

PROCEEDINGS OF THE
INTERNATIONAL LINEAR COLLIDER WORKSHOP

LCWS 2007

ILC 2007

VOLUME 2

Edited by
ARIANE FREY
SABINE RIEMANN

Impressum

Proceedings of the International Linear Collider Workshop LCWS 2007 and ILC 2007

Conference homepage:
<http://lcws07.desy.de/>

This document, the individual contributions and the talks are available at
<http://lcws07.desy.de/e262/e298/>

The proceedings are published with eConf:
<http://www.slac.stanford.edu/econf/C0705302/>

Slides are available at
<http://ilcagenda.linearcollider.org/conferenceTimeTable.py?confId=1296>

The copyright is governed by the Creative Commons agreement, which allows for free use and distribution of the articles for non-commercial activity, as long as the title, the authors' names and the place of the original are referenced.

Editors: Ariane Frey, Sabine Riemann
Technical Support: Ralf Diener
Cover Photo: Hamburg Tourismus GmbH
Photo of Participants: Margitta Müller, DESY
Cover: Experimente Support, DESY
October 2008
DESY-PROC-2008-03
ISBN 978-3-935702-27-0
ISSN 1435-8077

Published by
Deutsches Elektronen-Synchrotron, DESY
Notkestraße 85
22607 Hamburg
Germany

Committees

International Advisory Committee

S. Aronson (BNL), B. Barish (Caltech), J. Brau (Univ. Oregon), M. Calvetti (INFN-LNF), T. Camporesi (CERN), H.S. Chen (IHEP Beijing), J. Dainton (Cockcroft Inst.), M. Danilov (ITEP Moscow), J. Dorfan (SLAC), J. Engelen (CERN), A. Gurtu (Tata Inst.), R.D. Heuer (DESY/Univ. Hamburg), Y.B.Hsiung (Natl. Taiwan Univ.), P.W-Y. Hwang (Natl. Taiwan Univ.), J. Jaros (SLAC), A. Kakodkar (AEC & DAE India), J.S. Kang (Korea Univ.), D. Karlen (Univ. Victoria), S. Komamiya (Univ. Tokyo), A. Kronfeld (FNAL), F. LeDiberder (IN2P3), W.G. Li (IHEP Beijing), N. Lockyer (TRIUMF), K. Meier (Univ. Heidelberg), D. Miller (UCL), A. Miyamoto (KEK), P. Oddone (FNAL), M. Oreglia (Univ. Chicago), H. Park (Kyungpook Univ.), R. Patterson (Cornell Univ.), R. Petronzio (Univ. Rome), F. Richard (LAL), V. Rubakov (INR Moscow), A. Seiden (UCSC), R. Settles (MPI Munich), M. Shochet (Univ. Chicago), A. Shotter (TRIUMF), A. Skrinsky (Budker Inst.), A. Suzuki (KEK), F. Takasaki (KEK), G. Tayler (Univ. Melbourne), M. Tigner (Cornell Univ.), J. Timmermans (NIKHEF), A. Wagner (DESY), H. Yamamoto (Tohoku Univ.).

Programme Committee for ILC

J.-P. Delahaye (CERN), E. Elsen (DESY), B. Foster (Univ. Oxford), J. Gao (IHEP), M. Harrison (BNL), H. Hayano (KEK), M. Nozaki (KEK), T. Raubenheimer (SLAC), M. Ross (FNAL), N. Walker (DESY), B. Willis (Columbia Univ.), K. Yokoya (KEK).

Programme Committee for LCWS

U. Baur (Univ. Buffalo), T. Behnke (DESY), J. Brau (Univ. Oregon), T. Camporesi (CERN), M. Danilov (ITEP Moscow), R. Godbole (IISc), A. Gurtu (TIFR), R.-D. Heuer (DESY/Univ. Hamburg), B. Hsiung (Natl. Taiwan Univ.), J. Jaros (SLAC), D. Karlen (Univ. Victoria), A. Kronfeld (FNAL), D. Miller (UCL), A. Miyamoto (KEK), Y. Okada (KEK), M. Oreglia (Univ. Chicago), H. Park (KNU), R. Patterson (Cornell Univ.), F. Richard (LAL), R. Settles (MPI Munich), J. Timmermanns (NIKHEF), G. Weiglein (Univ. Durham), L. Weiguo (IHEP Beijing), H. Yamamoto (Tohoku Univ.).

Local Organising Committee

T. Behnke (DESY, Chair), K. Büsser (DESY), E. Elsen (DESY), M. Fleischer (DESY), A. Frey (MPI Munich), B. Kniehl (Univ. Hamburg), F. Lehner (DESY), S. Riemann (DESY), N. Walker (DESY)

Table of Contents

Committees iii

Volume 1

Plenary Sessions

Akiya Miyamoto <i>The Detector DCR</i>	3
Peter Zerwas <i>The ILC physics case</i>	16
Jim Brau <i>Charge to the meeting</i>	50
Klaus Desch <i>The LHC Early Phase for the ILC</i>	56
Roman Pöschl <i>Software Tools for ILC Detector Studies</i>	61
Tamaki Yoshioka <i>Particle Flow Calorimetry at ILC Experiment</i>	67
Jose Repond <i>Progress Report from Calice</i>	75
Ronald Lipton <i>Vertex Detector System Design</i>	85
Maury Tigner <i>Challenges for the ILC SCRF R&D</i>	94
Matthias Steinhauser <i>Loops for the ILC</i>	100
Daniel Haas <i>Summary of the data acquisition session for ILC detectors</i>	105
Maura Barone <i>ILC Project Tools: ILCagenda and ILCDoc</i>	110

Lars Hagge 112
E-Document Systems at ILC, Part II: ILC EDMS

Higgs and Electroweak Symmetry Breaking

Conveners: H. Logan, T. Barklow, S. Heinemeyer, A. Raspereza, Y. Gao, Y. Okada

Ilya Ginzburg 117
Different vacua in 2HDM

Pierre Lutz 122
The charged Higgs boson at LEP: Towards the final combinations

Djamel Boumediene 127
Higgs self coupling measurement

Rohini Godbole 131
Effects of polarisation on study of anomalous VVH interactions at a Linear Collider

Per Osland 137
Profile of Two-Higgs-Doublet-Model Parameter Space

Maria Krawczyk 141
The charged Higgs boson mass in the 2HDM: decoupling and CP violation

Victoria Martin 146
Searching for the Higgs with CDF

Stefan Dittmaier 150
Precision calculations for $H \rightarrow WW/ZZ \rightarrow 4\text{fermion}$ with PROPHECY4F

Sven Heinemeyer 155
Consistent Treatment of Imaginary Contributions to Higgs-Boson Masses in the MSSM

Martin Ohlerich 159
Prospects to Measure the Higgs Boson Mass and Cross Section in $e^+e^- \rightarrow ZH$ Using the Recoil Mass Spectrum

Thomas Underwood 166
A Natural Nightmare for the LHC?

Jürgen Reuter 171
Juergen Reuter

Koji Tsumura 176
New physics effect on the top-Yukawa coupling at ILC

Sara Bolognesi	181
<i>Higgs at CMS with 1, 10, 30 fb⁻¹</i>
Georg Weiglein	185
<i>CP-violating Loop Effects in the Higgs Sector of the MSSM</i>	
Marco Battaglia	190
<i>A Study of $e^+e^- \rightarrow H^0A^0$ Production at 1TeV and the Constrains on Dark Matter Density</i>	

SUSY Particles

Conveners: H. Baer, G. Wilson, A. Djouadi, J. List, S. Youl Choi, K. Fujii

Frank Deppisch	197
<i>Determining Heavy Mass Parameters in SUSY SO(10)</i>	
Hans-Ulrich Martyn	201
<i>Detection of long-lived staus and gravitinos at the ILC</i>	
Olaf Kittel	206
<i>How light can the lightest neutralino be?</i>	
Tania Robens	211
<i>Monte Carlo Simulations for NLO Chargino Production at the ILC</i>	
Per Osland	215
<i>Polarization-independent CP-odd Observable in e^+e^- Chargino Production at One Loop</i>	
Stefan Hesselbach	219
<i>CP Violation in SUSY Particle Production and Decay</i>	
Sven Heinemeyer	225
<i>Interplay of Electroweak Precision Observables and B Physics Observables</i>	
Luminita Mihaila	230
<i>About the Running and Decoupling in the MSSM</i>	
Jürgen Reuter	234
<i>Off-Shell and Interference Effects for SUSY Particle Production</i>	
Jan Kalinowski	238
<i>Dark Matter in the U(1) Extended SUSY</i>	
Caroline Milstene	242
<i>Precision measurement of a Particle Mass at the Linear Collider</i>	

Gudrid Moortgat-Pick 247
LHC/ILC interplay for challenging SUSY scenarios

Rohini Godbole 252
Distinguishing SUSY scenarios using τ polarisation and $\tilde{\chi}_1^0$ Dark Matter

New Physics at TeV Scale and Precision Electroweak Studies

Conveners: J. Hewett, K. Mönig, G. Moreau, S. Raychaudhuri

Tord Riemann 259
Two-loop Heavy Fermion Corrections to Bhabha scattering

Georg Weiglein 266
High-Precision Tests of the MSSM with GigaZ

Jürgen Reuter 272
ILC Sensitivity on Generic New Physics in Quartic Gauge Couplings

Ana Alboteanu 278
The Noncommutative Standard Model at the ILC

Jürgen Schreiber 283
Prospects of Discovering a New Massless Neutral Gauge Boson at the ILC

Ben Jeffery 290
LCFI Vertex Package: Precision Physics Opportunities with Heavy Flavour

Mihail Chizhov 296
The ILC Energy Requirements from Constraints on New Boson Production at the Tevatron

Jochum van der Bij 302
No Higgs at the LHC?! A case for the ILC.

Alexander Pankov 311
Discovery and Identification of Contactlike Interactions in Fermion-Pair Production at ILC

Top and QCD

Conveners: A. Juste, T. Teubner, R. Godbole

Yuichiro Kiyo 319
NNLO correction to the toponium and bottonium wave functions at the origin

Filimon Gournaris 324
Towards a Monte Carlo Event Generator for $t\bar{t}b\bar{b}$ production at threshold

Andre Sopczak <i>Scalar Tops from Morioka'95 to DESY'07</i>	328
Andre Hoang <i>Factorization Approach for Top Mass Reconstruction in the Continuum</i>	335
Rohini Godbole <i>Probing CP properties of the Higgs boson via $e^+e^- \rightarrow t\bar{t}\phi$</i>	342
Thomas Gehrmann <i>First results on $e^+e^- \rightarrow 3$ jets at NNLO</i>	347
Mathieu Segond <i>BFKL resummation effects in exclusive production of rho meson pairs at the ILC</i>	352

$\gamma\gamma, e-\gamma, e^-e^-$ **Physics and Technology**

Conveners: J. Gronberg, M. Velasco, M. Krawczyk, V. Telnov, E. Asakawa, K. Cheung

Aleksander Filip Zarnecki <i>H and A Discrimination using Linear Polarization of Photons at the PLC</i>	359
Ilya F. Ginzburg <i>Charge Asymmetry in $\gamma\gamma \rightarrow \mu^+\mu^- + \nu$'s / $\gamma\gamma \rightarrow W^\pm\mu^\mp + \nu$'s, effect of photon non-monochromaticity and p_\perp dependence</i>	363
Philip Yock <i>Anomalous Gamma Gamma Interaction</i>	367
James Monk <i>Using JetWeb to tune Monte Carlo for hadronic backgrounds from $\gamma\gamma$ events at a linear collider</i>	371
Maria Krawczyk <i>Heavy neutral MSSM higgs bosons at the Photon Collider - a comparison of two analyses</i>	375
Valery Telnov <i>Present status of the photon collider, what next?</i>	379

Loop Calculations

Conveners: D. Wackeroth, S. Dittmaier, Y. Yasui

Tord Riemann <i>New results on 5-point functions</i>	383
---	-----

Bernd Jantzen	392
<i>Two-loop electroweak NLL corrections: from massless to massive fermions</i>	
Christian Schwinn	398
<i>Effective Theory Approach to W-Pair Production near Threshold</i>	
Yoshiaki Yasui	404
<i>Status report from the GRACE group</i>	
Thomas Gehrmann	410
<i>Tools for NNLO QCD calculations</i>	
Marcus Weber	418
<i>Higgs Production by Gluon initiated Weak Boson Fusion</i>	
Christian Sturm	423
<i>Four loop QCD corrections and Master Integrals for the ρ-Parameter</i>	
Matthias Steinhauser	429
<i>Precise quark masses from sum rules</i>	
Dirk Seidel	433
<i>On-shell renormalization constants including two different nonzero masses</i>	

Cosmological Connections

Conveners: M. Battaglia, Z. Zhang, N. Okada

Genevieve Belanger	441
<i>Heavy Dirac Neutrino Dark Matter</i>	
Jenny List	444
<i>Model-independent WIMP Searches at the ILC</i>	
Zhiqing Zhang	450
<i>New Analysis of SUSY Dark Matter Scenarios at ILC</i>	

Volume 2

Tracking and Vertexing

Conveners: T. Nelson, D. Peterson, J. Timmermans, M. Winter, H. Park, Y. Sugimoto

Peter Wienemann	457
<i>MarlinTPC: A Marlin based common TPC software framework for the LC-TPC collaboration</i>	
Klaus Dehmelt	462
<i>Track Resolution Studies for a MPGD TPC</i>	
Alexander Kaukher	465
<i>Pad Occupancy in LDC TPC with TDC-based Readout Electronics</i>	
Winfried Mitaroff	468
<i>Track resolution studies with the “LiC Detector Toy” Monte Carlo Tool</i>	
Pawel Luzniak	472
<i>Study of Beamstrahlung in the Vertex Detector</i>	
Konstantin Stefanov	475
<i>Progress with the CPCCD and the ISIS</i>	
Erik Johnson	479
<i>ILC Vertex Detector Mechanical Studies</i>	
Yasuhiro Sugimoto	483
<i>R&D Status and Plan for FPCCD Vertex Detector</i>	
Devis Contarato	486
<i>Monolithic Pixel R&D at LBNL</i>	
Marco Battaglia	490
<i>Tracking with a Thin Pixel Telescope</i>	
Auguste Besson	494
<i>Status of the development of MIMOSA CMOS sensors</i>	
Jim Brau	497
<i>Development of an ILC Vertex Detector Sensor with Single Bunch Crossing Tagging</i>	
Daniel Haas	501
<i>A pixelated telescope for the E.U. detector R&D</i>	
Selcuk Cihangir	504
<i>Study of SOI, 3D and Laser Annealing as Candidate Technologies for the ILC</i>	

Andre Sopczak <i>Simulations of the Temperature Dependence of the Charge Transfer Inefficiency in a High Speed CCD</i>	507
Sergey Shulga <i>Digitization and hit reconstruction for silicon tracker in MarlinReco</i>	515
Robert Kutschke <i>Overview of SiD Tracking</i>	518
Dmitry Onoprienko <i>Calorimeter Assisted Tracking Algorithm for SiD</i>	522
Marcel Vos <i>SiLC simulation status report</i>	526
Wilfrid Da Silva <i>First test of a 180 nm prototype readout chip using a $^{90}_{38}\text{Sr}$ radiative source</i>	530
Akimasa Ishikawa <i>A GEM TPC End Panel Pre-Prototype</i>	533
Lea Hallermann <i>Status of the Large TPC Prototype Field Cage</i>	537
Hirotohi Kuroiwa <i>A Study of Spatial Resolution of GEM TPC with Ar-CF₄-iC₄H₁₀ Gas Mixtures</i>	540
Dean Karlen <i>Measuring Distortions in a TPC with Photoelectrons</i>	544
Nikolai Vlasov <i>Resolution Studies of GEM/Timepix Detector with 5 GeV electrons</i>	548
George Bashindzhagyan <i>Digital Active Pixel Array (DAPA) for Vertex and Tracking Silicon Systems</i>	552
Adrian Vogel <i>Geant4 Simulations of Machine-Induced Background in a TPC</i>	555
Akira Sugiyama <i>Simulation Study of GEM Gating at ILC-TPC</i>	559

Calorimetry and Muons

Conveners: R. Frey, J. Blazey, F. Sefkow, T. Takeshita, B.G. Cheon

Jaehoon Yu <i>Development of GEM Based Digital Hadron Calorimeter</i>	567
John Hauptman <i>Muon Identification without Iron</i>	573
Aldo Penzo <i>Photosensor Options for Dual-Readout Calorimetry in the 4th Concept</i>	576
Ekaterina Kuznetsova <i>First results of systematic studies done with different types of Silicon Photomultipliers</i>	578
Sandro Calcaterra <i>Beam Test of Scintillation Tiles with MPPC Readout</i>	581
Gerald Blazey <i>Preliminary Scintillator and Solid-State Photomultiplier Direct Coupling Tests</i>	584
Satoru Uozumi <i>Study of MPPC Performance for the GLD Calorimeter Readout</i>	587
Giovanni Pauletta <i>LC Scintillator - based Muon Detector/Tail-catcher R&D</i>	590
Laurent Royer <i>A 10-bits pipeline ADC dedicated to the VFE Electronics of Si-W Ecal</i>	595
Raymond Frey <i>A Silicon-Tungsten ECal with Integrated Electronics</i>	598
Marek Idzik <i>Readout electronics for LumiCal detector</i>	602
Anne-Marie Magnan <i>A MAPS-based Digital Electromagnetic Calorimeter for the ILC</i>	607
Denis Pierre Grondin <i>Mechanical R&D for CALICE ELECTROMAGNETIC CALORIMETER</i>	611
Cristina Carloganu, Anne-Marie Magnan <i>CALICE Si-W EM Calorimeter: Preliminary Results of the Testbeam 2006</i>	615
Niels Meyer <i>Preliminary Testbeam Results from the CALICE Tile Hadron Calorimeter</i>	623

Daniel Jeans 627
Scintillator+MPPC ECAL testbeam results

Simulation and Reconstruction

Conveners: N. Graf, M. Thomson, C. Gatto, A. Miyamoto

Andreas Gellrich 633
The ILC and the GRID

Wenbiao Yan 637
Full Simulation Study of WW Scattering at the ILC

Bruce Schumm 641
Simulation of an All-Silicon Tracker

Alexei Raspereza 645
LDC Tracking Package

Oliver Wendt 651
Track-Based Particle Flow

Mark Thomson 654
Progress with Particle Flow Calorimetry

Phillipe Gris 660
 π^0 Reconstruction within the full simulation framework

Daniel Jeans 663
 π^0 reconstruction in the GLD calorimeter

Sonja Hillert 666
The LCFI Vertex Package: vertex detector-based Reconstruction at the ILC

Tadashi Nagamine 672
Simulation Study of the FPCCD Vertex Detector for the ILC

Wolfgang Waltenberger 675
RAVE - First Vertexing and b-Tagging Results with LCIO Data

Tatsiana Klimkovich 679
Simulation Study for EUDET Pixel Beam Telescope using ILC Software

Machine Detector Interface

Conveners: T. Markiewicz, A. Seryi, E. Torrence, W. Lohmann, P. Bambade,
W. Kozanecki, K. Büßer, P. Burrows, T. Tauchi, T. Omori

Bill Morse <i>GamCal - A Beam-strahlung Gamma Detector for Beam Diagnostics</i>	685
Andrey Sapronov <i>ILC Beam Diagnostics using BeamCal and GamCal</i>	689
Oleg Eyser <i>Simulation Studies and Detector Scenarios for an ILC Polarimeter</i>	693
Daniela Käfer <i>Test Stand Measurements for an ILC Polarimeter</i>	697
Anthony Hartin <i>Simulation of ILC feedback BPM signals in an intense background environment</i>	701
Yuri Nosochkov <i>14 mrad Extraction Line Optics for Push-Pull</i>	705
Mila Pandurovic <i>Physics Background as a Systematic Effect in Luminosity Measurement at ILC</i>	710
Cecile Rimbault <i>Impact of Beam-beam Effects on Precision Luminosity Measurements at the ILC: Main results</i>	714
Adrian Vogel <i>Update on the Beam-Related Backgrounds in the LDC Detector</i>	719
Olivier Dadoun <i>Backscattering of Secondary Particles into ILC Detectors from Beam Losses Along the Extraction Lines</i>	722
Yosuke Takubo <i>Pair Monitor Studies</i>	727
Nickolai Muchnoi, Michele Viti <i>ILC Beam Energy Measurement Using Compton Backcattering</i>	731
Bino Maiheu <i>Progress Report for the BPM Energy Spectrometer Test Experiment at ESA</i>	741

Data Acquisition and Global Detector Network

Conveners: P. Le Du, D. Haas

Patrick Le Dû <i>Trigger/Data Acquisition Issues</i>	747
Daniel Haas <i>The DAQ for the EUDET pixel telescope</i>	755
David Bailey <i>Prototype DAQ for Calorimetry at Future ILC Experiments</i>	758
Valeria Bartsch <i>CALICE-DAQ communication and DAQ software</i>	761
Ray Larsen <i>ATCA for Machines</i>	764

Test Beam Contact

Conveners: M. Woods, J. Yu, F. Sefkow, K. Kawagoe

Kiyotomo Kawagoe <i>Overview on Test Beam Facilities</i>	771
---	-----

Beam Delivery System

Conveners: D. Angal-Kalinin, H. Yamamoto, A. Seryi

Taikan Suehara <i>R&D status of ATF2 IP Beam Size Monitor (Shintake Monitor)</i>	777
Tomoya Nakamura <i>High Resolution Cavity BPM for ILC Final Focal System (IP-BPM)</i>	781
Yoshihisa Iwashita <i>Permanent Magnet Final Quad</i>	785

Main Linac

Conveners: L. Lilje, H. Hayano, C. Adolphsen, N. Solyak

Ramila Amirikas, Alessandro Bertolini, Wilhelm Bialowons <i>Vibration stability studies of a superconducting accelerating module at room temperature and at 4.5 K</i>	791
--	-----

Igor Zagorodnov, Martin Dohlus 795
Coupler Kick

Damping Rings

Conveners: A. Wolski, S. Guiducci, J. Gao, M. Zisman

Xia Guoxing 801
Update on Ion Studies

Larisa Malysheva 807
Depolarisation in the damping rings of the ILC

Manfred Wendt 810
Status of the ATF Damping Ring BPM Upgrade Project

Sources

Conveners: D. Scott, M. Kuriki, A. Brachmann

Ian Bailey 819
Positron Source Target Development Update

Andriy Ushakov 822
Radiation Damage of ILC Positron Source Target

Leo Jenner 827
Robust Spin Polarisation Status

Leonid Kravchuk 830
Hardware Development and Study for ILC Positron Source Parameters

Accelerator Physics

Conveners: D. Schulte, K. Kubo, P. Lebrun

Stephen Malton 835
Update on the Status of BDSIM

Metrology

Conveners: M. Schlösser, R. Sugahara, R. Ford

Laurent Brunetti 841
Active Stabilization of a Mechanical Structure

Grzegorz Grzelak 849
Simulation of LiCAS Error Propagation

James Volk 853
Ground Motion Data for International Collider Models

Polarization

Conveners: G. Moortgat-Pick, S. Riemann

Olaf Kittel 861
Polarization aspects in radiative neutralino production

Anthony Hartin 866
Incoherent pair background processes with full polarizations at the ILC

Andreas Schälicke 871
Polarized Geant4 – Applications at the ILC

Vahagn Gharibyan 876
ILC Positron Production Target Simulation

Ralph Dollan 880
Low Energy Positron Polarimeter for the ILC

ATF2

Convener: E. Elsen

Benoit Bolzon 889
ATF2 Project: Final doublet support studies at LAPP

Yves Renier 892
Study of time-dependent corrections in the ATF2 beam-line

Tracking and Vertexing

Conveners: T. Nelson, D. Peterson, J. Timmermans, M. Winter, H. Park, Y. Sugimoto

MarlinTPC: A Marlin based common TPC software framework for the LC-TPC collaboration

Jason Abernathy¹, Klaus Dehmelt², Ralf Diener², Jim Hunt³,
Matthias Enno Janssen², Martin Killenberg⁴, Thorsten Krautscheid⁴,
Astrid Münnich⁵, Martin Ummenhofer⁴, Adrian Vogel² and Peter Wienemann⁴

1- University of Victoria - Department of Physics and Astronomy
PO Box 3055, V8W 3P6 Victoria BC - Canada

2- Deutsches Elektronen-Synchrotron
Notkestr. 85, 22607 Hamburg - Germany

3- Cornell University, Wilson Laboratory
Ithaca, NY 14853 - USA

4- University of Bonn, Department of Physics
Nussallee 12, 53115 Bonn - Germany

5- RWTH Aachen, III. Physikalisches Institut
Physikzentrum, 52056 Aachen - Germany

We describe the goals and present functionality of MarlinTPC, a common software framework for the LC-TPC collaboration based on LCIO, Marlin and other ilcsoft tools.

1 Introduction

Three of the four available designs for detectors at the International Linear Collider (ILC) envisage a large time projection chamber (TPC) as main tracking device. It is the task of the LC-TPC collaboration to perform the necessary R&D to be able to fulfil the TPC performance requirements derived from the ILC physics goals [1].

In the course of LC-TPC activities a rather large variety of simulation, analysis and reconstruction software packages has been developed. The usage of these packages ranges from studying TPC performance as part of an overall detector for different detector layouts and background conditions, optimising prototype designs, reconstructing and analysing cosmics and testbeam data from various small prototypes using different readout technologies to full detector physics analyses. Most of these individual software packages have become rather sophisticated in their particular field of application. Valuable experience was collected during usage and development of the software partly leading to novel techniques to cope with new challenges encountered in TPCs with new amplification or readout systems. The drawback of this specialisation is that the software often works smoothly only for particular applications or TPC setups. Exchanging code between different packages or analysing data from different sources with the same program can be very time consuming and errorprone since the different programmes do not use commonly accepted interfaces and conventions. The goal of MarlinTPC is to overcome these drawbacks.

2 Design considerations

In view of the converging hardware efforts like the planned common large prototype, to improve the mutual understanding of results and to avoid further double work, it seems

natural to converge on the software tools. In June 2006 an initiative was started to take the first step towards this direction. Representatives of six LC-TPC member institutes met at DESY to find an agreement on common software standards. It was decided to transfer the existing algorithms to a new, commonly used framework, called MarlinTPC [2], building on top of LCIO [3], the *de facto* standard data format for ILC related work, and the accompanying ilcsoft tools [4]. This choice is motivated by the possibility to profit from general ILC software developments and by the fact that ilcsoft tools are already used by many other subdetector, simulation and physics analysis software projects. In particular Marlin [5] was chosen as analysis and reconstruction framework. Its modularity and well defined interfaces between its modules, called processors, ensure that different developers can work on different processors in parallel without interference and to plug'n'play with processors to easily try out e. g. different algorithms.

Further important pillars of MarlinTPC are the Linear Collider Conditions Data (LCCD) toolkit [6] and GEAR (Geometry API for Reconstruction) [7]. LCCD allows writing and reading of conditions data describing the detector status as function of time. It allows to tag data sets for later easy reference and to request data valid at a particular point in time. GEAR allows to access geometry information needed for the simulation, digitisation and reconstruction of events. Thereby it is made sure that consistent geometry information is used throughout MarlinTPC.

3 Reconstruction

In the beginning the focus was laid on the development of reconstruction processors. Therefore the reconstruction code is currently the most evolved part of MarlinTPC. It will be briefly described in this section.

3.1 Processor chain

The event data model (EDM) for the reconstruction is provided by the LCIO classes `TrackerRawData`, `TrackerData`, `TrackerPulse`, `TrackerHit` and `Track`. These data structures represent well-defined interfaces between the different reconstruction steps. Every processor retrieves one or several input collections which contain the input data (e. g. `TrackerData` objects), processes them (e. g. applies a pulse finding algorithm) and finally provides output collections containing the results of the applied algorithm (e. g. `TrackerPulse` objects). The output collections in turn can be read in by subsequent processors to further process the event data.

The present processor chain for the MarlinTPC reconstruction is shown in Table 1. Additional correction processors e. g. to correct for electric or magnetic field inhomogeneities or gain fluctuations can be easily added in the appropriate places if needed.

3.2 Present functionality

This section briefly describes the functionality of the MarlinTPC reconstruction as it is available in September 2007.

`TrackerRawDataToDataConverterProcessor` converts `TrackerRawData` objects with integer FADC counts into `TrackerData` objects with floating point numbers for the channel time spectrum. This allows for pedestal subtraction by the `PedestalSubtractorProcessor`

Data structure	Processor name	input/output collection name
TrackerRawData		TPCRawData
	TrackerRawDataToDataConverterProcessor	
TrackerData		TPCConvertedRawData
	PedestalSubtractorProcessor	
	TimeShiftCorrectorProcessor	
TrackerData		TPCData
	PulseFinderProcessor	
	ChannelMapperProcessor	
	CountsToPrimaryElectronsConverterProcessor	
TrackerPulse		TPCPulses
	HitTrackFinderTopoProcessor	
TrackerHit, Track		TPCHits, TPCTrackCandidates
	TrackSeederProcessor	
Track		TPCSeedTracks
	TrackFitterLikelihoodProcessor	
Track		TPCTracks

Table 1: Present MarlinTPC reconstruction processors

since the pedestals are in general non-integer values. The pedestals are provided by LCCD and are read in using the Marlin `ConditionsProcessor`. Optionally further correction processors can be applied after the pedestal subtraction.

The next step is the search for pulses in the channel time spectra performed by the `PulseFinderProcessor`. It uses a threshold based method which has an individual threshold per channel depending on the noise width calculated from the pedestal. The algorithm is capable to handle signals with positive and negative polarity as well as zero suppressed data to support a large variety of possible readout electronics.

The `ChannelMapperProcessor` translates the hardware channel numbers of the electronics into GEAR pad indices. Afterwards the number of ADC counts per pulse is converted into primary electrons by the `CountsToPrimaryElectronsConverterProcessor`, using electronics and gas gain calibration factors. The channel map as well as the calibration constants are stored using LCCD.

The `HitTrackFinderTopoProcessor` performs a topological search for pulses on neighbouring pads. Pulses on contiguous pads in one pad row are grouped as hit candidates. Afterwards the hit coordinates are calculated. Contiguous hits in different pad rows within an adjustable time window are assembled to make up a track candidate. The algorithm does not make any assumption on the trajectory and thus works for straight tracks like cosmic muons in a prototype as well as for a low energetic particle curling up in the TPC, producing a helix with a changing curvature due to energy loss. It is implemented for the two available GEAR pad geometries (rectangular and circular pad row layout). An estimate for the track parameters is calculated analytically by the `TrackSeederProcessor` to have a good starting point for the succeeding fit.

The `TrackFitterLikelihoodProcessor` determines the track parameters by maximising the global likelihood for observing the measured charge distribution on all pads associated with the track. It has been shown to give better results than just minimising the mean squared distance of the reconstructed hits to the track using a χ^2 fit [8].

For bookkeeping every processor writes all its processor parameters like cuts etc. to the LCIO run header, as well as the subversion software revision of the code which was used to

process the data.

So far the code has just been validated with toy data. Thus the performance of the available processors still needs to be checked with real data or more realistic Monte Carlo samples.

4 Simulation, digitisation and analysis

Very recently sizable development work on simulation, digitisation and analysis code has started.

The simulation part of MarlinTPC started off with the package TPCGEMSimulation from [9]. It simulates primary ionisation using a parametrisation of HEED [10] output, drifting of the primary electrons to the endplates, amplification in a triple-GEM gas amplification system and electronics shaping. Optionally an ion backdrift processor can be added. The supported gases are Ar-CH₄ (95-5), Ar-CH₄ (90-10) and Ar-CH₄-CO₂ (93-5-2). The original package (which received geometry information as processor parameters) has been modified such that all geometry information is retrieved from GEAR now. At present it is not possible to simulate other gases or amplification systems. It is planned to separate out the digitisation components of the package and, in the long run, to make the simulation more generally usable to be able to simulate other gases or amplification systems.

Work has started on a set of digitisation processors which can be used to digitise both the output of detailed gas detector simulations generating individual ionisation clusters and the output of Geant4 [11] simulations providing rather large energy deposits instead of individual electron-ion pairs. This also includes the development of processors producing pile-up due to the large drift time of electrons (compared to the bunch crossing rate) and background from e^+e^- pairs from the fusion of beamstrahlung photons.

For analysis purposes several processors are under development which provide information according to the recommendations of the first ILC TPC Analysis Jamboree [12]. Examples are the residual distributions, the fraction of 1-pad, 2-pad, 3-pad hits, residuals as function of the position on the pad, etc.

5 Conclusions and outlook

Within its first year the MarlinTPC project has made significant progress. The most important reconstruction processors are available, partly using newly developed, more powerful algorithms than what was available in the old software packages. It is planned to extend the reconstruction to include algorithms needed to handle data from TPCs with pixel readout such as Medipix2 or Timepix readout chips. Efforts are under way to also get similarly powerful simulation, digitisation and analysis processors.

MarlinTPC will be finally put to the test with the completion of the common large TPC prototype. With the advent of data from this prototype it has to prove its capabilities.

6 Acknowledgments

This work is partly funded by the Commission of the European Communities under the 6th Framework Programme “Structuring the European Research Area”, contract number RII3-026126.

References

- [1] See e. g. ILC Reference Design Report <http://ilc.kek.jp/RDR>
- [2] MarlinTPC homepage http://ilcsoft.desy.de/portal/software_packages/marlintpc
- [3] LCIO homepage <http://lcio.desy.de>
- [4] ILCSOFT homepage <http://ilcsoft.desy.de>
- [5] Marlin homepage <http://ilcsoft.desy.de/marlin>
- [6] LCCD homepage <http://ilcsoft.desy.de/lccd>
- [7] GEAR homepage <http://ilcsoft.desy.de/gear>
- [8] See e. g. <http://ilcagenda.linearcollider.org/contributionDisplay.py?contribId=292&sessionId=74&confId=1296>
- [9] See http://web.physik.rwth-aachen.de/~tpcmgr/en/software_new.html
- [10] See <http://consult.cern.ch/writeup/heed>
- [11] Geant4 homepage <http://cern.ch/geant4>
- [12] See <https://twiki.cern.ch/twiki/bin/view/ILCTPC/JamboreeRecommendations>

Track Resolution Studies for a MPGD TPC

Klaus Dehmelt

DESY-FLC

Notkestr. 85, D-22607 Hamburg - Germany

Three out of the four concepts for the ILC detector will have a Time Projection Chamber (TPC) as the central tracking device. Due to physics' specifications track parameters have to be determined to a high degree of precision. In order to achieve this precision Micro Pattern Gaseous Detectors (MPGD) have to be used as the readout structure for the TPC.

A small sized prototype TPC with a Gaseous Electron Multiplier (GEM [1]) has been used in order to perform resolution studies. The results will be presented.

1 The Small Prototype TPC

A small sized prototype of a TPC (Fig. 1), built at DESY was used for resolution studies. The gas amplification was achieved with a triple GEM structure, with both, staggered and non-staggered pad readout. The sensitive volume was $660 \times 50 \times 53 \text{ mm}^3$. The pads had a pitch of $2.2 \times 6.2 \text{ mm}^2$, distributed over 24 columns and 8 rows. Two different gas mixtures were used for the studies: TDR-gas (Ar 93%, CH₄ 5%, CO₂ 2%), respectively P5-gas (Ar 95%, CH₄ 5%). Cosmic muons were measured and the provided tracks were investigated for determining the spatial point resolution.

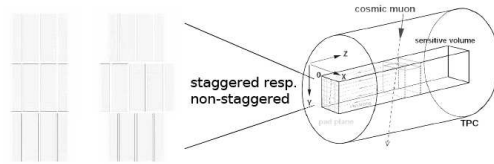


Figure 1: Small sized TPC prototype

2 The Reconstruction software

Analysis of the recorded tracks was performed with the software package "MultiFit" [2], based on C++, ROOT [3], and LCIO [4]. The reconstruction takes place in three steps:

- 1.) finding a cluster,
- 2.) finding a track,
- 3.) fitting the track.

Two different methods were used in order to analyze and fit the tracks.

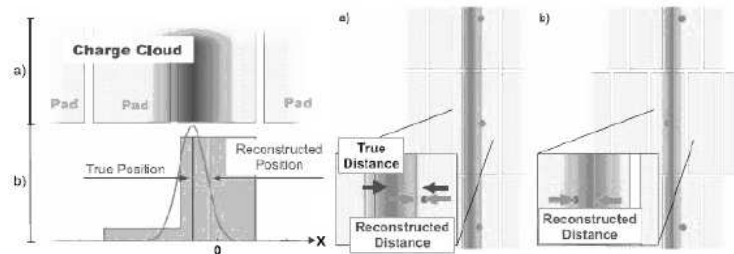


Figure 2: The effect of the pad response.

They were based on a least square, respectively a maximum-likelihood method. Both were capable to determine straight line and circular arc tracks.

The first method consisted of an adjustment of straight lines, respectively circular arcs for hits in the x-y-plane and subsequently minimizing χ^2 . The second method consisted of an adjustment of straight lines for pulses in the x-y-plane and subsequently maximizing the likelihood function [5].

Using the minimization method one needs to include a Pad Response Correction (PRC). This is due to the fact that the pad size is of finite geometry. Deposited charge on these pads can be insufficiently shared between neighboring pads if the signal's size is of the order of the pad size or narrower. Such charge distribution can lead to incorrect determination of the x-position (Fig. 2), since a center of gravity calculation would tend to reconstruct the position of the signal towards the center of a pad.

The PRC corrects for this effect, using a Pad Response Function (PRF). The PRF describes the measured charge on a pad as a function of the original charge and the pad geometry [6]. The PRF is a convolution of two Θ -functions, describing the pad's geometry, and a spatial charge distribution, assumed to be Gaussian distributed. The PRF is used to simulate the pad signal of a Gaussian distributed charge cloud. From these signals the x-position of the hit is determined with the center of gravity method and are being used to correct for the pad response. The minimization procedure is applied row wise, i.e. the responding pads are considered from row to row and subsequently a least square method is applied with respect to the residuals from the track parameters and positions of the track points.

Using the maximization method the correction due to the pad response is not necessary. In this case a charge density distribution due to primary ionization and a two-dimensional charge density function due to diffusion is used to describe the response of a signal on the pads. The convolution of these two functions leads to a charge distribution on the pad plane. After determination of the distributions on the individual pads a likelihood function is applied. The likelihood function consists of terms describing the probability of the expected charge deposition on the pads. The maximum for the sum of the probabilities will determine the best track parameters. The design of this fitting procedure includes intrinsically the pad response.

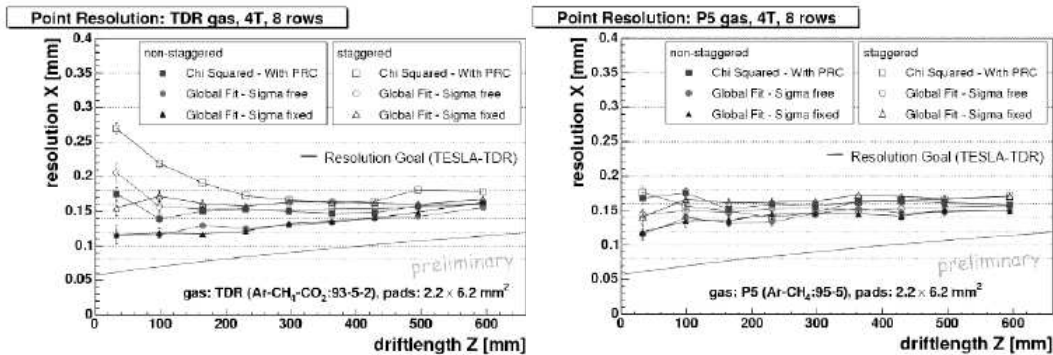


Figure 3: The track point resolution for two different gas choices and fitting methods.

3 Track Point Resolution

Both fitting methods described in Ch. 2 were applied in order to determine the track point resolution. Dependent on gas choice and pad layout the methods gave more or less similar results as a function of drift length. The results are summarized in Fig. 3. The track point resolution varied between $120 \mu\text{m}$ and $180 \mu\text{m}$ for drift distances less than 600mm . The best results were obtained with the maximum likelihood method when the width of the distributions were used as a fixed parameter. The resolution, needed for the ILC-TPC is not yet achieved and further evaluations have to be performed, in particular with larger prototypes of a TPC, i.e. with a larger number of readout pads.

4 Summary and Outlook

The software package “MultiFit” provides tools for reliable track reconstruction. With a small prototype of a TPC a track point resolution above the desired resolution for the ILC-TPC has been found. Further studies have to be performed in order to prove the feasibility of such a TPC.

Studies are ongoing for the determination of double track resolution. Important issues are the separation distance, the reconstruction efficiencies, and the influence of two nearby tracks on the fit and single point resolution. For these studies data from the cosmic as well from a laser track setup are being analyzed. First investigations show that an applied method for the hit separation yields a more efficient way for finding double tracks as compared to a hit merge method. For the hit separation a pulse splitting was performed such that a local minimum is found and subsequently reweighing of the charge sharing. This yields to an improvement of double track recognition.

References

- [1] F. Sauli, Nucl.Instr.Meth. **A386**, 531-534 (1997).
- [2] M. E. Janssen, Auflösungsstudien an einer Zeit-Projektions-Kammer (TPC) mit GEM Gasverstärkungssystem, December 2004, DESY-THESIS-2004-049.
- [3] Homepage: ROOT - Data Analysis Framework, CERN, CH, 2007, <http://root.cern.ch/> .
- [4] Homepage: LCIO - data model for ILC detector studies, DESY, D, 2007, <http://lcio.desy.de/> .
- [5] D. Karlen, P. Poffenberger, and G. Rosenbaum. Nucl.Instr.Meth. **A555**, 80 (2005).
- [6] T. Lohse and W. Witzeling, *The Time Projection Chamber*, Instrumentation in High Energy Physics (Advanced Series on Direction in High Energy Physics, Vol. 9) (June 1992).

Pad Occupancy in the LDC TPC with the TDC-based Readout Electronics

Alexander Kaukher *

Universität Rostock - Institut für Physik
Universitätsplatz 3, 18051 - Germany

Electron-positron background in the ILC puts a constrain on the design of a readout electronics for the LDC TPC. The memory size of a Time-to-Digit Converter is estimated from the simulation of the background.

1 Introduction

The requirement of high luminosity in ILC leads to necessity of the large number of electrons in a single bunch. Due to the pinch effect[2] a large number of hard beamstrahlung photons (order of 10^{11} per bunch crossing) is generated. Although the beamstrahlung photons produce no hits in a gaseous detector like Time Projection Chamber(TPC), they serve as a source of a secondary background. It is anticipated that the main contribution to the background in the TPC comes from the e^+e^- pairs, originating from the beamstrahlung photons.

Preliminary TPC studies[3] found occupancy in the TPC detector $\approx 1\%$, but give no information on the occupancy of a single pad. The subject of this work is to study the pad occupancy in the LDC TPC[4], which is one of the design constraints for the TPC readout electronics.

2 Simulation of the e^+e^- pair background in the LDC TPC detector

GUINEA-PIG program[2] was used to simulate the e^+e^- pair background. Input for the simulation is the beam parameters in a linear collider, for example the number of electrons in a bunch. For this simulation the TESLA parameter set is used, which is close to the nominal parameter set of the ILC[5]. Result of the simulation shows that on average, there are 10^5 pair particles in a single bunch crossing. Data from the GUINEA-PIG are used in the Monte Carlo simulation.

Simulation of the LDC TPC response has been performed with Mokka 06-03[6]. In the LDC01_02Sc model, maximal drift path of the TPC is 2 m. Energy cut in TPC set to 32 eV (twice larger the ionization potential of Argon).

On average, there are 5000 energy depositions(hits) in the TPC volume per bunch crossing. In the main, one observes tracks oriented along the z-direction in the TPC detector. These tracks come from low energy particles which have so small helix radius and many turns, that they appear as the tracks pointing to the end-plate of the TPC. Similar tracks will be found from muons, which appear at the earlier acceleration stages in the ILC, but there will be only 0.07 muons per bunch crossing. In both cases, such pointing tracks will occupy the readout of few neighbouring pads on the end-plate. In order to estimate the pad occupancy one needs to count the number of signals registered by a pad.

*This work is supported by the EUDET project.

3 Pad occupancy in the LDC TPC

Collisions of the beams in the ILC will occur every 369 ns[5], while the full drift time of the electrons in the TPC volume is $\sim 47 \mu s$. It is assumed that the drift velocity of electrons in the TPC gas is $4.5 \text{ cm}/\mu s$. This implies that the background signals from 128 bunch crossings will overlap in the TPC. Since no trigger is foreseen in the ILC TPC, signals during complete bunch train (2625 bunch crossings within 1 ms) have to be recorded by the TPC data acquisition. This sets stringent requirements on the compactness and the power consumption of the TPC readout electronics, if it is installed directly on the end-plate of the LDC TPC.

It is assumed, that there is no attachment. Diffusion is neglected in $r\phi$ and z directions. Due to the charge sharing, several pads can record a signal, but this currently not addressed.

In the Time-to-Digit Converter(TDC)-based readout electronics[7], charge of a signal from a pad is encoded into the pulse width of a digital signal with the help of a charge-to-time converter(QTC). Signals from the QTC are digitized with a TDC and stored in its memory. The QTC has a variable dead-time. For smaller input signals, the output pulse width is shorter, so that the QTC will be able to re-trigger earlier. If two hits arrive close in time they will not be resolved – the QTC will produce single pulse on the output.

The QT conversion characteristics has logarithmic dependence and was calibrated in such a way, that the output pulse width of 200 ns(corresponds to 1 cm in the drift direction of the TPC) relates to the energy deposit of hits appearing most often, Figure 1. For this simulation, a simple QT conversion was considered: a hit which arrives on a pad first, sets an integration window to 50 ns; the energy deposits from all hits which are found in this window are summed up; the pulse on the output of QTC is derived according to Figure 1.

The time of appearance of a hit on a pad for a given bunch crossing is given by

$$T_i = \frac{L_{half} - |Z_i|}{V_{drift}} + T_i, \quad (1)$$

where Z_i - z -coordinate of a particle in TPC volume, L_{half} - the maximal drift path in the LDC TPC, V_{drift} - the drift velocity, T_i - time of appearance of the hit in the TPC volume. With the help of equation (1) and QT-characteristics, signals from the QTC can be counted. 128 bunch crossing have been simulated and analyzed.

A distribution of the number of hits has the mean value of 2.6, Figure 2.

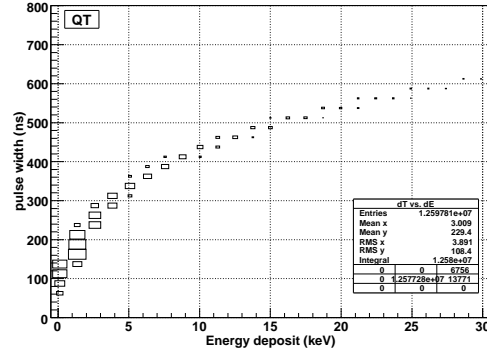


Figure 1: QT characteristics for the TDC-based readout electronics for the ILC TPC.

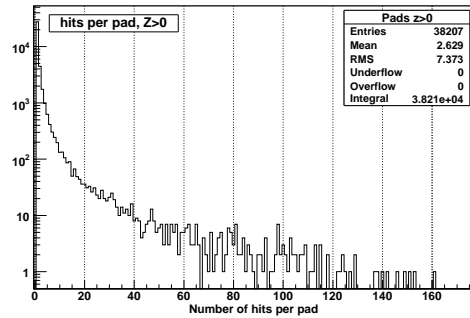


Figure 2: Hits per pad for 128 bunch crossings.

The maximal number of hits observed on a pad (size of a pad is 1 mm in the ϕ -direction and 6 mm in the radial direction) is ~ 160 . Assuming a 64 channel TDC chip and the maximum number of hits on all channels per 128 bunch crossings is equal to 160, one obtains 210000 data records (signal measurements) to be stored in the TDC memory. If a single “arrival time/charge/TDC-channel” data record is represented by a 32-bit word, the memory size would be 820 kbytes.

Consider, for example, 64 pads on the same radius of the TPC end-plate. Repeating analysis for such a cluster of pads and assuming that the TDC has a common memory for all 64 channels, one obtains ≈ 800 data records per TDC chip, Figure 3. In this case the TDC memory size is 64 kbytes.

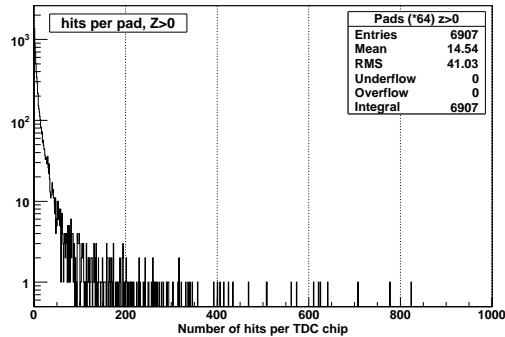


Figure 3: Hits per TDC chip for 128 bunch crossings.

4 Conclusion

Effective way of data readout with the TDC-based electronics leads to smaller size of the TDC memory. Collected data can be transferred with smaller number of cables, thus simplifying the design of the TPC end-plate and improving the material budget.

Energy depositions originating from the e^+e^- background will distort the electric field in the TPC volume. Corrections of the electric field distortions can be made if the background data is available.

5 Bibliography

References

- [1] Slides: <http://ilcagenda.linearcollider.org/contributionDisplay.py?contribId=293&confId=1296>
- [2] “Beam-beam simulations with GUINEA-PIG,” *In the Proceedings of International Computational Accelerator Physics Conference (ICAP 98), Monterey, California, 14-18 Sep 1998, pp 127-131.*
- [3] T. Behnke, S. Bertolucci, R. D. Heuer and R. Settles, “TESLA: The superconducting electron positron linear collider with an integrated X-ray laser laboratory. Technical design report. Pt. 4: A detector for TESLA,” DESY-01-011
- [4] Large Detector Concept Web Site: <http://www.ilcldc.org>.
- [5] International Linear Collider Reference Design Report, <http://www.linearcollider.org>
- [6] G. Musat, “Geant4 Simulation For The Flc Detector Models With Mokka,” *Prepared for International Conference on Linear Colliders (LCWS 04), Paris, France, 19-24 Apr 2004*
- [7] A. Kaukher, “A study of readout electronics based on TDC for the International Linear Collider TPC detector,” *IEEE Trans. Nucl. Sci.* **53** (2006) 749.

Track Resolution Studies with the “LiC Detector Toy” Monte Carlo Tool

W. Mitaroff, M. Regler, M. Valentan and R. Höfler

Institute of High Energy Physics – Austrian Academy of Sciences
A-1050 Vienna, Austria, Europe

LiC is a simple but powerful and flexible software tool, written in MATLAB, for basic detector design studies (geometries, material budgets). It is based on a helix track model including multiple scattering, and uses a Kalman filter for track fitting. We use this tool for comparing two variants of the LDC and one of the SiD layout, by studying track resolutions ($\Delta p_T/p_T$, $\Delta p_T/p_T^2$, transverse and spatial impact parameters) over the transverse momentum range $2.5 < p_T < 35$ GeV in the barrel region. Investigation of the forward/backward region is so far for LDC only.

1 The Monte Carlo Tool

A software tool for detector design, written in MATLAB[®], has been developed for tracking studies at the ILC. It aims at investigating the resolution of reconstructed track parameters in the vertex region for the purpose of comparing and optimizing the track sensitive devices and the material budgets of various detector set-ups. The detector model corresponds to a collider experiment with a solenoid magnet and a helix track model. The geometric surfaces are either cylinders (barrel region) or planes (forward/backward region). Material causing multiple scattering is assumed to be concentrated within thin layers.

A simplified simulation performs tracking with inclusion of multiple scattering, and simulates detector measurements including systematic and/or stochastic inefficiencies and uniform or Gaussian observation errors. Supported are *Si* strips (single or double sided, with any stereo angle), pixel detectors, and a TPC – all described by a simple text file. This is followed by track reconstruction by means of a Kalman filter [1], the fitted parameters and covariances being evaluated at the inner surface of the beam tube.

For a thorough description of its functionality and usage see [2].

2 Track resolution study

This study is based on about $2 \times 18,700$ (LDC barrel), 22,400 (SiD barrel) and 8,840 (LDC forward/backward) tracks, respectively, simulated and fitted by the “LiC Detector Toy” program. Definitions of the “barrel” and “forward/backward” regions in terms of the dip angle $\lambda \equiv \pi/2 - \vartheta_{polar}$ are given in section 3.

The true and fitted track data are passed to and further analyzed by a Java program, running within JAS3 and using AIDA [3]: calculating the deviations of fitted w.r.t. true transverse momenta $\Delta p_T = (p_T^{fitted} - p_T)$, and the impact parameters δ_T and δ_0 (transverse and in space, respectively); histogramming $\Delta p_T/p_T$, $\Delta p_T/p_T^2$, δ_T and δ_0 for separate intervals of true p_T ; extracting the rms or mean from each histogram; then using parametrizations (subsection 2.2) to fit $\text{rms}(\Delta p_T/p_T)$, $\text{rms}(\Delta p_T/p_T^2)$, $\text{rms}(\delta_T)$, and $\text{mean}(\delta_0)$ as functions of the central value of each p_T interval – see figs. 1 . . . 4.

Section 3 presents preliminary results and conclusions.

2.1 LDC and SiD detector descriptions

The geometry and material constants of the ILC “Large Detector” (LDC) and “Silicon Detector” (SiD) concepts have been taken from [4], and are summarized below.

LDC Detector description

$B_z = 4$ Tesla; efficiency Si = 95%; TPC = 100%; errors in μm

BARREL	$R[\text{mm}]$	$Z_{\text{min}}[\text{mm}]$	$Z_{\text{max}}[\text{mm}]$	Error distribution	$d[X_i]$	Remarks
Beam pipe	14			passive	.0025	0.4 mm Be
VIX 1	16	-50	50	pads 50*50 (25*25) equ. distrib.	.002	wafer + ladder
VIX 2	26	-120	120	idem	idem	idem
VIX 3	37	idem	idem	idem	idem	idem
VIX 4	48	idem	idem	idem	idem	idem
VIX 5	60	idem	idem	idem	idem	idem
Support structures	90	-110	-90	passive	.070	arbitrary
idem	idem	90	110	passive	idem	idem
SIT 1	150	-150	150	strips 2*50	.0175	$0^\circ - 10^\circ$
SIT 2	290	-360	360	idem	idem	idem
TPC inn. wall	340	-2160	2160	passive	0.140	
196 pad rings	<1580	idem	idem	$\sqrt{\sigma_{\theta_1}^2 + \sigma_{\theta_2}^2} \Delta z$ $\sigma_{\theta_1} = 50, 3.8$ in R ϕ	196^* $1.25E-5$	$\sigma_{\theta_2} = 15,$ 58 in z

FORWARD	$Z[\text{mm}]$	$R_{\text{min}}[\text{mm}]$	$R_{\text{max}}[\text{mm}]$	Error distribution	$d[X_i]$	Remarks
FTD 1	180	40.0	138	pads 50*300		.01
FTD 2	300	47.5	140	idem		idem
FTD 3	450	57.5	280	idem		idem
FTD 4	800	87.5	idem	strips 2*90		$\pm 45^\circ$
FTD 5	1200	122.5	idem	idem		idem
FTD 6	1550	157.5	idem	idem		idem
FTD 7	1900	187.5	idem	idem		idem

SiD Detector description

$B_z = 5$ Tesla; efficiency Si = 95%; errors in μm

BARREL	$R[\text{mm}]$	$Z_{\text{min}}[\text{mm}]$	$Z_{\text{max}}[\text{mm}]$	Error distribution	$d[X_i]$	Remarks
Beam pipe	12	-62.5	62.5	passive		.00253 0.4 mm Be + Ti
VXD 1	14.6	-62.5	62.5	pads 20*20 equ. distrib.		.00202 wafer + ladder
VXD 2	22.6	idem	idem	idem	idem	idem
VXD 3	35.4	idem	idem	idem	idem	idem
VXD 4	48.0	idem	idem	idem	idem	idem
VXD 5	60.4	idem	idem	idem	idem	idem
Dbl. support cylinders	168.7	-868.8	868.8	passive		2 * dbl. wall C fibre
TRK 1	184.2	-894.3	894.3	idem		.00152 single
TRK 2	218.0	-558.0	558.0	strips 50		.00800
TRK 3	468.0	-825.0	825.0	idem		idem
TRK 4	718.0	-1083.0	1083.0	idem		idem
TRK 5	968.0	-1347.0	1347.0	idem		idem
TRK 6	1218.0	-1606.0	1606.0	idem		idem

FORWARD	$Z[\text{mm}]$	$R_{\text{min}}[\text{mm}]$	$R_{\text{max}}[\text{mm}]$	Error distribution	$d[X_i]$	Remarks
not implemented so far						

Barrel region restricted to $|\lambda| < 20^\circ$, in order to avoid the “supporting membranes” of the VXD.

2.2 Parametrization of track resolutions

- The relative errors of the transverse momentum due to the magnet spectrometer resolution or caused by multiple scattering, respectively, are:

$$\sigma(p_T)/p_T = A \cdot p_T \quad \text{and} \quad \sigma(p_T)/p_T = B \cdot \sqrt{1 + (m/P)^2} \approx B$$

- Above terms are expected to add quadratically. However, for $p_T < 50$ GeV, a simpler linear addition fits the data quite well and has been used:

$$\sigma(p_T)/p_T = A \cdot p_T + B, \quad \text{thus} \quad \sigma(1/p_T) \equiv \sigma(p_T)/p_T^2 = A + B/p_T$$

- For lack of a theoretical model, the errors of the impact parameters w.r.t. the true vertex are heuristically parametrized for $p_T > 2.5$ GeV as:

$$\sigma(\delta_{T,0}) = a + b \cdot e^{-p_T/c} \quad (\text{for high } p_T, \text{ the asymptotic value} = a)$$

In the forward/backward region, only linear parametrizations in p_T have been used.

2.3 LDC and SiD track resolutions

- LDC and SiD barrel regions* for $p_T = 1 \dots 35$ GeV (figs. 1...4 at left):
the data points correspond to LDC $50 \times 50 \mu\text{m}$ pixels (blue dots), LDC $25 \times 25 \mu\text{m}$ pixels (red squares), and SiD $20 \times 20 \mu\text{m}$ pixels (purple triangles), respectively, of the barrel vertex detectors - for a detailed description, see subsection 2.1.
- LDC forward/backward regions* for $p_T = 1 \dots 25$ GeV (figs. 1...4 at right):
the data points correspond to dip angle ranges of $81^\circ < |\lambda| < 81.5^\circ$ (blue dots), $81.5^\circ < |\lambda| < 82^\circ$ (red squares), and $82^\circ < |\lambda| < 82.5^\circ$ (purple triangles).

The values are averages over p_T intervals of width 2.5 GeV. The error bars shown reflect only the statistics normalized to bin content.

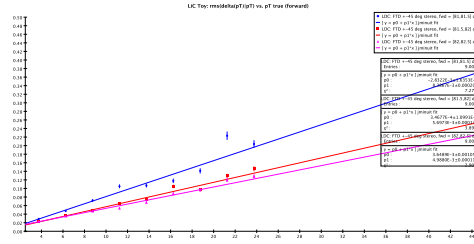
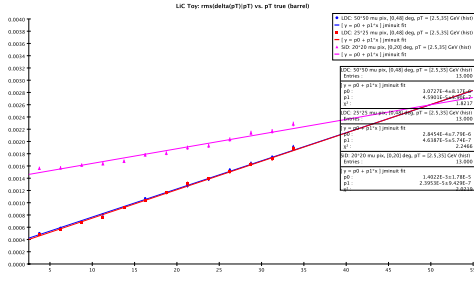


Fig. 1: rms($\Delta p_T/p_T$) vs. p_T for barrel (left) and forward/backward (right) regions.

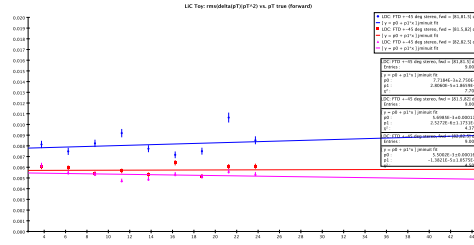
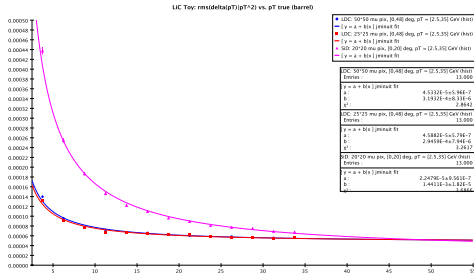


Fig. 2: rms($\Delta p_T/p_T^2$) [GeV^{-1}] vs. p_T for barrel (left) and forward/backward (right) regions.

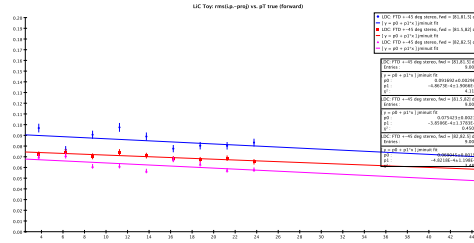
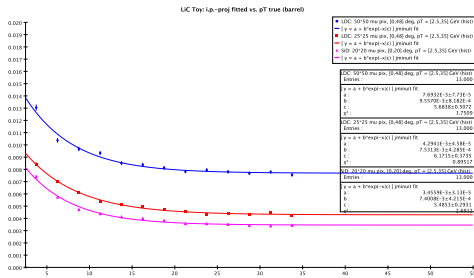


Fig. 3: rms(δ_T) [mm] vs. p_T for barrel (left) and forward/backward (right) regions.

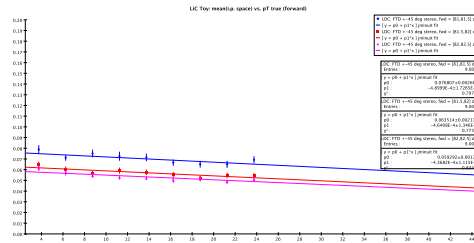
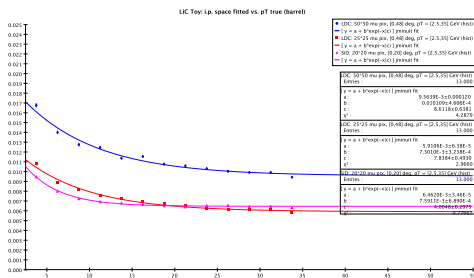


Fig. 4: mean(δ_0) [mm] vs. p_T for barrel (left) and forward/backward (right) regions.

3 Preliminary results

The results extracted from figs. 1...4 (subsection 2.3) are summarized below.

Barrel regions (LDC: $|\lambda| < 48^\circ$, SiD: $|\lambda| < 20^\circ$), $p_T = 2.5 \dots 35$ GeV:

Detector, px size	rms($\Delta p_T/p_T$)	rms($\Delta p_T/p_T^2$) [GeV $^{-1}$]	rms(δ_T) ^a	mean(δ_0) ^a
LDC $50 \times 50 \mu\text{m}$	$(4.6 \cdot p_T + 30.7) \cdot 10^{-5}$	$(4.5 + 31.9/p_T) \cdot 10^{-5}$	7.69 μm	9.56 μm
LDC $25 \times 25 \mu\text{m}$	$(4.6 \cdot p_T + 28.5) \cdot 10^{-5}$	$(4.6 + 29.5/p_T) \cdot 10^{-5}$	4.29 μm	5.91 μm
SiD $20 \times 20 \mu\text{m}$	$(2.4 \cdot p_T + 140.) \cdot 10^{-5}$	$(2.2 + 144./p_T) \cdot 10^{-5}$	3.46 μm	6.46 μm

Forward/backward regions ($81^\circ < |\lambda| < 82.5^\circ$), $p_T = 2.5 \dots 25$ GeV:

LDC $ \lambda $ range	rms($\Delta p_T/p_T$)	rms($\Delta p_T/p_T^2$) ^b	rms(δ_T) ^b	mean(δ_0) ^b
$81^\circ < \lambda < 81.5^\circ$	$(8.4 \cdot p_T - 2.83) \cdot 10^{-3}$	$8.36 \cdot 10^{-3}$ GeV $^{-1}$	86.7 μm	70.7 μm
$81.5^\circ < \lambda < 82^\circ$	$(5.7 \cdot p_T + 0.35) \cdot 10^{-3}$	$5.80 \cdot 10^{-3}$ GeV $^{-1}$	70.3 μm	57.1 μm
$82^\circ < \lambda < 82.5^\circ$	$(5.0 \cdot p_T + 3.65) \cdot 10^{-3}$	$5.37 \cdot 10^{-3}$ GeV $^{-1}$	63.1 μm	53.4 μm

Preliminary conclusions:

In the barrel region and for transverse momenta $p_T < 35$ GeV, the momentum resolution benefits dramatically from the low material budget of LDC's TPC; in contrast, SiD's all-*Si* tracker suffers from accumulated multiple scattering. However, extrapolation to higher momenta shows a break-even at $p_T \approx 50$ GeV. – The transverse impact parameters reflect the pixel sizes of each vertex detector's innermost layer(s).

In the forward/backward region $|\lambda| > 81^\circ$, the momentum resolution is sensitive to LDC's forward tracker strips stereo angle: $\pm 45^\circ$ is a good compromise between optimal $R - \Phi$ and $R - z$ resolutions. For $|\lambda| > 82.5^\circ$ (not shown), track reconstruction suffers extremely from inefficiencies, and might require non-standard treatment.

Acknowledgments

The software was designed and developed by the Vienna ILC Project Group in response to encouragement from the SiLC R&D Project. Special thanks are due to *R. Frühwirth* (HEPHY Vienna) for algorithms used by the LiC program.

References

- [1] M. Regler, R. Frühwirth and W. Mitaroff: *Int.J.Mod.Phys.* **C7**, 4 (1996) 521 - 542.
- [2] M. Regler, M. Valentan and R. Frühwirth: *The LiC Detector Toy Program*, Proc. 11th Vienna Conf. on Instrumentation (VCI) 2007, *Nucl.Instr.Meth.* **A** (in print).
User's Guide: http://wwwhephy.oeaw.ac.at/p3w/ilc/reports/LiC_Det_Toy/Reports/UserGuide.pdf
- [3] JAS3: <http://jas.freehep.org/>, AIDA: <http://aida.freehep.org/>
- [4] Detector Outline Documents:
LDC (July 2006): <http://www.ilcldc.org/documents/dod/outline.pdf>
SiD (May 2006): <http://hep.uchicago.edu/~oreglia/siddod.pdf>

^aasymptotic value,
^bweighted average.

Study of Beamstrahlung in the Vertex Detector

Paweł Luźniak¹ and Jacek Ciborowski² *

1- Łódź University - Institute of Physics
Pomorska 149/153, PL-90-236 Łódź - Poland

2- Warsaw University - Institute of Experimental Physics
Hoża 69, PL-00-681 Warsaw - Poland

This study, based on fast simulation, was aimed at evaluating the effect of e^+e^- pair background from beamstrahlung on performance of Vertex Detector (VTX) for jet flavour tagging in the International Linear Collider (ILC). Five layer VTX geometry with varying radius of the first layer was tested. Also possibility of rejection of background hits in the VTX, based on hit cluster shape and direction was studied.

1 Simulation

The e^+e^- pair background from beamstrahlung was simulated with Guinea-Pig [2] for nominal accelerator parameters at 500 GeV with 14 mrad crossing angle. The ILC detector response was modelled with Simulation á Grande Vitesse 2.30 (SGV), a fast simulation program allowing simplified definition of the detector geometry. A long barrel VTX with 5 coaxial layers, each made of 50 μm thick silicon plates with track spatial resolution of 5 μm and layer radii listed in Table 1 was simulated.

A beryllium beampipe of 0.25 mm thickness and radius 1 mm smaller than the first layer of the VTX was assumed. Dedicated software was developed to track charged particles through the VTX, taking into account multiple scattering and energy loss. VTX was assumed to be read out 20 times per bunch train, implying that background hits accumulated over 131 bunch crossings and overlaid “physics” hits. Tracks were reconstructed using own software. Tracks detected in the central tracker were refitted with hits from the VTX (both physics and background hits), selected with the Kalman Filter. Jet flavour tagging was performed with ZVTOP [3].

Layer	Radius	# of ladders
1	8,10,12,15 mm	8
2	26 mm	22
3	37 mm	32
4	48 mm	40
5	60 mm	50

Table 1: VTX detector layer specifications.

2 Background hits rejection

Hit density in a given layer of the VTX depends on beam parameters and the radius of the layer. Example distributions for the first layer with different radii are shown on Figure 1.

A track going through a silicon pixel plate deposits charge in several pixels forming a cluster. The shape of a cluster depends on the direction of a track with respect to the detector plane. This direction is described by two angles, γ and ξ , as shown on Figure 2.

*This work was partially supported by the Ministry of Science and Higher Education, research project no. EUDET/217/2006 (2006-2009).

Figure 5 shows that hits left by e^+e^- pair background have higher values of the ξ angle than hits left by physics tracks. Possibility of reconstructing the γ and ξ angles from the cluster shape would allow background rejection.

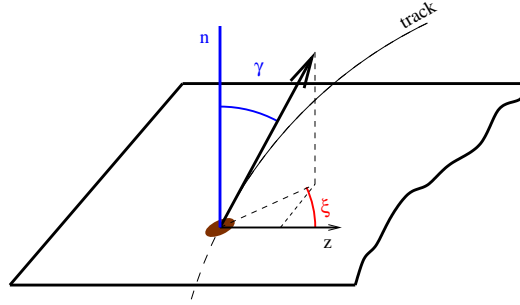
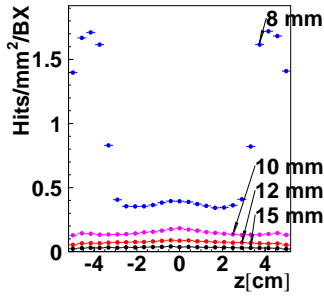


Figure 1: Hit density in the 1st layer Figure 2: γ and ξ in local coordinate frame, z coincides with the global detector Z coordinate

3 Jet flavour tagging performance

Jet flavour tagging performance was tested with 45.6 GeV jets in presence of e^+e^- background. Scenarios with 131BX, 66BX and no background were studied. For each scenario efficiency of selection at fixed purity and purity of the sample at fixed efficiency were studied. Results for “b” and “c” jet selection are shown on Figures 3 and 4. In the presence of the background the optimal radius of the first layer is 12 mm.

References

- [1] Slides:
<http://ilcagenda.linearcollider.org/contributionDisplay.py?contribId=296&sessionId=74&confId=1296>
- [2] C.Rimbault, P.Bambade, K.Moenig, D.Schulte, Study of incoherent pair generation in Guinea-Pig, EUROTeV-Report-2005-016-1
- [3] D. Jackson, ZvTop, NIM A388:247-253, 1997

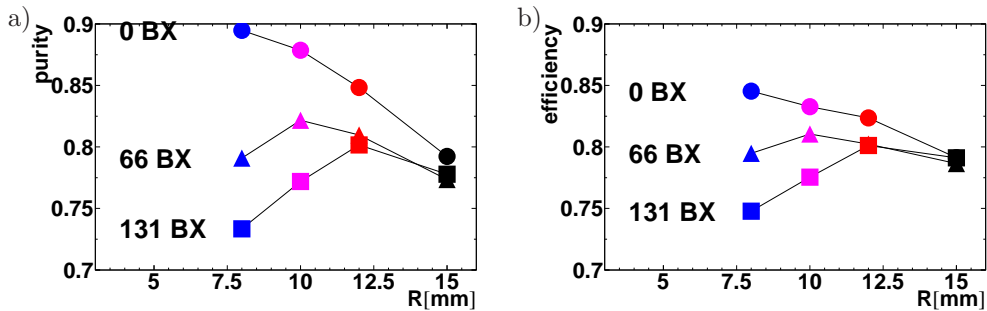


Figure 3: “b” jet selection a) purity at fixed efficiency of 0.8, b) efficiency at fixed purity of 0.8

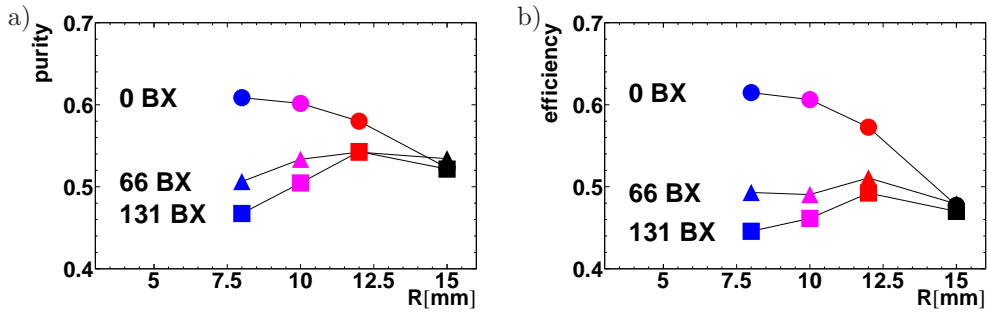


Figure 4: “c” jet selection a) purity at fixed efficiency of 0.6, b) efficiency at fixed purity of 0.6

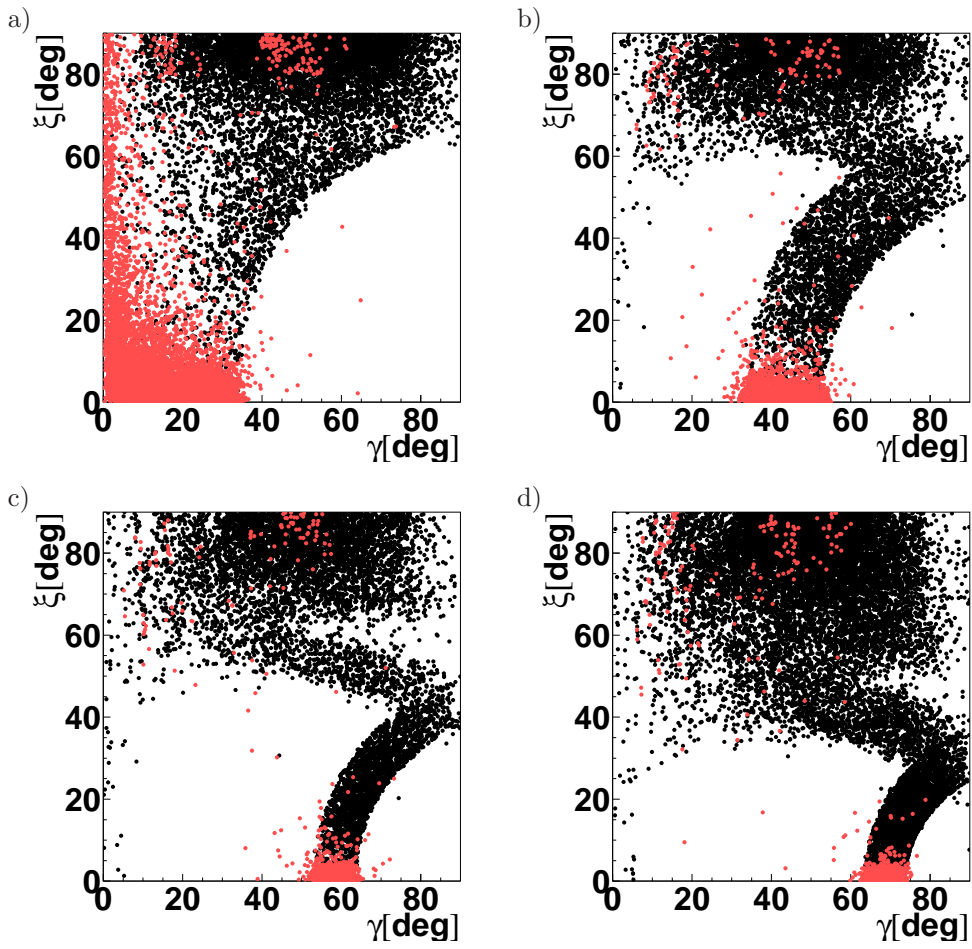


Figure 5: γ and ξ for signal (red/gray) and background (black) hits in the first layer at a) $|z| < 1$ cm, b) $1 \text{ cm} < |z| < 2$ cm, c) $2 \text{ cm} < |z| < 3$ cm, d) $|z| > 3$ cm (interaction point is at $z = 0$)

Progress with the CPCCD and the ISIS

Konstantin Stefanov *

STFC Rutherford Appleton Laboratory, Harwell Science and Innovation Campus,
Didcot OX11 0QX, UK

The Linear Collider Flavour Identification (LCFI) collaboration is continuing the R&D towards a CCD-based vertex detector for the International Linear Collider (ILC). We are working on two detector technologies, the Column Parallel CCD (CPCCD) and the In-situ Storage Image Sensor (ISIS). The evaluation of our second generation CPCCD (CPC2) and its readout and driver chips is presently in an advanced stage. In stand-alone mode CPC2 achieved operation at 45 MHz, which is a major milestone. After the successful proof-of-principle first generation ISIS1 we are now planning to continue with new, more advanced device. In this paper we present the status and the tests results from our CPCCD and ISIS developments.

1 Introduction

ILC will require high performance vertex detector for accurate reconstruction of decay chains, pure and efficient b and c tagging and vertex charge measurements [1, 2]. The vertex detector has to improve significantly upon the most accurate one built so far, the VXD3 [3], with several times better impact parameter resolution, lower mass and sparse readout. Charge coupled devices (CCD) were used as sensors in VXD3 due to their high resolution, excellent gain uniformity and small layer thickness, which makes them one of the most likely candidates for the vertex detector at the ILC.

CCDs are well suited for linear collider environments [4] because of the much cleaner interactions and low backgrounds compared to those at hadron colliders. The small CCD pixels ($20 \times 20 \mu\text{m}^2$ or below) allow excellent spatial resolution and two-track separation. This is helped by the low power dissipation, allowing the use of extremely low mass support mechanics. Large granularity, e.g. $2500 \text{ pixels}/\text{mm}^2$, permits integration of many events without loss of information due to overlaps. The CCD structure has 100% fill factor and all the active components are placed at the ends of the chip, which is very attractive for applications such as particle detection and imaging. Additionally, devices with an area of tens of square centimetres are readily available, which allows one to build detectors with optimal geometry.

2 Development of the CPCCD and its readout and drive systems

2.1 CPC2

Following the successful tests of our first CPCCD and its readout chip, the next generation devices CPC2 and CPR2 were designed and manufactured. An important new development in CPC2 is the busline-free design for clock distribution. In this architecture the clocks propagate on two separate metal layers covering the entire image area of the CCD. This drastically reduces the parasitic resistance and inductance associated with the conventional CCD buslines and enables efficient clocking at high speed.

*On behalf of the Linear Collider Flavour Identification (LCFI) Collaboration.

Three sensors with common design and functionality, but different size were manufactured by e2V Technologies. The largest CPC2-70 has an image area of $92 \times 15 \text{ mm}^2$ and total size of $105 \times 17 \text{ mm}^2$, allowing for 2 bump-bonded readout chips. This device is almost the size needed for the outer layers of the vertex detector at the ILC. The middle size CPC2-40 ($53 \times 15 \text{ mm}^2$ image area) represents half of the inner layer of the vertex detector and is being used for tests at speeds up to the design goal of 50 MHz. The smallest chip CPC2-10 ($13 \times 15 \text{ mm}^2$) covers most of the test program because of the large number of available devices.

In the first tests the busline-free CPC2 was driven by miniature air core transformers, embedded in a multi-layer PCB and fed from power RF amplifier. We observed X-ray signals from a ^{55}Fe source (5.9 keV, producing 1620 electrons) at clock frequency up to 45 MHz. The performance was dominated by the numerous parasitics of the PCB transformers and the high levels of noise from the RF amplifier. Despite this, the result is very close to the desired clock speed and an important milestone for the LCFI collaboration.

2.2 CPR2

The second generation readout chip CPR2 builds on the experience gained with CPR1 and has already been manufactured and delivered. In addition to the banks of voltage and charge amplifiers, matched to the outputs of CPC2, CPR2 implements cluster finding logic on 2×2 pixel kernel and sparse readout circuitry. Numerous test features have been provided, such as direct analog inputs and outputs from selected amplifiers, scan register for independent tests of the sparsifying logic and direct monitoring of any ADC channel. The clock distribution network has been improved to reduce the differential nonlinearity of the ADCs.

The chip logic continuously calculates the cluster sum of 4 pixel signals from every 2 adjacent columns. Upon exceeding a global threshold, an area of 4×9 pixels around the cluster is flagged for readout and later multiplexed to the 5-bit wide chip output. Using the scan register, the sparsification logic was tested with simulated clusters and showed good operation. It was found that CPR2 exhibits variable dead time between clusters separated in time by less than 60 to 100 pixels. The reason for this is understood and will be corrected in the next, improved version CPR2A.

The design of CPR2A is in an advanced stage. The local memory buffer for the sparsification logic has been increased to hold 3 separate readout clusters instead of just one in the CPR2. The size of the cluster has been reduced to 4×6 pixels and the logic has been re-designed to efficiently store up to 3 consecutive clusters using the same timestamp, thus saving memory space. In addition, each cluster finder column will have individual 7-bit threshold, needed to correct for gain non-uniformities in the signal amplifiers. These measures will significantly improve the chip's capabilities to process groups of dense hit patterns and reduce dead time.

2.3 CPCCD driver chip

The gate capacitance of the busline-free CPC2-40 is $40 \text{ nF/cm}^2/\text{phase}$ and current in excess of 20 Amps is required to drive it at 50 MHz. We designed a dedicated driver ASIC, the CPD1, made on $0.35 \mu\text{m}$ CMOS process. It uses optimised layout techniques for achieving minimum parasitic inductance in the clock and power paths. CPD1 is nominally supplied with 3.3 V and the user can switch each of the 8 sections individually, as well as control the slew rate of the output clocks via digital register. CPD1 has a built-in capacitor, internally

connected to one of the sections, which allows testing on an equivalent load of 32 nF with minimum parasitic impedance. The results at 50 MHz show excellent performance. We believe that similar performance could be achieved by bump bonding the CPD1 chip to a next generation CPCCD because of the very low interconnection impedance.

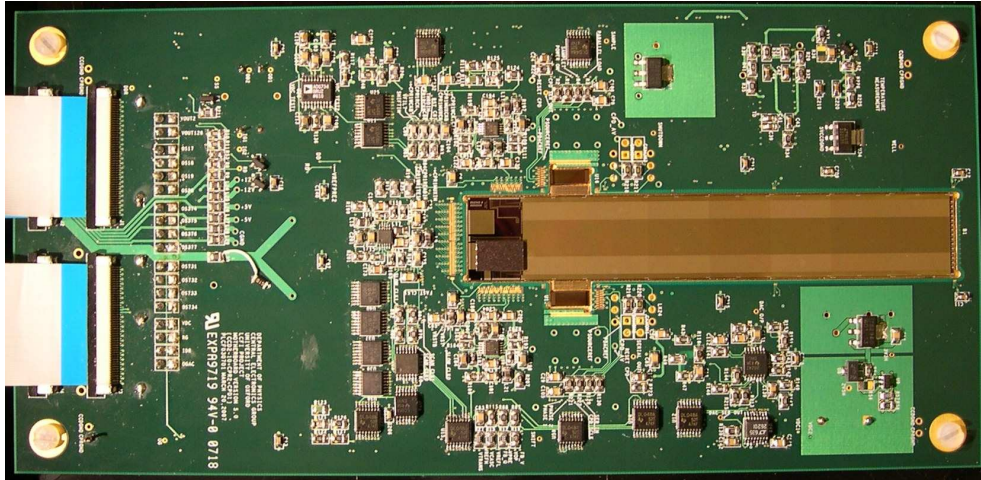


Figure 1: A prototype board with CPC2-70 (105 mm-long CPC2), bump-bonded to a CPR2 and driven by two CPD1 chips.

2.4 System tests

We developed a prototype board for testing all aspects of the three chips described above, shown on Fig. 1. Presently the driver chips are connected by wire bonds, which is not optimal for achieving the design readout rate due to their high parasitic inductance. However, the board has all the ingredients of a prototype ladder and is an important testbed towards building full-scale detector modules. Intensive tests of this configuration will be carried out in the following months.

3 Development of the ISIS

In parallel with the CPCCD development, LCFI is pursuing another CCD-based sensor, the In-situ Storage Image Sensor (ISIS) [5]. In every pixel of this device there is a CCD with 20 storage cells and 3-transistor readout circuitry, similar to that used in the Monolithic Active Pixel Sensors (MAPS). Charge generated by Minimum Ionising Particles (MIP) is transferred and stored in the CCD 20 times during the 1 ms-long bunch train at ILC. Readout is initiated in the 200 ms-long gap between the bunch trains at 1 MHz rate, using column parallel architecture. One of the main advantages of the ISIS is immunity to beam-related electromagnetic interference, because the signal is kept in the charge domain during the beam duration. In addition, the ISIS could be orders of magnitude more radiation resistant than the CPCCD due to the reduced number of charge transfers. One could also achieve lower readout noise because of the relaxed clock frequency, allowing longer shaping times.

Together with e2V Technologies, LCFI has designed and manufactured the first ISIS device (ISIS1), based on a standard CCD process, and utilising deep diffused p+ well for charge shielding of the CCD register. The device is an array of 16×16 ISIS pixels, each containing a 3-phase CCD with 5 cells, reset transistor, source follower and a row select transistor. Due to process limitations the pixels are laid on $40 \mu\text{m} \times 160 \mu\text{m}$ pitch and no on-chip logic for row selection and clocking is provided. The initial tests of the ISIS1 used pulsed light for charge generation and showed correct capture and transfer of signal into the CCD pixels corresponding to different time samples. Later the device was successfully tested with 5.9 keV X-rays as well, the results of which are shown in [6].

The development of a next-generation ISIS with $20 \times 20 \mu\text{m}^2$ pixel size is an ambitious goal which LCFI is actively pursuing. The combination of active transistors in every pixel, logic circuitry and CCDs in one monolithic device is challenging and will most likely require modifications to an existing CMOS process with feature size below $0.25 \mu\text{m}$.

4 Conclusions

The work at LCFI towards a CCD-based vertex detector for ILC is advancing. Our second generation CPC2 is a large device and a major step towards detector-scale demonstrator. Stand-alone tests have shown successful operation at 45 MHz using the developed busline-free devices. The readout chip for CPC2 has also been successfully designed, manufactured and tested. A new, improved version of the readout chip is in an advanced design stage. The CPD1 driver ASIC has shown satisfactory performance driving large currents at frequencies up to 50 MHz.

The CCD-based ISIS concept has numerous advantages tailored for the ILC environment and is an extremely promising device for the future vertex detector. The first prototype has already been manufactured and the initial tests have been successful. The second generation ISIS will be made on a smaller pitch which will take it a step closer to satisfying the challenging detector requirements.

5 Acknowledgements

Most of the work presented in this talk is funded by the UK Science and Technology Facilities Council (STFC), which support is greatly appreciated.

References

- [1] TESLA Technical Design Report part IV, DESY 2001-011 (2001).
- [2] S. Hillert, Nucl. Instr. and Meth. A560 (2006) 36.
- [3] K. Abe et al., Nucl. Instr. Meth. A400 (1997) 287.
- [4] K.D. Stefanov, Nucl. Instr. and Meth. A565 (2006) 157.
- [5] C.J.S. Damerell, Nucl. Instr. and Meth. A541 (2005) 178.
- [6] Slides:
<http://ilcagenda.linearcollider.org/contributionDisplay.py?contribId=297&sessionId=74&confId=1296>

ILC Vertex Detector Mechanical Studies

Erik Johnson*

Rutherford Appleton Laboratory
Oxfordshire, OX11 0QX, United Kingdom

The Linear Collider Flavour Identification Collaboration (LCFI) is conducting a research and development programme aimed towards building a vertex detector for the International Linear Collider (ILC). The latest mechanical ideas and study results are discussed along with future plans.

1 Introduction

The LCFI Collaboration's concept for a vertex detector is to have silicon detectors mounted on ladders. These ladders are then mounted in barrels around the detector. In the TESLA TDR[1] it is considered that 5 layers of barrels are needed, with the first barrel as close to the interaction point as possible and the other barrel layers spread evenly throughout the vertex detector. The detector needs to be lightweight, robust and have as uniform a distribution of material as possible within a layer.

In this design the ladders in layers 2-5 have an active length of 250 mm, with layer 1 much shorter at 100 mm. To hold the ladders in barrels around the beam pipe they are attached at their ends to a beryllium support shell with the entire vertex detector enclosed in a foam cryostat to allow cooling, illustrated in Figure 1.

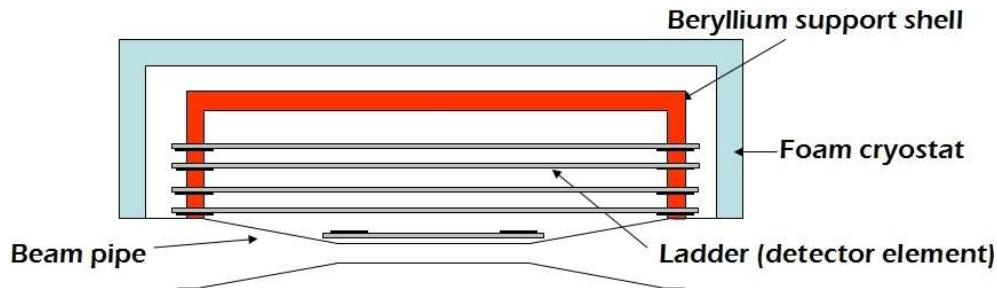


Figure 1: Conceptual design of ladders mounted on support shell, around beam pipe.

The ladders will be attached to the support shell by means of a pair of ceramic blocks, the annulus block attached to the support shell, and the ladder block attached to the ladder, illustrated in Figure 2. The blocks have a V and a flat machined into them to allow relative movement in one dimension, motion out of the plane being prevented by a compressive spring. The blocks at one end of the ladder are then fixed with a pin, those at the other being left free to slide to accommodate differential contraction.

Recent studies have concentrated on two different potential substrate materials: Silicon Carbide foam (SiC) and Reticulated Vitreous Carbon foam (RVC), both supplied by

*for the LCFI Collaboration.

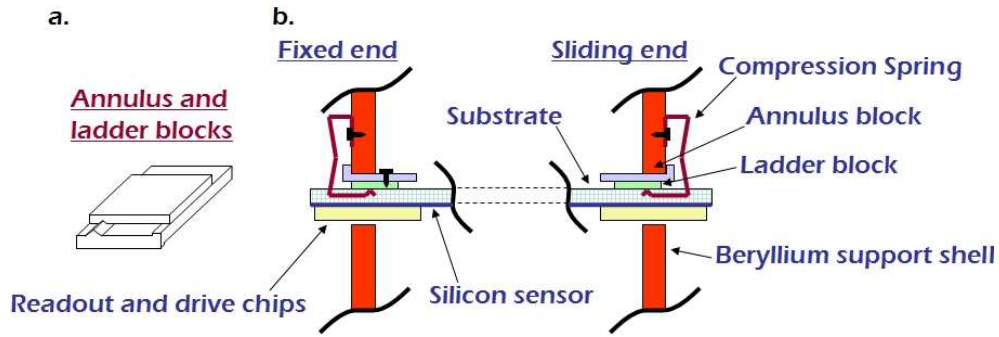


Figure 2: Conceptual designs, 2a showing how a ladder is attached to the support structure, 2b showing a close up of the ladder and annulus block.

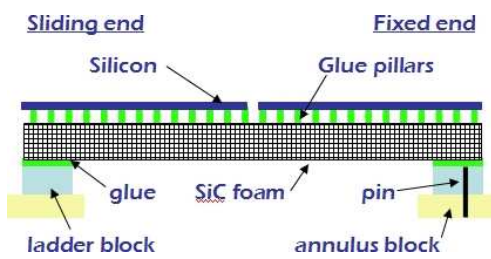


Figure 3: Conceptual design of an SiC ladder.

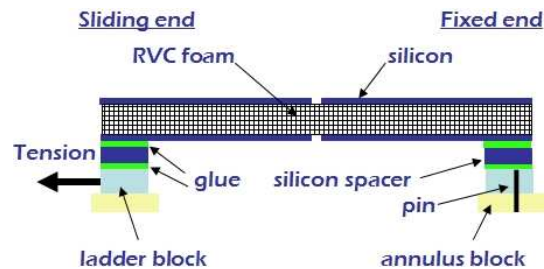


Figure 4: Conceptual design of an RVC ladder.

Erg Materials and Aerospace Corporation [2]. 20 micron thick unprocessed silicon rectangles supplied by Aptek Industries Inc [3] were used in both cases to simulate the detector elements.

2 SiC ladder

The SiC ladder was made by mounting a silicon rectangle on 1.5 mm thick silicon carbide foam. The foam was 8% the density of solid SiC. The silicon was attached to the foam by means of small adhesive pillars placed on a 5 mm grid with the silicon held above the foam such that once cured there was a 200 micron gap between substrate and silicon, illustrated in Figure 3. The material in the ladder corresponds to approximately 0.14% X_0 .

The ladder was cooled from room temperature to -50 degrees Celsius. On cooling the ladder bowed out of shape by approximately 160 microns. Figure 5 shows the profile of the ladder as it was cooled and heated back up towards room temperature. Figure 6 shows the difference between a profile at a particular temperature and room temperature; from this the overall change in shape and magnitude of that change may be seen (in both figures the feature 155 mm along the length is the gap between the two silicon rectangles).

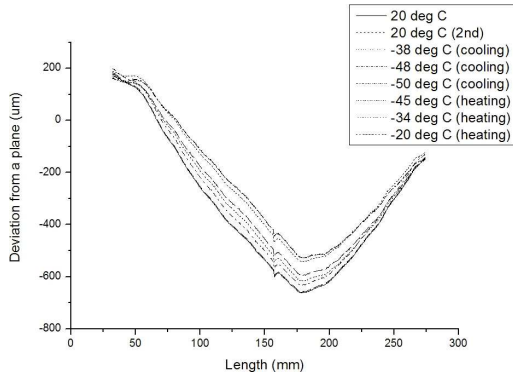


Figure 5: Profiles of an SiC ladder at various temperatures.

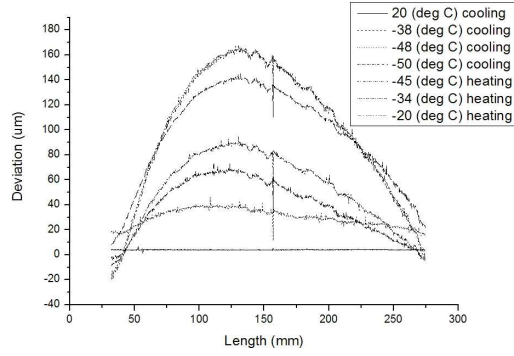


Figure 6: Difference between profiles at a particular temperature and room temperature.

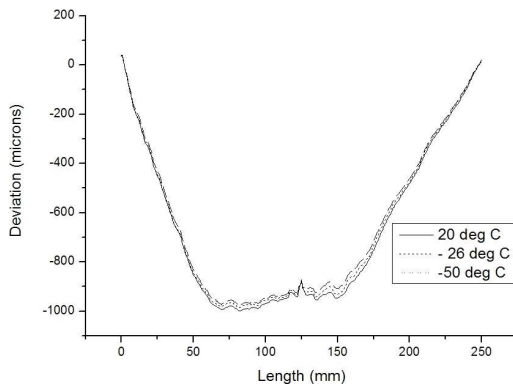


Figure 7: Profile of RVC ladder at various temperatures.

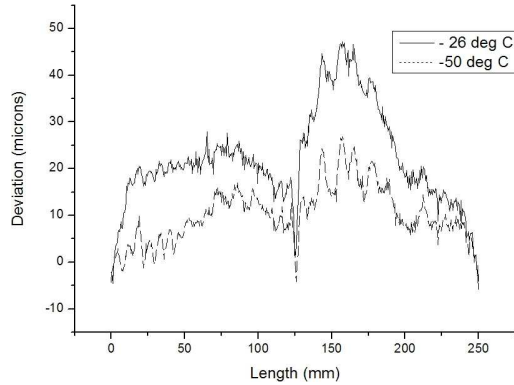


Figure 8: Plots of difference between temperature stated and room temperature for the RVC ladder.

3 RVC foam ladder

The RVC ladder was made by gluing silicon rectangles either side of a RVC foam to make a sandwich structure. The silicon was attached by adhesive pillars on a 5 mm grid sunk into the foam such that the silicon and foam were in contact. In order to keep its shape the ladder was kept tensioned along its length. Figure 4 shows the conceptual design of the RVC ladder.

This ladder was also cooled from room temperature to -50 degrees Celsius. Figure 7 shows the profile of the Ladder as it is cooled down and warmed up. Figure 8 shows the difference of the profiles at various temperatures to the profile at room temperature.



Figure 9: Picture of carbon fibre substrate with ripple.

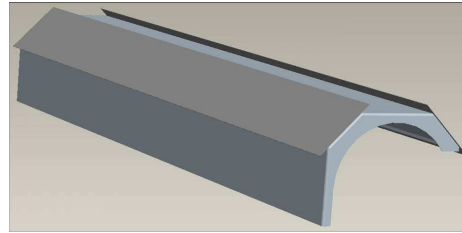


Figure 10: Illustration of half of a carbon fibre shell.

4 Future work

In addition to completing the studies on the above engineering models, alternative substrates and mounting schemes are under consideration. These include carbon fibre substrates, shell structures and double sided detectors using a foam substrate.

Figure 9 shows a carbon fibre substrate with a ripple effect along its length. This would increase the rigidity of the substrate across its width and would be tensioned to maintain its shape along its length.

Carbon fibre will also be investigated for use in shell structures as illustrated in Figure 10, with the first test carbon fibre shell structure under construction.

LCFI are also investigating the possibility of making double sided detectors using a foam substrate and the use of foams to make the shell structure.

References

- [1] TESLA TDR, Part 4, A Detector for TESLA
http://tesla.desy.de/new/pages/TDR_CD/PartIV/detect.html
- [2] Erg Materials and Aerospace Corporation, <http://www.ergaerospace.com>
- [3] Aptek Industries Inc., <http://www.aptekindustries.com>

R&D Status and Plan for FPCCD Vertex Detector

Y. Sugimoto

KEK, High Energy Accelerator Research Organization
1-1 Oho, Tsukuba, Ibaraki 305-0801, Japan

Fine Pixel CCD (FPCCD) is a candidate of for the sensor of the vertex detector at ILC. We have just started R&D for FPCCDs. We report on the status and plan of the FPCCD R&D.

1 Introduction

Many types of sensor technology have been proposed for the vertex detector at ILC experiment. Fine Pixel CCD (FPCCD) is one of the candidate technologies [2]. FPCCD has a pixel size of about $5 \mu\text{m}$ square. Because of large number of pixels per unit area, the pixel occupancy due to pair-background can be less than 1% even if the signal is accumulated for one train. By accumulating the signal during a train as electric charge and reading out between trains, FPCCD can be completely free from the electro-magnetic interference (EMI) caused by the beam bunches. Small pixel size of FPCCD gives excellent spatial resolution and two-track separation capability.

Standard CCDs usually have non-depleted region in the epitaxial layer. For charged particle detection, this non-depleted region causes spread of signal charge. For large pixel CCDs, this charge spread is preferable to get good spatial resolution using charge sharing method. In the case of FPCCD, this charge spread makes large number of hit pixels and pixel occupancy becomes unacceptable level. Therefore, fully depleted epitaxial layer is essential for FPCCD in vertex detector application at ILC.

As the first step of FPCCD R&D, we developed fully depleted CCDs. In this report, we describe study results of the sample CCDs, and mention about near future plan for FPCCD R&D.

2 Development of fully-depleted CCD

Several types of back-illuminating CCDs which are variants of type S7170 with higher resistive epitaxial layer have been developed by Hamamatsu Photonics. In order to see if the epitaxial layer is fully depleted, we injected focused laser light from the backside and measured the signal spread at the potential minimum. Substrate of back-illuminating CCDs is removed by back-thinning, and the image area consists of only epitaxial layer. If there is non-depleted region in the epitaxial layer, signal charge generated very close to the back surface spreads in the non-depleted region by thermal diffusion because there is no electric field in the non-depleted region. On the other hand, if the epitaxial layer is fully depleted, the signal charge quickly moves to the potential minimum near the gate, and the charge spread is very small.

In the test experiment, green laser light ($\lambda = 532 \text{ nm}$) was expanded to about 1 cm diameter beam by a laser beam expander, and then focused to a thin line using a cylindrical lens to illuminate a sample CCD. The width of the focused line was much less than the pixel width of $24 \mu\text{m}$, associated with broader tail due to spherical aberration of the cylindrical

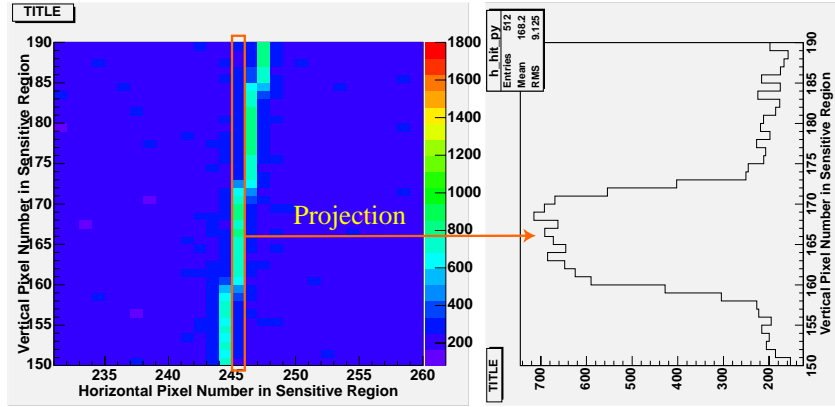


Figure 1: Image of one shot of line-focused laser illumination (left) and the projection of one column (right).

lens. By giving a small angle between the focal line and the direction of the pixel grid of the CCD, we can effectively make a scan inside a pixel. Figure 1 shows one shot of the laser illumination. From the histogram of the projection of one line, we can evaluate the charge spread.

We have measured the charge spread with gate voltages of $V_{gate} = -7$ V and $V_{gate} = +6$ V during the laser pulse illumination for each CCD sample. As shown in Figure 2, the thickness of non-depleted region changes with the gate voltage. If the distributions of the signal (right figure of Figure 1) for $V_{gate} = -7$ V and $V_{gate} = +6$ V are same, we can conclude that the CCD is fully depleted in both cases.

The results of the measurements are shown in Figure 3 and Figure 4 for typical samples. For the sample of S7170-Deep2-FF16-011, the distributions are widely spread and different in two gate voltage cases. On the other hand, for the sample of S7170-SPL24-22-20, the distributions have sharp edges and are same for both gate voltage cases. From this measurement, we can conclude that S7170-SPL24-22-20 is fully depleted even at the gate voltage of -7 V.

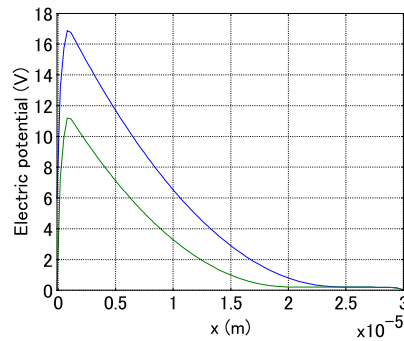


Figure 2: An example of potential as a function of depth for gate voltages of 0 V (lower peak) and 6 V (higher peak) for a CCD with $30 \mu\text{m}$ epitaxial layer thickness. The region where the potential is flat corresponds to non-depleted region.

3 Summary and future plan

Fully depleted epitaxial layer is the key issue of FPCCD vertex detector. The signal distributions of a newly developed CCD, S7170-SPL24, at two different gate voltages of -7 V and $+6$ V during the laser light illumination were same. From this result, we can conclude

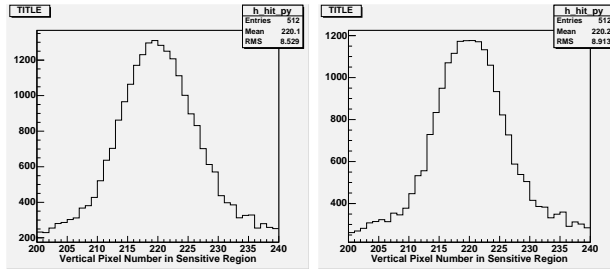


Figure 3: Charge distribution of S7170-Deep2-FF16-011 with gate voltage of -7 V (left) and $+6$ V (right).

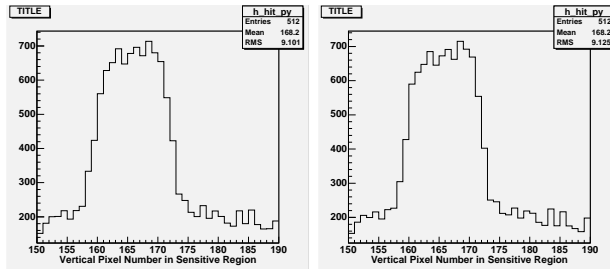


Figure 4: Charge distribution of S7170-SPL24-22-20 with gate voltage of -7 V (left) and $+6$ V (right).

that S7170-SPL24 is fully depleted even at the gate voltage of -7 V.

As a future plan, measurement of Lorentz angle and study of radiation hardness of the fully depleted CCD are planned in near future. Fabrication of smaller pixel, multi-port readout CCD and ASIC for readout of the multi-port CCD are also planned.

Acknowledgments

This work is partly supported by Grant-in-Aid for Scientific Research No. 17540282 and No. 18GS0202 from Japan Society for the Promotion of Science (JSPS), and No. 17043010 and No. 18034007 from Ministry of Education and Science in Japan.

References

- [1] Slides:
<http://ilcagenda.linearcollider.org/contributionDisplay.py?contribId=299&sessionId=74&confId=1296>
- [2] Y. Sugimoto, Proceedings of International Linear Collider Workshop LCWS05, Stanford, CA, March 2005, pp.550-554.

Monolithic Pixels R&D at LBNL

Devis Contarato¹, Marco Battaglia^{1,2}, Jean-Marie Bussat¹,
Peter Denes¹, Piero Giubilato³, Lindsay Glesener²,
Benjamin Hooberman² and Chinh Qu Vu¹

1- Lawrence Berkeley National Laboratory
Berkeley, CA - USA

2- University of California at Berkeley - Department of Physics
Berkeley, CA - USA

3- Istituto Nazionale di Fisica Nucleare - Sezione di Padova
Padova - ITALY

This paper reports recent results from the ongoing R&D on monolithic pixels for the ILC Vertex Tracker at LBNL [1].

1 Introduction

A Laboratory Directed Research and Development (LDRD) program has been on-going at LBNL since 2005. The main activity on sensor R&D is the development of CMOS monolithic pixels with integrated functionalities and fast readout in view of their possible application in the ILC Vertex Tracker. At each step of the development, various pixel architectures and layout options are explored, driving the choice for the design of subsequent prototypes.

The results obtained with the first prototype designed at LBNL (the LDRD-1 chip) have been reported in [2]. This paper summarizes the recent results obtained with the second prototype of the LDRD family, the LDRD-2 chip implementing in-pixel Correlated Double Sampling (CDS), outlines the main features of a forthcoming prototype with integrated digitization, and finally introduces a line of research recently started on Silicon-On-Insulator (SOI) pixels.

2 CMOS Monolithic Pixel Sensors

2.1 Prototype with in-pixel CDS and fast readout

The LDRD-2 chip was designed and fabricated in 2006 using the AMS 0.35 μm CMOS-OPTO technology with a nominal epilayer thickness of 14 μm . The array of 96×96 pixels of 20 μm pitch is divided in 6 subsections with different sizes of the charge collecting diode ($3 \times 3 \mu\text{m}^2$ and $5 \times 5 \mu\text{m}^2$) and different pixel architectures, standard 3-transistor (3T) pixels with and without a guard-ring around the diode and a self-biased pixel architecture, similar to the one first proposed in [3].

All sectors implement in-pixel CDS: the pixel dark level and charge signal are consecutively stored on two capacitors integrated in each pixel; both signals are then clocked to the chip analog outputs, after which the CDS difference is obtained either via FPGA or via the online DAS. The chip was designed to be operated up to a clocking frequency of 25 MHz. The readout scheme is based on a rolling-shutter scheme, i.e. rows are reset and read out in sequence, so that the integration time is constant for all pixels.

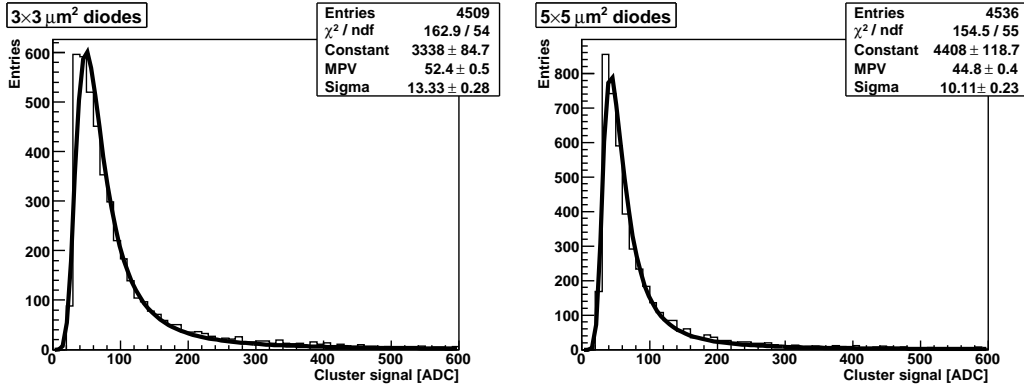


Figure 1: LDRD-2 chip beam-test results: cluster signal for 1.5 GeV electrons for two different sizes of the charge collecting diode.

The LDRD-2 has been extensively tested using the same measurement protocol used for the LDRD-1 chip: in-lab calibrations with a ^{55}Fe source and lasers of different wavelengths have been performed. The sensor charge collection time has been determined using a fast (0.5-5 ns) 1060 nm laser pulse focused on a single pixel and by following the collected charge signal during the pixel sampling time. The result of ~ 150 ns agrees well with the expectations coming from the typical resistivity of the epitaxial layer employed in the fabrication process.

The sensor response to minimum ionising particles has been tested on the 1.5 GeV electron beam at the BTS line of the Advanced Light Source (ALS) at LBNL. Figure 1 shows the cluster signal distribution obtained for the two different diode sizes on the chip sectors featuring a 3T pixel architecture. An average S/N ratio of ~ 20 was found to be similar for the two different diode sizes, with an average cluster multiplicity between 4 and 5, the larger being associated with pixels equipped with smaller diodes. The most probable value for the cluster charge signal for small and big diodes is ~ 750 and ~ 1000 electrons, respectively.

2.2 Prototype with integrated ADCs

The LDRD-3 chip, which is being designed and will be submitted in July in the $0.35 \mu\text{m}$ AMS CMOS-OPTO process, features the same in-pixel CDS architecture as in the LDRD-2 prototype, combined with integrated ADCs at the end of each column. The pedestal and signal levels from each pixel are sent to the bottom of the column, the CDS difference being performed by a 5-bit successive approximation, fully differential ADC running at 300 MHz clock frequency. The design of the LDRD-3 chip is driven by the results of a detailed study performed on data collected with the LDRD-1 chip for different pixel pitches, which had shown that 5-bit ADC accuracy is sufficient to achieve the desired single point resolution, provided that the pixel pedestal can be removed before digitization.

Figure 2 shows the chip layout and a sketch illustrating the chip working principle. The array consists of 96×96 pixel of $20 \mu\text{m}$ pitch. After a global reset, the sensor image is integrated, and then the pixel signal and reference levels are stored in the in-pixel capacitors. This is followed by a column-wise digitization of the pixel signals with concurrent storage

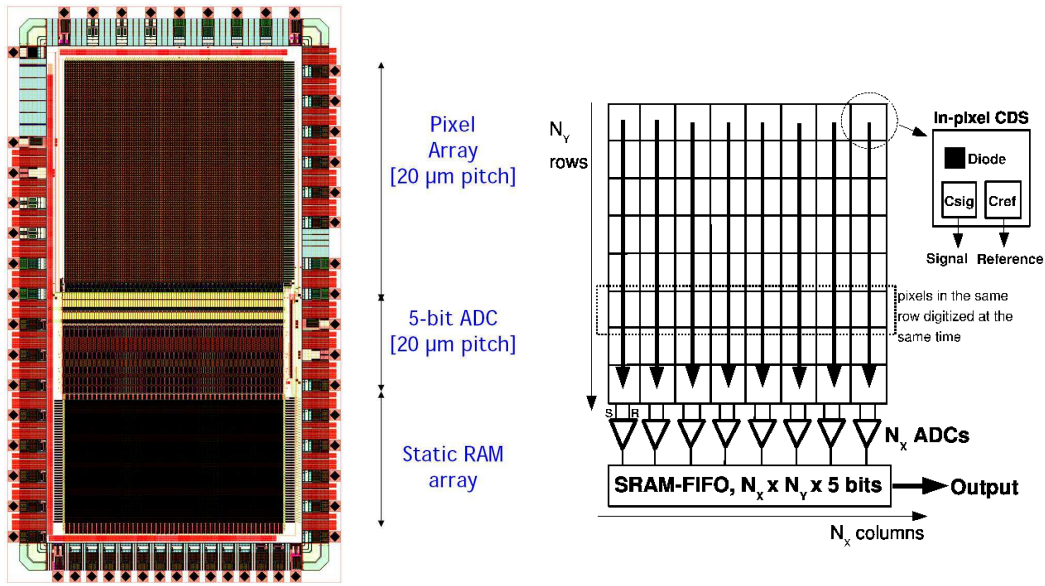


Figure 2: Layout (left) and schematic (right) of the LDRD-3 chip.

in a SRAM-FIFO memory cell integrated at the bottom of the column. The digital image is then read out serially from the SRAM-FIFO using a 50 MHz clock. The chip is expected to be back from fabrication in October 2007.

3 SOI monolithic pixels

A first prototype chip has been designed and submitted in a 0.15 μm fully-depleted SOI technology from OKI [4] in Fall 2006. The sensor is based on a 350 μm thick high-resistivity substrate, separated by the CMOS circuitry by a 200 nm thick buried oxide. The CMOS circuitry is implanted on a 40 nm layer of silicon on top of the buried oxide. The thickness of this CMOS layer is small enough that the layer can be fully depleted. This technology is expected to combine the advantage of a depleted substrate with the possibility of integrating complex functionalities by making use of both types of MOS transistor, in contrast with standard CMOS monolithic APS which feature only *n*-type transistors. Moreover, higher speed and lower power consumption can be achieved with the SOI process with respect to conventional CMOS processes.

The chip features 10 μm pitch pixels, two analog sections with 1.0 V and 1.8 V bias and a digital section; all three sections are divided in 2 subsections with 1×1 and 5×5 μm² charge collecting diodes. The total array size is of 160×150 pixels. The chip has been received back from foundry in May 2007. It is fully functional and is currently being tested.

4 Conclusions & Outlook

Recent progress in the development of the LDRD monolithic pixel chips at LBNL has been reviewed. A prototype with in-pixel CDS and fast readout has been successfully tested and will be used in June-July for tracking studies with 120 GeV protons at the MTBF facility at FNAL, in conjunction with the Thin Pixel Telescope described in [5]. Irradiation tests with 30 MeV protons and 1-20 MeV neutrons are also planned in Summer. The next prototype, implementing on-chip digitization, is expected in Fall 2007. In parallel, tests have started on a novel SOI chip, which combines a high-resistivity sensor substrate with a full CMOS circuitry implanted on top, so that higher circuitry complexity with low power dissipation can be implemented.

Acknowledgments

This work was supported by the Director, Office of Science, of the US Department of Energy under Contract no. DE-AC02-05CH11231.

References

- [1] Slides:
<http://ilcagenda.linearcollider.org/contributionDisplay.py?contribId=302&sessionId=74&confId=1296>
- [2] D. Contarato *et al.*, Proceedings of the LCWS06 International Linear Collider Workshop 2006, Bangalore, India.
- [3] G. Deptuch *et al.*, Nucl. Instrum. Meth. **A 511** (2003) 240.
- [4] OKI Electric Industry Co., Ltd., <http://www.oki.com>
- [5] M. Battaglia *et al.*, *Particle Tracking with a Thin Pixel Telescope*, these Proceedings.

Particle Tracking with a Thin Pixel Telescope

Marco Battaglia^{1,2}, Devis Contarato², Piero Giubilato^{2,3},
Lindsay Glesener², Leo Greiner², Benjamin Hooberman²

1- University of California - Dept of Physics, Berkeley, CA - USA

2- Lawrence Berkeley National Laboratory, Berkeley, CA - USA

3- Istituto Nazionale di Fisica Nucleare and Dip. di Fisica, Padova, Italy

We report results on a tracking performance study performed using a beam telescope made of 50 μm -thick CMOS pixel sensors on the 1.5 GeV electron beam at the LBNL ALS.

1 The Thin Pixel Prototype Telescope

The anticipated ILC physics program indicates that identification of heavy fermions with high efficiency and purity is of primary importance. The requirements in terms of track extrapolation accuracy are $\simeq 5 \mu\text{m} \oplus \frac{10 \mu\text{m}}{p_t (\text{GeV})}$. The Vertex Tracker design and the sensor R&D is driven by this requirement. CMOS pixel sensors are an attractive option for the ILC Vertex Tracker. In particular, they can be back-thinned to 50 μm or less, without significant performance deterioration [1].

While there has already been some experience with the reconstruction of well-isolated, high momentum particles with monolithic pixel sensors [2, 3], no data exists on low momentum particle tracking with thin pixel sensors with occupancy conditions comparable to those expected at the ILC. We present here results obtained with a Thin Pixel Prototype Telescope (TPPT) on the 1.5 GeV e^- beam at the LBNL Advanced Light Source (ALS) accelerator complex. The TPPT is the first beam telescope made of thinned CMOS pixel sensors. It consists of three planes of thin pixel sensors (layers 1 to 3), each spaced by 17 mm. One additional detector (layer 4) is added 17 mm downstream of the third layer. The MIMOSA 5 chip [4, 5], developed at IPHC in Strasbourg, France, has been selected for the TPPT. This chip, fabricated in the 0.6 μm AMS process, features a large active area of $1.7 \times 1.7 \text{ cm}^2$ and more than 1 M pixels. The epitaxial layer is 14 μm thick and the pixel pitch 17 μm . One sector of each MIMOSA 5 chip, corresponding to a 510×512 pixel array, is readout through a custom FPGA-driven acquisition board. The beam spill consists of a single bunch with a repetition rate of 1 Hz and the extraction signal is used as a trigger. For each spill we acquire three frames, one before the particles arrive on the TPPT. Four 14 bits, 40 MSample/s ADCs simultaneously read the four sensors, while an array of digital buffers drive all the required clocks and synchronisation signals. A 32 bits wide bus connects the FPGA to a digital acquisition board installed on a control PC. Data is processed on-line to perform correlated double sampling, pedestal subtraction, noise computation and cluster identification. To reduce the amount of data written to disk only the addresses and pulse heights of the pixels in a fixed matrix around the centre of a cluster candidate are recorded. The data is then converted in the `lcio` format and the offline analysis is performed by processors developed within the `Marlin` framework [6]. Each event is scanned for pixels with pulse height over a signal-to-noise (S/N) threshold of 4.5, these are designated as cluster ‘seeds’. Seeds are then sorted according to their pulse height values and the surrounding, neighbouring pixels are tested for addition to the cluster. Pixels with a

pulse height in excess to 2.0 time the noise are accepted. The neighbour search is performed in a 5×5 matrix. Clusters are not allowed to overlap and we require that clusters are not discontinuous, i.e. pixels associated to a cluster cannot be interleaved by any pixel below the neighbour threshold. The point of impact of the particle track on the detector is determined by reconstructing the charge centre-of-gravity of the cluster.

2 The ALS Beam Test with 1.5 GeV Electrons

The TPPT telescope is operated in an optical enclosure mounted on an optical rail and aligned on the ALS BTF beam line. We report here results of the first data taking performed in Fall 2006. The temperature was kept constant during operation at $\simeq 27^\circ\text{C}$ by forced airflow. The cluster S/N averaged on the TPPT layers is 14.5. Due to a drop of the voltage supplied to the chip, one of the planes of the telescope was not fully efficient during the ALS data taking. Because of that we also accept particle tracks reconstructed on two layers, provided they have a hit on the reference plane within $150 \mu\text{m}$. Detailed simulation of the TPPT has been carried out, using the `Geant-4` package [7] to generate the particle points of impact and energy deposits on the sensitive planes. These have been stored in `lcio` format and used as input to a CMOS pixel simulation program implemented in `Marlin` [8]. Noise values have been matched to those measured for the detectors in the telescope. Digitised simulation has been passed through the same cluster reconstruction program as the real data and reconstructed hits used to fit straight particle tracks, after pattern recognition. The single detector response is well reproduced by the simulation. Figure 1 compares the cluster pulse height and the pixels multiplicity in a cluster for simulation and ALS beam test data.

The TPPT at the ALS beam-line allows us to perform detailed studies of particle tracking with various, controllable, levels of track density under realistic conditions. Data have been collected at the BTS with different beam intensities ranging from $0.5 \text{ particles mm}^{-2}$ up to about $5 \text{ particles mm}^{-2}$. These particle densities resemble those expected in the core of hadronic jets at $\sqrt{s} = 500 \text{ GeV}$. In particular, the distribution of the distance between a hit associated to a particle track and its closest hit reconstructed on the same layer in the high intensity runs at the ALS reproduces that predicted by simulation for $e^+e^- \rightarrow Z^-H^0 \rightarrow q\bar{q}b\bar{b}$

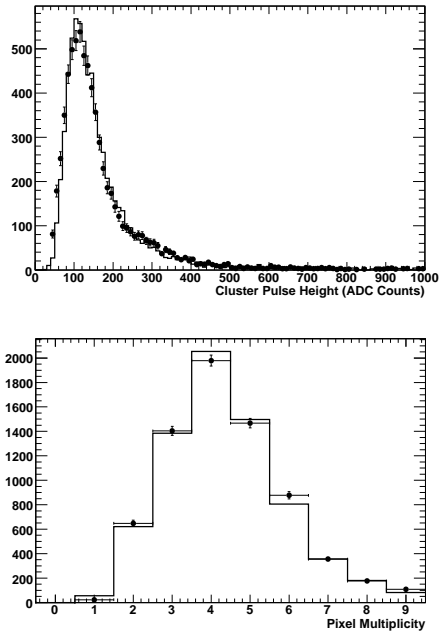


Figure 1: Detector response to 1.5 GeV e^- s in data (point with error bars) and in the `Geant-4+Marlin` simulation and reconstruction. The cluster signal pulse height (left) and pixel multiplicity in a cluster (right) are shown for clusters associated to reconstructed particle tracks.

for $M_H = 120$ GeV at 500 GeV.

After data taking, the beam telescope geometry has been surveyed using an optical metrology machine. The results of this survey have been used as starting point of the alignment procedure, performed on a sample of approximately 20000 well-isolated particle tracks with four correlated hits. After alignment, track candidates have been defined by matching hits on two layers. Each track candidate has been extrapolated to the third layer, where the closest hit has been added, if its residual was less than $50 \mu\text{m}$. Pattern recognition ambiguities have been solved based on the number of associated hits and on the difference between the track slope and the expected beam slope, determined from the settings of the beam-line final dipoles. Tracks have then been re-fitted using a modified least-square, to account for kinks due to multiple scattering on the measuring planes [9] and extrapolated to the reference layer, where the residual to the closest reconstructed hit has been computed. Since the beam contains a fraction of lower momentum particles, which increases moving away from the beam axis, only the central region of the beam was used and an additional cut was imposed on the residual on the second coordinate. The tracking performance has been characterised

by the residuals between the extrapolation of a track reconstructed using at least two layers and the point reconstructed on the reference layer using two different geometries. The first uses the extrapolation of the track back to the first layer. This resembles closely the case of track extrapolation from the vertex detector to the interaction point. Using all accepted tracks we measure a residual of $(9.4 \pm 0.2) \mu\text{m}$ (see Figure 2), which becomes $(8.9 \pm 0.4) \mu\text{m}$ when restricting to three-hit tracks. This should

be compared to $6.8 \mu\text{m}$ obtained from the simulation, which assumes perfect geometry. Subtracting in quadrature the estimated single point resolution of $x \mu\text{m}$, we obtain an extrapolation resolution of $8.5 \mu\text{m}$ for a 1.5 GeV particle, which is consistent with the impact parameter resolution required for the ILC. The second geometry adopted extrapolates the track on the second detector layer. In this case the multiple scattering effect is reduced by having measurements on both side of the extrapolation plane and we measure a residual of $(6.9 \pm 0.1) \mu\text{m}$.

Despite the multiple scattering effect, the extrapolation resolution of the TPPT at the ALS is significantly smaller than the MIMOSA-5 pixel pitch. This allows to perform studies

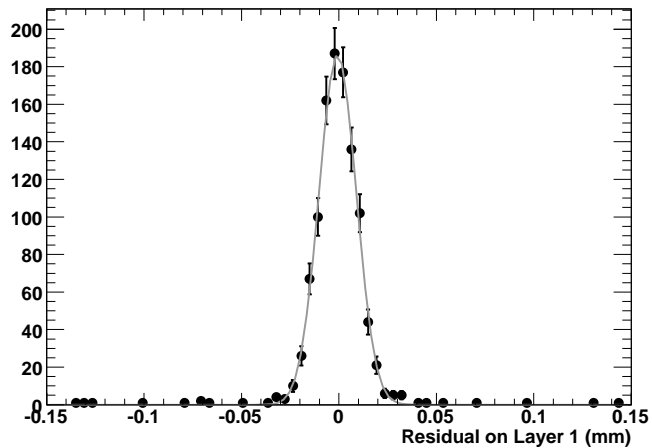


Figure 2: Residual on the vertical coordinate between the extrapolated track position on TPPT first layer and the associated hit reconstructed coordinate. The fitted Gaussian curve has a width of $9.4 \mu\text{m}$.

of cluster shape as a function of the track point of impact. We compared the number of pixels, along the horizontal coordinate, in clusters reconstructed on the first layer which are associated to two sets of tracks. In the first set tracks with extrapolation along the x horizontal axis within $4\ \mu\text{m}$ from the pixel centre are chosen: the average pixel multiplicity is 1.5. In the second set the track intercepts the detector more than $8\ \mu\text{m}$ away from the pixel centre: the average pixel multiplicity increases to 2.3.

3 The T-966 Telescope

A second thin pixel telescope (TPPT-2) has been built for use in the T-966 beam test experiment of the 120 GeV proton beam at the Fermilab MTest facility. The TPPT-2 consists of four layers of $50\ \mu\text{m}$ -thin MIMOSA-5 sensors mounted on new mezzanine cards with low profile components and larger clear region in the PC board below chip. The four layers are mounted using precision mechanics and are spaced by 15 mm. The chips have been positioned on the mezzanine boards using a precision vacuum chuck which gives a mounting accuracy better than $50\ \mu\text{m}$. Downstream from the TPPT-2, a detector under test (DUT) can be mounted on a computer-controlled XY stage which allows to remotely align it to the telescope. The DUT spacing from the TPPT-2 can be varied from 5 mm to 20 mm. The TPPT-2 has been tested in May 2007 on a 1.23 GeV e^- beam extracted from the ALS. An average S/N of 15.5 has been measured operating at 27°C . For the first T-966 data taking, planned for July and August 2007, an operating temperature of 20°C is foreseen, which will reduce the noise.

Acknowledgements

This work was supported by the Director, Office of Science, of the U.S. Department of Energy under Contract No.DE-AC02-05CH11231 and used resources of the National Energy Research Scientific Computing Center, supported under Contract No.DE-AC03-76SF00098. We are indebted to the staff of the LBNL Advanced Light Source for their help and the excellent performance of the machine.

References

- [1] M. Battaglia, D. Contarato, P. Giubilato, L. Greiner, L. Glesener and B. Hooberman, Nucl. Instrum. Meth. A **579** (2007) 675 [arXiv:physics/0611081].
- [2] S. Stanic *et al.*, Nucl. Instrum. Meth. A **568** (2006) 181.
- [3] M. Trimpl *et al.*, Nucl. Instrum. Meth. A **568** (2006) 201.
- [4] Yu. Gornushkin *et al.*, Nucl. Instrum. and Meth. A **513** (2003), 291.
- [5] G. Deptuch, Nucl. Instrum. and Meth. , A **543** (2005) 537.
- [6] F. Gaede, Nucl. Instrum. Meth. A **559** (2006) 177.
- [7] S. Agostinelli *et al.*, Nucl. Instrum. Meth. A **506** (2003), 250.
- [8] M. Battaglia, Nucl. Instrum. Meth. A **572** (2007) 274.
- [9] G. Lutz, Nucl. Instrum. Meth. A **273** (1988) 349.

Status of the development of MIMOSA CMOS sensors

A.Besson¹, M.Winter¹

on behalf of

DAPNIA - Saclay, LPSC - Grenoble, LPC - Clermont, DESY - Hamburg, Uni. Hamburg,
JINR - Dubna, IPN - Lyon, Uni.Frankfurt, GSI - Darmstadt, STAR coll. (LBNL, BNL).

1- IPHC/CNRS - DRS and Université Louis Pasteur
23 rue du Loess, BP28 F-67037 Strasbourg cedex 2 - France

This article provides a summary of the R & D activities on MIMOSA Monolithic Active Pixel Sensors. The performances and progress achieved with the fast readout architecture developed for the inner layers of the ILC-vertex detector are reviewed, complemented with a roadmap for the upcoming 2-3 years.

1 Introduction

CMOS sensors are developed for several years in order to achieve high performance in charged particle tracking[1][2]. One will review the main R&D activities driven by the ILC vertex detector (VD) constraints, requiring fast read-out, high granularity, low material budget, good radiation tolerance and moderate power dissipation.

The paper starts with an overview of the VD requirements, reminding that safety factors have to be attached to the simulated beam background rates governing the running conditions in the inner layers. Next, some major established performances of the MIMOSA sensors are recalled. The present R&D activity concentrates on the simultaneous development of fast pixel arrays with discriminated outputs, 4-5 bit ADCs and sparsification micro-circuits. Their status is briefly exposed, followed by their major next steps. The short and mid-term outcomes of this R&D program will meet the requirements of other, less demanding, applications (EUDET telescope[3], STAR HFT[4]), which will provide opportunities to operate large sets of sensors in real experimental conditions. More details on this vast R&D activity may be found in [5].

2 ILC requirements and vertex detector design

The main constraint driving the VD design comes from the beam background (beamstrahlung) which is expected to produce $\simeq 5 \text{ hits/cm}^2/\text{Bunch}$ crossing in the inner most layer, assuming a radius of 1.5 cm and a 4T magnetic field at $\sqrt{s} = 500 \text{ GeV}$. Accounting for a safety factor of 3 and a cluster multiplicity of 5-10, a read-out time of $\lesssim 25 \mu\text{s}$ was chosen to keep the occupancy at the per-cent level. This fast read-out time is achieved with sensors organised in short pixel columns perpendicular to the beam axes, read out in parallel. A 4-5 bit ADC integrated at the end of each column encodes the charge. The edge of the sensor hosts sparsification micro-circuits allowing to reduce the data flow. The VD equipped with such sensors will feature 5-6 cylindrical layers, $\sim 300\text{-}500$ million pixels, covering a total surface of $\sim 3000\text{-}4000 \text{ cm}^2$. The pixel pitch ranges from 20 to 40 μm , depending on the layer. A first complete ladder prototype is expected by 2010.

3 Review on CMOS sensors performances

Excellent particle tracking performances were repeatedly obtained with numerous small MIMOSA prototypes featuring analog outputs. The best performing fabrication technology found up to now (AMS 0.35 μm -OPTO), allows for a detection efficiency $\gtrsim 99.9\%$, a signal-to-noise ratio (SNR) of $\sim 20 - 30$ (fig.1) and a fake hit rate of $\lesssim O(10^{-5})$, at an operating temperature of up to 40°C . These performances were reproduced with real size sensors. One of them, MIMOSA-17 (256×256 pixels, $30 \mu\text{m}$ pitch), equips the demonstrator of the EUDET telescope.

The spatial resolution reaches $\simeq 1.5\mu\text{m}$ with a $20\mu\text{m}$ pitch and a 12-bit charge encoding (fig.2). The same data were used to show that encoding the charge on a compact 4-5 bit ADC integrated on the sensor edge would still allow for $\simeq 2\mu\text{m}$ single point resolution.

Radiation hardness has also been studied extensively. In particular, the MIMOSA-15 prototype, which features radiation tolerant pixels, was irradiated with 1 MeV neutrons and 10 keV X-rays. Both for a fluence of $\sim 10^{12} n_{eq}/\text{cm}^2$ and for an integrated dose of 1 Mrad, a SNR $\gtrsim 20$ and an efficiency $\gtrsim 99.5\%$ were observed at -20°C . Irradiation tests were also performed with 10 MeV e^- which are still to be completed. As a preliminary conclusion, at least 3 years of ILC running should be viable close at room temperature[6]. Performances of sensors featuring integrated single processing remain however to be evaluated.

4 Fast read-out architectures and integrated ADC

The MIMOSA-8 prototype[7], which features pixels with integrated CDS, organized in parallel columns ended with discriminators, has allowed to validate the fast architecture needed for the inner layers. A satisfactory charged particle detection was observed despite the thin epitaxial layer of the fabrication technology (TSMC $0.25 \mu\text{m}$), leading to a modest SNR.

The MIMOSA-8 architecture was translated in AMS 0.35 μm -OPTO technology, which features a thicker epitaxial layer. The sensor, called MIMOSA-16, was tested at the CERN-SPS. Preliminary results show a detection efficiency of $\gtrsim 99.8 \pm 0.2\%$ for a fake rate of $\lesssim 10^{-5}$ and a spatial resolution of $\sim 5 - 6\mu\text{m}$ despite the $25\mu\text{m}$ pitch. In parallel, the first zero

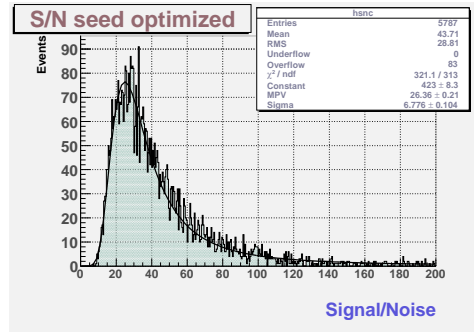


Figure 1: SNR measured at the CERN-SPS with MIMOSA-9, ($20 \mu\text{m}$ pitch) at $T = 20^\circ\text{C}$.

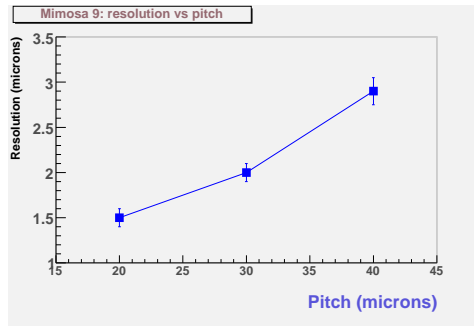


Figure 2: Single point resolution measured at the CERN-SPS with MIMOSA-9 (three pitch values: 20, 30 and $40 \mu\text{m}$)

suppression prototype (SUZE-1), foreseen to complement the MIMOSA-16 architecture, has been designed and will come back from foundry in October 2007. Finally, several laboratories are developing various 4-5 bits ADC architectures (semi-flash, flash, SAR, Wilkinson). Based on the results obtained with the prototypes tested up to now, a first mature ADC design is expected in 2008.

5 Roadmap

Here is a summary of the different prototypes foreseen in the period \sim 2007-2009:

- SUZE-01: zero suppression micro-circuit, back from foundry in October 2007;
- MIMOSA-22: extension of MIMOSA-16, $18.4 \mu\text{m}$ pitch, $(128+8) \times 576$ pixels, submission in October 2007,
- PHASE-1: extension of MIMOSA-22 with 640×640 pixels, $30 \mu\text{m}$ pitch, $2 \times 2 \text{ cm}^2$, for STAR HFT, submission in June 2008;
- ADC: integrated on pixel matrix, submission by Summer 2008;
- MIMOSA-22+: combination of MIMOSA-22 and SUZE-01, $1088 \times 544/576$ pixels, $1 \times 2 \text{ cm}^2$, final chip for EUDET telescope project, submission by Autumn 2008;
- ADC and zero suppression micro-circuit in the single chip : 2009.

6 Conclusion

MIMOSA sensors offer very attractive performances in terms of SNR, detection efficiency, spatial resolution and radiation tolerance for their application at the ILC vertex detector. They are however not yet adapted to the read-out speed required to cope with the expected beam background. Intense R&D is thus invested in achieving fast sensors with integrated analog-to-digital conversion and data sparsification. Encouraging results were obtained with a prototype composed of columns read out in parallel and ended with integrated discriminators. The development of ADCs foreseen to replace the discriminators and of zero suppression micro-circuits are also progressing well.

In the mid-term, sensors developed for the VD will equip less demanding devices (EUDET beam telescope, STAR HFT), which will allow to investigate how large sets of sensors can be operated in real experimental conditions and which added value they bring to charmed meson reconstruction.

References

- [1] Slides:
<http://ilcagenda.linearcollider.org/contributionDisplay.py?contribId=304&sessionId=74&confId=1296>
- [2] R. Turchetta et al., Nucl. Inst. Meth. **A458** 677 (2001);
- [3] EUDET home page: <http://www-zeus.desy.de/~haas/eudet-jra1/>
- [4] J.Thomas, talk at Int. Conf. on Strangeness in Quark Matter, Los Angeles (USA), March 2006;
- [5] M.Winter et al., DESY PRC reports R&D Nr 01/04 (2003, 2005 and 2007),
<http://www.iphc.cnrs.fr/Others,116.html>;
- [6] W.Dulinski et al., IEEE-Transactions on Nuclear Science (2007), 54-284;
A.Besson et al., Nucl. Inst. Meth. **A572** 300 (2007);
IPHC web site : <http://www.iphc.cnrs.fr/-CMOS-ILC-.html>;
- [7] Y. Degerli et al., IEEE Trans. on Nucl. Science, Vol.52, n°6, December 2005, pp. 3186-3193

Development of an ILC Vertex Detector Sensor with Single Bunch Crossing Tagging[1]

J.E. Brau, N. Sinev, D. Strom,
University of Oregon - Center for High Energy Physics
Eugene, OR USA 97403-1274

C. Baltay, W. Emmet, D. Rabinowitz.
Yale University - Physics Department
New Haven, CT USA 06520-8120 *

The hit density for an ILC vertex detector requires multiple hit capability within a bunch train. The ideal performance would be to associate uniquely each hit with a specific bunch crossing within the bunch train. We are developing a CMOS sensor with this capability, providing a four deep buffer per pixel to accumulate hit times during the one millisecond bunch train. The design of first prototypes for this sensor has been completed, with two buffers in $50\ \mu\text{m} \times 50\ \mu\text{m}$ pixels, and devices are expected to be produced during the coming year based on $0.18\ \mu\text{m}$ technology. The 4 deep buffer, with $\sim 10\ \mu\text{m}$ pixel sensors are planned in a later step with $45\ \text{nm}$ technology.

1 Introduction

A pixel vertex detector is a powerful tool for ILC experiments, capable of independent track reconstruction, as demonstrated by the 307 Mpixel CCD vertex detector at SLD.[2] The time structure of the ILC necessitates an extremely fast readout of the vertex detector elements. Monolithic CMOS pixel detectors that allow extremely fast non-sequential readout of only hit pixels have advantages over CCDs. We have initiated an R&D effort to develop such devices having time stamps with single bunch crossing precision for each hit. These "Chronopixel" detectors thereby significantly reduce the effective backgrounds relative to a sensor that integrates over many bunch crossings.

The ILC offers a unique environment in which to achieve exceptional physics goals due to the modest event rates, relative rates of background to signal, and relatively low radiation levels. Precision measurements of the branching ratios for many of the Higgs decay modes is a primary goal, and superb flavor tagging is needed to achieve this. The goal for the impact parameter resolution is $5\ \mu\text{m} \oplus 10\ \mu\text{m}/(p \sin^{3/2}\theta)$, requiring spacepoint precision of better than $4\ \mu\text{m}$. The transparency requirement is $\sim 0.1\%$ X_0 per layer. The $3.9\ \mu\text{m}$ spacepoint precision and 0.4% X_0 transparency of SLD encourages this goal.

2 Operational Constraints

The baseline time structure of the ILC results from bunchtrains of 2820 bunches spaced 337 nanoseconds, passing through the collider hall 5 times a second. Consequently, each bunch train is about 1 msec long, with about 200 msec between bunch trains.

In general, the requirements for the sensor are:

1. Good angular coverage with several layers close to the interaction point;

*This work is supported by the U.S. Department of Energy through the Linear Collider Detector R&D (LCDRD) grant.

2. Excellent spacepoint precision ($< 4 \mu\text{m}$);
3. Superb impact parameter resolution;
4. Transparency ($\sim 0.1\% X_0$ per layer);
5. Track reconstruction (in VXD alone);
6. Low occupancy ($< 10^{-3}$ hits/pixel);
7. EMI immunity; and
8. Power constraint (< 100 Watts for the entire vertex detector).

3 Progress on Monolithic CMOS Pixel Detector Design

During the past three years a conceptual design for a monolithic CMOS device that should meet the ILC vertex detector requirements has been developed by Oregon and Yale in collaboration with the Sarnoff Corporation[3] through an R&D contract. In this design each pixel (smaller than $15 \mu\text{m} \times 15 \mu\text{m}$) contains electronics to store the bunch number (time) of up to four hits above an adjustable threshold (thus “Chronopixels”). Hits are read out during the 199 msec between bunch trains. The pixels can achieve up to 3 to 4 micron precision without analog information. A simplified schematic of the in channel electronics design is shown in Figure 1.

3.1 General Description of the Design

The system design includes sensors up to $12.5 \text{ cm} \times 2.2 \text{ cm}$ with $10 \mu\text{m} \times 10 \mu\text{m}$ pixels. This is achieved with pixel electronics within each pixel area, on the same piece of silicon (monolithic CMOS) thinned to a thickness of 50 to $100 \mu\text{m}$. The electronics for each pixel records hits above an adjustable threshold. The time of each hit is stored in each pixel, up to a total of four hit times per pixel, with single bunch crossing precision (thus the name “Chronopixels” for this device). Hits will accumulate for the 2820 bunch crossings of a bunch train and the sensor is read out during the 200 msec between bunch trains. Only the coordinates (x,y,t) for hit pixels are read out. With 10 micron size pixels analog information is not needed to reach a 3 to 4 micron precision; only digital readout is planned, considerably simplifying the electronics.

Extensive background calculations[4] indicate that the maximum total hit rate in the innermost layer of the vertex detector will be $0.03 \text{ hits/mm}^2/\text{bunch crossing}$. With 2500 mm^2 per sensor (a total of 25×10^6 pixels) and 2820 bunch crossings per train we expect 2×10^5 hits/sensor/bunch train, or an occupancy of the order of one percent in these inner layers. This appears much too high to allow efficient pattern recognition. The crucial element of our design is the availability of the time information (i.e., bunch crossing number) with each hit. An event of interest at a known time in a subsystem, such as the tracker or calorimeter, are associated with vertex detector hits in time, and the occupancy is $< 10^{-5}$ per pixel (SLD worked well with a vertex detector occupancy of 10^{-3} per pixel).

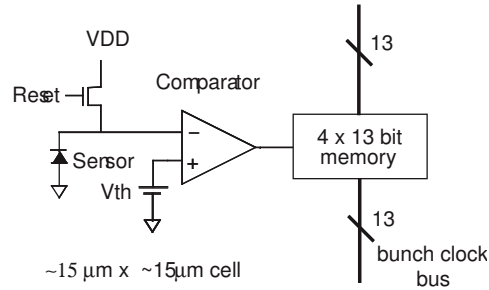


Figure 1: Pixel Architecture

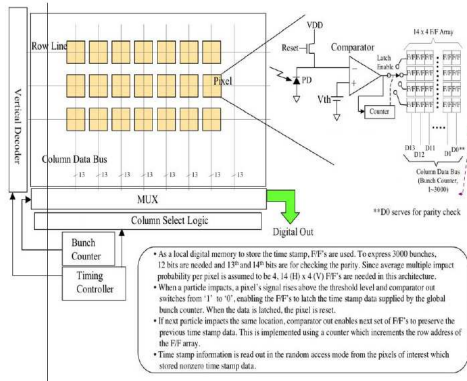


Figure 2: Chronopixel Array Architecture

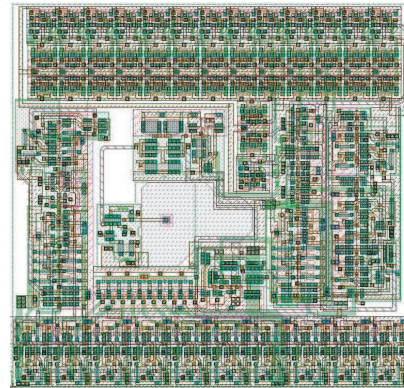


Figure 3: Image of the 645 transistor pixel design

3.2 Detailed Design

SARNOFF has designed the electronics under each pixel of the Chronopixel array, shown schematically in Figure 2. The functionality of this design has been verified by an hspice simulation.

The analog components of the circuit (the boxes labeled Detector and Comparator on Figure 2) are estimated to consume most of the power, ~ 15 milliwatts/mm². The remaining digital components are estimated to be around 0.05 milliwatts/mm². The analog components are only needed during the time when hits are accumulated during the bunch train, ~ 1 msec. The average power can thus be reduced by a factor of ~ 100 by turning off the analog parts during the 200 msec digital readout. This reduces the average power consumption to the vicinity of 0.5 watts per sensor or to the order of 100 watts for the vertex detector, which seems acceptable.

During the last year Sarnoff completed the design of the first prototype device. Using a TSMC 0.18 micron process they were able fit the circuitry needed for each pixel into a area slightly larger than 50μ by 50μ . An image of this design is shown in Figure 3. This design is complete and is awaiting LCDRD funding for production. As the purpose of the design is to test the pixel circuitry, the pixel has been designed to use a standard TSMC process and will not be active over the entire 50μ by 50μ area.

The circuitry in the pixels has been carefully designed to be scalable to smaller features sizes. To achieve a pixel that is $\sim 10 \mu$ by $\sim 10 \mu$ a smaller feature size CMOS, e.g. 45nm, will be used.

We produced a detailed simulation of the pixel active area and has investigated the ultimate pixel geometry which will need a process with a smaller feature size than 0.18 microns, a thick epitaxial layer and a deep-p well. As this will eventually require an expensive custom processes, we are presently concentrating on a proof of concept run with a standard

TSMC process.

3.3 Discussion

Readout Scheme Each sensor will consist of 2000 columns with 12500 pixels per column, divided into 40 readout regions of 50 columns each. At the end of the bunch train, when the electromagnetic interference due to the beam has died off, the 40 regions will be read out in parallel at 25 MHz into a FIFO buffer located at the end of each sensor. The contents of the FIFO buffer will be read out at 1 GHz. We thus expect to read out the full sensor (2×10^5 hits, with 38 bits per hit) in about 8 msec. This leaves a safety margin of 25 with the 200 msec gap between trains.

Charge Spreading. In order to optimize digital readout, charge spreading should be contained within the pixel volume. This is accomplished by maximizing the depletion depth, and benefiting from the effects of small stray fields extending into the undepleted region. The design depletes the charge sensitive epitaxial layer to the maximum extent possible. Employing the highest feasible silicon resistivity is important. Our detailed simulations of the chronopixel design indicate that full depletion of the epilayer is not possible. We will rely on the field extension into deep portions of the epilayer volume to constrain the drift of charge. Our simulations model this field, and the resulting drift.

Charge Statistics and Read Noise. A Monte Carlo calculation indicates that a 1 GeV pion at normal incidence has a most probable yield of 800 electrons for a 15 micron thick charge sensitive epitaxial layer.[5] The designed read noise is 25 electrons; if this is achieved in the prototype, it comfortably achieves the required signal to noise for high efficiency particle detection with low backgrounds. Two strategies are employed to achieve this low noise performance. A soft reset[6] is used, as well as a negative feedback circuit.

References

- [1] Slides:
<http://ilcagenda.linearcollider.org/contributionDisplay.py?contribId=305&sessionId=74&confId=1296>
- [2] K. Abe, et al., Nucl. Instrum. Meth. A400 (1997) 287.
- [3] Sarnoff Corporation, Princeton, NJ 08540-6449.
- [4] Takashi Maruyama, Backgrounds, 2005 ALCPG and ILC Workshop, ALCPG 0909.
- [5] Su Dong, Private Communication.
- [6] R. Turchetta, et al., Nucl. Instrum. Meth. A560 (2006) 139-142.

A pixelated Telescope for the E.U Detector R&D

Daniel Haas (Daniel.Haas@cern.ch) *

Université de Genève - Département de Physique Nucléaire et Corpusculaire
24, quai Ernest-Ansermet, 1211 Genève 4 - Switzerland

A beam telescope with up to six sensor planes based on monolithic active pixel sensors is currently constructed and evaluated within the EUDET collaboration. The telescope is lightweight, moveable and can be operated in magnetic fields of up to 1.2 T. It provides a convenient test environment for a wide variety of pixelated sensor technologies and can be used as a realistic test bed for tracking studies for a vertex detector at a future linear collider.

1 Introduction to EUDET

EUDET [2] is a project supported by the European Union in the 6th Framework Programme [3] structuring the European Research Area. The project comprises 31 European partner institutes from twelve different countries working in the field of High Energy Physics. In addition, over twenty associated institutes will contribute to and exploit the EUDET research infrastructure which the aim to support the detector R&D in Europe for the next large particle project, the International Linear Collider. The EUDET collaboration will provide test beam infrastructure, including a 1 Tesla solenoid magnet and a high resolution beam telescope as well as infrastructure for tracking detectors and calorimeters.

2 Requirements of the pixel telescope

The pixel telescope consists of a mechanical support structure, the sensor planes and a dedicated readout chain. It has to be used for a wide range of R&D activities and different devices under test (DUT), ranging in size from a few millimeters up to one meter. Its resolution should be high ($<4 \mu\text{m}$) even at low energies of a few GeV/c, like at DESY. This can be achieved providing sensors with individual plane resolutions of 2-3 μm or better and careful optimization of the telescope geometry. The lateral dimensions of the sensors should support the readout of high precision pixel devices without mechanical movement of the DUT. A minimum size of 20 mm is adequate for this. For larger structures, scanning of the DUT using mechanical actuators will be provided. The readout speed of the telescope should take advantage of testbeam environments and achieve around 1 kHz.

2.1 Pixel sensor

As mentioned before, the sensors for the telescope have to provide single point resolutions of 2 to 3 μm with a minimum of material and a reasonable size. R&D towards an ILC vertex detector is actively pursued on a number of different sensor technologies such as CCD [4], DEPFET [5] and CMOS [6] sensors. The EUDET collaboration will use sensors derived from the MIMOSA-5 [7] chip by CNRS/IRES Strasbourg.

*For the EUDET Collaboration

The initial MIMOTEL sensor shown in Figure 1 will provide 256 x 256 pixels with a 30 μm pitch and an active area of 7.6 x 7.6 mm^2 . A thinned down version of the MIMOTEL will be available as well in a next step. Also a high resolution tracker sensor (HRT) with 512 x 512 pixels, 10 μm pitch on an active area of 5 x 5 mm^2 with a single point resolution of about 1 μm is available. By the end of 2008, the 'final' sensor for the EUDET pixel telescope should be available. It will be based on the MIMOSA-22+ technology, providing integrated zero suppression, column parallel readout, 1088 columns of 576 pixels on 20.0 x 10.5 mm^2 , a readout time of around 100 μs and a thinned sensor.

2.2 Mechanics

Depending on the application of the beam telescope, different setups of the sensor planes need to be foreseen and the mechanical support structure has to provide a flexible solution. The mechanics will allow the usage of the telescope in different scenarios: A compact setup, with the telescope planes very close to the DUT, allowing the characterisation of a high precision device. The compact scenario can also be used inside a magnetic field. In addition, the telescope can be split up in a 2-arm geometry, with up to 3 sensors in front and up to 3 sensors behind larger structures. Lightweight DUTs can also be put on a moving table, allowing scanning of the device with high precision within the pixel telescope. The mechanics also provides cooling to the pixel sensors.

2.3 Data acquisition

The data of the pixel sensors is acquired via a dedicated readout board, the EUDET data reduction board (EUDRB) [8], situated in a VME64x crate.

Data acquired on the EUDRBs will be collected by an MVME6100 CPU on the VME and send to the central data acquisition system. The synchronization with the DUT is done via a dedicated trigger logic unit (TLU), designed by the University of Bristol for EUDET. The unit allows a simple trigger/busy/reset communication with the DUT, but also a more advanced mode, tagging events via a distributed event number. In such a way, users of the pixel telescope can choose their level of integration in the global DAQ scheme. They can run either completely independent, synchronizing only via a standard trigger/busy logic or they can use the provided event number for enhanced data synchronization. Even a full integration in the EUDET DAQ is possible. Sample producer tasks to do this are provided. Data taken is stored locally, but then converted to lcio format on the GRID for easy analysis and compatibility within the ILC software framework.

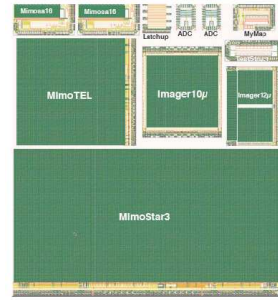


Figure 1: The MIMOTEL sensor (left) and the HRT imager sensor (center).



Figure 2: The demonstrator at the DESY testbeam.

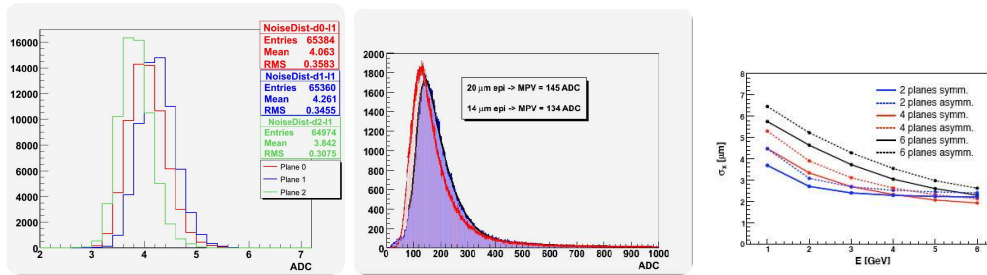


Figure 3: Noise (left) and cluster (middle) profile measurements of the demonstrator telescope. Right: Expected resolutions for different telescope geometries.

2.4 'Demonstrator' telescope

In the summer 2007, the 'demonstrator' telescope will be evaluated in different testbeams at DESY and CERN. The demonstrator will run with 3 to 6 planes and serve as a proof of concept. A first test has been performed already at DESY just after the end of the LCWS, using a 3 plane telescope as shown in Figure 2 and the full system has been proven to work.

3 Performance evaluation

Preliminary results of the demonstrator are shown in Figure 3 and show noise distributions on the sensors as well as the cluster profile for sensors with different epitaxial layers. The noise per plane is around 4 ADC counts and the most probably value for 3x3 signal clusters around 140 ADC counts. Further studies of the telescope are still ongoing to measure the resolution of the telescope as expected from simulations.

4 Summary

A first version of the EUDET pixel telescope is currently being evaluated and has been proven to work. First users of the telescope are expected by the end of this summer. The final version of the telescope with increased performance will be available in 2009. Interested parties are welcome to contact the EUDET collaboration for the exploitation of the device.

References

- [1] Slides:
<http://ilcagenda.linearcollider.org/contributionDisplay.py?contribId=306&sessionId=74&confId=1296>
- [2] <http://www.eudet.org>
- [3] <http://europa.eu.int/comm/research/fp6>
- [4] K.D. Stefanov, *CCD Vertex Detector for the Future LC*, Nucl. Instrum. Meth. **A 501** (2003) 245.
- [5] P. Fischer *et al.*, *Readout concepts for DEPFET pixel arrays*, Nucl. Instrum. Meth. **A 512** (2003) 318.
- [6] R. Turchetta *et al.*, *A monolithic active pixel sensor for charged particle tracking and imaging using standard VLSI CMOS technology*, Nucl. Instrum. Meth. **A 458** (2001) 677.
- [7] Y. Gornushkin *et al.*, *Tracking performance and radiation tolerance of monolithic active pixel sensors*, Nucl. Instrum. Meth. **A 512** (2003) 299.
- [8] C. Bozzi, *The data reduction board of the EUDET pixel telescope*, in these proceedings.

Study of SOI, 3D and Laser Annealing as Candidate Technologies for the ILC

Selcuk Cihangir¹

1 – Fermi National Accelerator Laboratory
Batavia, Illinois, USA

We have been studying SOI (Silicon On Insulator) and 3D technologies for integration of sensors and electronics as candidates for the ILC vertex detector. We have also been investigating laser annealing and its usage to form the ohmic contact at the backside of thinned sensor wafers. We will summarize these studies and present measurement results qualifying feasibility of these technologies at ILC.

1 Introduction

SOI consists of a thin silicon circuit layer over an insulator, usually SiO₂, placed on a “handle” wafer. The result is the suppression of bottom junction which leads to lower parasitic capacitance enabling faster switching and operation with lower power consumption. This, in turn, makes it possible to have denser layouts, operation at higher temperatures (250°C) with lower SEU (Single Event Upset) rate.

The technology has application in fields such as high speed processors (AMD Athlon-64), graphic processors (Play Station 3), high-speed serial data communications, ultra low power solar cells, satellite systems, spacecraft electronics and high energy physics (HEP). The handle wafer in SOI can be high resistivity silicon, making integration of detector and electronics possible.

The Fermilab group has initiatives in the following areas:

- Thinned, edgeless sensors
- Chip fabricated in OKI 0.15 μm SOI process, includes sensor and one layer of electronics for electron microscope
- Chip being designed in American Semiconductor 0.18 μm SOI process with pixel sensor layer and one or more electronics layers for ILC vertex detector
- 3D chip (VIP1) being fabricated in MIT LL 0.18 μm SOI multi-project run, a 3 tier demonstrator chip for ILC vertex detector
- Bonding Technologies being explored, such as Cu-Sn bonding of FPIX chips/sensors and DBI bonding of 3D chips to MIT sensors
- Laser annealing
- Simulations

2 SOI Concept for HEP

The SOI chip is formed by a high resistivity silicon handle wafer, thinned to 50-100 microns (fully depletable with large signal) separated from the transistor layer by a layer of Buried Oxide (BOX), as shown in Figure 1. The edges are activated and the back of the substrate has an Ohmic contact. The backside is implanted and laser annealed after thinning. SOI provides the possibility of monolithic fabrication of detectors and electronics, with low mode capacitance, full depletion and no parasitic charge collection as in CMOS MAPs.

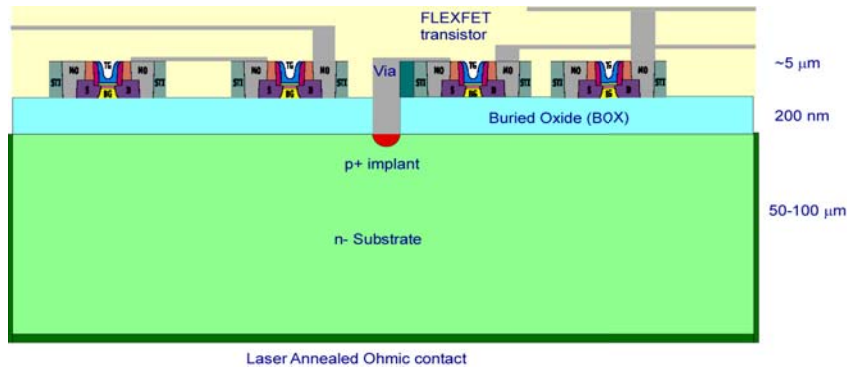


Figure 1: Schematic view of a SOI detector.

2.1 OKI 0.15 μm SOI process Mambo X-Ray Chip

Fermilab has submitted a design to a KEK sponsored multi project run at OKI which incorporates diode formation by implantation through a via formed in the BOX. The chip incorporates a 64 x 64 26 micron pitch, 12 bit counter array for a high dynamic range x-ray or electron microscope imaging. Maximum 13 μm implant pitch is determined by the “back gate” effect where the topside transistors thresholds are shifted by handle potential. It is 350 micron thick. We just received this chip and will test it at a laser test stand.

2.2 American Semiconductor 0.18 μm SOI process Flexfet Chip

Fermilab designed for American Semiconductor Company a demonstration SOI pixel cell with voltage ramp for time marker, sampling for crossing time, analog pulse height and counter for timestamp. All these features are simulated beforehand. Transistors in this chip have two gates. In addition to the conventional top gate, a bottom gate shields the transistor channel from charge buildup in the BOX caused by radiation, as well as from the voltage on the substrate and removes the “Back Gate Voltage” problem. Optimization is on-going on this chip and it is to be tested. Also, possibility of a pinning layer to shield the analog pixel from digital activity is considered.

2.3 VIP1 Chip

The goal of this chip, shown in Figure 2, which is being fabricated in MIT LL 0.18 μm SOI multi-project run, is to demonstrate the ability to implement a complex pixel design with all required ILC properties in a 20 micron square pixel. It is a three dimensional (vertical) integration of electronics and sensors, reducing R, L, C for higher speed, reducing chip I/O pads and providing increased functionality. Also, interconnects by through wafer via formation and metallization reduce the power and crosstalk.

Previous technologies limited to very simple circuitry or large pixels. This chip has three levels (also called tiers) of transistors, 11 levels of metal in a total vertical height of only 22 μm. Its key features are analog pulse height, sparse readout, and high resolution time stamps. Time stamping and sparse readout occur in the pixel. Hit address is found on array perimeter. It will be a 64 x 64 pixel demonstrator version of eventual 1K x 1K array. Edgeless sensor will be bonded to the chip later.

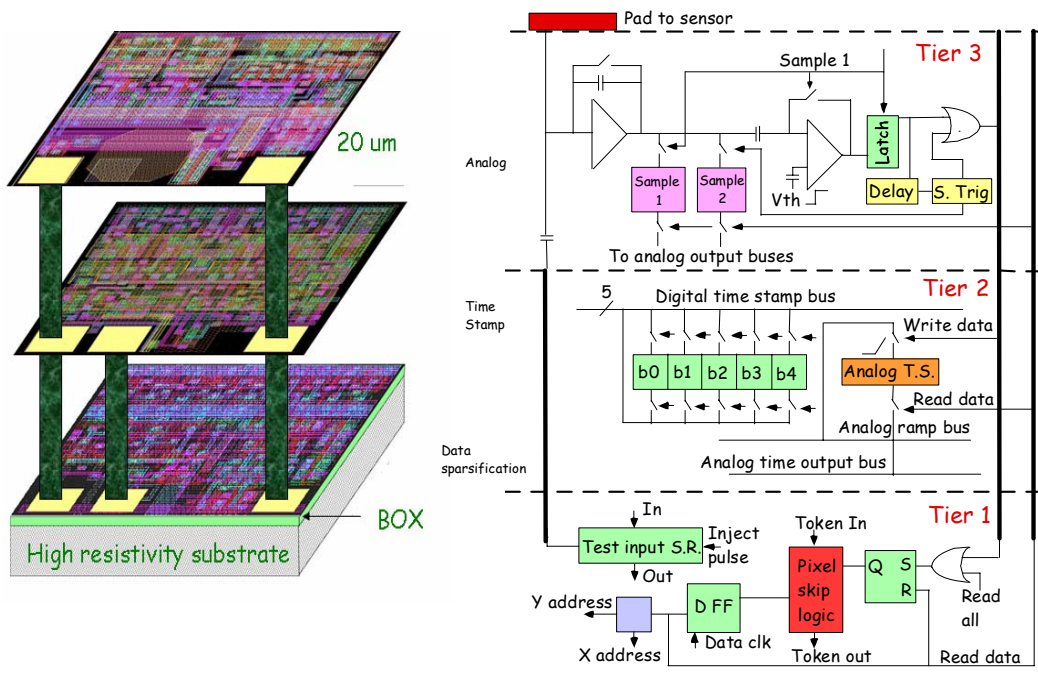


Figure 2: VIP1 Chip

2.4 Laser Annealing

After thinning a substrate, a backside contact must be formed. This is usually done by implantation and high temperature furnace annealing which will destroy the front side CMOS SOI circuitry. An alternative is the laser annealing of the backside implantation, which limits the front side temperature. Use of a raster scanned eximer laser melts the silicon locally. This activates the implant and repairs the implantation damage by recrystallizing the silicon. Diffusion time of phosphorus, the ohmic material, in molten silicon is much less than cooling time therefore we expect uniform distribution in melt region. This was demonstrated by SIMS (Secondary Ion Mass Spectroscopy) measurements which provided implant depth profiles by analysis of ions ejected from the surface upon ion bombardment.

3 Acknowledgements

The work presented here is a joint effort of groups from Fermilab, Bergamo, Cornell and Purdue. Slides can be viewed at:

<http://ilcagenda.linearcollider.org/contributionDisplay.py?contribId=309&sessionId=74&confId=1296>

Simulations of the Temperature Dependence of the Charge Transfer Inefficiency in a High-Speed CCD

André Sopczak*, on behalf of the LCFI collaboration

Lancaster University

Results of detailed simulations of the charge transfer inefficiency of a prototype serial readout CCD chip are reported. The effect of radiation damage on the chip operating in a particle detector at high frequency at a future accelerator is studied, specifically the creation of two electron trap levels, 0.17 eV and 0.44 eV below the bottom of the conduction band. Good agreement is found between simulations using the ISE-TCAD DESSIS program and an analytical model for the former level but not for the latter. Optimum operation is predicted to be at about 250 K where the effects of the traps is minimal; this being approximately independent of readout frequency in the range 7–50 MHz. The work has been carried out within the Linear Collider Flavour Identification (LCFI) collaboration in the context of the International Linear Collider (ILC) project.

1 Introduction

Particle physicists worldwide are working on the design of a high energy collider of electrons and positrons (the International Linear Collider or ILC) which could be operational sometime around 2019. Any experiment exploiting the ILC will require a high performance vertex detector to detect and measure short-lived particles, yet be tolerant to radiation damage for its anticipated lifetime. One candidate is a set of concentric cylinders of Charge-Coupled Devices (CCDs), read out at a frequency of around 50 MHz.

It is known that CCDs suffer from both surface and bulk radiation damage. However, when considering charge transfer losses in buried channel devices only bulk traps are important. These defects create energy levels between the conduction and valence band, hence electrons may be captured by these new levels. These electrons are also emitted back to the conduction band after a certain time.

It is usual to define a Charge Transfer Inefficiency (CTI), which is the fractional loss of charge after transfer across one pixel. An initial charge Q_0 after being transported across m pixels is reduced to $Q_m = Q_0(1 - \text{CTI})^m$. For CCD devices containing many pixels, CTI values around 10^{-5} are not negligible.

The CTI value depends on many parameters, some related to the trap characteristics such as: trap energy level, capture cross-section, and trap concentration (density). Operating conditions also affect the CTI as there is a strong temperature dependence on the trap emission rate and also a variation of the CTI with the readout frequency. Other factors are also relevant, for example the mean occupancy ratio of pixels (1% for a 50 MHz readout is assumed here), which influences the fraction of filled traps in the CCD transport region.

Previous studies have been reported in [1, 2, 3, 4, 5]. The novel features of this work are detailed 2D simulations using real device geometry without approximations for the charge storage volume and transport.

*Email: andre.sopczak@cern.ch

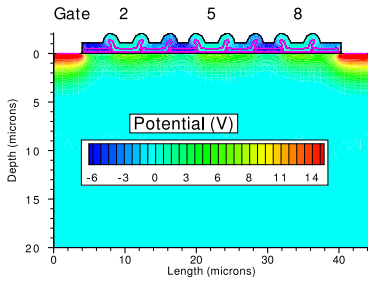


Figure 1: Detector structure and the potential under the gates after initialization. The signal charge is injected under gate 2 and is moved to the right. There are three gates for each pixel.

2 Simulations

The UK Linear Collider Flavour Identification (LCFI) collaboration [6, 7] has been studying a serial readout device produced by e2V Technologies, with a manufacturer’s designation ‘CCD58’. It is a 2.1 Mpixel, three-phase buried-channel CCD with $12\ \mu\text{m}$ square pixels.

Simulations of a simplified model of this device have been performed with the ISE-TCAD package (version 7.5), particularly the DESSIS program (Device Simulation for Smart Integrated Systems). It contains an input gate and an output gate^a, a substrate contact and nine further gates (numbered 1 to 9) which form the pixels. Each pixel consists of 3 gates but only one pixel is important for this study—gates 5, 6 and 7. The simulation is essentially two dimensional and assumes a $1\ \mu\text{m}$ device thickness (width) for calculating densities. Thus the model is equivalent to a short, thin slice of one column of CCD58 with rectangular pixels $12\ \mu\text{m}$ long by $1\ \mu\text{m}$ wide. The overall length and depth are $44\ \mu\text{m}$ and $20\ \mu\text{m}$ respectively (Fig. 1).

Parameters of interest are the readout frequency, up to 50 MHz, and the operating temperature between 120 K and 300 K although simulations have been done up to 500 K. The charge in transfer and the trapped charge are shown in Fig. 2.

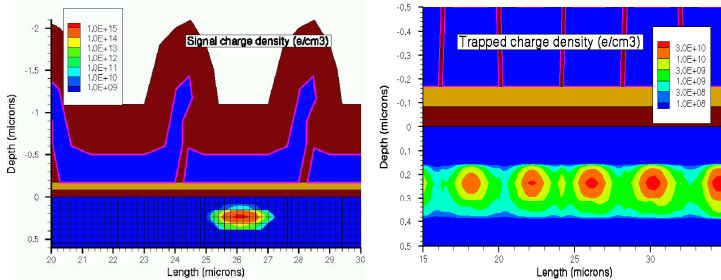


Figure 2: Left: signal charge density. The mesh size varies between 0.1 and 0.3 microns. During the analysis an integration under each gate is performed. Right: trapped charge density from transfer of signal charge at a time when the signal packet has passed under all

the gates. The trapped charge density decreases from the right to the left due to emission. The time the charge spends under the gates is much longer than the time spent in the gaps (which is of the order of a nanosecond), therefore the trapped charge density is much higher under the gates in comparison with the region between the gates. The legend box refers to the region with positive depth values. At negative depth values are an oxide layer, a nitride layer, polysilicon gates and finally an oxide layer. No metal is shown.

The signal charge used in the simulation is chosen to be similar to the charge generated by a minimum ionising particle (MIP), amounting to about 1620 electron-hole pairs^b for CCD58. DESSIS has a directive for generating heavy ions and this is exploited to create the charges. The heavy ion is made to travel in a downwards direction starting at $1.2\ \mu\text{m}$ below gate 2 at $1\ \mu\text{s}$ before charge transfer begins. This provides ample time for the electrons to be drawn upwards to the transport channel which is $0.25\ \mu\text{m}$ beneath the gate electrodes.

^aThese separate the area under study from the input drain and output diffusion pn junctions.

^bThis number has to be divided by 12 because the charge is assumed to be distributed over the whole pixel but the model has only 1/12th of the true pixel volume.

2.1 Calculating CTI

Charge Transfer Inefficiency is a measure of the fractional loss of charge from a signal packet as it is transferred over a pixel, or three gates. After DESSIS has simulated the transfer process, a 2D integration of the trapped charge density distribution is performed independently to give a total charge under each gate. The CTI for transfer over one gate is equivalent to $CTI = \frac{e_T - e_B}{e_S}$, where e_S = number of electrons in the signal packet, e_B = number of background trapped electrons prior to signal packet transfer, e_T = number of trapped electrons under the gate, after signal transfer across gate. In this way the CTI is normalised for each gate. The determinations of the trapped charge take place for gate n when the charge packet just arrives at gate $n + 1$. If the determination were made only when the packet has cleared all three gates of the pixel, trapped charge may have leaked out of the traps.^c

The total CTI (per pixel) is determined from gates 5, 6 and 7, hence $CTI = \sum_{n=5}^7 \frac{e_T - e_B}{e_S}$, where n is the gate number. The background charge is taken as the trapped charge under gate 1 because this gate is unaffected by the signal transport when the charge has just passed gates 5, 6 or 7.

2.2 0.17 eV and 0.44 eV traps

This CTI study, at nominal clock voltage, focuses only on the bulk traps with energies 0.17 eV and 0.44 eV below the bottom of the conduction band. These will be referred to simply as the 0.17 eV and 0.44 eV traps. An incident particle with sufficient energy is able to displace an atom from its lattice point leading eventually to a stable defect. These defects manifest themselves as energy levels between the conduction and valence band, in this case the energy levels 0.17 eV and 0.44 eV; hence electrons may be captured by these levels. The 0.17 eV trap is an oxygen vacancy defect, referred to as an A-centre defect. The 0.44 eV trap is a phosphorus-vacancy defect—an E-centre defect—that is, a result of the silicon being doped with phosphorus and a vacancy manifesting from the displacement of a silicon atom bonded with the phosphorus atom [2].

In order to determine the trap densities for use in simulations, a literature search on possible ILC radiation backgrounds and trap induction rates in silicon was undertaken. The main expected background arises from e^+e^- pairs with an average energy of 10 MeV and from neutrons (knocked out of nuclei by synchrotron radiation).

Table 1 shows results of background simulations of e^+e^- pairs generation for three proposed vertex detector designs (from three ILC detector concepts).

Simulator	SiD	LDC	GLD
CAIN/Jupiter	2.9	3.5	0.5
GuineaPig	2.3	3.0	2.0

Table 1: Simulated background results for three different detector scenarios. The values are hits per square centimetre per e^+e^- bunch crossing. SiD is the Silicon Detector Concept [8], LDC is the Large Detector Concept [9] and GLD is the Global Linear collider Detector [10].

Choosing the scenario with the highest expected background, that is the LDC concept, where the innermost layer of the vertex detector would be located 14 mm from the interaction point, one can estimate an e^+e^- flux around 3.5 hits/cm²/bunch crossing which gives a fluence of 0.5×10^{12} e/cm²/year. In the case of neutrons, from two independent studies, the fluence was estimated to be 10^{10} n/cm²/year [11] and 1.6×10^{10} n/cm²/year [12].

^cSince some of this leaked charge might rejoin the signal packet now under the next gate, this procedure may slightly overestimate the CTI.

Particle type	0.17 eV (cm ⁻³)	0.44 eV (cm ⁻³)
10 MeV e ⁻	3.0 × 10 ¹¹	3.0 × 10 ¹⁰
1 MeV n	(4.5...7.1) × 10 ⁸	(0.7...1.1) × 10 ¹⁰
total	3.0 × 10 ¹¹	4.1 × 10 ¹⁰

Table 2: Estimated densities of traps after irradiation for one year. For neutrons, the literature provides two values.

$E_t - E_c$ (eV)	Type	C (cm ⁻³)	σ (cm ²)
0.17	Acceptor	1 × 10 ¹¹	1 × 10 ⁻¹⁴
0.44	Acceptor	1 × 10 ¹¹	3 × 10 ⁻¹⁵

Table 3: Trap concentrations (densities) and electron capture cross-sections as used in the DESSIS simulations.

Based on the literature [13, 14, 15, 16, 17, 18, 19, 20, 21], the trap densities introduced by 1 MeV neutrons and 10 MeV electrons have been estimated with two established assumptions: the electron trap density is a linear function of dose, and the dose is a linear function of fluence. A summary is given in Table 2.

The actual trap concentrations and electron capture cross-sections used in the simulations are shown in Table 3.

2.3 Partially Filled Traps

Each electron trap in the semiconductor material can either be *empty* (holding no electron) or *full* (holding one electron). In order to simulate the normal operating conditions of CCD58, partial trap filling was employed in the simulation (which means that some traps are full and some are empty) because the device will transfer many charge packets during continuous operation.

In order to reflect this, even though only the transfer of a single charge packet was simulated, the following procedure was followed in all cases. During an initial 98 μ s period, the gates ramp up and all the traps are filled. The gates are biased in such a way so that charge moves to the output drain. The device is then in a fully normal biased state and corresponds to the situation of a charge packet having just passed through the pixel under investigation. Since another charge packet does not arrive immediately, a 2 μ s waiting time^d is introduced before readout clocking is started. During this period some of the traps become empty. The test charge is generated 1 μ s after the start of this waiting period so that 1 μ s, later when the waiting ends, there is a signal packet sitting under gate 2 just at the time when the three sinusoidally varying voltages (clock phases) are applied to cause the transfer of the produced signal charge packet through the device.

3 Simulation Results

The CTI dependence on temperature and readout frequency was explored.

3.1 0.17 eV traps

Figure 3 shows the CTI for simulations with partially filled 0.17 eV traps at different frequencies for temperatures between 123 K and 260 K, with a nominal clock voltage of 7 V.

^dThis waiting time corresponds to the mean time between the arrival of charge packets from a 1% mean pixel occupancy with a 50 MHz readout frequency and to larger values for lower frequencies.

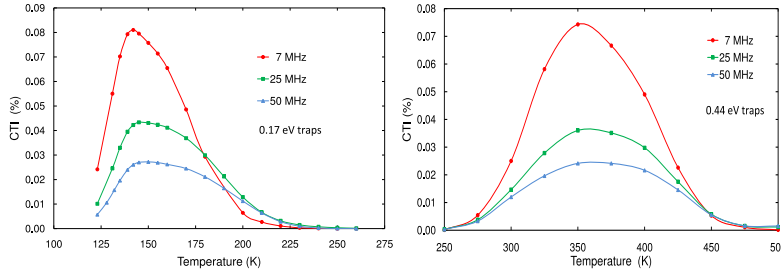


Figure 3: CTI values versus temperature for simulations with 0.17 eV (left) and 0.44 eV (right) partially filled traps at clocking frequencies 7, 25 and 50 MHz.

A peak structure can be seen. For 50 MHz, the peak is at 150 K with a CTI of 27×10^{-5} . The peak CTI is in the region between 145 K and 150 K for a 25 MHz clock frequency and with a value of about 43×10^{-5} . This is about 1.6 times bigger than the charge transfer inefficiency at 50 MHz. The peak CTI for 7 MHz occurs at about 142 K, with a maximum value of about 81×10^{-5} , an increase from the peak CTI at 50 MHz (27×10^{-5}) by a factor of about 3 and an increase from the peak CTI at 25 MHz (43×10^{-5}) by a factor of nearly 2. Thus CTI increases as frequency decreases. For higher readout frequency there is less time to trap the charge, thus the CTI is reduced. At high temperatures the emission time is so short that trapped charges rejoin the passing signal.

3.2 0.44 eV traps

Simulations were also carried out with partially filled 0.44 eV traps at temperatures ranging from 250 K to 500 K. This is because previous studies [5] on 0.44 eV traps have shown that these traps cause only a negligible CTI at temperatures lower than 250 K due to the long emission time and thus traps remain fully filled at lower temperatures. The results are also depicted in Fig. 3. The peak CTI is higher for lower frequencies with little temperature dependence of the peak position.

3.3 0.17 eV and 0.44 eV traps together

The logarithmic scale plot (Fig. 4) of the simulation results at the different frequencies and trap energies clearly identifies an optimal operating temperature of about 250 K.

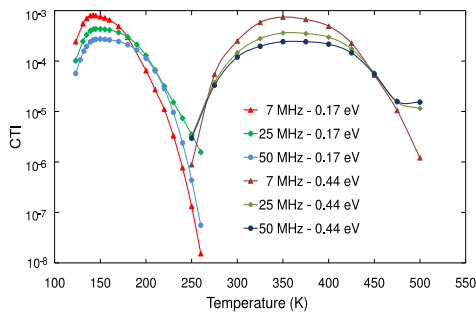


Figure 4: CTI values versus temperature for simulations for partially filled 0.17 eV and 0.44 eV traps at frequencies 7, 25 and 50 MHz (logarithmic scale).

4 Comparisons with an Analytical Model

The motivation for introducing an analytical model is to understand the underlying physics through making comparisons with the DESSIS simulations. This might then allow predictions of CTI for other CCD geometries without requiring a full simulation.

4.1 Capture and emission time constants

The charge transfer inefficiency is modelled by a differential equation in terms of the different time constants and temperature dependence of the electron capture and emission processes. In the electron capture process, electrons are captured from the signal packet and each captured electron fills a trap. This occurs at a rate determined by a capture time constant τ_c . The electron emission process is described by the emission of captured electrons from filled traps back to the conduction band, and into a second signal packet at the emission rate determined by an emission time constant τ_e .

Following the treatment by Kim [22], based on earlier work by Shockley, Read and Hall [23], a defect at an energy E_t below the bottom of the conduction band, E_c , has time constants

$$\tau_c = \frac{1}{\sigma_e \nu_{th} n_s} \quad \tau_e = \frac{1}{\sigma_e \chi_e \nu_{th} N_c} \exp\left(\frac{E_c - E_t}{k_B T}\right) \quad (1)$$

where σ_e = electron capture cross-section, χ_e = entropy change factor by electron emission, ν_{th} = electron thermal velocity, N_c = density of states in the conduction band, k_B = Boltzmann's constant, T = absolute temperature, and n_s = density of signal charge packet. It is assumed that $\chi_e = 1$.

At low temperatures, the emission time constant τ_e can be very large and of the order of seconds. The charge shift time for one gate, $t_{sh} = 1/(3f)$, where f is the readout frequency, is of the order of nanoseconds. A larger τ_e means that a trap remains filled for much longer than the charge shift time. Further trapping of signal electrons is not possible and, consequently, CTI is small at low temperatures. A peak occurs between low and high temperatures because the CTI is also small at high temperatures. This manifests itself because, at high temperatures, the emission time constant decreases to become comparable to the charge shift time so trapped electrons rejoin their signal packet.

4.2 Charge Transfer Model

The model by Hardy et al. [24] considers the effect of a single trapping level and includes only the emission time constant in the following differential equation $dn_t/dt = -n_t/\tau_e$ where n_t is the density of filled traps. The traps are initially filled for this model and $\tau_c \ll t_{sh}$.

When $\tau_c \gg t_{sh}$ and to be consistent with the DESSIS simulation (that uses partially filled traps), this model can be adapted by the use of the capture time constant. The solution of this differential equation leads to an estimator of the CTI:

$$CTI = \left(1 - e^{-t_{sh}/\tau_c}\right) \frac{3N_t}{n_s} \left(e^{-t_{join}/\tau_e} - e^{-t_{emit}/\tau_e}\right) \quad (2)$$

where N_t is the density of traps, t_{emit} is the total emission time from the previous packet, the mean waiting time between charge packets related to the mean occupancy of pixels in the device, and t_{join} is the time period during which the charges can join the parent charge packet. This definition is for the CTI for a single trap level. The factor of three appears since there is a sum over the three gates that make up a pixel. (The Hardy model solution does not have the terms inside the leftmost bracket.)

Figure 5 compares the full DESSIS simulation for 0.17 eV and 0.44 eV traps and clocking frequency of 50 MHz to this Analytical Model. It emphasises the good agreement between the model and full simulations at temperatures lower than 250 K with 0.17 eV traps, but shows a disagreement at higher temperatures for the 0.44 eV traps.

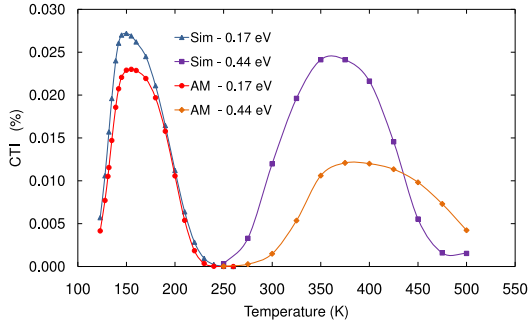


Figure 5: CTI values versus temperature for simulations for 0.17 eV and 0.44 eV partially filled traps at clocking frequency 50 MHz. Comparison of the Analytical Model (labelled AM) with the full DESSIS simulation (Sim).

However it is clear that there are limitations with the Analytical Model. They could relate to a breakdown of the assumptions at high temperatures, to ignoring the precise form of the clock voltage waveform, or to ignoring the pixel edge effects. Further studies are required.

5 Conclusions and Outlook

The Charge Transfer Inefficiency (CTI) of a CCD device has been studied with a full simulation (ISE-TCAD DESSIS) and compared with an analytical model.

Partially filled traps from the 0.17 eV and 0.44 eV trap levels have been implemented in the full simulation and variations of the CTI with respect to temperature and frequency have been analysed. The results confirm the dependence of CTI with the readout frequency. At low temperatures (< 250 K) the 0.17 eV traps dominate the CTI, whereas the 0.44 eV traps dominate at higher temperatures.

Good agreement between simulations and an Analytical Model has been found for 0.17 eV traps but not for 0.44 eV traps. This shows the limitations of the model with respect to the full simulation.

The optimum operating temperature for CCD58 in a high radiation environment is found to be about 250 K for clock frequencies in the range 7 to 50 MHz. However CCD58 is not really suited to high speed readout and attempts to make laboratory measurements have given inconsistent results. So in order to meet the demanding readout requirements for a vertex detector at the ILC, interest has now moved to an alternative CCD design with Column-Parallel (CP) and 2-phase readout. Our prototype CP-CCD has recently operated at 45 MHz. Thus our involvement with serial readout devices will probably now cease but the experience gained with DESSIS and building analytical models will transfer to our studies of CP-CCDs.

Acknowledgments

This work is supported by the Particle Physics and Astronomy Research Council (PPARC) and Lancaster University. The Lancaster authors wish to thank Alex Chilingarov, for helpful discussions, and the particle physics group at Liverpool University, for the use of its computers.

References

- [1] J.R. Janesick, “Scientific Charge-Coupled Devices”, SPIE Press, ISBN 0819436984 (2001).
- [2] K. Stefanov, PhD thesis, Saga University (Japan), “Radiation damage effects in CCD sensors for tracking applications in high energy physics”, 2001, and references therein; K. Stefanov et al., IEEE Trans. Nucl. Sci., 47 (2000) 1280.
- [3] O. Ursache, Diploma thesis, University of Siegen (Germany), “Charge transfer efficiency simulation in CCD for application as vertex detector in the LCFI collaboration”, 2003, and references therein.
- [4] J.E. Brau, O. Igonkina, C.T. Potter and N.B. Sinev, Nucl. Instr. and Meth. A549 (2005) 117; J.E. Brau and N.B. Sinev, IEEE Trans. Nucl. Sci. 47 (2000) 1898.
- [5] A. Sopczak, “LCFI Charge Transfer Inefficiency Studies for CCD Vertex Detectors”, IEEE 2005 Nuclear Science Symposium, San Juan, USA, Proc. IEEE Nuclear Science Symposium Conference Record, N37-7 (2005) 1494; A. Sopczak, “LCFI Charge Transfer Inefficiency Studies for CCD Vertex Detectors”, 9th ICATPP Conference on Astroparticle, Particle, Space Physics, Detectors and Medical Physics Applications, Como, Italy, Proc. World Scientific (Singapore) p. 876; A. Sopczak, “Charge Transfer Efficiency Studies of CCD Vertex Detectors”, on behalf of the LCFI collaboration, Int. Linear Collider Workshop, LCWS’05, Stanford University, USA, physics/0507028, Proceedings p. 544.
- [6] LCFI collaboration homepage: <http://hepwww.rl.ac.uk/lcfi/>
- [7] S.D. Worm, “Recent CCD developments for the vertex detector of the ILC - including ISIS (In-situ Storage Image Sensors)”, 10th Topical Seminar on Innovative Particle and Radiation Detectors (IPRD06) 1–5 October, 2006, Siena, Italy; T.J. Greenshaw, “Column Parallel CCDs and In-situ Storage Image Sensors for the Vertex Detector of the International Linear Collider”, 2006 Nuclear Science Symposium, October 29–November 4, 2006, San Diego, USA.
- [8] SiD collaboration homepage: <http://www-sid.slac.stanford.edu/>
- [9] LDC collaboration homepage: <http://www.ilcldc.org/>
- [10] GLD collaboration homepage: <http://ilcphys.kek.jp/gld/>
- [11] Private communication from Takahi Maruyama, Stanford Linear Accelerator Center, 2006.
- [12] A. Vogel, private communication (DESY Hamburg), 2006.
- [13] M.S. Robbins “The Radiation Damage Performance of Marconi CCDs” Marconi Technical Note S&C 906/424 2000 (unpublished).
- [14] M.S. Robbins et al., IEEE Trans. Nucl. Sci. 40 (1993) 1561.
- [15] M.S. Robbins, T. Roy and S.J. Watts, Proceedings of the First European Conference on Radiation and its Effects on Devices and Systems, RADECS 91, ISBN: 0-7803-0208-7 (1992) 327.
- [16] J.W. Walker and C.T. Sah, Phys. Rev. B7 (1972) 4587.
- [17] G.K. Wertheim, Phys. Rev. 110 (1958) 1272.
- [18] M. Suezawa, Physica B340-342 (2003) 587.
- [19] N.S. Saks, IEEE Trans. Nucl. Sci. 24 (1977) 2153.
- [20] J.R. Srour, R.A. Hartmann and S. Othmer, IEEE Trans. Nucl. Sci. 27 (1980) 1402.
- [21] E. Fretwurst et al., Nucl. Instr. and Meth. A377 (1996) 258.
- [22] Ch.-K. Kim, in *Charge-Coupled Devices and Systems*, M.J. Howes and D.V. Morgan, Eds. Wiley 1979, p. 57. A.M. Mohsen and M.F. Tompsett, IEEE Trans. Elec. Dev. 21 (1974) 701.
- [23] W. Shockley and W.T. Read, Phys. Rev. **87** (1952) 835; R.N. Hall, Phys. Rev., **87** (1952) 387.
- [24] T. Hardy, R. Murowinski and M.J. Deen, IEEE Trans. Nucl. Sci. 45 (1998) 154.

Digitization and hit reconstruction for silicon tracker in MarlinReco

S.Shulga and T.Ilicheva *

Joint Institute for Nuclear Research
141980 Dubna, Moscow reg., Russia
Fr.Scorina Gomel State University
245280 Gomel, Republic of Belarus

The program *SiliconDigi*, implementing a new *Marlin* processors for digitization and clustering in silicon tracker of LDC, is presented. Processors include member of class *Detector* which contains digitizer and clusterizer. Vector of samples of class *DetUnit* (simplest detector unit) are initialized by using *GEAR* interface. Digitizer and clusterizer take detector units to transform collection of simulated hits to collection of raw data and reconstructed hits for each detector unit. Current code contains barrel subdetectors. Codes of classes *Digitizer* and *Clusterizer* are taken from CMS software.

1 Design of package *SiliconDigi*

Simplest object of digitization is readout unit. The detector is a set of identical readout units. The detector should comprise process of digitization and clustering, receiving from the outside and making for external use corresponding hit information. It means that codes of digitizer and clusterizer should be parts of class describing detector.

To have flexible package it is useful to separate persistent part of the program (*MARLIN* [2] processors) from developing part. Developing part of codes describes detector including vector of detector units, interface to *GEAR* [2] initializing detector units, digitizer and clusterizer. Detector unit contains *LCIO* [2] collections (*SimTrackerHit*, *TrackerRawData* and *TrackerHit*) which are initialized or produced by processors.

That is why package *SiliconDigi* [3] consist of three sub packages (sub package in sense of *MarlinReco* [2]): *SiDetector* (includes classes *Detector*, *DetUnit*, *SiPixelDetUnitDigitizer* and *SiTrkDetUnitClusterizer*), *SiDigi* (class *SiTrkDigiProcessor*) and *SiClustering* (class *SiTrkClusterProcessor*).

Class *Detector* is container of layers and samples of *DetUnit*. Main method of *Detector* performs initialization of *DetUnit* by using *GEAR* xml-file. Abstract base class *DetUnit* is container of simulated/raw/reconstructed and temporary hits. *DetUnit* can read/write standard *LCIO* collection of hits. *Detector* contains digitizer and clusterizer. The object to be digitized/clusterized is a sample of *DetUnit*. Codes of digitizer and clusterizer are taken from CMS software [4, 5, 6, 7, 8, 9].

First function of digitizer is finding of ionization points in detector unit. Interval between hit entry and exit points is divided in N segments by using parameter of length of segment (0.01 mm by default). This function creates ionization points which contain information about positions of ionization points and energy loss in units of number of electrons. Energy losses are defined by using Landau distribution in thin silicon layer.

Next step of digitizer is transformation of ionization points to collection points defined at charge collection plane where sensor pixels are placed.

*This work is partially supported by BMBF(Germany).

Number of collection points is equal number of ionization points. Two physical phenomena are simulated at this step: Lorenz drift with the fixed Lorenz angle and diffusion around the drift direction. The collection point contains the calculated value of Gaussian charge diffusions along X and Y directions ($\sigma_X \times \sigma_Y$). Each collection point is mapped by pixel map to find low and upper bounds of fired pixels. Cluster of fired pixels is defined with sizes $3\sigma_X \times 3\sigma_Y$. In each fired pixel 2-dimensional integral is calculated according to Gaussian distribution of charge for each collection point separately. Charge fractions are summarized over the collection points for given fired pixel. For all simulated hits charge fractions are summarized over the simulated hits. All fired pixels are collected in *map<int channel, double charge>* where *channel* is packed 2-dimensional pixel number, *charge* is full charge from all simulated hits in the event. Map of signals is a last output result of digitizer. Digitizer translates this map to the sample of *DetUnit*. *DetUnit* modifies signal map adding noises and killing some channels according to the inefficiency. Method *DetUnit::add_noise* adds two types of noises. First one calculates noises in each hit pixels around zero by Gaussian distribution with σ_{noise} given by user parameter. After that noise charge is added to the hit pixel. Secondly, it calculates noise in not-hit pixels by so called noiser. The noises are ruled by two parameters: noise RMS in units of electrons and threshold in terms of σ_{noise} .

Method of pixel inefficiency kills some pixels, double columns of pixels or full readout chips. Two parameters are used to find readout chip inefficiency: sizes of readout chips along X and Y direction in units of number of pixels. One can introduce different inefficiencies for different layers.

The clustering is performed on a matrix with size which is equal the size of the pixel detector. Each cell contains the ADC count of the corresponding pixel. The search starts from seed pixels, i.e. pixels with sufficiently large amplitudes. Clusters are set of neighbor pixels including pixels which touched by corners.

2 Thresholds and efficiency of hit reconstruction

It is convenient to use σ_{noise} as an unit of collected charge. Then it is possible to define admissible thresholds, expressing them in terms of σ_{noise} . In the beginning we find a threshold defining a signal in the channel (pixel). Clearly, that this threshold should make few σ_{noise} , to avoid a plenty of false fired pixels. Simultaneously big threshold reduces efficiency of registration of hits.

To define a pixel threshold, we shall construct dependence of efficiency from value of pixel threshold, setting the threshold of seed pixels and a threshold of the cluster charge as equal to zero (seed pixel is a pixel from which the clustering is started). Noises also are switched off. From figure 1 (a) we see, that without essential decrease in efficiency of registration of a hit it is possible to choose pixel threshold not more than $4\sigma_{noise}$.

After that to build second plot (dependence of efficiency from seed threshold) the pixel threshold is fixed to $4\sigma_{noise}$, cluster threshold is set to zero. Seed threshold can be more than pixel threshold. Maximal value of seed threshold will be set $5\sigma_{noise}$.

Last plot is dependence of efficiency from cluster threshold with minimal pixel and seed thresholds which were found by previous pictures. Cluster threshold can be more then seed threshold. Maximal cluster threshold is restricted by decreased efficiency and will be set not more than $6\sigma_{noise}$.

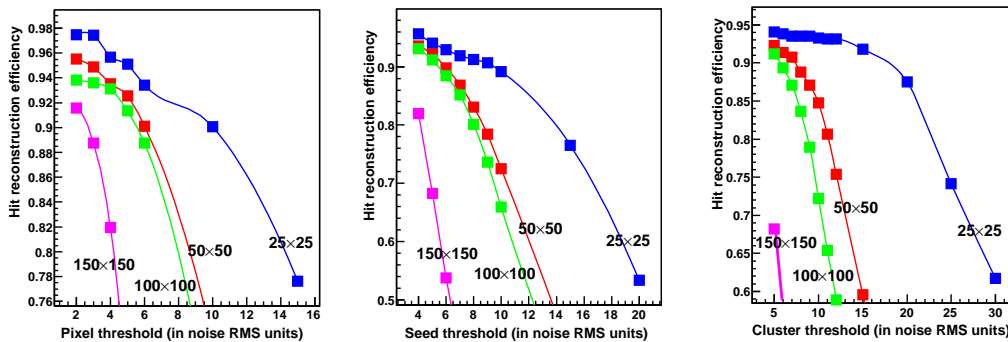


Figure 1: Efficiency of hit reconstruction as function of pixel, seed and cluster thresholds for pixel sizes 25×25 , 50×50 , 100×100 and $150 \times 150 \mu\text{m}^2$.

3 Conclusion

Classes *Detector*, *DetUnit* and *BarrelDetUnit* are developed to use in digitization and clustering processors for silicon tracker in framework of *Marlin-Reco*. Class *Detector* includes pixel digitizer and pixel clusterizer for rectangular detector units. Pixel, seed and cluster thresholds are investigated. The table 1 contains hit reconstruction efficiencies for different sizes of pixels with thresholds which were found above.

Pixel size, μm^2	Reconstructed hits, %	True hits, %
25×25	94.3	93.5
50×50	89.8	89.6
100×100	86.9	86.8
150×150	54.0	53.9

Table 1: Hit reconstruction efficiency for different sizes of pixels. Pixel, seed and cluster thresholds equal $4\sigma_{noise}$, $5\sigma_{noise}$ and $6\sigma_{noise}$ correspondingly.

References

- [1] Slides:
<http://ilcagenda.linearcollider.org/contributionDisplay.py?contribId=311&sessionId=74&confId=1296>
- [2] http://ilcsoft.desy.de/portal/software_packages
- [3] http://www-zeuthen.desy.de/lc-cgi-bin/cvsweb.cgi/SiliconDigi/?cvsroot=marlinreco;only_with_tag=v00-04
- [4] S.Cucciarelli, D.Kotlinsky, T.Todorov, CMS Note 2002/049
- [5] S.Cucciarelli, D.Kotlinsky, CMS IN 2004/014
- [6] D.Kotlinski, Pixel Software Workshop, 11-15/01/07 (CMS)
- [7] G.Giorgiu, Pixel Workshop, 01/12/07 (CMS)
- [8] D.Kotlinski, Pixel Software meeting, 19/09/06 (CMS)
- [9] S.Shulga, ILC software and Tools Workshop, LAL-Orsay, 2-4 May, 2007,
<http://ilcagenda.linearcollider.org/conferenceDisplay.py?confId=1446>

Overview of SiD Tracking

Rob Kutschke

Fermi National Accelerator Laboratory
Batavia, IL, USA

This report gives an overview of R&D done for the SiD tracker, including the baseline design plus options that are being considered.

1 Introduction

All of the elements in the tracking system of the SiD detector are made from silicon pixels or strips. Figure 1 shows an overview of this system, which comprises a silicon pixel vertex detector, a silicon strip tracker, and silicon forward disks. Figure 2 shows a detail of the elements near the beam line. Higher quality versions of these figures can be found in the slides that were shown at the workshop [1]. The vertex detector and the tracker are both built from cylindrical barrel layers plus planar disk endcap layers. The drivers for this design are the robustness of silicon against unexpected beam conditions, its excellent two-particle separation, its ability to resolve hits from a single beam crossing, and its exquisite spatial resolution which, when material is controlled, yields state of the art momentum resolution.

This report will focus on the tracker sub-system. Many additional details are available in the SiD report to the ILC Tracker Review [2], in its accompanying presentations [3], and in several contributions included in these proceedings [4]-[8].

2 Tracker Layout and Options

In the tracker barrel, the baseline design is for 5 layers of axial strips, in which a single module design tiles the entire barrel, using a pinwheel scheme to implement overlaps in φ and radial offsets to implement overlaps in z . The design is for $25\ \mu\text{m}$ trace pitch, $50\ \mu\text{m}$ readout pitch and $S/N > 25$. A module has a length of about 10 cm. Options include more layers, different placement of layers, shorter strips, and stereo angles, either large or small, on some layers. There is also a question about the large radial gap between the vertex detector and the tracker; is an additional layer required in this gap?

For the tracker endcap, the baseline design is for crossed pairs of one-sided sensors, but a detailed module design remains to be developed. An option is to use a single layer of two-sided sensors with crossed readout; if a vendor is identified who can supply sufficiently high quality devices, this would be the preferred option because of the potential for lower mass. A second option is to transition from strips to pixels at small radii; the options for pixels include square, rectangular, and hexagonal. Similar options are on the table for the design of the forward tracker.

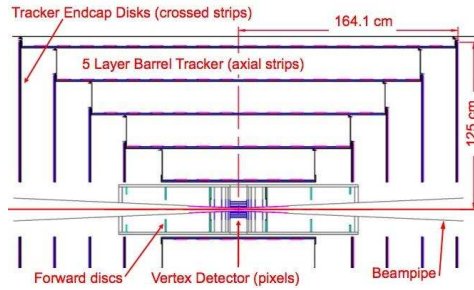


Figure 1: Vertical section of the SiD tracking system.

A mechanical design for the major support structures exists and was presented at the ILC Tracker Review [2] [3]. There is high confidence in this design because it derives from the experience of the D0 Central Fiber Tracker during Run IIa.

3 Readout Options

SiD is currently evaluating 3 readout options for the tracker, all of which have single bunch-crossing timing. The baseline readout option is to use the KPjX chip, which would be bump bonded (AC coupled) at a central location in each module. The chip has 4 sample and hold analog buffers, which will be digitized and read out between bunch trains. The design requires a double metal layer on the sensors to route signals and power; bench tests will be performed to verify that the power traces, which cross the signal traces, do not induce too much noise. The KPjX chip is also proposed for the SiD electromagnetic calorimeter (ECAL).

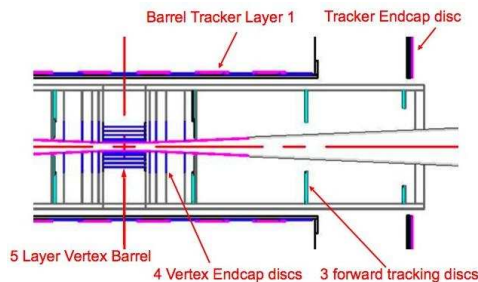


Figure 2: Detail of vertex detector and forward tracking system.

A second option is to read out each strip at both ends and to interpolate the z position using charge division. This design does not require double metal but it does require a longer shaping time. It is estimated that a spatial resolution of 5.5 mm can be achieved, which gives a resolution on $\tan \lambda$ of about 0.007, comparable to that of small angle stereo strips. Test sensors optimized for charge division will be ordered in the next SiD sensor submission.

The third option is a time over threshold scheme. Relative to the KPjX design, this has the advantage that it does not require analog buffering but it does require a shaping time of order 10 beam crossings. This option is discussed in detail elsewhere in these proceedings [4].

SiD is open to other read out options and is happy to evaluate sample chips from other R&D groups.

4 Alignment

The University of Michigan group in SiD is evaluating Frequency Scanned Interferometry (FSI) as a method for monitoring the alignment of the tracking system. In this technique, an absolute distance is measured by reflecting laser light from a reflector and counting fringe shifts as the laser frequency is scanned. The Michigan group has developed a method that uses two lasers to reduce systematics and has achieved a resolution of 0.20 μm in a bench test with a high degree of realism [5].

5 Power Cycling

In order to reduce generated heat, the SiD readout electronics will be powered down between pulse trains. The pulse trains come at a rate of 5 Hz, with duration of about 1 ms, and it is anticipated that the time averaged heat load can be reduced to about 1/80 of the powered-on load. Calculations show that the time averaged heat generation of the tracker, barrel plus

endcaps, will be about 500 watts, a level that can be cooled by flowing about 100 cfm of dry air through the tracker volume. While detailed air flow and heat flow calculations remain to be done, this is not a particularly fast air flow rate and there remains plenty of headroom.

Another concern is vibrations induced by Lorentz forces caused by the large currents required to power-up the electronics in a short time. SiD plans to design a support structure that has sufficient stiffness at 5 Hz so that these vibrations are not an issue. The design will be validated using optical measurements on prototypes driven at 5 Hz.

6 Software

The SiD R&D effort uses the ALCPG software suite that is described elsewhere in these proceedings [6].

Detailed simulations are required to evaluate many of the outstanding design issues. One task is to evaluate the occupancy of the candidate tiling solutions for the tracker endcap and forward tracker layers. Another task is to develop a set of pattern recognition algorithms that find all tracks of physics interest with high efficiency. A Kalman filter will be used to study the resolution on the track parameters as a function of the detailed design of material layout. Once these codes are available the final optimization of the tracker can take place, within the context of optimizing the integrated tracking system. Whenever possible, the optimization will use as its metrics the results of simulated analyses of benchmark physics processes.

Most tracks of physics interest originate inside of layer 2 of the vertex detector. These tracks can be found with high efficiency by using the pixel vertex detector as a stand-alone pattern recognition device to find track seeds. While the pair background from beamstrahlung is large, simulations have shown this to be sufficiently mitigated by SiD's high magnetic field (5 T) and the fine segmentation of the vertex detector. These so-called "vertex seeds" are extrapolated to the tracker to pick up additional hits. This algorithm has been demonstrated to work well in the barrel region.

In the endcap and forward regions, the main issue is resolving ambiguities caused by ghost hits in the crossed strips. Work on these algorithms will begin as soon as candidate tiling solutions are coded.

About 5% of tracks of physics interest originate outside of layer 2 of the vertex detector and do not have sufficient vertex detector hits to produce track seeds in the vertex detector. These tracks include the decay products of long lived B and D mesons and the decay products of kaons and hyperons. Two strategies have been developed to deal with these tracks, calorimeter assisted tracking and stand-alone pattern recognition, both of which will be run after excluding hits found by vertex detector seeded pattern recognition. These algorithms are most important for barrel tracks, which, in the baseline design, have only axial strip measurements. Both algorithms, however, could prove useful to improve track finding efficiency for tracks that go through the tracker endcap or the forward disks.

Most non-electron charged tracks leave a clearly identifiable track stub in the SiD ECAL, which is made from alternating layers of tungsten sheets with pixel detectors. These calorimeter stubs have 3D information about the track trajectory, albeit with poor resolution. Calorimeter assisted tracking begins by finding stubs in the calorimeter and then extrapolating them into the tracker to pick up additional hits. A detailed description of this algorithm and a presentation of results can be found elsewhere in these proceedings [7].

The final pattern recognition algorithm is to use the tracker as a stand alone pattern recognition device. In the baseline design, all of the barrel layers are axial so the projection of tracks in the $r\varphi$ plane will be easy to find. As will be discussed in the next paragraph crude z measurements are available in all scenarios but there are scenarios in which high precision z measurements can be added to the track. A detailed description of this algorithm and a presentation of results can be found elsewhere in these proceedings [8].

For calorimeter assisted and stand-alone pattern recognition there are several options for obtaining z measurements. Each barrel module has a length of about 10 cm, which provides a z measurement with a resolution of $10/\sqrt{12} \simeq 2.9$ cm. For tracks that traverse adjacent modules that overlap in z , a higher precision z measurement is available. If vertex detector pixel hits can be added to the track, they provide high precision z measurements. If the track comes from a calorimeter seed, that seed provides measurements of both a z position and $\tan \lambda$. Finally, if the charge division option is chosen, it provides z measurements; moreover charge division measurements will greatly simplify both calorimeter assisted tracking and stand-alone tracking.

7 Summary

The physics drivers of the ILC have lead the SiD R&D group to propose an all silicon tracking system with three subsystems that perform in an integrated fashion. This report has discussed the baseline design and the main options for one of these systems, the tracker. The present tracker design is complete in the big picture and additional detail will be added throughout the coming year. The most pressing issue is to demonstrate that the proposed design has both the required pattern recognition power and the required resolution on track parameters; this is particularly important for tracks that traverse the endcap or forward disk regions and for tracks that originate far from the interaction point.

The author thanks the United States Department of Energy for support of the SiD R&D at Fermilab.

References

- [1] Slides shown during this presentation:
<http://ilcagenda.linearcollider.org/contributionDisplay.py?contribId=499&sessionId=74&confId=1296>
- [2] ILC-NOTE-SID-TRK-2007-002, on the ILC document server.
- [3] SiD presentations at the ILC Tracker Review, Beijing, 2007.
<http://ilcagenda.linearcollider.org/conferenceDisplay.py?confId=1319>
- [4] B. Schumm, "Progress on long-shaping-time readout at SCIPP", in these proceedings.
- [5] H-J. Yang *et. al.*, Applied Optics **44**, 3937 (2005); H-J. Yang and K. Riles, arXiv:physics/0609187 (2006).
- [6] N. Graf, "ALCPG Software Summary", in these proceedings.
- [7] D. Ononprienko, "Non-Prompt Track Reconstruction with Calorimeter Assisted Tracking Algorithm", in these proceedings.
- [8] B. Schumm, "Tracking Simulation Studies at UC Santa Cruz", in these proceedings.

Calorimeter Assisted Tracking Algorithm for SiD

Dmitry Onoprienko¹ and Eckhard von Toerne^{1, 2}

1- Kansas State University - Physics Department
116 Cardwell Hall Manhattan, KS 66506 - USA

2- Bonn University - Institute of Physics
Nussallee 12, D-53115 Bonn - Germany

Calorimeter-assisted track finding algorithm takes advantage of the finely segmented electromagnetic calorimeter proposed for the SiD detector concept by looking for "MIP stubs" produced by charged particles in the calorimeter, and using them as seeds for pattern recognition in the tracker. The algorithm allows for efficient reconstruction of tracks that cannot be found using seeds provided by the vertex detector, even if standalone pattern recognition in the outer tracker is difficult. The algorithm has been implemented as a package in the org.lcsim framework. Current status of the package and its performance in non-prompt tracks reconstruction are described.

1 Introduction

The development of the calorimeter assisted tracking algorithm was originally motivated by the need to reconstruct long-lived particles in the SiD detector [2].

To minimize multiple scattering and energy loss in the central tracker while providing excellent vertex finding capabilities and high precision measurement of the charged tracks momenta, the SiD baseline design utilizes a compact five-layer silicon pixel vertex detector and a five-layer silicon strip outer tracker, possibly with no stereo and limited Z-segmentation in the barrel.

The standard track finding algorithm developed for the SiD relies on identifying tracks in the vertex detector, where pattern recognition is simplified by the fact that precise three-dimensional information is available for each hit. The tracks are then propagated into the outer tracker, additional hits are picked up, and the track curvature is measured. This algorithm has been demonstrated [3] to achieve high efficiency in reconstructing most types of tracks. However, its heavy reliance on seeds provided by the vertex detector raises a number of questions that need to be addressed. One obvious issue is that the tracks that originate outside the third layer of the vertex detector cannot be reconstructed using this approach, since they do not leave enough hits in pixels to generate a seed. Decay products of K_S^0 and Λ are important examples of particles producing such non-prompt tracks. The detector should also be capable of detecting new physics signatures that would include long-lived exotic particles like those predicted by some gauge-mediated supersymmetry breaking scenarios.

In order to address this issue, a track finding algorithm has been developed that uses electromagnetic calorimeter to provide seeds for pattern recognition in the tracker. Fine segmentation of the EM calorimeter allows for detection of traces left by minimum ionizing particles - so called MIP stubs - and using them to determine the track entry point, direction, and sometimes curvature with a precision sufficient for extrapolating the track back into the tracker.

2 Algorithm

With calorimeter assisted tracking, track finding goes through the following main steps:

1. The standard vertex detector seeded track finder is run. Tracker hits that are associated with successfully reconstructed tracks are removed.
2. MIP stubs in the electromagnetic calorimeter are identified. Several alternative algorithms can be used at this step, such as a generic nearest-neighbor clustering followed by user-controlled cluster quality cuts, or a dedicated MIP stub finder developed specifically for the SiD geometry. For each MIP stub, a seed track is created, and initial helix parameters are determined.
3. Seed tracks are extrapolated back into the tracker, picking up hits in each layer. Every time a hit is added to the track, the track is re-fitted to get a more precise estimate of its parameters. If multiple hit candidates are found in a given layer, the track finding process is branched and several independent track candidates are created.
4. Quality cuts are applied to track candidates; duplicate tracks that share too many hits are discarded.
5. Vertex finder is run; if track intersections are found, the original particles that produced these secondary vertices are reconstructed.

The algorithm has been implemented as a package (`org.lcsim.recon.cat`) in the Java based `org.lcsim` framework [4]. The package design is highly modular, allowing easy substitution of components implementing different algorithms at various stages of the event processing. Most of the track finder parameters can be set at run time, making it possible for the user to tune the algorithm and use it as a part of more complex reconstruction strategies that can involve multiple track finders and multiple passes through the data.

The code can be run both standalone and inside JAS3 interactive shell [5]. The implementation is largely decoupled from any particular geometry, which allows the algorithm to be used for studying and optimizing a wide range of SiD detector options, as well as other ILC detectors designs.

3 Performance

The package was tested by reconstructing simulated events in the SiD detector. For this study, the "SiD00" version of the detector design was used. Since proper charge deposition and digitization code was not yet available, point-like hits produced by the simulation software were smeared with the expected position resolution. In the outer tracker barrel, no stereo layers and 10 cm silicon strips parallel to the beam line were modeled. Strips on opposite sides of the endcap disks were assumed to be perpendicular to each other, forming 90 degrees stereo superlayers, with 10 cm strip length.

Figure 1 shows reconstruction efficiency obtained with the calorimeter assisted tracking algorithm for charged π mesons produced in single K_S^0 events, as a function of transverse momentum. Pions are considered reconstructable if they leave hits in at least 3 tracker layers. Figure 2 shows reconstruction efficiency for K_S^0 in the same type of events. Hollow points refer to the actual efficiency obtained with the current version of the package. Since

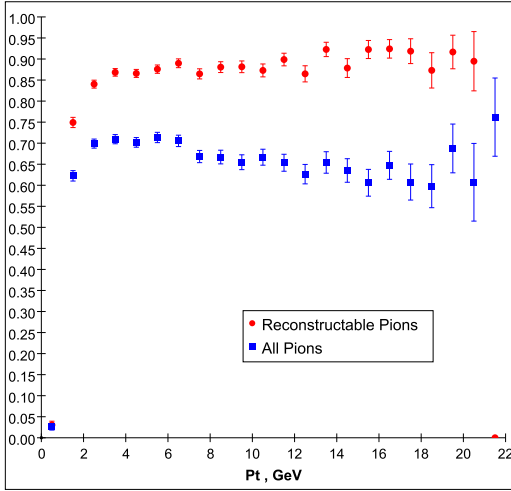


Figure 1: Reconstruction efficiency for charged π mesons from K_S^0 decays in single K_S^0 events, as a function of transverse momentum.

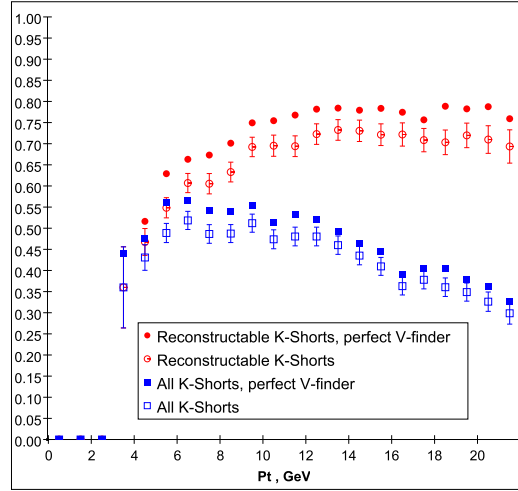


Figure 2: K_S^0 reconstruction efficiency as a function of transverse momentum. Single K_S^0 events.

the currently used vertex finder is a simplistic tool expected to be replaced by a more advanced algorithm once the latter is ported to the org.lcsim framework, the efficiency that would be obtained with a perfect vertex finder is also shown (filled points). K_S^0 is considered reconstructable if it decays in the sensitive area of the detector (inside the third layer of the outer tracker).

Figure 3 shows K_S^0 reconstruction efficiency in $t\bar{t}$ events at 500 GeV center-of-mass energy. For comparison, less than 3 % of all K_S^0 produced in such events would have been reconstructed by the vertex detector seeded algorithm. Figure 4 shows reconstructed K_S^0 mass peak in $t\bar{t}$ events.

4 Discussion

The calorimeter assisted tracking algorithm addresses one of the critical issues for the proposed SiD detector - reconstruction of long lived particles. It can also be instrumental in reconstructing kinked tracks that lose a substantial portion of their energy in the tracker, as well as calorimeter backscatters. Availability of this algorithm significantly improves overall robustness of the track reconstruction in SiD, reducing its reliance on the vertex detector.

The performance tests described in the previous section have been carried out using the current version of the algorithm implementation. Several enhancements are already in the works, and we expect substantial performance improvements.

One of the areas where improvements are desirable is reconstruction of low momentum tracks. As seen in Figure 1, the reconstruction efficiency falls sharply for charged pions with transverse momenta below 1 GeV. Many of these tracks never reach the calorimeter barrel and, after leaving many hits in the tracker, enter calorimeter endcaps at shallow angles, making accurate determination of track parameters from MIP stubs difficult. Our

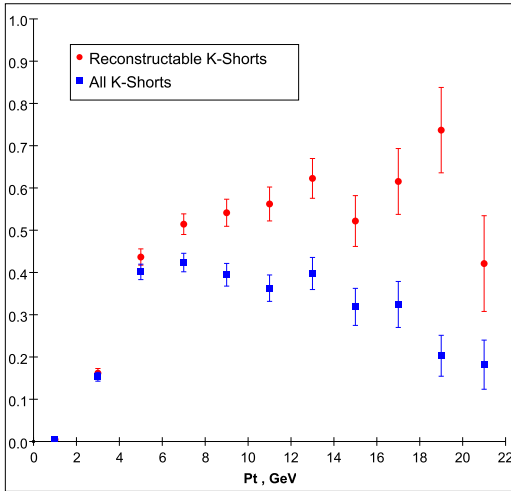


Figure 3: K_S^0 reconstruction efficiency as a function of transverse momentum. 500 GeV $t\bar{t}$ events.

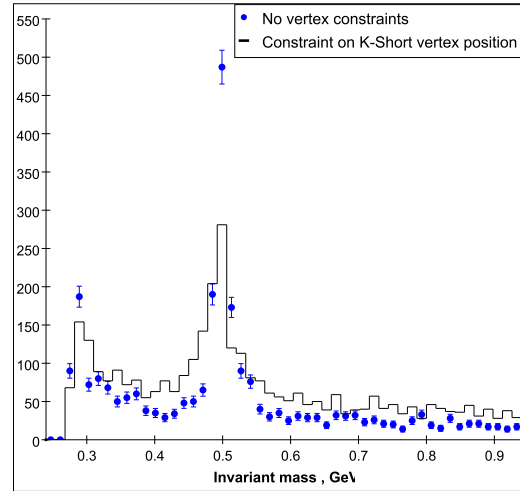


Figure 4: Reconstructed $\pi^+\pi^-$ mass. 500 GeV $t\bar{t}$ events.

preliminary studies indicate, however, that more flexible fitting and track extrapolation procedures may let us recover a substantial portion of these tracks. We expect to implement these procedures once the infrastructure required to support them becomes available in the org.lcsim framework.

The package implementing the calorimeter assisted tracking algorithm will remain under continuing development in the near future. However, a fully functional version will be maintained in the org.lcsim production area. It will be used for SiD geometry optimization and physics reach studies.

References

- [1] Slides:
<http://ilcagenda.linearcollider.org/contributionDisplay.py?contribId=312&sessionId=74&confId=1296>
- [2] SiD Detector Concept:
<http://www-sid.slac.stanford.edu/>
- [3] N. B. Sinev, *In the Proceedings of 2005 International Linear Collider Workshop (LCWS 2005), Stanford, California, 18-22 Mar 2005, pp 1009.*
- [4] org.lcsim framework:
<http://www.lcsim.org/software/lcsim/index.html>
- [5] T. Johnson, *In the Proceedings of CHEP'01: Computing in, High-Energy Physics and Nuclear, Beijing, China, 3-7 Sep 2001*

SiLC simulation status report

M.A. Vos

IFIC (U. Valencia/CSIC)
Apartado de Correos 22085,
E-46071 Valencia, Spain

The SiLC - Silicon for the Linear Collider - collaboration aims to develop silicon detector technology for tracking in the international linear collider experiments. The R & D programme involves a substantial effort in simulation of the response of detector designs. In this contribution, an overview of ongoing efforts in this area is given.

1 Introduction

The SiLC R & D collaboration [2] for the International Linear Collider involves over 200 people from 22 institutes. SiLC members are from three continents, and pertain to the three detector concepts: LDC, SiD and GLD. The aim of the collaboration is to develop silicon detector technology for tracking in the ILC experiments. Core activities include Front End chip design for micro-strip detectors, sensor development, (hardware) alignment and mechanics.

Monte Carlo simulation is an indispensable tool to guide the detector design. In the past, SiLC has played a mayor role in the development and maintenance of valuable fast simulation packages. Well-known examples are the Simulation a Grande Vitesse (SGV) [3]. More recently, the LicToy package - described elsewhere in these proceedings [4] - has been developed. Today, the attention of the SiLC simulation team is shifting towards *full simulation*: detailed Monte Carlo studies of the detector response.

Due to lack of space, several important areas of work will not be discussed in this contribution. Examples are the active line of development centered at Charles University in Prague towards a versatile digitization package for micro-strip detectors, and the investigation of the reconstruction of non-prompt tracks in the SiD concept.

In this contribution, an overview is given of recent progress in the SiLC simulation studies. In separate sections, three specific items are highlighted. The first two deal with two aspects of tracking in the very forward region of the ILC experiment - a complex area that has received relatively little attention. In section 2 estimates are presented of the hit density in the Forward Tracking Disks due to machine background. Section 3 deals with the impact of the material budget on the momentum resolution in the same region. The third aspect of tracking discussed in this contribution is the estimate of extrapolation uncertainties in the innermost part - the Silicon Intermediate Tracker - of the central tracker.

2 Background levels in the forward region

In an e^+e^- collider like the ILC there is one major source of machine-induced background: incoherent pair creation off beamstrahlung photons. An accurate generator for this complex process is available [5] and full detector simulations have been performed, primarily for the vertex detector. The effect on other sub-detectors - in particular the TPC [6] - is actively

being investigated. In this section, the background levels in the forward tracker are discussed briefly.

The inner radius of the forward tracking disks and therefore the angular coverage of the tracker is limited by a region - the accumulation zone - of extremely high background intensity. The radial extent of this zone at different distances along the beam axis is studied using an approach based on the work of reference [7]. The trajectory of the electrons and positrons is represented by a helix in a solenoidal field. Interactions with material are neglected.

For nominal machine parameters and a 4 Tesla magnetic field the accumulation zone is found to extend to a radius of less than 15 mm for z -positions below 320 mm. For alternative parameter sets of the final focus system, the accumulation zone reaches much larger radii. For the low-power (high-luminosity) option the radius at the first (at $z = \pm 20$ cm) and second ($z = \pm 32$ cm) disk of the LDC design become, respectively, 16 (21) mm and 24 (30) mm. Thus, the envisaged inner radius of the active region of the innermost LDC forward tracker disks (37.5 mm) leaves only approximately 7 mm for the beam pipe and the detector services.

A quantitative estimate of the pair background hit density in the forward tracker of the LDC geometry is obtained using a full GEANT4 simulation of the response of the detector to the pairs generated with GuineaPig [5]. The results for the seven disks of the LDC geometry are shown in figure 1. The three solid curves indicate the hit density in units of hits / mm^2 / BX for a 500 GeV collider with nominal final focus parameters. On the innermost two disks hit density reaches 2×10^{-4} , comparable to the level in the outermost layer of the vertex detector. For the outermost disks the background level is an order of magnitude lower.

The dashed curve corresponds to a variation of the final focus parameters known as the low power option. The dotted curve represents a 1 TeV linear collider with nominal parameters. The background level is quite sensitive to both parameters: both result in a factor two increase of the background level with respect to the nominal parameter set throughout the length of the forward tracker.

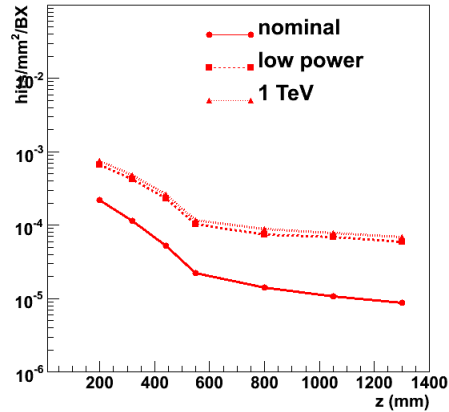


Figure 1: The hit density due to machine background in the LDC forward tracker.

3 Impact of the material budget in the forward region

The ILC detector concepts aim for a superb transverse momentum resolution. Compared to the central tracker, the momentum resolution in the very forward region is inevitably degraded by the less favourable orientation of the magnetic field. Only through the use of state-of-the-art instrumentation can the degradation of the performance towards small polar angle be limited.

In this section the performance of two possible detectors is compared. Both options correspond to the nominal LDC layout and identical assumptions are made regarding the space point resolution: $5 \mu m R\phi$ -resolution for the three innermost disks, $10 \mu m$ for the four outermost disks. The two setups differ the assumption made for the material budget. The first set-up corresponds to a rather conservative estimate of 1.2 % X_0 /disk for the first three disks and 0.8 % X_0 for the four outermost disks. For the second set-up the material in the three disks is reduced by a factor 10.

An estimate of the momentum resolution is obtained using a Kalman Filter track fit on a geometry representing the LDC layout for a track at a polar angle of 20° . As a cross-check, two independent implementations of the fitting algorithm were used, LicToy [4] and the CMS track fit. Both packages are found to yield compatible results.

The results for a range of particle momenta are parametrized as the quadratic sum of a constant (resolution) term and a (multiple scattering) term proportional to $1/p_T$:

$$\sigma(p_T)/p_T^2 = 2.0 \times 10^{-4} \oplus 5.8 \times 10^{-3}/p_T, \text{ if FTD 1-3 have 1.2 \% } X_0/\text{disk}$$

$$\sigma(p_T)/p_T^2 = 1.8 \times 10^{-4} \oplus 4.0 \times 10^{-3}/p_T, \text{ if FTD 1-3 have 0.12 \% } X_0/\text{disk}$$

Clearly, the reduction of the material budget in the challenging set-up leads to an improved momentum resolution performance. As expected, the effect is particularly significant at low momentum, where multiple scattering has the largest impact. In figure 2 the transverse momentum resolution for charged particles with a transverse momentum of 1 GeV and a polar angle of 20° is shown for a series of assumptions on the material budget of the three innermost forward tracking disks.

The improvement of the momentum resolution may seem small in comparison to the effort of reducing the material. It should be noted, however, that there are very few degrees of freedom in the FTD design. While the resolution for high-momentum tracks can be improved significantly by a better space point resolution, the material is the principal handle on the resolution of low-momentum tracks.

4 Pattern recognition in the central tracker

To meet the ILC requirement of efficient and clean reconstruction of charged particle tracks, the various sub-detectors should have excellent pattern recognition capabilities. Currently, the SiLC simulation team is investigating the constraints on the tracker design that derive from this requirement.

One key ingredient to pattern recognition is the precision with which track candidates can be extrapolated to the *next* layer. The uncertainty on the extrapolated position determines - together with the hit error - how many unrelated hits will be compatible with the track candidate. The extrapolation precision depends on the precision of the track parameter estimate and on the distance over which the track is extrapolated. For low momentum tracks, the amount of material in the last measurement layer is furthermore important.

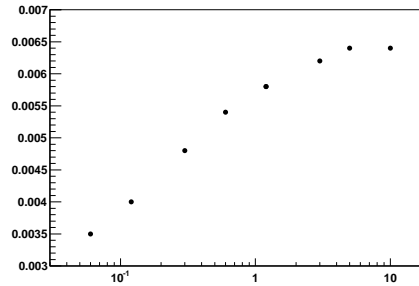


Figure 2: The transverse momentum resolution for 1 GeV tracks in the LDC forward tracker versus material budget in the innermost disks.

In the following, a track is “grown” by an iterative process of extrapolation to the next layer, a search for compatible hits, and update of the trajectory parameters. The track search is “inside-out”, i.e. seeds are created in the VXD. In the first detector layers, the track candidate is only weakly constrained. As a result of the excellent space point resolution and tight material budget, the prediction on the next vertex detector layer is quite precise. Assuming a $2 \mu m$ two-dimensional space point resolution and a material of $0.12 \% X_0$ the uncertainty in the predicted position when extrapolating a track candidate consisting of three VXD measurements to the outermost VXD layers is of the order of $5 \mu m$.

For the next step - the extrapolation of a 5-point track to the intermediate tracker layers - the extrapolation distance is significantly larger. In the various detector concepts the Intermediate Tracker has an innermost layer at a radius 9 cm (GLD), 16 cm (LDC) or 22 cm (SiD). In the LDC layout the extrapolation precision at the innermost SIT layer is given by: $\sigma(R\phi) = 61 \oplus 114/p_T$, whereas $\sigma(z) = 7 \oplus 43/p_T$. The larger $R\phi$ -uncertainty reflects the weakly constrained transverse momentum of the track. In table 1 the $R\phi$ extrapolation precision is listed for a variety of assumptions on the VXD performance and VXD-SIT distance.

5 Conclusions

The SiLC collaboration is actively pursuing a number of simulation studies. In this contribution, three highlights have been presented. In the coming year these studies should allow to determine the requirements of the intermediate central tracker and the forward tracker.

References

- [1] Slides:
<http://ilcagenda.linearcollider.org/contributionDisplay.py?contribId=314&sessionId=74&confId=1296>
- [2] <http://silc.in2p3.fr>
- [3] M. Berggren, Simulation a Grande Vitesse,
- [4] W. Mitaroff, the LicToy: a flexible tool for detector optimization, these proceedings.
- [5] D. Schulte, PhD. thesis, University of Hamburg 1996.
- [6] A. Vogel, Update on the beam related backgrounds in the LDC detector, these proceedings.
- [7] C. Rimbault et al., Study of incoherent pair generation in Guinea Pig, EuroTev report 2005-016.

VXD parameters	R ϕ uncertainty (μm)
LDC nominal	$61 \oplus 114 / p_T$
material $\times 2$	$61 \oplus 166 / p_T$
resolution $\times 2$	$122 \oplus 117 / p_T$
4-layer VXD	$105 \oplus 134 / p_T$
All-together	$211 \oplus 199 / p_T$
SIT radius	R ϕ uncertainty (μm)
R = 12 cm	$27 \oplus 47 / p_T$
R = 20 cm	$108 \oplus 215 / p_T$
R = 30 cm	$279 \oplus 624 / p_T$

Table 1: The $R\phi$ precision of the prediction position on the first Silicon Intermediate Tracker layer under a variety of assumptions for the detector layout.

First test of a 180 nm prototype readout chip using a ^{90}Sr radioactive source

W. da Silva, J. David and F. Kapusta *

LPNHE Paris
 Université Pierre et Marie Curie and CNRS/IN2P3
 4, Place Jussieu, Case 200, 75252 Paris Cedex 05, France

GLAST and CMS sensors equipped with a new 180 nm UMC readout chip have been tested with a ^{90}Sr source. S/N preliminary results obtained with a Common Mode Subtraction Method developed for few strips reading are presented.

1 Hardware and Software in the Paris Lab Test Bench

There were 3 kinds of detectors: a CMS detector with 3 modules fully equipped with 4 VA1 from IDEAS, another CMS detector with 3 modules equipped with 2 VA1 and 4 180 nm UMC and a GLAST detector with 10 modules equipped with 2 VA1 and 4 180 nm UMC. The GLAST detector is 90 cm strip long and 500 μ thick with a 228 μ pitch. The CMS detector is 28 cm strip long and 410 μ thick with a 183 μ pitch. A sequencer, called the Altera box, supplied all the signals needed for the smooth functioning of the preamps-shaper. A 14 Mbq Strontium source was used with a trigger based on a scintillator signal above some threshold. One PC had an ADC card for the proper reading of the analog signals from the detectors with LabView installed, for data taking and coordination of the all the test bench. Another PC was dedicated to the ROOT analysis software.

2 Source tests and results

A common mode noise subtraction method with a low number of adjacent channels has been developed and tested with simulated and real data. In the following figures the source raw data is shown, then pedestal and common mode subtracted. The final S/N value is obtained from a pedestal and signal fit.

2.1 VA1

The VA1 128 channels have been tested as a reference. A four channel analysis of CMS and GLAST sensors has been done as well as a reference. The Signal over Noise ratios found, respectively of 17, 13 and 12, are consistent with the length and quality of each sensors.

*On behalf of the SiLC Collaboration

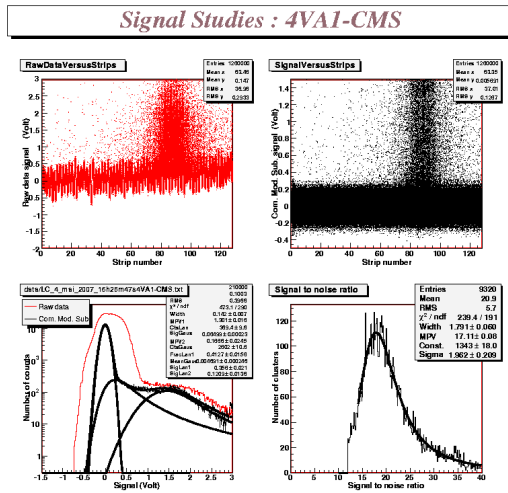


Figure 1: 4VA1

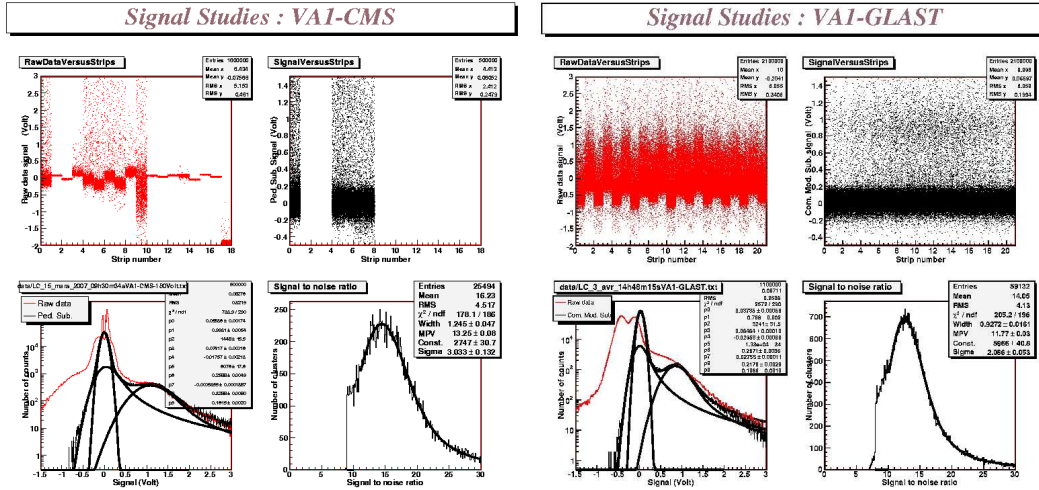


Figure 2: VAI-CMS and VAI-GLAST

2.2 180 nm

The method validated by the VAI data analysis has been applied to the new 180 nm data. The 180 nm sensor channels have a comparable noise : $\sigma^{Noise} \simeq 16 \text{ mV}$. The found S/N ratios are respectively of 11 and 8.

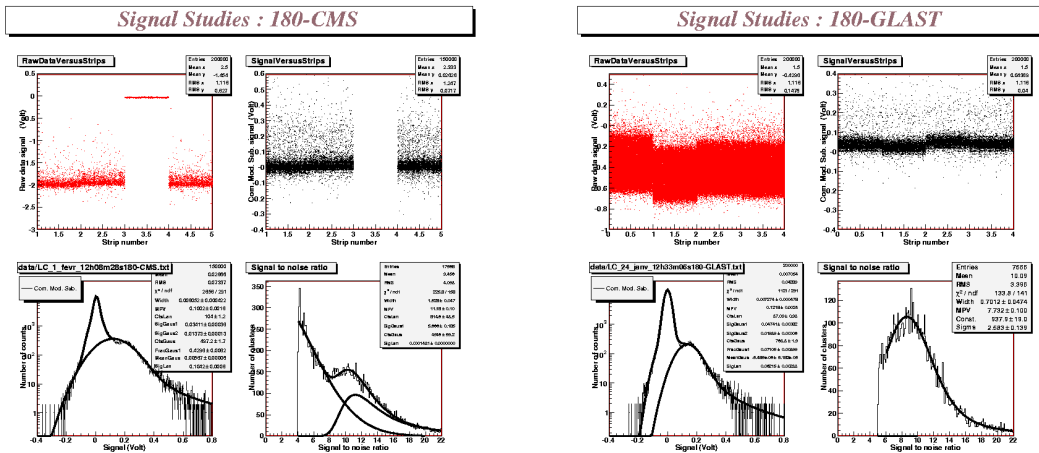


Figure 3: 180-CMS and 180-GLAST

3 Conclusions and outlook

A summary of the S/N results is given in the last figure, where a simulation was used to compute the ENC. The 180 nm chip is working. The global noise should be decreased. This source test will be followed by a beam test at DESY. It is a step towards the use of the new built 130 nm UMC chip with analog pipeline and digital output.

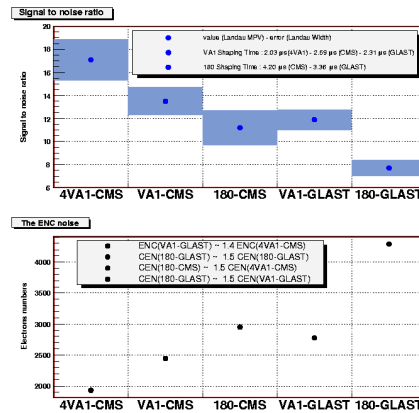


Figure 4: Results

References

- [1] Slides:
<http://ilcagenda.linearcollider.org/contributionDisplay.py?contribId=452&sessionId=74&confId=1296>

A GEM TPC End Panel Pre-Prototype

A.Ishikawa¹, A.Aoza¹, T.Higashi¹, A.Sugiyama¹, H.Tsuji¹, Y.Kato², K.Hiramatsu²,
T.Yazu², T.Watanabe³, O.Nitoh⁴, H.Ohta⁴, K.Sakai⁴, H.Bito⁴,
K.Fujii⁵, M.Kobayashi⁵, H.Kuroiwa⁵, T.Matsuda⁵, R.Yonamine⁵,
Y.Gao⁶, Y.Li⁶, J.Li⁶, L.Cao⁶, Z.Yang⁶, A.Bacala⁷, C.J.Gooch⁷, R.Reserva⁷, D.Arogoncia⁷

1- Saga University, Honjo-machi 1, Saga 840-8502, Japan

2- Kinki University, 3-4-1 Kowakae, Higashi-Osaka 577-8502, Japan

3- Kogakuin University, 1-24-2 Nishi-Shinjyuku, Tokyo 163-8677, Japan

4- Tokyo University of Agriculture and Technology, Koganei, Tokyo, 184-8588, Japan

5- IPNS, KEK, Oho 1-1, Tsukuba 350-0810, Japan

6- Tsinghua University, CN-100 084, Beijing, China

7- Mindanao State University Iligan Institute of Technology, 9200 Lligan, Philippines

A GEM TPC end panel pre-prototype was constructed for a large LC-TPC prototype to test its basic design philosophy and some of its engineering details. Its interim test results are presented.

1 Introduction

Three out of the four detector concepts for the ILC feature a Time Projection Chamber (TPC) as their main trackers. The LC-TPC is required to have more than 100 sampling points with a spatial resolution of $150\ \mu\text{m}$ or better and a two-track separability down to 2 mm. Beam tests of a small prototype [2, 3] have shown that the required performance is achievable if we adopt a pad width of as narrow as $\sim 1\ \text{mm}$ or a resistive anode to spread the signal charge on a pad plane. Basic properties of a TPC with a micro pattern gas detector (MPGD) readout plane are also understood through these small prototype tests. Our next target is to construct a large prototype having multi-MPGD-panels with small readout pads, and to demonstrate the required performance under more realistic experimental conditions with panel boundaries and distortions, thereby allowing a smooth extrapolation to the real LC-TPC. The LCTPC collaboration plans to have a beam test with a large prototype at DESY in the summer of 2008. For the beam test, we will prepare Gas Electron Multiplier (GEM) panels. Our basic design goals for the pre-prototype GEM end panel includes the following: to allow the required smallness and density of readout pads, to minimize dead spaces due to phi-boundaries of adjacent panels, and to allow easy replacement of GEM foils when necessary. Considering these requirements, we decided to use as large GEM foils currently available as possible, and to stretch the GEM foil in the radial directions so as to avoid thick mullions introducing dead regions for high momentum tracks. We also designed a GEM mounting system through which we can supply necessary high voltages to the GEM foils. Prior to the production of GEM panels for the beam test, we constructed a pre-prototype to test its basic design philosophy and some of its engineering details including fabrication methods for the GEM end panels.

2 Construction of the GEM TPC End Panel Pre-Prototype.

2.1 GEM

Our GEM foils are supplied by Scienergy Co. [4] and consist of $5\ \mu\text{m}$ thick copper electrodes sandwiching a $100\ \mu\text{m}$ thick liquid crystal polymer insulator. The thick GEM foils allow stable operation with higher gain than popular $50\ \mu\text{m}$ thick GEM foils. A double GEM configuration is hence enough to give a gain of more than 10^4 . The hole diameter and pitch are $70\ \mu\text{m}$ and $140\ \mu\text{m}$, respectively. The hole shape is cylindrical due to dry etching unlike that of CERN GEMs, which is biconical. The active area is fan-shaped spanning 9.2° in the ϕ direction with inner and outer radii of 128 and 139 cm ($\sim 20 \times 11\ \text{cm}^2$), which is about 2 times larger than the GEM foils we used for our small prototype. To keep the stored energy small enough, the GEM electrodes are divided into two in the radial direction with a boundary of $100\ \mu\text{m}$.

A set of G10 frames should be glued to each GEM foil in order to be mounted on a readout PC board. For the frame gluing we developed a GEM stretcher, which consists of two parts. One is an acrylic GEM stretcher frame and the other is a set of a middle frame and a GEM adjuster made of aluminum. The lower part of the acrylic stretcher frame has a groove with a depth of 2 mm and the upper part has screw holes aligned to it. The middle aluminum frame has the same size as the groove. By sandwiching a GEM foil with the lower and the upper parts of the acrylic stretcher frame together with the aluminum frame, and by screwing bolts into the holes of the upper piece and pressing down the aluminum frame into the groove, we could stretch the GEM foil. The GEM foil, the G10 frames, and the adjuster have through holes aligned to each other. We stacked them up together, put pins into the holes of the adjuster to align them, and glued the G10 frames with epoxy adhesive to the GEM foil. Notice that the frames covered only the inner and outer edges of the GEM foil to reduce the dead space pointing to the interaction point. This fabrication method has been established and allowed us to produce 3 panels per day.

2.2 Readout PC Board

The electrons multiplied by the GEM foils are read out by a PC board. The PC board is $2\ \text{mm}^t$ thick and has a size enough to cover the GEM foils, spanning 9.2° in ϕ and having inner and outer radii of 127 and 140 cm, which are about 1 cm extended in both inner and outer directions to facilitate the GEM mounting. It carries 20 pad rows on its front side of which the inner 10 have 176 pads each and the outer 10 have 192 pads each, with every two rows staggered by half a pad width to minimize the so-called hodoscope effect. A typical pad size is about $1.1 \times 5.5\ \text{mm}$ which is small enough for the intrinsic charge spread of $\sim 350\ \mu\text{m}$. The pads are wired to readout connectors on the back side of the PC board through a five-layer FR4. The PC board, being of six layers, has no through-holes due to wiring, thereby assuring the gas-tightness required for the TPC operation.

We used connectors supplied by JAE [5]. Each connector has 40 channels, of which 32 are used for signal readout and the remaining 8 for ground. Its size is about $15 \times 5\ \text{mm}^2$, which is one of the smallest connectors commercially available. Pre-amplifiers are connected to the PC board with flexible cables. For the large prototype, pre-amplifiers and flash ADCs will be mounted on small PC boards and are directly connected to the readout PC board. We will not use the connectors for the real ILC TPC, since pre-amplifiers and flash ADCs will be mounted on the surface of the PC board.

High voltage (HV) electrodes are also wired through the PC board. To apply the HVs to the GEM electrodes, we adopt a bolt-and-nut method. A brass nut is adhered to an electrode on the front side of the PC board. We tried two methods to fix the nut. One is soldering, the other is gluing with a conductive paste (dotite by Fujikura Kasei Co. [6]). It turned out that soldering is much stronger than the conductive paste, besides the dotite produces threads. We will hence use soldering for the large prototype construction. The lower and the upper GEM foils are stacked on the PC board, and bolted through their G10 frames to bite the GEM electrodes so as to supply required HVs through the bolts. The spacings between the GEM foils and the readout pad plane are determined by the thicknesses of the G10 frames, resulting in a transfer gap of 4 mm and an induction gap of 2 mm. An aluminum flange with a groove for an O-ring is glued to the back side of the PC board with epoxy adhesive to avoid mechanical distortion and to be mounted to a gas container. When we glued the aluminum flange, we aligned the flange and the PC board by hand since there are no alignment holes or posts in the PC board and the flange. The positions of the readout pads are determined by this flange, so some alignment posts should be prepared for the large prototype. The GEM end panel was mounted on a gas container with 16 M3 bolts.

3 Measurement of Gain Uniformity over the Panel.

The pre-prototype chamber is filled with a 90:10 mixture of Ar and iso-butane gases. We applied 410 V to each of the two GEM foils, and electric fields of 100, 2050, and 3075 V/cm to the 25 mm long drift, the 4 mm long transfer, and the 2 mm long induction regions, respectively. Under these conditions, the gas gain was about 2×10^4 and the signal spread was about $550 \mu\text{m}$. We irradiated the pre-prototype panel with X-rays from ^{55}Fe through the windows of the test chamber to measure the gain uniformity over the panel.

First, we checked the charge distribution over the readout pads. Since the signals sometimes spread over 2 pad rows, we required the signal charge be shared by 2 pad rows and summed the signals over 5 contiguous pads on each of these two rows to avoid mis-collection. Figure 1 shows the charge sum distributions for 10 pads. Both a 5.9 keV main peak and a 2.9 keV escape peak can be clearly seen.

Second, we checked the charge spread. A center of gravity was calculated from the measured pad signal charges and their ϕ positions as well as the charge fraction on each pad. By plotting the charge fraction as a function of the charge center measured from the middle of the central pad, we could get an image of the charge distribution over the pad plane. Gaussian fit to the distribution resulted in a $(1-\sigma)$ width of about $550 \mu\text{m}$ corresponding to half a pad width as expected (Fig. 2) from the diffusion.

We then measured the charge sum distributions at 28 positions over the panel for the uniformity test, usually requiring the charge sharing. We found, however, that charge sharing never happened near the boundary

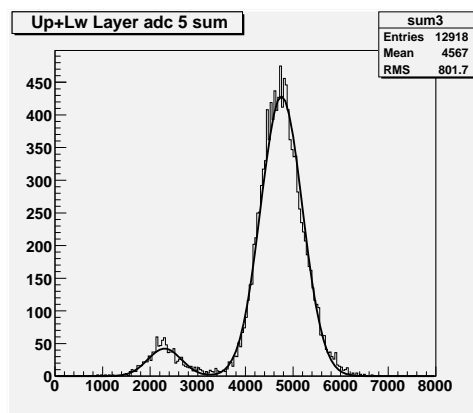


Figure 1: Charge sum distribution.

of the inner and the outer GEM electrodes. The exact reason is still unknown but it could be attributed to the charge-up of the insulator of the GEM boundary affecting the charge collection. The charge sharing was hence not required for the positions in the boundary region. After normalizing the charge sums to that of some reference position, we found that the normalized charge sums range from 0.49 to 1.08. The observed gain non-uniformity is 2.5 times larger than the expected 20% or less from the mechanical tolerance of the panel. We found a large field distortion near the panel edges, which partly explains the non-uniformity but not all of it. Further investigations for possible causes are needed including variations of operation conditions such as gas concentration, etc..

4 Summary

We have constructed and tested a pre-prototype of the GEM TPC end panels to verify basic design philosophy and some of engineering details including fabrication methods for the large prototype of the real ILC TPC. We have basically established a GEM framing scheme with some minor problems to be improved for the large prototype construction. We have also measured the gain uniformity over the pre-prototype panel and observed a 50% non-uniformity at maximum. The non-uniformity could partly be attributed to the field distortion due to the test chamber setup, but requires further studies to fully validate our basic design philosophy.

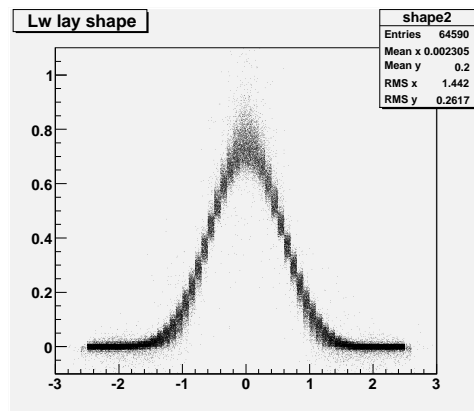


Figure 2: Signal spread.

Acknowledgements

This study is supported in part by the Creative Scientific Research Grant No. 18GS0202 of the Japan Society for Promotion of Science.

References

- [1] Slides:
<http://ilcagenda.linearcollider.org/contributionDisplay.py?contribId=317&sessionId=74&confId=1296>
- [2] D. C. Arogancia *et al.*, arXiv:0705.2210 [physics.ins-det].
- [3] M. S. Dixit, J. Dubeau, J. P. Martin and K. Sachs, Nucl. Instrum. Meth. A **518**, 721 (2004).
- [4] <http://www.scienergy.co.jp/>
- [5] <http://www.jae.co.jp/e-top/>
- [6] http://www.fkkasei.co.jp/english/index_e.html

Status of Large TPC Prototype Field Cage

Lea Hallermann^{1,2}, Peter Schade^{1,2}
for the LCTPC collaboration

1- DESY
Notkestraße 85, 22607 Hamburg - Germany
2- Universität Hamburg - Institut für Experimentalphysik
Luruper Chaussee 149, 22761 Hamburg - Germany

Four concepts for detectors at the International Linear Collider (ILC) have evolved. One of these proposals is the Large Detector Concept (LDC) [2]. It contains a large continuous gaseous tracker surrounded by a highly granular calorimeter all embedded in a solenoidal 4T magnetic field. Within the LDC concept and in the framework of the EUDET programme, the FLC TPC group at DESY in collaboration with the Department of Physics of the University of Hamburg develops a field cage for a large Time Projection Chamber (TPC) prototype. In the following, the status of its design and construction will be described.

1 The Large Prototype Proposal

The EUDET project [3] is an EU supported project to develop an infrastructure for detector R&D for the ILC. The construction of a Large Prototype (LP) for an TPC is part of it. This prototype is designed and will be operated by the LCTPC collaboration. With the LP studies of e.g. amplification systems, readout structures and electronics will be performed. A first series of tests is planned at the electron test beam at DESY. A superconducting magnet (PCMAG) from KEK is installed at the test beam area since winter 2006. Together with a high precision silicon telescope and the LP this will become a powerful research infrastructure for the development of TPC detectors at the ILC.

2 Field Cage Design

The dimensions and the field homogeneity of the magnet constrain the field cage dimensions. The LP will be 60 cm long and will have an outer radius of 77 cm. This leads to a gap of 4 cm all around between the field cage and the magnet, where silicon strip detectors will be mounted. In Figure 1 the LP is shown inside the inner region of PCMAG, where the field deviations are smaller than 3%.

The walls of the prototype will consist of composite material to obtain a lightweight but stable structure with the smallest possible amount of dead material. A technical drawing of the field cage is shown in Figure 2.

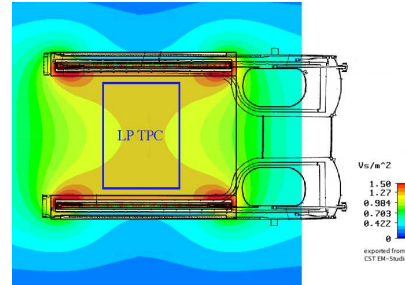


Figure 1: LP in simulated magnetic field of PCMAG

2.3 Drift Field Quality

Besides the design of the field strip foil, the accuracy of the used resistors and a potential tilt of the end plates will influence the drift field quality. The chosen surface mount device (SMD) resistors provide deviations of less than 0.1% at 1 M Ω . This yields slightly modified potentials on the strips. The resulting electrical field, which was calculated with a randomly generated set of these resistors, showed only deviations of $\Delta E/E < 10^{-4}$.

A tilt of the cathode of 0.2 mm leads to field deviations, which are shown in Figure 3. In the corners near the cathode, on the right hand side of the plot, the deviations are remarkably high but within 25 cm towards the anode the field strips level this out and the field reaches the aspired quality with $\Delta E/E < 10^{-4}$.

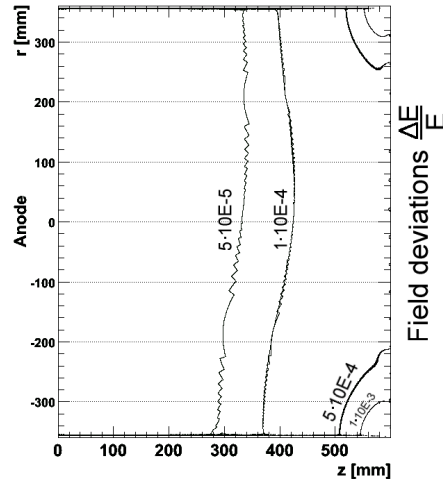


Figure 3: Calculated field deviations caused by tilted cathode. The figure shows a longitudinal cut through the LP.

3 Field Cage Production and Silicon Strip Detectors

The field strip foil as well as the field cage itself will be built by external companies, which are specialised in production of circuit boards respectively composite materials. The anode for the LP with the readout structure will be designed and built by the LCTPC collaboration. The silicon strip detectors will be mounted on the support structure between magnet and field cage. They are used to get independent reference points for particle tracks. The SiLC collaboration will install two perpendicular layers of silicon strips on both sides of the field cage. These modules will have a size of 10 × 10 mm² and are expected to provide a resolution of 10 – 12 μm in $r\varphi$ and 20 μm along the z axis.

4 Acknowledgments

This work is supported by the Commission of the European Communities under the 6th Framework Programme "Structuring the European Research Area", contract number RII3-026126.

5 Bibliography

References

- [1] Slides: <http://ilcagenda.linearcollider.org/contributionDisplay.py?contribId=319&sessionId=74&confId=1296>
- [2] LDC outline document: <http://www.ilcldc.org/documents/dod/>
- [3] <http://www.eudet.org>

A Study of Spatial Resolution of GEM TPC with Ar-CF₄-iC₄H₁₀ Gas Mixtures

H.Kuroiwa¹, K.Fujii¹, M.Kobayashi¹, T.Matsuda¹, R.Yonamine¹,
A.Aoza², T.Higashi², A.Ishikawa², A.Sugiyama², H.Tsuji²,
K.Hiramatsu³, Y.Kato³, T.Yazu³,
T.Watanabe⁴,
H.Bito⁵, O.Nitoh⁵, H.Ohta⁵, K.Sakai⁵,
D.Arogancia⁶, A.Bacala⁶, C.J.Gooc⁶, R.Reserva⁶,
R.D.Settles⁷,
L.Cao⁸, Y.Gao⁸, Y.Li⁸, J.Li⁸, and Z.Yang⁸

1 - IPNS, KEK, Oho 1 Tsukuba 350-0810, Japan
2 - Saga University, 1 Honjho-machi, Saga 840-8502, Japan
3 - Kinki University, 3-4-1 Kowakae, Higashi-Osaka 577-8502, Japan
4 - Kogakuin University, 1-24-2 Nishi-Shinjyuku, Tokyo 163-8677, Japan
5 - Tokyo University of Agriculture and Technology, Koganei, Tokyo 184-8588, Japan
6 - Mindanao State University Iligan Institute of Technology, 9200 Iligan, Philippines
7 - Max Planck Institute for Physics, Munich, Germany
8 - Tsinghua University, CN-100 084, Beijing, China

Preliminary results of the spatial resolution of a GEM TPC with Ar-CF₄ (3%)-iC₄H₁₀ gas mixtures are reported.

1 ILC TPC and Ar-CF₄ gas mixtures

The Time Projection Chamber (TPC) with the Micro-Pattern Gas Detectors (MPGD) is one of the candidates of the main tracker at the International Linear Collider (ILC). Three MPGD TPCs described in the ILC Reference Design Report [1] have the dimension of 2.8-4 m in diameter and 3-4.6 m in length. They are to provide 200 space points along each particle track with the R ϕ spatial resolution of 100 μ m or better. The momentum resolution of $\delta(1/p_t) \leq 0.5 \times 10^{-4} (\text{GeV}/c)^{-1}$ is envisaged in the magnetic field of 3-4 T.

The spatial resolutions of MPGD TPCs have been studied using small TPC prototypes [2]. It has been shown that the micromegas TPC with the resistive anode readout and the multilayer GEM TPC readout by narrow standard pads of around 1 mm wide can achieve the spatial resolution down to 50 μ m for the short drift distance up to a few 10s cm.

To realize the target resolution in the whole range of the drift length of the ILC TPC, we need to choose a gas mixture with small transverse diffusion or a large $\omega\tau$ in the high magnetic field. Ar-CF₄ gas mixtures are known to have the large $\omega\tau$ up to around 20 at 4T. Fig. 1 shows the spatial resolutions of GEM TPC with Ar(97%)-CF₄(3%) calculated by a new analytic formula [4]. Here the transverse diffusion constant was assumed to be 20 $\mu\text{m}/(\text{cm})^{1/2}$ based on the Magboltz simulation [5], and the

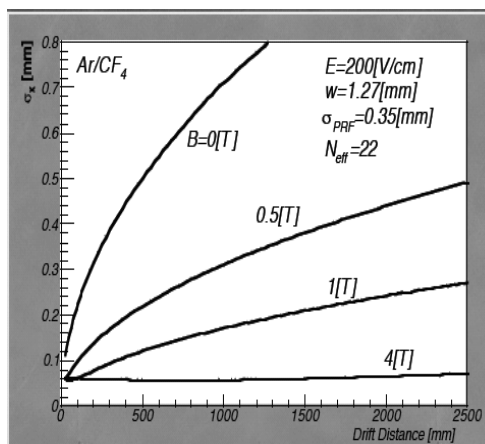


Fig.1 The R ϕ spatial resolution of GEM TPC calculated by the analytic formula for Ar(97%)-CF₄(3%) gas mixture in the magnetic field up to 4T [3].

width of the standard readout pads and the width of the pad response function of the multilayer GEM were taken to be 1.27 mm and 350 μm , respectively. The effective number of electron N_{eff} appears in the formula was assumed to be 22 [4].

The Ar-CF₄ gas mixtures are also known to have the high electron attachment at the high electric field above 1 kV/cm [5]. It is conjectured, however, that the region in the gas amplification gap of MPGD where the electron attachment dominated over the gas amplification might be limited so that MPGD should provide sufficient gas amplification. The attachment in the drift region (<400V/cm) is estimated to be negligible even for the large ILC TPC. The most recent work of the micromegas TPC readout by the resistive anode measured the excellent spatial resolutions of around 50 μm for Ar(95%)-CF₄(3%)-iC₄H₁₀(2%) gas mixture in the 5T magnetic field [6]. The resolutions measured at 0.5T in the same experiment gave the effective number of electrons N_{eff} of 28.8 proving the above conjecture. It was also reported that a three-layer GEM TPC worked successfully with the same gas mixture [7]. However the measured resolutions were limited by the large pad width of 8 mm and there was no report on N_{eff} .

Beside the standard characteristics of the TPC gas there are also special requirements to the TPC gas at ILC. The neutrons from the beam dumps of ILC may arise as a significant background in TPC [1]. To minimize their effects it may be advisable to avoid any gas mixture which contains much hydrogen. Also when we adopt the GEM gating [8] to prevent the ion feed back to the drift region from the amplification region, the selection of the TPC gas mixture may become even narrower. Although there is an argument against the Ar-CF₄ gas mixtures since the CF₄ is an etching gas, the Ar-CF₄ gas mixtures seem to have advantage in these two points.

2 GEM TPC with Ar-CF₄(3%)-iC₄H₁₀ gas mixtures

We report here preliminary results of our measurement of the spatial resolution of a GEM TPC with Ar-CF₄(3%)-iC₄H₁₀ gas mixtures.

The measurement was done using the MP-TPC prototype. The MP-TPC is a small TPC prototype with the cylindrical drift region of 14.5 cm in diameter. It has a detachable endplate which carried a GEM detector in this measurement. The maximum drift length with the GEM detector was 25.4 cm.

The GEM detector consists of 3-layers of the standard CERN GEM (10 x 10 cm²) mounted on a pad plane. The transition gaps between the three GEMs were set to be 1.5 mm for this measurement and the induction gap to the pad plane 1.0mm. The pad plane has 12 pad rows. The width (pitch) of each pad is 1.17 (1.27) mm and the length (pitch) 6 (6.3) mm. The pads in the adjacent rows are staggered by one half of the pad pitch. In this measurement the central 32 pads of 7 pad

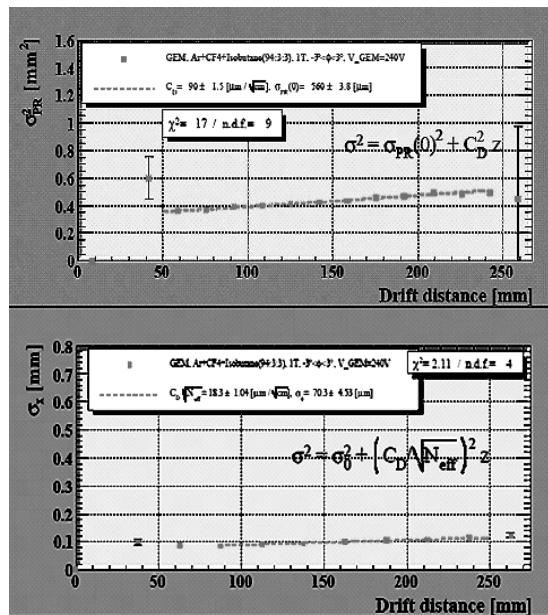


Fig.2 The width of the pad response (top) and the spatial resolution (bottom) as functions of the drift length. The gas is Ar(94%)-CF₄(3%)-Isobutene(3%) gas mixture. The dotted line in each plot is the best fit to the data by the function given in the plot.

rows were actually readout by the ALEPF TPC electronics. Some more details of the MP-TPC and the readout electronics may be found elsewhere [4].

The MP-TPC was placed at the center of a superconducting solenoid of the MRI model at the KEK cryogenic center. The inner bore is 80 cm in diameter and 1.6 m in length. The uniform magnetic field of 1T is generated by a multilayer superconducting coil. An iron yoke of about 10 cm thick surround the cryostat improves the field uniformity.

The TPC gas was mixed on the site using three mass flow controllers (MFC). The flow rate of the mixed gas was typically 100cc/min during the measurement. The MFC for Ar gas has the maximum flow rate of 1 liter/min, and the other two for CF₄ and iC₄H₁₀ 20 cc/min. The MFCs were calibrated recently. The actual flow rates during the measurement are estimated to be within 5% or better to the preset values.

The measurement was made with the cosmic ray tracks triggered by two scintillator counters immediately above and below the MP-TPC. Each scintillator counter was readout by a fine-mesh PMT.

3 Spatial resolutions and N_{eff}

The data were collected for the two different values of the iC₄H₁₀ concentration; (1) Ar(94%)-CF₄(3%)-iC₄H₁₀(3%) and (2) Ar(96%)-CF₄(3%)-iC₄H₁₀(1%). The lower concentration of iC₄H₁₀ is preferred when the neutron background becomes an important issue. The voltage applied to each GEM was 240 V for the gas mixture (1) and 230 V for the gas mixture (2) keeping the gas gain to be same. The voltages of the transition gaps and the induction gap were set to be same to the GEM voltage. The drift velocity was tentatively chosen to be around 80V/cm in this measurement; 80.4V/cm and 77.6V/cm for the gas mixture (1) and (2), respectively. For each gas mixture, we accumulated about 60,000 cosmic ray triggers. The magnetic field was 1T.

Before the data taking we tried to operate our GEM TPC with Ar(97%)-CF₄(3%) but without any iC₄H₁₀ concentration. We could not see the GEM signal up to the GEM voltage of 340V, confirming the observations by other people [9].

The cosmic ray tracks were found by using the Double-Fit program [4] which performed the χ^2 fit to hit points found in the 7 pad rows. The circle fit was applied. In the following discussion the comics rays were selected in $-3^\circ < \phi < 3^\circ$, where the angle ϕ was the angle of the projected track on the pad plane relative to the normal of the pad rows, to minimize the pad angle effect.

For the gas mixture (1) with the 3% iC₄H₁₀ the drift velocity was measured to be 3.4 cm/ μ s while the Magboltz simulation predicts 3.15 cm/ μ s. The drift velocity was measured by the endpoint of the time distribution of the cosmic ray tracks. In the upper plot of Fig.2 shows the widths of the pad response $\sigma_{\text{PR}}(z)$ as a function of the drift length z . The linear fit to the data by the formula $\sigma_{\text{PR}}(z)^2 = \sigma_{\text{PR}}(0)^2 + C_{\text{DT}} z$ gives the transverse diffusion constant C_{DT} of $90 \pm 1.5 \mu\text{m}/\text{cm}^{1/2}$ to be compared

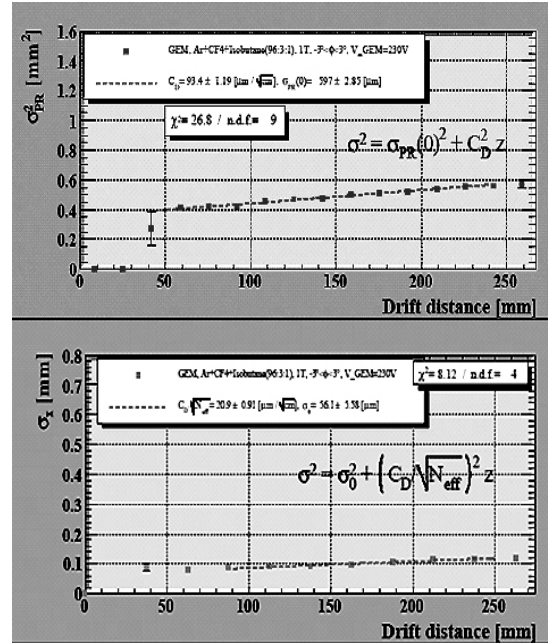


Fig.3 The width of the pad response (top) and the space resolution (bottom) as functions of the drift length. The gas is Ar(96%)-CF₄(3%)-iC₄H₁₀(1%) gas mixture. The dotted line in each plot is the best fit to the data by the function given in the plot.

to $88 \mu\text{m}/\text{cm}^{1/2}$ calculated by the Magboltz simulation. The measured spatial resolutions $\sigma_x(z)$ are shown in the lower plot of Fig.2. Fitting the spatial resolutions with the formula $\sigma_x(z)^2 = \sigma_x(0)^2 + [(C_{DT})^2/N_{\text{eff}}]z$ [4], we obtain the effective number of electrons N_{eff} of 24 ± 2 . Here the fitting was made in the region of the drift length larger than 80 mm to avoid the hodoscopes effect.

Fig 3 shows the results for the gas mixture (2) with the 1% $i\text{C}_4\text{H}_{10}$. The diffusion constant measured is $93 \pm 2.0 \mu\text{m}/\text{cm}^{1/2}$ while the Magboltz simulation predicts $71 \mu\text{m}/\text{cm}^{1/2}$. From the measured spatial resolutions in the lower plot of Fig. 3 the N_{eff} is found to be 20 ± 1 . The drift velocity measured is $4.2 \text{ cm}/\mu\text{s}$ while the Magboltz simulation predicts $3.9 \text{ cm}/\mu\text{s}$.

These measured N_{eff} are comparable to those for the micromegas TPC operated with $\text{Ar}(95\%)-i\text{C}_4\text{H}_{10}(5\%)$ gas mixture [4] and the 3-layer GEM TPC with the TDR gas and P5 gas [10].

4 Conclusions

We measured the spatial resolutions of the 3-layer GEM TPC with the $\text{Ar}-\text{CF}_4(3\%)-i\text{C}_4\text{H}_{10}$ gas mixtures at 1T. In the limited operational conditions we found no serious problem to operation the GEM TPC for the gas mixtures while we could not operate it without $i\text{C}_4\text{H}_{10}$. The effective number of electrons N_{eff} were found to be comparable to those found for the other standard gases. We need to understand the somewhat (10%) higher drift velocities and the significantly (30%) lower diffusion constant obtained for the gas mixture with the 1% $i\text{C}_4\text{H}_{10}$ concentration. We continue our study of the GEM TPC with the $\text{Ar}-\text{CF}_4(3\%)-i\text{C}_4\text{H}_{10}$ gas mixtures, in particular, toward higher drift fields.

5 Acknowledgements

This study is supported in part by the Creative Scientific Research Grant No. 18GS0202 of the Japan Society of Promotion of Science. We thank to the KEK Cryogenic Center and the IPNS cryogenic group for their sincere cooperation.

6 References

- [1] ILC Global Design Effort and World Wide Study, ILC, Reference Design Report, August, 2007: <http://www.linearcollider.org/cms/?pid=1000025>
- [2] LC-TPC group, LC-DET-2007-005. Also <http://ilcagenda.linearcollider.org/sessionDisplay.py?sessionId=37&slotId=0&confId=1212#2007-02-05>
- [3] K. Fujii and M. Kobayashi, private communications.
- [4] D.C Arogancia et.al., arXiv: 0705.2210v1 [hep-ex] 15 May 2007.
- [5] S. Biaggi, Magboltz 2 version 7.1, (2004) CERN library.
- [6] M. Dixit et. al., CARLETON-HP-732, Mar 2007.
- [7] E. Radicioni et. al., MP3-3, 2006 IEEE Nuclear Science Symposium Conference Record.
- [8] A. Sugiyama et. al., in this workshop: <http://ilcagenda.linearcollider.org/getFile.py/access?contribId=323&sessionId=74&resId=0&materialId=slides&confId=1296>
- [9] Y. Lie and P. Colas, private communications.
- [10] M. Kobayashi et. al., LCWS06: <http://indico.cern.ch/getFile.py/access?contribId=137&sessionId=4&resId=1&materialId=slides&confId=568>

Measuring Distortions in a TPC with Photoelectrons

Dean Karlen

University of Victoria and TRIUMF
Canada

In order to reach the desired momentum resolution with the large TPCs proposed for the ILC detectors it will be necessary to measure and correct distortions of the electron drift, particularly that due to non-uniform magnetic fields. This paper presents a proposal for using photoelectrons generated at the central cathode to provide critical information for distortion corrections.

1 Introduction

The large TPCs proposed to perform the central tracking for the ILC detectors will be very sensitive to non-uniformities in the electric and magnetic fields because of the long drift distance for the electrons. When operated with a fast gas in a strong magnetic field, the electrons will move nearly parallel to the magnetic field lines which reduces any distortions from electric field non-uniformities while increasing the sensitivity to non-uniform magnetic fields. With the finite beam crossing angle for the ILC, it is expected that a so-called anti-DID field will be introduced to reduce the background from low energy particles entering the detector. The effect of this non-uniform field component needs to be very well understood and corrected for, in order to attain the desired momentum resolution for the TPCs.

This paper presents a proposal for using photoelectrons as a controlled and reproducible pattern of electrons with which to monitor all aspects of electron transport in the TPC, including drift velocity, diffusion, gas gain, and the distortions from straight line paths arising from electric and magnetic field non-uniformities and from positive ion effects.

2 Producing photoelectrons

The proposed approach to produce a pattern of photoelectrons involves placing a set of aluminum elements on the copper surface of the central cathode. By flashing regions of the central cathode with a diffuse pulse of 266 nm wavelength light, photoelectrons are emitted from the aluminum and not the copper, due to the different work functions of those two metals. The aluminum pattern would be accurately surveyed during the central cathode construction, allowing for absolute measurements of the transverse displacements of the drifting electrons. This technique was used in the STAR TPC and will be used in the T2K TPCs that are now under construction [1].

For the test pattern to be useful to help empirically correct distortions that arise from imprecise knowledge of the fields or from positive ions, it is important to consider the ambiguities in solving the inverse problem: given the known positions of the test-pattern, and images from the device, determine the transverse displacements that electron clouds experience. If the test pattern consists only of long strips to mimic tracks, as was done in the STAR TPC, it is not possible to determine these displacements, as illustrated in Figure 1.

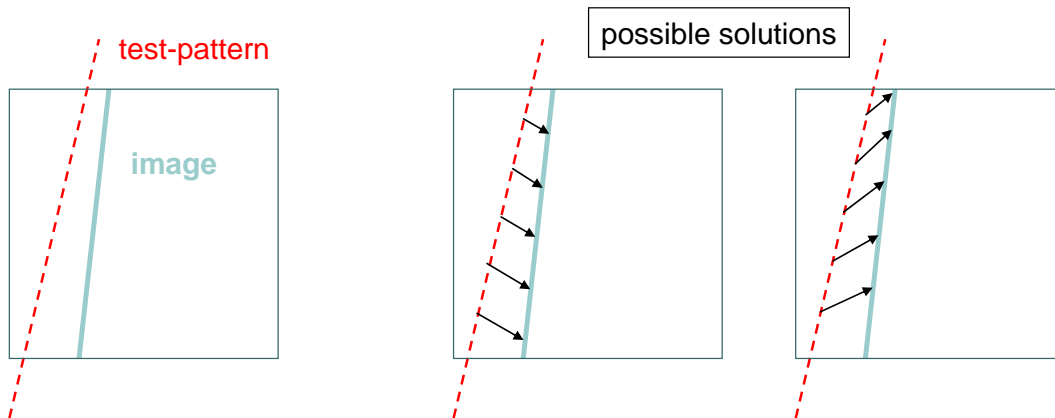


Figure 1. The left figure shows the test pattern projected onto the endplate and an observed image in the case of a large distortion in the drift lines of the electrons. On the right are shown two possible solutions that can produce the observed effect to illustrate the ambiguity that arises when using strips as test patterns.

To deduce the transverse displacements of the electron clouds, a pattern of dots should be used rather than lines. In order for the same system to also measure the diffusion constant for the gas, a few line patterns need to be incorporated, so that the same method as for tracks produced by traversing charged particles can be used.[2]

3 Demonstration of the system

As part of the tests for the T2K TPC design, this type of photoelectron calibration system was incorporated into the large T2K prototype TPC built in Canada in 2005. The test pattern consists of lines only, with thin aluminum tape applied manually and cut into 2,3, and 4 mm wide strips. Two contrast materials for central cathode surface were used, copper and carbon loaded kapton (the latter being the STAR design). In early 2007, a yag laser was acquired to test the photoelectron system. The UV light was introduced through the TPC endplate through a fibre terminated by two small lenses to defocus the light over the entire central cathode. The aluminum pattern and one of the first observed images is shown in Figure 2.

The jtpc analysis package was used to fit the track parameters for each strip separately. With laser images taken every second, it is possible to monitor the drift velocity at the precision of about 0.01% every few minutes. At the same time the diffusion constant and relative gain can both be monitored at the precision of about 1%.

The amplitude observed for any set of pads is seen to fluctuate by more than 10% from one laser event to the next. Power meters confirm that the pulse to pulse energy from the laser has a standard deviation of about 3%. The observed fluctuations can be attributed to the photoelectron production itself, which should follow a Poisson distribution. In fact, the variance is found to be proportional to amplitude, as expected for a Poisson distribution, and therefore the measure of variance and amplitude allows a direct estimate of the absolute gain, as shown in Figure 3.

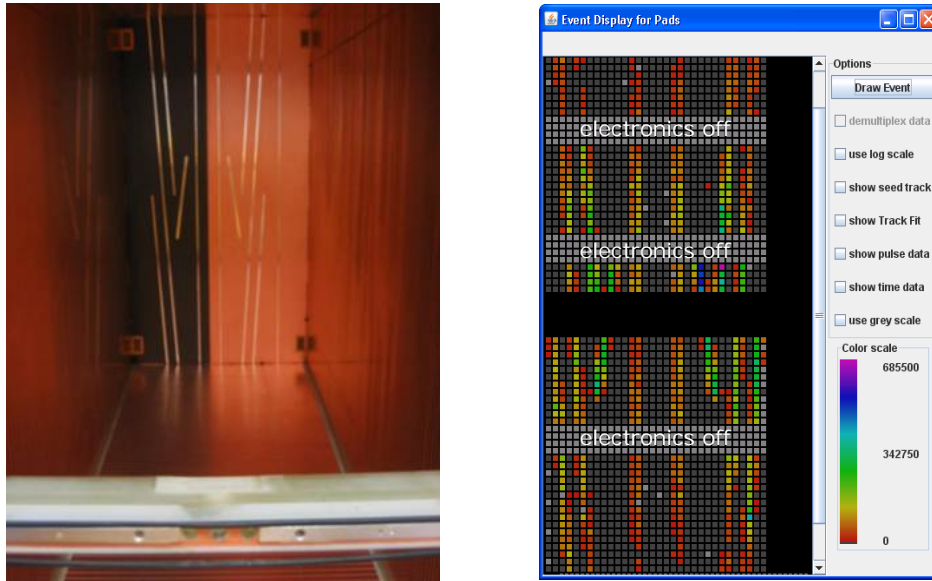


Figure 2. The photograph on the left shows a view inside the T2K prototype TPC built in Canada in 2005. The central cathode surface on the left is carbon loaded kapton, and copper on the right. The aluminum strips are clearly visible. On the right is an event display, showing the amplitude of the signals on the readout pads after a single flash of the UV laser.

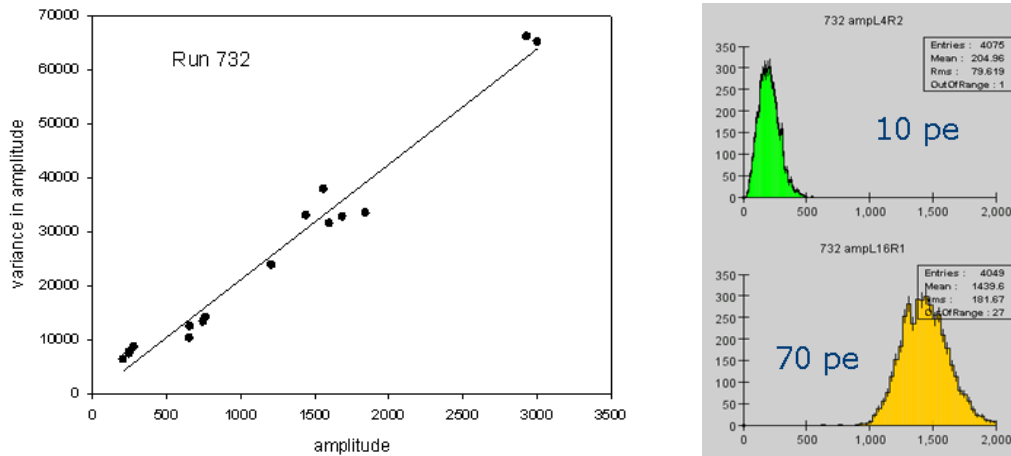


Figure 3. On the left is shown the observed relation between variance and amplitude for different sets of pads from laser events. This appears to be linear as expected for a Poisson process, thereby allowing for a direct estimate of the absolute gain of the system. On the right are shown the distribution of amplitudes for two selected pad groups and the estimated mean number of photoelectrons responsible for the signals.

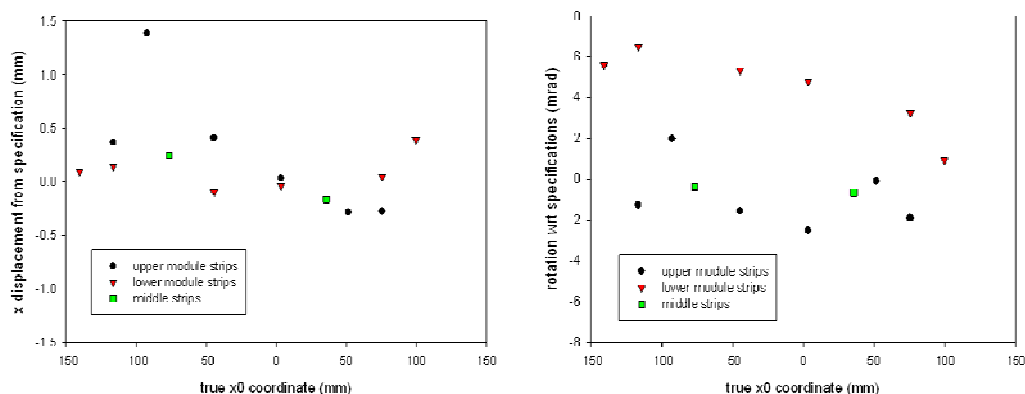


Figure 4. On the left is shown the difference between the specified and measured horizontal coordinates for the aluminum strips at the centre line of the TPC. The right figure shows the difference between the specified and measured azimuthal angles of the strips.

The track parameters for the horizontal coordinate (at the vertical center of the TPC) and the azimuthal angle for each strip pattern are compared to the specified locations for the strips in Figure 4. The horizontal displacements are seen to be all within 0.5 mm apart from one strip. There appears to be an effective rotation for the images in the lower module. When incorrect field cage potentials are applied, distortions greater than 10 mm are observed.

4 Considerations for the ILC TPC

For the ILC TPC photoelectron calibration system, a combination of dots and some radial (or nearly radial) strips should be applied to the central cathode. Dots of radius 1 mm produce an electron cloud with transverse standard deviation of 0.5 mm, allowing for measurements of displacements with precision of about 50 μm with just a few light pulses. Some gaps must be designed into the endplate readout to allow for the source of UV light to enter. This can be done with a few radial gaps – so that the azimuthal acceptance is uniform around the TPC. The system will require that the light intensity not vary across the surface of a dot by more than about 3%. The same specification is necessary for the knowledge of the relative gains from one pad to the next. A 3% difference results in a systematic shift of about 40 μm . In order to verify the utility of this system for the high precision requirements of the ILC TPC, we propose to install a photoelectron calibration system in the large prototype currently being designed by the LCTPC collaboration. Two fibers entering the endplate next to the readout modules will allow most of the central cathode to be exposed.

5 References

- [1] T2K TPC Technical design report, T2K TPC collaboration, January 2007.
- [2] D. Karlen, G. Rosenbaum, P. Poffenberger, Nucl. Inst. Meth. A555 (2005) 80.

Resolution Studies of GEM/Timepix Detector with 5 GeV electrons

A. Bamberger¹, K. Desch², U. Renz¹, M. Titov^{1,3}, N. Vlasov¹, P. Wienemann²,
S. Zimmermann¹ and A. Zwerger¹

1- Albert-Ludwigs University of Freiburg, Physics Institute, Freiburg, Germany

2- Rheinische Friedrichs-Wilhelms-Universität, Physics Institute, Bonn, Germany

3- CEA Saclay, DAPNIA/SPP, Gif sur Yvette, France

This contribution investigates a prototype of a TPC readout with a highly pixelated CMOS ASIC, which is an option for charged particles tracking of the ILC. A triple GEM stack was joined with a TimePix and MediPix2 chip (pixel size of $55 \times 55 \mu\text{m}^2$) and its readout properties were investigated with 5 GeV electrons. The spatial resolution of the cluster center reconstruction was determined as a function of drift distance using different cluster algorithms and compared with Monte Carlo predictions.

1 General consideration

The recent development of Micro-Pattern-Gas-Detectors (MPGD) allows an extended field of application for detectors with gas multiplication. For Time-Projection-Chambers (TPC) the readout with Gas-Electron-Multipliers (GEM) [1] has been demonstrated in conjunction with an unconventional readout option with high pixelation using the MediPix2 chip [2]. The TimePix [3] and MediPix2 is investigated the first time with 5 GeV electrons from DESY II. They have the virtue of negligible multiple scattering. An external tracking with Si-telescope provides information on the track position which is used for resolution determination and for the drift velocity measurements using a TimePix chip.

2 Basic setup for the GEMs and the MediPix2/TimePix chip

A cross sectional view of the triple GEM plus Medipix2 and Timepix detector with an electron beam crossing the drift region is shown in Fig.1 (left part). The drift volume of 6 mm thickness and $10 \times 10 \text{ cm}^2$ in size serves for charged track detection. The drift field is about 1.1 kV/cm. Three CERN-produced GEMs of the same area as the drift volume with $70 \mu\text{m}$ holes of $140 \mu\text{m}$ pitch are arranged in a stack above the readout plane with 2 mm (2-2-1) or 1 mm distances (1-1-1) for the transfer gaps, the latter provides a collapsed setup in order to study possible effects on the spatial resolution. With the triple GEM stack gas amplification of $\approx 10^5$ can be achieved with Ar/CO₂ and He/CO₂-mixtures for the high resolution detection of minimum ionizing particles. The MediPix2 and TimePix chip is positioned at a distance of 1 mm from the last GEM exposed to a field of $E_I = 4.0 \text{ kV/cm}$. The advantage of a GEM setup is the robust operation, since the fields of the gas multiplication region ($\approx 70 \text{ kV/cm}$) are well shielded inside GEM holes, see [2].

3 The test beam setup

The MediPix2 and Timepix chip has a surface of $14 \times 14 \text{ mm}^2$ and a pixel size of $55 \times 55 \mu\text{m}^2$. It is positioned close to the border of the GEM stack, see Fig. 1 (right part). The remaining

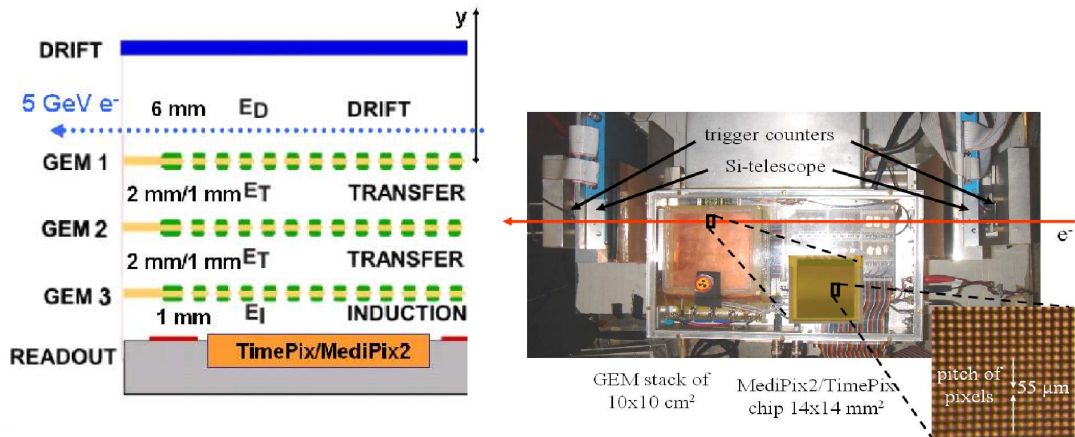


Figure 1: Setup of drift volume: stack and MediPix/TimePix (left) and test beam setup where inserts show size of MediPix2/TimePix and the size of a pixel (right)

surface of the GEMs is covered with 24 anode pads of $2 \times 2 \text{ cm}^2$ size for monitoring purposes. The gas tight box contains the GEMs, the resistor chain, the TimePix and MediPix2 chip and the readout electronics of the pads.

The readout of the MediPix2 and TimePix is done with MUROS2 using the fast shutter option. The thresholds for the pixels used were $990 e^-$ and $830 e^-$ for the MediPix2 and the TimePix, respectively. The electron beam is defined by trigger scintillating counters of $1 \times 1.5 \text{ cm}^2$ in size and a Si-telescope with 3 planes of strips (two planes allow measurement of the x-coordinate in front and behind the GEM plus Medipix2 and Timepix, and one plane is used for the y-coordinate measurement in front of the detector). The effective readout pitch of Si-telescope is $50 \mu\text{m}$.

4 TimePix: The TIME, TOT and MIXED modes

The TimePix has a clock, which is distributed throughout the entire chip. A register on each pixel counts the number of clock cycles in a way depending on the chosen mode of operation. For each pixel this mode can be set individually. In TIME-mode the cycles are counted from the point when the signal crosses the threshold till a common stop by the gate signal (= "Fast shutter"). The other mode "Time-Over-Threshold" records the clock cycles as long as the pulse is above the threshold. The maximum number of counts in this measurement is limited by the chosen gate width of $12.6 \mu\text{s}$, which is about 600 counts at a given clock frequency of 48 MHz.

In a special configuration "Mixed Mode" every other pixel switches the TIME and TOT mode in checker board fashion. This results in 1/2 of all pixels are of TIME-type and another 1/2 of the TOT-type. This allows a proximity information of both TIME and TOT.

5 Cluster reconstruction and point resolution

Typically, 8 - 9 non-separated clusters per track were observed, see Fig. 2 (left part). Images with double tracks were not considered in the current analysis. The following three clustering methods were used, where last two can separate the overlapping clusters using the charge deposition information (TOT or MIXED modes) resulting in average 10 - 11 clusters per event:

- “Contiguous areas” method leaves overlapping clusters not separated. That method is applicable for any TimePix mode. The result is a lower number of clusters depending on the effective threshold settings and therefore not covered here
- “Saddle Point” method separates the contiguous clusters making a line for secondary maximum in a projection transverse to track. The line divides the merged clusters at the saddle point
- “Island” method joins the adjacent pixels with a nonzero TOT values into clusters in the way that a pixel is joined into the cluster of its neighbor with a highest TOT value. The procedure is repeated for each pixel to produce a unique assignment of pixels to clusters. It results in a separation in two spacial coordinates available compared with the above case

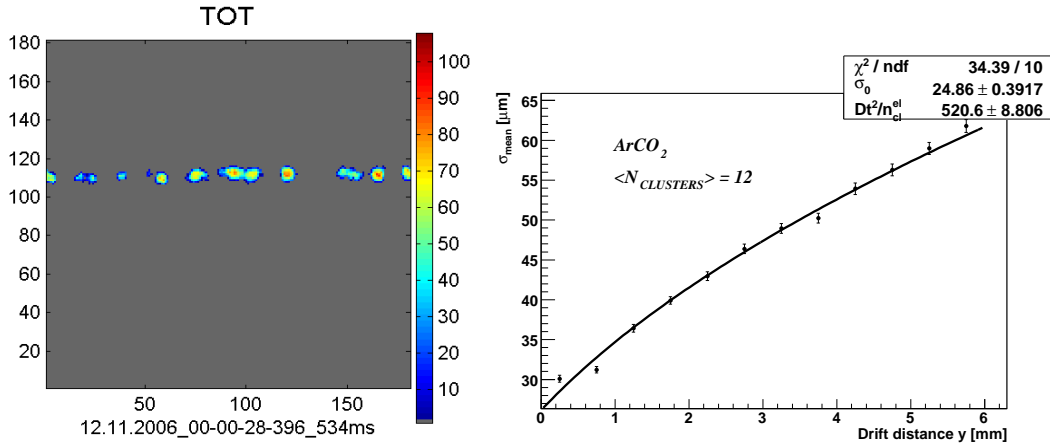


Figure 2: Image of 5 GeV electron track (left part) and σ_0 and D_t^2/n_{cl}^{el} for Ar/CO₂ (right part)

The evaluation follows basically [2]: A cluster is rejected if it contains less than 9 hits. The noise is removed beyond the cluster region. Two different methods of the straight line fits to the centers of the clusters result in an unbiased estimation of the standard deviation. Residuals of the fit to all cluster centroids (N) and a fit to (N-1) centroids resulting in a residual of the exempt cluster which is permuted over all clusters. These residuals enter into two Gaussian fits which produce $\sigma_{unbiased} = \sqrt{\sigma_N \times \sigma_{N-1}}$.

The left part of Fig. 2 shows a measured dependence of the resolutions versus the drift space for Ar/CO₂. In the drift region to separate the lateral diffusion within the drift space from the intrinsic GEM plus TimePix and MediPix2 resolution the y-coordinate information of the external telescope is used. The following parametrisation is applied for the fit: $\sigma^2 = \sigma_0^2 + \frac{D_t^2 \times y}{n_{cl}^{el}}$. The σ_0 equal to 24.9 ± 0.4 results from the fit for Ar/CO₂.

6 Comparison with Monte Carlo simulations

The results of spatial resolution σ_0 and D_t^2/n_{cl}^{el} corresponding to different clustering methods for Ar/CO₂ and He/CO₂ are summarised in Tab. 2. The comparison with HEED simulations [4] is also given in the table.

	DATA			Simulations	
	Gas	σ_0	D_t^2/n_{cl}^{el}	σ_0	D_t^2/n_{cl}^{el}
“Island”	Ar/CO ₂	24.9 ± 0.4	521 ± 9	–	–
	He/CO ₂	29.4 ± 0.5	660 ± 14	–	–
“Saddle Point”	Ar/CO ₂	18.4 ± 2.7	467 ± 36	15.2 ± 3.8	726 ± 41
	He/CO ₂	27.1 ± 4.9	547 ± 78	19.4 ± 4.0	989 ± 54

Table 1: The values of σ_0 and D_t^2/n_{cl}^{el} for the data and Monte Carlo simulations. The comparison with Monte Carlo simulation is present at the moment only for the “Saddle Point” clustering method.

The agreement between two clustering methods is found to be good for both σ_0 and D_t^2/n_{cl}^{el} values. It is found that simulations considerably overestimate the slope D_t^2/n_{cl}^{el} comparing to the measurements for both gases.

The slope depends on the size of merged clusters because a higher number of electrons per detected cluster than for an ideally resolved cluster is present. This leads to a reduction of the effective transverse diffusion through the active volume and reduces the slope parameter. Based on this observation it is possible that the discrepancy of the Monte Carlo with respect to the slope is present, since the average number of detected clusters lower by a factor of 2 than expected from simulations [4].

7 Acknowledgments

We would like to thank the EUDET project for its financial support and the MediPix collaboration for supporting us work with readout software and hardware, especially with respect to the TimePix chip used for the very first time in an experiment. We would also like to thank Michael Campbell, Erik Heijne, Xavier Llopart and Fabio Sauli for stimulating discussions and a lot of valuable advices.

References

- [1] Nucl.Instr.Meth.A386(1997)531
- [2] A. Bamberger et al., “Readout of GEM Detectors Using the MediPix2 Chip”, NIMA573, 361-370(2007)
- [3] X. Llopart, see this conference
- [4] M. Hauschild, <http://hausch.cern.ch/hausch/MediPix.html>

Digital Active Pixel Array (DAPA) for Vertex and Tracking Silicon Systems

G. Bashindzhagyan¹, N. Korotkova¹, R. Roeder², Chr. Schmidt³ and N. Sinev⁴

1 - Skobel'syn Institute of Nuclear Physics - Moscow State University
Moscow, 119992 - Russia

2 - CiS Institut für Mikrosensorik
Konrad-Zuse-Straße 14, 99099 Erfurt - Germany

3 - Gesellschaft für Schwerionenforschung mbH
Planckstraße 1, 64291 Darmstadt - Germany

4 - University of Oregon/Stanford Linear Accelerator Center
Eugene, OR 97403-1274/Stanford, CA 94025 - USA

The concept of digital silicon sensor for vertex and tracker application is proposed. It is based on advanced type of active element and sophisticated digital architecture. Very fast binary readout is combined with approximately $8 \mu\text{m}$ space resolution.

1 Introduction

The concept of digital silicon sensor for vertex and tracker application is proposed. It is based on advanced type of active element and sophisticated digital architecture. Very fast binary readout is combined with approximately $8 \mu\text{m}$ space resolution.

$4 \times 4 \text{ cm}^2$ sensor composed of four $2 \times 2 \text{ cm}^2$ quarters should be produced as a regular microelectronic device on low resistivity silicon wafers. Basic element is about $25 \times 25 \mu\text{m}^2$ pixel with binary readout. It includes active sensor, low power amplifier and a few logical elements with parallel and serial outputs (Figure 1).

Active sensor is a fully depleted diode in $10 \mu\text{m}$ thick epitaxial layer on regular low resistivity silicon wafer with individual very low power amplifier and FF. The pixel outputs are connected into DAP "strips". Each strip consists of about 800 pixels. 2 cm long strips have $25 \mu\text{m}$ pitch according to the pixel size plus gap. Individual strip electronics and memory are positioned on the end of the strip near the quarter's edge.

2 DAPA overview

Within each strip all pixel signals are connected to one wire OR line through gate A. If a charged particle crosses ANY pixel which belongs to that strip, a short pulse (not potential) appears on the wire OR line. This pulse activates circuits which register signal arrival time. It can also be used to generate a fast first level trigger. This stage of DAPA activity can be used as microstrip detector with $25 \mu\text{m}$ pitch and binary readout. The same signal from the charged particle hit sets individual FF in the given pixel into "1" logical state. Serially connected FFs within strip work as a shift register. Every clock period information about hits in the entire strip is shifted one step toward strip end. After certain number of shifts, hit signal will reach strip end, where it's arrival time will also be registered. Delay between first (wire OR) signal and this (shift register output) signal is used to determine hit position within the strip. We suppose that about 100 MHz frequency can be used if DAPA detectors works as independent system without collider (bunch) synchronization (at GSI, for

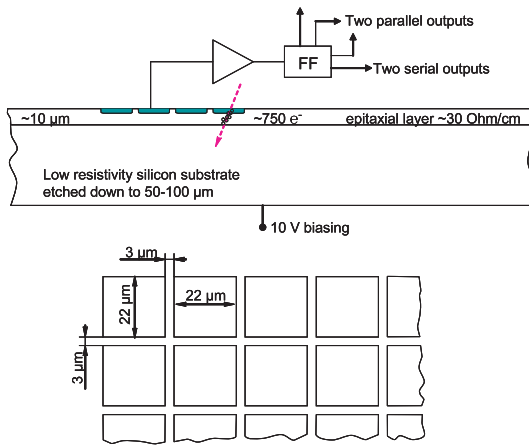


Figure 1: DAPA individual pixel

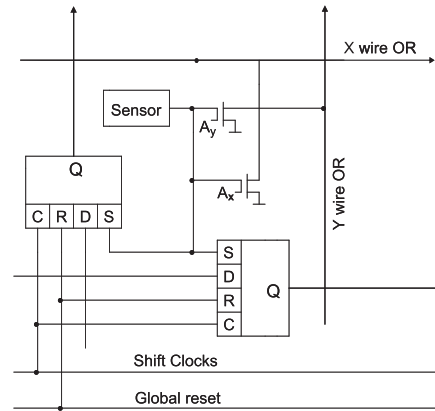


Figure 2: DAPA two orthogonal readout structure

example). If a few particles hit the same strip during one circle, it creates an ambiguity in pixel identification along a strip. It could be a case when occupancy and event rate are very high (CBM Vertex, for example). To prevent ambiguity identical readout schematic exists in perpendicular direction (Figure 2). A probability to get occasional coincidence in two lines of 800 pixel each is negligible. For LC application clock period corresponds to bunch period within a bunch train. This case we don't need shift register to work permanently. It has to be a clock train synchronized with bunch train +800 additional pulses to read out the whole of strip pixels. Rather simple controller is positioned on the edge of each quarter. It collects already zero suppressed information from all 800 strips and sends it via one serial output as its (quarter) number, strip number, time stamp and pixel on strip number. Actually it's complete event address is space and time for a further on-line and off-line analysis. Additional fast output exists for a first level trigger generation.

3 Two orthogonal readout properties

With two orthogonal readouts two wire ORs transfer fast signals to both perpendicular sides of the $2 \times 2 \text{ cm}^2$ DAPA quarter (Figure 2). The same is organized for serial readout (shift register). Double number of strip end modules is required accordingly. This DAPA version gives very serious advantages and can be used in a few ways:

1. As a regular DAPA device with fast strip/time registration and pixel position determination through the shift register. Using only X wire OR and registers.
2. As a double sided microstrip detector with binary readout. Only X and Y wire ORs are in use. Both shift registers are stopped by switching off the shift clock.
3. Two fast OR readouts can be combined with one shift register serial readout. It saves power which is required to operate digital electronics.

4. Both fast and both shift readouts are in use. Probability of ambiguity will be negligible in this case and clock frequency can be seriously decreased to reduce power consumption. By switching on and off shift clocks and changing its frequency, one can adjust DAPA properties during the experiment depending on current situation.

4 DAPA advantages

1. Completely integrated electronics.
2. Completely integrated zero suppression.
3. One line serial output.
4. Good space resolution on both coordinates. Even according to simplest scenario it works as a thin double sided microstrip detector with binary readout, $8\ \mu\text{m}$ resolution and all mentioned advantages.
5. DAPA with two orthogonal readouts can appear as very flexible device, which properties can be adjusted according to experimental requirements in any moment without any hardware changes.
6. Because of single side structure it can be produced on a thick regular substrate and after that thinned down to 50-100 microns.
7. DAPA has to be radiation hard detector due to very thin sensors.
8. More simple mechanical support and assembly procedure comparing with double sided microstrip detectors because of DAPA single side structure.
9. Much higher reliability because of an absence of many interconnections.
10. It is expected that DAPA system cost will be approximately the same as silicon microstrip detector system which requires electronic chips, interconnections and a lot of qualified manpower for sensor/chip assembly and tests.

5 Conclusion

- DAPA device can appear as a charged particle detector Nuclear physicists were dreaming about.
- It will be simple, convenient and reliable device for many future experiments including ILC, GSI and Super LHC, when dE/dX measuring is not required.

References

- [1] Slides:
<http://ilcagenda.linearcollider.org/contributionDisplay.py?contribId=473&sessionId=74&confId=1296>
- [2] G. Bashindzhagyan and N. Sinev, *Digital active pixel array for LC tracker*, 2005 International Linear Collider Workshop, SLAC, Stanford, California, USA (2005).

Geant4 Simulations of Machine-Induced Background in a TPC

Adrian Vogel

DESY – FLC
22603 Hamburg – Germany

In this talk [1] I present simulation results for machine-induced backgrounds in a TPC, which is foreseen as the main tracker of the LDC detector. Using Guinea-Pig as a particle generator and Mokka as a full detector simulation, background occupancies and space charges are estimated. Some special attention is paid to neutrons.

1 Backgrounds at the ILC

Even though the ILC is expected to provide a very clean experimental environment, its operation will not be perfectly background-free. A main source of backgrounds are electron-positron pairs which are created during the collision of the very strongly-focussed bunches. Due to the high space charge, the particles in the bunches can emit “beamstrahlung” photons [2] which can in turn scatter and create electron-positron pairs with typical energies in the GeV range. Other background sources are either supposed to be negligible (such as the beam dump or synchrotron radiation from the final focus) or have to be studied in further detail (e. g. the beam halo or losses in the extraction line).

In the order of 10^5 pairs are created per bunch crossing, but they very rarely reach the TPC directly because of their forward boost and the focussing effect of the strong magnetic field. Instead, they hit the forward calorimeters (mostly the BeamCal, which is in fact designed to observe the spatial distribution of the pairs) and the magnets of the beam delivery and/or the extraction line. There they create charged particles and photons in large quantities, and also neutrons can be released by photonuclear reactions.

Some of these shower products are backscattered, and while most of the charged particles will be confined to the innermost parts of the detector by the magnetic field, photons and neutrons can easily reach the TPC. The chamber gas can then be ionised through photon conversion, Compton scattering, and – in the case of neutrons – recoiling protons, provided that the quencher gas contains hydrogen.

2 Simulation Tools

2.1 Guinea-Pig – Particle Generator

Guinea-Pig [3] is used to simulate the beam-beam interaction. Given a set of beam parameters (energy, bunch sizes, emittances, bunch charge, etc.), Guinea-Pig writes out the electron-positron pairs which are created in one bunch crossing. For this talk, 100 bunch crossings with nominal ILC beam parameters [4] at $\sqrt{s} = 500$ GeV are used.

2.2 Mokka – Full Detector Simulation

The Geant4-based application Mokka [5] is used for a full simulation of the detector. The geometry corresponds to the “LDC version 2” [6], featuring a TPC with a sensitive volume

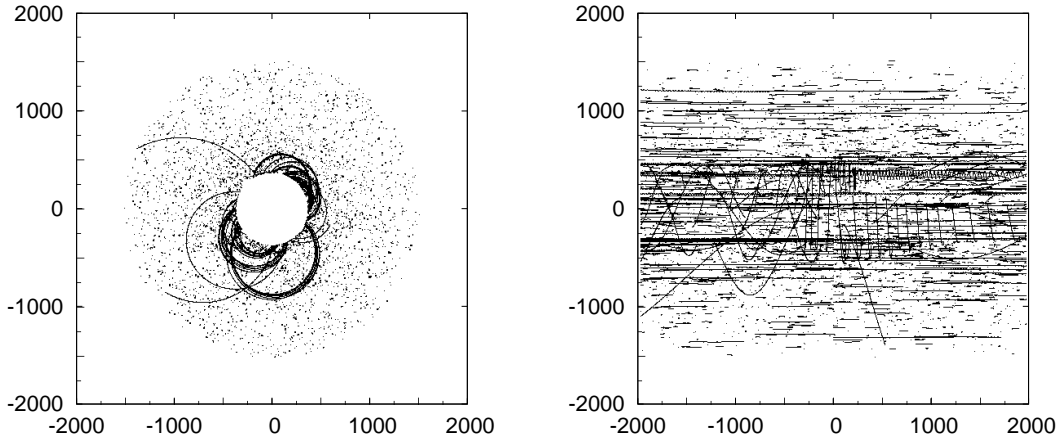


Figure 1: Front view (left) and side view (right) of Mokka hits from 100 bunch crossings

of $371 \text{ mm} < r < 1516 \text{ mm}$ and $|z| < 1970 \text{ mm}$. In the forward region there is a rather large distance of 1080 mm between LumiCal and BeamCal, which helps in shielding backscatterers from the BeamCal and therefore reduces the number of photons being able to reach the TPC.

Since the transportation of neutrons should be modelled as precisely as possible, the simulation uses a Geant4 built-in physics list named `QGSP_BERT_HP` which has high-precision models for low-energy neutrons (below 20 MeV).

3 Digitisation and Analysis

Mokka writes out the energy deposits which happen during each single simulated step of a particle in the TPC volume (Figure 1). These steps are currently limited to a maximum length of 5 mm [7], which is a trade-off between accuracy and output file size. The energy deposits are afterwards assigned to discrete volume elements (so-called voxels), the sizes of which correspond to the size of the readout pads on the anode (in ρ and ϕ) and the readout sampling of the signals (in z).

All 100 bunch crossings are overlaid with proper drift behaviour and bunch spacing, thereby forcing all signals into the “readout window” by a simple modulus operation – this should provide a sufficiently realistic picture from the middle of a long bunch train. (A few signals are created with very long delays, presumably because of nuclear reactions, but their fraction is negligibly small.) An ideal charge sharing over three pads is assumed, but z -dependent diffusion, gain fluctuations, or electronics effects such as shaping are not simulated yet.

3.1 Occupancy and Primary Space Charge

In Figure 2 the occupancy (i. e., the percentage of non-empty voxels) is calculated for different voxel sizes. Starting from $5 \times 5 \times 10 \text{ mm}^3$, the radial size (height of a pad row in ρ), the azimuthal size (width of a pad in ϕ), and the longitudinal size (depth of a time bin in z) are varied independently. The resulting overall occupancies stay well below 1% as long as the voxel dimensions do not get too large.

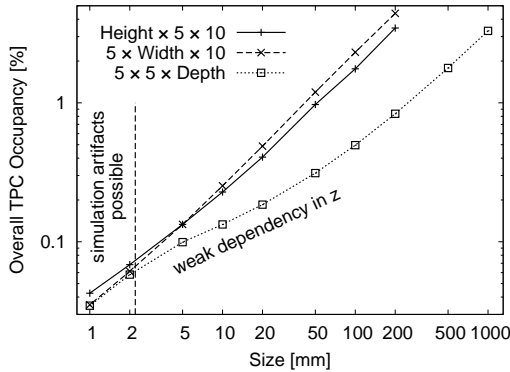


Figure 2: Occupancy in the TPC from 100 bunch crossings, calculated for different voxel sizes (note the logarithmic scale)

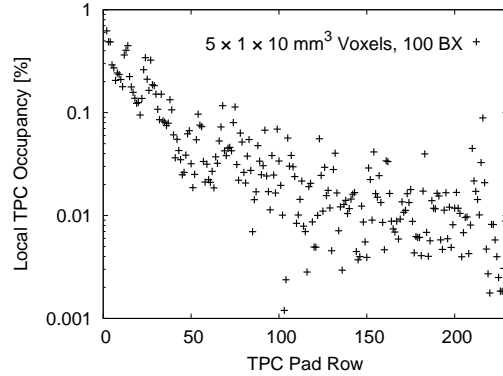


Figure 3: Local occupancy in the TPC from 100 bunch crossings, shown in dependence of the radial position

For height and width, the occupancy – as one would expect – scales almost linearly with the voxel size. However, for the depth, there is only a weak dependency on the voxel size over a large domain. This is a consequence of the many microcurlers which travel a relatively long distance in z , but which only occupy very few pads in ρ and ϕ (cf. Figure 1). Only when the voxel depth reaches approximately the size of the large curler structures, the corresponding curve in Figure 2 begins to rise as steeply as the other two. Even though this is irrelevant for a TPC (which would never have such a coarse longitudinal sampling), it might matter for other detector technologies.

Using the more-or-less realistic voxel size of $5 \times 1 \times 10 \text{ mm}^3$, Figure 3 shows that the local occupancy strongly depends on the radial position within the chamber. The innermost regions almost reach 1%, whereas in the middle and outer regions, occupancies of no more than 0.01% to 0.1% have to be expected.

The mean primary space charge ranges from almost 10^{-3} fC/cm^3 in the inner regions down to approximately $5 \cdot 10^{-5} \text{ fC/cm}^3$ in the middle and outer parts of the TPC. The distribution of the charge per voxel varies over a large range (from a few primary electrons up to several thousands in the extreme case), but it does not follow a Landau-like shape due to the large contribution from photons which cause local energy deposits.

3.2 Influence of Neutrons and Hydrogen

It has been assumed that neutrons might have a significant influence on the TPC background by hitting protons and producing short recoil tracks, provided the chamber gas uses a quencher which contains hydrogen. To test this, another simulation run with 20% of CH_4 (instead of the usual 5%) is carried out. The results are shown in Table 1: One can in fact recognise a fourfold increase in signals created by protons (as far as the low statistics permits), but their fraction is negligible compared to the other ionisation processes. It should therefore be safe to use a conventional hydrocarbon-based quencher in typical concentrations instead of a surrogate which might introduce new kinds of problems.

	5% CH ₄	20% CH ₄
Neutrons	142 ± 20	146 ± 25
Photons	947 ± 57	955 ± 44
Electrons	6 ± 13	6 ± 12
Electrons	292 ± 130	303 ± 121
Protons	2 ± 2	9 ± 4

Table 1: Number of particles which are entering the TPC (top part) and which are created in the TPC due to secondary processes (bottom part) per bunch crossing. The error values indicate the fluctuation per bunch crossing, not the total statistical error from all 100 bunch crossings.

4 Summary and Outlook

The occupancy of the TPC caused by machine-induced backgrounds stays well below the value of 1% which is often quoted as an approximate critical limit [8]. This single number still does not take the spatial structure of the background signals into account: Microcurlers will often blind only a few pads for a longer time. Such patterns will have less impact on data readout and pattern recognition than a set of truly randomly-distributed hits which might – numerically – yield the same value for the occupancy.

A pattern recognition algorithm should easily manage to remove most of these background signals before track finding and fitting, thus presumably minimising the direct influence on the tracker resolution as long as background levels do not get significantly higher. Furthermore, due to the strong radial dependency of the background occupancy, there will always be the option to start pattern recognition in the sparsely-populated outer regions of the TPC and then continue by tracking inwards.

However, background particles will still cause primary ionisation and possibly field distortions from backdrifting ions, thereby having at least an indirect influence on the performance of the tracker. These effects will have to be studied in further detail – a large-scale production of background events is foreseen for this purpose. Another plan is to include hadronic beamstrahlung scattering products (so-called minijets) in the simulations.

References

- [1] Slides: <http://ilcagenda.linearcollider.org/contributionDisplay.py?confId=1296&contribId=322>
- [2] K. Yokoya, KEK Report 85-9 (1985).
- [3] D. Schulte, DESY Report TESLA 97-08 (1997).
- [4] ILC@SLAC Beam Parameters Web Site, <http://www-project.slac.stanford.edu/ilc/acceldev/beamparameters.html>
- [5] Mokka Web Site, <http://mokka.in2p3.fr>
- [6] Large Detector Concept Web Site, <http://www.ilcldc.org>
- [7] A. Vogel, *Simulation of a TPC for the ILC Detector*, ILC Software and Physics Meeting, Cambridge, UK (2006), <http://ilcagenda.linearcollider.org/conferenceDisplay.py?confId=165>
- [8] D. Kisiielewska *et al.*, *Detector Outline Document for the Large Detector Concept* (2006), <http://www.ilcldc.org/documents/dod/>

Simulation Study of GEM Gating at ILC-TPC

A.Sugiyama¹, A.Aoza¹, T.Higashi¹, A.Ishikawa¹, H.Tsuji¹, Y.Kato², K.Hiramatsu²,
T.Yazu², T.Watanabe³, O.Nitoh⁴, H.Ohta⁴, K.Sakai⁴, H.Bito⁴,
K.Fujii⁵, M.Kobayashi⁵, H.Kuoiwa⁵, T.Matsuda⁵, R.Yonamine⁵, S.Uno⁵,
Y.Gao⁶, Y.Li⁶, J.Li⁶, Q.Huirong, L.Cao⁶, Z.Yang⁶, A.Bacala⁷, C.J.Gooc⁷, R.Reserva⁷, D.Arogancia⁷

Saga University, 1 Honjho-machi, Saga 840-8502, Japan

Kinki University, 3-4-1 Kowakae, Higashi-Osaka 577-8502, Japan

Kogakuin University, 1-24-2 Nishi-Shinjyuku, Tokyo 163-8677, Japan

Tokyo University of Agriculture and Technology, Koganei, Tokyo 184-8588, Japan

IPNS, KEK, Oho 1 Tsukuba 350-0810, Japan

Tsinghua University, CN-100 084, Beijing, China

Mindanao State University Iligan Institute of Technology, 9200 Iligan, Philippines

The feasibility of GEM gating under LC-TPC condition such as high magnetic field and high $\omega\tau$ gas has been studied by simulation. We found the best electron transmission is 70% at a current condition due to the high magnetic field.

1 Introduction

Future ILC experiment is a dedicated experiment for precise measurement of nature of Higgs particle and beyond the standard model with its clear experimental condition comparing to Hadron experiments. However beam bunch trains squeezed to the order of nano meter at the interaction point introduce various beam background as well as physics background such as two photon processes. Time Projection Chamber (TPC) is one of candidates for tracking system in ILC detector concepts.

TPC suffers huge background activities such as photon and neutron as well as charged particles during bunch train crossing at IP (1msec) every 200msec. It takes $50\mu\text{sec}$ for electrons to drift a full length of drift distance (2m), while ions take 10^4 longer time than electron. As ions cannot be swept away from TPC drift region before the next beam train, they will be piled up by following bunch trains. But the most of ions are produced at gas multiplications and these ions must be blocked at the gate device near the sensor which has to transmit electrons from drift region to the sensor when gate is open. Gate system must be about 1cm above a gas amplification device in order to hold all ions produced at gas multiplications during 1msec beam collision.

F.Sauli had applied Gas Electron Multiplier (GEM) [2] as a gating device by just reversing the electric field in GEM hole when Gate is closed. The electron transmission is the key issue for this and has been measured for several gas mixtures and two different GEM [3]. He shows the clear improvement in the electron transmission at a low voltage operation by changing a hole radius larger (Figure 1-a). The best transmission is 70% at 10 volts for $50\mu\text{m}$ thick GEM with $100\mu\text{m}$ diameter hole and 150 V/cm , 300 V/cm for a drift and transfer field in Argon CO_2 gas mixture (70:30).

2 Method to understand electron transmission

We have tried to understand a mechanism of this improved electron transmission at low V_{GEM} operation and hope to find a reliable gate condition for LC-TPC. In order to understand behavior of a electron transmission, it is divided into two factors, a collections efficiency and extraction efficiency. Each efficiency is evaluated by GARFIELD [4] simulation based on 3 dimensional electric field map calculated by Maxwell3D [5].

The collection efficiency is defined as the number of electron reach to a entrance of GEM hole divided by the number of generated electrons uniformly over a cell unit at $500\mu\text{m}$ above GEM surface, while the extraction efficiency is defined as the number of electrons which could come out from holes divided by the number of electrons reach to hole entrance. Electric field is calculated $500\mu\text{m}$ above and below GEM as well as its inside.

When we use Garfield, STEP size is always defined by a length, where STEP size is an interval to update electron position in Garfield. In Monte Carlo simulation, results of calculation sometime depend on a choice of STEP size especially under rapidly changing field. After studies of efficiency dependence on a step size, we compromised to choose $2\mu\text{m}$ because it seems to provide a result close enough to one with a finer step size, and we could not choose finer step size due to the limited maximum number of steps.

Though we try to use a precise field map with fine elements, GARFIELD could only accept $\mathcal{O}(10^5)$ elements. A systematic difference in the extraction efficiency at higher field is still observed when we change a size of elements by twice larger under the same geometry. While the collection efficiency is not sensitive to the element size as electric field associated to this effect is lower. As the gating GEM is used at low voltage, the limited number of elements seems not to be a big problem here. But we have to notice these calculations always include an ambiguity, but it must not exceed 5%.

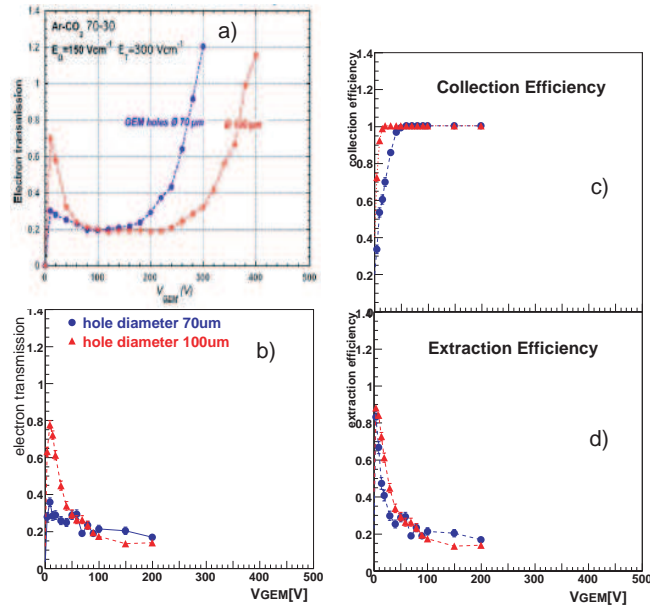


Figure 1: Comparison of electron transmission between Sauli's data (a) and simulation(b). (c) and (d) show collection and extraction.

3 Comparison to experimental results

Comparing to the Sauli's data of Ar : CO₂ = 70 : 30 with 2 different hole sizes, the electron transmissions are well reproduced by the simulation quantitatively below 150 volts in

V_{GEM} though above 150 volts results of simulation are different (shown in Figure 1) as they don't include gas amplification effect, where 150 V/cm and 300 V/cm is applied for drift and transfer regions respectively. GEM with 100 μm diameter hole provides 70~80 % efficiency in the electron transmission at 10 volts in V_{GEM} though the standard GEM provides less than 40% transmission at the best. This difference can be attributed to the different behavior of the collection efficiency largely depend on a hole aperture. A behaviour of the collection efficiency has been studied by Aachen group based on a ratio of hole field (E_h) to outer field (E_d) [6] and our result is also well explained by this.

The extraction efficiency is rather complicated. The area of field lines passing through GEM hole is shrunk as E_h and the effect of transverse diffusion become important. Electrons are easily get out from the area of passing-through field lines due to the diffusion and move along returning field line to the bottom electrode of GEM. It explains why extraction efficiency decrease as E_h . On the other hand very low E field ($E_h \sim 0$), the diffusion is very large where electrons can reach to wall of the hole and decrease the extraction efficiency.

4 Effect of magnetic field

When we use TPC at Linear Collider experiment, the strong magnetic field is necessary for a good jet energy resolution ensured by neutral-charged particle separation for Particle Flow Algorithm as well as for a good local position resolution due to low transverse diffusion. In order to achieve 100 μm accuracy for 2 m long drift, ArCF₄ gas mixture is a promising candidate for LC-TPC.

ArCF₄ provides a good transmission under 0 magnetic field as shown in Figure 2. However, once 3 Tesla field is applied, transmission becomes below 40% because the collection efficiency become very worse at low E_h (distribution seems to be shift to higher E_h).

The degradation of the collection efficiency seems to be coming from $E \times B$ effect when electron move towards holes near the GEM surface. ArCF₄ gas provides large Lorentz angle to electron drifting under non parallel electric and magnetic field which disturb electron motion toward hole center and increase a chance to be absorbed at the upper electrode of GEM. Increasing of E_h field initiate this electron motion high above the GEM surface and increase a probability of electron going into a hole.

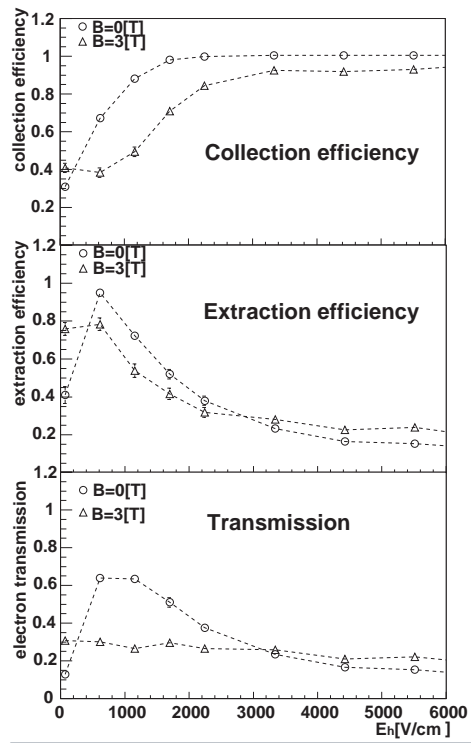


Figure 2: Collection and extraction efficiency and electron transmission under magnetic and non-magnet field for ArCF₄ with 100 μm diameter hole, $E_d = 150V/cm$ and $E_t = 300V/cm$.

Comparing to the case without magnetic field, the extraction efficiency is increased at low $E_h \sim 0$ due to the low transverse diffusion under magnetic field. It is less at $E_h < 2000 \text{ V/cm}$ as an electron does not follow electric field line and may move into hole at a distant place from the center due to $\mathbf{E} \times \mathbf{B}$ effect. But it is increased again at high E_h due to the same effect happened at the collection efficiency.

Under 3 Tesla magnetic field, we can obtain 60% electron transmission with $E_d=50 \text{ V/cm}$ which results in an unacceptable low drift velocity for LC-TPC. However these results are based on a standard GEM which is developed as a gas multiplication device and there must be a room to optimize GEM itself and an operation condition as a gate specific device.

5 Optimization of GEM

Parameters we can change in GEM itself are 1) hole size/pitch, 2) hole shape and 3) GEM thickness (insulator thickness and metal thickness). However there are limitations of parameter space in each item mainly due to production techniques.

5.1 Hole size/pitch

Making hole size larger in the same pitch seems to improve the collection efficiency at low E_h region due to a geometrically larger hole aperture. However hole size in the same pitch is limited by technical reasons when GEM is produced in any kind of etching. While hole pitch is related to local resolution as local position information of each electron will disappear through hole due to diffusion and $\mathbf{E} \times \mathbf{B}$ effects. We cannot enlarge pitch size unlimited. The best local resolution achieved in the similar condition is about $50 \mu\text{m}$ at zero drift distance and $\text{pitch}/\sqrt{12}$ should not be beyond this number.

5.2 Hole shape

Shape of hole is largely dependent on processing method when holes are drilled. Chemical etching is used to produce bi-conical shape hole, while dry etching provides more straight cylinder like hole. When magnetic field is not applied to the detector, hole shape would not affect the extraction efficiency as almost all electrons pass through the near central region of hole. But electrons can pass through near a hole wall under magnetic field and straight hole provides slightly better extraction efficiency.

5.3 GEM thickness

Thickness of insulator is related to a chance of electron absorption at a wall of hole because transverse diffusion of electrons increases as traveling distance. $25 \mu\text{m}$ -thick insulator improves transmission by 10% and $12.5 \mu\text{m}$ does another 10%. Electrode thickness also contributes to a total length of hole and improves transmission by 10% reducing thickness to $1 \mu\text{m}$ from $5 \mu\text{m}$. A production of very thin GEM would not be easy, but it is worth trying if the obtained result is good enough.

5.4 Operation condition

GEM operation is determined by the field at drift and transfer region and V_{GEM} . E_d is determined by the drift velocity and diffusion of electron in order to obtain the best performance of TPC. The transmission is largely depend on a gas property(transverse diffusion as a function of electric and magnetic field) as well as the field ratio. E_d has the largest contribution to the transmission. When E_d is reduced to 100V/cm , you will get another 10% increase.

In any case, back-drifting ions are blocked more than 99.9% when a reversed V_{GEM} is applied to the gating GEM by 10 volts.

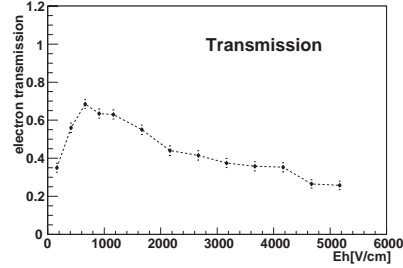


Figure 3: The best electron transmission with a special GEM having $12.5\mu\text{m}$ thick insulator and $1\mu\text{m}$ thick electrodes.

6 Summary

We may achieve 70% electron transmission with very thin GEM gate under LC-TPC operation condition. We are not sure this number is acceptable or not but we need some more improvements as well as experimental understanding of GEM gating scheme rather than just a simulation.

7 Acknowledgments

This study is supported in part by the Creative Scientific Research Grant No. 18GS0202 of the Japan Society for Promotion of Science.

References

- [1] Slides:
<http://ilcagenda.linearcollider.org/contributionDisplay.py?contribId=323&sessionId=74&confId=1296>
- [2] F. Sauli, Nucl. Inst. and Meth. **A386** 531-534 (1997).
- [3] F. Sauli *et al.*, Nucl. Inst. and Meth. **A560** 269-277 (2006).
- [4] R. Veenhof, Nucl. Inst. and Meth. **A419** 726-730 (1998).
- [5] Commercial Finite Element Computation Package, Ansoft Co. Pittsburg,PA,USA.
- [6] M. Killenberg *et al.*, Nucl. Inst. and Meth. **498** 369-383 (2003).

Calorimetry and Muons

Conveners: R. Frey, J. Blazey, F. Sefkow, T. Takeshita, B.G. Cheon

Development of GEM Based Digital Hadron Calorimeter

Jaehoon Yu^{1*}

*Presented on behalf of Heather Brown¹, Chang Hie Han³, Kwon Pyo Hong⁴, Wonjeong Kim³, Jia Li¹, Carlos Medina¹, Seong Tae Park³, Jacob Smith¹, Andrew P. White¹ and Tianchi Zhao²

1. Department of Physics, University of Texas at Arlington, Arlington, TX
2. Department of Physics, The University of Washington, Seattle, WA
3. Department of Physics, Changwon National University, Changwon, Korea
4. Korea Atomic Energy Research Institute, Daejeon, Korea

1. Introduction

The International Linear Collider (ILC) [1] is a precision machine with high physics potential thus ILC must be accompanied by detectors capable of disentangling and deciphering complex signatures that are densely packed in both space and time. Excellent energy and angular resolution of parton-initiated "jets" are essential to precise measurements of cross sections and invariant masses of resonance states. In particular, accurate measurements of jet energy and missing energy are critical for discovery and characterization of the Higgs bosons and supersymmetric particles.

The Particle Flow Algorithm (PFA) [2] initially developed by the ALEPH experiment [3] at LEP is considered to be a solution to improve jet energy resolution. PFA exploits the relatively superior resolution of tracking systems, by replacing calorimeter cluster energies with the momenta of the associated charged tracks, thereby improving jet energy resolution. PFA requires fine calorimeter segmentation and a large tracking volume to precisely associate energy clusters with the track and to remove only the energy corresponding to the track. Fine segmentation requires a large number of readout channels, consequently instrumentation of the next generation of detectors capable of exploiting PFA using the current analog calorimeter technology may be prohibitively costly.

Digital calorimetry [4] measures the energy deposit by simply counting cells above the threshold. Such counting requires only binary information with little dynamic range, thus reducing costs for readout electronics relative to an analog calorimeter of the same granularity. Over the past several years the University of Texas at Arlington (UTA) team has been developing a digital hadronic calorimeter (DHCAL) using a Gas Electron Multiplier (GEM) [5] as the sensitive gap detector. GEM can provide flexible configurations which allow small anode pads for high granularity. It is robust and fast with only a few ns rise time and has a short recovery time which allows higher rate capability. It operates at a relatively low voltage across the amplification layer, uses simple gas (ArCO₂) which prevents the detector from long term issues and is stable.

In this report, we present the recent results of the GEM based DHCAL R&D activities including some preliminary results of beam tests at Fermilab's Meson Test Beam Facility (MTBF) and the plans for the near and mid-term future.

2. GEM-Based Digital Hadron Calorimetry Prototypes

Our development effort using GEM for a DHCAL is essential for PFA approach to achieve the required jet energy and jet-jet mass resolution. The ionization signal from charged tracks passing through the drift section of the active layer is amplified using a double GEM layer

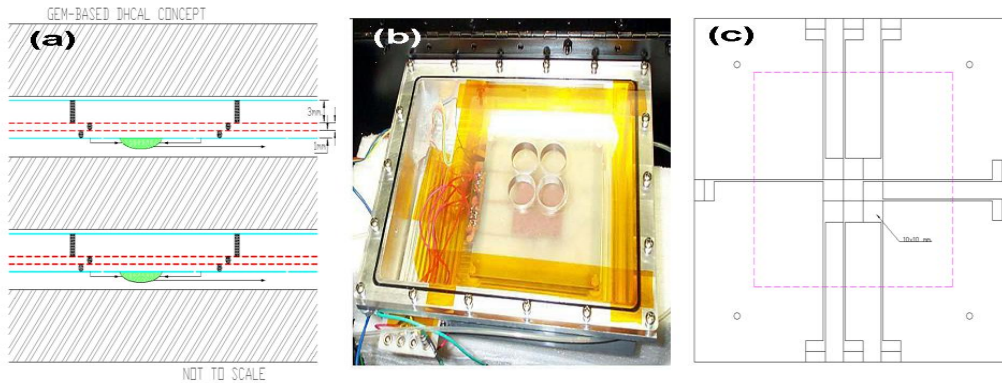


Figure 1. (a) GEM DHCAL concept diagram (b) UTA GEM prototype chamber constructed with 10 cm×10 cm CERN GDD GEM foils (c) Prototype readout anode pad with nine 1 cm×1 cm cells

structure. The amplified charge is collected at the anode layer with 1cm×1cm pads at zero potential.

The potential differences, required to guide the ionization, are produced by a resistor network, with successive connections to the cathode, both sides of each GEM foil, and the anode layer. The pad signal is amplified, discriminated, and a digital output produced. As pointed out above, GEM design allows a high degree of flexibility with, for instance, possibilities for microstrips for precision tracking layer(s), variable pad sizes, and optional ganging of pads for finer granularity future readout if allowed by cost considerations. Figure 1.(a) depicts how the GEM approach can be incorporated into a DHCAL scheme.

Initial studies were conducted on signal characteristics and gain from a small prototype GEM detector shown in Fig. 1.(b). The signals from the chamber are read out using the QPA02 chip developed by Fermilab for Silicon Strip Detectors. The gain of the chamber was determined to be of the order 3,500, consistent with measurements done by the CERN GDD group. The MIP efficiency was measured to be 94.6% for a 40 mV threshold, which agrees with a simulation of chamber performance. The corresponding hit multiplicity for the same threshold was measured to be 1.27, which will be beneficial for track following and cluster definition in a final calorimeter system. A gas mixture of 80% Ar/20% CO₂ has been shown to work well and give an increase in gain of a factor of 3 over the 70% Ar/30% CO₂ mixture. A minimum MIP signal size of 10 fC and an average size of 50 fC were observed from the use of this new mixture. The prototype system has proved very stable in operation over many months, even after deliberate disassembly and rebuilding, returning always to the same measured characteristics. We also investigated cross talk properties using nine 1 cm×1 cm cell anode pad layout shown in Fig.1(c). We also used collimated gamma rays from a ¹³⁷Cs source to study signal sharing between adjacent pads.

3. Development and Beam Tests of 30cm×30cm Chambers

As the first step for the full-size (1m×1m) test beam chambers, we have developed a 30cm×30cm GEM foils as shown in Fig. 2.(a) together with Microinterconnect Systems

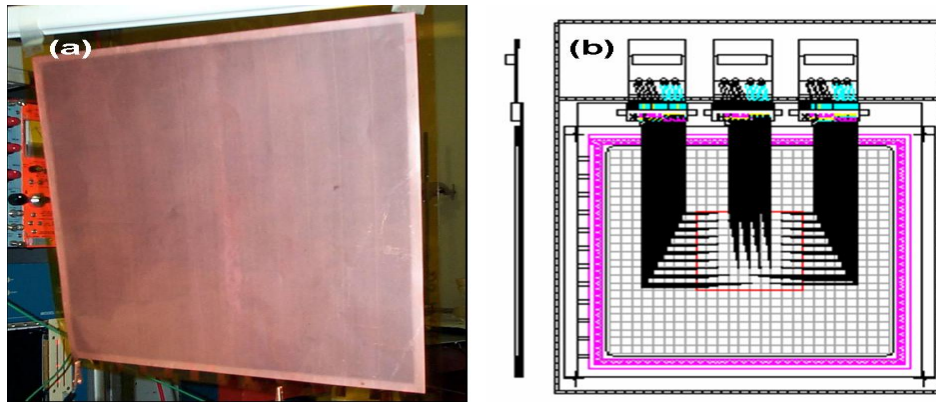


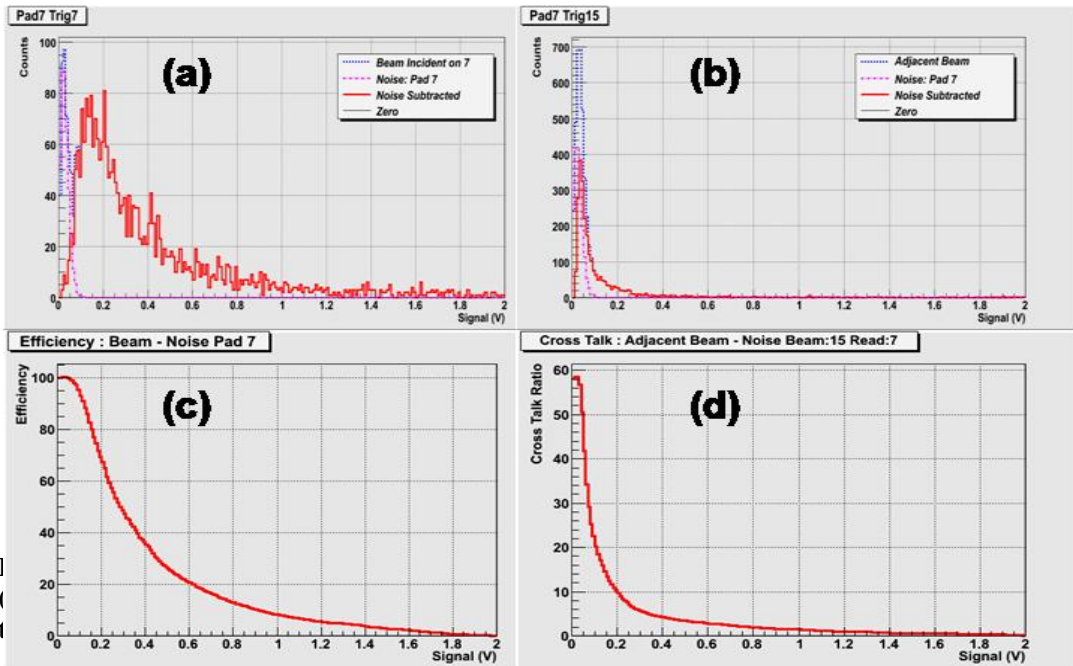
Figure 2. (a) A photo of one of the $30 \times 30 \text{ cm}^2$ 3M GEM Foils (b) A schematic diagram of a 96 channel anode board with three 32 channel Fermilab QPA02 front end electronics

Division of 3M Corporation [6]. The foil is divided into 12 independent HV strips for operational safety which we had to disconnect a few during beam test experiments. For mechanical assembly, we have developed tools to handle large area foils, maintaining flatness of the foils, and the detector walls that provide gas and HV feed through. A modification of this foil design will allow sections of $1 \text{ m} \times 30 \text{ cm}$ foils for the unit chamber. We constructed several prototype chambers using these foils and the readout boards shown in Fig.2.(b) and expose them into various beams. These chambers were read out using the 32-channel QPA02 chip based Fermilab preamp cards.

In order to test the chambers properly with sufficient statistics, they need to be exposed to particle beams. We conducted three beam tests to measure rate capability of the chamber, its MIP characteristics, cross talk between the channels and occupancy from this exercise. The output signals from the amplifier cards will be sent to discriminator boards which contain discriminator chips, multiplexer stages, and data output interface. The output from the discriminator boards were read out by a PCI based ADLink ADC controlled by LabView software.

The first beam exposure of our $30 \text{ cm} \times 30 \text{ cm}$ prototype chamber took place in May 2006, at the high intensity, low energy (10 MeV) electron beam at the Korean Atomic Energy Agency (KAERI). This beam exposure was a joint effort between UTA and the Radiation Detector Development (RDD) Group at Changwon National University (CNU), Changwon, Korea. Since the beam consists of 30 ps pulses of 10^{10} electrons every $43 \mu\text{s}$ in 5 cm radius, the detector and the electronics measured responses to 10^9 electrons per pad. While the electronics was saturated, the chamber was able to see the beam clearly and provided a good measure of the time structure of the beam. As a test, we directly exposed a broken GEM foil to the beam. In both the chamber and the broken GEM foil, we did not see any physical damages. In addition, while the signal shapes were distorted by the hit from 10^9 electrons per pad, the chamber responded well to such a large signal, giving us confidence that the chamber will function in the ILC environment without damage.

In order to continue testing GEM-based DHCAL for in-beam characterization, we performed additional beam tests at Fermilab's Meson Test Beam Facility (MTBF). We tested



a single multi-channel chamber using the 100 channel readout system for one week in March 2007 for joint run with CNU as a secondary user behind a straw channel detector group and one week in April, 2007, as the primary user. Most the useful data taking was done using 120 GeV proton beams from the Main Injector. Labview based online analysis software complimented the DAQ software and allowed us to monitor the data as they got accumulated. Since the DAQ card required sufficiently long signal for an efficient sampling, we developed a pulse shaper to stretch the signal to a suitable level for the ADLink DAQ card to sample. We also used a commercial shaper for a verification purposes.

The trigger was formed of coincidences of three $1\text{cm}\times 1\text{cm}$ and two $19\text{cm}\times 19\text{cm}$ counters to constrain the beam to smaller than $1\text{cm}\times 1\text{cm}$ region, which is the size of a readout pad. The two $19\text{cm}\times 19\text{cm}$ counters enveloped the GEM prototype chamber to ensure the beam passage through the active area of the detector. In addition to the beam trigger, we employed two additional triggers: chamber self trigger with the signal above 30mV, utilizing the negative output from Fermilab QPA02 preamplifier, and the coincidence between the five counters and a pad signal above 30mV to constrain the beam on a particular target pad.

Using the data collected in the MTBF beam tests, we were able to determine relative efficiency and fractional cross talk ratio. In order to verify the proper functionality of the chamber, we took data using a high intensity Sr^{90} radioactive beta source. Figure 3.(a) shows the signal without noise subtraction (blue), noise (purple) and noise subtracted signal (red) when 120GeV proton beam is incident to the target pad. Noise subtracted signal distribution demonstrates Landau shape as expected. We, however, observed that the width of the distribution from proton beams is much wider than the source.

Figure 3.(c) shows the relative efficiency measured on this pad as a function of threshold, which demonstrates that at the efficiency about 94% at 40mV. It, however, should be noted that a sizable number of events have more than one proton entering the detector within the 200ns gate. This is the apparent reason why we observed differences in the widths in noise subtracted signal distributions. An initial estimate of the multiple proton events shows about 20% multiple proton event contamination. A more detailed analysis using the differences between the data obtained from the Sr^{90} source and the proton beams is in progress.

In order to measure the cross talk rate, we read out the pad immediately next to the pad with the trigger. Figure3.b shows the pulse height distributions of the pad number 7 when beam is incident on the immediate neighboring pad. Blue dotted lines represent the signal before noise subtraction, the purple lines represent noise, and the red line is the noise subtracted signal. The difference between the two cases is apparent from the two figures. From these, we can extract the fractional cross talk rate on a pad, as shown in Fig.3.d. From these studies, while the probability of the cross talk is small for both the pads, it should be emphasized that given the size of the trigger paddle this distribution includes charge sharing between the neighboring pads and the multiple proton events. As in the cases before, a more systematic analysis is in progress to take into account these different effects.

4. Future Plans

We plan to conduct a beam test using both the digital readout chip (DCAL) developed jointly by ANL and FNAL and the kPiX analog readout chip developed by SLAC in fall 2007. The prerequisite for this test is the verification of the functionality of the chamber with these readout chips in bench tests. We are working with the ANL RPC team to establish a DCAL chip test station at UTA for more efficient chamber construction and testing.

The next phase is the beam test of the full scale 1m^3 GEM DHCAL prototype together with an electromagnetic calorimeter. We plan to construct a total of 50 or so (40+10 spares) chamber layers using $1\text{m}\times 30\text{cm}$ GEM foils produced by 3M. Three of these unit chambers will make up one sensitive layer of size $1\text{m}\times 1\text{m}$. This test will be performed at the MTBF in late 2008 or 2009. The goal of this test is to measure the responses and energy resolution of a GEM-based DHCAL. This result should be compared to that of a DHCAL using RPCs and other analog HCALs. This full scale prototype will be tested jointly with CALICE Si/W or Scintillator/W ECAL and a tail catcher (TCMT), using the CALICE mechanical support structure which was used in this year's CERN beam test. This phase, however, depends heavily on the availability of funds.

5. Possible Alternatives to Standard Thin GEM Foils

We have been considering an alternative to the standard GEM foil technology. Recent work [7] has shown that a so-called "thick-GEM" (TGEM) can, in a single layer achieve multiplication levels typical of at least a double-GEM device. A TGEM is a printed circuit board, clad with copper on both sides through which holes have been drilled. A typical configuration might be a 0.4 mm thick board with 0.3 mm diameter holes spaced 1 mm apart. Since in our application we use relatively large pads compared say to a microstrip tracker the sparser array of holes should not be an issue. With the detector costs scaling as $+\$12\text{M}/\text{mm}$ increase of the superconducting coil diameter, this could be a significant cost saving.

We have obtained a few TGEM samples from the Weizmann Institute and are in the process of constructing a prototype for feasibility study. In addition, the recent development

of resistive-electrode TGEM (RETGEM) [8] will also be investigated as an alternative solution for the overall ILC detector.

6.0 Conclusions

Gas electron multiplier technology demonstrates exceptional possibilities of use, from time projection chambers to digital hadron calorimeter to muon tracking chambers. The development of large area GEM foils enables a wide variety of use in various detectors. The research and development work in progress of using GEM is at the stage to measure the performance of the conceptual GEM-based DHCAL. Following the three single chamber beam tests, we plan to perform additional tests using multi-channel ASIC chips. We also plan to construct a 40 layer 1m^3 calorimeter prototype to measure the calorimetric performance. TGEM foil developed by Weizmann institute and the RETGEM are of great interest due to their potential for cost savings in large area production.

7.0 References

1. The International Linear Collider, <http://www.linearcollider.org/cms/>
2. ALEPH Collaboration, Nucl. Inst. Meth. **A360**, 481 (1995)
3. D. Decamp et al., ALEPH Collaboration, "ALEPH: A Detector for Electron-Positron Annihilations at LEP", NIM, **A294**, 121 (1990).
4. J. Repond, "A Digital Hadron Calorimeter with Resistive Plate Chambers," Proc. of the VII Workshop on Resistive Plate Chambers and Related Detectors, Clermont-Ferrand, France (October 2003), Nucl. Inst. Meth. **A518**, 54 (2004); V. Ammosov *et al.*, "RPC as a Detector for High Granularity Digital Hadron Calorimetry," Serpukhov, IHEP, DESY-04-057, March (2004).
5. F. Sauli, Nucl. Inst. Meth., **A386**, 531 (1997); S. Bachmann *et al.*, "Performance of GEM detectors in high intensity particle beams," Nucl. Inst. Meth., **A470**, 548 (2001); P. S. Barbeau *et al.*, "A First Mass Production of Gas Electron Multipliers," hep-ex/0304013 (2003); I. Shipsey, American Linear Collider Workshop, July 13 – 16, Cornell University, Unpublished (2003).
6. 3M Interconnect Solutions Division, http://www.3m.com/us/electronics_mfg/interconnects/
7. R. Chechik, A. Breskin, C. Shalem, D. Mormann, Nucl. Instrum. Meth. **A535**, 303 (2004); R. Chechik, A. Breskin, C. Shalem, Nucl. Instrum. Meth. **A553**, 35 (2005); C.K. Shalem, R. Chechik, A. Breskin, K. Michaeli, N. Ben-Haim, Nucl. Instrum. Meth. **A558**, 475 (2006); C.K. Shalem, R. Chechik, A. Breskin, K. Michaeli, N. Ben-Haim, Nucl. Instrum. Meth. **A558**, 468 (2006).
8. R. Olivera *et al.*, to be published in Nucl.Instrum.Meth. **A** (2007).

Muon Identification without Iron

John Hauptman *

Iowa State University, Department of Physics and Astronomy
Ames, IA 50011 USA

Muons can be identified with high efficiency and purity and reconstructed with high precision in a detector with a dual readout calorimeter and a dual solenoid to return the flux without iron. We show CERN test beam data for the calorimeter and calculations for the magnetic fields and the track reconstruction. For isolated tracks, the rejection of pions against muons ranges from 10^3 at 20 GeV/c to 10^5 at 300 GeV/c.

1 Introduction

Big detectors at high energy colliders require the detection of electrons (e) and muons (μ) with high efficiency, high purity and high precision for the reconstruction of the decays $W \rightarrow e\nu$, $W \rightarrow \mu\nu$, $Z \rightarrow e^+e^-$, $Z \rightarrow \mu^+\mu^-$, for the identification of τ lepton decays to e and μ , for searches for lepton number violation, for the positive tagging of events with missing neutrinos, and for the isolation of event samples with supposed decays of supersymmetric or other massive states decaying partly to leptons. The muon system of the 4th Concept, Fig. 1, achieves almost absolute muon identification for isolated tracks.

2 Separation of muons (μ^\pm) from charged pions (π^\pm)

We achieve excellent $\mu - \pi^\pm$ separation using three independent measurements: (a) energy balance from the tracker through the calorimeter into the muon spectrometer, (b) a unique separation of the radiative component from the ionization component in the dual-readout calorimeter; and, (c) a measurement of the neutron content in the dual-readout fiber calorimeter.

2.1 Separation energy and momentum balance

The central tracking system has a resolution of about $\sigma_p/p^2 \sim k_1$ ($k_1 \sim 3 \times 10^{-5} (\text{GeV}/c)^{-1}$) and the muons spectrometer in the annulus between the solenoids with a B=1.5 T field has resolution of about $\sigma_p/p^2 \sim k_2$

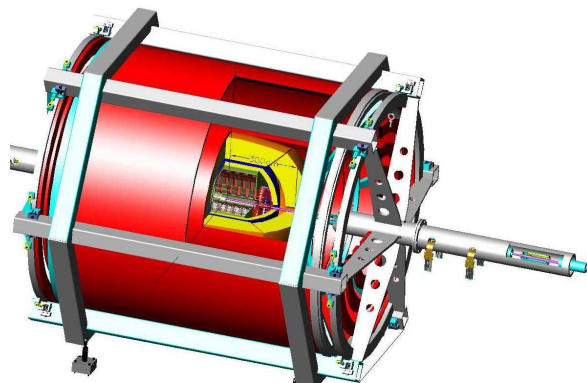


Figure 1: 4h Concept detector showing the dual solenoids. The annulus between the solenoids is filled with cluster counting wires inside precision tubes.

*This work has been supported by the US Department of Energy through DE-FG02-91ER40634 and LCRD Project 6.18.

($k_2 \sim 5 \times 10^{-4} \text{ (GeV/c)}^{-1}$). A muon of momentum p which radiates energy E in the volume of the calorimeter that is measured with a resolution of $\sigma_E/E \sim 0.20/\sqrt{E}$ will have a momentum-energy balance constraint of $[k_1 p^2 \oplus 0.2\sqrt{E} \oplus k_2(p - E)^2]/p$ which yields a rejection of about 30 for a 100 GeV muon radiating 20 GeV.

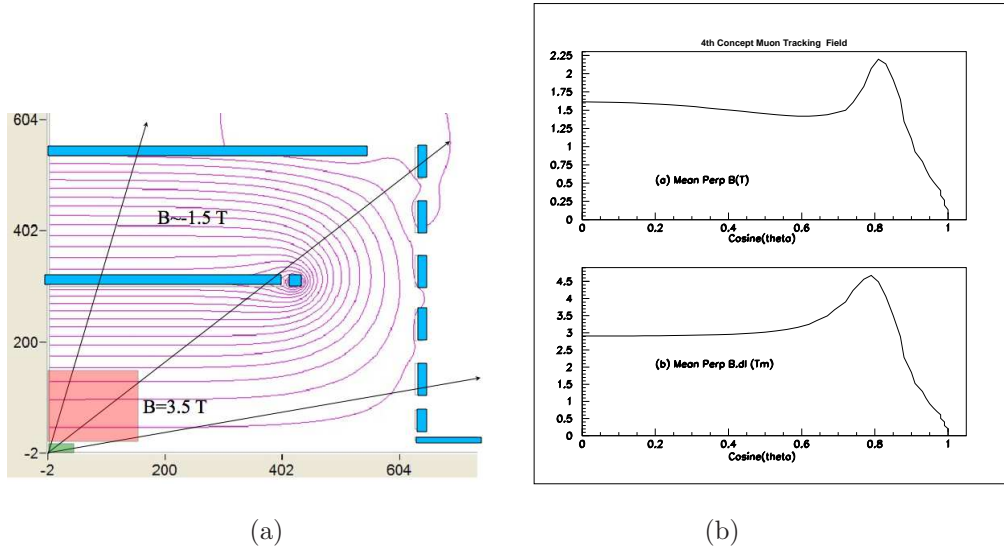


Figure 2: (a) The field map of the dual solenoids showing the wall of coils and the almost completely confined field; (b) the mean bending field (1.5 T) along muon trajectories from the origin and the integral of the mean bending field (3 Tm).

2.2 Separation by dual-readout

A non-radiating muon penetrating the mass of a fiber dual readout calorimeter will leave a signal in the scintillating fibers equivalent to the dE/dx of the muon, which in DREAM is about 1.1 GeV. There will be no Čerenkov signal since the Čerenkov angle is larger than the capture cone angle of the fiber. A radiating muon will add equal signals to both the scintillating and Čerenkov fibers and, therefore, the difference of the scintillating (S) and Čerenkov (C) signals is

$$S - C \approx \overline{dE/dx} \approx 1.1 \text{ GeV}$$

independent of the degree of radiation. The distributions of $(S - C)$ vs. $(S + C)/2$ for 20 GeV^a and 200 GeV π^- and μ^- are shown in Fig. 3 in which for an isolated track the π^\pm rejection against μ is about 10^3 at 20 GeV and 10^4 at 200 GeV. The distribution of $(S - C)$ as a mean that is very nearly 1.1 GeV as expected, and the radiative events are evident at larger $(S + C)/2$.

^aThere were no μ^- left in the H4 beam at 20 GeV/c, so these data are from 40 GeV/c μ^- .

2.3 Separation by neutron content measurement

The DREAM collaboration has succeeded in the measurement of neutron content in hadronic showers event-by-event in the DREAM module by summing the scintillating channels of the module in three radial rings and digitizing the PMT output at 1.25 GHz. These data, now being analyzed, show clearly the long-time neutron component in hadron showers that is absent in electromagnetic showers (and also absent in the Čerenkov fibers of the DREAM module for both e and π).

We expect to estimate a neutron fraction, f_n , each event the same way we estimate f_{EM} each event, and be able to reject localized hadronic activity in the calorimeter with factors of 10-50.

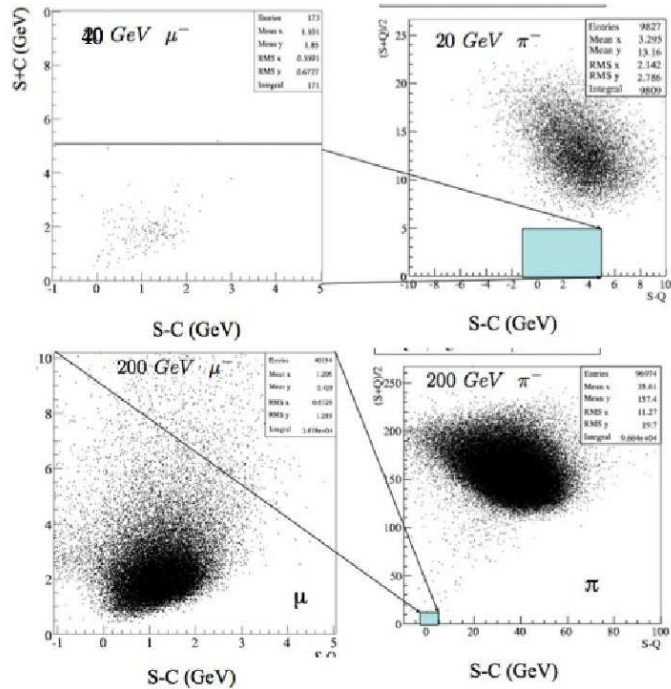


Figure 3: Dual-readout separation of $\mu - \pi^\pm$.

3 Summary

Any simple product of these three rejection factors, or any estimate of the muon efficiency and purity, gives an optimistic result that will clearly be limited by tracking efficiencies, overlapping shower debris in the calorimeter, or track confusion either in the main tracker or the muon spectrometer before these beam test numbers are reached. Nevertheless, we expect excellent muon identification.

References

- [1] Slides:
<http://ilcagenda.linearcollider.org/contributionDisplay.py?contribId=377&sessionId=108&confId=1296>
- [2] 4th Concept Detector Outline Document is available at the WWS-OC website
<http://physics.uoregon.edu/~lc/wwstudy/concepts/>.
- [3] "Muon Detection with a Dual-Readout Calorimeter", N. Akchurin, *et al.*, *Nucl. Instr. Meths.* **A 533** (2004) 305-321.
- [4] "Electron Detection with a Dual-Readout Calorimeter", N. Akchurin, *et al.*, *Nucl. Instr. Meths.* **A 536** (2005) 29-51.

Photosensor Options of Dual-Readout Calorimetry for the 4th Concept

Aldo Penzo*

Sezione INFN and Dipartimento di Fisica, Università di Trieste
Via A. Valerio 2, Trieste - Italy

The 4th Concept calorimeter design is built upon criteria that result from the DREAM prototype: by using two types of fibers, scintillator and quartz, to sample a shower, its electromagnetic fraction can be determined, and strong fluctuations of this fraction in the overall energy resolution can be suppressed. The next foreseen steps are to extend the dual-readout principle to homogeneous calorimeters (for instance scintillating crystals containing heavy elements) and to tackle another source of fluctuation in hadronic showers, originating from binding energy losses in nuclear break-up (measuring low energy neutrons, which often remain unobserved in standard calorimeters). A new generation of photodetectors with suitable properties, may represent a special asset for dual-readout calorimetry, making it simple, reliable and cheap.

1 Introduction

The 4th Concept design proposes a calorimeter system of a relatively simple construction and moderate costs, however with excellent properties, built upon experience gained with the extensively beam-tested DREAM (Dual REAdout Module) prototype [1]. The main idea of dual(/multiple) readout (DR) calorimetry is to independently measure for each hadronic shower those physical quantities that have large fluctuations and lead to large spread in energy response, mainly the electromagnetic content of a shower, and the binding energy losses, but to sum over the depth development of the shower, that should not affect the energy response in case of sufficient containment.

This choice is quite different from the currently popular trend in calorimetry, based on Particle Flow Analysis (PFA)[2], that emphasizes a high degree of transverse and longitudinal segmentation. The 4th Concept, with one longitudinal calorimeter section, has relatively few channels, about 20K, contrasted with about 50M for PFA. Even reading each channel twice (scintillating and quartz fibers separately) the DR system would be much simpler and cheaper. Furthermore it should be possible to apply the DR principle by distinguishing scintillation and Cherenkov light in a single radiator coupled to a single photodetector, according to their different time characteristics: very fast Cherenkov signal (few ns) - slower scintillation pulse (tens ns); low energy neutrons from nuclear fragmentation would produce a signal much later, on a scale of hundreds ns.

Therefore the two different methods emphasize different experimental aspects: redundancy and fine granularity in space for PFA, and high resolution in the time domain for DR. Almost all related R&D activities are widely different for these two calorimetric approaches; however at least one item is of common interest, and may have promising perspectives for both methods: new photodetectors with high quantum efficiency, photon counting capability and no sensitivity to magnetic fields. In particular this last requirement rules out the classic vacuum photo-multiplier tubes (PMT).

*on behalf of 4th Concept and DREAM

2 New Developments

An interesting alternative to PMT's has been recently developed [3] and a number of different types of solid state photon counting devices (SiPM) from various manufacturers are presently becoming commercially available. The potential of these photo-detectors has become soon clear but work still needs to be done towards a detailed specification and evaluation in view of different applications and in particular the application of these photo-sensors to calorimetry. In Italy this development has been undertaken by FBK-IRST [4] in Trento, with the support of INFN, where a number of research groups have launched activities for using SiPM in medical applications (PET), astrophysics, calorimetry, large area scintillatorbased muon counters and scintillation fiber trackers.

One of these projects (FACTOR), with participation of people involved in DREAM and 4th Concept, is engaged in a campaign of R&D and tests in Messina, Trieste and Udine laboratories and on test beams at CERN and FNAL. Static and dynamic measurements of various IRST devices compare well with other manufacturers' products, and show reduction of the dark count rate. IRST has also made considerable progress in the design and on the geometric efficiency of SiPMs for their application to calorimetry. Sensitivity of the IRST SiPM in the blue region may be another important advantage for the readout of quartz (Cherenkov emitting) fibers. Present progress and future plans for the collaborative effort of FBK-IRST and INFN have been presented and discussed at a recent meeting in Perugia. The two partially overlapping communities of DREAM and 4th are carrying on intense R&D and test activities. The plans and objectives for these activities are described in documents [5]. Some tasks for the 4th Concept design group are listed in [6]: these include construction of a cubic-meter dual-fiber readout module to overcome the leakage fluctuations that limit the performance of the 1-tonne DREAM module. When this new module will be constructed (provided enough money becomes available) it will be also a benchmark for the design criteria of a full-scale ILC multiple-readout calorimeter prototype. One realistic option could involve using the upgraded SiPM from IRST for the readout of this module; initial tests will be performed on a smaller-scale tower.

References

- [1] "Hadron and Jet Detection with a Dual-Readout Calorimeter", N. Akchurin, *et al.*, NIM **A537** (2005) 537.
- [2] Mark Thomson, "Progress with Particle Flow Calorimetry", These Proceedings, LCWS07, DESY, June 2007 [arXiv:0709.1360v1].
- [3] P.P. Antich *et al.*, NIM **A389**(1997) 491; V. Saveliev, V. Golovin, NIM **A442**(2000) 223; G. Bondarenko, *et al.*, NIM **A442**(2000) 187
- [4] C. Piemonte, NIM **A568**(2006) 224; N.Dinu *et al.*, NIM **A572**(2007) 422; C. Piemonte *et al.*, IEEE Trans. Nucl. Science, vol. 54, No. 1 (2007) 1.
- [5] "Dual-Readout Calorimetry for the Linear Collider"; "Ultimate Hadron Calorimetry", N. Akchurin *et al.*, LCRD proposals, Feb. 2005.
- [6] "Comprehensive Study, Construction and Testing of Multiple Readout Calorimeters", J. Hauptman *et al.*, 4th Concept, Proposal to ALCPG/LCDRD, June 2006

First results of systematic studies done with different types of Silicon Photomultipliers

C. Bosio¹, S. Gentile², E. Kuznetsova¹, F. Meddi²

1- INFN Roma 1
Piazzale Aldo Moro 5, 00185 Roma, Italy

2- Università degli Studi di Roma "La Sapienza"
Piazzale Aldo Moro 5, 00185 Roma, Italy

The presented results are obtained during the first steps taken in order to develop a setup and measurement procedures which allow to compare properties of diverse kinds of silicon photomultipliers. The response to low-intensity light was studied for silicon photomultipliers produced by CPTA (Russia), Hamamatsu (Japan), ITC-irst (Italy) and SensL (Ireland).

1 Introduction

Fast development of the silicon photomultiplier technology results in a number of different sensor types available on market and produced by various manufacturers. Despite the different commercial names of the devices, here all of them are referred as SiPM.

The measurements discussed here include current-voltage characteristics and studies of the SiPM response to low-intensity light. The results of the former measurements are mostly used to check the sample operability and to define the range of bias voltages for the latter studies. The measurements of the SiPM response to the light provide a number of parameters suitable for the comparison of different samples.

Five samples of silicon photomultipliers produced by the following manufacturers have been studied: CPTA^a produced samples distributed by Obninsk University and Forimtech^b, HAMAMATSU produced Multi-Pixel Photon Counter S10362-11-025C [1], ITC-irst^c and SensL^d produced samples were compared on the base of the measurement results.

2 Measurement Setup

In order to obtain the SiPM response to low-intensity light, the sensors were illuminated with a light emitting diode operated in a pulse mode. The LED drive developed by Institute of Physics ASCR (Prague) was used. The drive provides current pulses with tunable amplitude and duration with a sharp rise time down to 2 ns [2]. The signal from SiPM was read out with a charge-sensitive preamplifier and digitised with an integrating ADC. The LED pulse of about 6 ns duration and ADC gate of 65 ns width were synchronised by means of a common trigger.

The measurements were done at room temperature. Temperature variation during the measurements done for one sample did not exceed 2°C, for all measurements discussed here the total variation was less than 4°C.

^aCPTA, Russia, <http://www.zao-cpta.ru>

^bForimtech SA, <http://www.forimtech.ch>

^cITC-irst, Italy, <http://www.itc.it/irst>

^dSensL, Ireland, <http://www.sensl.com>

3 Measurement Results

Fig. 1 shows an example of the SiPM response to low-intensity light measured with the described setup. The peaked structure indicates the number of cells fired during one light pulse, starting with the pedestal for no cells fired. The distance between peaks corresponds to the SiPM gain.

The spectrum is fitted as a sum of gaussian distributions:

$$\sum_i G(N_i, \mu_i, \sigma_i) = \sum_i G(N_i, \mu_0 + i \cdot g, \sigma_i), \quad (1)$$

where μ_0 corresponds to the pedestal position and g is gain in units of ADC counts. From statistical considerations the width of i^{th} peak σ_i can be expressed as

$$\sigma_i = \sqrt{\sigma_0^2 + i \cdot \langle \sigma_{px} \rangle^2}, \quad (2)$$

where σ_0 is the pedestal width and $\langle \sigma_{px} \rangle$ represents fluctuations of the one-cell response averaged over the active area of the sample.

The gain as a function of the overvoltage $U_{bias} - U_{brd}$ was studied for several values of the bias voltage. The breakdown voltage U_{brd} is defined here as the bias voltage corresponding to the gain equal to one. The results are shown in fig. 2 (left). Fig. 2 (right) shows the dark current as function of the overvoltage.

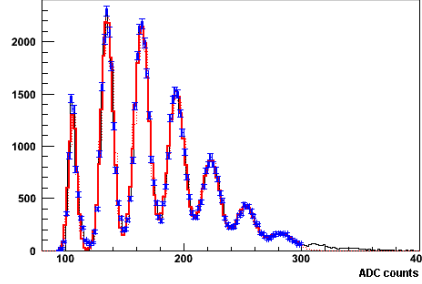


Figure 1: ADC spectrum of the SiPM response to the low-intensity pulsed light fitted to a superposition of seven gaussian peaks.

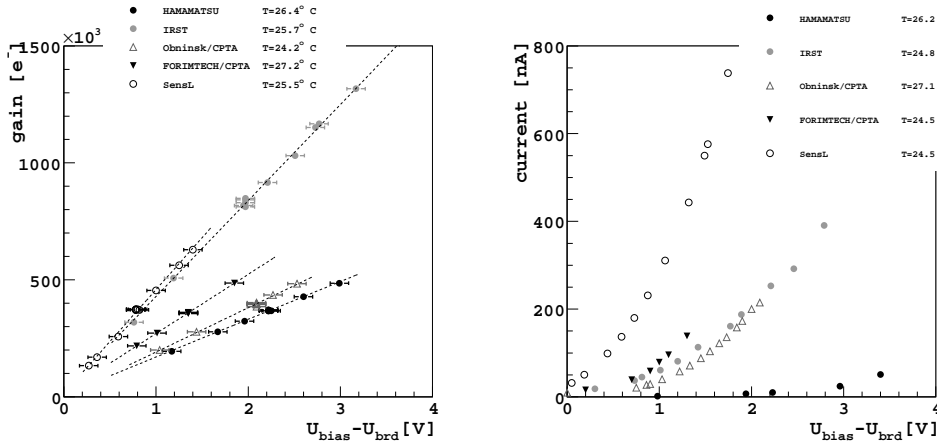


Figure 2: Gain (left) and dark current (right) as a functions of the overvoltage.

Fig. 3 shows gain normalised to the corresponding values of pedestal width σ_0 (left) and $\langle \sigma_{px} \rangle$ (right) as functions of the overvoltage. Being averaged over the active area of SiPM,

$\langle\sigma_{px}\rangle$ contains statistical and systematic parts:

$$\langle\sigma_{px}\rangle \sim \sqrt{N + \sigma_{nu}^2}, \quad (3)$$

where N is the average number of charge carriers in the avalanche and σ_{nu} represents non-uniformity of the amplification over the SiPM active area. Since gain is proportional to the carriers number, $g \sim N$, the ratio $g/\langle\sigma_{px}\rangle$ shown in fig. 3 (right) tends to a linear behaviour for the low gain values $N \ll \sigma_{nu}^2$. For the high gain values $N \gg \sigma_{nu}^2$ the dependence would correspond to square root low $g/\langle\sigma_{px}\rangle \sim \sqrt{N}$ in the case of a constant σ_{nu} . As seen from fig. 3 (right), the ratio $g/\langle\sigma_{px}\rangle$ obtained for some of the samples indicates growth of the non-uniformity factor σ_{nu} with the bias voltage.

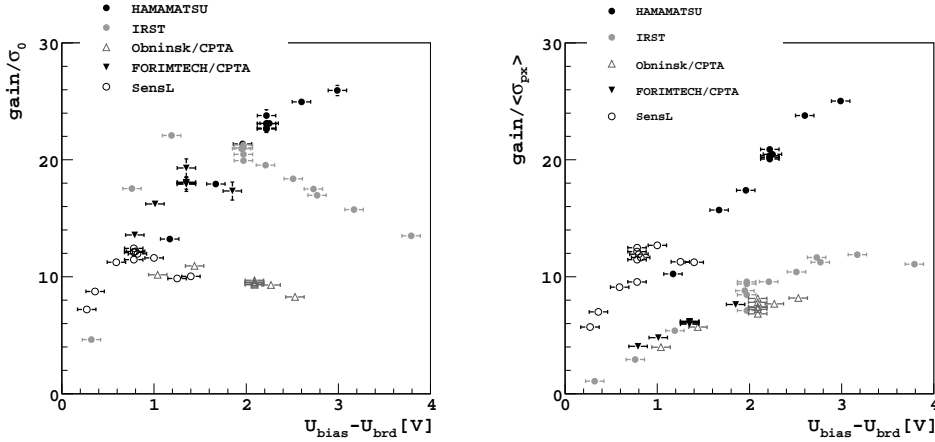


Figure 3: The gain normalised to the corresponding values of pedestal width (left) and $\langle\sigma_{px}\rangle$ (right) as functions of the overvoltage.

4 Conclusion

The obtained results demonstrated operability and potential of the developed setup. Further development and tune of the setup, measurement procedure and data treatment will allow to obtain comparative characteristics of diverse types of silicon photomultipliers.

5 Acknowledgements

We would like to thank Prof. R. Battiston (University and INFN of Perugia), Prof. V. Saveliev (Obninsk State University and DESY), Dr. I. Polak (Institute of Physics of the ASCR, Prague), Dr. E. Popova (MEPhI) and Mr. N. D'Ascenzo (DESY) for their support and fruitful discussions.

References

- [1] HAMAMATSU PHOTONICS K.K, Product catalogue No. KAPD0002E02, 2007.
- [2] I. Polak. Talk at ILC Workshop, Valencia, 2006.

Beam Test of Scintillation Tiles with MPPC Readout

A. Calcaterra, R. de Sangro, G. Finocchiaro, P. Patteri, M. Piccolo and M. Rama

Laboratori Nazionali di Frascati dell'INFN, Via E. Fermi,40 - I-00044 Frascati (Rome) Italy

This paper [1] describes measurements made using counters composed of a small (3 by 3 by 0.5 cm³) scintillation tile coupled to a Multi-Photon Pixel Counter (MPPC) and exposed to an electron beam at the Beam Test Facility in Frascati. We show our first results for charge spectra and efficiency, and a very preliminary measurement of device linearity.

1 Introduction and motivation for this study

Silicon photomultipliers [2], often called “SiPM” in literature, are semiconductor photon detectors built from a square matrix of decoupled avalanche photodiodes (APD’s) on common silicon substrate. The dimension of each single APD square microcell can vary from 20 to 100 μm . The applications of silicon photon detectors are very wide [3]; in particular, at the ILC, the demands imposed to calorimetry are so stringent that they may be met only with a very fine granularity of individual detection elements; a tile of 30 by 30 by 5 mm³, and possibly thinner, being typical.

2 The Beam Test Facility in Frascati

The Beam Test Facility [4] exploits by means of a transfer line the DAΦNE ϕ -factory LINAC, and is optimized for the production of electron and positron bunches in a wide range of multiplicities.

The beam profile from the BTF has typical horizontal and vertical dispersions of $\sigma_h = 2$ mm and $\sigma_v \leq 5$ –10 mm. The BTF equipment includes a Pb-glass calorimeter, placed downstream the user setup. The beam pulse is totally absorbed in the calorimeter, and the integrated signal from the PM gives a measurement of the number of MIPs in every pulse (see Figure 1).

In most of this work, and unless otherwise stated, only events having a Pb-glass calorimeter signal in the second peak in Figure 1 have been used: those corresponding 1-MIPs beam pulses.

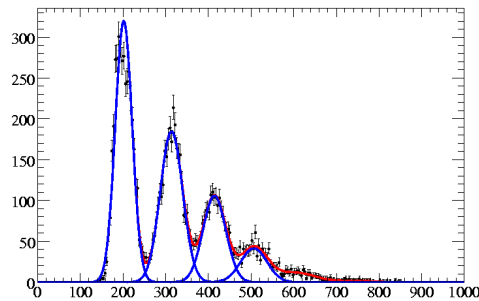


Figure 1: Beam pulse multiplicity. 0-MIPs beam pulses appear at ~ 200 counts.

3 Description of the setup and measurements

The setup is composed of 3 counters using MPPC detectors [5] and a 6-layer, two-dimensional tracker made of mechanically-quenched Resistive Plate Counters [6].^a The trigger is obtained for every beam pulse via a signal synchronous with the LINAC radiofrequency; it is thus unbiased, and completely independent from our measurements.

The counters (one appears in Fig. 2) in these measurements were: n.“1”, with a scintillation tile made of St. Gobain BC-400 coupled to the MPPC using a 1 mm thick green fiber, inserted into a groove machined along the tile center, and read by an MPPC with 1600 pixels in a square matrix of 1 by 1 mm, and 25 μm pixel pitch; n.“2”, with a tile made of green-scintillating material, similar to Scionix EJ260, coupled as in n.“1” to an MPPC with 400 pixels, and 50 μm pixel pitch; n.“3”, with a tile like counter “1”, directly coupled without a fiber to an MPPC like the one in counter “2”. In all 3 counters the MPPC were biased using a power supply HP6614C, with a stated accuracy of 0.03%, in quadrature with 12 mV.



Figure 2: A counter assembly, showing the 3 by 3 cm^2 tile and the preamplifier.

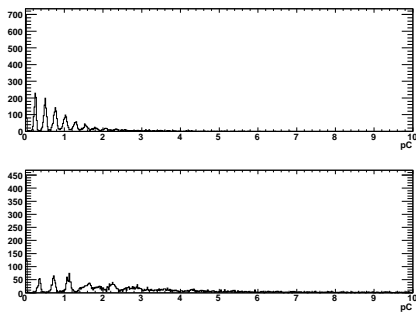


Figure 3: Charge spectra (pC) for counters 2(up) and 3 ($V_{bias} = 69.5$ V for both).

beyond ~ 1.5 pC for counter n.3 seems not attributable to channel electronics, the RMS noise figure (width of the peak at 0 pC) being about the same for both.

We use Fig. 4 to measure the efficiency of counters 2 and 3, where we plot the signal from counter 2 along the horizontal axis and the signal from counter 3 vertically.

^aThe tracker is meant to measure the beam impact point on the counters but, as this paper does not address the issue of pulse height vs impact points, its information was not used.

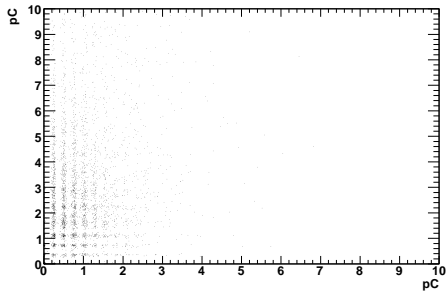


Figure 4: Integrated charge from counter 2 (horizontal axis) and 3.

Landau distributions we obtain the Most Probable Values (MPV's) plotted in the bottom right part of Fig. 5 against the number of MIPs. The points lie very close to the fitted line, with an intercept close to 0. The most probable number of pixels per MIP is 14.

The results described in this paper, although still in an initial stage, encourage us to proceed with the study of the performance in a beam test and in cosmic rays of complete counters, employing a SiPM as detection element: with a small and relatively fast assembly we have obtained charge spectra and efficiency, and a first very preliminary measure of linearity. We plan to increase the number of counters studied by an order of magnitude to gather more statistics and to implement a measure of temperature in our setup.

The authors of this paper wish to express their thanks to G. Mazzitelli and P. Valente, and all operators of the BTF facility for successful and time-efficient running, and to L. Daniello for his skill and dedication in the assembling of the MPPC counters.

Due to the very close proximity of the 2 scintillating tiles, we select events $\sim 4\sigma$'s above the pedestal for one of the two, and evaluate the efficiency of the other one as the ratio of counts above-pedestal to the total. These proximity-defined efficiencies are of $(91 \pm 1)\%$ and $(84 \pm 1)\%$ for counters 2 and 3 respectively. We judge that the difference in efficiencies is due to the different working point of the 2 MPPC's, that were identically biased at 69.5 V.

In Fig. 5 (top, and bottom left) one may see the charge spectrum for counter 1, biased at 72.0 V, in units of "pixels", for 1, 2, and 3-MIPs events. Fitting these data to

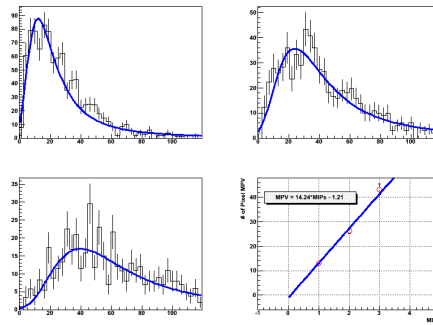


Figure 5: Linearity of counter 1 readings.

References

- [1] Slides at this link:
<http://ilcagenda.linearcollider.org/contributionDisplay.py?contribId=381&sessionId=108&confId=1296>
- [2] Dolgoshein B. *et al.* Nucl. Instrum. Meth. A5632006368, and references therein.
- [3] for a recent review, see N. Otte in Proceedings of the SNIC April 2006 Symposium, SLAC, Stanford, available online at <http://www-conf.slac.stanford.edu/snic/default.htm>
- [4] Mazzitelli G. *et al.* Nucl. Instrum. Meth. A515/32003516. See also the web page <http://www.lnf.infn.it/acceleratori/btf/publications.html>
- [5] The present paper is about devices S10362-11-050U and S10362-11-025U, for a description of these and other devices see <http://www.hahamatsu.it>.
- [6] Calcaterra A. *et al.* Nucl. Instrum. Meth. A565/22006444.

Preliminary Scintillator and Solid-State Photomultiplier Direct Coupling Tests

Gerald C. Blazey

Northern Illinois University – Northern Illinois Center for Accelerator and Detector Development
Department of Physics, DeKalb, Illinois – USA

Initial cosmic ray measurements show strong minimum ionizing particle response for scintillator directly coupled to solid-state photomultipliers. Source scans show strong dependence on scintillator thickness.

1 Introduction

An excellent candidate for the highly segmented calorimeters required for particle flow algorithms (PFA) appears to be a scintillator based detector with solid-state photomultipliers directly coupled to scintillator pads and both mounted on a multi-layer printed circuit board (PCB). Calorimeter prototypes utilizing the scintillator and solid-state photomultiplier combination have recently been built and beam tests show the technology suitable for precision calorimetry. These prototypes coupled the scintillator cells to the photomultipliers with wave-length shifting fiber. Direct coupling of the cells with solid-state sensors represents an attractive alternative for construction and assembly of the highly segmented mega-channel detectors required for PFAs. We describe direct coupling measurements with green emitting scintillator. Tests were performed with sensors from different vendors and with different cell geometries. Uniformity across the scintillating cell was measured with a radioactive source. Minimum ionizing particles were used as a source of cosmic rays.

2 Source Scans

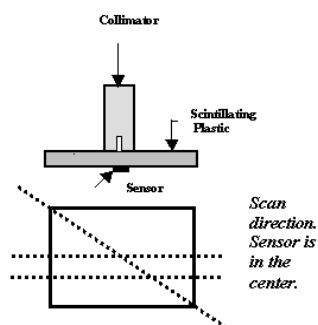


Figure 1: Scan apparatus

As illustrated in Fig. 1 we performed scan measurements with a Sr90 radioactive source collimated to 0.8mm. A Hamamatsu sensor (MPPC S10362-11-025C) [1] was placed at the center of the scintillating cell and current from the sensor recorded. The source was moved along the cell surface. All cells had the same coating and the edges were unpolished and painted white. Two layers of Tyvek on the top and the bottom of the scintillator served as a reflective material. The sensor opening in the reflective coating was 3x3 mm². Positioning was accurate within ± 0.5 mm. The maximum signal to background ratio was ~ 150 . The measurements were reproducible to within ~ 3 %.

We performed three different scans with four different thicknesses of scintillator. Scans were performed through the center of the scintillating cell, across the scintillator with a 10mm offset with respect to the center, and from corner-to-corner. As shown in Fig. 2, the uniformity improves with thickness and the non-uniformity is greatest at cell edge. For 6mm

thick scintillator, the edge response (normalized to the central position) was 54% for the scan through the center and 52% for the diagonal scan (at a distance of 15mm from the center).

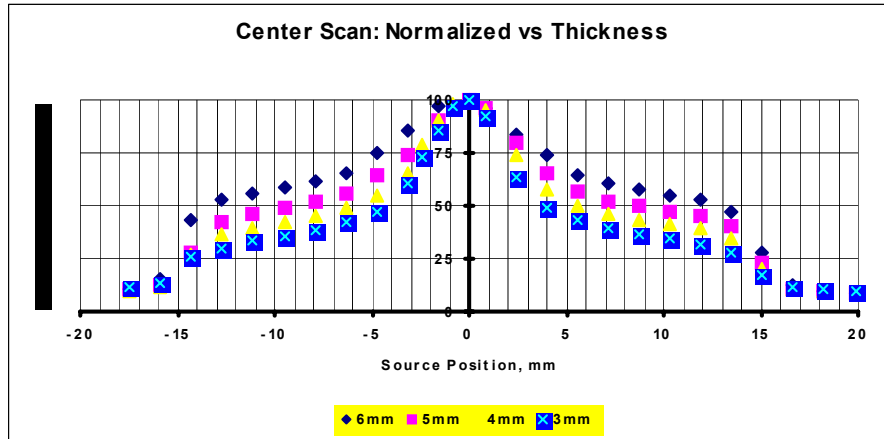


Figure 2: Scan measurements through the center for different thicknesses.

3 Cosmic Ray Measurements

The experimental apparatus used to measure the response to cosmic muons is illustrated in Fig. 3. The trigger utilized two 3x3 cm² scintillating cells with sigma type grooves and glued Y-11 WLS fibers 1 mm in diameter. The optical signal from the trigger scintillating pads was amplified with an Optical Interface Amplifier (OIA) made by CPTA [2]. The OIA includes solid-state photomultipliers with bias circuits, amplifiers, and shapers. The CPTA photomultiplier detection efficiency was about 35% at 450nm. The discriminator transforms the analog signal into NIM signals and a coincidence unit finalizes the trigger. The threshold for each trigger counter was set at five photoelectrons. The random coincidence rate was approximately one event per 30 minutes. The 3x3 cm² scintillating test cell was made of EJ-260 green emitting plastic scintillator [3] and located between the two trigger counters which were positioned 10 cm from one another. The scintillator thickness was 6 mm. The photo-sensor was placed directly on the scintillator and coupled with optical grease. The cell was wrapped with VM2000 film. For each measurement a 3x3 mm² opening was made in the film and a solid-state photomultiplier placed at the center of the opening. The signal was read out with a data acquisition system developed by the CALICE collaboration, running on a PC controlling a VME DAQ board [4].

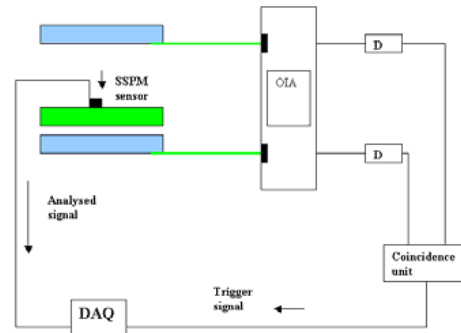


Figure 3: Cosmic ray apparatus

The response to cosmic rays was measured for the three different likely sensor positions (Fig. 4). A CPTA sensor distribution for the central position in ADC units is shown in Fig. 5. The pedestal can be distinguished from the most probable value. We used the most probable

value to evaluate the difference in the light output for the three different sensor positions; these are shown in Table I normalized to the central position. The uncertainty is estimated at 15% and includes statistical uncertainties and photomultiplier gain variations due to temperature changes. As shown in Table I, we performed a second set of calibrated measurements with a Hamamatsu photomultiplier (MPPC S10362-11-100C) [1]. Although not shown, the signal is far from the pedestal, suggesting high registration efficiency. We measured a 10.8 ± 1.5 PE response without optical grease at the central position, implying opportunity to optimize the coupling.

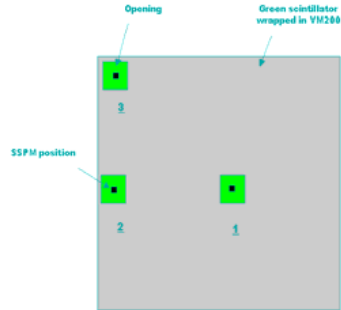


Fig.4: Measurement positions

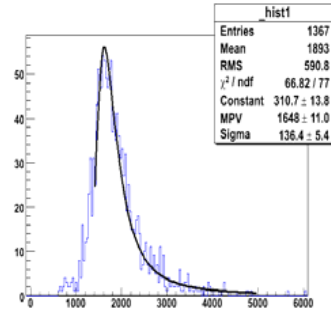


Fig 5: Response at center position

TABLE I: Sensor Response at Various Locations (with optical grease)

Position	CPTA (Normalized to Center Position)	Hamamatsu (PE)
Center	100%	16.8 +/- 2.5
Edge	92%	19.3 +/- 3.0
Corner	71%	Not measured

4 Conclusions

Detailed source scans show that uniformity improves with scintillator thickness. Cosmic ray measurements are encouraging, both CPTA and Hamamatsu sensors generate strong MIP signals which indicates that highly efficient directly coupled detectors are feasible. R&D continues with different scintillator, surface treatments, and sensors. An integrated PCB board with scintillator and SiPMs both mounted on the surface is in preparation for beam tests this year. Slides can be found at Reference [5].

5 References

- [1] Catalog N KAPD0002E01, Jan. 2007, DN Hamamatsu Photonics K.K.
- [2] D. Beznosko, et al., NIM A545 727 (2005).
- [3] Eljen Technology 2010 E. Broadway, Sweetwater, Texas 79556, United States.
- [4] CALICE Collaboration, <http://www.hep.ph.ic.ac.uk/calice/elecProduction/electronics.html>
- [5] Slides: <http://ilcagenda.linearcollider.org/contributionDisplay.py?contribId=383&sessionId=108&confId=1296>

Study of MPPC Performance for the GLD Calorimeter Readout

Satoru Uozumi *for the GLD Calorimeter Group*

Shinshu University - Faculty of Science
3-1-1 Asahi, Matsumoto, Nagano 390-8621 Japan

The Multi Pixel Photon Counter (MPPC) is a semiconductor photon sensor which has a multi micro-APD pixel structure which works in limited Geiger mode. Since the MPPC has many attractive features, such as good performance, low cost, compact size and tolerance for magnetic fields, we are developing and studying it, aiming to use it for the scintillator-strip calorimeter readout for the GLD detector. As a result of this study, we have found that the latest 1600 pixel MPPC has satisfactory performance and is feasible for calorimetric use. However further study and development are still needed and are in progress, especially with regards to dynamic range, robustness and radiation hardness.

1 Introduction

The Multi Pixel Photon Counter (MPPC)[1][2] is a semiconductor photon sensor which is one of the Pixelated Photon Detectors (PPD) family, similar to the Silicon Photomultiplier or MRS-APD [3]. As shown in Figure 1, it has multi micro-APD pixels which work in limited Geiger mode. If a photon is injected into a pixel and creates a photoelectron, an avalanche is induced in the strong electric field and is read as a signal. Since the MPPC has many attractive features, such as low cost, compact size and tolerance for magnetic fields, we are developing and studying the 1600 pixel MPPC aiming to utilize it as the readout sensor of the GLD scintillator-strip calorimeter[4].

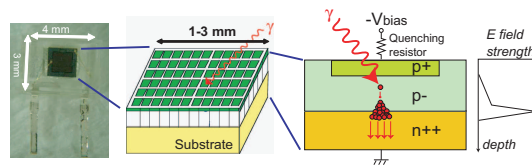


Figure 1: Picture and structure of the MPPC.

Since the MPPC has many attractive features, such as low cost, compact size and tolerance for magnetic fields, we are developing and studying the 1600 pixel MPPC aiming to utilize it as the readout sensor of the GLD scintillator-strip calorimeter[4].

2 Performance of the 1600 pixel MPPC

2.1 Gain, Dark Noise Rate, Inter-pixel Cross-talk

The basic performance of the MPPC – gain, dark noise rate and inter-pixel cross-talk probability – are summarized in Figure 2. The gain is measured as function of bias voltage and fitted by a linear function $\text{Gain} = C(V_{\text{bias}} - V_0)/e$, where C and V_0 denote the pixel capacitance and breakdown voltage, and e is the electron charge. The quantity $V_{\text{bias}} - V_0$ is the over-voltage and is denoted as ΔV . In the plot one can see that the breakdown voltage depends on temperature with a coefficient $\Delta V_0/\Delta T = 56 \text{ mV/K}$. The gain is typically of order a few 10^5 , which is large enough for the requirements of the GLD calorimeter. The dark noise rate and the inter-pixel cross-talk probability are measured as functions of the

over-voltage. The dark-noise is caused by thermal electrons, and thus has a strong temperature dependence. Typical values of the dark noise and cross-talk probability are of order 100 kHz and ~ 0.1 respectively, acceptably small for the GLD calorimeter readout.

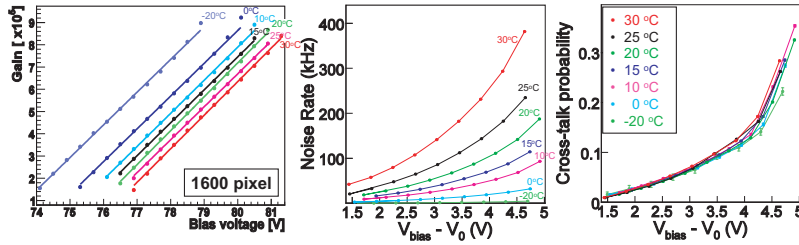


Figure 2: Measured gain, noise rate, inter-pixel cross-talk probability of the 1600 pixel MPPC, as a function of over-voltage and temperature.

2.2 Photon Detection Efficiency

The photon detection efficiency (PDE) of the 1600 pixel MPPC is measured as shown in Figure 3. The LED light pulse is collimated and injected into both the MPPC and Photomultiplier, and its light yield is measured by both sensors. From the ratio of observed light yields and the PDE of the photomultiplier, one can extract the PDE of the MPPC. The measured PDE is also shown in Figure 3. It is observed that PDE increases with over-voltage, and saturates at around 17%. Since the geometrical acceptance of photo-sensitive region of the 1600 pixel MPPC is $\sim 20\%$, this number is considered to be reasonable. The PDE of 17% is comparable with conventional photomultipliers and is satisfactory for the requirements of the GLD calorimeter.

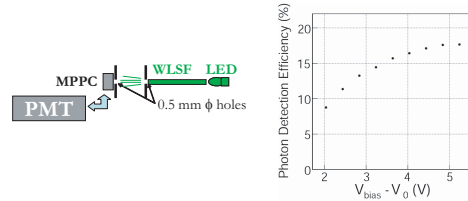


Figure 3: Setup and result of the measurement of photon detection efficiency.

2.3 Recovery Time

The recovery time of the MPPC is another interesting property to measure. The setup and result of the recovery time measurement is shown in Figure 4. Two successive light pulses from a laser and LED are injected with a delay of Δt , and by measuring the pulse height of the MPPC for the second light pulse at different Δt , the recovery of the MPPC can be observed. The right plot in Figure 4 shows the recovery fraction (f_r) measured as a function of Δt . By fitting the measured points with an empirical function $f_r = A(1 - e^{-(\Delta t - b)/\tau})$, the recovery time τ is measured to be $\tau = 4.1 \pm 0.1$ ns. This number is consistent with the CR time constant of the quenching resistor and pixel capacitance.

2.4 Response Function

The MPPC has a non-linear response to input light strength, since in principle each pixel can count only one photon. However since the recovery time of the 1600 pixel MPPC is

~ 4 ns, similar to the width of the light pulse from plastic scintillator, light created by a charged particle crossing the scintillator can fire an identical pixel several times. Due to this effect the dynamic range of the MPPC, basically determined by the number of pixels, can be enhanced. We have measured the actual response of the MPPC as a function of the true number of photoelectrons, as shown in Figure 5. In this measurement, PMT is used to determine the number of photoelectrons from the LED. In the result one can see that the shape of response function changes with the duration of the input pulse. This enhancement may be useful for calorimetric use, where a large dynamic range is needed. However a precise determination of the input light pulse is necessary to take advantage of this effect.

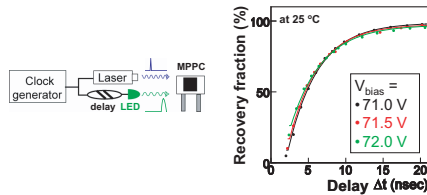


Figure 4: Setup and result of the recovery time measurement. Recovery fraction is ratio of responses for 2nd pulse, measured after a delay of Δt and after complete recovery ($\Delta t = \infty$).

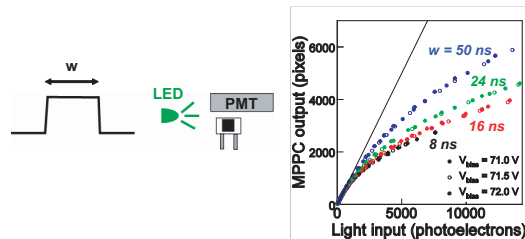


Figure 5: Setup and result of the response function measurement.

3 Summary

We are studying and developing the 1600 pixel MPPC with Hamamatsu Photonics, aiming to utilize it for the GLD calorimeter readout. Results of the several measurements performed so far show satisfactory performance for the GLD calorimeter readout. However development is still underway, and further studies on stability, robustness, and radiation hardness will be performed. The dynamic range and temperature dependence of V_0 will also be improved in the near future.

References

- [1] Hamamatsu Photonics K.K.
http://jp.hamamatsu.com/products/sensor-ssd/4010/index_en.html
- [2] Satoru Uozumi *for the KEKDTP photon sensor group*, “Development and Study of the Multi Pixel Photon Counter”, proceedings for the 10th Vienna Conference on Instrumentation, Vienna, 19-24 Feb 2007.
- [3] G. Bondarenko *et al.*, Nucl. Phys. Proc. Suppl. **61B**, 347 (1998); G. Bondarenko *et al.*, Nucl. Instrum. Meth. A **442**, 187 (2000); P. Buzhan *et al.*, ICFA Instrum. Bull. **23**, 28 (2001); P. Buzhan *et al.*, Nucl. Instrum. Meth. A **504**, 48 (2003).
- [4] GLD Detector Outline Document, GLD collaboration
<http://ilcphys.kek.jp/gld/documents/dod/g1ddod.pdf>

LC Scintillator-based Muon Detector/Tail-catcher R&D

R. Abrams¹, G. Blazey², A. Driutti⁶, A. Dychkant², H.E. Fisk³, A. Gutierrez⁴, P. Karchin⁴,
M. McKenna⁵, C. Milstene³, A. Para³, G. Pauletta⁶, R. Van Kooten¹, M. Wayne⁵, V. Zutshi²

1 – Department of Physics, Indiana University, Bloomington, IN 47405, U.S.A.

2 – Department of Physics, Northern Illinois University, DeKalb IL 60115, U.S.A.

3 – Fermilab, P.O. Box 500, Batavia, IL 60510, U.S.A.

4 – Department of Physics and Astronomy, Wayne State University, Detroit MI 48201, U.S.A.

5 – Department of Physics, University of Notre Dame, Notre Dame, IN 46556, U.S.A.

6 – Università di Udine 33100 Udine, UD Italy

Preliminary analysis of test beam data from strip scintillator planes read-out with multi-anode PMTs (MAPMTs) is presented along with a description of the independent systematic measurements of relative response for all channels of several MAPMTs used in the tests. Test beam measurements for the response of a scintillator strip, read out with Si photo-sensors, is also described.

1 Introduction

This report[1] describes tests of four 2.5 m X 1.25 m area ILC pre-prototype strip-scintillator planes exposed to a +120 GeV/c hadron beam in the Meson area at Fermilab. The objectives of the tests were to measure the response of the strip scintillator (1cm thick X 4.1cm wide) equipped with a 1.2 mm diameter green light collecting wavelength shifting (WLS) fiber glued in a longitudinal channel along the length of the strip. For readout purposes the WLS fiber was thermally fused to a clear fiber of the same diameter near the exit of the strip to transmit light pulses, generated by charged hadrons, to the multi-anode photo-multiplier that was used to convert the light pulses to signals that were then digitized.

The parallel strip-scintillator that makes up the planes is oriented at $\pm 45^\circ$ relative to the boundaries of each plane. Two of the four planes had a single clear fiber per strip to carry the light to its photo-sensor. These planes are labeled S+ and S- to indicate single-ended readout strips.

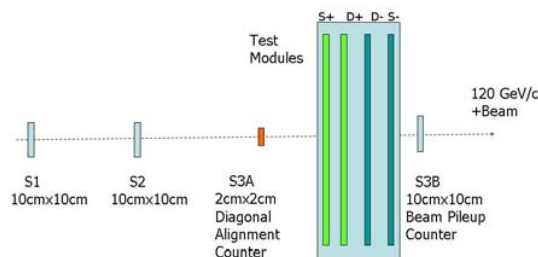


Figure 1: MTest beam setup of four planes of scintillator strips and the beam defining counters.

The other two planes have clear fibers fused to each end of the WLS fiber to provide dual paths for light to reach two photo-sensors. These two planes are labeled D+ and D-. The two ends of each D-plane fiber are labeled D(a) or D(b). Each plane has 22 full length strips (1.87 m) and 42 partial length strips, 21 to fill each of the two corners of a given plane. This geometry is chosen to

limit the maximum length of scintillator bars, WLS fibers and consequent attenuation of scintillator generated light and the possible need for double-ended readout.

2 Test-beam Set-up

Figure 1 shows schematically the four planes of strips and beam defining counters. The MTest (primarily) proton beam was approximately 1 cm FWHM in diameter. The 2 cm X 2 cm S3A counter was mounted diagonally to define the fixed beam position. The four planes were mounted on a movable cart so they could be positioned vertically and horizontally to put beam through one strip in each plane. The beam trigger required a four-fold coincidence of the counters as indicated in Fig. 1. The pulse height for S3B was digitized for use in the analysis to veto multiple beam particles during the ADC gate.

The 64 channel multi-anode PMTs, Hamamatsu 7546B run at 970 V, were used to convert light to electrical signals. The anode signals passed via a special printed circuit board from the MAPMT base to paddle cards that separated the output from 16 channels into RG-174 coaxial cable that terminated at a patch panel. From there RG-58 cables carried the signals to LeCroy X10 amplifiers where they were split and delayed for timing purposes before they entered LeCroy 2249A ADCs. The LRS 2249A's digitized the delayed signals that were contained in an ADC gate that was triggered by the four-fold beam coincidence. The ADC gate was 170ns to accommodate signals from any of the instrumented strips. The digitized ADC outputs were readout with a standard CAMAC system at a rate that was restricted to about 50 Hz. When we were the prime user we had low intensity beam, ~ 1000 p/sec, two 1 s spills per minute, 12 hours per day. Ten percent of the ADC gates contained additional beam particles, even at low rates. This fraction was measured by digitizing the output of the SC3B counter for all recorded beam triggers. During the data analysis events, with a pulse height in SC3B that was more than a single minimum ionizing particle, were rejected from further analysis.

There were a total of 384 channels associated with the MAPMTs. Due to our limited DAQ rate we used a total of slightly less than 40 ADC channels. Each LRS 2249A ADC channel was separately calibrated. The nominal calibration was 0.25 pC/count for this 10 bit system. Several channels were significantly different than this.

3 Test Beam Data

Measurements were done for a selected sample of points on the grid of intersections of positive and negative strips. A total of 78 strips were selected for beam studies based on limited running time, our ability to position the strip intersection points in the beam and performance of necessary checks to qualify the data. We performed pedestal measurements for channels whose strips were not in the beam during beam spills. A typical set of pedestal subtracted histograms for the six channels with beam for strips +38 and -38 is shown in Fig. 2.

The triggers for the data shown in Fig.2 depend only on the beam counters shown in Fig. 1. None of the scintillator strips are included in the trigger. This allows for an independent measurement of the efficiency of any strip through which the beam is passing. For the plot shown there are 11,450 events. A careful examination of the six plots shows that there are no events with a pulse height near zero. If there were a single event missing the inefficiency would be $1/11450 = 8.7 \text{ E-}05$.

Assuming Poisson statistics this inefficiency, implies the mean number of photo-electrons is > 9 . With this simple analysis the mean number of photo-electrons from light pulses produced at the far end of a strip would decrease the efficiency to about 99%, which seems tolerable since strip wrapping, etc. will introduce inefficiencies of a few percent.

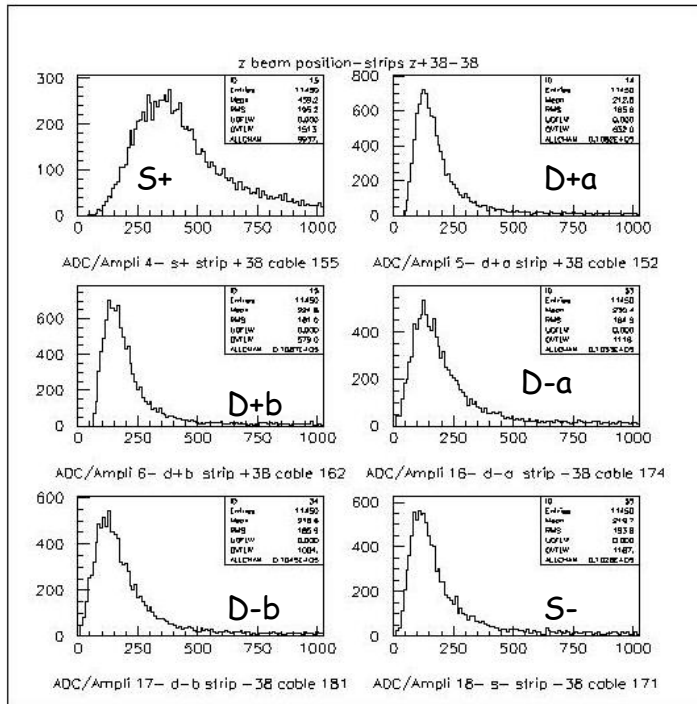


Figure 2: Pulse height histograms for beam exposure of the four strips centered on the four planes: +38 and -38.

Another observation from Fig. 2 is that the mean pulse height for these six channels is quite varied. This comes primarily from the different responses of the multi-anode cells to light pulses. Other factors that affect the observed pulse-height distributions from different PMT channels, include the ADC calibration (# of pC/ADC count), variations in the X10 amplifiers, and the light transmission through the thermally-fused splice joint between the clear and WLS fibers. The latter, $\sim 80\%$, has been measured for each of the 384 fiber splices but it has not been applied in our analysis.

4 Measurement of MAPMT Relative Response

There are various schemes that can be used to measure the response of each MAPMT channel. We used a custom setup that mimics green light generated in strips. It is a piece of scintillator that has two 1.01 m long, 1.2 mm diameter Kuraray Y11 fibers embedded in it, with a 5 mCi Sr-90 source (with housing) placed on top of it to produce light pulses. A precision-drilled template with 64 1.2mm diameter holes was used to accurately position the free end of the WLS fiber adjacent to the Hamamatsu 7546B MAPMT photocathode window. The assembled PMT with base voltage divider circuit, cables, and light source were operated in a light-tight box. The output of the MAPMT channel that was illuminated was carried from the light-tight box to a commercial electrometer connected via commercial DAQ apparatus to a PC. One of the two WLS fibers was connected to a given channel for monitoring purposes throughout the measurements[2].

Each of six MAPMTs had their relative response measured with the HV set to 800V. At this voltage the typical current was $\sim 1 \mu\text{A}$. We also measured cross-talk, i.e. the output of physically adjacent channels when light was incident on one channel. The cross-talk varied from a maximum

of 4.9% to an average of 3.9% for the four nearest channels to 1% for the next nearest channels. There was no saturation in the output of any channel as the voltage was varied between 600V and 970V as evidenced by a linear dependence of the logarithm of the current as a function of the voltage. The variation in response over six MAPMTs that were measured is substantial. For all tubes measured the maximum to minimum output varied by a roughly a factor of 5. The mechanical structure of the MAPMT is reflected in a periodic variation in the relative output over the 64 channels[2].

5 Test Results

Figure 3. shows the calibrated response of several channels in pC as a function of distance from beam intersection with a particular strip to the WLS-to-clear splice joint. Included are the ADC calibration and the MAPMT channel's relative response as described by A. Dyshkant et al [2]. The data show that when both ends are readout the summed signal is larger by 30 – 50% than that of a strip with single ended readout.

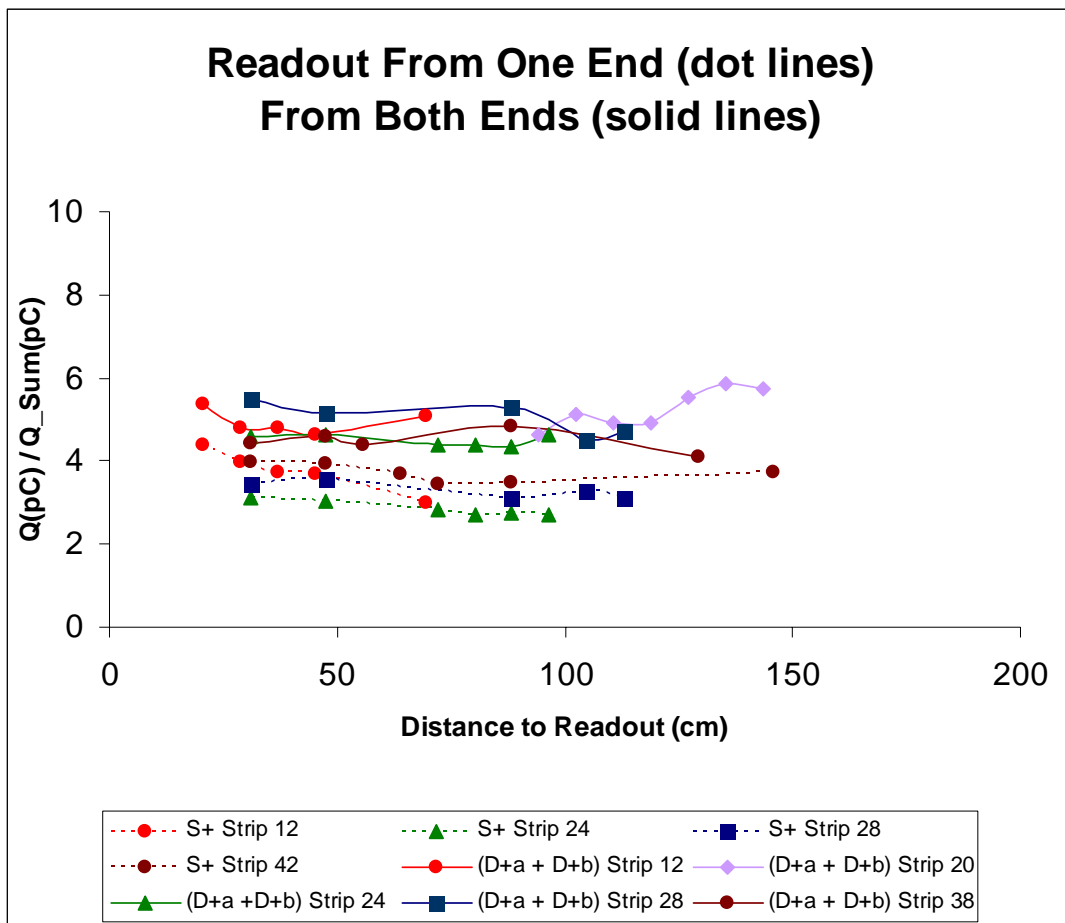


Figure 3: Signals from scintillator strips after corrections for relative response of different MAPMT channels. The data points connected by dashed (solid) lines are for strips with single-ended (double-ended) readout.

This is about what was expected based on the attenuation length for green light in the WLS fiber and the reflection coefficient for the mirrored surface that was sputtered on the polished far end of each WLS fiber of the S-planes.

6 Testing Si Photo-sensors

Near the end of our MTest running the Udine group attached a few of their IRST photo-sensors [3] to strips that were essentially the same as those tested with MAPMTs. Their installation at the test beam was relatively simple as we were able to attach them on the front face of our movable array of four MAPMT planes. The outputs of the photo-sensors were sent to X10 amplifiers and then to ADCs for digitization. An example of the digitized output is shown in Figure 4 below.

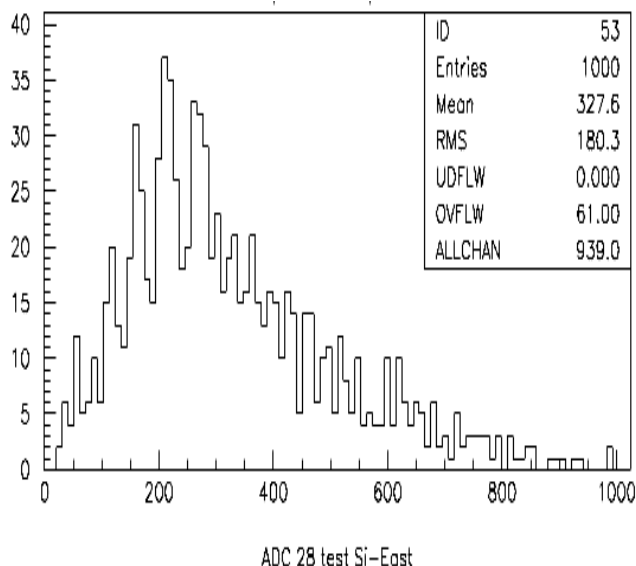


Figure 4: Test results from an IRST photo-sensor optically coupled to a WLS fiber embedded in a extruded scintillator bar.

Individual photo-electron peaks are clearly visible. The beam was primarily 120 GeV/c protons with the intensity similar to running with the MAPMT tests. Discriminator thresholds were set above electronic noise but below the single photo-electron amplitude; the dark count did not exceed 1.5 KHz. Data were taken with a trigger based only on beam line scintillation counters as were used in the MAPMT tests. The Si photo-sensor gain is estimated to be $1.6 \text{ E}+06$; the efficiency is 99% and the mean number of photo-electrons is ~ 6.5 .

References

- [1] Slides: <http://ilcagenda.linearcollider.org/contributionDisplay.py?contribId=509&sessionId=108&confId=1296>
- [2] A.Dyshkant, G.Blazey, K.Francis, D.Hedin, V.Zutshi, H.E..Fisk, et al, MAPMT H7546B Anode Current Response Study for ILC SiD Muon System Prototype, FERMILAB-PUB-07-485-E, Fermilab (2007).
- [3] C. Piemonte, et al IRST-INFN Trieste/Udine <http://www.sipm.itc.it>

A 10-bits pipeline ADC dedicated to the VFE Electronics of Si-W Ecal

Laurent Royer and Samuel Manen

Laboratoire de Physique Corpusculaire, 24 avenue des Landais
63177 AUBIERE Cedex - France

A 10-bits pipeline Analog-to-Digital Converter (ADC) has been designed in a $0.35\ \mu\text{m}$ CMOS technology and prototypes tested. This ADC is a building block of the very-front-end electronics dedicated to the Si-W electromagnetic calorimeter. Based on a 1.5-bit resolution per stage architecture, it reaches the 10-bits precision at a sampling rate of 4 MSamples/s with a consumption of 35 mW. Integral and Differential Non-Linearity measured never exceed respectively ± 1 LSB and ± 0.6 LSB over the 2V dynamic range, with a level of noise limited to 0.47 LSB at 68% C.L.

1 Introduction

The very-front-end readout electronics of the Si-W Electromagnetic Calorimeter (ECAL) of ILC has to process 10^8 channels which deliver a 15-bits dynamic range signal with a precision of 8 bits. Moreover, the minimal cooling available for the embedded readout electronics imposed an ultra-low power limited to $25\ \mu\text{W}$ per channel. This issue will be reached thanks to the timing of ILC which allows the implementation of a power pulsing with a duty ratio of 1%. A key component of the very-front-end electronics is the Analog-to-Digital Converter (ADC) which has to reach a precision of 10 bits. In order to save the die surface of the chip and to limit the power consumption, one ADC will be shared by several channels. To fulfill this request, an ADC operating at a sampling rate of the order of one MSamples/s has been designed and tested.

2 Description of the pipeline ADC

The ADC designed is based on a pipeline architecture [2]. A resolution of 2 bits per stage has been chosen in order to attenuate the contributions to the non-linearity of the gain error and of the offset voltages. As the two output bits of each stage are combined with the next one and the combination "11" avoided, the effective resolution per stage is 1.5 bit [3]. This 1.5-bit/stage pipeline ADC architecture [3] involves two comparators per stage, with separate threshold voltages V_{Th}^{Low} and V_{Th}^{High} , and two reference voltages V_{Ref}^{Low} and V_{Ref}^{High} . A 2-bits word $[b_2 b_1]_i$ is delivered by each stage i .

The global schematic of one ADC stage with resolution of 2 bits is given on Fig. 1. In order to reject the common mode noise, a fully differential structure has been adopted. As represented on Fig. 1, the value of the reference signal added to the $(V_{In})_i$ input signal is selected by comparators outputs through switches. Then the circuit operates on two clock phases: during the sampling phase, the input signal and the reference signal are summed through capacitors $2C$, while during the hold phase, the summed signal is amplified by factor 2. The gain-2 amplifier is built with a differential amplifier and a capacitive feedbacked loop. A better matching is obtained with capacitors and they have been preferred to resistors.

This matching is particularly important because it affects the precision of the gain 2, and therefore, the linearity of the ADC. Thus, feedback capacitors must be large enough to minimize both the thermal noise kT/C and the components mismatch proportional to $1/\sqrt{C}$. In contrast, both the small die surface and the dynamical performance achieved with low supply current have to be carry out. Then capacitors values of 300 fF and 600 fF are used.

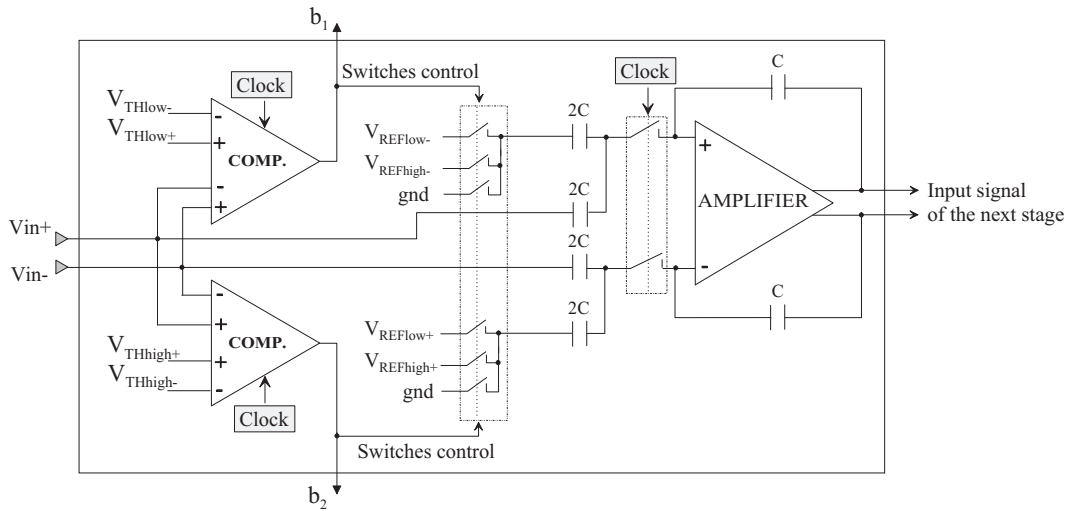


Figure 1: Simplified schematic of one ADC stage: 2 comparators give the output bits of the stage and determine the reference signals subtracted to the input signal; the amplifier amplifies by a factor 2 the residual voltage and delivers it to the next stage.

3 Measurement Results

Architecture	1.5-bit/stage
Technology	0.35 μm 2-P 4-M CMOS
Area	1.5 mm x 0.9 mm
Supply Voltage	0-5 V
Resolution	10 bits
Full scale	2 V differential
Sample rate	4 MS/s
Consumption	35 mW @ 4 MHz
INL	+0.85/-0.70 LSB
DNL	+0.56/-0.46 LSB
Noise	0.47 LSB @ 68% C.L.
Gain Error	0.8% of full scale
Zero Error	0.5% of full scale

Table 1: Performance of the pipeline ADC.

A 10-bits ADC prototype has been fabricated using the Austriamicrosystems 0.35 μm 2-poly 4-metal CMOS process. The total area of the ADC is 1.35 mm^2 and the chip is bounded into a JLCC 44 pins package. The circuit is measured with a 5.0 V supply and a differential input swing of $2.0V_{pp}$, at a frequency clock of 4 MHz.

Main performance is reported on table 1. A dynamic input range of 2.0 V is measured with zero and gain errors respectively of 5 LSB and 8 LSB. The standard deviation of the noise is lower than 0.5 LSB at 68% C.L.

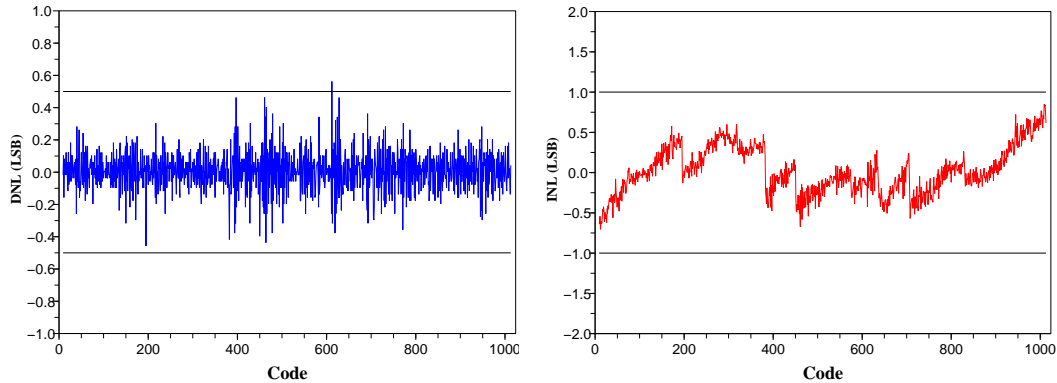


Figure 2: Differential (left) and integral (right) nonlinearity measurements

The static linearity curves of the 1.5-bit/stage ADC are given in Fig. 2. The Differential Non-Linearity (DNL) is defined as the difference between an actual step width and the ideal value of one LSB. The DNL measured is within a ± 0.6 LSB range. The Integral Non-Linearity (INL) refers to the deviation, in LSB, of each individual output code from the ideal transfer-function value. The INL curve plotted in Fig. 2 never exceeds $+0.85/-0.70$ LSB over the 2V dynamic range.

At a sampling rate of 4 Msamples/s the dissipation of the chip is 35 mW. With a time of 250 ns to convert one analogue signal and considering the number of events stored per channel to be less than 5, the power consumption integrated during the ILC duty cycle of 200 ms is evaluated to $0.22 \mu\text{W}/\text{channel}$. Assuming that the ON-setting time and the pipeline latency of the conversion are neglected when the ADC is shared by tens of channels, the integrated power dissipation of the ADC is then limited to 1% of the total power available for the very front-end electronics of the ECAL.

4 Conclusion

A 10-bit 4-MSamples/s 35-mW CMOS ADC based on a pipeline 1.5-bit/stage architecture has been designed and tested. Its performance confirms that this architecture fulfill the ADC requirements of the ECAL at ILC. Bearing in mind that the consumption is a key point, the next step will consist on a portage in 3V supply.

References

- [1] Slides:
<http://ilcagenda.linearcollider.org/contributionDisplay.py?contribId=388&sessionId=108&confId=1296>
- [2] R. Van de Plassche, *Integrated analog to digital and digital to analog converters*. Kluwer Academic (1994).
- [3] A.M. Abo and P.R. Gray, "A 1.5V, 10-bit, 14.3-Ms/s CMOS pipeline analog to digital converter," *IEEE journal of Solid State Circuits*, vol. 34, no. 5, pp. 599–606, May 1999.

A Silicon-Tungsten ECal with Integrated Electronics

R. Frey¹, J. Brau¹, M. Breidenbach², D. Freytag², G. Haller², R. Herbst², R. Lander³,
T. Nelson², V. Radeka⁴, D. Strom¹, and M. Tripathi³ *

1- University of Oregon - Dept of Physics and Center for High Energy Physics
Eugene, Oregon - USA

2- Stanford Linear Accelerator Center
Stanford, California - USA

3- University of California - Dept of Physics
Davis, California - USA

4- Brookhaven National Laboratory - Physics Division
Upton, New York - USA

We summarize recent R&D progress for a silicon-tungsten electromagnetic calorimeter (ECal) with integrated electronics, designed to meet the ILC physics requirements.

1 Overview

A basic physics requirement for ILC detectors is that they provide excellent reconstruction of hadronic final states. This allows access to new physics which is complementary to the LHC. One statement for a requirement on jet reconstruction is that intermediate particles which decay into jets, such as W, Z, or top, can be identified and isolated. This places unprecedented requirements on 2-jet or 3-jet mass resolution, typically at the level of 3-5% using the PFA technique, which makes challenging demands on the calorimeters. The electromagnetic energy resolution is not expected to limit jet resolution using a PFA. However, particle separation—photon-photon and charged hadron-photon—is crucial. In addition, if one provides this kind of imaging calorimeter to meet the PFA needs, these same features will also be put to good use for reconstruction of specific tau decay modes (to enable final-state polarization measurement), to “track” photons (even if originating from a vertex displaced from the interaction point), to track MIPS, and so forth. Figure 1 and Table 1 provide some context for our ECal design within the SiD detector concept, along with some main design parameters. More detail is included in the presentation[1].

inner radius of ECal barrel	1.27 m
maximum z of barrel	1.7 m
longitudinal profile	(20 layers \times 0.64 X_0) + (10 layers \times 1.3 X_0)
silicon sensor segmentation	1024 hexagonal pixels
pixel size	13 mm ²
readout gap	1 mm (includes 0.32 mm silicon thickness)
effective Moliere radius	13 mm
pixels per readout chip	1024

Table 1: Main parameters of the silicon-tungsten ECal for SiD.

*This work supported in part by the U.S. DoE LCDRD program.

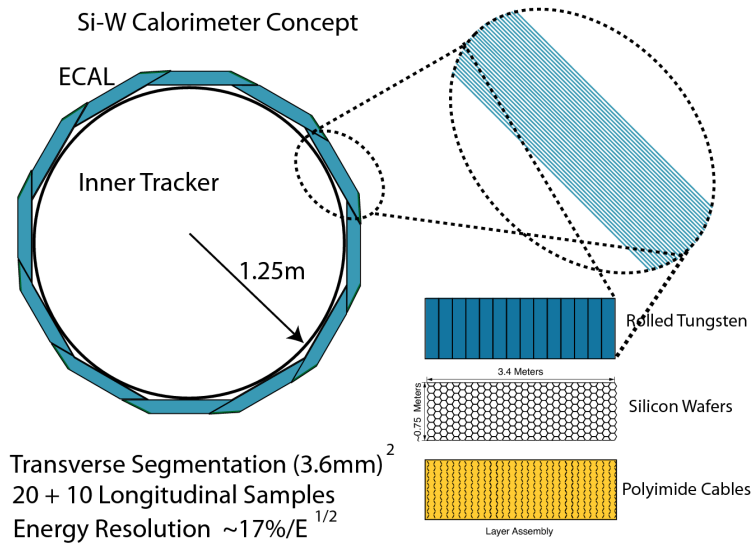


Figure 1: Silicon-tungsten ECal as envisioned for the SiD concept.

The thrust of our R&D project is to integrate detector pixels on a large, commercially feasible silicon wafer, with the complete readout electronics, including digitization, contained in a single chip (the *KPiX* ASIC) which is bump bonded to the wafer. We take advantage of the low beam-crossing duty cycle (10^{-3}) to reduce the heat load using power cycling, thus allowing passive-only thermal management. Our design then has several important features: The electronics channel count is effectively reduced by a factor of 1024; the transverse segmentation down to a few mm can be naturally accommodated (with the cost, to first order, not dependent on the segmentation choice); the readout gaps can be small (1 mm). This last property is crucial for maintaining the small Moliere radius intrinsic to tungsten.

2 Sensor and electronics progress

Based on the lab measurements[2] performed on the version 1 silicon sensor prototypes, we have developed a design for new (version 2) sensors which can be used to fabricate a full-depth (30-layer) ECal module. The new sensor design is depicted in Fig. 2. The layout minimizes capacitive and resistive noise contributions from the signal traces, especially in the vicinity of the *KPiX* chip. A typical trace contributes $C \sim 20$ pF and $R \sim 300$ Ω .

The readout of the Si pixels must accommodate a very large dynamic range. Based on EGS4 simulations, the largest signals in a single pixel—arising from 500 GeV Bhabha electrons—correspond to about 2000 MIPs at shower max. At the low end, one requires measuring MIPs well above the electronic noise ($\text{SNR} \approx 7$ or better). The *KPiX* design incorporates this large dynamic range in a novel way, using on-the-fly range switching. Figure 3 shows this range-switching function in action in the lab. In the plot, as the injected charge is increased, we see the range switch at about 700 fC. For 320 micron silicon, 1 MIP

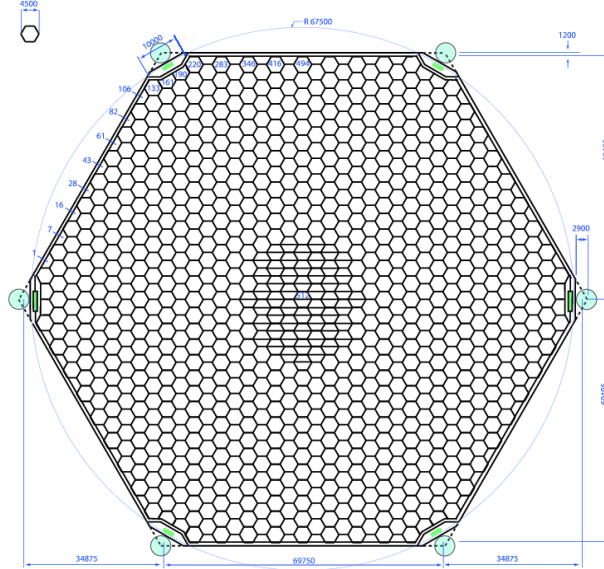


Figure 2: Schematic of version 2 silicon sensors. The central region includes a pad array to which the KPiX ASIC is to be bump or gold-stud bonded.

is equivalent to about 4.1 fC. Thus the upper end of the plot corresponds to about 2500 MIPs, more than the expected maximum.

If the KPiX heat load is kept below about 40 mW, the temperature gradient across an ECal module (≈ 75 cm) can be kept at an acceptable level ($< 10^\circ$ C) using only passive heat conduction via the tungsten radiators. Clearly, this is desirable, and is achievable by taking advantage of the beam-timing structure of the ILC, where beams are only present for 1 ms out of each 200 ms cycle. By cycling off most of the (analog) KPiX power between beam-crossing times, lab measurements of the prototypes confirm that the heat load of the full KPiX chip will be about 20 mW. This heat is to be passively conducted to the module edges behind the ECal (see Fig. 1), where it can be extracted.

Recently, a KPiX v4 prototype was connected to a spare CDF silicon-strip detector and placed in a test beam at the SLAC End Station A (ESA). The data set is still being analyzed. A preliminary result is given in Fig. 4, which shows the detected charge distribution. Since the beam rate averaged 0.25 electron per pulse, and the beam diameter was much larger than the active detector region, the distribution is dominated by the electronic noise, which is gaussian over several orders of magnitude. The single-MIP contribution is clearly visible.

References

- [1] Slides:
<http://ilcagenda.linearcollider.org/contributionDisplay.py?contribId=389&sessionId=108&confId=1296>
- [2] D. Strom *et al.*, *Proc. LCWS 2005, Stanford, California, 18-22 Mar 2005, pp 0908*;
<http://www.slac.stanford.edu/econf/C050318/papers/0908.PDF> .

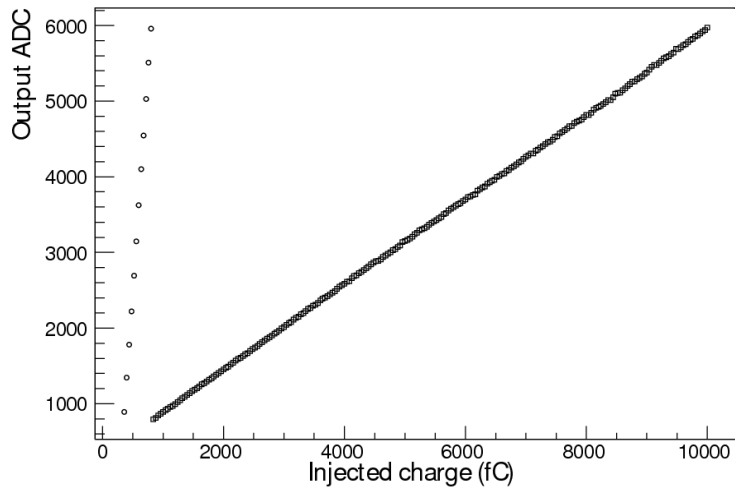


Figure 3: KPiX output as a function of input charge, showing the dynamic gain change at about 700 fC.

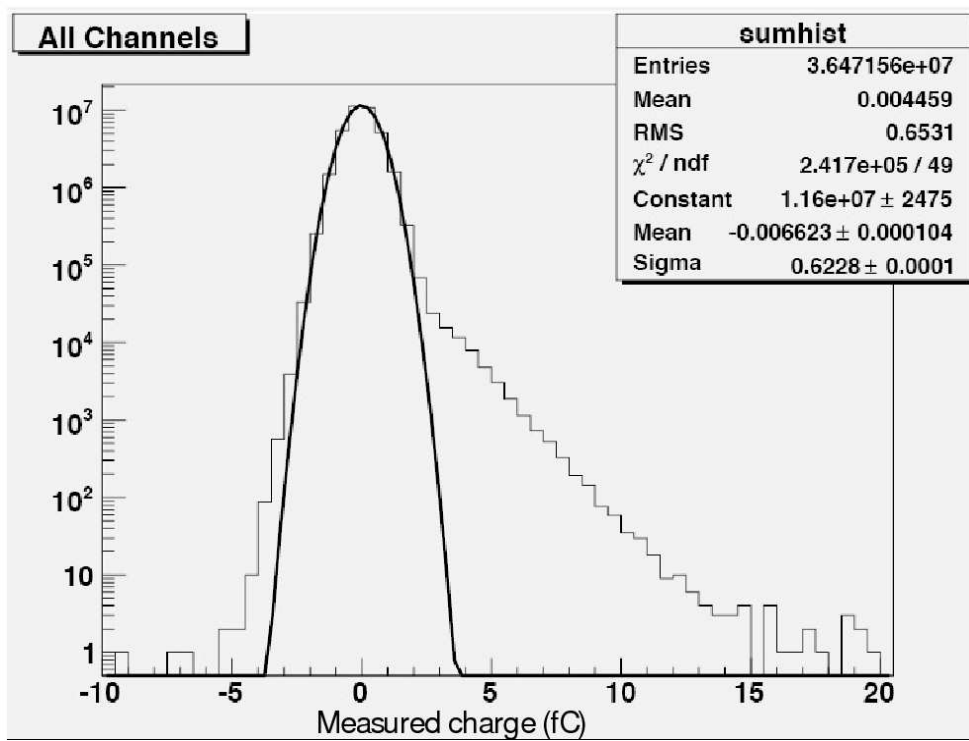


Figure 4: Distribution of charge collected by the KPiX v4 chip at the SLAC ESA.

Readout electronics for LumiCal detector

Marek Idzik, Krzysztof Swientek and Szymon Kulis

AGH University of Science and Technology
Faculty of Physics and Applied Computer Science
Cracow - Poland

The readout electronics for the luminosity detector (LumiCal) at ILC is discussed. First, the challenges of LumiCal and the proposed solutions are described together with the overall readout architecture chosen. Then a more detailed description of the front-end and the analog to digital conversion blocks follows. In particular the design and simulation results of the prototype preamplifier, shaper and basic ADC blocks are presented.

1 Introduction

The project of LumiCal readout electronics depends on several assumptions concerning detector architecture. At present development stage it is assumed that the LumiCal detector is built of 30 layers of 300 μm thick DC-coupled silicon sensors whereas each layer is divided into 48 azimuthal sectors. Each sector, with the inner radius of 8 cm and the outer of 35 cm, is segmented into 96 radial strips with a constant pitch. Such design results in very wide range of sensor capacitance which will be connected to the front-end.

The LumiCal readout should work in two modes: the physics mode and the calibration mode. In physics mode the detector should be sensitive to electromagnetic showers of high energy deposition (up to about 15 pC of ionized charge) in a single sensor. In calibration mode it should detect signals from relativistic muons, i.e. it should be able to register the minimum ionizing particles (MIPs). Because of very high occupancy expected the front-end electronics should resolve signals from particles in subsequent beam bunches and so should be very fast. The requirements on power dissipation can be strongly relaxed if a total or partial power supply switching off is applied in the periods between the bunch trains.

To fulfill all the requirements the general concept of the readout electronics was outlined as shown in fig. 1. The main blocks in the signal flow are: the front-end electronics, the A/D conversion plus zero suppression and the data concentrator with optical driver. The

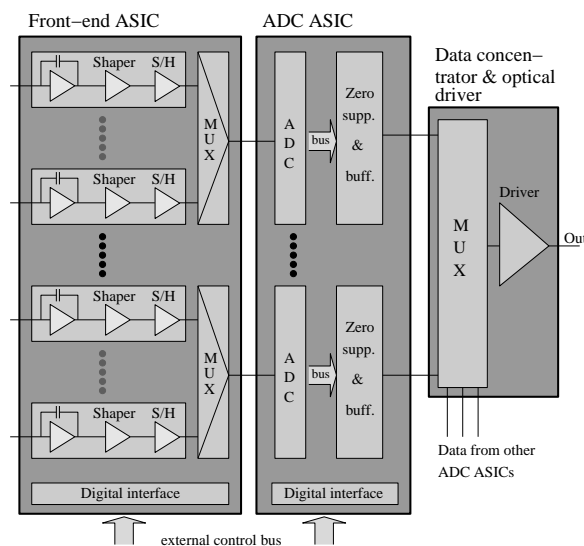


Figure 1: Block diagram of the LumiCal readout electronics

first two blocks of fig. 1, i.e. the front-end and the ADC need to be designed as dedicated multichannel ASICs. In the following the designs of these blocks are discussed and simulation results are presented [1]. The data concentrator and optical driver block will be studied on further development stage. The prototype designs of discussed ASICs are done using the AMS $0.35\mu\text{m}$ technology.

2 Front-end electronics

The front-end electronics detect signals from silicon sensor, amplify and shape them in order to obtain the required signal to noise ratio and finally sample and store their amplitudes. The memorized amplitudes are sent to an A/D conversion block. These operations are done in parallel in all channels of the front-end ASIC. The features of LumiCal already mentioned set important constraints and requirements on the front-end. They concern mainly the wide input capacitance range 10-100 pF per channel, the wide range of charge 2 fC-15 pC deposited in a single sensor and the high speed (pulse duration of about 360 ns). The low noise requirements are driven by calibration mode operation where a S/N ratio of about 10 should be sustained even for the largest sensor capacitance. At present stage the power dissipation per channel is constrained to 10 mW. In order to fulfill the requirements concerning low noise operation and wide range of input capacitance a charge sensitive preamplifier configuration was chosen. Two architectures of front-end using this configuration are currently under study: one with continuous pulse shaping and other based on Switched-Reset scheme. Both architectures with simulation results are discussed below. The sample and hold circuit (S/H) and the multiplexer circuit (MUX) are not discussed here since they have not been designed yet.

2.1 Front-end with continuous pulse shaping

Each front-end channel is built of the preamplifier, pole-zero cancellation circuit (PZC) and shaper as shown in fig. 2. The preamplifier integrates the signal from a sensor on the feedback capacitance. The PZC circuit is used in order to shorten a slow tail of the preamplifier response and in this way to improve high input rate performance. To optimize the signal to noise ratio and high speed performance the preamplifier and PZC is followed by a pseudo-gaussian shaper with a peaking time of about 70 ns.

In order to cover the amplitude range of input signals, from MIPs in the calibration mode to more than 10 pC in the physics mode a variable gain scheme is implemented. The gain control is realized by the switches in the preamplifier and shaper feedback. As can be easily calculated the transfer function of circuit in fig. 2 is equivalent to a standard CR-RC first order shaping. Both the preamplifier and shaper circuits are designed as folded cascodes

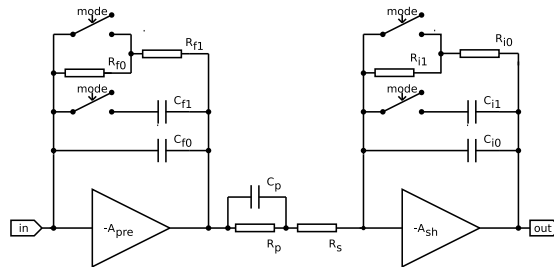


Figure 2: Schematic of preamplifier, PZC and shaper. Switches set to calibration mode

with active loads, which are followed by buffers.

The front-end is designed as a multichannel ASIC. In order to match the sensor segmentation a single ASIC containing 32, 48 or 64 channels is considered for the final version.

Simulations of the proposed front-end were done using Cadence package with Hspice and Spectre simulators. The typical simulated responses for sensor capacitances in the range 10-100 pF are shown in fig. 3 for the calibration mode (mode0) and for the physics mode (mode1). One can notice that in the calibration mode the amplitude

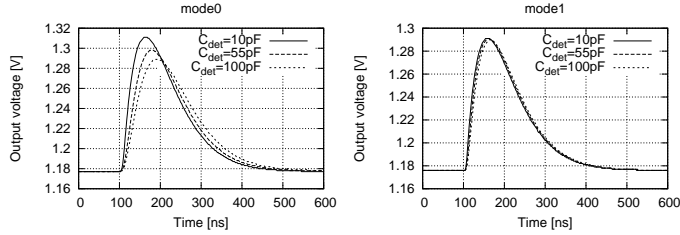


Figure 3: Example of shaper output in calibration mode for 10fC input charge (mode0) and in physics mode for 1pC input charge (mode1)

and peaking time depend on input capacitance. This happens because in the calibration mode, where the preamplifier's feedback capacitance C_f is small ($\sim 400fF$), the ratio of the sensor capacitance C_{det} to the effective input capacitance $C_{eff} \approx A_{pre} \cdot C_f$ is not negligible since the preamplifier gain A_{pre} is below 1000 while the sensor capacitance reaches 100 pF. In such case some part of input charge is lost on sensor capacitance and the preamplifier can not be considered as purely charge sensitive. On the contrary, in the physics mode where the feedback capacitance is large ($\sim 10pF$) the aforementioned ratio may be neglected and the preamplifier behaves as charge sensitive. This is seen in fig. 3 (mode1) where the dependence on input capacitance is hardly noticeable. The simulations were done for a wide range of input charge. The circuit is linear up to about 7 pC and fully saturates above 15 pC. In all simulated cases the S/N ratio stays above 10.

2.2 Switched-Reset front-end

The preamplifier with feedback reset instead of feedback resistance could be a very attractive configuration because such solution does not need a shaper and has large output dynamic range. For this reason a charge sensitive configuration equipped with reset switch as shown in fig. 4 is also investigated. The preamplifier is designed as a folded cascode. To allow variable gain operation different values of feedback capacitances are implemented. The calibration mode configuration is obtained using the smallest capacitance C_{f0} . Simulations of this configuration were performed for a wide range of input capacitancies and input charges. In all cases signal risetime is below 300 ns. Since the simulated reset time of the preamplifier never exceeds 40 ns the full cycle of pulse response and the reset can be kept between two bunches. In the calibration mode the circuit is linear up to about 300 fC and saturates for higher input charges. In the physics mode the linearity region can be extended to tens of pC by increasing the feedback

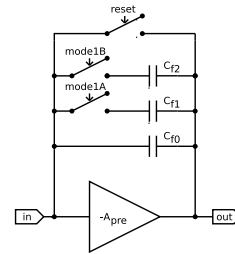


Figure 4: Schematic of switched-reset preamplifier

capacitance. The circuit noise performance is currently under study.

3 Analog to Digital conversion

In the LumiCal detector the energy deposited in a sensor, detected and amplified in the front-end electronics, needs to be digitized and registered for further analysis. This is done in the ADC and zero suppression block. Simulations of LumiCal indicate that the reconstruction procedure needs about 10 bit precision on the measurement of deposited energy. Considering the number of detector channels needed and the limitations on area and power, the best choice for the analog to digital conversion seems a dedicated multichannel ADC. To save the area a reasonable solution is to make one faster ADC for 8 channels of the front-end electronics. Since the LumiCal detector requires a sampling rate of about 3 MHz per channel an ADC should sample the data with at least 24 MHz rate. On the other hand a single 3 MHz ADC per each channel would be the simplest solution from the designer point of view. Both solutions are still under consideration.

One of the most efficient architecture assuring a good compromise between the speed, area and power consumption is a pipeline ADC, and this architecture was chosen for the LumiCal data conversion. Below, the design of main blocks of pipeline ADC is briefly described. The part of ADC block responsible for zero suppression is not discussed here since it is not implemented yet.

3.1 ADC Architecture

Pipeline ADC is built of several serially connected stages as shown in fig. 5. In the proposed solution a *1.5 bit stage* architecture was chosen because of its simplicity and immunity to the offsets in the comparator and amplifier circuits. Since single stage generates only three different values coded on 2 bits it is called *1.5 bit stage*. Each stage from fig. 5 generates 2 bits which are sent to digital correction block. In the correction block 18 output bits from 9 stages are combined together resulting in 10 bits of ADC output.

The block diagram of a single stage is shown in fig. 6. Each *1.5 bit stage* consist of two comparators, two pairs of capacitors C_s and C_f , an operational transconductance amplifier, several switches and small digital logic circuit. To improve the ADC immunity to digital crosstalks and other disturbances a fully differential architecture is used. The operation of the stage is performed in two phases. In phase φ_1 capacitors C_s and C_f connected to ground through S_1 (in reality to common voltage, ground is used in description only for simplicity) are charged to voltages $V_{i\pm}$. In phase φ_2 the switches S_2 and S_3 change positions and S_1 is open. The C_f are now in the amplifier feedback while the C_s are

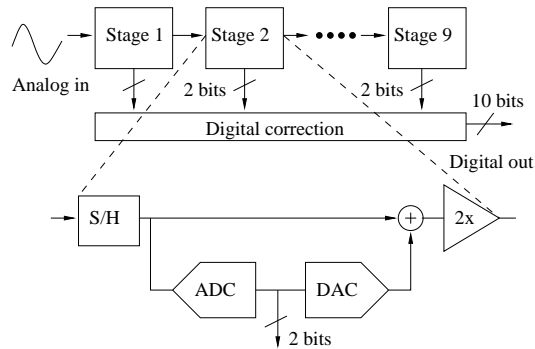


Figure 5: Pipeline ADC architecture

connected to DAC reference voltages ($\pm V_{ref}$ or 0 depending on comparators decision). In the *1.5 bit stage* architecture $C_f = C_s$ is chosen to obtain a gain of two in the transfer function.

The critical block of pipeline ADC is the fully differential amplifier. A telescopic cascode amplifier configuration is used here since it represents the most efficient solution with respect to speed vs power. In order to obtain high enough gain (of about 80 dB) required for 10 bit resolution a gain boosting amplifiers are used in both upper and lower cascode branches. Since the *1.5 bit stage* architecture leaves very relaxed requirements on the comparators ($\sim 100\text{mV}$ threshold precision) a simple dynamic latch architecture was chosen. For the present prototype all reference voltages are assumed to be applied externally.

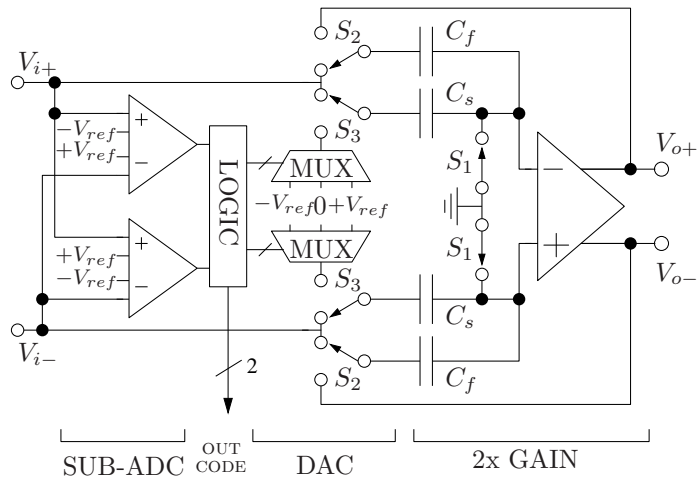


Figure 6: Simplified schematic of a 1.5 bit stage. Switches set to φ_1 phase

Figure 6: Simplified schematic of a 1.5 bit stage. Switches set to φ_1 phase

4 Summary

To summarize it should be stressed that the work on the LumiCal readout electronics has just started. The main readout circuits i.e. the front-end and the ADC are being simulated and first prototypes are submitted. In the next evaluation stage the sub-circuits not yet designed like sample and hold (S/H) or multiplexer (MUX) will be integrated and prototyped as well. Then the integration of multichannel ASICs with all channels and full functionality comprising all necessary controls, DACs, zero suppression etc. will be added.

Acknowledgments

This work was partially supported by the Commission of the European Communities under the 6th Framework Programme "Structuring the European Research Area", contract number RII3-026126.

References

- [1] Slides:
<http://ilcagenda.linearcollider.org/contributionDisplay.py?contribId=390&sessionId=108&confId=1296>

A MAPS-based Digital Electromagnetic Calorimeter for the ILC

J. A. Ballin, P. D. Dauncey, A.-M. Magnan[†], M. Noy¹
Y. Mikami, O. Miller, V. Rajović, N. K. Watson, J. A. Wilson²
J. P. Crooks, M. Stanitzki, K. D. Stefanov, R. Turchetta, M. Tyndel, E. G. Villani³

1 - Department of Physics, Imperial College London, London, UK

2 - School of Physics and Astronomy, University of Birmingham, Birmingham, UK

3 - Rutherford Appleton Laboratory, Chilton, Didcot, UK

[†] - Contact: A.Magnan@imperial.ac.uk

A novel design for a silicon-tungsten electromagnetic calorimeter is described, based on Monolithic Active Pixel Sensors (MAPS). A test sensor with a pixel size of $50 \times 50 \mu\text{m}^2$ has been fabricated in July 2007. The simulation of the physical sensor is done using a detailed three-dimensional charge spread algorithm. Physics studies of the sensor are done including a digitisation algorithm taking into account the charge sharing, charge collection efficiency, noise, and dead areas. The influence of the charge sharing effect is found to be important and hence needs to be measured precisely.

1 Introduction and pixel design

The MAPS R&D program is part of the CALICE [2] collaboration and proposes a swap-in solution to the existing analogue electromagnetic calorimeter (ECAL) design [3], leaving the mechanical design unchanged. A first proof of concept sensor has been fabricated.

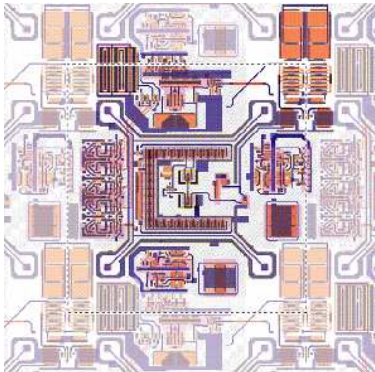


Figure 1: Example of sensor layout: the so-called presampler design.

around 11% of dead area. Figure 1 shows an example of the pixel layout, where one pixel is represented inside the dash-lined area, and the four diodes can be seen on the four corners. The components inside the diodes form the analogue circuitry, whereas the comparator and logic are distributed around the edges. The diodes are N-well to P-substrate. The in-pixel

The concept is to develop a digital electromagnetic calorimeter where each pixel reports only a single bit. This requires a low probability for multiple particles within a pixel, and that probability is reduced to an acceptable level with a cell size of $50 \times 50 \mu\text{m}^2$.

The charge collection is done mainly by diffusion: four diodes placed near the corners of each pixel have been optimised in order to minimise the charge sharing between pixels while maximising the charge collection (see Section 2). To limit the charge sharing effect, the sensitive thickness of the silicon epitaxial layer has been set to $12 \mu\text{m}$. The total silicon thickness remains $300 \mu\text{m}$.

The readout electronics are mainly inside the pixel. A column of 5 pixels every 42 is however needed for the electronic logic, which accounts for

N-wells needed for the PMOS transistors would also collect charge, leading to losses in signal. In order to minimise this effect, a novel process has been devised: the INMAPS process isolates the insensitive N-well region by screening it with a $1\ \mu\text{m}$ thick deep P-well implant.

The main challenge for a full calorimeter will be the power dissipation. The current test sensor has not been optimised at all in terms of power, and consumes on average $40\ \mu\text{W}/\text{mm}^2$, whereas the analogue CALICE design target is $1\ \mu\text{W}/\text{mm}^2$. This will be improved in the second design.

2 Sensor simulation

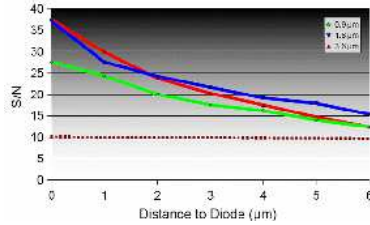


Figure 2: Sensor simulation: signal over noise ratio as a function of the distance of the input MIP to the diodes. The green, blue and red curves are respectively for 0.9, 1.8 and $3.6\ \mu\text{m}$ diodes.

The simulation of the charge collection of the sensor is done using Sentaurus TCAD [4], a tool taking a precise description of the components in 3D.

Figure 2 shows the signal over noise ratio as a function of the distance of the input MIP to the diodes, for three different diode sizes. The size of $1.8\ \mu\text{m}$ seems appropriate to maximise the signal over noise ratio, while keeping the collected charge level to a reasonable level.

Due to time constraints, results covering the whole pixel, with a $5\ \mu\text{m}$ step in both direction, have been done using two approximations: a pessimistic scenario, where no deep P-well is added, and the N-well is represented by a large central square collecting around 50% of the total charge deposited in a pixel, and an optimistic scenario with a perfect deep p-well implant isolating completely the N-well.

3 Physics simulation

The physics simulation of the whole detector using a Tesla-like design [5], and a MAPS-based ECAL is done using GEANT4 [6]. The distribution of the energy per hit for photon events is found to be stable from 500 MeV up to 200 GeV, confirming the assumption of having 1 MIP per cell on average. The energy resolution will then be given by:

$$\sigma_E/E \propto \sqrt{\sigma_{N_{pixels}}^2 + N_{noise}/N_{pixels}}.$$

Due to their small size, the charge sharing between pixels is expected to be important, and will have a big influence on the number of hits above threshold, and hence on the energy measurements. Understand this phenomenon will be crucial, as well as a precise measurement of its effects, to prove the validity of such a calorimeter.

The digitisation, required for a realistic simulation, is done in several steps, with results displayed in Figure 3 in terms of energy per hit, where the charge spread model assumes a perfect p-well. The simulation of the energy deposited in $5 \times 5\ \mu\text{m}^2$ cells is done with the Mokka [7] application. The charge sharing results from the sensor simulation (see Section 2) are then applied, giving for each deposition the percentage of energy seen by the pixel and by its eight closest neighbours. The results before applying the charge spread are displayed in

dark blue. The other coloured curves show various intermediate contributions, and the black curve is the result per pixel when the different contributions have been summed. A noise of $\sigma = 100$ eV (which corresponds to 30 electrons, to be cross-checked with the sensor test setup) is then added. The influence of the noise on the energy resolution is found negligible for a threshold value above 600 eV, or 6σ of the noise. This is close to the region where the energy resolution is found minimal (see Figure 4). Dead areas of 5 pixels every 42 pixels are removed, giving the yellow histogram, Figure 3. This was found to degrade the energy resolution measurement by 6%, for single photon events at 20 GeV. A basic MIP clustering algorithm is finally applied, according to the number of closest neighbours, and gives a 16% improvement when calculating the energy resolution versus threshold, for a 20 GeV photon.

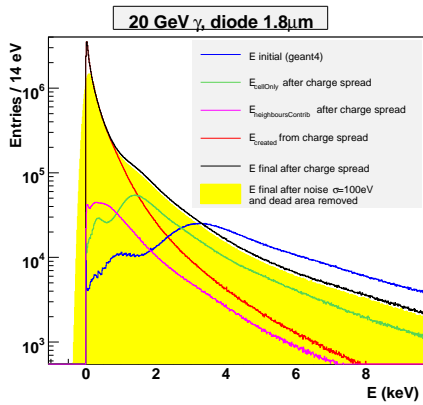


Figure 3: Energy per hit for the different digitisation steps.

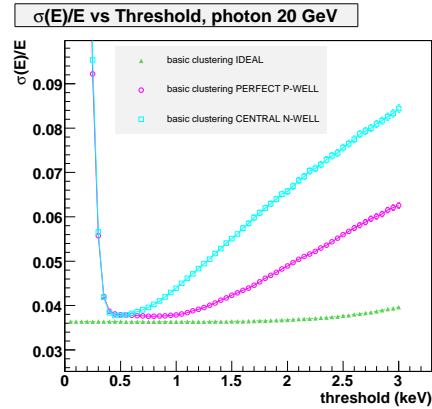


Figure 4: Energy resolution versus threshold before digitisation (“IDEAL”) and for the two charge spread models.

Figure 4 displays the energy resolution versus threshold for 20 GeV photons for the two extreme models we have taken into account up to now. From these curves, two very positive remarks can be drawn. Firstly, the value of the threshold corresponding to the minimum in terms of energy resolution lies outside the noise region, i.e. above 5σ . Secondly, the minimum value stays constant over a range of threshold settings and is close to the value found when no charge spread is assumed. In the pessimistic N-well scenario, the minimum region is quite narrow, whereas the optimistic scenario predicts a flat region between 5 and 10σ of the noise. The reality is expected to lie in between. The influence of the charge spread model is therefore crucial, and hence needs to be measured precisely, and compared with the sensor simulation results.

4 Conclusion

The sensor test setup is now completed, with several designs received from the foundry beginning of July 2007. Simulation shows a MAPS-based calorimeter has the potential to give good energy resolution but several aspects of the sensor response must be measured to cross-check the simulation.

References

- [1] Slides:
<http://ilcagenda.linearcollider.org/contributionDisplay.py?contribId=392&sessionId=108&confId=1296>
- [2] The CALICE collaboration: calorimeter studies for a future linear collider, 2002.
<http://www.ppd.clrc.ac.uk/AnnReps/2004/exp/Calice-317.pdf>
- [3] ECAL mechanical design, available from
<http://polywww.in2p3.fr/activities/physique/flc/calice.html>
- [4] Sentaurus TCAD, available from
<http://www.synopsys.com/products/tcad/tcad.html>
- [5] Tesla Technical Design Report, available from
http://tesla.desey.de/new_pages/TDR_CD/start.html
- [6] GEANT4, a simulation toolkit, S. Agostini et al., Nucl. Instr. and Meth. **A 506 (2003) 250-303**.
- [7] **Mokka, a detailed Geant4 simulation for the ILC detectors. Available from**
<http://polywww.in2p3.fr/activities/physique/geant4/tesla/www/mokka/mokka.html>

Mechanical R&D for CALICE ELECTROMAGNETIC CALORIMETER

Marc Anduze¹ and Denis Grondin²

1- LLR - IN2P3/CNRS
Palaiseau - France

2- LPSC - IN2P3/CNRS - UJF- INPG
Grenoble - France

This paper presents mechanical R&D for the CALICE Silicon-tungsten electromagnetic calorimeter. After the physics ECAL prototype tested in 2006 (DESY-CERN) and before the design of different "module 0" (barrel and end-cap), a technological prototype, called EUDET module, is under study and design in order to have "full scale" technological solutions which could be used for the final detector (moulding process, thermal cooling, inlet/outlet, integration tools...). These solutions will take into account of the industrial point of view.

1 Electromagnetic Si-W Calorimeter design

The electromagnetic calorimeter has been optimized for the reconstruction of photons and electrons and for separating them properly from debris coming from charged hadron interactions in the device. The range of energies for photons and electrons suggests a thickness close to 24 radiation lengths for the ECAL. The following sampling is then under consideration: 20 layers of 0.6 X_0 thick tungsten absorbers (2.1 mm) and another 9 layers of tungsten 1.2 X_0 thick (4.2 mm). The detector design with a solenoid outside the calorimeter imposes an overall cylindrical symmetry. The global design has been developed with an attempt to simplify the device as much as possible, by reducing the number of different module and different technologies used.

1.1 The barrel geometry

One of the requirements for the calorimeter is to ensure the best possible hermeticity. To minimize the number of cracks in the barrel, a design with large modules is preferred, with boundaries not pointing to the vertex. As shown in Figure 1 the perfect ϕ symmetry of the coil has been approximated by an eight-fold symmetry and the modules are installed in such a way that the cracks are at very large angle with respect to the radial direction (trapezoidal shape). This octagonal shape seems to optimize the barrel modules size and their mechanical properties without diverging too far from a circle.

One eighth of the barrel calorimeter is called a stave. At the back of a stave, between the ECAL and the HCAL, some space is left which is used to house different services like cooling

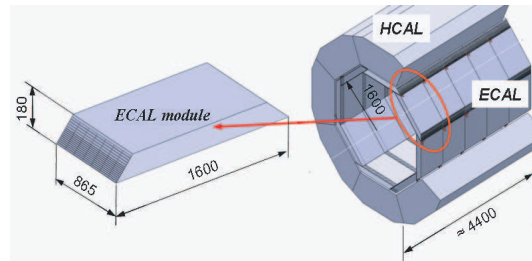


Figure 1: Structure of modules of the ECAL barrel General design of the calorimeter system

or electrical power and signal distribution. Along the beam axis, a stave is subdivided into five modules.

1.2 The end-cap geometry

The ECAL end-caps (Figure 2) could be constructed from very similar modules but with different shapes. To ensure that the depth of the calorimeter remains sufficient, the octagonal shape of the end-cap at the outer radius (1900 mm) follows the barrel part (1770 mm). Each end-cap consists of twelve modules (4x3 types), and can be split vertically into two halves for opening. With this design, no crack is pointing to the origin.

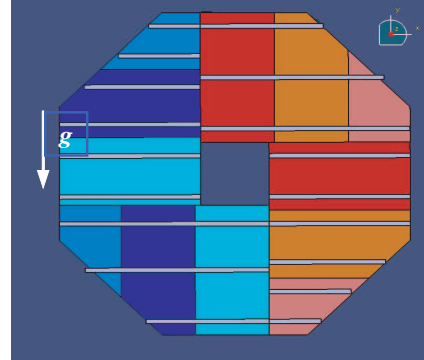


Figure 2: End-cap design for ECAL

2 The mechanical R&D

2.1 The alveolar structure

The design and construction of a module presents an interesting technological challenge. A design has been adopted where half of the tungsten layers are part of a solid mechanical structure, by embedding them into a light composite structure made of carbon fiber reinforced with epoxy. In between these plates and the carbon fiber partitions, free spaces are left into which detector elements, called "detector slabs", are inserted. This design has been validated on the physics prototype.

The method of an "assembled structure" has been chosen. Each alveolar layer is done independently, cut to the right length (with 45°) and assembled with tungsten plates in a second curing step. This principle will limit risks losing tungsten plates compared to an "one block" solution where all the structure is made in one step. After curing, the place holders (core) for the detector slabs are removed, leaving empty spaces called alveoli. This principle reduces also the cost of the industrial process: simpler moulds (one for barrel + 10 for end-caps) and the final piece is obtained in 2 simple polymerization processes, avoiding curing problems like thermal inertia, weight of metal mould, or the control of curing parameters. This method allows the possibility to integrate optical fiber with Bragg grating for Tests-Simulations Dialogue to. The first samples will be used to study mechanical behavior (destroying tests, dimensional controls...). The mechanical strength of "glued" structures has to be validated for these multi-curing steps to obtain the final structure (weight 650kg for the EUDET module, up to 2T for the End-cap modules).

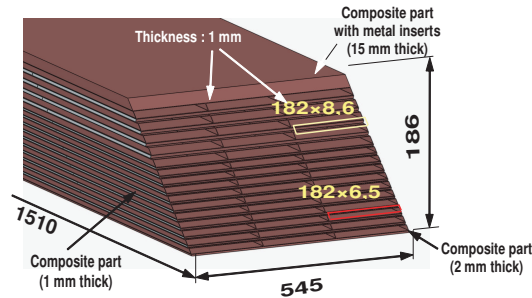


Figure 3: Alveolar structure design of the EUDET module

2.2 The detector slab

A slab (see Figure 4) has a tungsten plate core wrapped with an "H" structure made of carbon fibres. The silicon layers are attached on each side of the "H". Each silicon matrix is glued on a thin short PCB layer where the front end electronics is embedded. The silicon diodes are made of square pads of $5 \times 5 \text{ mm}^2$, the thickness of this one is currently about $300 \mu\text{m}$. A detector slab consists also of several "unit" PCBs, allowing more flexibility for different length of slabs. Indeed the length of each long slab will be obtained by the variation of the length of one "end" PCB.

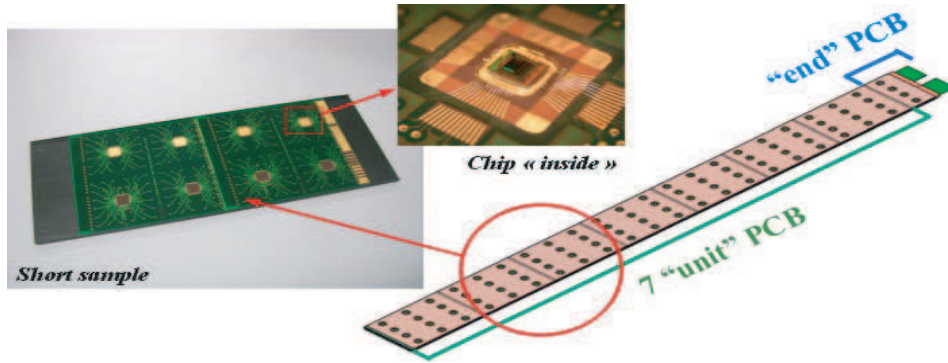


Figure 4: Detector slab to be inserted into the ECAL structure . Principle

2.3 Cooling system and power dissipation

Power dissipation is the key issue for this electronics. Indeed, the front-end electronics is located inside the calorimeter and has to have a very low consumption. The first slab thermal analysis is encouraging: assuming that the chip power is $25 \mu\text{W}$ per channel (power dissipation for the overall electronic chain including the digitization), a simulation of heat conduction just by the heat shield (copper), added along the slab direction, leads to an estimation of the temperature gradient along the slab of around 7°C . This simulation is probably pessimistic since only copper is used and not the other material of the slab (PCB, tungsten, carbon fibers...). Therefore, passive cooling inside the slab could be sufficient for the full scale ECAL. Then, the main cooling system could be at the end of each slab. For

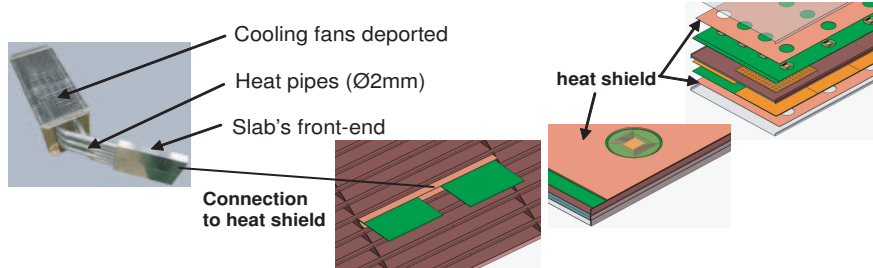


Figure 5: Possible cooling system for ECAL barrel and endcaps

each module, on the front end, cooling pipes connected to each heat shield, could be located in the gap between ECAL and HCAL, with all slab's input/output for the readout and power supply. Total power to dissipate will be approximately 2055 W for about $82,2 \text{ M}$ of channels

for the whole ECAL. After thermal study, design and tests of heat pipes technology has to be done, testing connection to slab and prototype of full system for 1 slab and 1 layer.

2.4 The interface with the HCAL: mounting and alignment

Alignment and cooling system are both crucial to ensure the needed detector performances from the point of view of good functioning and precisions and heavy withstanding. The ECAL will be fastened to the HCAL stave by stave, through accurate rail systems. The main issue designing this rail system is to reduce as small as possible the gap between ECAL and HCAL to keep the continuity between the 2 calorimeters (typically less than 4 cm). However, this gap has to be sufficient to install all the different services like cooling pipes and fans, electrical power and signal distribution. A fastening system, based on rails which will be fixed by metal inserts, directly inside the composite structure of the ECAL could solve this problem (see Figure 6). But this gap has to be optimized according to mechanical simulations and destructive tests of the ECAL/HCAL interface and the needs of cooling and fluid systems.

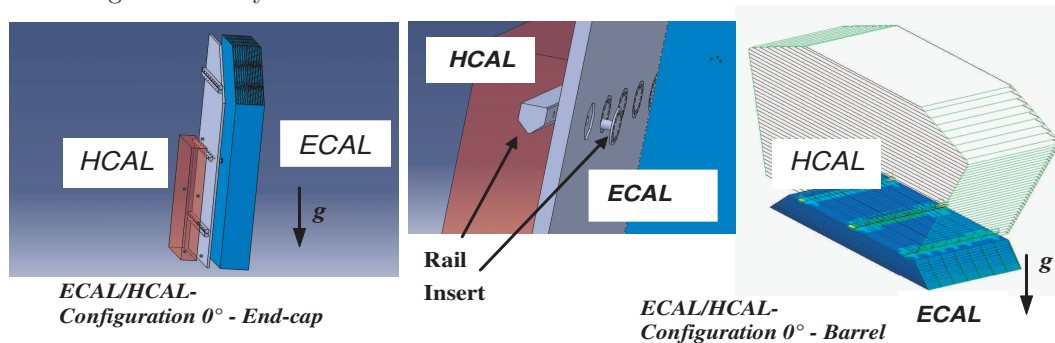


Figure 6: Barrel and endcap ECAL/HCAL interface with its fastening and guiding system

3 The scope of work

Before the design of one "full scale" modules (barrel and specific module geometry 45°/end-cap) the technological demonstrator, or EUDET module, should allow to solve several technological issues: long composite structures moulding, thermal cooling, ECAL/HCAL interface, tools... In this way, Finite Element models of modules have to be continued to estimate the global behaviour of the ECAL, overall deflection for all configuration ECAL/HCAL, thermal dissipation, and start the optimization of the thickness of composite sheets to reduce the dead zones. In parallel, the mould design and fabrication, with its specific difficulty in long alveoli fabrication will be demonstrated with the EUDET module, using news materials and taking into account the industrial process and constraints. A first prototype of alveolar structure (1500 mm long) should be built mid 2008, allowing a cost estimate of the future Si/W ECAL clearly driven in first by the silicon diodes and the tungsten price.

References

- [1] Slides of our presentation in ILCWS07 in Hamburg:
<http://ilcagenda.linearcollider.org/contributionDisplay.py?contribId=393&sessionId=108&confId=1296>

CALICE Si-W EM Calorimeter: Preliminary Results of the Testbeams 2006

C. Cârloganu¹ and A.-M. Magnan² on behalf of the CALICE Collaboration

1- LPC Clermont-Ferrand, IN2P3/CNRS, UBP, France

2- Imperial College London, United Kingdom

The CALICE [1] Si-W electromagnetic calorimeter [2] has been tested with electron beams (1 to 6 GeV) at DESY in May 2006, as well as electrons (6 to 45 GeV) and hadrons (6 to 80 GeV) at CERN in August and October 2006. Several millions of events have been taken at different incident angles (from 0° to 45°) and three beam impact positions. The ECAL calibration is performed with muon beams and shows a good uniformity for nearly all channels. The large statistics available allows not only to characterise the ECAL physics performance, but also to identify subtle hardware effects.

1 Introduction: the Calice ECAL Prototype

The Si-W ECAL physics prototype is composed of 30 layers of 3×3 wafers, each wafer having an array of 6×6 pixels of $1 \times 1 \text{ cm}^2$. The two top rows of wafers are completed for the full depth in July 2006. The mechanical structure consists of tungsten sheets wrapped in carbon fibre, providing 15 alveola where slabs are inserted. One slab is made of two PCBs on each side of a tungsten layer, with the wafers conductively glued to the PCB. The very front end electronics (VFE) provide preamplification and are located outside the active area, but mounted on the same PCB as the silicon wafers. The prototype is built of three stacks, each of ten layers of alternating tungsten and silicon. Each stack has a different tungsten thickness: 1.4 mm or $0.4X_0$ per layer in the first stack, 2.8 mm or $0.8X_0$ per layer in the second stack and 4.2 mm or $1.2X_0$ per layer in the rear stack. This choice should ensure a good resolution at low energy, due to the thin tungsten in the first stack, combined with a good containment of the electromagnetic showers, with an overall thickness of about 20 cm or $24X_0$ at normal incidence. To rotate to angles of 10° , 20° , 30° and 45° with respect to the beam axis, the three stacks, mechanically separate, are also translated laterally so that the beam still passes through all of them.

The purpose of the testbeam phase is to validate the simulation against a realistic detector, as well as allowing to detect the potential hardware problems. Once the simulation is trusted, full detector studies will lead to the optimisation of the calorimeter for a Particle Flow approach. The test setup at CERN is presented on Figure 1, and is simulated using Mokka [3].

Three drift chambers are used for the tracking at CERN and four at DESY. The ECAL, HCAL [4] and TCMT [5] follow, with the ECAL mounted on a movable stage for angle scans.

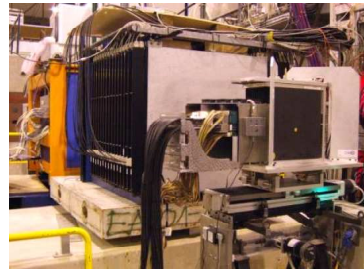


Figure 1: Testbeam setup at CERN, in August 2006. The ECAL is in front, followed by the analogue HCAL and TCMT.

2 Summary of the data taken

Eight million triggers were taken at DESY during 14 days in May 2006, for seven beam energies (1, 1.5, 2, 3, 4, 5, 6 GeV), five angles (0° , 10° , 20° , 30° , 45°) and three positions of the beam on the ECAL front face (center, border and corner of a wafer), with a minimum of 200,000 events per configuration. Six layers were not instrumented: the last eight layers had one dummy slab, one instrumented slab, and two dummy slabs.

The August 2006, CERN beams allowed to take another 8.6 million triggers in ECAL only mode, with the full depth instrumented, for six beam energies between 6 and 45 GeV, and four angles. Pions were taken between 30 and 80 GeV in combination with the HCAL and TCMT. For calibration purposes, 30 million muon events were also taken parasitically to an experiment upstream.

The setup in October 2006 was slightly different, with ECAL and HCAL at 6 cm from each other. 3.8 million triggers were taken with electrons and positrons from 6 to 45 GeV, and 22 million with pions from 6 to 80 GeV. Another 40 million muon events were added for calibration purposes.

3 ECAL Calibration

3.1 Gain Calibration

The current calibration of the ECAL prototype is performed by using a set of 74 high-statistics muon runs ($\sim 250,000$ events each), taken during October 2006 with another experiment upstream, providing a wide spread of the muon beam over the front face of the prototype. The events are triggered with a 1 m^2 scintillator counter.

After pedestal subtraction (see Section 3.2), the runs are reconstructed using a fixed global noise cut of half a Minimum Ionising Particle (MIP), 1 MIP being estimated to 50 ADC counts by former studies. To reject any remaining noise hits, it is required that the hits of one event form tracks characteristic of a MIP.

The distributions obtained by channel are described by a convolution of a Gaussian and a Landau function. The calibration constant is defined as the most probable value (MPV) of the Landau function, while the standard deviation of the Gaussian defines the noise value for each cell. For 6403 out of the 6480 channels of the prototype, a calibration constant can be obtained via this method without further investigations. The remaining cells show a noise value that is unusually high, and are treated by estimating the additional noise contribution, or by applying the calibration constant from one of their neighbours.

An entire wafer (36 channels) seems to not be fully depleted at the applied voltage of 200V, resulting in a MIP peak at half the normal value. A relative value between the mean

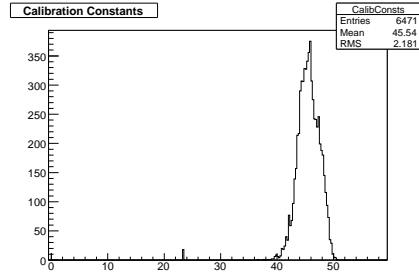


Figure 2: Equivalent ADC value for the energy deposit of 1 MIP for the live cells of the ECAL prototype.

MIP signals of the wafer and its neighbours can be estimated, allowing a relative calibration of the cells. 0.14 % of the channels give no output and were considered as dead. The calibration constants for all calibrated channels are histogrammed in Figure 2. The distribution is narrow, with almost all pads in the range 40 to 50 ADC counts per MIP. The small peak at 23.5 corresponds to the single incompletely depleted wafer.

3.2 Pedestal

For all beam tests performed, the data acquisition consists of a fixed sequence of 500 pedestal events, 500 events with charge injection via the calibration chips, and then 20,000 beam events. The pedestal events are used to make a first estimate of the pedestal (mean value) and noise (RMS) per channel.

It has been observed that the pedestals are not necessarily stable, but subject to a random shift affecting all channels of one layer with the same drift. This effect concerns several particular PCBs, is time dependant, and is attributed to the instabilities of the power supplies giving the pedestal lines, which are not isolated. To correct for these instabilities, the pedestals are recalculated on an event by event basis, by discarding all cells recording a signal, and iterating until the RMS of the distribution obtained with the remaining channels is of the order of the expected noise.

3.3 Noise

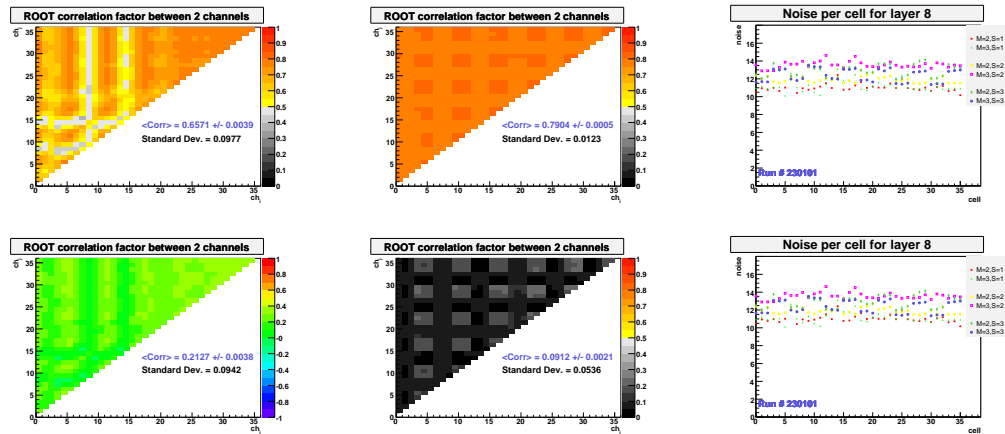


Figure 3: Layer 8, *left*: module recording a signal, *middle*: neighbouring wafer, *right*: mean noise per wafer. *Upper row*: without corrections, and *bottom row*: with corrections.

In order to identify coherent noise, the correlation between pairs of channels is calculated in signal events. No clear correlation is seen in an entire PCB, except the one coming from the pedestal drift discussed above. The results are thus shown only on a wafer basis. Figure 3 displays the correlation factors (colour scale) as a function of the channel indices, numbered from 0 to 35, for a particular wafer affected by the pedestal drifts described above, and a run recorded at DESY with an energy of 6 GeV. Channels numbered 0 to 17 and 18 to 35 correspond to two different chips. The corresponding noise level per layer, for all wafers,

is also presented in Figure 3, on the right column.

The results before any corrections are shown in the upper row of Figure 3. The left plot represents the module in which the beam was directed. It can be seen that the region with signal shows less correlations, due to the fact that most pixels are discarded in the noise calculation. The middle plots show a neighbouring module, affected only by the global pedestal drift. The difference between these two wafers allows the identification of a crosstalk issue. All the channels of some wafers recording a high signal, like the one presented in Figure 3 on the left, suffer from a pedestal shift towards negative values. This effect does not propagate to the neighbouring wafers. This seems to be random in space and in time, but it is clearly correlated with the intensity of the signal recorded. This effect is not yet understood, but under investigation. In order to correct for the induced correlated noise, the mean and standard deviation are calculated on an event-by-event basis, per wafer, after discarding the signal hits, and iterating over the channels taken into account in the sum. The bottom row on Figure 3 shows the results after all the pedestal corrections described above. The corrections are performing well, bringing the noise back to the normal level of 6 ADC counts. For this particular layer, affected by both problems (i.e. coherent noise on the PCB level due to an instability in the power supply, and crosstalk affecting the wafer recording a high signal), the wafer recording a signal still shows a remaining 20% of correlations. The correlation is however completely removed for wafers affected only by the crosstalk problem, which confirms that the corrections are performing well.

4 Background for physics performance studies: electron selection

The selection of the single electron events is loose, in order to avoid bias:

- $E_{cell} \geq 0.6$ MIP removes the noise. The threshold is about five times the average noise measured per cell.
- the total energy recorded in the ECAL, E_{raw} , should be in the range $125 < (E_{raw}(\text{MIP})) / (E_{beam}(\text{GeV})) < 375$. E_{raw} is computed with the three stacks weighted in the ratios 1:2:3, according to the tungsten thickness.

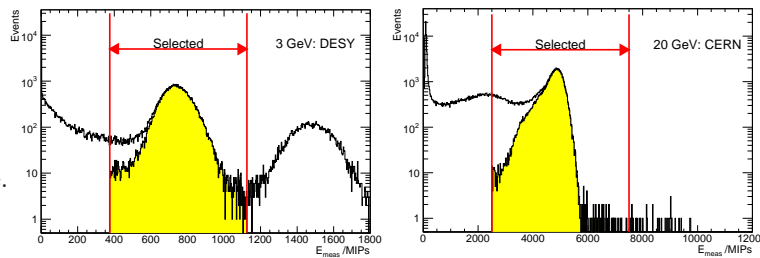


Figure 4: Total ECAL energies for a 3 GeV e^- DESY beam (*left*) and for 20 GeV at CERN (*right*), with the energy selection windows. The shaded areas show the effect of the cuts on the shower barycentre (*left*) and on the Čerenkov counter signal (*right*).

Further cuts are applied to some particular samples: the significant pion content of some high energy electron runs at CERN is reduced by using the threshold Čerenkov counter, whereas the low energy halo coming with some low energy DESY beams is rejected with

additional cuts on the shower barycentre. The effect of these two additional cuts is indicated by the shaded regions in Figure 4.

5 Energy Response, Linearity and Resolution

The total response of ECAL is computed by summing the hit energies in the three sections of the detector. If E_1 , E_2 , E_3 are the recorded energies in the first, second and third stack respectively, the total response is $E_{\text{tot}} = (\alpha_1 E_1 + \alpha_2 E_2 + \alpha_3 E_3) / \beta$. The naive choice for the weights $(\alpha_1, \alpha_2, \alpha_3) = (1, 2, 3)$ is generally used. It reflects the relative thicknesses of the tungsten layers in each of the stacks, and hence the relative sampling fractions. However, a weighting scheme optimisation for energy resolution was performed as well, leading to the slightly different values of $(1.1, 2., 2.7)$. The normalisation β has been arbitrarily fixed to 250 MIP/GeV.

The guard rings create 2 mm non-active inter-wafer gaps, causing non-uniformities in the ECAL response, as illustrated in Figure 5, left, where the mean energy is plotted as a function of the shower barycentre, $(\bar{x}, \bar{y}) = \sum_i (E_i x_i, E_i y_i) / \sum_i E_i$. Dips in response are clearly visible and account for the asymmetric tail on the low side of the distribution of total energy (Figure 5, right), which is reasonably well modelled by the simulation. The correction of these non-uniformities will be discussed in Section 6.

The beam profile, and thus the fraction of beam particles traversing the inter-wafer gaps, depends on the beam energy. Therefore, in order to avoid bias, a cut is applied on the shower barycentre position such as to select showers not affected by the gaps.

To estimate the energy resolution and the mean calorimeter response, the distribution from Figure 6, left, is fitted by a Gaussian in the asymmetric range of $[-\sigma, +2\sigma]$ in order to reduce sensitivity to pion background and to radiative effects upstream of the calorimeter, as well as to any residual influence

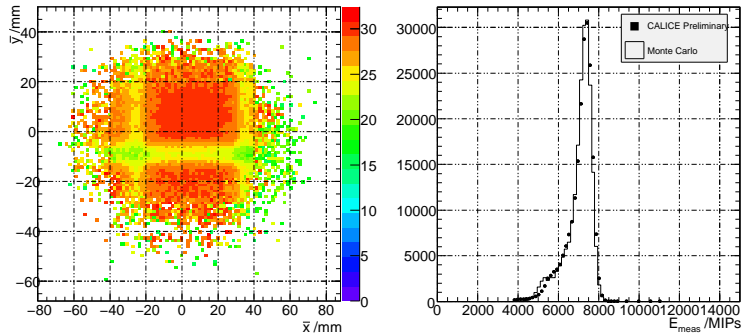


Figure 5: *Left:* mean ECAL energy as a function of the shower barycentre (\bar{x}, \bar{y}) . *Right:* total ECAL energy for a 30 GeV e^- beam, for data (points) and Monte Carlo (open histogram).

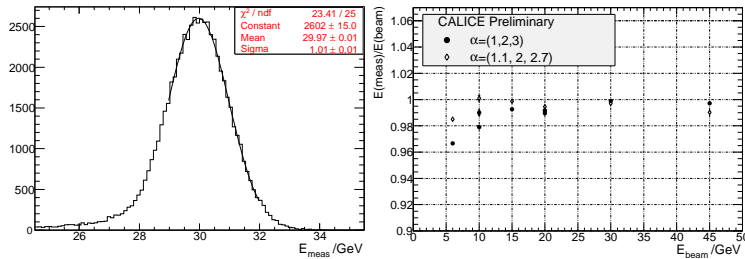


Figure 6: *Left:* a Gaussian fit to the measured energy, for 30 GeV e^- data. *Right:* ECAL energy response, divided by beam energy, as a function of beam energy.

of the inter-wafer gaps.

The ratio of the reconstructed energy to the beam energy, as function of the beam energy is shown in Figure 6, right, for the two choices of weights. Non-linearities are at the % level. The linearity is somewhat better for the optimised weights.

The energy resolution, similar for both weightings, is shown in Figure 7. The Monte Carlo prediction, with the naïve weights, also shown, is in reasonably good agreement with the data. The resolution can be parametrised, for the naïve choice of weights and, respectively, the optimised one, as

$$\frac{\Delta E}{E}(\%) = \frac{17.7 \pm 0.1}{\sqrt{E(\text{GeV})}} \oplus 1.1 \pm 0.1 \quad \frac{\Delta E}{E}(\%) = \frac{17.1 \pm 0.1}{\sqrt{E(\text{GeV})}} \oplus 0.5 \pm 0.2,$$

6 Interwafer gap corrections

The method used for correcting the interwafer gaps operates at the event level and relies only on the calorimeter information: it parametrises the mean calorimeter response as function of the shower position in the calorimeter and applies subsequently corrective factors for each event according to this parametrisation. It is only geometrical, independent in \bar{x} and \bar{y} and without any explicit dependence on the shower energy.

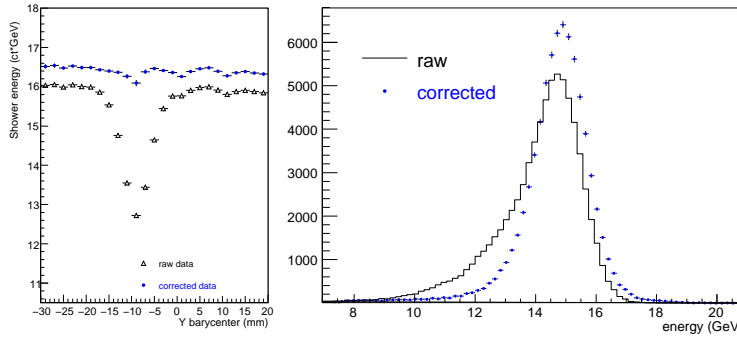


Figure 8: 15 GeV e^- , before (black triangles) and after corrections (blue circles): total energy as function of the shower barycentre \bar{y} (*left*), and energy distribution (*right*).

The impact of the corrections is clearly illustrated in Figure 8, left, where the y scan of ECAL is shown for the raw and, respectively the corrected data. The low energy tail of the energy distribution is greatly reduced (Figure 8, right). The resolution loss when going from the out of gap events to all the events (with corrections applied on the energy) is of the order of 10%. The corrections do not degrade the linearity.

When tracking information is available, it is possible to precisely calculate the shower position within each wafer. Subsequently, the ratio of the active to non-active areas crossed

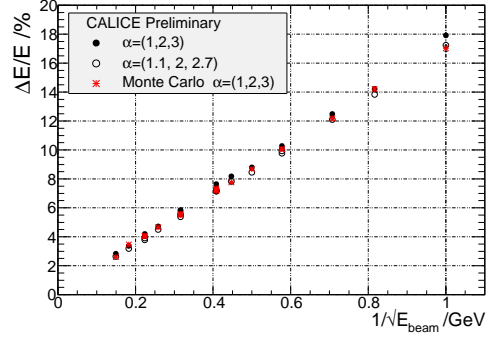


Figure 7: ECAL energy resolution as function of $1/\sqrt{E}$. Two possible weightings of the ECAL stacks are compared.

by the shower according to a mean shower shape can be estimated and used to correct the energy recorded in each layer.

7 Shower development

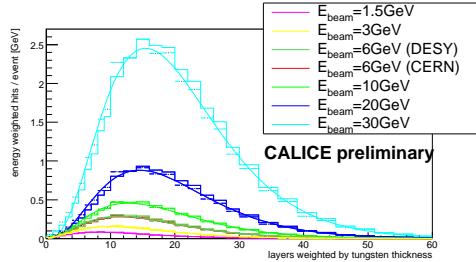


Figure 9: Longitudinal shower profile for the data (points with statistical uncertainties) and Monte Carlo simulation (histogram). The smooth curve is the used parametrisation of the shower profile.

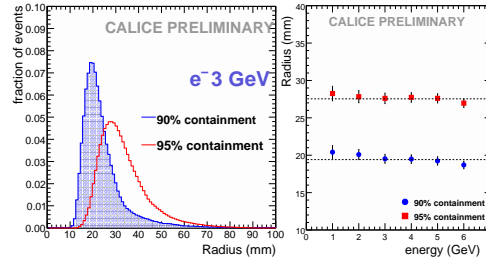


Figure 10: *Left*: distribution of radii for 90% and 95% signal containment (3 GeV e^- , normal incidence, centre of wafers). *Right*: radii for 90% and 95% signal containment of e^- as function of the beam energy.

Only events outside the interwafer gaps were used to characterise the longitudinal development of the shower. The mean energy distribution is well fitted by the standard parametrisation, $\gamma(t) = ct^\alpha \exp(-\beta t)$, where t is the calorimeter depth, c is an overall normalisation, α and β are constants (Figure 9). The position of the shower maximum grows logarithmically with the beam energy.

An important issue in the development of a calorimeter is to achieve the smallest possible effective Molière radius, in order to provide the best shower separation. It requires the use of an absorber with a small intrinsic Molière radius (R_M), but also the minimisation of the gaps between the absorber layers.

Figure 10, left shows the event distribution for 90% and 95% levels of signal containment with respect to the radius. The results for the various energies studied are summarised in Figure 10, right. The points correspond to the peak position of each radius distribution. At 90% (95%) shower containment the corresponding radius, often quoted as $1 R_M$, is about 20 (28) mm.

The geometry of the ECAL prototype, with 2.2 mm thick interlayer gaps leads to an effective Molière radius which is expected to be larger by a factor of about 2 with respect to R_M of solid tungsten. The results from the test beam studies are therefore in agreement with expectations. R&D effort towards the use of Si pads with integrated readout is under way and will hopefully lead to a significant decrease of the interlayer gap and therefore of the ECAL effective Molière radius.

8 Spatial and angular resolution of ECAL

The spatial and angular resolution of the ECAL are studied with the DESY data at normal incidence. The shower direction and position at the ECAL front face are constructed on

an event-by-event basis using a linear two-parameter chi-square fit to the shower barycentre positions in each layer for the x and y coordinates separately. The correlation matrix is determined from simulations for each beam energy.

The fit results are compared with the position and angle measured by the tracking system. The expected e^- position and direction at ECAL front face is obtained from a linear fit of the drift chambers. Sources of systematic uncertainties as residual misalignment, material modelling, and background rate are estimated for the extrapolation to the ECAL front face.

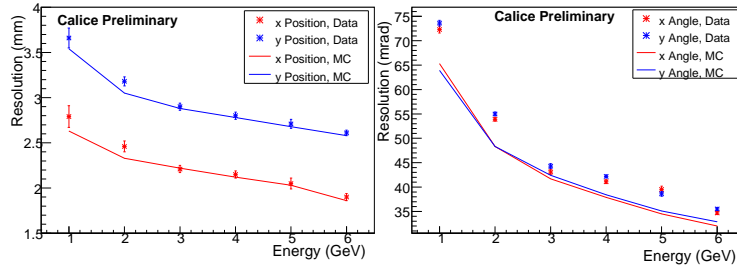


Figure 11: Resolutions in position (left) and angle (right) as a function of the beam energy. The data are shown as points with error bars. The simulation expectation is shown by the continuous line.

The ECAL resolution, deconvoluted from the tracking errors, is displayed in Figure 11.

9 Conclusion

The Si/W ECAL prototype was presented, as well as the results of the first beam tests at DESY and CERN during 2006. The prototype calorimeter was further exposed to beam at CERN in summer 2007. Analysis of the data collected is in progress.

References

- [1] The CALICE collaboration: calorimeter studies for a future linear collider, 2002. <http://www.ppd.clrc.ac.uk/AnnReps/2004/exp/Calice-317.pdf>
- [2] ECAL mechanical design, available from <http://polywww.in2p3.fr/activities/physique/flc/calice.html>
- [3] Mokka, a detailed Geant4 simulation for the ILC detectors. Available from <http://polywww.in2p3.fr/activities/physique/geant4/tesla/www/mokka/mokka.html>
- [4] F. Sefkow, "Tile Hadron Calorimeter", Calorimeter R&D Review, these proceedings.
- [5] D. Chakraborty, "Tail Catcher and Combined Analysis", these proceedings.

Preliminary Testbeam Results from the CALICE Tile Hadron Calorimeter

Niels Meyer for the CALICE collaboration

Deutsches Elektronen-Synchrotron
Notkestr. 85, 22607 Hamburg - Germany

The CALICE collaboration has constructed a testbeam hadron calorimeter based on scintillator tiles, individually read out by novel multi-pixel Geiger mode photodiodes. The purpose is to establish the technology and to record hadron shower data with unprecedented granularity for the validation of simulation models and the development of clustering algorithms. First testbeam results of the partially instrumented calorimeter from electron and pion beams at CERN are presented, the latter taken together with an electromagnetic calorimeter in front and a tail-catcher and muon-tracker behind.

1 Introduction

The CALICE collaboration has constructed a physics prototype hadronic tile calorimeter (HCAL), a 38-layer plastic-scintillator/steel sandwich structure with a lateral dimension of about 1 m^2 and a total depth of 4.5λ . The scintillator is segmented in tiles between 3×3 and $12 \times 12 \text{ cm}^2$ in size. The 216 tiles of one layer are mechanically mounted inside a cassette with side-lying readout electronics, which are inserted into the mechanically independent stack of absorber plates. For calibration and monitoring, each HCAL module is equipped with a versatile LED system allowing to inject controlled light signals to each individual tile. A wavelength-shifting fiber inside a groove collects and converts the UV scintillation light of one tile and guides it to one green sensitive Silicon Photo-Multiplier (SiPM) [2].

SiPM are multi-pixel Geiger mode photodiodes with 1156 pixels on $1 \times 1 \text{ mm}^2$ sensitive area. Each pixel has a resistor of few $\text{M}\Omega$ for passive quenching of the Geiger avalanche initiated by electron-hole-pairs in the depleted region of the silicon. The gain reached is of order 10^6 despite the relatively low operation voltage below 100 V. The resulting dead-time in conjunction with the readout gate lead to non-linear behavior at high signal amplitudes.

The HCAL with an initial instrumentation of 15 (23) active modules distributed over 29 layers of the absorber stack as illustrated in Fig. 1 has been installed at the CERN SPS testbeam area and took data from electron, muon, and pion beams during two periods in summer 2006. Data has been taken stand-alone as well as together with an electromagnetic calorimeter (ECAL) upstream and a tail-catcher and muon-tracker (TCMT) downstream of the HCAL. The ECAL

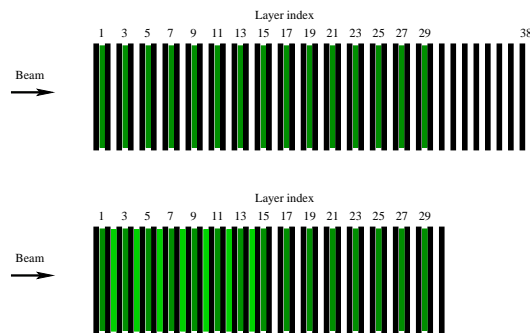


Figure 1: Configuration of active HCAL modules and absorber plates in August/September 2006 (top) and October 2006 (bottom), respectively.

is a silicon-tungsten sampling calorimeter, and the TCMT is also a scintillator/steel sampling detector based on SiPM readout. All three calorimeters with more than 10,000 channels use the same data acquisition, which also includes scintillator triggers, a threshold Cerenkov counter and three multi-wire proportional chambers as further beam instrumentation.

In the following, the calibration and reconstruction strategies [3] of the HCAL are introduced. The response of the detector to electrons is analyzed from data recorded with 15 active HCAL modules and no ECAL in front in order to validate the reconstruction procedure by means of well understood electromagnetic showers. A preliminary analysis of pion data recorded with 23 active HCAL layers together with both ECAL and TCMT is also presented.

2 Calibration and reconstruction

By convention, equalization and energy calibration of all channels is achieved by the most probable energy deposition of a minimum ionizing particle crossing the tile at normal incidence, the so-called MIP scale. This scale is available in data as well as in simulations and has been measured using muons behind a closed beam dump during parasitic running to another upstream experiment. The muon beam was wide enough to cover the whole HCAL front face and has been triggered with two $1 \times 1 \text{ m}^2$ scintillator plates firing in coincidence. Besides calibration, the MIP scale is also used for zero-suppression by rejecting amplitudes below 0.5 MIP.

Non-linearity of SiPMs is an effect scaling with the number of pixels firing. Any correction therefore depends on the possibility to translate a given amplitude to the pixel scale. Low light intensities from the LED system and a special high-amplification mode of the readout electronics allow the separation of single photon signals, the so-called gain calibration. Beam data is taken with lower amplification of the readout electronics for a larger dynamic range. A second measurement with the medium LED intensities therefore is needed to relate the response to identical signals with the two different electronics modes, the so-called electronics inter-calibration. Two different approaches for non-linearity correction are used: an analytic method assumes binomial saturation correction, while a more complex method involves the saturation curve measured with a calibrated light source before mounting each SiPM on its tile [4].

The number of pixels firing at an amplitude equivalent to one MIP is referred to as lightyield and is an important figure-of-merit for the HCAL. This value can directly be determined as ratio of the three calibration constants. Channels with a small lightyield are characterized by large statistical fluctuations of the amplitude (which is always an integer number of pixels) and yield larger noise contributions above 0.5 MIP, while channels with large lightyield exhibit a stronger non-linear behavior and are limited in their dynamic range. It is therefore desirable to operate the calorimeter at an average lightyield close to the design value of 15 pixels/MIP. This goal has not quite been matched for the first 2006 data taking period, but could be corrected for the second period by raising the bias voltage.

3 Response to electrons

High energetic electromagnetic showers are in contrast to hadron showers very well understood and are therefore best suited to assure full understanding of the detector response. In case of the tile HCAL, they in addition mark a special benchmark scenario, since they are

much more compact than hadron showers, lead to higher hit amplitudes, and consecutively end up at higher levels of non-linearity to be corrected for. For 123 out of 3240 channels from 15 active modules, one or more calibration constants could not be extracted. Although some of these channels can be calibrated in principle, all of them are excluded for this analysis.

The amplitude measured in each channel is reconstructed to the MIP level, amplitudes below 0.5 MIP are removed from the event. For all others, non-linearity is corrected using the channel-dependent saturation measurements.

The reconstructed energy sum after this steps is shown in Fig. 2 (top) for various electron beam energies. The mean response is extracted from Gaussian fits to the core of the distributions and subtracted by the mean energy in random trigger events (noise) of the same run. The energy scale is fixed by the difference in response between the 10 GeV and 20 GeV beam, which minimizes the impact of noise contributions.

The comparison between beam and reconstructed energy is shown in Fig. 2 (bottom). The green band indicates the uncertainty region from the calibration measurements, and the blue line corresponds to digitized simulations including various experimental effects: realistic geometry and material budget of beam instrumentation and HCAL, sensitivity holes due to excluded cells, leakage of scintillation light to neighboring cells, SiPM saturation, pixel statistics, electronic noise, and SiPM dark current. Inhomogeneities due to varying SiPM properties (lightyield, saturation behavior, noise and dark current) are taken into account as well, based on the calibration measurements described above.

Expectations from simulations show perfect linearity, which is expected since identical functions have been used for simulation and correction of SiPM saturation. Non-linearity of order 5% is observed in data for the highest shower energies, but remains smaller than the calibration uncertainties up to 30 GeV beam energy. The excess of reconstructed energy in data w.r.t. simulations have been found to be due to coherent noise, which has not been simulated. For the second data taking period, coherent noise could be reduced to uncritical level by modifications of the readout electronics.

4 Response to pions

Pion showers from beam energies between 6 and 20 GeV are studied using combined data taken with the ECAL, the HCAL (with 23 layers, see bottom of Fig. 1), and the TCMT.

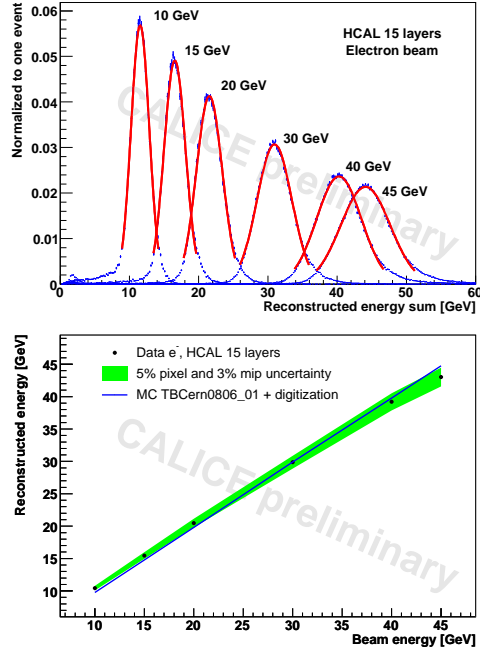


Figure 2: Reconstructed energy sum (top) and the correlation between reconstructed and beam energy (bottom) for electron beams between 10 and 45 GeV.

The ECAL is used as a pre-shower veto in order to discard showers which started before the HCAL, and the TCMT is used to identify those showers fully contained in the HCAL.

Calibration and reconstruction is done similar to the analysis of electron showers described before, only that the energy scale is fixed from the 10 GeV beam alone and that the analytic ansatz for saturation correction is used. An obvious effect of leakage into the TCMT is observed as shown in Fig. 3 (top). The bottom part of the same figure illustrates that linearity between beam and reconstructed energy is observed. For illustrative purposes, equivalent curves for two shower simulations based on GEANT3 without digitization are shown as well. Good level of agreement with data is only achieved if the energy scaling factor from the MIP to the GeV scale is determined independently for each of the three curves.

5 Outlook

The CALICE testbeam program successfully continued in summer 2007 with the same subsystems as presented. The HCAL was fully equipped with 38 active modules and was positioned together with the ECAL on a movable stage allowing for horizontal, vertical, and angular scans. The analysis of this data set is ongoing and will give a much more comprehensive picture of the capabilities of the CALICE tile calorimeter than this initial analysis of data taken with the partially instrumented detector.

References

- [1] Slides:
<http://ilcagenda.linearcollider.org/contributionDisplay.py?contribId=396&sessionId=108&confId=1296>
- [2] G. Eigen, *AIP Conf. Proc.* **867**, 565 (2006).
- [3] E. Garutti, *AIP Conf. Proc.* **867**, 574 (2006).
- [4] M. Danilov [CALICE Collaboration], *Nucl. Instrum. Meth. A* **582** (2007) 451

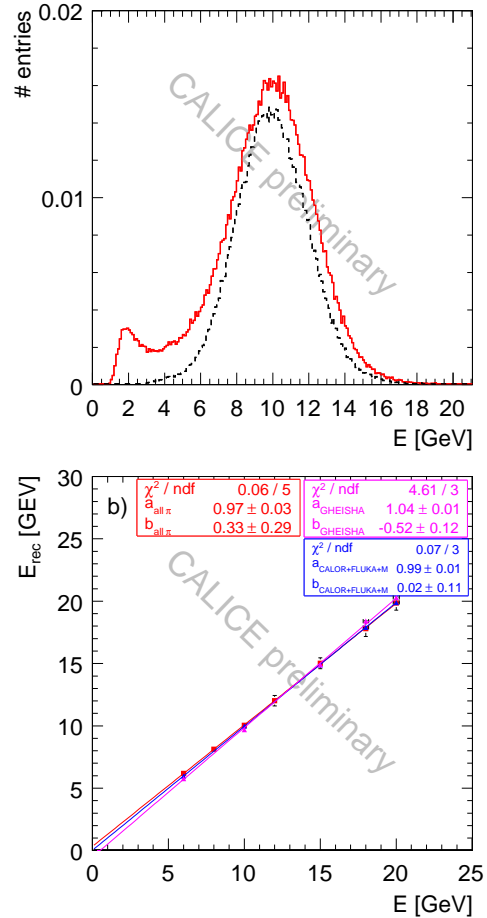


Figure 3: Top: Reconstructed energy for all showers starting after the ECAL (solid) and those which in addition are contained in the HCAL (dashed) from 10 GeV π^- . Bottom: Correlation between reconstructed and beam energy for π^- beams between 6 and 20 GeV for data and two different shower simulations.

Scintillator+MPPC ECAL Testbeam Results

Daniel Jeans for the GLD-CAL group and the CALICE collaboration

Kobe University, Department of Physics
1-1 Rokkodai-cho, Nada-ku, Kobe, Japan

A scintillator-tungsten ECAL prototype with full MPPC readout was constructed and exposed to positron beams at DESY. We describe the detector and present the results of a preliminary analysis of its performance.

1 Introduction

At the future ILC experiments, the success of the physics program will depend, among other things, on the jet energy resolution. One way to achieve excellent jet energy resolution is by means of a Particle Flow Algorithm, which relies on the accurate separation of calorimeter energy deposits due to charged and neutral particles. The momentum of charged tracks, accurately measured in the tracking detector, are used to estimate the charged jet energy, while the energy deposits in the calorimeter not associated to charged particles are used to estimate the neutral energy. To achieve the separation of charged and neutral energy, a highly granular calorimeter is required. We are studying the design of such a calorimeter, and have produced a prototype electromagnetic calorimeter, whose performance we have tested in a positron beam at DESY.

2 Prototype Design

The calorimeter prototype is a sampling calorimeter, with alternating layers of scintillator and tungsten. Each scintillator layer consists of 18 scintillator strips, arranged in two rows of 9 strips. Each strip has a size of $4.5 \times 1 \text{ cm}^2$, and a thickness of 3 mm. The thickness of the tungsten plates is 3.5 mm. The light produced in each scintillator strip is read out by a Multi Pixel Photon Counter (MPPC), manufactured by Hamamatsu Photonics. The orientation of strips in successive layers is orthogonal, giving an effective overall granularity of $1 \times 1 \text{ cm}^2$.

We tested three types of scintillator layers.

- WLS “megastrip”: scintillator plates (of size $90 \times 45 \times 3 \text{ mm}$) produced by Kuraray. Grooves were machined into the plate and filled with white PET film, giving 9 optically isolated strips, each with width 10mm. A wavelength shifting fibre was inserted into a 1 mm diameter hole drilled along the central axis of each strip. The MPPC was placed at one end of this fibre. The faces of the megastrip were covered in radiant mirror film produced by 3M.
- direct readout “megastrip”: as above but without the WLS (or its hole). The MPPC was directly attached to one end of the scintillator strip.
- KNU extruded: extruded scintillator strips, developed by Kyungpook National University, Korea, with a co-extruded coating of TiO_2 and a central WLS.

Three modules, each with 13 scintillator-tungsten layers, were constructed, one for each scintillator type. Two modules were combined to make the detector prototype. Of the various combinations tested, only the results with the two Kuraray megastrip modules, the WLS module placed upstream of the direct readout module, are reported here.

The effective Moliere radius of this detector is around 21 mm, and the effective radiation length 8 mm.

3 DESY testbeam setup

The prototype detector was taken to DESY in February/March 2007, and exposed to secondary positron beams at the DESYII accelerator, in the energy range 1 – 6 GeV.

The beamline was instrumented with two scintillator trigger counters, a scintillator veto counter and four drift chambers upstream of the ECAL detector, which was placed on an automated movable stage. One additional trigger counter and one veto counter were placed downstream of the detector. The detector was read out using the readout electronics and DAQ developed for the CALICE Analogue HCAL prototype detector.

In four weeks of running, around 10^8 events were collected.

4 Detector calibration

At several points during the data taking, the detector was calibrated. The tungsten plates were removed, and the detector was exposed to positron beams. The detector was scanned, aiming the beam at the centre of each scintillator strip.

Calibration events were selected by requiring appropriate signals in the trigger and veto counters up- and down-stream of the detector. Each strip in the detector was separately calibrated. To select events in which a positron (considered to be a MIP) passed through a particular strip in the detector, almost all similar strips in the other same polarity layers were required to have recorded a signal inconsistent with being purely pedestal. The other strips in the same layer as the one being considered were required to have measured a signal consistent with the pedestal. This event selection provides a clean sample of events in which a MIP passed through a particular strip.

The distribution of the signals from the selected strip were then used to measure the response of the strip. It was fitted by a Landau distribution convoluted with a Gaussian, and the most probable value of the Landau was used as the calibration constant for that strip.

5 Energy scan

The detector was exposed to positron beams of energy 1, 2, 3, 4, 5 & 6 GeV (with the tungsten plates inserted). For the data analysed here, the beam was directed at the centre of the detector; beam scans across the detector were also performed, but these data have not yet been analysed.

To estimate the energy deposited in the detector, the signal from each strip was converted, by means of the calibration constants, to a number of MIP equivalents. This was then summed over all detector strips to give the total energy, in terms of MIP equivalents, reconstructed in the detector.

These distributions were then used to measure the detector's basic performance. The linearity of the energy response is shown in Fig. 1: the detector is relatively linear, with residual non-linearities on the order of 4%. The cause of this non-linearity is presently under study. The widths of the response curves were used to measure the detector's energy resolution. The evolution of the resolution with beam energy is shown in Fig. 2; this was fitted by the quadratic sum of a statistical and constant term, giving an energy resolution of $\sigma_E/E = 13.45\%/\sqrt{E} \oplus 2.87\%$.

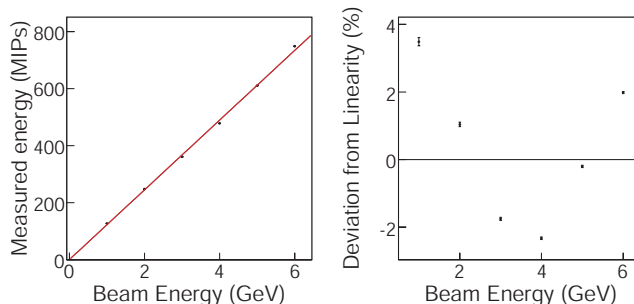


Figure 1: Linearity of the detector energy response.

6 Future refinements

There are several effects which we know we need to correct for, and which are presently being studied. One example is the nonlinear behaviour of the MPPC, which affect the response, particularly at large light yields. Another example is a correction due to temperature variations, which can have a strong effect on the characteristics of the MPPC.

We will also measure the dependence of the performance on the position at which the positron enters the calorimeter, and measure the performance using modules made of different scintillator types. This will help us to choose the best scintillator to use in the ILC detector.

Another area of current work is the development of a more sophisticated simulation of the detector: the simple simulation we have at present does not model the detector sufficiently well.

7 Conclusions

A prototype ECAL was constructed using scintillator strips readout by MPPCs, and exposed to positron beams at DESY. The results of a preliminary analysis of its performance were presented: the detector is linear to within 4% in the energy range considered, and the energy resolution for positrons was measured to be $\sigma/E = 13.5\%/\sqrt{E} \oplus 2.9\%$.

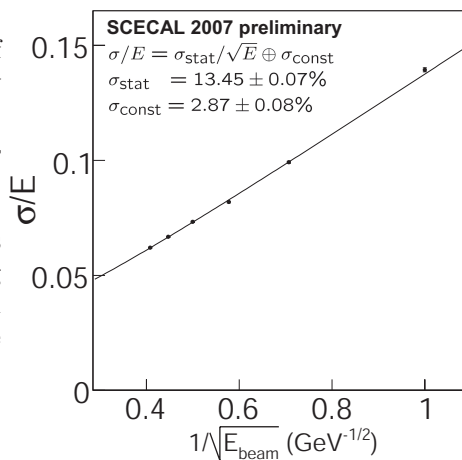


Figure 2: Energy resolution of the detector response.

Simulation and Reconstruction

Conveners: N. Graf, M. Thomson, C. Gatto, A. Miyamoto

The ILC and the Grid

A. Gellrich*

Deutsches Elektronen-Synchrotron (DESY)
Notkestr. 85, 22607 Hamburg, Germany

Already today major computing resources for HEP are available in the Grid only. For the ILC project two Virtual Organizations were founded which are supported by many Grid sites world-wide. The ILC community has started to use Grid resources for *Monte Carlo* production, data analysis, and data storage. The development of specific tools for ILC has recently been initiated.

1 Introduction

Driven by the computing needs of the four LHC experiments, a global computing infrastructure is under construction, the so-called *world-wide LHC Computing Grid* (WLCG) [2]. It incorporates compute and data storage resources that are distributed all over the world. Access to the resources is provided by means of a service infrastructure. People, institutions, and resources are collected within *Virtual Organizations* (VO) that are based on common sharing rules. Users authenticate against the Grid services by way of personal certificates and are authorized to use resources within a VO.

The European part of WLCG is operated in the context of the EU-project *Enabling Grids for E-Science* (EGEE) project [3]. EGEE brings together scientists and engineers from more than 240 institutions in 45 countries world-wide to provide a seamless Grid infrastructure for e-Science that is available to scientists 24 hours-a-day. Conceived from the start as a four-year project, the second two-year phase started on 1 April 2006, and is funded by the European Commission. Currently EGEE is planning for a third period, starting in 2008.

Within the EGEE project two VOs for the ILC project [5] were founded and officially registered: *'ilc'* and for the CALICE collaboration [6] *'calice'*. Both VOs are supported by a large number of sites within the EGEE.

This paper complements a talk given at LCWS2007 in the 'LCWS: Sim/Reco' parallel session [1].

2 The Grid

2.1 Grid Infrastructure

The EGEE Grid infrastructure consists of Grid services and Grid resources. The compute and data storage resources are contributed by the participating Grid sites and are distributed globally. Sites operate *Computing Elements* (CE), which act as logical entry points to clusters of *Worker Nodes* (WN), and *Storage Elements* (SE), which provide interfaces to data storage systems.

Core Grid services are *VO Membership Services* (VOMS), *VO Membership Registration Service* (VOMRS), *LCG File catalogues* (LFC), *Workload Management Systems* (WMS), and *Resource Brokers* (RB). Those services must exist at least once per VO.

*<http://www.desy.de/~gellrich>

2.2 Grid Middleware

As Grid software – called *middleware* which mediates between the user’s application and the operating system – the EGEE development *gLite* [9] is deployed. *gLite* provides software to implement the Grid services as well as client software to communicate with the Grid services. Usually the user’s workgroup servers or desktops deploy this *User Interfaces* (UI) client software.

3 The ILC VOs

DESY hosts the ILC VOs ‘*calice*’ and ‘*ilc*’ as a part of its EGEE Grid infrastructure. The membership to the VOs is managed by VOMS [12]. User registration is handled by VOMRS [13]. In order to register files, LCG File Catalogues are operated for both VOs. DESY also operates Workload Management Systems and Resource Brokers for the VOs.

3.1 Communications within ILC

The following communication channels are available for ILC. DESY operate the mailing lists

- `calice-vo-support(@)desy.de`
- `calice-vo-users(@)desy.de`
- `ilc-vo-support(@)desy.de`
- `ilc-vo-users(@)desy.de`

A web page with instructions to site administrators and users is available [7].

3.2 Testbeam Data

DESY enabled its mass storage system as a Storage Element, including a large tape library, for the ILC VOs. Read and write access to the data is possible by way of Grid tools.

The CALICE collaboration [6] decided a year ago to use DESY mass storage as the main repository for testbeam data. To date (October 2007) a total of $30TB$ of data was transferred through the Grid to DESY. It is planned to also transfer testbeam data from FNAL via the Grid to DESY.

A similar approach has recently been chosen by the detector development group of EUDET-JRA1 [10]. To date (October 2007) a total of $1.3TB$ have been transferred to DESY via the Grid.

All CALICE and EUDET-JRA1 (Grid) users benefit from the presence of the testbeam data in the Grid which allows seamless access within hours after data transfer world-wide.

3.3 ILC Application Software on the Grid

The WLCG is close to finishing the transition from Scientific Linux 3 (SL3) to SL4 as the Operating System on the Worker Nodes. Most of the HEP software – also in ILC – is supported for SL4.

In HEP, geometry and calibration data are typically stored in central database systems which leads to severe bottlenecks when many jobs try to access them concurrently. For ILC

the tool set *MyGridDB* [17] was developed which decouples production jobs from the central ILC database. Necessary database entries are simply dumped into files and stored in the Grid. At run-time, jobs create local database instances with these files.

4 Perspectives

So far, the Grid has been used by ILC on a basic level only. Data transfers as well as data analyzes and *Monte Carlo* production have been carried out by way of simple scripts which utilize the generic gLite command suite. In order to make most efficient use of the Grid resources high level user tools will be needed. As a product of the LCG developments, a number of elaborated tools are available that might well be applicable to the ILC needs. Among those tools are GANGA [14] and DIRAC [15]. A working group was set up recently to evaluate those tools for ILC.

Up to now, all software, that is needed to run ILC jobs, including the libraries of the persistency framework /em LCIO [16], are either submitted with the job or are downloaded from at run-time. The WLCG Grid infrastructure foresees a mechanism to install VO-specific software on the various sites locally. This mechanism includes a software *tag* which is published by way of the information system. This *tag* can be evaluated by the Work-load Management System to ensure the presence of the requested software on the picked Computing Element.

In EGEE, sites usually provide Grid resources to supported VOs on one infrastructure. Resource distribution is performed by virtual shares rather than dedicating hardware directly to VOs. This ansatz allows to very efficiently utilize resources and makes it easy to add more. Many Grid sites have already committed a fraction of their Grid resources to ILC. With the increase of resources in the Grid, more resources will be available for ILC computing too.

To date two instances of the VO *'ilc'* live concurrently in EGEE and in the American *Open Science Grid* (OSG) [4]. Methods to synchronize the members of the VOs are being developed. Again, it is planned to benefit from WLCG developments on interfaces between those two Grids.

5 Summary

Grid computing is a strategic technology for the future. It is about virtualization of computing resources, such as compute cycles and data storage, in a *global* context. Already now large computing resources outside the Grid are not available anymore in HEP.

For the ILC project two VOs were set up which use the existing EGEE/WLCG infrastructure; all core Grid services are hosted at DESY. Various sites world-wide support the ILC VOs and provide compute and data storage resources to the ILC VOs.

Though tools for the ILC *Monte Carlo* mass production and user analysis as well as data transfer are still rudimentary, considerable amounts of resources have already been exploited by ILC.

Recently, working groups within ILC were founded to evaluate and adapt software tools and frameworks to the needs of ILC.

ILC strongly benefits from the existing Grid infrastructure with its increasing resources as well as from products which have been developed for LHC.

Acknowledgments

We would like to thank the DESY Computer Center for their support in installing and operating the Grid infrastructure.

EGEE-II is a project funded by the European Commission with the contract number INFSO-RI-031688C.

References

- [1] Slides:
<http://ilcagenda.linearcollider.org/contributionDisplay.py?contribId=233&sessionId=76&confId=1296>
- [2] <http://cern.ch/lcg/>
- [3] <http://www.eu-egee.org/>
- [4] <http://www.opensciencegrid.org/>
- [5] <http://www.linearcollider.org/>
- [6] <http://polywww.in2p3.fr/activites/physique/flc/calice.html>
- [7] <http://grid.desy.de> and <http://grid.desy.de/ilc/>
- [8] <http://www.dcache.org/>
- [9] <http://glite.web.cern.ch/glite/>
- [10] <http://www-zeus.desy.de/~haas/eudet-jra1/>
- [11] <http://www.desy.de/>
- [12] <https://grid-voms.desy.de:8443/voms/calice/> and <https://grid-voms.desy.de:8443/voms/ilc/>
- [13] <https://grid-voms.desy.de:8443/vo/ilc/vomrs/>
- [14] <http://ganga.cern.ch/>
- [15] <http://dirac.cern.ch/>
- [16] <http://lcio.desy.de/>
- [17] <http://www.desy.de/~hhoelbe/>

Full Simulation Study of WW Scattering at the ILC

David Ward and Wenbiao Yan

University of Cambridge, Cavendish Laboratory, JJ Thomson Avenue,
Cambridge CB3 0HE, United Kingdom

We study full simulation of WW scattering with a linear collider detector model at $\sqrt{s} = 800$ GeV for the process $e^+e^- \rightarrow \nu_e\bar{\nu}_e WW \rightarrow \nu_e\bar{\nu}_e q\bar{q}q\bar{q}$ and $e^+e^- \rightarrow \nu_e\bar{\nu}_e ZZ \rightarrow \nu_e\bar{\nu}_e q\bar{q}q\bar{q}$, and obtain the limits on α_4 and α_5 in the electroweak chiral Lagrangian.

1 Introduction

The standard model introduces the Higgs boson to explain the breaking of electroweak symmetry, and hence we should not observe strong WW scattering. However, one can imagine that there is no Higgs boson, and that electroweak symmetry breaking is broken by a strong interaction. The W bosons become strongly interacting particles at TeV energies in this case [2]. WW scattering is a useful probe of breaking of electroweak symmetry. The WW scattering at low energies can be described by an effective Lagrangian approach, in which there are two anomalous couplings α_4 and α_5 in the theory [3]. α_4 and α_5 are model dependent, and are zero in the standard model. The sensitivity of α_4 and α_5 has already been studied for the CERN LHC case [4] and linear collider TESLA case with fast simulation at $\sqrt{s} = 800$ GeV [3, 5] and $\sqrt{s} = 1000$ GeV [6]. The motivation of this work is study the sensitivity α_4 and α_5 by full detector simulation (*not* fast simulation !) for the different linear collider detector models and different Particle Flow Algorithms (PFA) for the detector design studies. However, in this talk, we only show preliminary results on the linear collider detector model LDC00Sc, which is implemented in the Mokka [7] Monte Carlo, with Pandora PFA [7].

2 Analysis setup

The Monte Carlo samples are generated at $\sqrt{s} = 800$ GeV, beam polarisations of 80% for electrons and 40% for positrons are assumed. For the $t\bar{t}$ events, PYTHIA [8] is used without beam polarisations. For the other event samples, WHIZARD [9] is used. The hadronization is done by JETSET. Table 1 shows the summary of all Monte Carlo samples for the analysis. The single weak boson process is generated with an additional cut on $M(q\bar{q}) > 130$ GeV to reduce the number of generated events [6]. According to the results in [3, 5], the processes $e^+e^- \rightarrow WW/ZZ \rightarrow q\bar{q}q\bar{q}$ and $e^+e^- \rightarrow q\bar{q} \rightarrow X$ can be neglected. Because WHIZARD calculates matrix elements for all diagrams for the process $\nu_e\bar{\nu}_e q\bar{q}q\bar{q}$, it is necessary to separate the signal events and background events. The suggestions in [3, 5] are followed to choose doubly resonant signals $\nu_e\bar{\nu}_e WW$ and $\nu_e\bar{\nu}_e ZZ$: (1) $147.0 < m_{q\bar{q}}^1 + m_{q\bar{q}}^2 < 171.0$ GeV for $\nu_e\bar{\nu}_e WW$; $171.0 < m_{q\bar{q}}^1 + m_{q\bar{q}}^2 < 195.0$ GeV for $\nu_e\bar{\nu}_e ZZ$. (2) $|m_{q\bar{q}}^1 - m_{q\bar{q}}^2| \leq 20.0$ GeV. (3) $m_{\nu_e\bar{\nu}_e} \geq 100.0$ GeV, where $m_{q\bar{q}}^1$ and $m_{q\bar{q}}^2$ are the invariant masses of two pairs of quarks. The cut $m_{\nu_e\bar{\nu}_e} \geq 100.0$ GeV is used to reject WWZ and ZZZ events, where the Z decays into a neutrino pair. The rest of the events are considered as 6-fermion background events.

The Mokka 6.2 [7] program is used for the detector simulation, and Marlin 0.9.6 [7] is used for the event reconstruction. The output of Pandora PFA [7] is used in the analysis.

Channel	$\sigma_{800\text{GeV}}$ (fb)	Generator
$\nu_e\bar{\nu}_e WW \rightarrow \nu_e\bar{\nu}_e q\bar{q}q\bar{q}$	8.55	Whizard 1.50
$\nu_e\bar{\nu}_e ZZ \rightarrow \nu_e\bar{\nu}_e q\bar{q}q\bar{q}$	3.97	Whizard 1.50
$\nu_e\bar{\nu}_e q\bar{q}q\bar{q}$ (background)	5.46	Whizard 1.50
$e\nu_e WZ \rightarrow e\nu_e q\bar{q}q\bar{q}$	38.75	Whizard 1.50
$ee WW/ZZ \rightarrow ee q\bar{q}q\bar{q}$	289.43	Whizard 1.50
$t\bar{t} \rightarrow X$	299.63	PYTHIA 6.1
$\nu_e e W \rightarrow \nu_e e q\bar{q}$	108.59	Whizard 1.50
$\nu_{\mu,\tau}\bar{\nu}_{\mu,\tau} WW/ZZ \rightarrow \nu_{\mu,\tau}\bar{\nu}_{\mu,\tau} q\bar{q}q\bar{q}$	8.85	Whizard 1.50

Table 1: The Cross section of signal and background Monte Carlo samples in the analysis.

3 Event selection

The WW scattering events are selected with some cuts similar to paper [3, 5], and are unified for the WW/ZZ events. In order to suppress background events, the following cuts are used in the analysis. (1) The recoil mass $M_{recoil} \geq 200.0$ GeV. (2) Total transverse momentum $P_T \geq 40$ GeV. (3) Total transverse energy $E_T \geq 150$ GeV. (4) Total missing momentum and most energetic track have $|\cos\theta| < 0.99$. (5) Energy in a 10° cone around the most energetic track $E_{cone} \geq 2.0$ GeV. (6) The PFA objects in the detector are forced into four jets with the Ktjet package [10]. The events with four good jets (i.e. $E_{jet} > 10.0$ GeV and $|\cos\theta_{jet}| < 0.99$) and $Y_{34} > 0.0001$ ^a are used in the analysis. The number of charged tracks in each jet ≥ 2 .

The jet pairing is chosen by requiring the product $|m_{ij} - m_{W/Z}||m_{kl} - m_{W/Z}|$ to be minimum for three possible pairs [3]. For the $\nu_e\bar{\nu}_e WW$ events, the reconstructed W mass is between 60 GeV and 88 GeV. For the $\nu_e\bar{\nu}_e ZZ$ events, the reconstructed Z mass is above 85 GeV and below 100 GeV. The separation power of W and Z is an important issue in the WW scattering. In the Figure 1 shows the hadronic mass separation for $\nu_e\bar{\nu}_e WW$ (blue) and $\nu_e\bar{\nu}_e ZZ$ (red) at $\sqrt{s} = 800$ GeV at primary parton level (left) and detector level (right). There is no W/Z selection at detector level in the right-hand part of Figure 1, which suggests the W and Z could be separated by reconstructed mass via jets.

4 Fitting method and results

The distribution $d^2\sigma/(dM_{VV}d|\cos\theta_V^*|)$ ($V = W, Z$) in 10×10 bins at detector level is used to extract α_4 & α_5 with a binned likelihood fit, where M_{VV} is the event mass, and $\cos\theta_V^*$ is the polar angle of V in the VV rest frame. The SM Monte Carlo sample with ($\alpha_4 = 0.0$, $\alpha_5 = 0.0$) is the "data" sample in the fitting, and the integrated luminosity of the "data" sample is 1000 fb^{-1} . The Poisson distribution $p(n) = e^{-\lambda}\lambda^n/n!$ is used for each bin, where n is the observed number in the "data" sample and background event samples, and $\lambda = m^{signal}(\alpha_4, \alpha_5) + m^{bcg1}(\alpha_4, \alpha_5) + m^{bcg2}$ is the expected number. $m^{signal}(\alpha_4, \alpha_5)$ is the contribution from doubly resonant signal events, $m^{bcg1}(\alpha_4, \alpha_5)$ is for background events with α_4 & α_5 dependence, e.g. $e\nu_e WZ$ events. m^{bcg2} is due to background events without α_4 & α_5 dependence, e.g. $t\bar{t}$ events. Finally, the likelihood function $-\ln\mathcal{L}$ is defined as

^a Y_{34} is the jet resolution parameter in the Ktjet package [10] at which an event is reclassified from four to three jets.

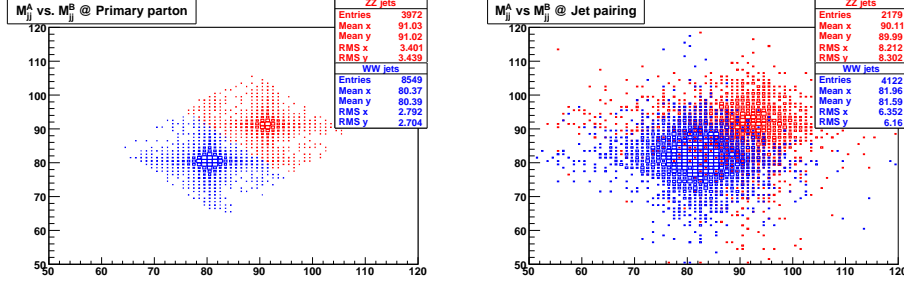


Figure 1: Hadronic mass separation for $\nu_e\bar{\nu}_e$ WW (blue) and $\nu_e\bar{\nu}_e$ ZZ (red) at $\sqrt{s} = 800\text{GeV}$ at primary parton level (left) and detector level. There is no W/Z selection at detector level.

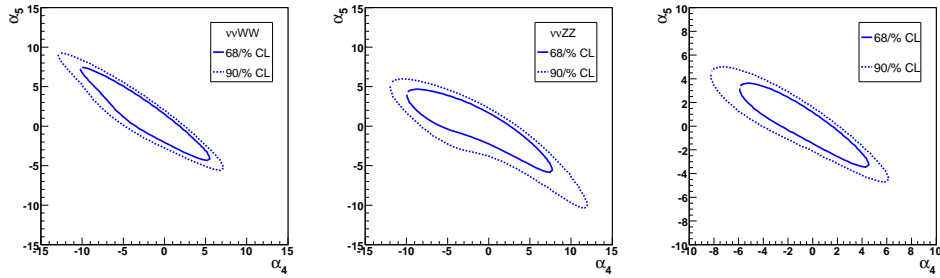


Figure 2: The left (middle) plot shows the 68% (continuous line) and 90% (dashed line) C.L. contours obtained by $\nu_e\bar{\nu}_e$ WW ($\nu_e\bar{\nu}_e$ ZZ), the right plot shows the C.L. contours obtained by combination of $\nu_e\bar{\nu}_e$ WW and $\nu_e\bar{\nu}_e$ ZZ events.

$-\sum \ln p(n_i) = -\sum n_i \ln \lambda_i + \sum \lambda_i + \sum \ln(n_i!)$, here $\sum \ln(n_i!)$ is a constant and is ignored in the fitting.

Each Monte Carlo SM event (i th event) of the signal is weighted by $R_i(\alpha_4, \alpha_5) = 1.0 + A_i\alpha_4 + B_i\alpha_4^2 + C_i\alpha_5 + D_i\alpha_5^2 + E_i\alpha_4\alpha_5$, where $R_i(\alpha_4, \alpha_5)$ is obtained in the following way: using the generated SM events, we recalculate matrix elements for each event with 20 sets of (α_4, α_5) values, and decide $(A_i, B_i, C_i, D_i, E_i)$ by TMinuit fitting to 20 R for i th event. $m^{signal}(\alpha_4, \alpha_5)$ is obtained by counting selected events with weight $R_i(\alpha_4, \alpha_5)$. $m^{bkg1}(\alpha_4, \alpha_5)$ is obtained a similar way.

The fitted α_4 & α_5 are shown in Figure 2. The left (middle) plot shows the 68% (continuous line) and 90% (dashed line) C.L. contours obtained by $\nu_e\bar{\nu}_e$ WW ($\nu_e\bar{\nu}_e$ ZZ), the right plot shows the C.L. contours obtained by combination of $\nu_e\bar{\nu}_e$ WW and $\nu_e\bar{\nu}_e$ ZZ events. The results are also comparable with TESLA results based on fast simulation [3, 6], and are shown in the slides [1].

5 Acknowledgments

We would like to thank Wolfgang Kilian on the WHIZARD generator, Predrag Krstonsic and Andres F. Osorio on the WW scattering, Mark Thomson on the Pandora PFA.

References

- [1] Slides:
<http://ilcagenda.linearcollider.org/contributionDisplay.py?contribId=236&sessionId=76&confId=1296>
- [2] E. Boos *et al.*, Phys. Rev. **D57** 1553 (1998);
Michael E. Peskin and James D. Wells, Phys. Rev. **D64** 093003 (2001);
Michael S. Chanowitz, arXiv:hep-ph/0412203 (2004).
- [3] R. Chierici, S. Rosati and Michael Kobel, " Strong electroweak symmetry breaking signals in WW scattering at tesla", LC-PHSM-2001-038.
- [4] A. S. Belyaev *et al.*, Phys. Rev. **D59** 015022 (1998).
- [5] Andres F. Osorio, University of Manchester. PhD thesis, 2006.
- [6] M. Beyer *et al.*, arXiv:hep-ph/0604048 (2006);
P. Krstonsic *et al.*, arXiv:hep-ph/0508179 (2005).
- [7] ILC software packages, <http://ilcsoft.desy.de/portal>.
- [8] PYTHIA 6.1, <http://www.thep.lu.se/~torbjorn/Pythia.html>.
- [9] WHIZARD 1.50, <http://www-ttp.physik.uni-karlsruhe.de/whizard>.
- [10] J. M. Butterworth *et al.*, Comp. Phys. Comm. **153** 85 (2003).

Simulation of an All-Silicon Tracker

Chris Meyer, Tyler Rice, Lori Stevens, Bruce A. Schumm

University of California at Santa Cruz and the Santa Cruz Institute for Particle Physics
1156 High Street, Santa Cruz, California 95062, USA

We present recent improvements in the performance of the reconstruction of non-prompt track in the SiD Detector Concept Design, including initial results on the effect of longitudinal segmentation in the SiD tracker. We also describe a generic tracking validation package developed at SCIPP.

The SiD Detector Concept offers a number of potential advantages in the reconstruction of ILC collisions, but to be confident of the quality of this reconstruction, several of the SiD's innovative features need to be studied via realistic simulation. In particular, it must be demonstrated that the use of a limited number (five in the baseline design) of precise silicon layers for track reconstruction is sufficient to exploit the physics potential of the ILC machine. While there is little question that such a device can provide superior transverse momentum resolution, the capability of the design to recognize and reconstruct tracks – particularly those that originate outside the first layer or two of the vertex detector – is less clear.

To explore the performance of the tracker under realistic settings, we have developed a tracking performance package that evaluates the tracking efficiency and reconstruction accuracy of tracking algorithms. This package has been developed as a stand-alone C++ package, and thus is fully versatile, being easily applied to any ILC detector concept within any reconstruction framework (in fact, it is generally applicable to any cylindrical geometry track reconstruction package). In the interest of space, we do not present further details of this package here; sample output is to be found in reference [1]. We encourage interested groups to contact us for details.

One of the novel aspects of the baseline SiD design is that it proposes to do tracking reconstruction with only ten tracking layers, of which five are concentrated around the beampipe in a pixelated vertex detector. While previous studies [2, 1] have suggested that such an approach can be sufficiently efficient for prompt tracks, the reconstruction algorithm used in these prior studies was unable to reconstruct tracks originating outside of the first layer of the vertex detector. Over the past year, the SCIPP ILC simulation group has explored the capability of the SiD tracker to reconstruct such non-prompt tracks, and how that capability depends upon the longitudinal segmentation of the tracker. The results presented here are somewhat updated relative to the results presented at the workshop in May 2007.

The SCIPP group's work on non-prompt track reconstruction has been based on refining and extending *AxialBarrelTracker*, an algorithm originally written by Tim Nelson (SLAC) to reconstruct SiD tracks in the absence of the vertex detector. This algorithm works inward from the outside of the SiD tracker, beginning with three-hit seeds that lie on circles in the plane transverse to the beam line that miss the collision point by no more than 1 centimeter. To search for non-prompt tracks, the SCIPP group relaxed the miss-distance requirement to 10 centimeters, finding that, once the hits from prompt tracks were removed, the number of seeds remained tractable with the relaxed DOCA constraint.

The group explored the nature of the hits remaining after the hits from prompt tracks were removed. Roughly 5% of hits were due to tracks that went through three or more tracking layers and then exited the tracker. Approximately 45% of the hits appeared to be coming from tracks that looped through the tracker, striking each tracking layer a number of times. Roughly 35% of hits were due to material interactions of prompt tracks. The remaining 15% were hits from tracks with momentum too low to reconstruct.

In this light, a set of ‘findable’ non-prompt particles was identified by requiring that the underlying (‘Monte-Carlo Truth’) tracks lie within $|\cos\theta| < 0.8$, have a radius of origin between 2 and 40 cm and a path length in the tracker of at least 50cm, not arise via back-scatter off of the calorimeter, and have a transverse momentum of no less than 0.75 GeV/c. In a sample of 137 Z-pole $b\bar{b}$ events with thrust greater than 0.94 and a thrust axis with $|\cos\theta_{thrust}| < 0.5$, these selection requirements identified 304 findable non-prompt particles. This set of findable particles represents approximately 5% of the number of findable particles that would be identified if there were no restriction on the radius of origin (in other words, approximately 5% of all tracks are non-prompt).

Tracks found by AxialBarrelTracker were accepted provided they were comprised of at least four hits, had a reconstructed transverse momentum of at least 0.75 GeV/c, and a reconstructed distance of closest approach in the plane perpendicular to the beam of no more than 10 cm. The results that follow were achieved under the assumption that the tracker was composed of two unsegmented halves: one extending to positive value of z and the other to negative values; only tracks for which all hits had the same sign z coordinate were accepted.

Findable particles were deemed ‘found’ provided they were associated with accepted tracks that had at least four hits caused by the findable particle under consideration. No more than one accepted track was permitted to be associated with each findable particle. Any accepted track not associated with a findable particle was deemed ‘fake’.

With these criteria, 131 (43%) of findable non-prompt particles were found with 5 hits, with only one fake five-hit track. Another 100 non-prompt tracks were found with 4 hits; however, these were accompanied by an additional 270 four-hit fake tracks, rendering four-hit tracks too impure for use. The remaining findable particles (73, or 24% of the sample) had no associated accepted track.

Upon examination, it was discovered that AxialBarrelTracker was often being confused by three-hit seeds for which not all of the hits came from the same underlying particle. Thus, to improve the efficiency as well as reduce the number of fake tracks, we added to AxialBarrelTracker a requirement that all the hits on the seed lie within an azimuthal slice of width $\pi/2$. This requirement was also applied to the larger set of hits as additional hits were added to the seed.

After application of this azimuthal restriction, the sample of 304 findable particles were reconstructed as follows. 145 (48%) were reconstructed with five hits, 112 (37%) were reconstructed with four hits, and 47 (15%) had no associated accepted track. The number of five-hit fake tracks remained unchanged at one, while the number of four hit fake tracks was reduced from 270 to 157. It should be point out that, of the 304 findable particles, only 166 left one and only one hit in each of the five layers; for this set of tracks, the reconstruction efficiency with the azimuthal restriction approached 85%.

Thus, it appears that non-prompt particles leaving hits in all five central tracking layers can be reconstructed with reasonable efficiency and good purity, but that more work needs to be done to reconstruct particles leaving only four hits (the majority of four-hit particles

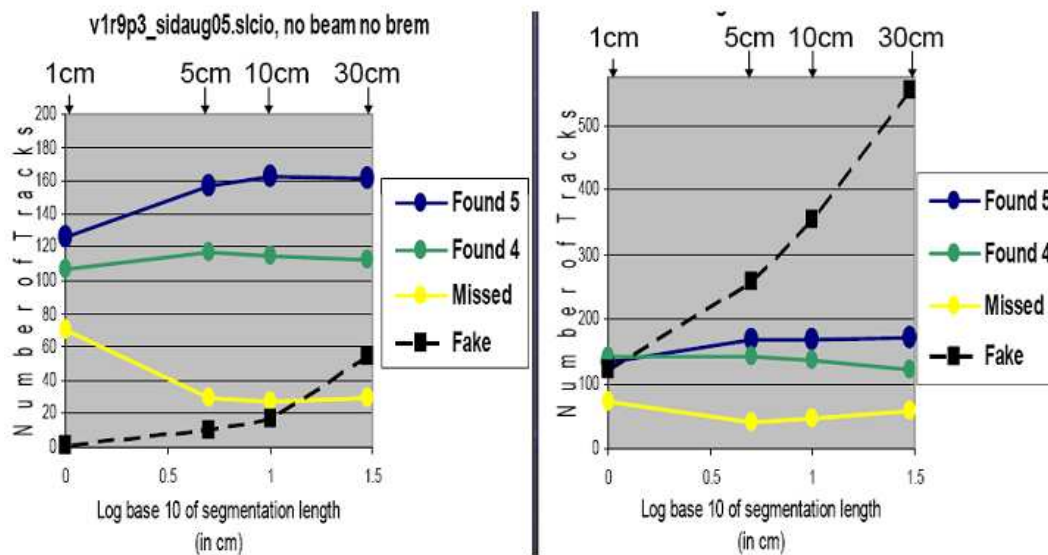


Figure 1: Performance of AxialBarrelTracker as a function of the z length of the tracker modules for Z pole $b\bar{b}$ events (left) and uds events at $E_{cm} = 500$ GeV. The trajectories correspond to the numbers of findable particles found with five hits and four hits, the number of findable particles with no associated track, and the number of fake tracks.

originate outside of the first central tracking layer, rather than originating at smaller radius but curling up or leaving the detector before reaching the fifth tracking layer). To this end, the group developed code that takes advantage of longitudinal segmentation, testing for the consistency of the pattern of struck modules with the hypothesis that the pattern was produced by a single particle. The performance of AxialBarrelTracker as a function of the z length of the tracker modules is shown in Figure 1, for two data samples: $b\bar{b}$ events at the Z pole and uds events at $E_{cm} = 500$ GeV. As stated above, the $b\bar{b}$ events contained 304 findable non-prompt tracks; the $E_{cm} = 500$ GeV events contained 352 findable non-prompt tracks. It is seen that 10 cm segmentation (the SiD baseline) can be very helpful for intermediate energy (~ 50 GeV) jets, but does not appear to make too a qualitative difference for high energy (~ 250 GeV) jets.

In summary, the SCIPP simulation group has optimized Tim Nelson's AxialBarrelTracker routine to find non-prompt tracks. The efficiency and purity for non-prompt tracks hitting all five tracking layers is good, but without z segmentation, it seems difficult to reconstruct tracks that hit four or fewer layers. The inclusion of z segmentation can provide a substantial benefit by reducing the number of fake four-hit tracks. However, the degree of segmentation needed to reduce the fake-track contribution enough to make four-hit tracks usable depends upon the physics being studied. For low-energy (~ 45 GeV) jets, the proposed 10cm segmentation of the SiD baseline may be sufficient. For high-energy (~ 250 GeV) jets, however, the current reconstruction seems to require segmentation on the order of 1cm or less to recover four-hit tracks. The SCIPP simulation group continues to explore the capability of the SiD

baseline tracker to reconstruct non-prompt tracks, and is in the process of implementing the GARFIELD tracker [3], which uses minimum-ionizing calorimeter stubs to seed tracks, as an additional layer in the SiD reconstruction.

References

- [1] B. Schumm, *VXDBasedReco Track Performance Studies*,
http://scipp.ucsc.edu/~schumm/talks/national_meetings/snowmass/.
- [2] N. Sinev, *The Efficiency of Track Reconstruction using the Vertex Detector as the Primary Tracking Device*, 2005 International Linear Collider Workshop, Stanford, CA, 2005.
- [3] The Garfield Calorimeter-Assisted Tracking package was authored by Eckhard von Toerne and Dima Onoprienko of Kansas State University.

LDC Tracking Package

Alexei Raspereza, Xun Chen and Ariane Frey

Max-Planck-Institut für Physik
Föhringer Ring 6, 80805 Munich

This note describes the software, performing tracking in the detector at the International e^+e^- Linear Collider (ILC). The code is designed specifically for the Large Detector Concept (LDC). It is implemented within the framework of MARLIN and uses LCIO as the data format. Results of initial performance studies are presented for the tracking system of the LDC detector. The note is based on the talk given at the LCWS07 Conference [1].

1 Introduction

The ambitious physics program at the ILC sets stringent requirements on the detector. For the tracking system this means:

- excellent momentum resolution $\delta(1/p_T) \leq 5 \cdot 10^{-5} \text{ (GeV/c)}^{-1}$;
- very good flavour tagging capability, the vertex detector must measure impact parameter of tracks with the resolution $\delta(IP) \leq 5\mu\text{m} \oplus 10\mu\text{m}/p[\text{GeV/c}] \cdot \sin^{3/2} \theta$;
- efficient reconstruction of tracks in the dense jets, characterized by high local multiplicities of charge particles;
- full reconstruction of low p_T loopers, enabling precise extrapolation of tracks to the endcap calorimeters with subsequent linkage of tracks with calorimeter clusters.

Several detector concepts have emerged as a result of intensive R&D program for the ILC detector [2]. This note describes the tracking software designed within the framework of the Large Detector Concept (LDC). The LDC tracking system consists of the following components.

1. Microvertex pixel detector (VTX) surrounds the primary interaction point. The detector has 5 coaxial silicon layers. The innermost layer has radius 1.55 mm and the outermost - 6.0 mm.
2. Large volume Time Projection Chamber (TPC) ($r \sim 170\text{cm}$, $L \sim 2 \times 270\text{cm}$) represents the main component of the LDC tracking system.
3. Intermediate Si Tracker (SIT) has two cylindrical layers with radii 160 and 300 mm. Strip-wise readout is foreseen for this detector. SIT serves as a linker between VTX and TPC.
4. Forward Si tracking discs (FTD's) ensure good track reconstruction in the forward region. In the baseline LDC detector design, the forward tracking detector consists of 7 discs in both hemispheres placed at distance between 200 and 1300 mm from the interaction point. The three innermost discs on both sides will be instrumented with hybrid pixels, while for the remaining discs the strip readout is planned.

2 Structure of the Package

The LDC tracking code is implemented within the framework of MARLIN [3] and constitutes a part of the MARLINRECO package [4]. The code includes:

- MARLIN processors performing digitization of the signal in various tracking subdetectors;
- MARLIN processors implementing pattern recognition in TPC and silicon detectors;
- the track fitting code based on the Kalman filter approach;
- utility classes facilitating fast and efficient pattern recognition;
- class `MarlinTrackFit` providing an interface to the FORTRAN based DELPHI code;
- FORTRAN code from DELPHI, which performs pattern recognition in TPC, the interface of the FORTRAN code to the MARLINRECO package is realized in the form of C++ wrappers.

The software is compliant with the LCIO data format [5]. The track parameterization follows the ILC convention documented in Ref. [6]. The track parameters and corresponding covariance matrix are evaluated with the Kalman filter at the point of closest approach to the nominal e^+e^- interaction point.

2.1 Digitization Processors

The digitization of the simulated tracker hits (`SimTrackerHits`), produced during the detector simulation run, is performed in two different ways. The first approach is based on the Gaussian smearing of `SimTrackerHits` according to a-priori known and specified spatial point resolutions. This approach is implemented in the processors `VTXDigiProcessor`, `FTDDigiProcessor` and `TPCDigiProcessor`. The module `VTXDigiProcessor` performs digitization of `SimTrackerHits` in the vertex detector and SIT, `FTDDigiProcessor` - in the forward tracking discs and `TPCDigiProcessor` - in TPC. All processors require `SimTrackerHit` collection names as an input parameters. The `VTXDigiProcessor` treats VTX and SIT as cylindrical detectors. The two spatial point resolutions, one in the $r - \phi$ projection and another - along z , should be provided by user as a processor parameter. `FTDDigiProcessor` treats forward tracking discs as a rigid measurement planes at fixed positions in z . It is assumed that the hit position in the FTD's is measured "isotropically", thus a user has to provide only spatial point resolution in the $r-\phi$ projection. The TPC spatial resolution in $r-\phi$ is given by $\sigma^2(r - \phi) = \sigma_0^2 + D^2 \cdot L_{drift}$ where σ_0 is the constant term, D is the diffusion coefficient and L_{drift} is the drift length. Resolution along z axis is assumed to be independent of L_{drift} .

For the DEPFET-based microvertex detector, a detailed digitization procedure is implemented in the MARLIN processor `VTXDigitizer`. The procedure takes into account Lorentz effect, charge diffusion, electronic noise and energy loss fluctuations along the charged particle trajectory within the sensitive silicon layer.

All digitization processors produce as an output LCIO collections of the digitized tracker hits (`TrackerHit`s). Each `TrackerHit` is attributed with the 3D position and covariance matrix of the position measurement. The covariant matrix of the hit position measurement is then used in the track fitting procedure.

2.2 Pattern Recognition in TPC

Pattern recognition in TPC is done using C++ wrappers of the LEP code. The main MARLIN module is `LEPTrackingProcessor`, which invokes FORTRAN routines, which perform inward search for spatially continuous sequences of hits, compatible with the helix hypothesis, and fits these sequences. The LEP code is capable of finding only semiloops of the tracks. As a consequence, the low p_T loopers are splitted into several segments, which are then identified and merged by the `FullLDCTracking` processor described below. `LEPTrackingProcessor` requires as an input LCIO collection of the TPC `TrackerHits` and produces LCIO collections of the TPC tracks and inter-relations between tracks and Monte Carlo particles.

2.3 Pattern Recognition in Silicon Detectors

Combined pattern recognition in all silicon tracking devices (VTX, FTD and SIT) is implemented in the processor `SiliconTracking`. The procedure starts with the search for hit triplets in the outermost layers of the combined VTX-SIT tracking system and in FTD. Once such triplets are found, an inward extrapolation of the track candidates is performed and additional hits in the inner layers of VTX and FTD are assigned to the track candidates. The `SiliconTracking` processor requires as an input collections of VTX, FTD and SIT `TrackerHits` and produces the collections of silicon tracks and track - particle relations.

2.4 Association of the Silicon and TPC track segments. Full LDC Tracking.

The final step of the track reconstruction in the LDC detector consists of the association of track segments found in TPC and silicon detectors, merging splitted loopers in TPC and assignment of the left-over hits to the found tracks. All this is done by the `FullLDCTracking` processor. It requires as an input collections of VTX, FTD, SIT and TPC `TrackerHits` and collections of silicon and TPC tracks. An output is produced in the form of the fully reconstructed LDC tracks and track – MC particle relations.

2.5 TrackCheater Processor

The `TrackCheater` processor is designed to construct true Monte Carlo tracks from the hits attributable to the same Monte Carlo particles. Thus, this processor just emulates perfect pattern recognition. An user can optionally set track parameters, using generated values of the 4-momentum of charged particles or perform a fit of the cheated tracks. The `TrackCheater` processor requires as an input collections of `TrackerHits` in various sub-detectors and produces collections of true Monte Carlo tracks and track – MC Particle relations.

2.6 Detector Geometry and Material Description

The information on the detector geometry and material properties is needed both at the stage of the signal digitization and the track reconstruction. Description of the detector is provided via GEAR interface [7].

3 Performance Studies

Performance of the code has been evaluated on the samples produced with MOKKA program [8] simulating the LDC detector response. The detector model LDC01Sc was used. The following spatial point resolutions were assumed for various tracking subdetectors:

- VTX : $\sigma_{r-\phi} = \sigma_z = 4\mu\text{m}$,
- FTD : $\sigma_x = \sigma_y = 10\mu\text{m}$,
- SIT : $\sigma_{r-\phi} = \sigma_z = 10\mu\text{m}$,
- TPC : $\sigma_{r-\phi} = 55\mu\text{m} \oplus 3\mu\text{m}^{1/2} \sqrt{L_{\text{drift}}}$, $\sigma_z = 0.5\text{mm}$

Simple digitization procedure, performing Gaussian smearing of the simulated hit positions, is applied for each tracking subdetector.

The resolution on the track parameters has been investigated with the samples of single muons. Both momentum and polar angle of muons have been varied to study the dependence of resolution on the track momentum and polar angle. In the central part of the detector, the overall momentum resolution asymptotically reaches $\delta(1/p_T) = 3.5 \cdot 10^{-5} (\text{GeV}/c)^{-1}$ with increasing particle momentum. The multiple scattering degrades the resolution at lower momenta. For the charged particles with momentum around 1 GeV, the resolutions varies from $\delta(1/p_T) = 1.5 \cdot 10^{-3}$ to $3 \cdot 10^{-3} (\text{GeV}/c)^{-1}$ depending on the polar angle. The impact parameter resolution is found to be $\delta(IP) = 4\mu\text{m} \oplus 9\mu\text{m}/p[\text{GeV}/c] \cdot \sin^{3/2} \theta$. In the central region, the polar and azimuth angles are measured with precision better than 0.1 mrad for particle momenta $p > 50$ GeV. The resolution degrades to few mrad at $p < 1$ GeV.

The track finding efficiency has been studied on the sample of the pair produced top quarks at 500 GeV. Figure 1 shows the efficiency as a function of the particle momentum and polar angle. The overall efficiency is found to be 99(97.5)% for track momenta $p > 1(0.4)$ GeV/c.

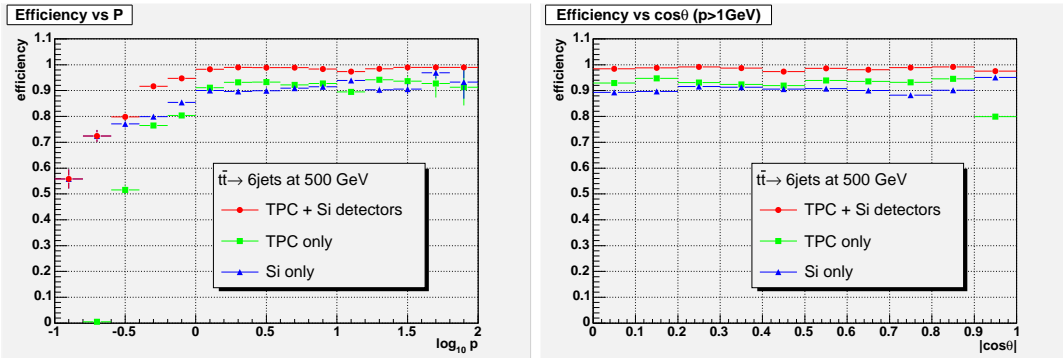


Figure 1: The track finding efficiency as a function of the track momentum (left plot) and polar angle (right plot) in the sample of the $e^+e^- \rightarrow t\bar{t}$ events at 500 GeV. The dependence of the track efficiency on the polar angle is presented only for tracks with momentum greater than 1 GeV.

The tracking code has been also tried in combination with the particle flow algorithms (PFA). The PFA-related performance has been evaluated in two ways. First, the tracking code has been combined with the ideal PFA, implementing perfect clustering in the calorimeters and fully efficient cluster-track association. In the second trial, the tracking code has been interfaced to the realistic algorithm Wolf-PFA [9]. The performance has been estimated in terms of the di-jet mass resolution in the sample of the Higgs boson production via the W -fusion mechanism, $e^+e^- \rightarrow W^+W^-\nu\bar{\nu} \rightarrow H\nu\bar{\nu}$. The center-of-mass energy is chosen to be 800 GeV, the Higgs boson mass is set to 120 GeV.

To eliminate the impact of missing neutrinos from b and c -hadrons decays on the di-jet mass resolution, the Higgs boson is forced to decay to $s\bar{s}$ pairs. Thus, only those effects, which are related to the event reconstruction efficiency and detector resolution, are studied.

Figure 2 shows the reconstructed Higgs boson mass for the runs with the perfect and Wolf particle flow algorithms. For each of the considered cases, the results are compared between the perfect tracking, performed by the `TrackCheater` processor, and realistic LDC tracking. Only slight deterioration of the di-jet mass resolution is observed for the realistic LDC tracking when compared to the runs with `TrackCheater`.

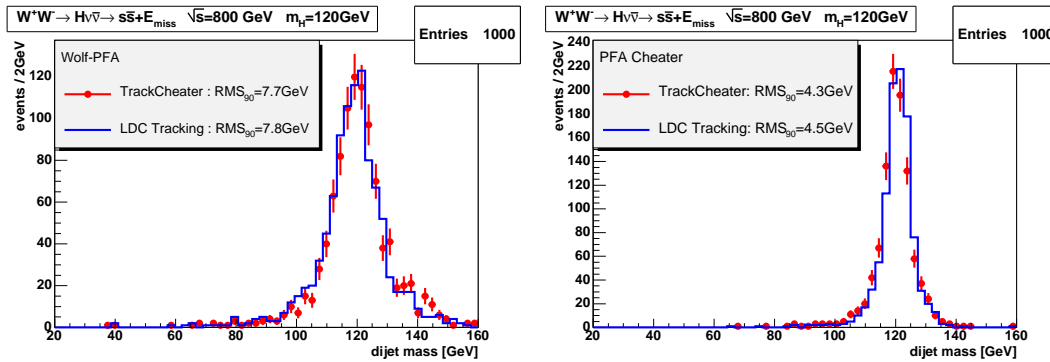


Figure 2: The di-jet mass distribution in the sample of the $e^+e^- \rightarrow W^+W^-\nu\bar{\nu} \rightarrow H\nu\bar{\nu}$ events. Left plot shows results obtained with the realistic Particle Flow Algorithm Wolf-PFA. Right plot - with the perfect PFA. Dots with error bars correspond to the runs with the perfect tracking, solid histograms - with the realistic LDC tracking.

4 Conclusion

The LDC tracking software has been developed as a part of the MARLINRECO package. The code performs digitization of the signal in various tracking subdetectors, followed by track finding and fitting in the LDC detector. Initial studies showed that the LDC detector supported by the designed code meets the performance requirements imposed by the ILC physics program. The package can be used in future detector optimization and performance studies and in physics analyses relying upon the full detector simulation and event reconstruction.

References

- [1] Slides:
<http://ilcagenda.linearcollider.org/contributionDisplay.py?contribId=284&sessionId=76&confId=1296>;
- [2] GLD, LDC, SiD and 4-th Outline Documents:
<http://physics.uoregon.edu/~lc/wwstudy/concepts>;
- [3] http://ilcsoft.desy.de/portal/software_packages/marlin/index_eng.html;
- [4] http://ilcsoft.desy.de/MarlinReco/v00-02/manual_html/manual.html;
- [5] <http://lcio.desy.de>;
- [6] T. Kraemer, LC Note LC-DET-2006-004;
- [7] http://ilcsoft.desy.de/portal/software_packages/gear/index_eng.html;
- [8] <http://polywww.in2p3.fr/geant4/tesla/www/mokka/mokka.html>;
- [9] A. Raspereza, arXiv:physics/0601069.

Track-Based Particle Flow

Oliver Wendt^{1,2}

1- DESY - FLC

22603 Hamburg - Germany

2- University of Hamburg - Department of Physics

Luruper Chaussee 149, 22761 Hamburg - Germany

One of the most important aspects of detector development for the ILC is a good jet energy resolution σ_E/E . To achieve the goal of high precision measurements $\sigma_E/E = 0.30/\sqrt{E(\text{GeV})}$ is proposed. The particle flow approach together with highly granular calorimeters is able to reach this goal. This paper presents a new particle flow algorithm, called Track-Based particle flow, and shows first performance results for 45 GeV jets based on full detector simulation of the Tesla TDR detector model.

PACS numbers: 07.05.Kf, 29.40.Vj, 29.85.+c

Keywords: particle flow, event reconstruction, calorimetry

1 Introduction

The International Linear Collider (ILC) will provide the potential for high precision measurements at center-of-mass energies between several hundred GeV and one TeV. Many interesting physics processes in this regime will be composed of multi-jet final states originating from hadronic decays of heavy gauge bosons. To reach the goal of high precision measurements it is suggested to achieve a mass resolution for $W \rightarrow q'\bar{q}$ and $Z \rightarrow q\bar{q}$ decays which is comparable to their widths. This leads to a jet energy resolution of $\sigma_E/E = 0.30/\sqrt{E(\text{GeV})}$ considering the typical di-jet energies ranging from 100 to 400 GeV. Studies based on full detector simulation have shown that particle flow algorithms (PFA) are able to reach this goal [1, 2]. The basic concept of any PFA is to reconstruct the four-momenta of all visible particles in an event. The four-momenta of charged particles are measured in the tracking detectors, while the energy of photons and neutral hadrons is obtained from the calorimeters. The accuracy of momentum measurement in the tracking systems is by orders of magnitude better than the accuracy of energy measurement in the calorimeters. This leads to a theoretical limit on the jet energy resolution of approx. $\sigma_E/E = 0.20/\sqrt{E(\text{GeV})}$, considering the characteristic ratio of charged and neutral particles in a jet. The given limit is obtained if the PFA is able to disentangle all charged from close-by neutral showers. Since this is not possible in a realistic PFA the performance degrades due to this *confusion*. Any PFA relies strongly on pattern recognition in the highly granular calorimeters and it is not possible to distinguish between pure detector and algorithmic effects on the reconstructed jet energy. Hence, for reliable detector optimisation studies using a PFA it is necessary to study different PFA and compare their results.

2 The Track-Based Particle Flow Algorithm

The Track-Based PFA is a new proposal of a PFA at the ILC. Basis of this PFA is a collection of tracks. Sequentially, the tracks are extrapolated into the calorimeter and correlated energy depositions are assigned to the track. Related MIP-like track segments are identified

as well. Additionally, a collection of photon candidates can be used as an input to improve the performance of the reconstruction. As soon as all tracks have been extrapolated their assigned hits are removed from the collection of calorimeter hits. Afterwards, a clustering procedure is applied on the remaining hits to reconstruct neutral particles. A simple particle identification (PID) is done for charged and neutral particles. The Track-Based PFA is implemented in C++ within the `Marlin` [3, 4] framework. Events for the reconstruction are created with `Mokka` [3], a `GEANT4` [5] simulation of the Large Detector Concept (LDC) [6]. `LCIO` [7] serves as persistent data format. The Track-Based PFA consists of six main stages:

i) Photon Finding: Photon finding is done with the “PhotonFinderKit” proposed by [8]. Only ECAL hits are taken into account. The output of this stage is a collection of clusters labeled as photon candidates.

ii) Tracking and Track-Extrapolation: Tracks, either provided by Monte Carlo information or by realistic tracking [9], are the basis of the Track-Based PFA. They are sequentially extrapolated into the calorimeter using a trajectory interface. The trajectory is given by a simple helix model at the moment, not taking into account energy loss. If such an extrapolation traverses one of the photon candidates it is removed from the collection of photon candidates, since it could be the electro-magnetic core of a hadron shower or an electron.

iii) MIP-Stub Finding: The collection of MIP-like energy depositions along a track extrapolation is done by a simple geometrical procedure. A system of two cylindrical tubes are assigned to the track extrapolation, surrounding it concentrically. Calorimeter hits in the vicinity of the track extrapolation are sorted with respect to their path lengths on the extrapolated trajectory. Starting from hits with small path lengths those hits are assigned to the MIP-stub which are located within the inner cylindrical tube. Hits beyond the outer cylindrical tube are not taken into account. As soon as a hit located in-between both tubes is found the procedure is stopped. The position of the last hit collected and its direction given by the tangent on the trajectory at this point are stored as initial parameters for the clustering procedure performed in the next step.

iv) Clustering and Cluster-Assignment: The Trackwise Clustering, proposed in [10], has been modified to take the start point and direction given by the MIP-stub finding into account. Additionally, it is adapted to produce more but smaller clusters. The center of gravity and orientation is calculated by the inertia tensor of each cluster. The clusters are assigned to the track by proximity and direction criteria. The track momentum is taken into account to prevent from assigning clusters with too much energy.

v) Particle Identification and Removal of “Charged” Calorimeter Hits: The PID of charged particles is done by a cut on the fraction of energy deposited in ECAL compared to the HCAL. It distinguishes only between electrons and charged pions. Additionally, muons are identified if a MIP-stub has been assigned to the track only. Afterwards, all calorimeter hits assigned to tracks are removed from the collection of calorimeter hits.

vi) Clustering and Particle Identification on “Neutral” Calorimeter Hits: The Trackwise Clustering is applied on the remaining calorimeter hits using the direction to the interaction point as a start direction. The PID is done in the same way as for the charged particles assigning a PID of photons or neutral kaons.

All reconstructed particles are filled into a collection assigned to the event. The Track-Based PFA described in this note is included in the `MarlinReco` package [3].

3 Performance

Figure 1 shows an example of a reconstruction of 45 GeV jets from a $Z^0 \rightarrow uds$ decay at $\sqrt{s} = 91.2$ GeV using the Track-Based PFA (circles). The detector simulation has been done with Mokka, using the TESLA TDR detector model [1, 3]. The initial direction of the quarks is restricted to a polar acceptance of $|\cos\theta| < 0.8$. The tracks as described in stage ii) of Section 2 are reconstructed by Monte Carlo information. Additionally, a histogram is shown which indicates the same reconstruction using a perfect assignment of hits to tracks by Monte Carlo information (dashed lines). It is getting close to the theoretical limit of approx. $0.20/\sqrt{E}(\text{GeV})$. The performance of the reconstruction is measured by the root-mean-square of the smallest range of reconstructed energies containing 90% of the events (RMS_{90}) [11]. The Track-Based PFA reaches a jet energy resolution of $0.41/\sqrt{E}(\text{GeV})$. There are two other PFA available within the Marlin framework. The first one (Wolf) reaches approx. $0.52/\sqrt{E}(\text{GeV})$ [12] for the same detector model and physics process, whereas the second one (PANDORAPFA) already reaches the goal of $0.30/\sqrt{E}(\text{GeV})$ [2].

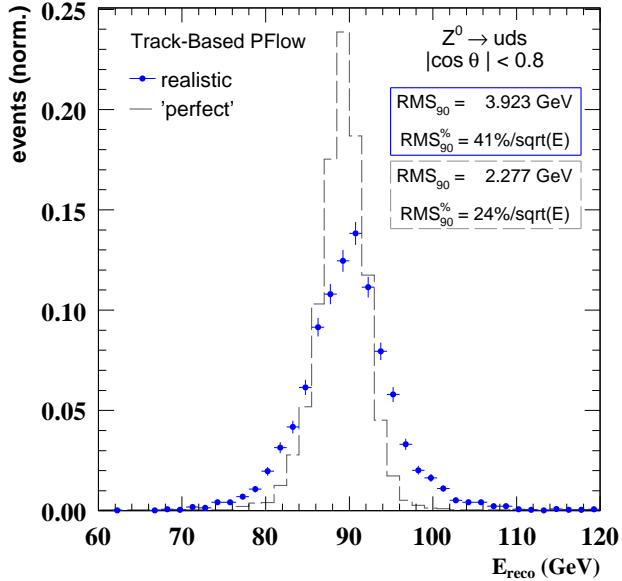


Figure 1: Total reconstructed energy for $Z^0 \rightarrow uds$ at $\sqrt{s} = 91.2$ GeV, realistic Track-Based PFA (circles) and assignment of calorimeter hits to tracks by Monte Carlo information (dashed lines).

References

- [1] TESLA Technical Design Report, DESY 2001-011, ECFA 2001-2009 (2001).
- [2] M. A. Thomson, arXiv:0709.1360 [physics.ins-det].
- [3] ILC software portal, <http://ilcsoft.desy.de>
- [4] F. Gaede, Nucl. Instrum. Meth. A **559**, 177 (2006).
- [5] GEANT4 collaboration, S. Agostinelli *et al.*, Nucl. Instr. and Meth. **A506** (2003) 3;
GEANT4 collaboration, J. Allison *et al.*, IEEE Trans. Nucl. Sci. 53 (2006) 1.
- [6] LDC web page, <http://www.ilcldc.org>
- [7] F. Gaede, T. Behnke, N. Graf and T. Johnson, eConf **C0303241**, TUKT001 (2003)
- [8] P. Krstonsic, "Photon Reconstruction", to appear in the proceedings of LCWS07, Hamburg
- [9] A. Raspereza, "LDC Tracking Software", to appear in the proceedings of LCWS07, Hamburg
- [10] A. Raspereza, arXiv:physics/0601069.
- [11] M. A. Thomson, AIP Conf. Proc. **896**, 215 (2007).
- [12] O. Wendt, F. Gaede and T. Kramer, arXiv:physics/0702171.

Progress with Particle Flow Calorimetry

Mark Thomson

University of Cambridge, Cavendish Laboratory
J.J. Thomson Avenue, Cambridge, CB30HE, UK

One of the most important requirements for a detector at the ILC is good jet energy resolution. It is widely believed that the particle flow approach to calorimetry is the key to achieving the ILC goal of a di-jet invariant mass resolution $\sigma_m/m < \Gamma_Z/m_Z$. This paper describes the current performance of the PANDORAPFA particle flow algorithm. For simulated light quark jets in the Tesla TDR detector, the jet energy resolution achieved is better than $\sigma_E/E \approx 3.4\%$ for jet energies in the range 45 – 250 GeV. This represents the first demonstration that Particle Flow Calorimetry can reach the ILC jet energy resolution goals.

1 Introduction

Many of the interesting physics processes at the ILC will be characterised by multi-jet final states, often accompanied by charged leptons and/or missing transverse energy associated with neutrinos or the lightest super-symmetric particles. The reconstruction of the invariant masses of two or more jets will provide a powerful tool for event reconstruction and identification. Unlike at LEP, where kinematic fitting[1] enabled precise jet-jet invariant mass reconstruction almost independent of the jet energy resolution, at the ILC this mass reconstruction will rely on the detector having excellent jet energy resolution. The ILC goal is to achieve a mass resolution for $W \rightarrow q'\bar{q}$ and $Z \rightarrow q\bar{q}$ decays which is comparable to their natural widths, i.e. $\sigma_m/m = 2.7\% \approx \Gamma_W/m_W \approx \Gamma_Z/m_Z$. For a traditional calorimetric approach, a jet energy resolution of $\sigma_E/E = \alpha/\sqrt{E(\text{GeV})}$ leads to a di-jet mass resolution of roughly $\sigma_m/m = \alpha/\sqrt{E_{jj}(\text{GeV})}$, where E_{jj} is the energy of the di-jet system. At the ILC typical di-jet energies will be in the range 150 – 350 GeV, suggesting the goal of $\sigma_E/E \sim 0.3/\sqrt{E(\text{GeV})}$. This is more than a factor two better than the best jet energy resolution achieved at LEP, $\sigma_E/E = 0.6(1 + |\cos\theta|)/\sqrt{E(\text{GeV})}$ [2]. Meeting the jet energy resolution goal is a major factor in the overall design of a detector for the ILC.

2 The Particle Flow Approach to Calorimetry

It is widely believed that the most promising strategy for achieving the ILC jet energy goal is the particle flow analysis (PFA) approach to calorimetry. In contrast to a purely calorimetric measurement, PFA requires the reconstruction of the four-vectors of all visible particles in an event. The reconstructed jet energy is the sum of the energies of the individual particles. The momenta of charged particles are measured in the tracking detectors, while the energy measurements for photons and neutral hadrons are obtained from the calorimeters. The crucial step in PFA is to assign the correct calorimeter hits to reconstructed particles, requiring efficient separation of nearby showers.

Measurements of jet fragmentation at LEP have provided detailed information on the particle composition of jets (e.g. [3, 4]). On average, after the decay of short-lived particles, roughly 62% of the energy of jets is carried by charged particles (mainly hadrons), around 27% by photons, about 10% by long-lived neutral hadrons (e.g. n/K_L^0), and around 1.5%

by neutrinos. Assuming calorimeter resolutions of $\sigma_E/E = 0.15/\sqrt{E(\text{GeV})}$ for photons and $\sigma_E/E = 0.55\sqrt{E(\text{GeV})}$ for hadrons, a jet energy resolution of $0.19/\sqrt{E(\text{GeV})}$ is obtained with the contributions from tracks, photons and neutral hadrons shown in Tab. 1. In practise it is not possible to reach this level of performance for two main reasons. Firstly, particles travelling at small angles to the beam axis will not be detected. Secondly, and more importantly, it is not possible to perfectly associate all energy deposits with the correct particles. For example, if a photon is not resolved from a charged hadron shower, the photon energy is not counted. Similarly, if part of charged hadron shower is identified as a separate cluster the energy is effectively double-counted. This *confusion* degrades particle flow performance. Because confusion, rather than calorimetric performance, determines the overall performance, the jet energy resolution achieved will not, in general, be of the form $\sigma_E/E = \alpha/\sqrt{E(\text{GeV})}$.

The crucial aspect of particle flow is the ability to correctly assign calorimeter energy deposits to the correct reconstructed particles. This places stringent requirements on the granularity of electromagnetic and hadron calorimeters. Consequently, particle flow performance is one of the main factors driving the overall ILC detector design. It should be noted that the jet energy resolution obtained for a particular detector concept is the combination of the intrinsic detector performance and the performance of the PFA software.

Component	Detector	Energy Fraction	Energy Res.	Jet Energy Res.
Charged Particles (X^\pm)	Tracker	$\sim 0.6 E_{\text{jet}}$	$10^{-4} E_{X^\pm}^2$	$< 3.6 \times 10^{-5} E_{\text{jet}}^2$
Photons (γ)	ECAL	$\sim 0.3 E_{\text{jet}}$	$0.15 \sqrt{E_\gamma}$	$0.08 \sqrt{E_{\text{jet}}}$
Neutral Hadrons (h^0)	HCAL	$\sim 0.1 E_{\text{jet}}$	$0.55 \sqrt{E_{h^0}}$	$0.17 \sqrt{E_{\text{jet}}}$

Table 1: Contributions from the different particle components to the jet-energy resolution (all energies in GeV). The table lists the approximate fractions of charged particles, photons and neutral hadrons in a jet and the assumed single particle energy resolution.

3 The PandoraPFA Particle Flow Algorithm

PANDORAPFA is a C++ implementation of a PFA algorithm running in the MARLIN[5, 6] framework. It was designed to be sufficiently generic for ILC detector optimisation studies and was developed and optimised using events generated with the MOKKA[7] program, which provides a GEANT4[8] simulation of the Tesla TDR[9] detector concept. The PANDORAPFA algorithm performs both calorimeter clustering and particle flow in eight main stages:

i) Tracking: for the studies presented in this paper, the track *pattern recognition* is performed using Monte Carlo information[5]. The track parameters are extracted using a helical fit. The projections of tracks onto the front face of the electromagnetic calorimeter are calculated using helical fits (with no accounting for energy loss along the track). Neutral particle decays resulting in two charged particle tracks (V^0 s) are identified by searching from pairs of non-vertex tracks which are consistent with coming from a single point in the central tracking chamber. Kinked tracks from charged particle decays to a single charged particle and a number of neutrals are also identified, as are interactions in the tracking volume (prongs).

ii) Calorimeter Hit Selection and Ordering: isolated hits, defined on the basis of proximity to other hits, are removed from the initial clustering stage. The remaining hits are

ordered into *pseudo-layers* which follow the detector geometry so that particles propagating outward from the interaction region will cross successive pseudo-layers. The assignment of hits to pseudo-layers removes the dependence of the algorithm on the explicit detector geometry whilst following the actual geometry as closely as possible. Within each pseudo-layer hits are ordered by decreasing energy.

iii) Clustering: the main clustering algorithm is a cone-based forward projective method working from innermost to outermost pseudo-layer. In this manner hits are added to clusters or are used to seed new clusters. Throughout the clustering algorithm clusters are assigned a direction (or directions) in which they are growing. The algorithm starts by *seeding* clusters using the projections of reconstructed tracks onto the front face of the calorimeter. The initial direction of a track-seeded cluster is obtained from the track direction. The hits in each subsequent pseudo-layer are then looped over. Each hit, i , is compared to each clustered hit, j , in the previous layer. The vector displacement, \mathbf{r}_{ij} , is used to calculate the parallel and perpendicular displacement of the hit with respect to the unit vector(s) $\hat{\mathbf{u}}$ describing the cluster propagation direction(s), $d_{\parallel} = \mathbf{r}_{ij} \cdot \hat{\mathbf{u}}$ and $d_{\perp} = |\mathbf{r}_{ij} \times \hat{\mathbf{u}}|$. Associations are made using a cone-cut, $d_{\perp} < d_{\parallel} \tan \alpha + \beta D_{\text{pad}}$, where α is the cone half-angle, D_{pad} is the size of a sensor pixel in the layer being considered, and β is the number of pixels added to the cone radius. Different values of α and β are used for the ECAL and HCAL with the default values set to $\{\tan \alpha_{\text{E}} = 0.3, \beta_{\text{E}} = 1.5\}$, and $\{\tan \alpha_{\text{H}} = 0.5, \beta_{\text{H}} = 2.5\}$ respectively. Associations may be made with hits in the previous 3 layers. If no association is made, the hit is used to seed a new cluster. This procedure is repeated sequentially for the hits in each pseudo-layer (working outward from ECAL front-face).

iv) Topological Cluster Merging: by design the initial clustering errs on the side of splitting up true clusters rather than clustering energy deposits from more than one particle. The next stage of the algorithm is to merge clusters from tracks and hadronic showers which show clear topological signatures of being associated. A number of track-like and shower-like topologies are searched for including looping minimum ionising tracks, back-scattered tracks and showers associated with a hadronic interaction. Before clusters are merged, a simple cut-based photon identification procedure is applied. The cluster merging algorithms are only applied to clusters which have not been identified as photons.

v) Statistical Re-clustering: The previous four stages of the algorithm were found to perform well for jets with energy less than ~ 50 GeV. However, at higher energies the performance degrades rapidly due to the increasing overlap between hadronic showers from different particles. To address this, temporary associations of tracks with reconstructed calorimeter clusters are made. If the track momentum is incompatible with the energy of the associated cluster re-clustering is performed. If $E_{\text{CAL}} - E_{\text{TRACK}} > 3.5\sigma_E$, where σ_E is the energy resolution of the cluster, the clustering algorithm, described in *iii*) and *iv*) above, is reapplied to the hits in that cluster. This is repeated, using successively smaller values of the α s and β s in the clustering finding algorithm (stage *iii*) until the cluster splits to give an acceptable track-cluster energy match. Similarly, if $E_{\text{TRACK}} - E_{\text{CAL}} > 3.5\sigma_E$ the algorithm attempts to merge additional clusters with the cluster associated with the track. In doing so high energy clusters may be split as above.

vi) Photon Recovery and Identification: A more sophisticated photon identification algorithm is then applied to the clusters. The longitudinal profile of the energy deposition, ΔE , as a function of number of radiation lengths from the shower start, t , is compared to

that expected for an electromagnetic shower:

$$\Delta E \approx E_0 \frac{(t/2)^{a-1} e^{-t/2}}{\Gamma(a)} \Delta t \quad \text{where} \quad a = 1.25 + \frac{1}{2} \ln \frac{E_0}{E_c},$$

E_0 is the shower energy and E_c is the critical energy which is tuned give the appropriate average shower profile in the ECAL. The resulting level of agreement is used to improve the tagging of photons and to recover primary photons merged with hadronic showers.

vii) Fragment Removal: At this stage there is still a significant number of “neutral clusters” (not identified as photons) which are *fragments* of charged particle hadronic showers. An attempt is made to identify these clusters and merge them with the appropriate parent cluster. All non-photon neutral clusters, i , are compared to all clusters with associated tracks, j . For each combination a quantity, e_{ij} , is defined which encapsulates the evidence that cluster i is a fragment from cluster j . The requirement, R_{ij} , for the clusters to be merged, *i.e.* the cut on e_{ij} , depends on the location of the neutral cluster and the change in the χ^2 for the track–cluster energy consistency that would occur if the clusters were merged, $\Delta\chi^2 = (E_{\text{TRACK}} - E_j)^2/\sigma_E^2 - (E_{\text{TRACK}} - E_i - E_j)^2/\sigma_E^2$. If $e_{ij} > R_{ij}$ the clusters are merged. This *ad hoc* procedure gives extra weight to potential cluster matches where the consistency of the track momentum and associated cluster energy improves as a result of the match.

viii) Formation of Particle Flow Objects: The final stage of the algorithm is to create Particle Flow Objects (PFOs) from the results of the clustering. Tracks are matched to clusters on the basis of the distance closest approach of the track projection into the first 10 layers of the calorimeter. If a hit is found within 50 mm of the track extrapolation an association is made. If an identified kink is consistent with being from a $K^\pm \rightarrow \mu^\pm \nu$ or $K^\pm \rightarrow \mu^\pm \nu$ decay the parent track is used to form the PFO. The reconstructed PFOs are written out in LCIO[5] format.

4 Current Performance

Fig. 1a) shows an example of a PANDORAPFA reconstruction of a 100 GeV jet from a $Z \rightarrow u\bar{u}$ decay at $\sqrt{s} = 200$ GeV. The ability to track particles in the high granularity Tesla TDR calorimeter can be seen clearly. Fig. 1b) shows the total PFA reconstructed energy for $Z \rightarrow uds$ events with $|\cos\theta_{q\bar{q}}| < 0.7$, where $\theta_{q\bar{q}}$ is the polar angle of the generated $q\bar{q}$ system. These events were generated at $\sqrt{s} = 91.2$ GeV using the Tesla TDR detector model with a HCAL consisting of 63 layers and in total 6.9 interaction lengths. The root-mean-square deviation from the mean (rms) of the distribution is 2.8 GeV. However, quoting the rms as a measure of the performance over-emphasises the importance of the tails. It is conventional to quote the performance in terms of rms_{90} , which is defined as the rms in the smallest range of reconstructed energy which contains 90% of the events. For the data shown in Fig. 1b) the resolution achieved is $\text{rms}_{90}/E = 0.23/\sqrt{E(\text{GeV})}$, equivalent to a single jet energy resolution of 3.3%. The majority of interesting ILC physics will consist of final states with at least six fermions, setting a “typical” energy scale for ILC jets as approximately 85 GeV and 170 GeV at $\sqrt{s} = 500$ GeV and $\sqrt{s} = 1$ TeV respectively. Fig. 2 shows the jet energy resolution for $Z \rightarrow uds$ events plotted against $|\cos\theta_{q\bar{q}}|$ for four different values of \sqrt{s} . The current performance is summarised in Tab. 2. The observed jet energy resolution in simulated events is not described by the expression $\sigma_E/E = \alpha/\sqrt{E(\text{GeV})}$. This

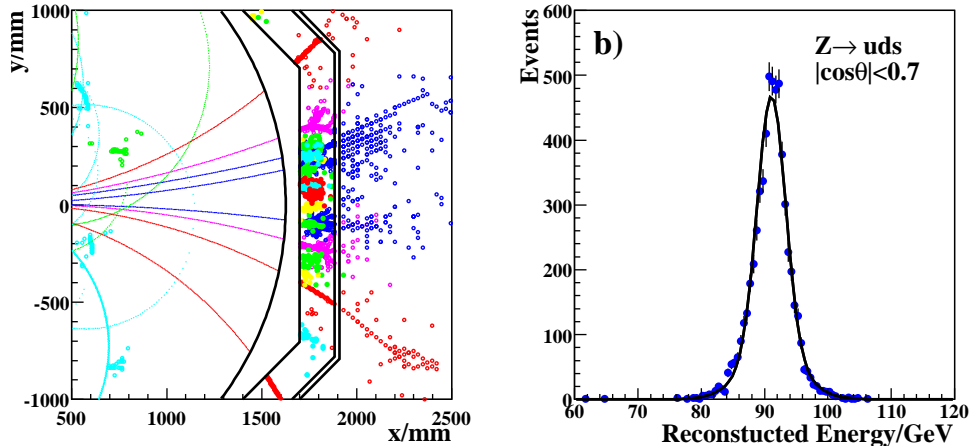


Figure 1: a) PANDORAPFA reconstruction of a 100 GeV jet in the MOKKA simulation of the Tesla TDR detector. b) The total reconstructed energy from reconstructed PFOs in $Z \rightarrow uds$ events for initial quark directions within the polar angle acceptance $|\cos \theta_{q\bar{q}}| < 0.7$. The solid line shows a fit to two Gaussians with a common mean; the broader Gaussian is constrained to contain 25 % of the events. The narrow Gaussian has a width of 2.2 GeV.

is not surprising, as the particle density increases it becomes harder to correctly associate the calorimetric energy deposits to the particles and the confusion term increases. A table also shows a measure of the single jet energy resolution, obtained by dividing rms_{90} by $\sqrt{2}$. For the jet energies considered (45 – 250 GeV) the fractional energy resolution is significantly better than the ILC requirement of 3.8 % obtained from the consideration of gauge boson di-jet mass resolution. It should be noted that in a real physics analysis the performance is likely to be degraded by jet finding, jet-pairing and the presence of missing energy from semi-leptonic heavy quark decays. Nevertheless the results presented in this paper already provide a strong indication that Particle Flow Calorimetry will be able to deliver the ILC jet energy goals and it is expected that the performance of PANDORAPFA will improve with future refinements to the algorithm.

5 Conclusions

Particle flow calorimetry is widely believed to be the key to reaching the ILC jet energy resolution goal of a di-boson mass resolution of $\sigma_m/m < 2.7\%$. Consequently, the design and optimisation of detectors for the ILC depends both on hardware and on sophisticated software reconstruction. Based on the PANDORAPFA reconstruction of simulated events in Tesla TDR detector concept, it has now been demonstrated that particle flow calorimetry can meet this goal at the ILC. This was not true at the time of LCWS06 and, thus, represents a significant step forward in the design and future optimisation of the ILC detector(s).

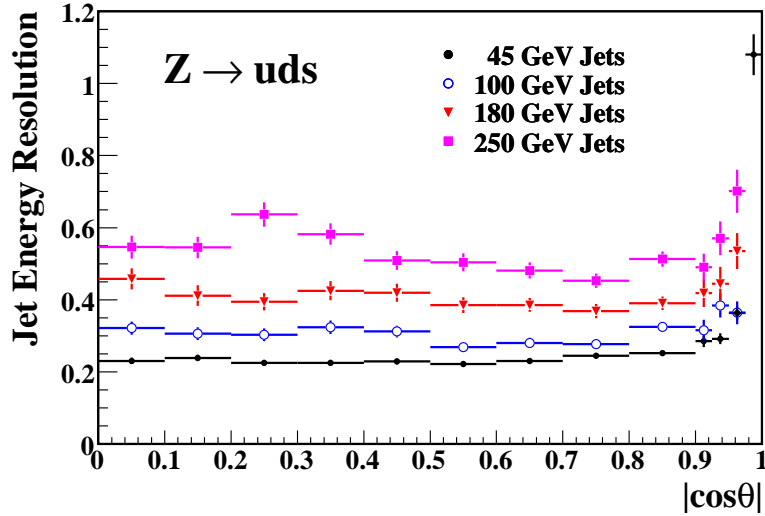


Figure 2: The jet energy resolution, defined as the α in $\sigma_E/E = \alpha\sqrt{E(\text{GeV})}$, plotted versus $\cos\theta_{q\bar{q}}$ for four different values of \sqrt{s} .

Jet Energy	rms ₉₀	rms ₉₀ / $\sqrt{E_{jj}(\text{GeV})}$	rms ₉₀ / $\sqrt{2}E_j$
45 GeV	2.2 GeV	23 %	3.3 %
100 GeV	4.1 GeV	29 %	2.9 %
180 GeV	7.4 GeV	39 %	2.9 %
250 GeV	12.0 GeV	54 %	3.4 %

Table 2: Jet energy resolution for $Z \rightarrow uds$ events with $|\cos\theta_{q\bar{q}}| < 0.7$, expressed as, rms₉₀ for the di-jet energy distribution, the effective constant α in $\text{rms}_{90}/E = \alpha(E_{jj})/\sqrt{E_{jj}(\text{GeV})}$, and the fractional jet energy resolution for a single jet.

References

- [1] M. A. Thomson, Proc. of EPS-HEP 2003, Aachen. Topical Vol. of Eur. Phys. J. C Direct (2004).
- [2] ALEPH Collaboration, D. Buskulic et al., Nucl. Inst. Meth. **A360** (1995) 481.
- [3] I.G. Knowles and G.D. Lafferty, J. Phys. **G23** (1997) 731.
- [4] M. G. Green, S. L. Lloyd, P. N. Ratoff and D. R. Ward, “Electron-Positron Physics at the Z”, IoP Publishing (1998).
- [5] <http://www-flc.desy.de/ilcsoft/ilcsoftware/>.
- [6] F. Gaede, “Status of ILC-LDC Core Software”, Proceedings of LCWS07, DESY, June 2007.
- [7] <http://polywww.in2p3.fr/activites/physique/geant4/tesla/www/mokka/>.
- [8] GEANT4 collaboration, S. Agostinelli et al., Nucl. Instr. and Meth. **A506** (2003) 3;
GEANT4 collaboration, J. Allison et al., IEEE Trans. Nucl. Sci. 53 (2006) 1.
- [9] TESLA Technical Design Report, DESY 2001-011, ECFA 2001-2009 (2001).

π^0 Reconstruction within the full simulation framework

Philippe Gris

Laboratoire de Physique Corpusculaire - IN2P3/CNRS
63177 Aubière Cedex - France

A study of π^0 's reconstruction within the full simulation of the LDC detector at ILC is presented. The impact of constrained fits is shown and a method to reconstruct π^0 's in physics events is exposed.

1 Introduction

Neutral pions are an important part of the particle content in hadronic events: in $t\bar{t}$ or hZ events at $\sqrt{s}=500$ GeV, they represent 20% of the visible energy. This result points out that π^0 's reconstruction has an impact on Particle-Flow and on detector optimisation. It is thus important not only to identify and reconstruct photons but to go further and to identify π^0 's.

Studies aiming at reconstructing π^0 's within the full simulation framework are exposed in this document. The software context is developed in a first part. Details on the calibration of the electromagnetic (EM) calorimeter are given in a second part. The constrained fit method applied on single π^0 's is described in a third section. An approach to reconstruct π^0 's in physics events is exposed in a fourth part.

2 Framework of the study

The full simulation chain was composed of the following steps: event generation has been performed with `Pythia v6.321`[1], the `GEANT4` based full Monte Carlo simulation with `Mokka v06.02`[2] and the reconstruction with `Marlin v00-09-05` [3] and `MarlinReco v00-02` [4]. Analyses were performed with `Root v5.10.00` [6]. The detector model used was `LDC00`[2]. Events generated were composed of single photon, of single π^0 or of all π^0 's coming from $hZ \rightarrow b\bar{b}\nu\bar{\nu}$ at $\sqrt{s}=500$ GeV.

3 EM calorimeter calibration

The EM calorimeter has to be calibrated before addressing the π^0 's reconstruction. For this single photons have been generated with `Mokka` and reconstructed with `Marlin` at the following energies: 0.25, 0.30, 0.35, 0.40, 0.50, 1, 2, 4, 10, 25, 50 GeV (angular coverage: $0 \leq \theta \leq \pi/2$ with a step of 0.1 and $0 \leq \Phi \leq 2\pi$ with a step of $2\pi/16$). The goal of the calibration procedure was to evaluate α_0 and β_0 in $E_\gamma^{clus} = \alpha_0(E_1^{30} + \beta_0 E_{31}^{40})$ where E_i^j is the sum of the raw energies deposited in the silicon cells of the i -to- j layers. All the hits were used (no clustering algorithm applied). The β_0 parameter is firstly evaluated by minimizing $\sigma(E_1^{30} + \beta E_{31}^{40}) / \langle E_1^{30} + \beta E_{31}^{40} \rangle$. α_0 is then given by the mean value of $E_\gamma^{truth} / (E_1^{30} + \beta_0 E_{31}^{40})$ where E_γ^{truth} is the Monte-Carlo truth energy of the generated photon. The results are $\beta_0 = 3.0 \pm 0.1$, $\alpha_0 = 27.62 \pm 0.03$ and $\alpha_0 = 28.83 \pm 0.05$ for the central and the endcap parts respectively.

Once the EM calorimeter is calibrated, the performance in terms of energy and angular resolution as well as on linearity may be evaluated. Results are summarized in table 1.

	Barrel		Endcap	
Energy resolution	$\frac{\sigma_E}{E} = 1.6\% \oplus \frac{12.4\%}{\sqrt{E}}$		$\frac{\sigma_E}{E} = 1.4\% \oplus \frac{12.1\%}{\sqrt{E}}$	
Non linearity	< 2.5%		< 5%	
	E<1.5 GeV	E>1.5 GeV	E<1.5 GeV	E>1.5 GeV
θ resolution σ_θ (mrad)	$0.34 + \frac{0.94\sin\theta}{\sqrt{E}}$	$0.02 + \frac{1.4\sin\theta}{\sqrt{E}}$	$0.26 + \frac{0.55\cos\theta}{\sqrt{E}}$	$0.007 + \frac{0.96\cos\theta}{\sqrt{E}}$
Φ resolution σ_Φ (mrad)	$0.39 + \frac{1.01}{\sqrt{E}}$	$0.01 + \frac{1.56}{\sqrt{E}}$	$0.94 + \frac{1.5}{\sqrt{E}}$	$0.02 + \frac{2.9}{\sqrt{E}}$

Table 1: LDC00 EM calorimeter resolutions after calibration

4 Single π^0 fit

To study neutral pion reconstruction within the full simulation framework, single π^0 have been generated with **Mokka** at the following energies: 0.4, 0.6, 0.7, 1.2, 4.9, 12.4, 29.5 GeV and for similar values in (θ, Φ) as indicated in part 3. A clustering has been performed with the **TrackWiseClustering** processor [5]. Events with exactly two clusters were selected.

To correct for mismeasurements and fluctuations, a constrained fit has been applied on cluster pairs with the minimization of the following χ^2 :

$$\chi^2 = \sum_{i=1}^2 \frac{(E_i^{cl} - E_i)^2}{\sigma_{E_i}^2} + \sum_{i=1}^2 \frac{(\theta_i^{cl} - \theta_i)^2}{\sigma_{\theta_i}^2} + \sum_{i=1}^2 \frac{(\Phi_i^{cl} - \Phi_i)^2}{\sigma_{\Phi_i}^2} \quad (1)$$

where $E_i^{cl}, \theta_i^{cl}, \Phi_i^{cl}$ are the energy and angles of the i -th cluster. E_i, θ_i, Φ_i are the corrected energy and angles coming out of the fit procedure. The values of the variances $\sigma_{E_i}^2, \sigma_{\theta_i}^2, \sigma_{\Phi_i}^2$ were set to the estimation of table 1.

Only events for which the fit has converged, the number of iterations was less than 5, and the χ^2 of the fit is less or equal than 3.9 were selected. The impact of the fit on the energy resolution is shown on figure 1. The gain is spectacular at very low energies (few hundred MeV) where the resolution is ten times better after the fit. A similar study with single π^0 's coming from $hZ \rightarrow b\bar{b}\nu\bar{\nu}$ events has shown that the constrained fit divides the relative energy resolution by a factor of two (from 7.4% to 3.4%).

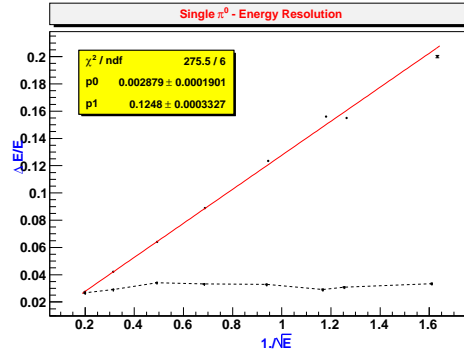


Figure 1: Energy resolution $\Delta E/E$ as a function of $1/\sqrt{E}$ for single π^0 before (full line) and after (dashed line) application of a constrained fit.

5 Method to reconstruct π^0 in physics events

The number of π^0 's produced in a given physics event can be quite large: for $hZ \rightarrow b\bar{b}\nu\bar{\nu}$ events at $\sqrt{s}=500$ GeV, 12 to 13 π^0 on average are produced leading to more than 20 clusters in the EM calorimeter.

Cluster pairs have to be formed so as to reconstruct π^0 's. A strategy is thus needed to perform a correct pairing (ie association of clusters coming from the same π^0) and to minimize fake pair production. A study has been performed using MC-truth information of photons coming from π^0 decays in $hZ \rightarrow b\bar{b}\nu\bar{\nu}$ events at $\sqrt{s}=500$ GeV and $hhZ \rightarrow b\bar{b}b\bar{b}\nu\bar{\nu}$ at $\sqrt{s}=800$ GeV. Energies and angles of the photons were smeared according to the resolutions given in table 1. The "clusters" (here defined as the smeared MC-truth photons) were then associated on the basis of a probability depending on the mass of the pair, and/or the angle between the two objects. The pair giving the highest probability was selected and the corresponding clusters were removed from the cluster list. To quantify the quality of the procedure, we have used the ratio of the energy sum of pairs coming from π^0 's (which we know from MC) divided by the total π^0 energy of the event. The figure 2 shows clearly the importance of the reconstructed mass in our estimator. When the angle is also used, a slight improvement is observed: the mean value of the $E_{\pi^0}(goodpairs)/E_{\pi^0}(all)$ is 75% (rms:23%) when the mass is used. It increases to 78% (rms: 21%) when the mass and the angle information are combined.

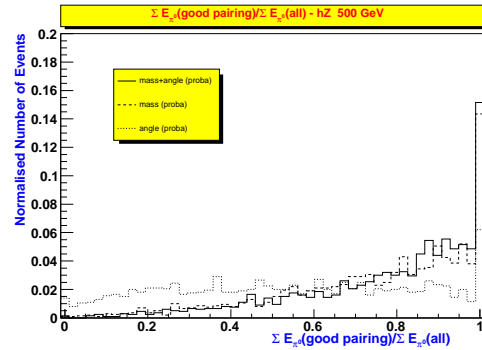


Figure 2: Fraction of good π^0 energy for $hZ \rightarrow b\bar{b}\nu\bar{\nu}$ events at $\sqrt{s}=500$ GeV. The results are given for three estimators using the mass, the opening angle and the mass+the opening angle of the cluster pairs.

6 Conclusion

A study on various aspects of π^0 reconstruction was presented in this document. It was shown that constrained fits on single π^0 greatly improve the energy resolution in particular at low energies. A strategy to reconstruct π^0 's in physics events was developed. Using an estimator based on the mass and the angle of cluster pairs, it was shown that 77% to 78% of the total π^0 energy in $hZ \rightarrow b\bar{b}\nu\bar{\nu}$ events at $\sqrt{s}=500$ GeV could be tagged properly.

References

- [1] T.Sjostrand, S.Mrenna and P.Skands JHEP05 (2006) 026
- [2] <http://polywww.in2p3.fr/activites/physique/geant4/tesla/www/mokka/mokka.html>
- [3] <http://ilcsoft.desy.de/marlin>
- [4] <http://www-flc.desy.de/ilcsoft/ilcsoftware/MarlinReco>
- [5] TrackwiseClustering in MARLIN presented by Dennis Martsch - ILC Software Workshop June 2005
- [6] <http://root.cern.ch>
- [7] <http://lcio.desy.de/>

π^0 reconstruction in the GLD calorimeter

Daniel Jeans for the ACFA-SIM-J group

Kobe University, Department of Physics
1-1 Rokkodai-cho, Nada-ku, Kobe, Japan

The baseline design of the GLD calorimeter has active layers made of 5×1 cm scintillator strips. Adjacent layers have strips orientated in orthogonal directions. An algorithm is being developed to perform clustering in this geometry, which should give an effective granularity of almost 1×1 cm.

1 Introduction

Many physics processes produced at ILC are expected to produce hadronic jets, and the success of the ILC physics program depends in part on the precise measurement of their energies. GLD plans to use a PFA based approach to the measurement of jet energies. The identification of π^0 decays to pairs of photons is expected to lead to some improvement of the jet energy resolution, since a kinematic fit can be applied to the two photons, constraining their invariant mass to be equal to the known π^0 mass, and thereby improving the estimate of the photons' energies.

The identification of high energy π^0 decays requires a calorimeter of fine granularity, since the two photons may only be separated by a small distance (\sim cm). The GLD calorimeter seeks to achieve this granularity by means of a strip structure, where alternate layers of the calorimeter consist of long scintillator strips orientated in orthogonal directions.

This paper describes the current status of an algorithm which is being developed to perform clustering in such a strip calorimeter, initially applied to the identification of π^0 decays.

2 Strip clustering

We develop a clustering algorithm which attempts to reconstruct maximal information about calorimetric shower shapes; later stages of the algorithm will decide which groupings of energy deposits correspond to single incident particles. Clustering in a strip calorimeter presents some complications with respect to calorimeters with square cells. Two nearby clusters (from the two photons from π^0 decay, for example) may be resolved in layers of one polarity, but merged into a single cluster in the other layers.

The algorithm proceeds as follows:

- perform a nearest neighbour clustering separately in each calorimeter layer.
- look for evidence of substructure in the resulting clusters: considering only strips with an energy deposit above some value (half the maximum energy deposit in the cluster, for example), perform a second nearest neighbour clustering. If this re-clustering gives more than one cluster, split the original cluster, assigning low energy cells below the energy cutoff to the closest cluster.

- search for neighboring clusters in the layers immediately above and below the one being considered; if neighbours are found both above and below, check if these two are also each others neighbors: if yes, make a “triplet” with these three clusters.
- if a single cluster is the central member of more than one triplet, split it cell-by-cell, assigning cells to the closest triplet.
- a figure-of-merit (“quality”) is then defined for each identified triplet, considering all combinations of the three clusters which make up the triplet. This essentially tests how many cells in the clusters are each others neighbours, and weights this with the cells’ energies.

Once a series of triplets has been identified in the calorimeter, the next step is to combine them, in a step we call calorimeter “tracking”. Starting from the innermost triplet, we search for triplets starting in the next layer, whose first two clusters are the same as the last two layers of the initial triplet. We continue to move deeper into the calorimeter in this way, adding matching triplets to the “track”. In cases where more than one triplet matches a track, the one with highest “quality” is chosen. When one “track” has finished, the innermost unassigned triplet is used as the seed triplet for the next “track”. If this seed triplet is matched to an existing track (but was not used because of low “quality”), a “mother”/“daughter” relationship between the two tracks is established.

3 Photon- π^0 separation

The performance of this algorithm was studied by comparing single 10 GeV photon events to single 10 GeV π^0 events, fully simulated in the GLD detector. The distance between the two photons from a 10 GeV π^0 decay at the front face of the ECAL (at a radius of 210cm in the barrel) is expected to be around 6cm, just a little larger than the length of the scintillator strips (of size 5×1 cm). The extent to which the algorithm could distinguish two photons in the π^0 decays was measured. To do this, we consider only calorimeter “tracks” which start in the first two layers of the calorimeter, and do not have any “mothers”. In photon events, we expect to find only one such track, in π^0 events we expect to find two, one from each photon.

Figure 1 is an event display of a single 10 GeV π^0 event, reconstructed in three different ways. The first two use a 1×1 cm cell size, the first reconstructed with the current GLD clustering algorithm, the second with the new “track” clustering algorithm. The standard algorithm (based on nearest neighbours) resolves only a single cluster, while the “track” clustering detects much more substructure. The third figure shows the results of “track” clustering with strips of 5×1 cm size. The structure is again reconstructed, although it also looks rather fragmented: many tracks are found inside the cluster. More work is clearly needed to combine these small tracks together to create a pair of photon objects.

In Fig. 2 we show the number of such early, mother-less tracks reconstructed in single 10 GeV photon and π^0 events, when different strip sizes are used, from 1×1 cm to 20×1 cm, and some configurations with larger strip width. We see that for photon events (left hand plot), the number of such tracks is indeed usually 1, with some fraction of events reconstructed with either zero or two tracks. The number of misreconstructed events depends relatively weakly on the strip length: for longer strips, more events are reconstructed with two tracks. The reason for this feature is not yet fully understood.

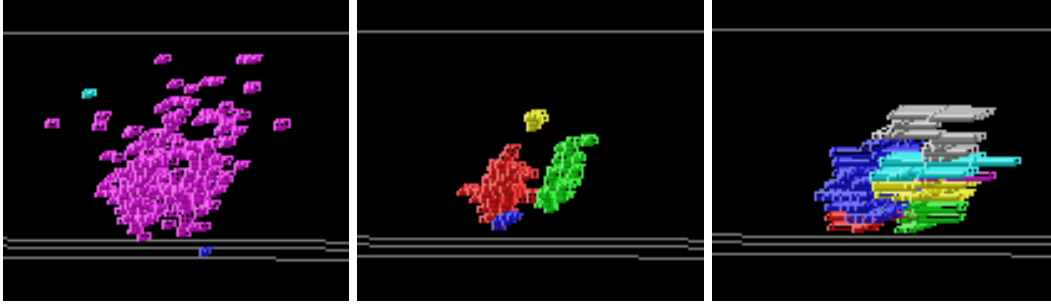


Figure 1: Display of a single 10 GeV π^0 event. Left: standard GLD clustering with 1×1 cm cell size; Centre: “track” clustering with 1×1 cm cell size; Right: “track” clustering with 5×1 cm cell size. Different colours denote separate “tracks”.

The right hand plot, for π^0 events, shows that these events are usually reconstructed with two early tracks, although a relatively large fraction is reconstructed with only one. Smaller fractions are reconstructed with zero or 3 tracks. The relative populations of two-track and one-track events depend quite strongly on the strip size and shape: when the strips are larger, the event is more often reconstructed with only a single “track”: this is to be expected, since the granularity of the calorimeter is less fine, and the photons more difficult to resolve.

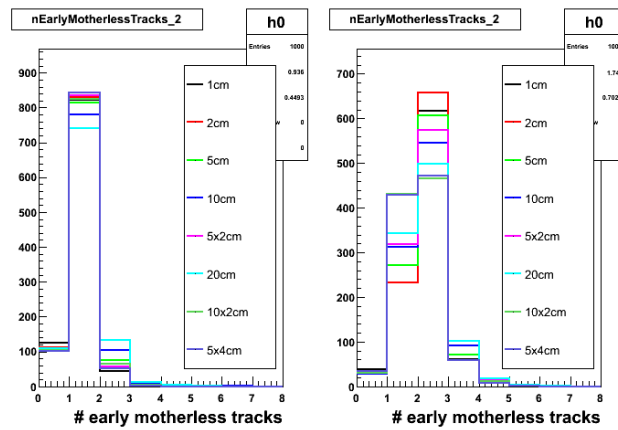


Figure 2: Number of early mother-less tracks reconstructed in 10 GeV photon (left) and π^0 (right) events. Different color histograms are the results of different strip shapes and sizes.

4 Conclusion

We are developing a clustering algorithm to be used in the GLD strip calorimeter. We are studying its performance in single photon and π^0 events, attempting to distinguish the two types of events. Preliminary results look reasonable: the two photons from a 10 GeV π^0 decay can usually be resolved, and the performance depends on the strip size in the expected way. The algorithm will be further developed, and eventually be integrated in a full PFA algorithm.

The LCFIVertex Package: vertex detector-based Reconstruction at the ILC

S. Hillert on behalf of the LCFI collaboration

University of Oxford - Department of Physics
Denys Wilkinson Building, Keble Road, Oxford OX1 3RH - UK

The contribution gives an overview of the LCFIVertex package, providing software tools for high-level event reconstruction at the International Linear Collider using vertex-detector information. The package was validated using a fast Monte Carlo simulation. Performance obtained with a more realistic GEANT4-based detector simulation and realistic tracking code is presented. The influence of hadronic interactions on flavour tagging is discussed.

1 Introduction

At the International Linear Collider (ILC), the vertex detector is expected to provide high-precision measurements with a point resolution of $\sim 3\mu\text{m}$ or below over an unprecedented acceptance region of $|\cos\theta| < 0.98$, where θ is the track polar angle. The ambitious detector design will result in excellent vertexing and flavour tagging performance. This contribution [1] describes scope, validation and resulting performance of the LCFIVertex package, a software package for vertex detector-based event reconstruction at the ILC.

The LCFIVertex package provides tools for vertexing, flavour tagging and the determination of the heavy quark charge sign of the leading hadron in heavy flavour jets. For vertexing, the ZVTOP topological vertex finding algorithm developed by D. Jackson for SLD is implemented [2]. For the first time within an ILC software environment, the more specific ZVKIN branch of the algorithm is provided in addition to the widely used ZVRES branch.

The ZVRES approach uses a vertex function calculated from “probability tubes” representing the tracks in a jet. Maxima of the vertex function in three-dimensional space are sought and the χ^2 of the vertex fit is minimised by an iterative procedure. In contrast, ZVKIN initially determines the best approximation to the direction of flight of the B -hadron in candidate b -jets and uses the additional kinematic information provided by this “ghost track” to find 1-prong decay vertices and short-lived B -hadron decays not resolved from the interaction point.

Flavour tagging is accomplished using a neural net approach. The software includes a full neural network package written by D. Bailey. By default, the flavour tag is obtained from the algorithm developed by R. Hawkings [3], however it should be noted that the implementation is highly flexible, allowing the user to change the input variables for the network, its architecture and training method.

Determination of the quark charge is initially limited to cases in which the leading hadron is charged using an approach developed at SLD and modified as described at a previous LCWS workshop [4]. With ZVKIN, the basis is provided for extending the functionality to cover also neutral hadrons, using the SLD charge dipole technique [5].

The C++-based package uses the LCIO data format [6] for input and output and is interfaced to the analysis and reconstruction framework MarlinReco [7]. An interface to the

JAS3-based US software framework `org.lcsim` [8] is planned to be written in the near future. The code is available at the ILC software portal [9] and the Zeuthen CVS repository [10]. To facilitate comparisons of results from ILC physics studies performed by different groups, in addition a new CVS repository called “tagnet” has been set up in Zeuthen for providing trained neural networks in the format used by this package. Users training their own neural networks, e.g. for specific physics processes, are encouraged to make them available to the community in this way.

2 Code validation

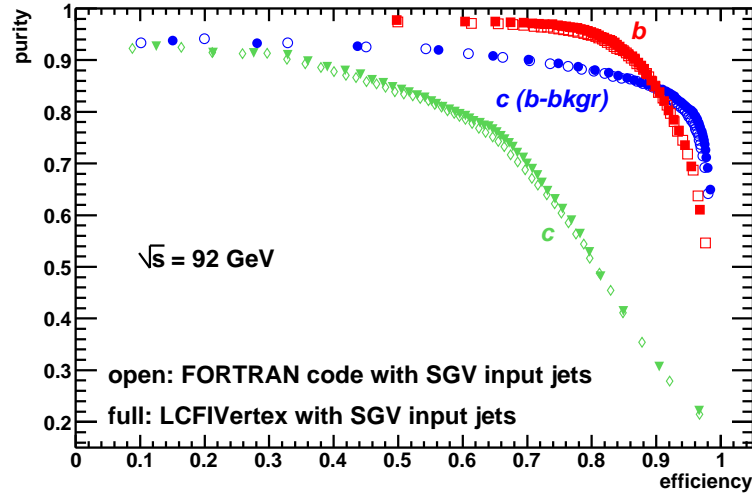


Figure 1: Comparison of tagging performance achieved with the LCFIVertex package and the previous FORTRAN code, using identical input events at the Z -resonance. Tagging purity is shown as function of efficiency for b -jets and c -jets. Performance for c -jets assuming only b -background is also shown. All tagging results are in excellent agreement.

Prior to development of the LCFIVertex package, part of its functionality was available in the form of FORTRAN routines which had been used in conjunction with the BRAHMS Monte Carlo (MC) simulation and reconstruction [11] used for the TESLA-TDR [12]. The fast MC program Simulation a Grande Vitesse, SGV, developed by M. Berggren [13] and interfaced to this FORTRAN flavour tag [14], allowed detailed cross checks to be performed during the development phase. Results from tests of various separate parts of the package were presented at the 2006 ECFA ILC workshop [15].

As final step of the code validation, the resulting flavour tagging performance achieved with the FORTRAN/SGV code and with our package was compared, using identical $e^+e^- \rightarrow q\bar{q}$ events ($q = u, d, s, c, b$) at the Z -resonance and at a centre of mass energy of $\sqrt{s} = 500 \text{ GeV}$, generated with the PYTHIA MC program [16]. The SGV MC simulation was extended to write out the relevant information in LCIO format as input to our code using the FORTRAN interface provided within LCIO.

Figure 1 shows the resulting tagging performance from the LCFIVertex package compared to that of the FORTRAN code in terms of tagging purity vs efficiency, for events at the Z -resonance. Excellent agreement is seen for the b - and the c -tag as well as for the c -tag when considering b -background only, as is relevant for some physics processes. Agreement at the higher energy is equally good.

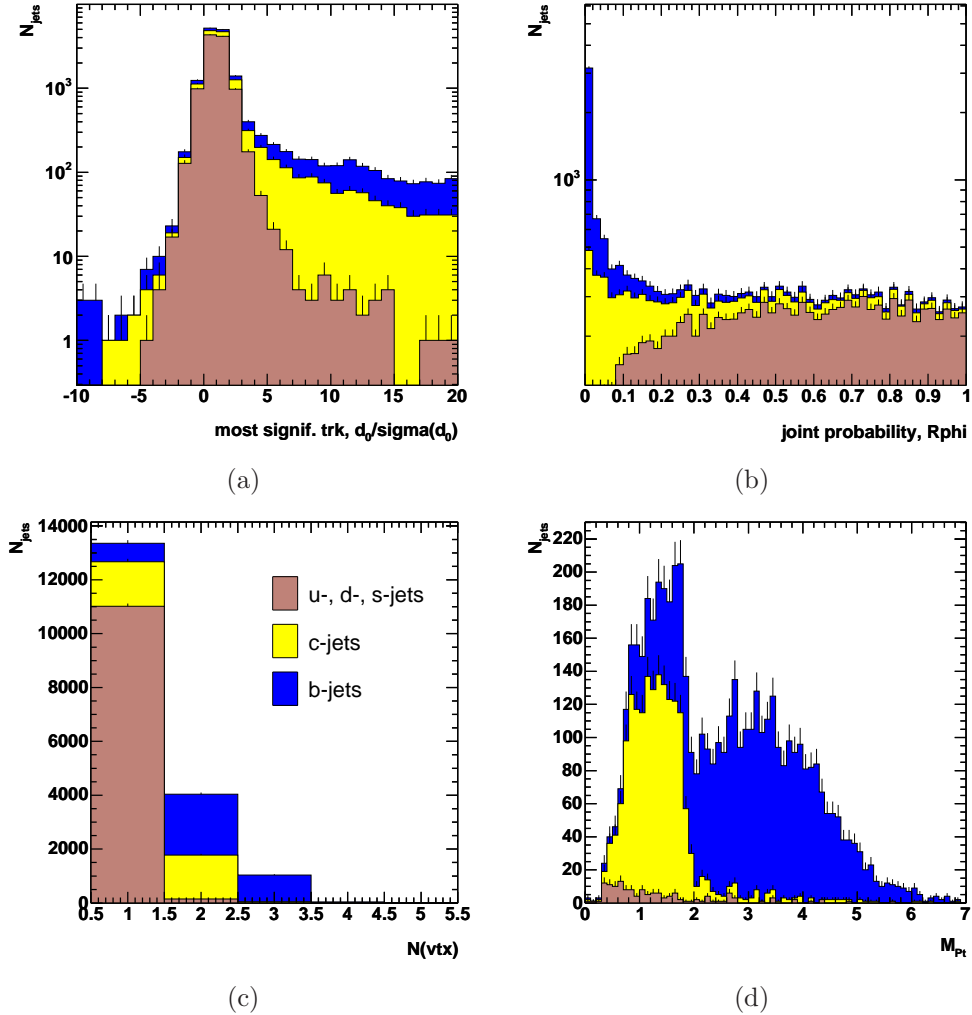


Figure 2: Some of the variables used to distinguish the different jet flavours. Shown are (a) the impact parameter significance of the most significant track in the jet, (b) the “joint probability” for all tracks in the jet to originate at the event vertex, (c) the vertex multiplicity in the jet and (d) the P_t -corrected vertex mass.

3 Performance obtained with full MC

Following the successful code validation, performance of the LCFIVertex package with more realistic input was studied. For this purpose, the same PYTHIA events used for the validation were passed through the GEANT4-based full MC simulation MOKKA, version 06-03 [17], assuming the detector model LDC01Sc, in which the vertex detector layers are approximated by cylinders.

Photon conversions were switched off in GEANT, as these can easily be suppressed later. Tracks stemming from hadronic interactions in the beam pipe and in the vertex detector layers were suppressed at the track selection stage using MC information.

The LDCTracking package by A. Raspereza [18] was used to simulate tracker hit digitization assuming simple Gaussian smearing of the hits, and for track reconstruction. Resulting tracks were fed into the Wolf particle flow algorithm [19] to obtain ReconstructedParticle objects, which were passed on to the Satoru jet finder [20] to perform jet finding using the Durham kT -cluster algorithm with a y -cut value of 0.04.

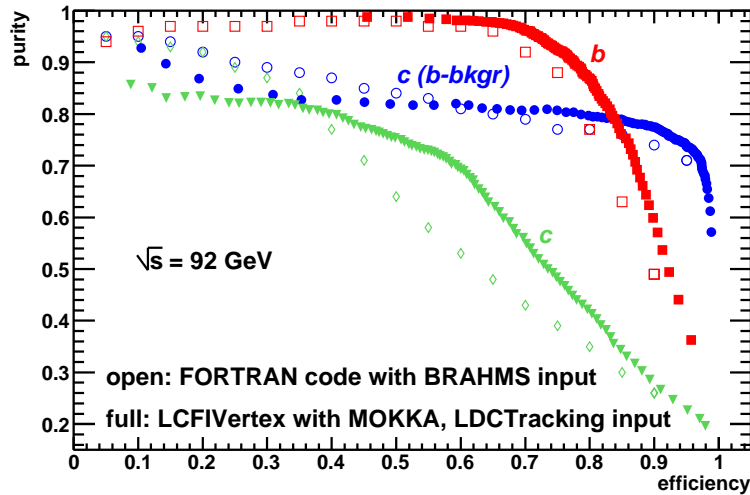


Figure 3: Comparison of tagging performance achieved with the LCFIVertex package and the previous FORTRAN code, using identical input events at the Z -resonance. For the FORTRAN case, events were passed through the BRAHMS simulation and reconstruction, for the LCFIVertex package the detector response was simulated using MOKKA and event reconstruction performed using MarlinReco. The new code, run with this input, yields better tagging performance, see text.

The default track selection used in the LCFIVertex package is based on a previous study [21] using the BRAHMS MC and reconstruction, with the modification that tracks stemming from the decays of K -shorts and Lambdas are suppressed using MC information.

Figure 2 shows the most sensitive input variables for the flavour tag as used in the Hawkings approach. Compared to the previous BRAHMS result [21], these variables provide somewhat better separation power. The resulting flavour tagging performance, presented in Figure 3, is hence improved. Reasons for the difference seen may include a better detector

resolution of $2\ \mu\text{m}$ being assumed for the new result, compared to the former value of $3.5\ \mu\text{m}$, as well as the suppression of K-short and Lambda-decays, photon conversions and hadronic interactions, all of which will need to be taken into account properly in a future version of the software.

The LDCTracking code can be run in different modes. The results shown in Figure 2 and Figure 3 correspond to the “track cheater”, which uses MC information to assign tracker hits to the different tracks, run with only the Silicon-based detectors, i.e. vertex detector, Silicon intermediate tracker (SIT) and forward tracker (FTD). It was shown that when including the hits in the TPC and replacing the track cheater with an algorithm including realistic pattern recognition, the resulting tagging performance does not change significantly.

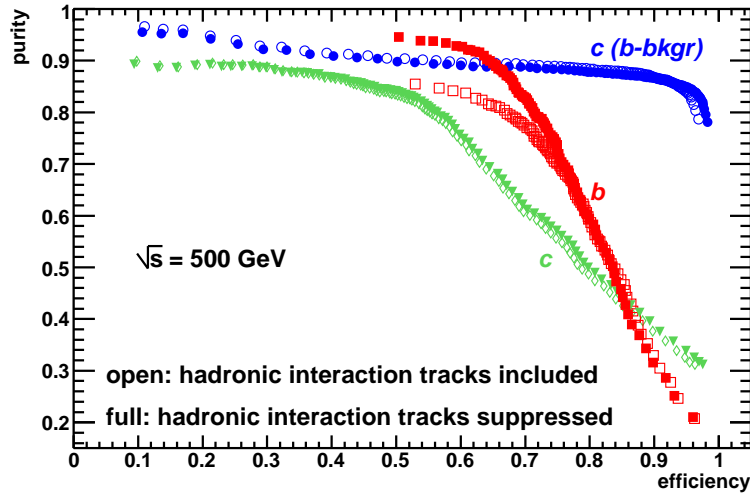


Figure 4: Effect of including tracks arising from hadronic interactions in the detector material and the beam pipe in the reconstruction, compared to the case, in which these tracks are suppressed using MC information. At a centre of mass energy of $\sqrt{s} = 500\ \text{GeV}$, b -tagging performance clearly degrades.

The effect of including tracks arising from hadronic interactions in detector material and beam pipe is shown in Figure 4, compared to the current default settings of the package that suppress these tracks using MC information. At a centre of mass energy of $500\ \text{GeV}$, the b -tag degrades significantly when tracks from hadronic interactions are included. At the Z -resonance this effect is negligible. Note that the current implementation of the suppression of the effect is based on MC information and only works for the specific detector model used for the initial full MC study (LDC01Sc).

4 Summary

The LCFIVertex package provides the topological vertex finder ZVTOP, a flexible flavour tag with the Hawkings approach as default and determination of quark charge in heavy flavour jets. Validation of this C++ based code using the fast MC program SGV to simulate detector

response and event reconstruction has shown it to be in good agreement with results from an earlier FORTRAN implementation, in comparison to which the new code has extended functionality, a higher degree of flexibility and improved documentation.

With input from the GEANT4-based detector simulation MOKKA and the event reconstruction package MarlinReco, the LCFIVertex package yields results comparable to those previously obtained from BRAHMS, with the differences being likely to be accounted for by a number of unrealistic simplifications made in the current first release version of the new code. One of these is the suppression of hadronic interaction effects using MC information, giving a clear improvement at high centre of mass energies.

References

- [1] Slides:
<http://ilcagenda.linearcollider.org/contributionDisplay.py?contribId=76&sessionId=76&confId=1296>
- [2] D. J. Jackson, Nucl. Instrum. Meth. A **388** (1997) 247;
- [3] S. M. Xella Hansen, C. Damerell, D. J. Jackson and R. Hawkings,
Prepared for 5th International Linear Collider Workshop (LCWS 2000), Fermilab, Batavia, Illinois, 24-28 Oct 2000, <http://www-flc.desy.de/lcnotes/notes/LC-PHSM-2001-024.ps.gz>
- [4] S. Hillert [LCFI Collaboration], *In the Proceedings of 2005 International Linear Collider Workshop (LCWS 2005), Stanford, California, 18-22 Mar 2005, pp 0313*, <http://www.slac.stanford.edu/econf/C050318/papers/0313.PDF>;
- [5] J. Thom, "Search for B/s0 - anti-B/s0 oscillations with a charge dipole technique at SLD", DESY-THESIS-2002-006;
T. R. Wright, "Parity violation in decays of Z bosons into heavy quarks at SLD. ((C))", UMI-30-33372;
- [6] F. Gaede, T. Behnke, N. Graf and T. Johnson, *In the Proceedings of 2003 Conference for Computing in High-Energy and Nuclear Physics (CHEP 03), La Jolla, California, 24-28 Mar 2003, pp TUKT001* arXiv:physics/0306114;
- [7] O. Wendt, F. Gaede and T. Kramer, arXiv:physics/0702171;
- [8] org.lcsim web page at <http://www.lcsim.org/software/lcsim/>;
- [9] ILC software portal at <http://ilcsoft.desy.de/portal>;
- [10] Zeuthen CVS web interface <http://www-zeuthen.desy.de/lc-cgi-bin/cvsweb.cgi/>;
- [11] T. Behnke and G. A. Blair, <http://www-flc.desy.de/lcnotes/notes/LC-T00L-2001-005.ps.gz>;
- [12] T. Behnke, S. Bertolucci, R. D. Heuer and R. Settles, ECFA-2001-209;
- [13] SGV web page at <http://delphiwww.cern.ch/~berggren/sgv.html>;
- [14] V. Adler, "Optimising of design parameters of the TESLA vertex detector and search for events with isolated leptons and large missing transverse momentum with the ZEUS-experiment (HERA II)", DESY-THESIS-2006-012;
- [15] B. Jeffery, *Contribution to International Linear Collider Workshop (ILC-ECFA and GDE Joint Meeting), Valencia, 6-10 November 2006*,
- [16] T. Sjostrand, S. Mrenna and P. Skands, JHEP **0605** (2006) 026 arXiv:hep-ph/0603175;
- [17] P. Mora de Freitas, *Prepared for International Conference on Linear Colliders (LCWS 04), Paris, France, 19-24 Apr 2004*;
- [18] A. Raspereza, "LDC Tracking Software", *in these proceedings*;
- [19] A. Raspereza, arXiv:physics/0601069;
- [20] S. Yamashita, OPAL Technical Note TN579 (1998);
- [21] S. M. Xella Hansen, M. Wing, D. J. Jackson, N. De Groot and C. J. S. Damerell, "Update on flavour tagging studies for the future linear collider using the BRAHMS simulation", <http://www-flc.desy.de/lcnotes/notes/LC-PHSM-2003-061.ps.gz>.

Simulation Study of the FPCCD Vertex Detector for the ILC

Tadashi Nagamine

Tohoku University - Department of Physics
Sendai, Miyagi - Japan

Performance of the FPCCD based vertex detector for the ILC has been studied using Geant4 based simulation program developed for GLD. We present impact parameter resolutions, impact on track-hit matching efficiencies at the inner most layers by high background rates, performance of pair background rejection using cluster sizes.

1 Introduction

We have studied a vertex detector design based on CCD with very small pixels, FPCCD, using a Geant4 based simulation program developed for the GLD detector concept [2]. In the ILC, very large amount of pairs of e^+ and e^- are produced in collisions of very small beams, those pairs are expected to be very severe background in the vertex detector. From the study based on beam interaction simulation program, CAIN, a hit rate in an inner most layer of the vertex detector is estimated to be more than 50 hits / mm^2/train . Since FPCCD accumulate signals during a whole beam train, those pixels have to be as small as $5\mu\text{m}$ by $5\mu\text{m}$ to lower the background occupancy less than 1% level. Since those pairs have low transverse momentum, thus large incident angle tracks, FPCCD have to be $15\mu\text{m}$ thick fully depleted sensitive layers to reduce the background cluster sizes. Another feature of the vertex detector is that every two adjacent layers are put close together, gaps of those pair of layers are 2 mm. Here we show some geometrical configuration of the vertex detector in this simulation study in the Table 1. The thickness of each layer is $50\mu\text{m}$ with $30\mu\text{m}$ Si which is equivalent to materials of ladder supports, total material budget per layer is $80\mu\text{m}$ Si or 0.09 % of X_0 . We assume Be beam pipe with $250\mu\text{m}$ thick and 18 mm radius. Details of the FPCCD vertex detector and other sub-detectors in GLD detector concept is described in GLD Detector Outline Document [2].

2 Expected Impact Parameter Resolutions

We use a Kalman filter based track fit program to study the impact parameter resolutions. In the track fitting procedure, only true hits of tracks in TPC, SIT and the vertex detector are used for the track fits. Using helix parameters of the fitted tracks,

Layer #	1	2	3	4	5	6
Radius (mm)	20	22	32	34	48	50
Length (mm)	65	65	100	100	100	100

Table 1: Radius and Length of the layers

the impact parameters are calculated for muons with momentum between 0.5 GeV/c through 100 GeV/c. The impact parameters in the $R-\phi$ plane are show in Figure 1. As seen in the figure, the resolutions over momentum of 1GeV/c are comparable to that shown in [2], which is expressed as $\sigma_b \leq 5 \pm \frac{10}{p\beta \sin^{3/2} \theta}$ (μm).

3 Effects of Background in Track Finding

To evaluate track finding capability in very high background rate, which are expected more than 50 hits/mm²/track in the two inner most layers, Layer 1 and Layer 2. Due to lack of a track finding program in software tool we used currently, we follow a procedure described below. In this procedure, we assume sizes of the clusters are negligible.

1. Perform track fitting with true hits of TPC, SIT and the vertex detector except for the hits of the two inner layers, Layer 1 and Layer 2.
2. Extrapolate the track onto Layer 2.
3. Calculate a distant between the extrapolated hit point and the true hit on Layer 2 and make a probability distribution function(PDF).
4. Generate true hit according to the PDF and background hits uniformly at 50, 100 and 200 hits/mm²/train.
5. Accept that track fit successful if a distance of the true hit is less background hits from the expected hit point.

The procedure are carried out for tracks at $\cos\theta = 0$ and momentum between 0.5 through 4.0 GeV/c to evaluate the efficiencies to find true hits of the tracks. The results are show in Figure 3. As seen in the figure, inefficiencies are less than 10% below momentum of 0.5 GeV/s at background rate at 100 hits/mm²/train. Since Layer 1 is very close to Layer 2, efficiencies of Layer 1 is almost same as ones of Layer 2. Thus, requiring two hits that one on Layer 1 and the other on Layer 2 are close enough to the track, inefficiency caused by background hits is reduced. Since in this study, cluster size and cluster overlaps are not taken into account yet, more detailed study is necessary.

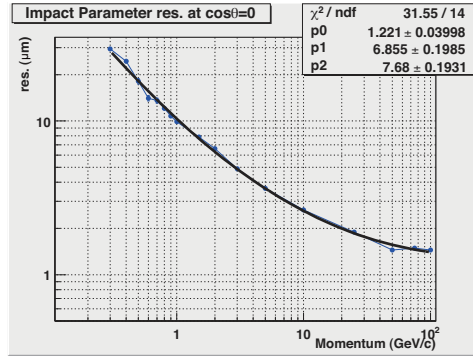


Figure 1: The momentum dependence of the impact parameter resolution.

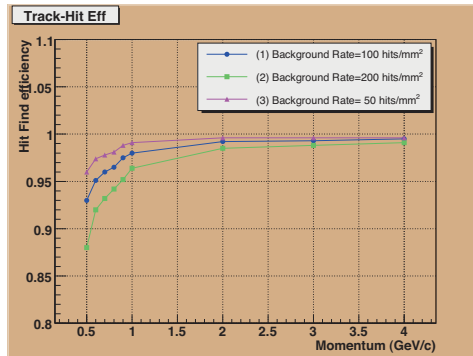


Figure 2: Efficiencies on Layer 2 under the background levels at 50, 100 and 200 hits/mm²/train.

4 Rejection of Pair Background Clusters

Since the pair background tracks have large curvatures, those traverse several pixels as many as 8 pixels in the ϕ direction and as many as 6 in the z direction. And those numbers of traversed pixels are independent of the hit positions. On the other hand, the incident angles of the high momentum tracks to the vertex detector layers in R - ϕ plane are close to normal and traverse one or two pixels in the ϕ direction. Numbers of pixels traversed in the z directions depend on polar angles of tracks and are proportional to z positions from the interaction point. Using these differences of the cluster sizes, we can discriminate clusters of the pair background. Figure 3 shows the results after the rejection using cluster sizes. The figure shows that rejection factor for the pair background at large Z position is about 20, while the losses of the efficiencies for high momentum tracks are at level of 1%.

5 Conclusions

We have studied the performances the vertex detector design using the FPCCD sensor technology. The impact parameter resolutions are close to the requirements in GLD. The impact on tracking by very high level of background hits has been studied and is small enough at high momentum and tolerable at low momentum. The discrimination using cluster sizes is found to be very useful.

6 Acknowledgements

This study is supported in part by the Scientific Research Grant No. 17540482 and the Creative Research Grant No. 18GS020 of the Japan Society for Promotion of Science.

7 Bibliography

References

- [1] Slides:
<http://ilcagenda.linearcollider.org/contributionDisplay.py?contribId=272&sessionId=76&confId=1296>
- [2] <http://ilcphys.kek.jp/gld/documents/dod/glddod.pdf>
GLD Detector Outline Document
- [3] K.Yokoya and P.Chen, *Frontiers of Particle Beams: Intensity Limitations*, edited by M.Month and S.Turner, *Lecture Notes in Physics Vol. 400* (Springer-Verlag, Berlin, 1990),pp.415-445.
Beam-beam phenomena in linear colliders

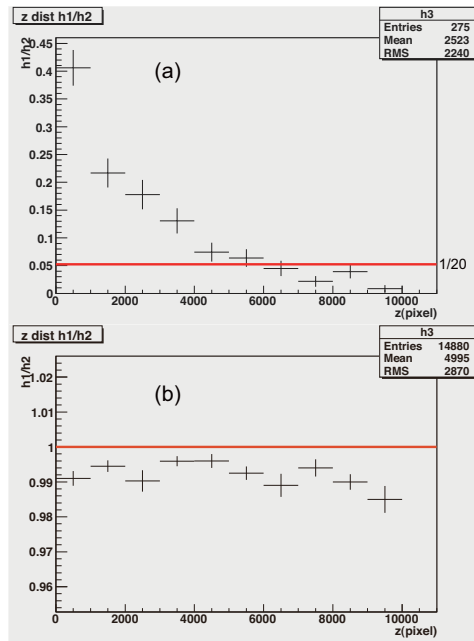


Figure 3: Z-dependent of Rejection factor for the pair background (a), and 1 GeV/c muon tracks (b), where unit of horizontal axis is a pixel.

RAVE – First Vertexing and b -Tagging Results with LCIO Data

Wolfgang Waltenberger, Bernhard Pflugfelder and Herbert Valerio Riedel

Institute of High Energy Physics – Austrian Academy of Sciences
A-1050 Vienna, Austria, Europe

We demonstrate the potential of the RAVE event reconstruction toolkit for the ILC experiments. RAVE has been run embedded both in the Marlin and the org.lcsim frameworks. It has been used to reconstruct primary as well as secondary interaction vertices – the first results with LCIO data are promising. RAVE already has a lengthy and diverse list of platforms on which it has been run – it is portable. RAVE is ready for the ILC challenges.

1 Introduction

RAVE (Reconstruction in an Abstract Versatile Environment) is a project for creating a detector-independent embeddable event reconstruction toolkit that could be used by a wide range of high energy physics collision experiments. Originating from the CMS vertex community, it features powerful novel adaptive algorithms. RAVE has been successfully integrated both in the Marlin [1] and the org.lcsim [2] frameworks.

2 Input data

The following analyses have been performed against 10000 Zh_{120} di-jet events, with both heavy (b and c) and light quark flavors. Marlin’s standard track reconstruction method has been employed.

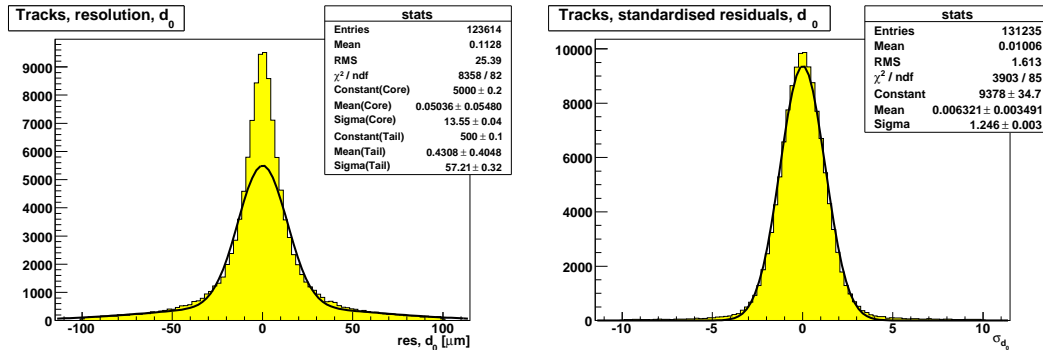


Figure 1: Track resolutions (left) and standardised residuals (right) of the tracks transverse impact parameters (d_0).

Fig. 1 shows the resolutions and the standardised residuals (“pulls”) of the tracks’ transverse impact parameters d_0 . The impact parameters d_0 are systematically underestimated by about 25 %. The same is true for all other track parameters, see [3].

3 Algorithms

On the vertex reconstruction side, the following algorithms are available in RAVE:

- A standard least squares kalman filter [4].
- An adaptive method – implemented as an iterative, re-weighted kalman filter [5].
- An iterative adaptive method, calling the adaptive method iteratively, in order to both find and fit vertices (see [6]).
- A multi-vertex method [7] which fits several vertices concurrently at once.

Work is in progress for making the ZvRes algorithm [8] available within RAVE.

In this paper, only results from the adaptive and iterative adaptive methods are shown.

4 Fitting the primary interaction point

All di-jet events have been used to fit the collision point. No prior selection has been applied on the tracks. Note that this cannot be considered the optimal reconstruction technique, since under such circumstances heavy flavor events tend to worsen the resolutions of the interaction points. Such effects must be kept in mind but are graciously ignored in this paper. Fig. 2 shows the resolutions and the standardised residuals (“pulls”) of the z coordinate of the reconstructed vertices. It can be seen that resolutions of $6 \dots 7 \mu\text{m}$ can be expected in this coordinate. The standardised residuals are similar to those of all track parameters; the systematic bias in the errors has propagated from the tracks to the vertices. Identical results (apart from rounding errors) have been obtained both within Marlin and org.lcsim, see [3].

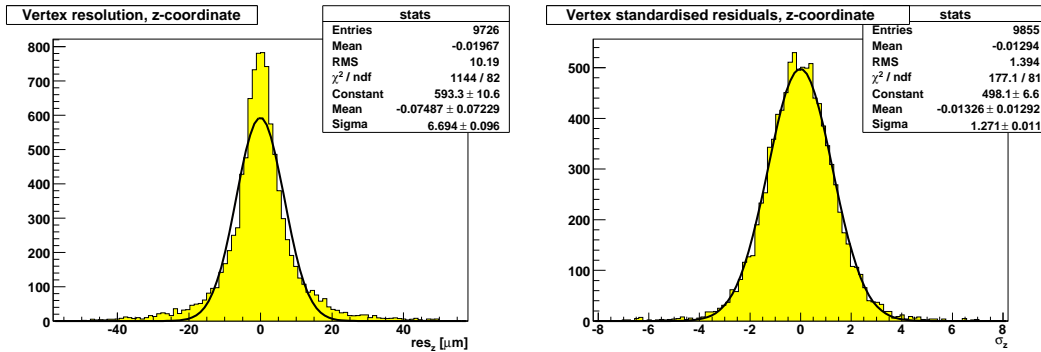


Figure 2: Fitting the interaction points with the adaptive method; the resolution (left) and the standardised residuals (right) of the z coordinates of the reconstructed vertices

5 Secondary Vertices and Flavor Tagging

It has been tried to find and fit the decay (secondary) vertices, also. Here we restrain ourselves to depicting a screenshot of a successful reconstruction of all interaction vertices

(Fig. 3) of a charmed di-jet event. The iterative adaptive method has been employed in this example with default parameter settings.

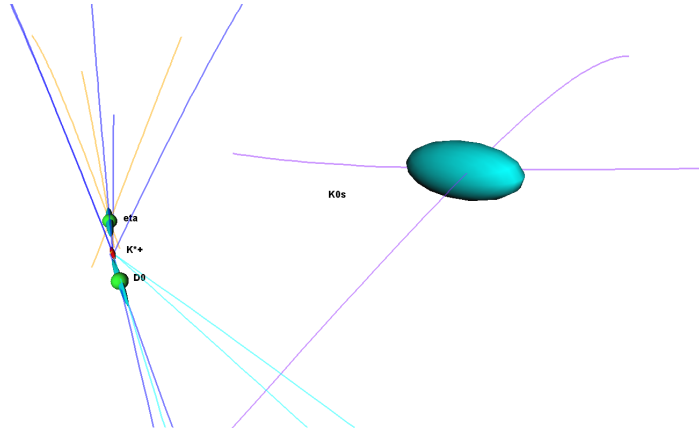


Figure 3: A screenshot of a fully reconstructed charmed di-jet event; all interaction vertices have been reconstructed successfully – the ellipsoids depicted the reconstructed vertices’ errors, magnified by a factor of ten.

A simple b -tagging algorithm has been tried on the event samples. For very preliminary results see [3].

6 Availability

RAVE has been successfully tested on Intel and on PPC CPUs, on two Linux platforms (Debian, Scientific Linux 4) and Mac OS X. Recently, native Windows DLLs have successfully been created and used. RAVE has been reported to compile and run on SLAC Linux workstations [9].

The RAVE toolkit has been used from C++, Java, and Python. Interface to the latter two languages are provided via the SWIG [10] interface generator. RAVE interfaces (“glue code”) exist for Marlin [11] and org.lcsim [12].

RAVE is now hosted at HepForge [13]. It can be downloaded from there.

7 Conclusions and Outlook

RAVE has been shown to be easily embeddable into two major ILC reconstruction frameworks. It compiles and runs on various platforms. Application of the standard vertex reconstruction techniques with standard parameter settings immediately produced acceptable results. RAVE vertex reconstruction is thus ready for several applications, such as the reconstruction of the primary interaction point, or secondary vertex finding and fitting. It could be shown that RAVE’s flavor tagging indeed works; this part of RAVE should still be considered experimental, though.

Refitting the tracks with the information of the reconstructed vertex (“smoothing”) is a near-term goal. Also, using the information of the interaction region (i.e. the “beamspot

constraint”) to improve upon the vertex reconstruction is a feature that will appear soon in RAVE. Longer term developments are a production-quality flavor tagger, and kinematic fitting.

Acknowledgments

The software was designed and developed by the Vienna ILC Project Group. Thanks are due to *Fabian Moser* who significantly contributed to RAVE, *Winni Mitaroff* for valuable discussions, *Rudi Frühwirth* for formulating much of the algorithmic base of RAVE, *Ben Jeffery* for supplying simulated ILC data, and *Jan Strube* and *Jeremy McCormick* for testing Java-RAVE at SLAC.

References

- [1] *Marlin – Modular Analysis and Reconstruction for the Linear Collider*
<http://ilcsoft.desy.de/marlin>
- [2] *org.lcsim – the Java-based Reconstruction and Analysis Software* <http://lcsim.org/software/>
- [3] Slides:
<http://ilcagenda.linearcollider.org/contributionDisplay.py?contribId=273&sessionId=76&confId=1296>
- [4] M. Regler, R. Frühwirth and W. Mitaroff: *Int.J.Mod.Phys.* **C7**, 4 (1996) 521 - 542.
R. Frühwirth et al.: *Comp.Phys.Comm.* **96** (1996) 189-208.
- [5] R. Frühwirth et al., *Proc. Int. Conf. for Computing in High Energy and Nuclear Physics (CHEP 03)*, La Jolla (USA), 24 - 28 March 2003, SLAC, Menlo Park 2003 – ref. TULT013, SLAC-R-636 / eConf C0303241.
R. Frühwirth et al.: *Adaptive vertex fitting*, Report CMS-NOTE-2007-008, CERN, Geneva 2007 (submitted to *J.Phys.G*).
- [6] Wolfgang Waltenberger: *Development of Vertex Finding and Vertex Fitting Algorithms for CMS*, TU Wien, 2004, CMS TS-2006/12. http://publications.teilchen.at/walten/ww_diss.pdf
- [7] R. Frühwirth, W. Waltenberger: *Adaptive Multi-Vertex Fitting*, CMS CR-2004/062, http://cmsdoc.cern.ch/documents/04/cr04_062.pdf *Proc. Int. Conf. for Computing in High Energy and Nuclear Physics (CHEP 04)*, Interlaken (CH), 27 Sep. - 1 Oct. 2004, CERN, Geneva 2005 – vol. 1, p. 280, CERN-2005-002-V1.
- [8] D.J. Jackson: *Nucl.Instr.Meth. A* 388 (1997) 247-253.
<http://www.physics.ox.ac.uk/LCFI/Physics.html>.
- [9] RAVE Installation at SLAC. See:
<http://confluence.slac.stanford.edu/display/ilc/RAVE+installation+instructions>
- [10] SWIG Simple Wrapper Interface Generator: <http://www.swig.org/>
- [11] RAVE Glue Code for Marlin. See:
<http://stop.itp.tuwien.ac.at/websvn/listing.php?replname=marlinrave>
- [12] RAVE Glue Code for org.lcsim. See:
<http://stop.itp.tuwien.ac.at/websvn/listing.php?replname=lcsimrave>
- [13] RAVE at HepForge: <http://projects.hepforge.org/rave>

Simulation Study for EUDET Pixel Beam Telescope using ILC Software

Tatsiana Klimkovich

DESY

Notkestr. 85, 22607 Hamburg - Germany

A pixel beam telescope which is under development within the EUDET collaboration will provide a test environment for different pixel sensor technologies as well as for large tracking devices such as TPC. The telescope will consist of 4-6 sensor planes. The setup has already passed first tests at a 1-6 GeV/c electron beam at DESY in Hamburg. The device is flexible for using at other beam lines, e.g. at CERN pion beam. In this paper a simulation study for different telescope configurations will be presented [1].

1 Introduction

EUDET is a coordinated European effort towards research and development for the next generation of large-scale particle detectors [2]. The project covers different activities for vertexing, tracking, calorimetry as well as networking activities which support information exchange. The JRA1 subgroup is dedicated to develop a test beam infrastructure and a pixel beam telescope. The planes of the beam telescope are equipped with monolithic active pixel detectors constructed in CMOS technology. The objective of the future device is to achieve a precision of the predicted impact position of beam particles on the DUT plane of less than $3 \mu\text{m}$ at 5 GeV/c. To fulfil this requirement it is necessary to find an optimum configuration of the telescope mechanics. For this purpose a simulation study of different telescope geometries has been done.

The general layout of the considered beam telescope geometries is shown in Fig. 1. The setup consists of three separate insulating boxes (for two telescope arms and the device under test (DUT)), which allows better flexibility for the overall setup. In the cases of 2- and 4-plane geometries the closest telescope planes to the DUT have been considered in the simulation. The thickness of the telescope planes has been assumed to be $110 \mu\text{m}$ which corresponds to the thickness of the thinned sensors. The DUT is assumed to be $300 \mu\text{m}$ thick.

The simulation of the beam telescope has been done using the package Mokka [3], which is a Geant4-based simulation program for a future International Linear Collider (ILC). All parameters for different detector models have been stored in a MySQL database. The output files are in LCIO format [4, 5]. For the analysis of simulated data the Linear Collider analysis framework Marlin [6] as well as C++ and ROOT software have been used. For every detector setup 50000 events have been simulated (without magnetic field) with a 1-6 GeV/c electron beam. In the simulation the effects of multiple scattering (MS) have been taken into account. The validity of the MS model has been verified by comparing simulation results with theoretical description [1, 7]. For every event hit

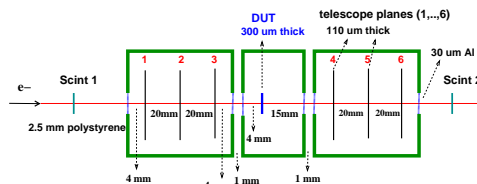


Figure 1: Geometry layout of the pixel beam telescope.

positions and deposited energies in every telescope plane and the DUT have been stored. An intrinsic resolution of $3 \mu\text{m}$ for every telescope plane has been assumed. For this purpose in the analysis every hit position in telescope plane has been smeared.

2 Simulation results

The analysis procedure is done as follows. Through the hits in the telescope planes a straight line as a track model using a least squares fit has been fitted [8]. The telescope planes have been considered as perfectly aligned. To reduce the effects of multiple scattering the cuts for χ_{track}^2 and the track slope have been introduced. The residuals in the DUT plane $r_{x \text{ DUT}}$ and $r_{y \text{ DUT}}$ are calculated as the difference between the DUT hit position predicted by the extrapolated track and the real hit position in the DUT. After fitting a Gaussian function to the DUT residual distributions $r_{x \text{ DUT}}$ and $r_{y \text{ DUT}}$ the standard deviation values σ_x and σ_y have been extracted. The dependence of σ_x on the electron beam energy is shown for different telescope configurations in Fig. 2.

At low energies the contribution of multiple scattering is large and, therefore, the 2-plane configuration gives better results. With increasing energy the 4-plane geometry is an optimal variant. For the case of the availability of two closest to the DUT telescope planes of higher resolution ($1.5 \mu\text{m}$), which can be achieved by using sensors with smaller pixel size, the performance of the telescope will improve significantly [1].

The present telescope setup is foreseen to be used in different test beam environments. The performance of the telescope within hadronic beams has been investigated by simulating a pion beam of $100 \text{ GeV}/c$. The same intrinsic plane resolution of $3 \mu\text{m}$ is assumed. The results of the study are presented in Fig. 3. As is expected, the 6-plane geometry will show the best performance due to negligible multiple scattering effects.

When the detector is ready a proper software alignment will be an important issue for telescope precision. Therefore it is useful to test different alignment procedures in order to arrange the setup in such a way as to make alignment later on easy. A popular alignment program in use is Millepede [9] which is widely exploited in H1, ZEUS and

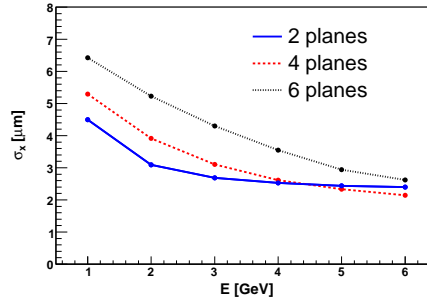


Figure 2: Standard deviation value of the residual distribution in the DUT plane σ_x as a function of the electron energy for different telescope geometries.

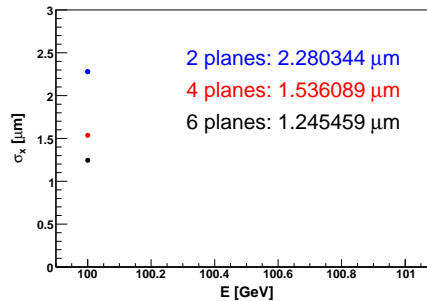


Figure 3: Standard deviation value of residual distributions in the DUT plane σ_x as a function of the pion beam energy.

CMS experiments for tracker alignment. The package is based on a linear least squares fit and especially suited for systems with big numbers of fitted parameters. There are two types of parameters used in the fit:

- local parameters: track parameters (here, track slopes and curvatures);
- global parameters: alignment coefficients (here, x and y shifts).

For testing the package 50000 events for 6 GeV/c electron beam have been simulated for 6-plane telescope geometry without the DUT. A misalignment has been introduced into the analysis by randomly shifting hit positions in telescope planes. Very preliminary results of the alignment procedure are shown in Fig. 4 for x shifts. Blue dots indicate true shifts which have been introduced in the analysis and red dots represent the output of the alignment package Millepede. In general good performance of the program is demonstrated however more detailed and systematic study is needed, e.g. for taking into account rotations of the telescope planes as well as finding a minimal number of events necessary for precision alignment.

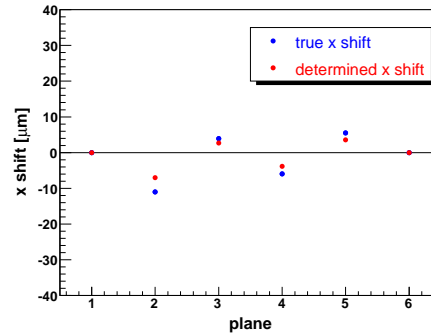


Figure 4: The results of the alignment procedure for x shifts as a function of the plane number.

Currently, a common analysis framework based on Marlin for the telescope operation is under development [10]. It will comprise all the steps of data analysis and possibility of its comparison with the simulation.

References

- [1] Slides: <http://ilcagenda.linearcollider.org/contributionDisplay.py?contribId=274&sessionId=76&confId=1296>
- [2] URL: <http://www.eudet.org>
- [3] P. Mora de Freitas, *Prepared for International Conference on Linear Colliders (LCWS 04), Paris, France, 19-24 Apr 2004*
- [4] F. Gaede, T. Behnke, N. Graf and T. Johnson, *In the Proceedings of 2003 Conference for Computing in High-Energy and Nuclear Physics (CHEP 03), La Jolla, California, 24-28 Mar 2003, pp TUKT001 [arXiv:physics/0306114]*
- [5] F. Gaede, *Prepared for International Conference on Linear Colliders (LCWS 04), Paris, France, 19-24 Apr 2004*
- [6] F. Gaede, Nucl. Instrum. Meth. A **559** (2006) 177
- [7] T. Klimkovich, EUDET-Memo-2007-06, available from: <http://www.eudet.org/zms/content/e62/e144/e190/eudet-memo-2007-06.pdf>
- [8] V. Blobel, E. Lohrmann, “Statistische und numerische Methoden der Datenanalyse”, Stuttgart and Leipzig, Teubner (1998)
- [9] V. Blobel, a program description for Millepede and the code is available from <http://www.desy.de/~blobel/>
- [10] URL: http://ilcsoft.desy.de/portal/software_packages/eutelescope/index_eng.html

Machine Detector Interface

*Conveners: T. Markiewicz, A. Seryi, E. Torrence, W. Lohmann, P. Bambade, W. Kozanecki,
K. Büßer, P. Burrows, T. Tauchi, T. Omori*

GamCal - A Beam-strahlung Gamma Detector for Beam Diagnostics

William M. Morse

Brookhaven National Lab - Physics Dept.
Upton, NY 11973 - USA

The ILC bunches experience intense electro-magnetic fields during the collision which produce a prodigious number of beam-strahlung gammas. A small fraction of the gammas convert into pairs. We discuss the use of the beam-strahlung gamma detector GamCal and the pair detector BeamCal as Luminosity Feedback Detectors to optimize the ILC luminosity. These two detectors provide complimentary information. Both have adequate statistical significance at full ILC beam current, but only the GamCal has adequate statistical significance if the ILC starts up at low beam currents.

1 Introduction

The ILC beams experience intense electro-magnetic fields due to the other bunch as they pass each other. The maximum equivalent magnetic field is 1KT. This causes a large amount of beam-strahlung gamma radiation. The power radiated by a beam electron is

$$P_e = \frac{2}{3} \frac{e^2}{m^2 c^3} \gamma^2 F^2 \tag{1}$$

where $F = e(E + c\beta B)$. A small fraction of the gammas convert into pairs, mainly by the Bethe-Heitler process [2] $\gamma e \rightarrow eee$. These pairs spiral in the magnetic field and some strike the BeamCal, about 3m away from the IP [1]. There are a smaller number of pairs from the Landau-Lifshitz ($ee \rightarrow eeee$) process [2]. The beam-strahlung gammas continue un-deflected by magnetic fields to a converter $10^{-4} - 10^{-5} X_0$ thick, about 180m from the IP.

Beam-strahlung	Number	E
ee	94K	180 TeV
BeamCal	7K	14 TeV
γ	2.5×10^{10}	110 MTeV
GamCal	10^5	300 TeV

Table 1: Number and energy per beam crossing of beam-strahlung gammas and pairs with the nominal ILC parameters.

The conversion positrons are then deflected by a dipole magnet into the GamCal detector. Table 1 gives some of the ILC beam-strahlung parameters. The GamCal converter thickness is $10^{-5} X_0$ for this calculation. The BeamCal calculation is for the small crossing angle, or the 14mrad crossing angle with the anti-DiD.

2 GamCal Detector

Figure 1 shows the GamCal concept. The converter could be a gas jet or a foil. The acceptance of the GamCal for the converted positrons is large: about half for the nominal ILC parameters. The main background is Landau-Lifshitz pair production by the electron beam:

$eZ \rightarrow eZe$. This background is about 6% of the beam-strahlung signal for the nominal ILC parameters.

Furthermore, the background from the electron beam can be measured by accelerating only one beam, and thus it can be subtracted. At the ILC we get only about 10^4 Higgs events per year at the nominal luminosity of $2 \times 10^{34} \text{cm}^{-2} \text{s}^{-1}$. Attaining the design luminosity will be challenging. The nominal ILC beam height is only 5nm; two orders of magnitude less than the SLC beam height. We need to find a signal for feedback which is proportional to the instantaneous luminosity and has statistical precision of $\sim 1\%$ for each beam crossing.

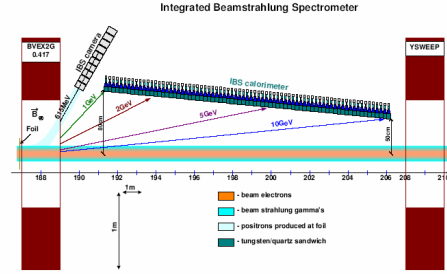


Figure 1: Concept for the GamCal.

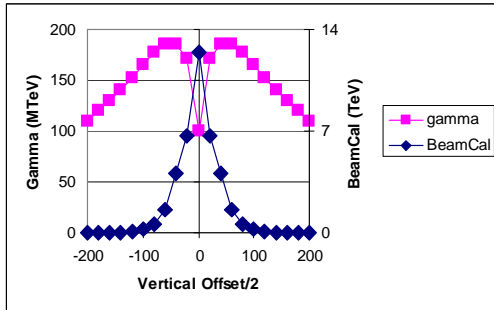


Figure 2: Beam-strahlung gamma energy and energy deposited in the BeamCal vs. vertical offset of the bunches.

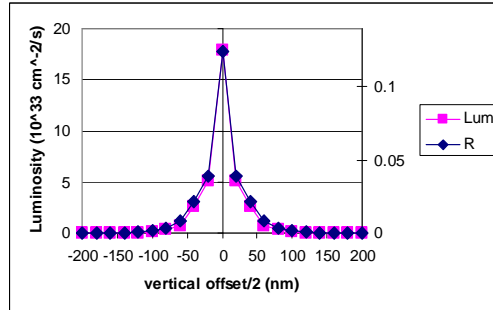


Figure 3: Luminosity and the ratio R of the BeamCal energy to the gamma energy.

The instantaneous luminosity is proportional to:

$$L_i \propto \frac{N_o^2}{A_o} \quad (2)$$

where A is the effective area and the o subscript denotes the overlapping part of the distribution. The production of Bethe-Heitler pairs at the IP is proportional to:

$$N_{BH} \propto \frac{\sigma_{BH} N_\gamma N_o}{A_o} \quad (3)$$

For the above equation, N_o is the number of overlapping positrons for the left BeamCal and GamCal detectors, and the number of overlapping electrons for the right detectors. Thus the ratio of the number of produced pairs divided by the gammas gives us the information needed to evaluate equ.2. This analytical result works remarkably well, as can be seen in the Guniea Pig based simulation results [3] shown in Figures 2 and 3. The bunch electric fields cancel when the bunches overlap perfectly, while the bunch magnetic fields add, giving a local minimum in the average Lorentz force, and thus a local minimum in the gamma

beam-strahlung (see equ. 1). Thus GamCal and BeamCal detectors provide complementary information, and the ratio tracks the instantaneous luminosity.

3 Luminosity Feedback Detectors

The ILC Reference Design Report describes the luminosity feedback process: “Because the luminosity may be extremely sensitive to bunch shape, the maximum luminosity may be achieved when the beams are slightly offset from one another vertically, or with a slight nonzero beam-beam deflection. After the IP position and angle feedbacks have converged, the luminosity feedback varies the position and angle of one beam with respect to the other in small steps to maximize the measured luminosity”.

The BeamCal and GamCal detectors provide the instantaneous luminosity feedback, as discussed above. The BeamCal statistical accuracy is $\simeq 1\%$ per beam crossing at the ILC nominal parameters; however, it becomes statistically marginal if the ILC starts up with lower beam currents. Figure 4 shows the number of pairs produced and those hitting the BeamCal from a simulation program [3] vs. N . Both the number of produced pairs and the BeamCal acceptance drops rapidly as N is reduced by an order of magnitude. A simple simulation program [4] shows that the GamCal acceptance drops by about a factor of two when N is reduced by an order of magnitude. The background from the electron beam hitting the GamCal converter will rise from $\simeq 6\%$ to $\simeq 60\%$ of the beam-strahlung signal, but this can be subtracted, as discussed above. Figure 5 shows the number of conversion positrons produced, and those hitting the GamCal vs. N for a converter of 10^{-4} and $10^{-5}X_0$. It appears that the damage issues for this foil of $10^{-5}X_0$ ($10^{-4}X_0$) are less challenging than for the SNS stripping foil at full (10%) ILC beam current. We would plan to have several foils remotely controllable in vacuum, as the SNS does.

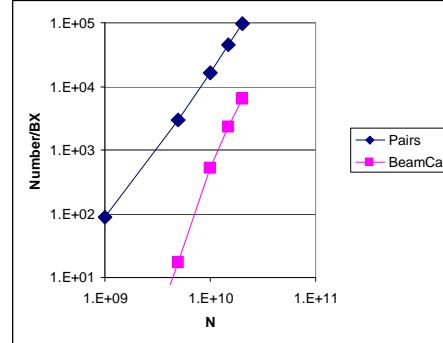


Figure 4: Number of Beam-strahlung pairs produced per beam crossing and the number hitting the BeamCal vs. the number of beam electrons N .

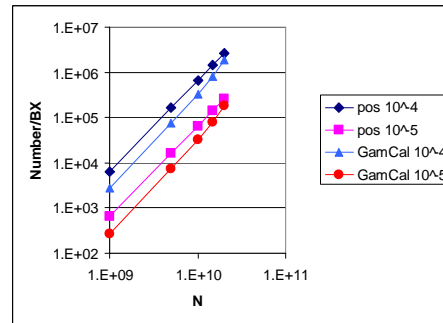


Figure 5: Number of positrons from the GamCal converter and the number hitting the GamCal vs the number of beam electrons N .

4 Conclusions

The BeamCal and GamCal detectors will be used to optimize the ILC instantaneous luminosity. The BeamCal will be statistically challenged at low beam currents, but the GamCal has good statistical validity even at 10% nominal beam current.

References

- [1] <http://www-zeuthen.desy.de/ILC/fcal/>.
- [2] C. Rimbault *et al.*, Phys. Rev. Special Topics - Acc. and Beams **9** 034402 (2006).
- [3] M. Ohlerich *et al.*, *Monitoring the ILC Luminosity with Beam-strahlung Measurements*, FCAL Report in Prep.
- [4] W. Morse and T. Rao, submitted as an ILC Note.

ILC Beam Diagnostics using BeamCal and GamCal

Andrey Saprionov on behalf of FCAL Collaboration *

Joint Institute for Nuclear Research - Dzhelapov Laboratory of Nuclear Problems
Joliot-Curie 6, 141980 Dubna Moscow Reg. - Russia

Two detectors in the very forward region of ILC apparatus, BeamCal and GamCal, are going to be used for beam monitoring purposes. Their potential in this field is being studied and several optimization possibilities are considered. A few preliminary results are presented in this report [1].

1 Introduction

Due to the high bunch charge density ILC is expected to have the largest amount of beamstrahlung background ever. This situation will result in a noticeable energy loss of about 1.5% of bunch energy but instead of dumping it into beam pipe it was proposed to utilize it for beam diagnostics. This duty is planned to be performed by two detectors in very forward region, GamCal and BeamCal.

The GamCal is projected to consist of two parts - the IBS Calorimeter for spectral measurement of beamstrahlung gammas energy, and the IBS Camera to obtain the profile of those gammas having their energies in a narrow range [2]. For the current preliminary studies only total energy of gammas was used as an input from GamCal.

Electromagnetic calorimeter BeamCal aims to capture electron-positron pairs produced by beamstrahlung gammas. It is positioned around outgoing beam pipe 3.5 meters from IP and contains thirty disks of tungsten separated by segmented layers of sensor made of diamond or other suitable radiation hard material. Each of two parts of BeamCal has about 45000 sensor sells and only part of them will be used for beam monitoring.

2 Beam diagnostics using beamstrahlung analysis

This analysis procedure was proposed by Achim Stahl in [3]. Majorly consists in reconstruction of beam parameters from distribution of beamstrahlung pairs energy that was deposited in BeamCal. Considered there are several observables can be calculated from the shape of this energy distribution, they can be approximately bonded with beam parameters by first order Taylor series:

$$O_{meas} = M \times [P_{act} - P_{nom}] + O_{nom} \quad (1)$$

Here O_{meas} is a vector of observables measured for actual beam parameters P_{act} , O_{nom} - one that would be measured in case of nominal parameters P_{nom} and M is a non-square matrix of first order Taylor series. To obtain an expression for beam parameters that has to be reconstructed one must apply Moore-Penrose inverse to the matrix M .

$$P_{rec} = M_{inv} \times [O_{meas} - O_{nom}] + P_{nom} \quad (2)$$

*Supported with INTAS funding.

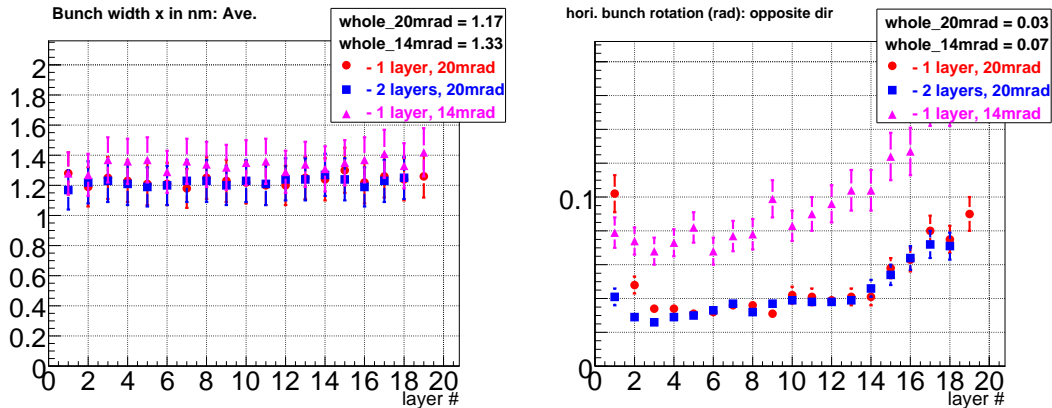


Figure 1: Beam parameters resolution depending on number of layer used as signal one.

Using simulated data with varied beam parameters it is possible to get this Moore-Penrose inverse which will serve for real-time reconstruction. A list of observables used for reconstruction may vary depending on detector geometry and magnetic field type.

The real-time reconstruction process follows several steps. First, same observables are calculated from energy deposition in calorimeter for several consequent bunch collisions. For each of them a vector of beam parameters is calculated by (2). These vectors are averaged to get a vector of current beam parameters which can be sent to beam adjustment systems.

The whole process should take no longer than few bunch-crossings to be effective as beam monitoring. This is why the speed optimization is essential. Naturally it can be done reducing the amount of readout channels, but should not lead to significant resolution drop.

3 Read-out scheme optimization

This research is carried to study the potential of various read-out schemes from the point of view of the beam diagnostics system performance. It largely employs the simulation code written by Achim Stahl and standalone Geant4 simulation of BeamCal calorimeter. The main course consists in comparison of reliability and resolution of different read-out patterns and picking those which fit performance and precision requirements. Another important option is the construction feasibility: there are several design features to deal with on a hardware level.

Beamstrahlung gammas and e^+e^- pairs are simulated using Guinea-Pig generator [4]. These pairs are given as an input to Geant4 simulation of BeamCal and resulting energy distribution is used to calculate sets of observables. According to the technique described above, part of these sets is used to build Moore-Penrose inverse matrix, another part serves for beam parameters reconstruction.

The sets of observables and beam parameters involved in these studies are largely the same as those described in Achim Stahl's note mentioned above. There are several differences in list of observables, they include additional asymmetries and phi momenta.

Table 1 generally represents significance of GamCal data for the reconstruction. The beam parameters resolution is compared for two crossing angles with and without observable

bp, unit	nom.	BeamCal		BeamCal+GamCal(E_γ)	
		20mrad	14mrad	20mrad	14mrad
σ_x , nm	655.	654.1 ± 2.47	654.9 ± 2.60	653.6 ± 1.17	653.9 ± 1.33
$\Delta\sigma_x$, nm	0.0	-0.06 ± 6.77	3.51 ± 5.59	-1.71 ± 2.40	-0.96 ± 2.12
σ_z , μm	300	308.0 ± 4.72	306.2 ± 3.72	299.8 ± 1.69	301.1 ± 1.65
$\Delta\sigma_z$, μm	0.0	2.43 ± 7.94	-0.37 ± 3.98	-0.15 ± 2.21	-0.67 ± 1.90
ε_x , 10^{-6}	10.0	— \pm —	9.94 ± 2.16	— \pm —	9.94 ± 2.16
$\Delta\varepsilon_x$, 10^{-6}	0.0	— \pm —	0.61 ± 1.21	— \pm —	0.61 ± 1.21
Δx , nm	0.0	4.55 ± 8.14	-3.86 ± 11.07	4.57 ± 8.13	-3.84 ± 11.08
Δy , nm	0.0	-2.22 ± 1.19	-1.26 ± 0.84	0.15 ± 1.26	-0.39 ± 0.84
w_x , μm	0.0	— \pm —	$286. \pm 593.$	— \pm —	$286. \pm 593.$
w_y , μm	0.0	$-8. \pm 14.$	$9. \pm 27.$	$-8. \pm 14.$	$9. \pm 27.$
α_h , rad	0.0	-0.036 ± 0.045	0.017 ± 0.092	-0.036 ± 0.045	0.005 ± 0.092
$\Delta\alpha_h$, rad	0.0	0.052 ± 0.033	-0.011 ± 0.064	0.053 ± 0.033	-0.008 ± 0.070
N , 10^{10}	2.0	1.999 ± 0.005	2.005 ± 0.004	1.999 ± 0.002	2.000 ± 0.003
ΔN , 10^{10}	0.0	-0.006 ± 0.023	0.005 ± 0.012	-0.005 ± 0.016	0.002 ± 0.010

Table 1: Beamstrahlung gamma energy influence on reconstruction precision.

representing total beamstrahlung gamma energy. Some positive influence of this observable can be noticed for bunch sizes and other parameters.

The read-out optimization studies consisted of several parts and so far were performed only for single parameter reconstruction. First part considered the possibility to reduce amount of layers from which the information is collected. This was done by changes in script calculating observables by setting it to include only selected layers at various positions along calorimeter axis. The plots on Figure 1 show that there is slight dependence in resolution on geometry and number of signal layers and their position, but not for all beam parameters. For most of them the reconstruction precision does not vary dramatically for the first twenty layers and also doesn't differ greatly from precision that whole calorimeter allows to obtain.

The second part of studies included calorimeter re-segmenting with a purpose of reducing amount of parallel processed data. There were two styles of re-segmentation proposed – unifying 16 and 32 original segments into super-segments. Re-segmentation scheme for 32 channel unification is shown on Figure 2. The results for 6th layer used as signal one obtained for 14mrad crossing angle geometry are summarized in Table 2. It can be seen that for most parameters the resolution is not getting much worse.

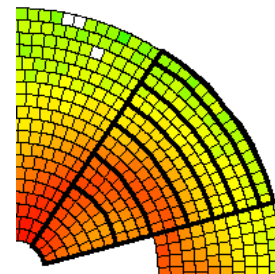


Figure 2: 32 channel re-segmentation scheme.

4 Summary

The results presented here are obtained for single parameter reconstruction and therefore are very preliminary. However one can see promising reconstruction stability and persistence of resolution as the amount of input information is reduced. Inclusion of beamstrahlung gamma energy into observables list was noticed to

bp	unit	nom.	RO scheme		
			detailed	16 channel	32 channel
σ_x	nm	655.0	653.72 ± 1.29	653.97 ± 1.30	654.04 ± 1.27
$\Delta\sigma_x$	nm	0.	-1.72 ± 2.01	-1.65 ± 2.01	-1.65 ± 2.02
σ_z	μm	300.	300.90 ± 1.69	300.48 ± 1.56	300.39 ± 1.47
$\Delta\sigma_z$	μm	0.	-0.59 ± 1.82	-0.41 ± 1.77	-0.33 ± 1.82
ε_x	10^{-6}m rad	10	10.18 ± 2.62	10.18 ± 2.62	10.18 ± 2.62
Δx	nm	0	-5.35 ± 11.52	-7.26 ± 9.80	-7.78 ± 9.76
α_v	rad	0	-0.056 ± 0.019	-0.076 ± 0.025	-0.077 ± 0.025

Table 2: Resolution of beam parameters reconstructed from re-segmented 6th layer of Beam-Cal.

have positive influence on reconstruction precision.

For the next step one has to broaden the studies to simultaneous reconstruction of several or, if possible, all beam parameters in order to approach to real life situation. The effectiveness of this beam monitoring system can be tested using more realistic bunches provided by ILC simulation software.

References

- [1] Slides:
<http://ilcagenda.linearcollider.org/contributionDisplay.py?contribId=171&sessionId=78&confId=1296>
- [2] W. Morse, *GamCal, a Device for Beam Diagnostics*, these proceedings.
- [3] A. Stahl, *Diagnostics of Colliding Bunches from Pair Production and Beam Strahlung at the IP*, LC-DET-2005-003, 2005
- [4] D. Schulte, TESLA-97-08 (1996)

Simulation Studies and Detector Scenarios for an ILC Polarimeter

K.Oleg Eyser¹, Christian Helebrant^{1,2}, Daniela Käfer¹, Jenny List¹ and Ulrich Velte^{1,3}

1 - DESY Hamburg, Germany

2 - Universität Hamburg, Germany

3 - Leibniz Universität Hannover, Germany

High energy longitudinal electron polarimetry will be based on Compton scattering for the International Linear Collider. An unobtrusive measurement has to include a magnet chicane setup serving as a spectrometer. Current proposals make use of Cerenkov detectors for electron detection. A fast simulation has been developed to study the basic properties of scenarios for the polarimeter setup.

1 Introduction

Electron polarimetry at the International Linear Collider (ILC) will be based on Compton scattering using a laser colliding head-on with the incident lepton beam in the beam delivery system. The shape of the differential Compton cross section depends strongly on the helicity states of electron beam and laser. Asymmetries can then be determined from different helicity configurations, which scale with the longitudinal polarization of the electron bunches [2].

At ILC energies of 250 GeV or more, the angular distributions of both the scattered photons and the recoil electrons are constrained to within a few μrad for all but the most highly energetic photons. The polarimeter, therefore, will be placed in a magnet chicane serving as a spectrometer for the recoil electrons (see figure 1). The setup consists of four sets of dipoles in such a way that the emittance of the incident electron beam should not be impaired by more than 1%. The electrons are first displaced parallel to their original direction by about 2 cm to the side by two sets of dipoles. After that, a pulsed laser (10 ps with 35 μJ) hits the bunches head-on and deflects about 10^3 out of the $20 \cdot 10^9$ electrons.

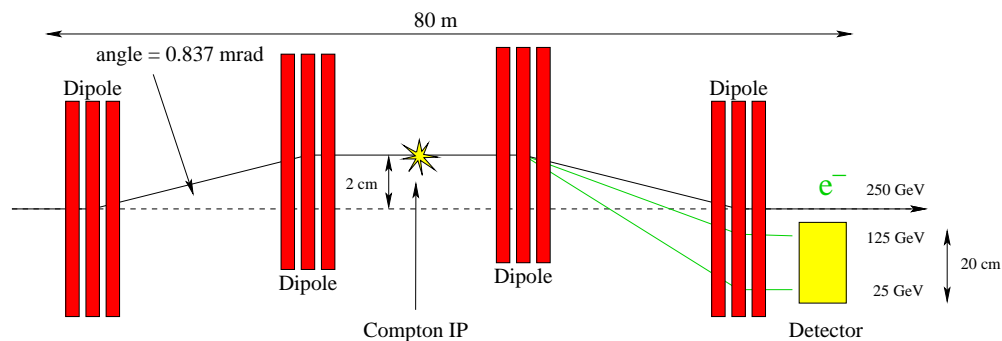


Figure 1: Proposed layout of the upstream electron polarimeter in a magnet chicane.

The second pair of dipole sets puts the undisturbed electrons back on their original track and serves as a spectrometer for the recoil particles which are deflected more strongly due to their reduced energy.

The Compton electron yield will then be determined after the last dipole set in a Cerenkov detector. The detector needs to cover less than 20 cm horizontally and only a fraction of that in vertical direction due to the orientation of the dipoles. The overall length of the polarimeter is reaching almost 80 m to accomplish this spread and to comply with the accelerator emittance demands at the same time. Cerenkov light will be produced by the electrons in gas tubes or quartz fibers, alternatively. The light is then transferred further to photo-detectors which are placed out of the accelerator plane in order to reduce background from beam related interaction or other effects from the beam delivery system.

The polarimeter location and setup have to be chosen carefully, since the polarization needs to be known as close to the electron-positron interaction point as possible. Especially the direction of the polarization vector can change easily in the magnetic fields of the beam delivery system. Beam orbit alignment accuracies have been estimated to be smaller than $80 \mu\text{rad}$ at 250 GeV for the measurement to be in compliance with the physics demands for the polarization determination ($\Delta P/P \leq 0.25\%$, [2, 3]). The polarimeter setup is such that the Compton edge does not change its position in the detector with respect to the incident beam energy. This is especially of value during commissioning of the accelerator in order to keep track of polarization preservation and also in threshold scans.

2 Fast Simulations

A fast Monte Carlo simulation has been developed which is used for first analyses of the basic properties of the polarimeter layout and the detector design. Bunches of $20 \cdot 10^9$ electrons at 250 GeV and 80% polarization are coupled to the circularly polarized, green laser pulses (2.33 eV) by a Compton generator. Both beams have an assumed circularly distributed width with a gaussian shape of $\sigma = 50 \mu\text{m}$. Also, there is a slight crossing angle of 10 mrad which is necessary in the experimental setup later.

The Compton recoil electrons are tracked through the dipoles and translated into Cerenkov photons at the location of the detector through a refraction index of 1.0014 for C_4F_{10} or pressurized propane (1.1 atm). Light transmission to the photo-detectors is currently covered by a global efficiency of 55%.

The light yield detected by the photo-detectors is determined from the wavelength dependent quantum efficiency. It has been taken from conventional HAMAMATSU R6094 photo-multiplier tubes. Between $300 \text{ nm} \leq \lambda \leq 650 \text{ nm}$, the quantum efficiency reaches a maximum of 25% around 350 nm and drops to zero elsewhere due to the opacity of the entrance window glass. ADC-counts are finally derived from the detected photons. These counts can be distorted by a quadratic function that describes the general behaviour of differential non-linearities in the electronics read-out chain. The distortion is maximal for medium values and vanishes at zero counts and when reaching saturation level.

The ADC-counts are determined for same and opposite helicity configurations and accumulated over several bunches. From these, an asymmetry is calculated as a function of channel number, see left side of figure 2. The channel number reflects the transverse position of the Compton electrons at the detector surface ($2 \text{ cm} \leq x \leq 20 \text{ cm}$) and is, therefore, a function of the inverse recoil energy.

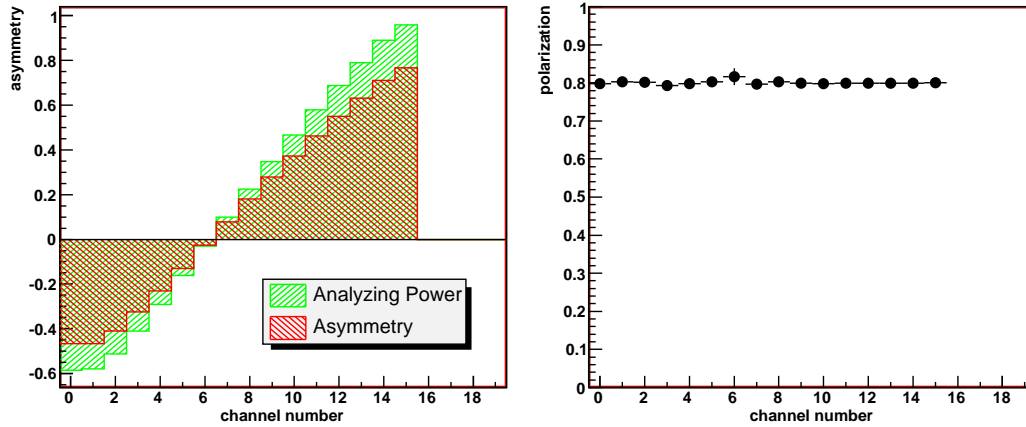


Figure 2: Asymmetry ϵ and analyzing power A as functions of channel number. The ratio of both leads to the electron longitudinal polarization P .

The polarization P is calculated from the *measured* asymmetry ϵ and the calculated analyzing power A , i.e., the Compton asymmetry for completely polarized electron bunches:

$$\epsilon = A \cdot P = \frac{N_{Adc}^+ - N_{Adc}^-}{N_{Adc}^+ + N_{Adc}^-}, \quad (1)$$

where N_{Adc}^+ and N_{Adc}^- are the integrated ADC-counts.

Polarizations are determined for each channel separately and then combined to a weighted mean (see right side of figure 2). This way, problematic channels can be excluded from the average value, which is especially important for the zero crossing of the asymmetry (channel 6 in figure 2). Statistical errors diminish after accumulation over many bunch trains of each 2820 bunches and reveal systematic uncertainties.

Experimentally, the polarization will be extracted from the output ADC-counts without proper knowledge of integral or differential non-linearities. In the simulation, one can compare the experimental values with the primary Compton electrons or with the secondary Cerenkov photons, so the effect of the distorted ADC-readout becomes traceable for single channels. Also, the measured polarization can be checked with respect to the *real* (input) electron polarization. Figure 3 shows the deviations between measured and real polarizations as a function of the quadratic non-linearities for a 20-channel detector.

In order to meet the physics demand for the polarization measurement, it is necessary to be in control of differential non-linearities in the range of 0.5%, contributing less than 0.1% to $\Delta P/P$. This effect is decreasing with increasing channel numbers. However, for Cerenkov tubes, a channel width of 1 cm seems to be a reasonable size. First non-linearity measurements have been carried out in a test stand [4] and more detailed studies of the whole detector setup are planned.

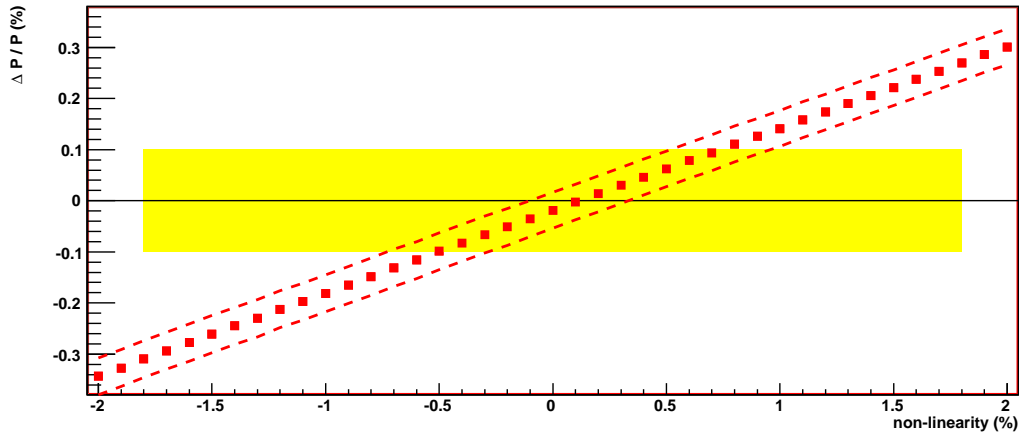


Figure 3: Effect of electronics differential non-linearities on the determination of the electron polarization. The yellow box represents the range of the desired maximum contribution to the total error $\Delta P/P \leq 0.25\%$.

3 Outlook

The simulation so far is very limited and only includes non-linearities of the electronics read-out after tracking the Compton electrons towards the detector surface and transforming them into Cerenkov photons. In the future, a full picture of the polarimeter has to include other details of the magnet chicane and the detector setup. This includes a proper description of the gas (or possibly other) volumes, the geometry for the transmission with reflectivities and absorption, and light extraction in the photo-detectors. There are on-going efforts to use BDSIM^a [5] for a description of the magnet chicane and add an accurate GEANT4 model of the complete detector setup. This simulation would also serve as a comprehensive tool to study the possibilities of combining the beam emittance measurement or others with the polarimeter chicane. Such an additional measurement might induce additional downstream background which has to be considered carefully.

4 Acknowledgments

The authors acknowledge the support by DFG Li 1560/1-1.

References

- [1] Slides:
<http://ilcagenda.linearcollider.org/contributionDisplay.py?contribId=173&sessionId=78&confId=1296>
- [2] V. Gharibyan, N. Meiners and P. Schüler, LC-DET-2001-047 (2001) and references therein.
- [3] G. Mortgaat-Pick et al., CERN-PH-TH/2005-036 and references therein.
- [4] D. Käfer et al., these proceedings (2007).
- [5] <http://cvs.pp.rhul.ac.uk/cvsweb.cgi/BDSIM/docs/>

^aBeam Delivery Simulation

Test Stand Measurements for an ILC Polarimeter

Daniela Käfer¹, Oleg Eyser¹, Christian Helebrant^{1,2}, Jenny List¹, Ulrich Velte³

1- Deutsches Elektronen Synchrotron (DESY) - Hamburg, Germany

2- Universität Hamburg, Germany

3- Leibniz Universität Hannover, Germany

The setup of two different small scale teststands for measurements regarding an electron Cherenkov detector as part of the ILC polarimeters is presented. Component measurements already carried out are analyzed and others, foreseen for the near future, are discussed. The larger one of the two teststands features the old Cherenkov detector of the SLD experiment, which will be used as a reference for a number of crucial measurements. Especially, the requirements for the non-linearity of the read-out chain are studied in greater detail and methods for its precise measurement before and during operation are being developed accordingly.

1 Polarisation: Measurement Principle

At the ILC it will be necessary to measure the beam polarisation with a precision of 0.25% to fully exploit the physics potential of machine and detectors [2]. These measurements will be realised via Compton polarimeters, where Cherenkov counters detect the backscattered Compton electrons. The Compton cross sections for different configurations of the laser light and e^+/e^- spin helicities are different, allowing for an asymmetry measurement, from which the polarisation level of the e^+/e^- -beams can finally be determined. For the upstream polarimeter a special magnetic chicane (Fig. 1(a)) is envisioned, so that the Compton edge of the backscattered electron beam will always be at the same position in the Cherenkov detector regardless of the energy of the original electron/positron beam.

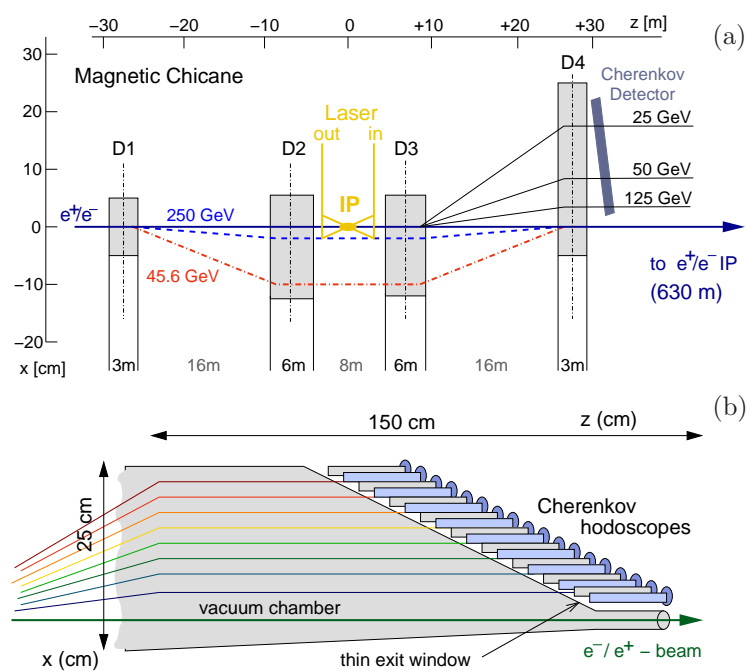


Figure 1: (a) The magnetic spectrometer and (b) the layout of the gas cherenkov hodoscope for the polarisation measurements.

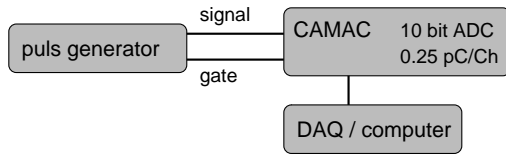
The scattered e^+/e^- are then deflected by the dipole magnetic fields of

the chicane and led to the detector, whose current baseline design [3] consists of gas tubes read out by photomultipliers (Fig. 1(b)). The incident e^+/e^- generate Cherenkov radiation inside the gas tubes, which is then detected by photomultipliers. However, alternative design possibilities, using quartz fibers and silicon photomultipliers, are also being studied.

For the detector R&D, many different aspects have to be taken into account and optimised. Among these are not only the choice of gas or the inside mirror-coating of the Cherenkov gas tubes (currently similar to those used for the polarimeter of the SLD detector at SLAC), but also different aspects of the photomultiplier and read-out electronics. It will, for example, be necessary to optimise the quantum efficiency, the sensitive area and the dynamic range of the photomultipliers, but also the reflectivity and the light extraction from the gas tubes. Furthermore, since the goal of achieving a polarisation measurement with a precision of 0.25% is very ambitious, the linearity of all detector components is extremely important. All non-linear effects (photodetectors, electronics, etc.) need to be measured precisely and corrected for if necessary.

2 The Component Test Stand

This test stand is based on CAMAC electronics and is used to develop different techniques for on- and off-line linearity measurements of various electronics components and different photodetectors. Up to now, two different methods for measuring the linearity of a QDC have been studied. The first method, of which Fig. 2 illustrates the setup, uses a sine wave as input to the QDC. The transition codes, or rather, the probability P_{code} for each transition to occur at a certain ADC-



code is measured and compared to the response of an ideal QDC, see Fig. 3(a):

$$P_{code} = \frac{N_{meas}}{\pi \cdot \sqrt{\frac{A^2}{2} - (code - offset)^2}},$$

Figure 2: The setup for the electronics tests.

where $A = 256$ pC is the charge amplitude at full scale range. Figure 3(b) shows the differential non-linearity (DNL), i.e., the difference between the measured and ideal QDC codes, while Fig. 3(c) displays the corresponding

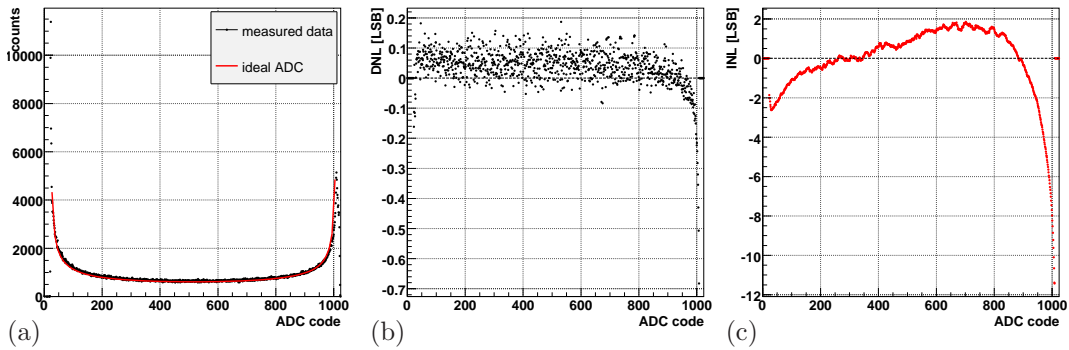


Figure 3: Linearity test: (a) measured and ideal prob. density function of QDC transition codes, (b) differential non-linearity, (c) gain and offset corrected integral non-linearity.

integral non-linearity (INL) after gain and offset correction, exemplary for channel 1. If a straight-line-fit is applied in the mid range of codes, from 200 to 800 ADC-counts, the INL ranges from 1 to 2 LSBs (least significant bit, or ideal QDC code width), corresponding to 0.1-0.2% of the full scale range.

The second method is a QDC self-test, integrated in the readout software. A DC-voltage from 0 to 20 V is applied to the QDC ($1 \text{ V} \hat{=} 12.5 \text{ pC}$) and the measured charge is compared to the input charge for multiple charge injections. This second method is less precise and, moreover, requires many steps and thus a very long measurement time.

In the near future, the component test stand will be used for a variety of other measurements, including the characterisation of different photo detectors (conventional PMTs and rather new developments, e.g. Silicon Photomultipliers), further linearity measurements regarding the photo detectors and, possibly, the entire readout chain. Longer term plans for this test stand also foresee measurements of temperature effects, the gain stability and other issues.

3 The SLD Cherenkov Detector Test Stand

As of early May 2006, the SLD Cherenkov detector is located at DESY. However, the necessary hardware components for its setup are not yet available, but a VME-PCI interface as well as charge-sensitive ADC (QDC) have been ordered. (For a description of the entire SLD-detector and the Compton polarimeter see Ref. [4].) For the detector commissioning it is planned to first test all nine channels for functionality – with a system of blue (and green) LEDs. Furthermore, the reflectivity and light yield (\leftrightarrow geometry), the sensitivity of the photo detectors, and the light extraction from the gas tubes will be studied. Later on, temperature effects will also be investigated, which might lead to an active regulation / stabilisation via thermo-electric elements. A proposal from April 18, 2007 lists further planned measurements, that will serve as a reference for studying new design features. Each measurement will either be performed as component and readout test of a single channel or of the entire detector system (Fig. 4), including:

- the characterisation of different types of photomultipliers (regarding sensitivity)
 - ▷ dark rate / light response;
 - ▷ voltage and/or temperature dependence;
 - ▷ dynamic range / sensitivity;
- the Pros/Cons of different types of photo detectors and connecting fibers:
 - ▷ photo detectors: conventional PMs, APDs, and SiPMs;
 - ▷ fiber types: optical, wavelength-shifting fibers;
- and the analysis of different couplings: (direct, air gap, etc.) between gas tubes & fibers, and between fibers & photo detectors;
- Linearity / non-linearity measurements for different configurations

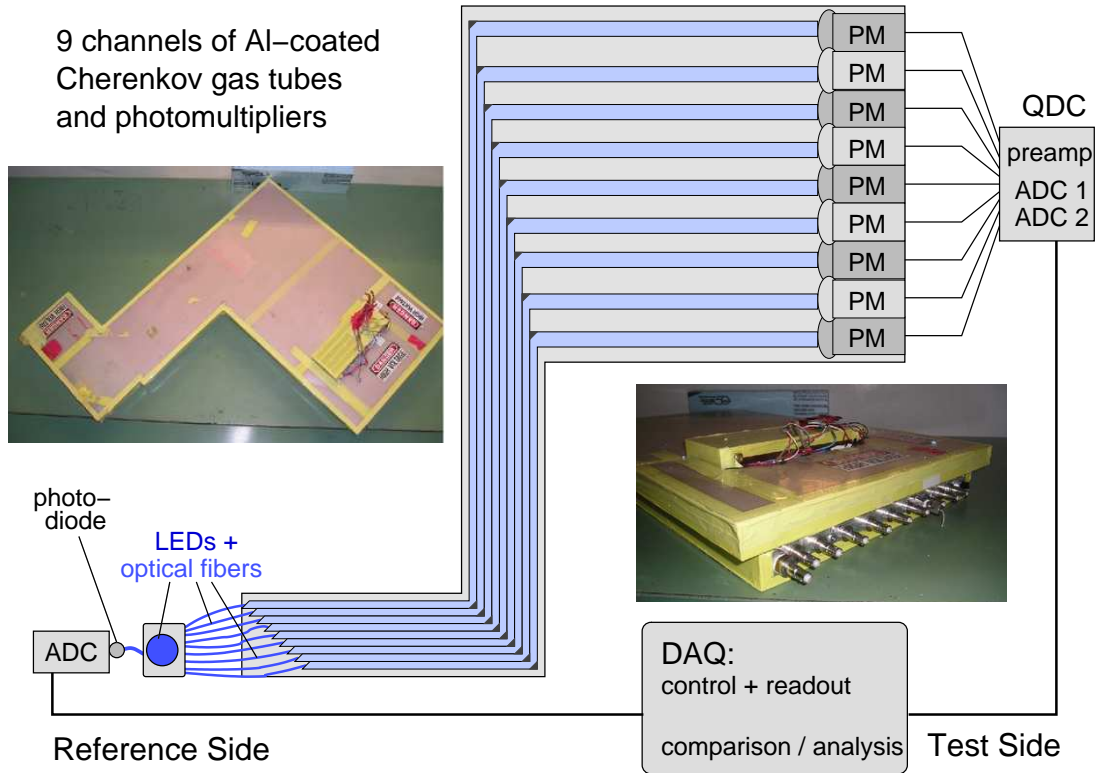


Figure 4: Schematic illustration of the setup of the old Cherenkov gas detector at DESY. The two photographs show a birdseye view (left), and the frontend (right).

4 Acknowledgments

The authors acknowledge the support by DFG Li 1560/1-1.

References

- [1] Slides:
<http://ilcagenda.linearcollider.org/contributionDisplay.py?contribId=172&sessionId=78&confId=1296>
- [2] G.A. Moortgat-Pick and H. Steiner, LC-TH-2000-055, 2000, [<http://www.desy.de/~lcnotes>];
G.A. Moortgat-Pick et al., ILC Reference Design Report, [[arXiv:hep-ph/0507011](http://arxiv.org/abs/hep-ph/0507011)].
- [3] TESLA Report 2001-23, Part III, DESY 2001-011, March 2001, [<http://tesla.desy.de>];
V. Gharibyan, N. Meyners, and K.P. Schüler, LC-DET-2001-047, DESY, Feb. 2001.
- [4] R.D. Elia, SLAC-Report-429, SLAC, Apr. 1994, (Ph.D. Thesis);
R.C. King, SLAC-Report-452, SLAC, Sep. 1994, (Ph.D. Thesis);
The SLD Collaboration (M. Woods), SLAC-PUB-7319, SLAC, Oct. 1996; [[arXiv:hep-ex/9611005](http://arxiv.org/abs/hep-ex/9611005)].

Simulation of ILC feedback BPM signals in an intense background environment

A. Hartin¹, P Burrows¹, G Christian¹, C Clarke¹, B Constance¹, H Khah¹, C Perry¹, C Swinson¹
R Arnold², S Molloy², S Smith², G White², M Woods², A Kalinin^{3*}

1- Oxford University - Physics Department
Keble Road, Oxford OX3 7TF- UK

2- Stanford Linear Accelerator Centre
Menlo Park, California USA

3- CCLRC - ASTeC Daresbury Laboratory
Daresbury, Warrington, Cheshire WA4 4AD, U.K.

Experiment T-488 at SLAC, End Station A recorded distorted BPM voltage signals and an accurate simulation of these signals was performed. Geant simulations provided the energy and momentum spectrum of the incident spray and secondary emissions, and a method via image charges was used to convert particle momenta and number density into BPM stripline currents. Good agreement was achieved between simulated and measured signals. Further simulation of experiment T-488 with incident beam on axis and impinging on a thin radiator predicted minimal impact due to secondary emission. By extension to worst case conditions expected at the ILC, simulations showed that background hits on BPM striplines would have a negligible impact on the accuracy of beam position measurements and hence the operation of the FONT feedback system

1 Introduction

The ILC beam-beam interaction produces a background environment that may affect the operation of feedback systems for beam alignment. One crucial element of the ILC feedback system is a stripline BPM placed near the interaction point in the extraction line. The operation of this feedback BPM in an intense background environment was tested at the T-488 experiment at SLAC EndStation A. T-488 operated in two modes. Firstly, a "high spray mode" in which the primary beam was directed off axis into a graphite torus producing a large background spray flux. Secondly, a "low spray mode" in which an on-axis beam impinging on a thin radiator resulted in a strong central beam and a lower flux of background charges [2].

In the high spray mode, BPM voltage signals visibly distorted from the usual bipolar doublet, were recorded (see figure 6). Accurate simulations that reproduced these high spray mode signal shapes were developed and are discussed in the first part of this paper. Experimental data from the low spray mode and high spray mode was combined to predict, by interpolation, the feedback BPM signal shapes expected at the ILC.

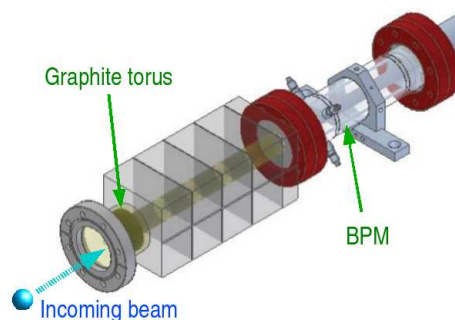


Figure 1: ESA T-488 module.

*This work is supported in part by the Commission of the European Communities under the 6th Framework Programme "Structuring the European Research Area", contract number RIDS-011899.

2 Simulations

The T-488 experimental module, containing the lowZ graphite torus, stripline BPM and connecting flanges (see figure 1) was modelled using Geant. With an incident flux of 10^4 electrons at different offsets on the x-axis, the x-profile of the scattered beam at the upstream end of the BPM strips was recorded (figure 2).

The x-profile of the beam was considered to consist of two current components; an azimuthally symmetric background spray I_{spray} and a remnant of the original beam I_b . I_{spray} was taken to be a constant average from the axis to radius of 1.5cm, and thereafter neglected. The contribution of both components to an image current in the BPM striplines $I_s = I_s^b + I_s^{\text{spray}}$ can be calculated by solving the Laplace equation in 2 dimensions [3]. The stripline current from a beam current I_b situated at (r, θ) from the axis of a beampipe of radius b, which subtends the stripline with angle ϕ (figure 3) is

$$I_s^b = -\frac{\phi}{2\pi} I_b \left[1 + \frac{4}{\phi} \sum_{n=1}^{\infty} \frac{1}{n} \left(\frac{r}{b}\right)^n \sin\left(\frac{n\phi}{2}\right) \cos(n\theta) \right] \quad (1)$$

The contribution to the BPM current I_s^{spray} is found by writing a current element ΔI_{spray} in terms of the current density J_{spray} and a volume element.

$$\Delta I_{\text{spray}} = J_{\text{spray}} r dr d\theta \quad (2)$$

Substituting ΔI_{spray} for I_b on the right hand side of equation 1 and integrating over all r and θ gives the contribution for the whole beampipe filling spray. The second term in equation 1 becomes zero and the first term contains the entire beampipe spray current.

$$I_s^{\text{spray}} = -\frac{\phi}{2\pi} I_b^{\text{spray}} \quad (3)$$

Much of the beam spray has significant transverse momentum which leads to direct hits on and secondary emission from the BPM striplines (figure 4). The time dependency of hits and secondary emission is determined with the aid of Geant's time of flight (TOFG) parameter. The electrical weight of each hit is determined by the method of image charge. A single charge e moving effectively from infinity to the strip surface contributes an image charge of e. Emitted charges e moving from the surface to effective infinity, contribute -e.

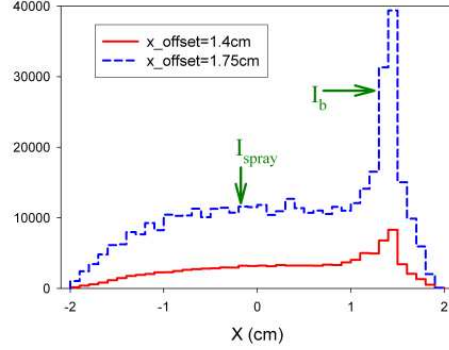


Figure 2: X-profile of beam at upstream end of BPM.

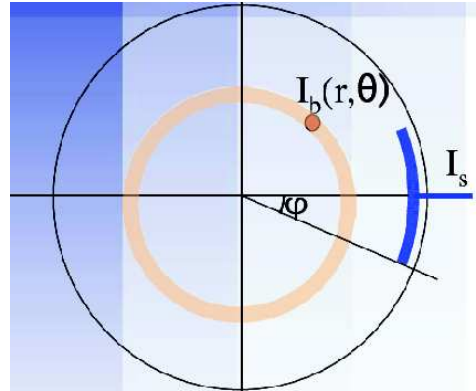


Figure 3: BPM x-y cross-section.

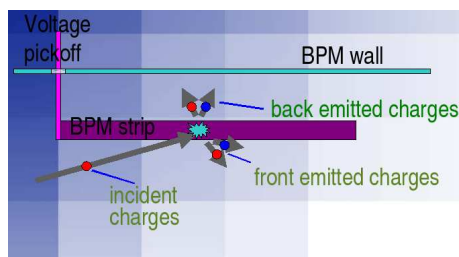


Figure 4: Hits and emission from BPM striplines.

Charges ejected from the back surface of the BPM strip quickly cross the 1mm gap between the strip and BPM wall and their contribution to the stripline current was taken to be entirely at the instant of emission. However for charges approaching or leaving the stripline tangentially, the contribution is a proportion of the charge. The extent of the tangential contribution is calculated by the transverse distance from the charge to the strip at either the upstream or downstream end of the strip, and the amount of image charge subtended by the stripline at that distance (see figure 5)

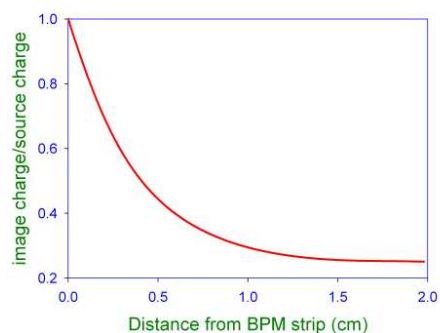


Figure 5: Stripline image charge variation with source charge distance.

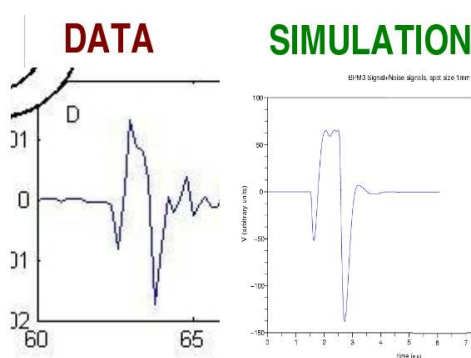


Figure 6: high spray mode BPM voltage signals.

3 Numerical Results

All the contributions to the stripline current were combined and the response of the oscilloscope that recorded them experimentally was simulated by use of a numerical second order, 1.2 GHz Butterworth low pass filter. Numerical calculations were performed using the Scilab program [4]. Comparison of experimental and simulated stripline signal showed good agreement, with the secondary emission signal superimposing a reverse bipolar doublet over the usual bipolar doublet (figure 6)

The distortion in BPM signal due to secondary emission may affect the amplitude of the difference signal used to drive the beam kicker in the feedback loop of the FONT system. The high spray mode of the ESA T-488 experiment however provides a background flux to beam signal ratio 3-4 orders of magnitude worse than that expected at the ILC. The ESA T-488 low spray mode provided a more realistic secondary emission to BPM signal ratio. No discernible effect on difference signal amplitude due to secondary emission could be determined beyond a 2% variation probably due to beam jitter, again in agreement with simulation (figure 7).

The expected effect on the ILC feedback BPM position measurements due to secondary emission was estimated by using Geant to simulate the number of incident hits on striplines for the T-488 low

spray mode and ILC parameter set 14 with anti-DiD field (figure 8). The ILC secondary emission to BPM signal ratio would be at least an order of magnitude smaller than that of the T-488 low spray mode and were therefore considered negligible

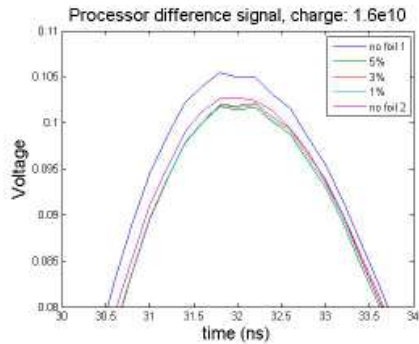


Figure 7: BPM difference signal in low spray mode (error bars of 2% not shown).

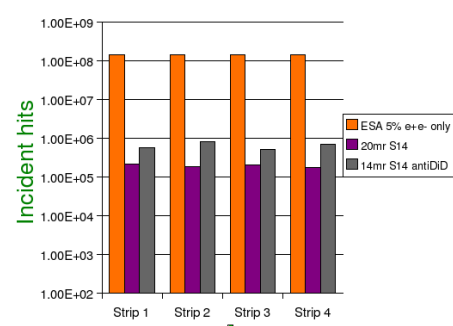


Figure 8: BPM stripline hits.

4 Conclusion

Distorted stripline BPM voltage signals were recorded at the ESA T-488 experiment with the incident beam off-axis and impinging on a lowZ graphite torus. The resultant charge spray was modelled using Geant and separated into a number of components. The effect on stripline current was calculated using the method of image charges, and the time response was filtered through a low pass numerical filter. Matching experimental and simulated signals gave confidence in the method employed. The simulations were applied to the T-488 low spray mode and no variation in BPM difference signal voltage amplitude beyond a 2% beam jitter was observed. The extent of background hits on the feedback BPM at the ILC, operating in its "worst case scenario" (in terms of pair background numbers) - parameter set 14 and anti-DiD solenoid field - was simulated. Since the effect at the ILC would be at least an order of magnitude smaller than that of the T-488 low spray mode, it was considered that pair backgrounds incident on BPM striplines at the ILC would have a negligible effect.

References

- [1] Geant - Detector Description and Simulation <http://wwwasd.web.cern.ch/wwwasd/geant>
- [2] P.N. Burrows et al, Electromagnetic Background Tests for the ILC Interaction Point Feedback System, PAC07 Proceedings
- [3] R.E. Shafer, AIP Conference Proceedings vol 212 (1989)
- [4] Scilab - open source platform for numerical computation <http://www.scilab.org>

14 mrad Extraction Line Optics for Push-Pull

Y. Nosochkov¹, K. Moffeit¹, W. Morse², B. Parker², A. Seryi^{1*}

1- Stanford Linear Accelerator Center
2575 Sand Hill Road, Menlo Park, CA 94025, USA

2- Brookhaven National Laboratory
Upton, NY 11973, USA

The ILC design [1] is based on a single Interaction Region (IR) with 14 mrad crossing angle and two detectors in the “push-pull” configuration, where the detectors can alternately occupy the Interaction Point (IP). Consequently, the IR optics must be compatible with different size detectors designed for different distance L^* between the IP and the nearest quadrupole. This paper presents the push-pull optics for the ILC extraction line compatible with $L^* = 3.5$ m to 4.5 m, and the simulation results of extraction beam loss at 500 GeV CM with detector solenoid.

1 Introduction

The ILC design [1] is based on a single Interaction Region (IR) with 14 mrad crossing angle and two detectors in the “push-pull” configuration, where the detectors can alternately occupy the Interaction Point (IP). The impact on the IR optics is that the two detectors may have different size and require different free space L^* between the IP and the nearest Final Doublet (FD) quadrupole. Below, we present the push-pull optics for the ILC extraction line compatible with L^* of 3.5 m to 4.5 m, and discuss tracking simulations of extraction beam loss at 500 GeV CM with detector solenoid.

2 Extraction optics

The push-pull optics near IP must be compatible with different detector designs and provide space for the detector exchange procedure. Fig. 1 shows the proposed layout of the incoming and extraction magnets on one side of the IP for three values of $L^* = 3.51, 4.0$ and 4.5 m. Here, the QD0, QF1 and SD0, SF1 are the incoming superconducting (SC) quadrupoles and sextupoles, and the QDEX1 and QFEX2A are the extraction SC quadrupoles. These magnets will be based on the compact SC design [2] in order to fit into the tight space provided by the 14 mrad crossing angle. To maximize the separation and magnet aperture, the first extraction quadrupole QDEX1 is placed farther from the IP at distance of 5.5, 5.95 and 6.3 m, in these options. Since the QD0,

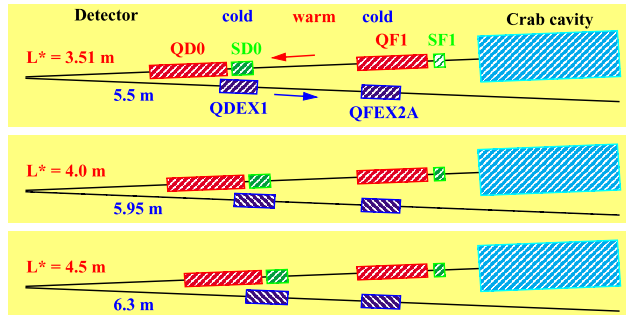


Figure 1: Magnets near IP for $L^* = 3.51, 4.0, 4.5$ m.

*Work supported by the Department of Energy Contract DE-AC02-76SF00515.

SD0, QDEX1 are inside the detector area, in order to facilitate a rapid push-pull exchange, each detector will have its own set of these magnets integrated into the detector cryostat. Consequently, the parameters of QD0, SD0, QDEX1 are optimized for each detector. For a uniform optics, the magnets outside of the detector will not change with L^* , except for field adjustment. The second set of SC magnets QF1, SF1, QFEX2A will be housed in a separate cryostat outside of the detector. The 2–3 m warm space between the 1st and 2nd cryostats, as shown in Fig. 1, will provide a breakpoint for detector detachment from the beamline. After the Final Doublet, there is a dedicated free space in the extraction line to accommodate the large size incoming crab-cavity.

The complete extraction optics and lattice functions are shown in Fig. 2, based on the earlier design in [3]. The SC and warm quadrupoles provide focusing to the 2nd focal point at $s = 148.6$ m with $R_{22} = -0.5$ required for the polarization diagnostics. After the quadrupoles, there are two vertical bending chicanes: for energy and polarization measurements [4] and gamma calorimeter (GamCal) [5]. The 6-bend polarimeter chicane is adjusted for 50% higher field in the 3rd and 4th bends for improved acceptance of Compton backscattered electrons in the Cherenkov detector, while the 5th and 6th bends close the trajectory bump and provide space and bending for GamCal.

The chicanes are followed by a system of 5 vertical and 5 horizontal fast cycling kickers. They will protect the dump window from damage and prevent water boiling in the tank in situations with a very small beam size such as in cases of an undisrupted beam or accidental focusing at dump. The kicker field will oscillate with ~ 1 kHz frequency to sweep the bunches in 1 ms train on 3 cm circle at the dump as shown in Fig. 3, thus reducing the beam density to acceptable level [6]. Finally, a system of 5 collimators is included: to clip off the disrupted low energy tail, to protect the extraction magnets and diagnostic devices from high beam loss and synchrotron radiation, and to limit the beam size at dump to within the 15 cm radius of the dump window. The dump is located ~ 300 m from the IP and > 3.5 m from the incoming line. The parameters of extraction magnets at 500 GeV CM are listed in Tables 1,2. The extraction magnets are compatible with 1 TeV CM energy, except the SC quads QDEX1, QFEX2A which require upgrade.

3 Detector solenoid

The detector solenoid field downstream of IP creates vertical orbit, dispersion, coupling and focusing in the extraction line. The orbit and dispersion are created due to the 7 mrad

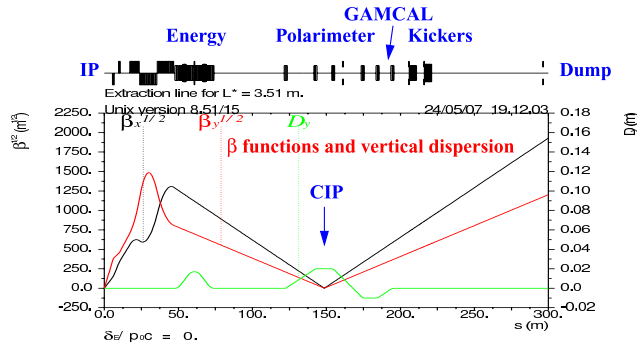


Figure 2: Extraction lattice functions.

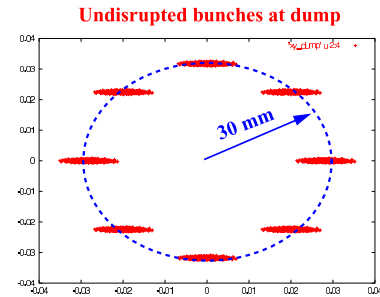


Figure 3: Swept bunches at dump.

Table 1: Quadrupole gradient (T/m), length (m) and aperture radius (mm) at 500 GeV CM.

Name	Qty	L* = 3.51 m			L* = 4.0 m			L* = 4.5 m		
		B'	L	R	B'	L	R	B'	L	R
QDEX1 (SC)	1	98.00	1.060	15	89.41	1.150	17	86.39	1.190	18
QFEX2A (SC)	1	31.33	1.100	30	33.67	1.100	30	36.00	1.100	30
QFEX2 (B,C,D)	3	11.12	1.904	44	11.27	1.904	44	11.36	1.904	44
QDEX3 (A,B,C)	3	11.39	2.083	44	11.37	2.083	44	11.36	2.083	44
QDEX3D	1	9.82	2.083	51	9.81	2.083	51	9.80	2.083	51
QDEX3E	1	8.21	2.083	61	8.20	2.083	61	8.19	2.083	61
QFEX4A	1	7.05	1.955	71	7.04	1.955	71	7.04	1.955	71
QFEX4 (B,C,D,E)	4	5.89	1.955	85	5.88	1.955	85	5.88	1.955	85

Table 2: Bend and kicker parameters at 500 GeV CM.

Name	Qty	L (m)	B (T)	Half-gap (mm)	Region
BVEX1E,...,8E	8	2.0	0.4170	85	Energy
BVEX1P,2P	2	2.0	0.4170	117	Polarimeter
BVEX3P	1	2.0	0.6254	117	
BVEX4P	1	2.0	0.6254	132	
BVEX1G,2G	2	2.0	0.4170	147	GAMCAL
XSWEEP	5	0.8	0.071	120	Fast kickers
YSWEEP	5	0.8	0.071	120	

angle between the solenoid and beam directions. Without correction, they will cause higher particle amplitudes and increased beam loss, and will alter trajectory and dispersion at the 2nd focus Compton IP (CIP). The other negative effect of the solenoid angle is deflection of e^+e^- secondary pairs away from the detector beam hole, thus increasing the detector background. The second source of extraction orbit is a non-zero incoming angle of beam trajectory at IP. The effect of solenoid focusing is weak, but it can shift the beam waist from the CIP by a few mm. It has been shown [7] that the e^+e^- background can be minimized by including the anti-DID horizontal field in the detector, as shown in Fig. 4 for the 5 T SiD solenoid model. The SC quadrupoles QDEX1 and QFEX2A will include the corrector coils which can be used to cancel the solenoid orbit and focusing effects. Fig. 4 shows the orbit cancellation using the QDEX1, QFEX2A dipole coils for $L^* = 3.51$ m and 50 μ rad angle at IP. This correction also compensates most of the residual dispersion.

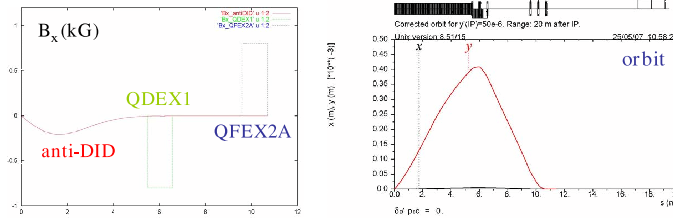


Figure 4: Cancellation of solenoid orbit for $L^* = 3.51$ m.

4 Extraction beam loss at 500 GeV CM

The following ILC beam options were used in tracking simulations: nominal (option c11), large vertical emittance (c13) and low beam power (c14). The disrupted beams are characterized by a low energy tail, with energies reaching 50% to 20% of nominal 250 GeV value,

and by a large angular spread. Beam in the nominal option has the lowest disruption. Option c13 has a larger angular spread, and option c14 has larger both the energy and angular spread. Additional disruption occurs when the beams are vertically offset at IP. The effects of energy and angular spread are the overfocusing of low energy electrons, large particle amplitudes and beam loss. The quadrupole focusing and magnet apertures are optimized for minimal loss of both the primary electrons and beamstrahlung (BS) photons which share the same beamline. The magnet aperture accepts photons with up to ± 0.75 mrad angles.

Table 3 shows the beam power loss for the three beam options, including the worst case IP offset Δy , for optics with $L^* = 3.51$ m without solenoid. The loss is small in options c11 and c13, and manageable in option c14. The three dump collimators located in the final 100 m drift have a larger beam load, because they trim the final beam size to within the 15 cm radius of the dump window. The IP offset may significantly increase the loss on collimators. For this reason, a protection system should be considered to detect and prevent beam running with large IP offsets. Example of beam loss in the first 200 m of extraction line for option c14 is shown in Fig. 5 for $L^* = 3.51$ m without solenoid. The two high peaks correspond to losses on the two diagnostic collimators COLE and COLCD.

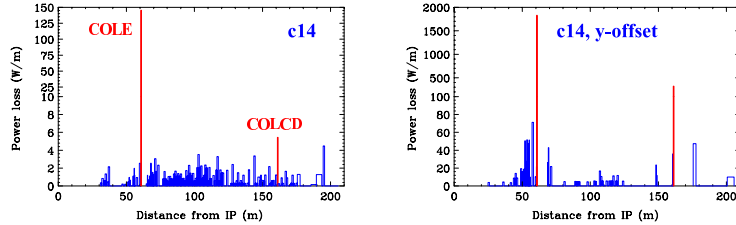


Figure 5: Beam loss in option c14 without (left) and with (right) IP y-offset for $L^* = 3.51$ m without solenoid.

Table 3: Power loss (kW) without solenoid for $L^* = 3.51$ m.

Option	Primary electrons						BS photons	
	All magnets and pipe	Diagnostic collimators		Dump collimators			Dump collimators	
		COLE	COLCD	COLW1	COLW2	COLW3	COLW1	COLW2
c11	0	0	0	0	0	0.272	0	0
c11+ Δy	0.001	0.001	0.0003	1.12	2.59	11.2	0.0001	0.025
c13	0.007	0.001	0.0001	1.02	1.57	6.54	0.570	0.820
c13+ Δy	0	0.0001	0	1.08	1.76	9.05	0.138	1.82
c14	0.126	0.044	0.003	2.62	6.18	26.3	0.035	0.171
c14+ Δy	0.581	0.549	0.161	85.9	43.7	82.1	10.9	20.1

Comparison of beam loss in the three configurations with $L^* = 3.51$ m, 4.0 m, 4.5 m without solenoid, and using option c14 without IP offset, showed that the electron losses are very similar and BS photon loss is evidently the same. For this reason, the remaining discussion will be limited to the optics with $L^* = 3.51$ m.

Tracking simulations with 5 T SiD solenoid, including anti-DID field and orbit correction, showed that solenoid effect on beam loss is small if the incoming vertical orbit has zero angle at IP. But in case of non-zero (under-corrected) y-angle at IP the losses at the diagnostic collimators would increase. The reason is the higher dipole field required for orbit correction which, in turn, increases non-linear dispersion and amplitudes of lowest energy electrons. Example of beam loss with solenoid and $50 \mu\text{rad}$ initial y-orbit angle is shown in Fig. 6 for the low power option c14. One can see that although the losses on magnets remain reasonably small, the load on diagnostic collimators (high peaks) is increased. Similar behavior is in the nominal ILC option c11, but the level of losses is a factor of 100 smaller.

The most increase of beam loss occurs when both the y -orbit angle at IP is non-zero and there is large vertical offset between beams at IP. It may be not desirable to cancel the IP orbit angle since it may not be optimum for highest luminosity. Therefore, to mini-

mimize the load on collimators, as mentioned earlier, a protection system is needed to detect and prevent running with large IP offsets. Further optimization of the diagnostic collimators may be needed to minimize the losses near the diagnostic devices. Bringing the corrector field closer to IP may also help to reduce the unwanted effects of non-linear dispersion.

5 Summary

The 14 mrad extraction optics compatible with push-pull detector configuration for a range of L^* from 3.5 m to 4.5 m is designed. The recent optics modifications also include the 6-bend polarimeter chicane which improves acceptance of Compton backscattered electrons in the Cherenkov detector and provides optics for GamCal, and the system of fast sweeping kickers for dump protection in cases of the small undisturbed or accidentally focused beam. Tracking simulations with 5 T SiD solenoid model, including the anti-DID field and orbit correction, showed that the increase of beam loss due to solenoid field is small. However, it increases with non-zero incoming vertical orbit angle and with large vertical beam offset at IP. The combination of these conditions produces the largest effect. The beam loss in the nominal parameter option still remains small to moderate. But more care is required in high disruption options. In order to minimize the unwanted power load on collimators, a protection system is needed to efficiently prevent beam running with large IP offsets. Secondly, more optimization of diagnostic collimators and orbit correction may be needed to minimize the unwanted losses and non-linear dispersion.

References

- [1] ILC Reference Design Report, ILC-Report-2007-001, August 2007.
- [2] B. Parker *et al.*, "Compact superconducting final focus magnet options for the ILC," SLAC-PUB-11764, PAC-2005-RPPP017 (2005).
- [3] Y. Nosochkov *et al.*, "ILC Extraction Line for 14 mrad Crossing Angle," SLAC-PUB-11591 (2005).
- [4] K. Moffeit *et al.*, "Proposal to Modify the Polarimeter Chicane in the ILC 14 mrad Extraction Line," SLAC-PUB-12425, IPBI-TN-2007-1 (2007).
- [5] W. Morse, "GamCal, a device for beam diagnostics," these proceedings.
- [6] L. Keller, <http://www-project.slac.stanford.edu/lc/bdir/Meetings/beamdelivery/2006-08-22/index.htm>.
- [7] A. Seryi *et al.*, "IR Optimization, DID and anti-DID," SLAC-PUB-11662 (2006).

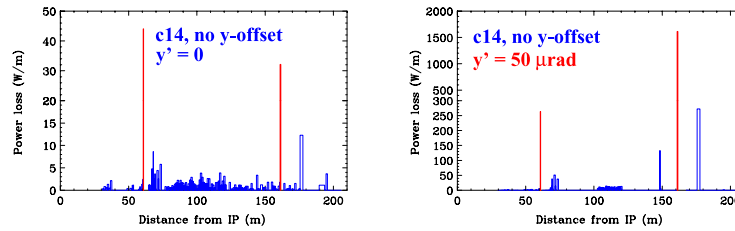


Figure 6: Beam loss in option c14 with solenoid, without (left) and with (right) 50 μ rad y -orbit angle at IP.

Physics Background as a Systematic Effect in Luminosity Measurement at ILC

M. Pandurović and I. Božović - Jelisavčić

“Vinča” Institute of Nuclear Sciences - Laboratory of Physics
M. Petrovića Alasa 12-14, Belgrade - Serbia

In order to achieve required precision of luminosity measurement at the International Linear Collider (ILC), that is of order of 10^{-4} , systematic effects have to be understood at the level of this precision. Apart from machine background originating from pairs converted from beamstrahlung and the beam-beam interaction effects, physics background from 2-photon processes is one of the main systematic effects. Properties of these processes, as well as their separation from the Bhabha signal have been studied.

1 Introduction

The International Linear Collider is anticipated to be used to make precision measurements of the properties of particles related to physics beyond the Standard Model. Error on luminosity affects many precision measurements, and limits some of them, as the additional component of a systematic error. Precision of luminosity measurement is driven by physics requirements for the cross-section measurements (i.e. the total hadronic cross-section at Z^0 resonance, 2-fermion production at high energy) and precision EW measurements (EWSB - anomalous gauge boson couplings, GigaZ).

2 Method

Integrated luminosity at ILC will be determined from the total number of Bhabha events N_{th} produced in the acceptance region of the luminosity calorimeter and the corresponding theoretical cross-section σ_B .

$$L_{int} = \frac{N_{th}}{\sigma_B} \quad (1)$$

The number of counted Bhabha events N_{exp} has to be corrected for the number of background events N_{bck} misidentified as Bhabhas, and for the selection efficiency ϵ .

$$L_{int} = \frac{N_{exp} - N_{bck}}{\epsilon \cdot \sigma_B} \quad (2)$$

Background to signal ratio is the bias to correct the measured total luminosity, as can be derived from (2).

Luminosity calorimeter has been designed [2] for the precise determination of the total luminosity. This is compact electromagnetic sandwich calorimeter consisting of 30 longitudinal layers of silicon sensor followed by tungsten absorber and the interconnection structure. It is located at $z = 2270$ mm from the IP, covering the polar angle range between 44 and 155 mrad, for the 14 mrad crossing-angle between the beams. Layout of the forward region as in the ‘Large Detector Concept’ (LDC) [3] has been assumed. Luminosity calorimeter is centered along the outgoing beam in order to avoid azimuthal angle dependence of $\Delta L/L$.

3 Results

Bhabha scattering at small angles is precisely calculable in QED ($\Delta\sigma_{th} \approx 10^{-4}nb$) [4] and has a sufficiently large cross-section to deliver high statistics for luminosity measurement of the required precision. With the cross-section of approximately 4 nb in the luminosity calorimeter angular range, at 500 GeV centre-of-mass energy and the nominal luminosity of $2 \cdot 10^{-34}cm^{-2}s^{-1}$ about 10^9 events will be collected per year, corresponding to the statistical error of order of 10^{-5} .

Bhabha events are characterized by the two electromagnetic clusters, with the full beam energy, that are back-to-back in azimuthal and polar angle. Based on this topology, separation criteria for signal from background will be derived. Signal of 10^5 Bhabha events has been generated with BHLUMI [5] small angle Bhabha generator, integrated into BARBIE V4.1 [6] detector simulation package. Both s and t channels have been included, vacuum polarization, as well as the the initial state radiation. We assumed head-on collisions, with luminosity detector that is axially symmetric around beam axis, and the corresponding detector acceptance between 26 and 82 mrad. Sensor planes of the luminosity calorimeter are segmented into 120 azimuthal sectors and 64 radial strips, alternately.

Four-fermion NC processes $e^+e^- \rightarrow e^+e^-f^+f^-$ ($f = l, q$) are considered to be one of the main sources of physics background for luminosity measurement. They are dominated by the multiperipheral processes (2-photon exchange). Both this study and an independent study [7] of two-photon processes ($2\gamma \rightarrow e^+e^-$), using Vermaseren generator [8], found occupancy in the luminosity calorimeter acceptance region of 10^{-3} particles per bunch crossing. These are rates comparable to the signal. The maximal occupancy of a sensor plane is given per train, for signal and background, in Figure 1. In terms of the detector occupancy, physics background contributes approximately 10 times less then the signal.

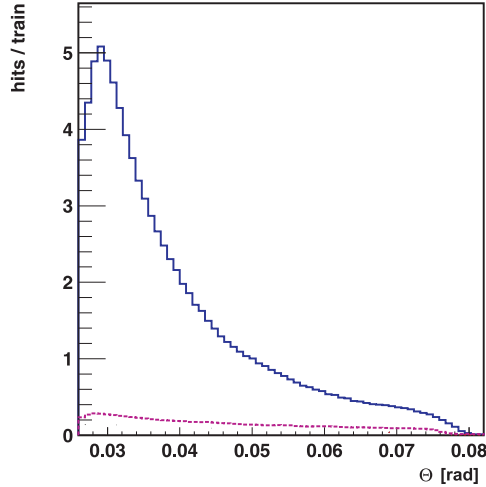


Figure 1: Occupancy in the sensors of the luminosity calorimeter for signal (solid line) and total background (dashed line).

To simulate physics background, the sample of 10^6 four-lepton events $e^+e^- \rightarrow e^+e^-l^+l^-$

($l = e, \mu$) and corresponding 10^5 hadronic events $e^+e^- \rightarrow e^+e^-q\bar{q}$ ($q = u, d, s, c, b$) have been generated with WHIZARD multiparticle event generator [9], with the total cross section of (1.68 ± 0.03) nb, assuming event generation through contributions of all neutral current tree-level processes. Though rates of signal and background are comparable in the luminosity calorimeter, well known characteristics of Bhabha events (colinearity, complanarity, energy distribution) allow isolation cuts to be applied. Discrimination of the signal from physics background is based on the set of cuts exploiting these symmetries of Bhabha topology [10]:

- Acolinearity cut $|\Delta\theta| \leq 0.06 \text{ deg}$,
- Acomplanarity cut $|\Delta\phi| \leq 5 \text{ deg}$,
- Energy balance cut $|E_R - E_L| \leq 0.1 E_{min}$, $E_{min} = \min(E_R, E_L)$,
- Relative energy cut $E_{rel} > 0.75$, $E_{rel} = (E_R + E_L)/2 \cdot E_{beam}$,

E_R, E_L being the total energy deposited on the right (front) and left side (back) of the luminosity calorimeter, respectively, and E_{beam} is the energy of the beam. All isolation cuts are applied assuming ideal reconstruction, since detector resolution does not affect the suppression of background, and assuming 100% reconstruction efficiency.

As illustrated in Table 1, starting from the comparable presence of signal to background, physics background can be reduced to the level of 10^{-4} , with the loss of signal efficiency of $\sim 20\%$.

	ε_s	R_l	R_h
1. $ \Delta\theta < 0.06 \text{ deg}$	81.87%	95.20%	95.27%
2. $ \Delta\phi < 5 \text{ deg}$	97.96%	89.53%	90.42%
3. $E_{bal} < 0.1 \cdot E_{min}$	90.61%	94.58%	95.45%
4. $E_{rel} > 0.75$	99.08%	88.73%	95.96%
5. $E_{rel} > 0.8$	98.50%	90.74%	96.57%
6. $30 < \theta < 75 \text{ mrad}$	64.99%	42.11%	41.95%
$B/S(1, 2, 3)$	$1.3 \cdot 10^{-4}$	80.60%	99.38%
$B/S(1, 2, 4)$	$2.6 \cdot 10^{-4}$	80.80%	99.26%
$B/S(5, 6)$	$1.8 \cdot 10^{-3}$	64.33%	93.69%

Table 1: Selection and rejection efficiency for signal and background, where ε_s denotes Bhabha selection efficiency, R_l - leptonic background rejection efficiency, R_h - hadronic background rejection efficiency.

Signal and background will be additionally affected by the beam-beam interaction effects. They will modify both initial state, through beamstrahlung, and the final state through electromagnetic deflection, resulting in the total suppression of the Bhabha cross-section (BHSE) of order of 4.4% [11]. In order to minimize the effect of the beam-beam interaction, the following set of cuts can be applied [11]:

- $E_{rel} > 0.8$
- $30 < \theta < 75 \text{ mrad}$

where the second cut has been subsequently applied to forward and backward side of the detector, allowing tolerance for the enhanced acolinearity of Bhabha tracks, due to the beamstrahlung. Alternation of this cut largely reduces the sensitivity of the luminosity measurement to the longitudinal position of the interaction point [4].

As shown in Table 1, asymmetric cuts are cutting-off more than one third of the signal, with the presence of background ten times larger than with symmetric cuts. In principal, annual Bhabha statistics of 10^9 events should allow a flexibility for 30% loss of the signal to still keep the statistical error of order of 10^{-4} . Uncertainty of background to signal ratio will influence the luminosity measurement as a component of the total systematic error. If the only of this ratio comes from the (generated) cross-section, the corresponding systematic error is of order of 10^{-6} , for colinearity based cuts, and 10^{-5} for asymmetric cuts.

4 Summary

The background to Bhabha events from the four-fermion NC processes has been studied for the luminosity calorimeter designed for ILC. It is shown that, due to the characteristic topology, Bhabha processes can be separated from physics background at the level of 10^{-4} . In the luminosity measurement, background to signal ratio will introduce a bias to be corrected for. Contribution to the systematic error of luminosity comes from the uncertainty of that bias. Under the assumptions used in this study, the uncertainty of background to signal comes from the error of the generated background cross-section, leading to the uncertainty of the bias of 10^{-6} for symmetric and 10^{-5} for asymmetric cuts.

Considering that beam-beam effects in the luminosity measurement are of order of 10^{-2} (BHSE) and that, in addition, uncertainty of the bias from beam-beam deflection is not known, a holistic study of systematic effects in luminosity measurement is needed in order to optimize selection of the signal in the presence of various sources of systematic error.

References

- [1] International Linear Collider; Reference Design Report, April 2007, [.http://www.linearcollider.org/cms](http://www.linearcollider.org/cms)
- [2] H. Abramowicz, I. Bozovic-Jelisavcic, M. Pandurovic et al [FCAL Collaboration], R&D for the ILC-Detector: Instrumentation of the Very Forward Region, DESY PRC R&D 02/01, April 2006.
- [3] Detector outline document for the Large Detector Concept, LDC Working Group for the Reference Design Report of the International Linear Collider, August 2006, <http://www.ilcldc.org/documents/dod>.
- [4] A. Stahl, Luminosity Measurement via Bhabha Scattering: Precision Requirements for the Luminosity Calorimeter, LC-DET-2005-004, May 2005.
- [5] S. Jadach, W. Placzek, E. Richter-Was, B.F.L. Ward and Z.Was, BHLUMI, A Monte Carlo Event Generator for Bhabha Scattering at Small Angles, Version 4.04.
- [6] B. Pavlik, BARBIE Version 4.1, Simulation package of the TESLA luminosity calorimeter.
- [7] L. Suszycki, LumiCal background studies, talk given at FCAL Research Workshop of the Israel Science Foundation, Tel Aviv, Israel, 18-22 September, 2005.
- [8] J.A.M Vermaseren, Nucl. Phys. B229(1983)347.
- [9] W. Killian, WHIZARD 1.40 A Generic Monte Carlo integration and event generation package for multi-particle processes (LC-tool 2002-039).
- [10] R. Ingbir, Luminosity detector design recommendation, talk given at the 4th International Linear Collider ECFA Workshop, Vienna, Austria, 14-17 November, 2005.
- [11] C. Rimbault, Limitation on precision luminosity measurement from beam-beam effects, European LC Workshop, Daresbury, UK, January 2007.

Impact of Beam-beam Effects on Precision Luminosity Measurements at the ILC: Main Results

Cécile Rimbault¹, Philip Bambade¹, Klaus Mönig² and Daniel Schulte³ *

1- LAL, Univ Paris-Sud, IN2P3/CNRS, Orsay, France

2- DESY, Zeuthen, Germany

3- CERN, Geneva, Switzerland

This note summarizes the results [1] of the first study done to quantify the impact of beam-beam effects on the precision luminosity measurement at the International Linear Collider, using GUINEA-PIG, a beam-beam interaction simulation tool.

1 Introduction

A way to determine luminosity at the International Linear Collider (ILC) is to measure the event rate of the Bhabha scattering process in a finely segmented calorimeter (LumiCal) at very low polar angles in the very forward region of the ILC detector. An absolute precision between 10^{-4} and 10^{-3} is needed for a number of key physics measurements [2, 3]. Besides theoretical uncertainties on the cross section of the Bhabha process [4] and different experimental errors when identifying Bhabha events in the LumiCal [5], the very strong beam-beam space charge effects which characterise the ILC e^+e^- collisions can lead to large biases in the counting rate. These must be corrected accurately enough not to limit the precision of the luminosity measurement.

A first study of such biases has been performed using the following procedure [6]. A sample of Bhabha events is first produced with BHLUMI, a multiphoton Monte-Carlo event generator for small-angle Bhabha scattering [7] providing four-momenta of outgoing electron, positron and photons. The center-of-mass energy is 500 GeV and the scattering angles are generated in the range $25 \text{ mrad} < \theta < 90 \text{ mrad}$.

The four-momenta of the two charged final state particles of a generated event are then read into GUINEA-PIG [8], a beam-beam interaction simulation tool, and associated to one of the e^+e^- interactions occurring during the simulated bunch collision. GUINEA-PIG computes the subsequent electromagnetic transport through the remaining part of the colliding bunch and the distribution of the resulting deflection is then obtained.

2 Effect of Beam-Beam Space Charge on Bhabha Scattering

Prior to the hard Bhabha scattering, the interacting particles are likely to have been deflected by the space charge of the opposite bunch and their energies reduced due to the emission of beamstrahlung. To take into account the cross section dependence with s , the probability used to produce Bhabha scattering events during the beam-beam collision is rescaled by s/s' , where s' is the effective centre-of-mass energy. The four-vectors of the Bhabha event particles are also rescaled by $\sqrt{s'/s}$, to satisfy energy and momentum conservation, as well as boosted from the centre-of-mass system of the two interacting particles to the laboratory

*This work is supported by the Commission of the European Communities under the 6th Framework Programme "Structuring the European Research Area", contract number RIDS-011899.

frame. Finally the coordinate system is rotated to take into account the deflection angles of the interaction particles in the initial state.

Just like the initial state radiation present in the initial sample generated with BHLUMI, the beamstrahlung emissions often occur asymmetrically, with either the electron or the positron losing most of the energy. Hence the acollinearity of the final state can be significantly enhanced.

The final state particles scattered in the acceptance of the LumiCal following a Bhabha interaction can cross a significant part of the opposite bunch. They can thus be focused by the electromagnetic field from the corresponding space charge. In the GUINEA-PIG simulation, the existing procedure to track secondary charged particles can be used conveniently to predict both the final deflection angle and any additional radiation. The resulting changes in scattering angles are displayed in Figure 1, where the differences between the initial polar angles before including the electromagnetic deflection, θ_1 and the final ones including it, θ_2 are shown as a function of θ_1 . The typical magnitudes of the induced electromagnetic deflections are a few 10^{-2} mrad, with the largest values at the lower edge of the LumiCal acceptance. Small energy losses due to radiation are also found.

Both the beamstrahlung radiation and electromagnetic deflection effects described above lead to a suppression of the Bhabha counting rate in the defined experimental acceptance in comparison to the theoretically predicted one. This Bhabha Suppression Effect (BHSE) can be expressed as:

$$BHSE = \frac{N_{final} - N_{init}}{N_{init}}, \quad (1)$$

where N_{init} and N_{final} are the numbers of Bhabha events selected within the specified cuts, respectively before and after including the different transformations to take into account effects from the beam space charge.

Because beamstrahlung radiation emitted prior to the hard Bhabha scattering enhances the acollinearity between the two final state charged particles, asymmetrical angular cuts [5] can help to minimise the BHSE and the resulting biases, for instance:

$$30 \text{ mrad} < \theta_{+/-} < 75 \text{ mrad} \quad \text{and} \quad 26.2 \text{ mrad} < \theta_{-/+} < 82 \text{ mrad} . \quad (2)$$

applied randomly, respectively to either the electron and positron, or vice-versa.

Similarly asymmetrical cuts on the energies are also advantageous. Choosing a global energy cut based on the sum of the final state energies:

$$E_- + E_+ > 0.8\sqrt{s}, \quad (3)$$

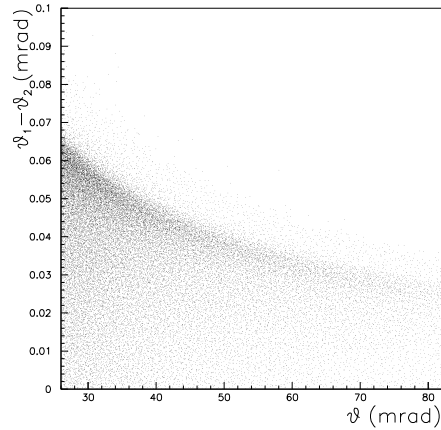


Figure 1: Change in Bhabha scattering final state polar angle due to the deflection induced by the space charge of the opposite bunch as a function of the polar angle at production.

as well as the angular cut in 2, the magnitude of BHSE is of the order of -0.015 for the ILC Nominal beam parameter set, two thirds of which is due to beamstrahlung emissions. Without such asymmetrical cuts, the BHSE bias is enhanced by a factor of about three.

3 Sensitivity to Beam Parameters

Both the beamstrahlung emissions and the electromagnetic deflection vary with the bunch parameters and the energy of the collision, and thus also the corresponding biases on the integrated luminosity. The reconstruction of the luminosity spectrum, based on the scattered Bhabha angles [9], provides a good way to measure the amount of beamstrahlung and thus to predict the corresponding contribution to the bias, because the electromagnetic deflections do not modify significantly this spectrum [6]. However, this also means that such a method does not allow probing effects from electromagnetic deflections experimentally.

In the following, the sensitivity of the BHSE on bunch parameters at the collision point and the residual dependencies which can be expected after correcting for the main contribution arising from beamstrahlung are discussed.

During operation of the ILC, bunch sizes and alignment at the interaction point can be expected to vary over time, due to dynamical imperfections in the acceleration and optical transport and through injection errors. Dedicated feedback control loops are included in the ILC design to maintain the bunch parameters constant within appropriate tolerances [10]. In this context, it is interesting to evaluate the precision needed on the knowledge of the main parameters to keep the BHSE within a given level of accuracy.

It was found that the BHSE only depends on both the horizontal size σ_x (see Fig. 2) and the bunch length σ_z . This can be understood because these parameters are directly related to the beamstrahlung emission. From the non-linear curves can be estimated the uncertainty on the BHSE resulting from a given precision assumed on the knowledge of σ_x and σ_z . Since the main uncertainty on the BHSE arises through the contribution from beamstrahlung, this part can in principle be measured and corrected from the luminosity spectrum reconstruction, the residual uncertainty which remains comes from the contributions of electromagnetic deflections. From the curves it can be deduced that to limit the error on the BHSE from this part to about 10^{-3} , a precision at the 20% level is needed on the knowledge of σ_z and

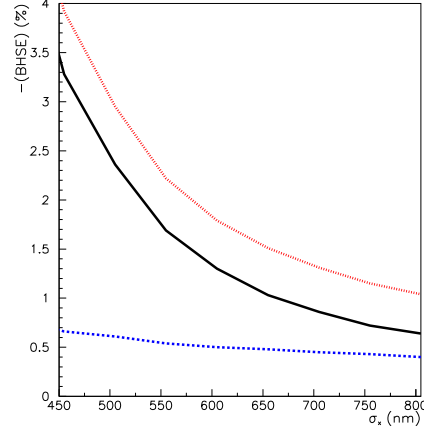


Figure 2: BHSE as a function σ_x . The contributions due to beamstrahlung (full line) and electromagnetic deflections (dashed line) are shown as well as the combined effect (top dotted line).

σ_x .

ILC should allow physics runs initially for energies between the Z boson mass and $\sqrt{s} = 500$ GeV [11]. In this energy range beam-beam effects are strongly modified. The dependence of BHSE with energy is shown in Figure 3, in the assumption that all optical parameters and the bunch length and intensity are kept constant. At the lower end of the energy range, the beamstrahlung contribution to the BHSE decreases to a few 10^{-4} . But on the other hand, electromagnetic deflections become rapidly stronger, dominating the bias below 400 GeV.

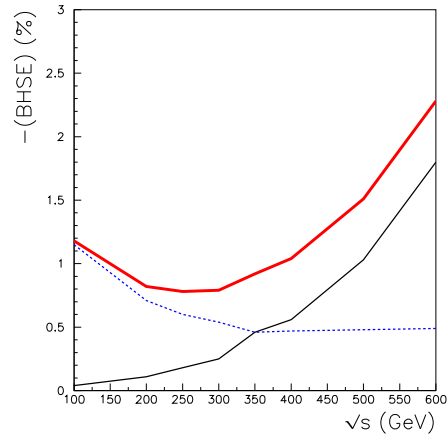


Figure 3: BHSE as a function of energy. The contributions due to beamstrahlung (thin line) and electromagnetic deflections (dashed line) are shown as well as the combined effect (top thick line).

4 Conclusion

In this study, it was shown, for the first time, that taking into account beam-beam interactions, the precise knowledge of the theoretical cross section is no longer sufficient to measure the luminosity with high precision (better than 10^{-3}), because strong collective effects modify drastically the kinematics of the Bhabha process. The first changes come from beamstrahlung, which induces a perturbation of the initial state. A second set of transformations arises from electromagnetic deflections which modify the kinematical phase space of the scattered Bhabha events. Using the beam-beam interaction simulation tool GUINEA-PIG, it was estimated that the bias induced on the luminosity measurement at low angle is about -0.015 for the Nominal beam parameter set. Two thirds of this bias are due to beamstrahlung emissions.

Both beamstrahlung emissions and electromagnetic deflections vary with the bunch length, σ_z , the horizontal size, σ_x , and the energy of the collision, and hence also the resulting biases on the integrated luminosity. Reconstructing the luminosity spectrum from the scattered Bhabha angles provides a good way to measure the amount of beamstrahlung, and thus to predict the corresponding contribution to the bias, because the electromagnetic deflections do not modify significantly this spectrum. Once this is done, controlling σ_x and σ_z at the 20% level around the nominal values is enough to limit the remaining contribution to the luminosity bias, from the deflections, to 10^{-3} .

Unlike the beamstrahlung emissions, no direct way to control experimentally the bias from the electromagnetic deflections is available from the data. Nevertheless, measurements of the beam angular divergence in the beam extraction line could be a way to monitor it. Further studies are needed on this point. Numerical simulations such as GUINEA-PIG [8] and CAIN [12] are essential estimation tools in all of this. A practical implementation to compute these effects is available at [13] and can be used for further studies.

In particular, physics running on the Z boson resonance is planned as an option in the ILC program (the GigaZ option). The accuracy on the luminosity is specified to be 10^{-4} in this case, while the bias from the electromagnetic deflections is at least a hundred times larger. Further more complete studies will then be particularly important, to explore all relevant dependencies and to devise data-driven correction methods.

References

- [1] Slides:
<http://ilcagenda.linearcollider.org/contributionDisplay.py?contribId=175&sessionId=78&confId=1296>
- [2] TESLA Technical Design Report, DESY 2001-011, March 2001.
- [3] The Forward Calorimetry Group, *R&D for the ILC-Detector: Instrumentation of the Very Forward Region*, DESY PRC R&D 02/01, April 2006.
http://www-zeuthen.desy.de/ILC/fcal/doc/PRC06/prc_rd_02-01_update_04-06.pdf
- [4] S. Jadach, *Theoretical error of luminosity cross-section at LEP*, June 2003. [hep-ph/0306083]
- [5] A. Stahl, *Luminosity Measurement via Bhabha Scattering: Precision Requirements for the Luminosity Calorimeter*, LC-DET-2005-004, 2005.
- [6] C. Rimbault, P. Bambade, K. Mönig, D. Schulte, *Impact of beam-beam effects on precision luminosity measurements at the ILC*, EUROTeV-Report-2007-017, JINST 2 09001, Septembre 2007.
- [7] S. Jadach, W. Placzek, E. Richter-Was, B.F.L. Ward, Z. Was, *Upgrade of the Monte-Carlo program BHLUMI for Bhabha scattering at low angles to version 4.04*, June 1996, CERN-TH/96-158. UTHEP-96-0601.
- [8] D. Schulte, Ph. D. Thesis, University of Hamburg 1996. TESLA-97-08.
- [9] K. Mönig, *Measurement of the Differential Luminosity using Bhabha events in the Forward-Tracking region at TESLA*, LC-PHSM-2000-60-TESLA, December 2000.
- [10] International Linear Collider Reference Design Report, first draft, february 2007.
http://media.linearcollider.org/rdr_draft_v1.pdf
- [11] A. Djouadi, J. Lykken, K. Mönig, Y. Okada, M. Oreglia, S. Yamashita, *The Physics Case for the International Linear Collider*, Frozen draft for the ACFA meeting in Beijing, February 2007.
http://www-zeuthen.desy.de/ILC/dcr_physics/dcr_beijing.pdf
- [12] K. Yokoya, User's Manual of CAIN - Version 2.35, April 2003.
<http://lcdev.kek.jp/~yokoya/CAIN/cain235/CainMan235.pdf>
- [13] <http://flc.web.lal.in2p3.fr/mdi/BBSIM/bbsim.html>

Update on the Beam-Related Backgrounds in the LDC Detector

Adrian Vogel

DESY – FLC
22603 Hamburg – Germany

In this talk [1] recent simulation results for beam-related backgrounds in the LDC detector are presented, using Guinea-Pig as a particle generator and Mokka as a full detector simulation. Different beam parameter sets and designs of the forward region are compared with respect to the background hits on the vertex detector.

1 Backgrounds at the ILC

Electron-positron pairs are a main source of background at the ILC. The very strongly-focussed bunches of the ILC interact through their high spatial charge densities and can emit photons, the so-called “beamstrahlung” [2]. These can in turn scatter and create electron-positron pairs – typically in amounts in the order of 10^5 per bunch crossing and with energies in the GeV range. Other sources of background are either supposed to be negligible (such as the beam dump or synchrotron radiation from the final focus) or have to be studied in further detail (e. g. the beam halo or losses in the extraction line).

The pairs can hit the forward calorimeters (mostly the BeamCal, which is in fact designed to observe the spatial distribution of the pairs) and the magnets of the beam delivery system and/or the extraction line, where they are over-focussed and deflected into the magnet material. In these processes, large amounts of photons and charged particles are created, and also neutrons can be released by photonuclear reactions.

Some of these particles (either directly from the IP or backscattered from the forward region) can reach the inner parts of the detector, most notably causing hits from charged particles on the inner silicon trackers, but also gradually damaging the silicon bulk and sometimes reaching the main gaseous tracker or the calorimeters.

2 Simulation Tools

2.1 Guinea-Pig – Particle Generator

Guinea-Pig [3] is used to simulate the beam-beam interaction. Given a set of beam parameters (energy, bunch sizes, emittances, bunch charge, etc.), Guinea-Pig writes out the electron-positron pairs which are created in one bunch crossing. Simulated data exists for the TESLA and various ILC beam parameter sets [4].

2.2 Mokka – Full Detector Simulation

The Geant4-based application Mokka [5] is used for a full simulation of the detector. The default detector geometry corresponds to the shortened “LDC version 2” [6], with an increased distance between LumiCal ($z = 2270 \dots 2470$ mm, $r = 100 \dots 350$ mm) and BeamCal ($z = 3550 \dots 3750$ mm, $r = 20 \dots 165$ mm), thus resulting in a better shielding against backscattering from the BeamCal. The geometry is implemented with a crossing angle of

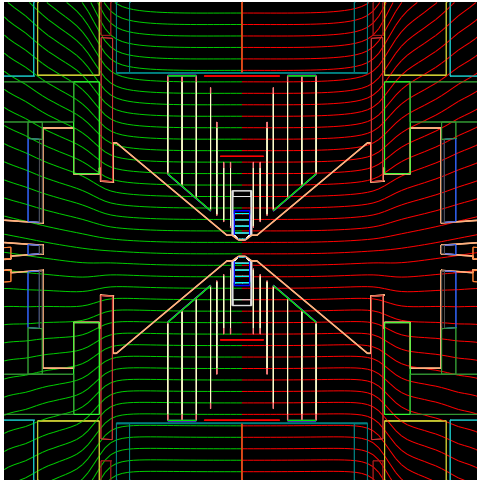


Figure 1: Overall detector geometry and anti-DID field (compressed view 1:10)

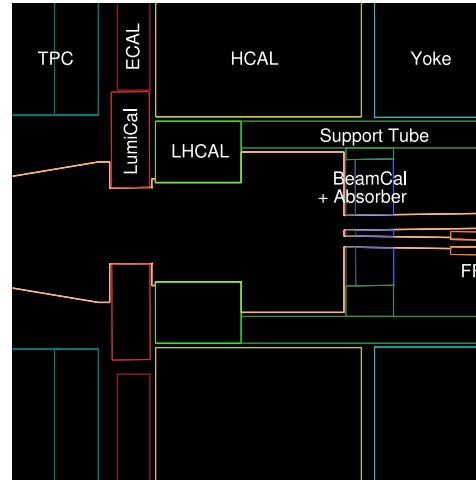


Figure 2: Design of the forward region (compressed view 1:2)

14 mrad and an anti-DID field [7] which bends the magnetic field lines from the IP towards the holes for the outgoing beams (Figures 1 and 2).

3 Hits on the Vertex Detector

The number of hits per layer generally decreases with the layer number, even though the innermost layer is only half as long as the rest and the outer layers have steadily increasing radii. The error bars of the following plots indicate the fluctuation (i.e., the standard deviation) per bunch crossing, not the statistical error of all 100 simulated bunch crossings.

3.1 Beam Parameter Sets

In the comparison of various beam parameter sets (Figure 3), the number of hits on the vertex detector clearly correlates with the number of primary electron-positron pairs. The nominal ILC parameters (at $\sqrt{s} = 500$ GeV) produce the least backgrounds, whereas the “low power” option with its even stronger-focussed beams gives more than twice the amount of background hits per bunch crossing. The old TESLA parameters are shown just for illustrational purposes – the original TESLA detector [8] had a completely different forward design than the LDC.

3.2 Influence of the Low-Z Absorber

About one third of the vertex detector hits are caused by backscatterers, most of which originate from the BeamCal. In the current design, the BeamCal is covered by a graphite absorber with a thickness of 50 mm which is intended to reduce backscattering.

Figure 4 shows that the graphite absorber in fact serves its purpose well: With a thickness of only 20 mm, the number of hits on the critical first layer increases by a factor of almost two, whereas the minimal profit from an increased thickness of 100 mm would hardly be justified

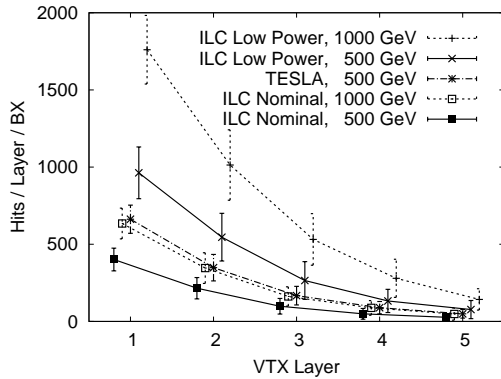


Figure 3: Number of hits on the vertex detector for various beam parameter sets

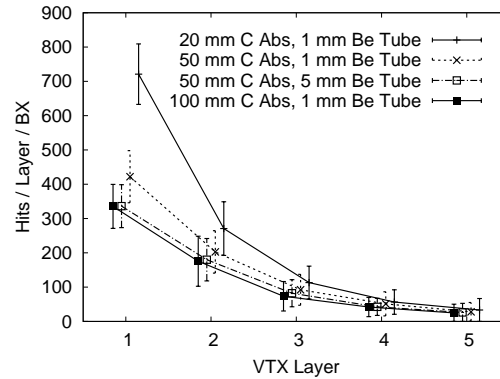


Figure 4: Number of hits on the vertex detector in relation to the thickness of the low-Z absorber

in comparison with the degraded resolution of the BeamCal itself – this is in agreement with previous dedicated studies of the absorber thickness [9]. However, a cladding of the inner surface of the BeamCal with 5 mm of beryllium would be an advantageous option.

4 Summary and Outlook

Backgrounds from backscattering particles have an important impact on the vertex detector, but they can be suppressed by appropriate means: The forward region has to be designed carefully in order to avoid “hot spots”, and the anti-DID helps in the reduction of backgrounds by preventing backscattered particles from hitting the vertex detector. For the low-Z graphite absorber in front of the BeamCal, a thickness of 50 mm looks reasonable, but additional absorber material inside the BeamCal could reduce backscattering further.

To study the impact of backgrounds on the whole reconstruction chain (including vertex detector, main tracker, and possibly the calorimeters), a large-scale production of background events is foreseen.

References

- [1] Slides: <http://ilcagenda.linearcollider.org/contributionDisplay.py?confId=1296&contribId=176>
- [2] K. Yokoya, KEK Report 85-9 (1985).
- [3] D. Schulte, DESY Report TESLA 97-08 (1997).
- [4] ILC@SLAC Beam Parameters Web Site, <http://www-project.slac.stanford.edu/ilc/acceldev/beamparameters.html>
- [5] Mokka Web Site, <http://mokka.in2p3.fr>
- [6] Large Detector Concept Web Site, <http://www.ilcldc.org>
- [7] B. Parker and A. Seryi, Phys. Rev. ST Accel. Beams **8**, 041001 (2005).
- [8] T. Behnke *et al.*, DESY-2001-011, Part IV (2001).
- [9] S. Niehage, Private communication

Backscattering of Secondary Particles into the ILC Detectors from Beam Losses Along the Extraction Lines

Olivier Dadoun and Philip Bambade *

LAL Univ Paris-Sud, IN2P3/CNRS, Orsay, France.

At the International Linear Collider (ILC) the beams will be focused to extremely small spot sizes in order to achieve the desired luminosity. After the collision the beams must be brought to the dump with minimal losses. In spite of all the attention put into the design of the extraction line, the loss of some disrupted beam particles, beamstrahlung or synchrotron radiation photons is unavoidable. These losses will generate low-energy secondary particles, such as photons, electrons and neutron, a fraction of which can be back-scattered towards the Interaction Point (IP) and generate backgrounds into the detector.

In this paper we present an evaluation of such backgrounds, using the BDSIM [2] and Mokka [3] simulations. The event reconstruction in the detector is made with the MarlinReco package from the Marlin tool [4].

1 Introduction

In an e^+e^- linear collider such as ILC, the beams will be focused to extremely small transverse sizes to reach the desired luminosity. This leads to intense beam-beam effects which result in large angular divergence and energy spread for the post-collision disrupted beams, as well as the emission of beamstrahlung photons. The disrupted beams and the beamstrahlung must be brought from the IP to their respective dumps with minimal losses.

The description of the present baseline extraction line design with a 14mrad horizontal crossing angle at the IP can be found in [6]. Several alternative extraction line studies, with a 2 mrad [7] crossing angle or with head-on collision [8] are also being pursued.

The paper presented here concentrates on the evaluation of the backgrounds in the Large Detector Concept (LDC [5]) from back-scattered photons induced by disrupted beam losses for the specific case of the first collimator in the 2mrad scheme. The methods developed are however general and can be applied to other extraction line designs and detector concepts. sectionParticles losse on the first collimator in the 2 mrad extraction line The new layout of the 2 mrad crossing angle has relatively good beam transport properties for all machine energies and beam parameter sets [7]. In the case of the 500 GeV center-of-mass machine, beam losses at the kW level are however expected at the first collimator QEX1COLL located at 45 m from the IP. These losses generate back-scattered photons. A fraction of these can reach the detector via direct lines of sight passing through the BeamCal mask aperture.

1.1 Disrupted beam losses at the first collimator

After having simulated the beam-beam collision with GuineaPig [9], the disrupted beam is tracked from the IP to QEX1COLL. The horizontal distribution of the particles lost at QEX1COLL is offset by a mean value of 20 cm with respect to the incoming beam line. The

*This work is supported by the Commission of the European Communities under the 6th Framework Programme "Structuring the European Research Area", contract number RIDS-011899.

number of lost particles represents less than 0.1% of the initial distribution. The energy spectrum of these lost particles is shown in figure 1. The interaction of these high energy

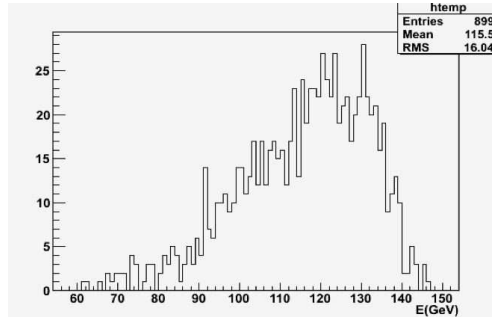


Figure 1: Energy distribution of disrupted beam particles lost at the first collimator QEX1COLL, located at 45 m from the IP.

electrons (with a mean energy of 115 GeV) in the collimator material is simulated using the BDSIM Geant4 based toolkit. In this study, copper was considered.

1.2 Back-scattered photons

The interaction of the high energy electrons in the material produces high energy photons from bremsstrahlung (main process at these energies) which generate a cascade of processes. The high energy photons are converted into a large number of lower energy particles, among which low energy photons travelling backwards. The corresponding spectrum is shown in figure 2. Three main processes relevant to the production of these back-scattered photons

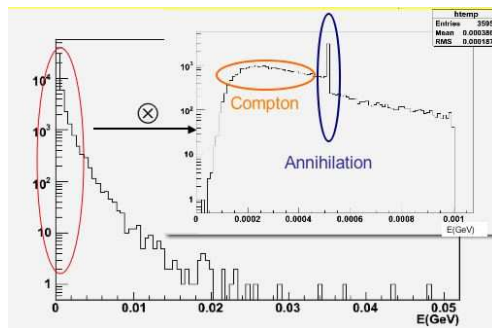


Figure 2: Back-scattered photon energy distribution, including zoom below 1 MeV in the insert.

are :

- Compton scattering
This process takes place between the incident bremsstrahlung photon and an electron in the material, producing a spectrum with typically an edge at 250 keV.

- Pair production
If the photon energy exceeds $2 \times m_e$ (m_e is the electron mass), the production of a e^+e^- pair is energetically possible. After thermalisation, the e^+ annihilates in the material, producing two back-to-back photons carrying each of them an energy of m_e , one of which is typically back-scattered.
- Photoelectric effect
When an electron is ejected from the K shell, the vacant place is filled by a free electron with a X-ray emission at 9keV. Due to the 10 keV energy threshold used in Geant4, this peak is not present in figure 2.

subsection Photon rate reaching the Vertex Detector The back-scattered photon angular distribution is shown in figure 3. As can be seen, it is broadly isotropic, even if some

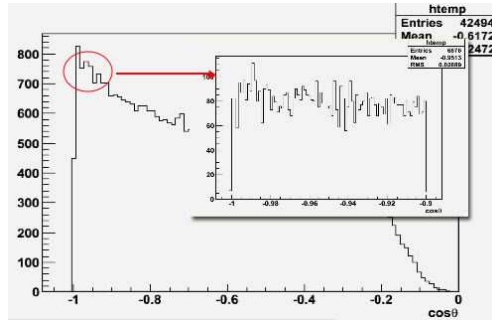


Figure 3: Polar angle distribution of back-scattered photons, including zoom around the backward direction at $\cos \theta = -1$ in the insert.

peaking occurs in the backward direction. For this reason, the fraction which can reach the IP directly without rescattering is very small, as it is limited by the apertures in the beam line. The tightest of these apertures is that of the BeamCal located inboards of the last final focus magnet, thus serving as an efficient mask for these photons. In the 2 mrad extraction line design, a 12 mm radius is used in order to shadow the innermost vertex detector layer at 15 mm. To estimate the fraction of back-scattered photons passing through this small hole, the flatness of the $\cos \theta$ distribution around the backward direction is exploited to obtain the number of photons and the probability distribution within the corresponding solid angle, by rescaling.

With this method, after appropriate normalisation to the total beam power, 40 photons per bunch crossing are estimated into the detector volume per kW of beam power lost at the QEX1COLL collimator 45 m after the IP. sectionHits in the LDC VD

1.3 Mokka simulation

The geometry of the LDC detector in the Geant4 based Mokka simulation is shown in figure 4. At 3.5 m, photons are generated within the 12 mm radius of the BeamCal with a flat spatial distribution, the energy spectrum shown in figure 2 and a fixed horizontal angle of 4.4 mrad corresponding to the 20 cm mean offset of the lost beam particles at 45 m. The Mokka output is then treated using the MarlinReco package from the Marlin reconstruction software.

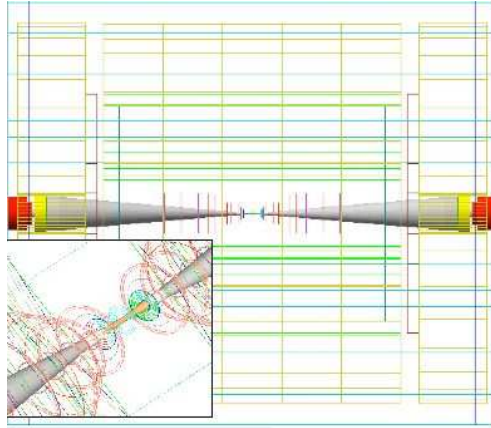


Figure 4: LDC concept detecteur simulated in Mokka.

1.4 VD hits

The spatial distribution of the hits in the VD is shown in figure 5. Most of hits occurred at 15 mm, corresponding to the first layer ^a. A strong left-right assymetry is visible, resulting from the fact that the emission points of the photons are offset to one side. The distribution

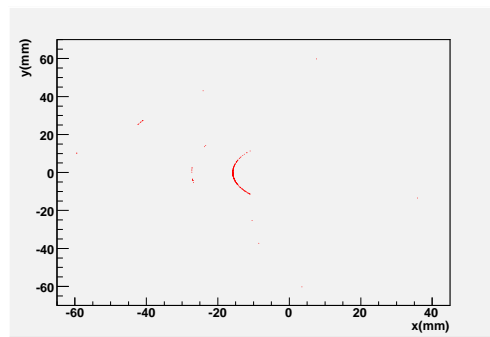


Figure 5: Location of the hits in the VD.

of deposited hit energies in the silicon is shown in figure 6.

The most probable value is about 15 keV, corresponding to approximately twice that obtained for high energy muons in similar conditions. This large value is explained by the very low electron momenta involved.

The number of hits observed in the VD is about 3% of the incident photon rate. A 1 kW beam power loss at QEX1COLL would hence amount to about 1 hit per bunch crossing. This is negligible in comparison to the number of hits from incoherent e^+e^- pairs produced in the beam-beam interaction and reaching the VD directly (estimated to be around 250 per bunch crossing [10]).

^aThe VD in LDC has a total of 5 layers.

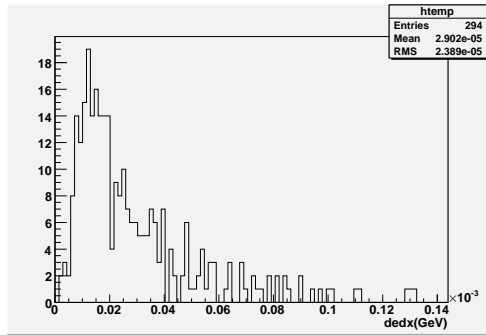


Figure 6: Distribution of deposited hit energies in unit of GeV.

2 Conclusion and prospects

It has been shown that photon back-scattering from disrupted beam losses at the first collimator QEX1COLL in the 2 mrad crossing angle scheme produce negligible effects in the detector.

Further studies planned include a more complete analysis of all photon emission sources along both the 2 mrad extraction line and the other IR geometries under consideration, including from the main beam dump and taking into account multiple reflections in the beam pipe.

References

- [1] Slides:
<http://ilcagenda.linearcollider.org/contributionDisplay.py?contribId=177&sessionId=78&confId=1296>
- [2] I. Agapov et al, The BDSIM Toolkit EUROTeV-Report-2006-014-1.
- [3] G. Musat, GEANT4 simulation for the FLC detector models with MOKKA. Proceedings of the International Conference on Linear Colliders,437-439
- [4] T. Kraämer et al, A Marlin based Reconstruction Package
- [5] On the web: <http://www.ilcldc.org/>
- [6] A. Seryi et al, Design of the Beam Delivery System for the International Linear Collider, in these Proceedings.
- [7] R. Appleby et al, Minimal 2 mrad extraction line layout for the International Linear Collider, in these Proceedings.
- [8] O. Napoly et al, Technical Challenges for Head-On Collisions and Extraction at the ILC, in these Proceedings.
- [9] C. Rimbault et al, An Upgraded Version of the Linear Collider Beam-Beam Interaction Simulation Code GUINEA-PIG, in these Proceedings
- [10] C. Rimbault et al, Incoherent pair generation in a beam-beam interaction simulation Phys. Rev. ST Accel. Beams 9, 034402 (2006)

Pair Monitor Studies

Yosuke Takubo¹, Hirokazu Ikeda², Kazuto Ito¹, Tadashi Nagamine¹, Rei Sasaki¹
and Hitoshi Yamamoto¹

1- Department of Physics of Tohoku University
Research Center for Neutrino Science, Tohoku University Sendai Miyagi, Japan
2- Institute of Space and Astronautical Science, Japan Aerospace Exploration Agency
3-1-1 Yoshinodai Sagami-hara Kanagawa, Japan

We study for the pair monitor which measures the beam profile at the interaction point by using the distribution of e^+e^- pair generated from the beam crossing. The simulation study confirmed that the pair monitor can measure the vertical beam size with 8% level with the e^+e^- distributions accumulated for 150 bunches. As the hardware study, the readout ASIC is developed. The shift register to specify the readout cell was verified to work correctly.

1 Introduction

The pair monitor is used to check the beam profile at the interaction point (IP), measuring the distribution of the e^+e^- pairs generated during beam crossing [2]. The particles of concern have the same charge as that of the oncoming beam, and are hereafter called “same-charge” particles. Most of them are deflected at larger angles than their inherent scattering angles by a strong electromagnetic force due to the oncoming beam, while the “opposite-charge” particles must oscillate inside the oncoming beam because of a focusing force between them; they are deflected with small angles. They can be well described by a scattering process of $e^- (e^+)$ in a two-dimensional Coulomb potential that is Lorentz boosted to the rest frame of the oncoming beam. Since this potential is produced by the intense electric charge of the oncoming beam, it is a function of the transverse size (σ_x, σ_y) and intensity of the beam. Therefore, the deflected particles should carry this information, especially in their angular distribution. The pair monitor uses this principle to extract information of the beam profile at IP.

We study the pair monitor to be used for the ILC beam profile monitor. The performance check and its optimization are performed by the simulation. In addition, we develop a readout ASIC suitable for the pair monitor. In this paper, the current status of these studies are reported.

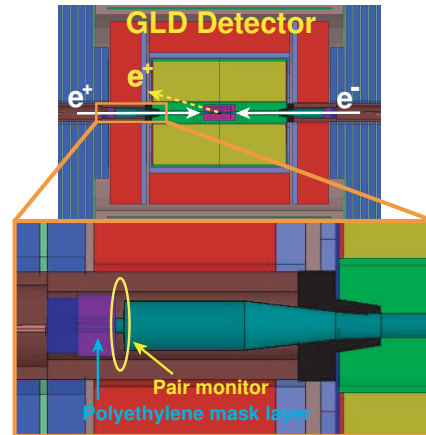


Figure 1: The simulation setup. The pair monitor is located at 400 cm from IP, that is in front of the Polyethylene mask layer.

2 Simulation Study

The performance and optimization of the pair monitor is studied with the simulator based on the Geant4, which is used for the GLD detector (Jupiter). In the simulation, e^+e^- events from the beam crossing are generated by CAIN, in which the standard beam size is defined as $(\sigma_X, \sigma_Y, \sigma_Z) = (639 \text{ nm}, 5.7 \text{ nm}, 300 \text{ }\mu\text{m})$. Figure 1 shows the simulation setup. The pair monitor is located at 400 cm from IP, that is in front of the Polyethylene mask layer to absorb γ s and e^\pm s created in the BCAL. The magnetic field is set to 3 T with anti-DID.

In this study, the e^+e^- distribution is studied at the left side in Figure 1, where the oncoming beam is e^+ . Therefore, e^+ distributions on the pair monitor have the beam information, since e^+ is scattered with large angle whereas the e^- is not scattered so much.

As the first step, the performance to measure the vertical beam size is checked. Figure 2 shows the relation between r and ϕ for e^+ , where r is the radius from the center of the extraction beam pipe for the e^- beam and ϕ is the angle around it. We select the L-region ($\phi = -3.14 \sim -1.8$ rad. and $r = 2 \sim 7$ cm) and H-region ($\phi = -1.4 \sim 2.5$ rad. and $r = 2 \sim 5$ cm) as shown in Figure 2, where the number of events depends on the vertical beam size largely. In the L-region, the number of the events decreases for larger vertical beam size, and that increases in the H-region. To extract information of the beam size, the peak-to-valley ratio is defined as N_L/N_H , where N_L and N_H are the number of events in the L-region and H-region, respectively. Changing the vertical beam size, we compare the peak-to-valley ratio.

Figure 3 shows the peak-to-valley ratio as a function of the ratio between the vertical beam size used in the simulation (σ_Y) and the standard vertical beam size ($\sigma_{Y0} = 5.7 \text{ nm}$). To make the figure, data for 21, 26, 27, and 50 bunches is accumulated for the vertical beam size of σ_{Y0} , $2\sigma_{Y0}$, $3\sigma_{Y0}$, $4\sigma_{Y0}$, and $5\sigma_{Y0}$, respectively. In Figure 3, the statistical error is assigned to the error bar. The peak-to-valley

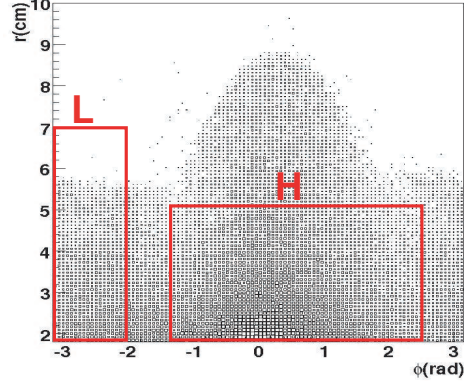


Figure 2: r v.s. ϕ distribution for e^+ , where r is the radius from the center of the extraction beam pipe for the e^- beam and ϕ is the angle around it.

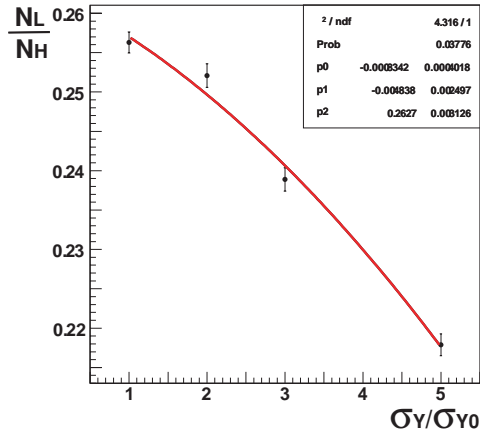


Figure 3: Peak-to-valley ratio as a function of the ratio between the vertical beam size used in the simulation (σ_Y) and the standard vertical beam size ($\sigma_{Y0} = 5.7 \text{ nm}$).

ratio depends on the vertical beam size clearly.

The performance to measure the vertical beam size is investigated when the data is accumulated for 150 bunches. The statistical error in Figure 3 is scaled to that for 150 bunches. Then, it is transformed to the uncertainty of the horizontal axis by using the fitting function obtained in Figure 3, that corresponds to the measurement accuracy of the vertical beam size. As the result, 8% accuracy is obtained when the vertical beam size is the standard one.

3 Development of Readout ASIC

We develop the readout ASIC for the pair monitor. It is designed to count a number of the hit to obtain the hit distribution on the detector. The statistics for about 150 bunches is enough to extract the beam information from the simulation study. Therefore, the number of the hit is counted for 16 timing parts in one train, which corresponds to 167 (= 2670/16) bunches in the current nominal ILC design. The hit counts for each timing parts are read within the timing width between each train (200 ms).

A silicon pixel sensor with the thickness of about $200\ \mu\text{m}$ is assumed as a detector candidate, whose signal level is about 15,000 electrons. The readout ASIC is designed to satisfy these concept.

The readout ASIC consists of the distributor of the operation signals, shift register to specify a readout cell, data transfer to the output line, and 36 readout cells. A readout cell consists of the amplifier, comparator, 8-bit counter, and 16 count registers. They are aligned to 6×6 for the X and Y directions. The prototype ASIC was produced with $0.25\ \mu\text{m}$ process. Its layout was made by Digian Technology, Inc. [3], and the production was done by the MO-SIS Service [4]. The chip size is $4 \times 4\ \text{mm}^2$, and the readout cell size is $400 \times 400\ \mu\text{m}^2$. To test the response of the readout chip, it is covered with MQFP package produced by I2A Technologies [5].

As the first test, the response of the shift register was checked. The shift register is used for the specification of the readout cells. The specification is done by inputting the shift clocks for the X and Y direction when the enable gate is opened. At the timing of the seventh shift clock for the X or Y directions, the shift register is designed to output the shift-done signal. Therefore, the response of the shift register can be confirmed by checking the shift-done signal after inputting the 7 shift clocks

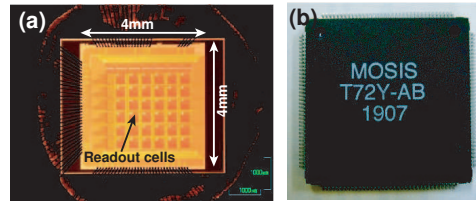


Figure 4: A prototype of the readout chip: (a) before package (b) after package.

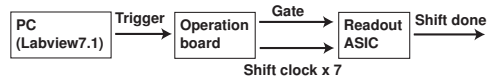
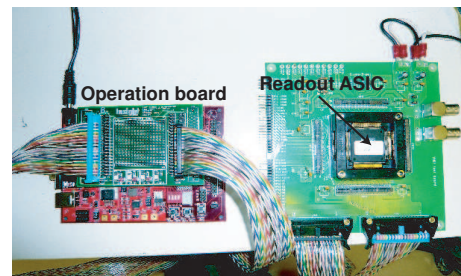


Figure 5: Experimental setup for the response test of the readout ASIC.

to one direction.

Figure 5 shows the experimental setup for the response test of the readout ASIC. The trigger signal is sent to the operation board (Spartan3 starter kit) from a computer, whose operation is done by using LABVIEW 7.1. The operation board is mounted a FPGA (Field Programmable Gate Array) which realizes flexible modification of the logic. An enable gate and shift clocks are sent to the readout ASIC by the operation board. The shift-done signal is monitored by an oscilloscope.

The first prototype is produced in 2005. The shift-done signal is output without regard to the timing of the shift clock. After the investigation, all the digital inputs were insulated by mistake in the production of the prototype. Therefore, the digital input was short-circuited in the second prototype, which was produced in 2007.

Figure 6 shows the test result of the shift register for the second prototype. We can see the shift done-signal at the timing of the seventh shift clock. From this result, it is confirmed that the shift register works correctly.

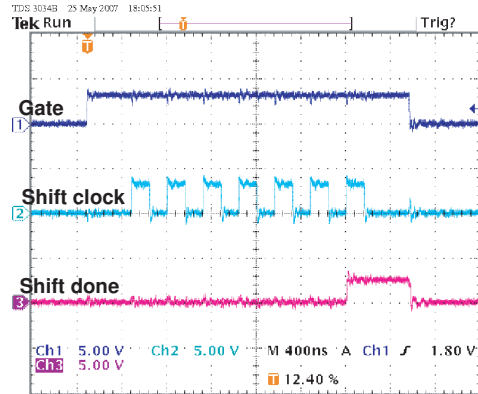


Figure 6: The test result of the shift register for the second prototype. The shift-done signal is output at the timing of the seventh shift clock.

4 Conclusions

We study the detector optimization and the readout ASIC for the pair monitor. The simulation study confirmed that the pair monitor can measure the vertical beam size with 8% level with the e^+e^- distributions accumulated for 150 bunches. The readout ASIC is developed for the pair monitor. Although the digital input was insulated in the first prototype, it was modified for the second prototype. The shift register to specify the readout cell was verified to work correctly.

5 Acknowledgments

This study is supported in part by the Creative Scientific Research Grant No. 18GS0202 of the Japan Society for Promotion of Science.

References

- [1] Slides:
<http://ilcagenda.linearcollider.org/contributionDisplay.py?contribId=178&sessionId=78&confId=1296>
- [2] T. Tauchi and K. Yokoya, Phys. Rev. E 51, 6119, 1995.
- [3] <http://www.digian.co.jp> in Japanese.
- [4] <http://www.mosis.com>.
- [5] <http://www.ipac.com>.

ILC Beam Energy Measurement Using Compton Backscattering

N. Muchnoi¹, H.J. Schreiber² and M. Viti²

1- Budker Institute for Nuclear Physics BINP
Novosibirsk 630090 - Russian Federation

2- Deutsches Elektronen-Synchrotron DESY
15738 Zeuthen, Germany

An alternative approach to measure the ILC beam energy is suggested. Beam electrons interact with monochromatic laser light so that downstream of the interaction point unscattered beam particles (most of them) and strongly collimated Compton backscattered electrons and photons exist. After passing a dipole, these particles are divided into non-deflected high energy photons, less deflected beam particles and scattered electrons with some larger deflection. Measuring the spatial distributions of these types of particles permits to infer the beam energy with an accuracy 10^{-4} or better. Since the systematics of the Compton backscattering approach are quite different from those of the BPM-based energy spectrometer, Compton backscattering provides an independent beam energy calibration system with comparable accuracy. The approach has no strict limitations on the beam energy, so it might be experimentally tested at lower energy machines.

1 Introduction

Accurate knowledge of the energy of colliding beams plays an important role in the physics program of the ILC. For example, masses of particles can be precisely determined either by means of threshold scans of cross sections of pair produced particles or by improving the 4-momenta of particles produced in the continuum. At circular lepton colliders the energy scale was accurately calibrated by means of the resonant depolarization technique, which is however not applicable at linear colliders. So at linear colliders some new approaches for beam energy monitoring are needed to be addressed.

Compton backscattering of monochromatic laser light on beam particles permits access to the beam energy utilizing precise information of the Compton backscattered electrons and photons. This approach is thought to be complementary to the canonical method of beam position monitor (BPM)-based magnetic spectrometers [2]. In the past, Compton backscattering has been applied to perform precise beam energy measurements at low energy storage rings such as BESSY-I, BESSY-II (Berlin) [3], the Taiwan Light Source [4] and the VEPP-4M collider (Novosibirsk) [5].

2 Outline of the experiment

A sketch of the scheme suggested for beam energy monitoring at the ILC is shown in Fig. 1. Beam electrons collide with monochromatic laser radiation at some small angle α . Downstream of the laser-electron interaction point (IP) non-interacting beam particles (most of them), Compton scattered electrons and photons are strongly collimated in the forward direction. A dipole magnet separates them into through-going high-energy photons, less deflected beam electrons and scattered electrons with some larger deflection. If a photon

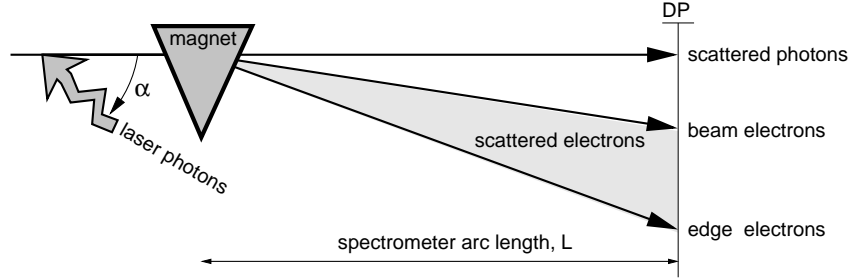


Figure 1: Sketch of the beam energy monitoring scheme at the ILC.

with energy ω_L is scattered head-on with a relativistic electron of energy ε (or E_{beam}) at some small angle α , the maximum energy of the scattered photon is

$$\omega_{max} = \frac{\varepsilon^2}{\varepsilon + \frac{m^2}{4\omega_0}}, \quad \text{where } \omega_0 = \omega_L \cos^2(\alpha/2). \quad (1)$$

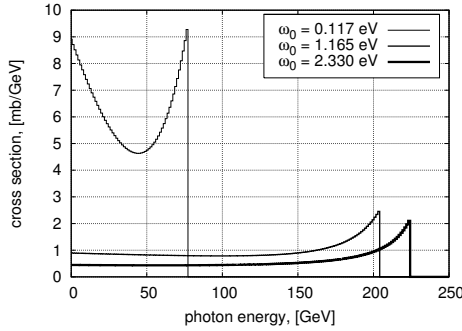


Figure 2: Backscattered photon energy spectra for three laser energies ω_0 , $\varepsilon=250$ GeV and $\alpha=8$ mrad.

These photons are scattered exactly along the momentum of the incident electron^a. Fig. 2 shows the Compton cross section as a function of the energy of backscattered photons for three laser energies. Photons with energy ω_{max} form a sharp high energy edge, which is mirrored by energy conservation to the electron energy spectrum as shown in Fig. 3. Electrons with minimum energy, given by $\varepsilon + \omega_L - \omega_{max}$, are called edge electrons and their energy is related to the beam energy ε via

$$E_{edge} = \frac{\varepsilon}{1 + \frac{4\varepsilon\omega_0}{m^2}}. \quad (2)$$

If monochromatic laser light scatters with beam electrons, the luminosity of the

^aThat is the reason of taking about Compton backscattering.

Compton process can be adjusted such that only a small fraction of the beam particles interact and the scattered photons, respectively, electrons possess a clear step-like peculiarity in their respective energy spectrum, from which ω_{max} , respectively, E_{edge} can be inferred. The relation of ω_{max} or E_{edge} with the beam energy, given by (1) respectively (2), permits then to extract the incident electron energy. However, precise spectrometry of the beam energy at the ILC is still challenging because, as seen from Figs. 2 and 3, Compton backscattered particles have frequently energies close to E_{beam} .

After passing the B-field of the spectrometer magnet, the deflection range of the scattered electrons has to be smaller than the magnet pole length, so that both the beam as well as the Compton electrons 'see' the same B-field integral $\int Bdl$. The amount of deflection is given by the bending angle, which in turn is inverse proportional to the particle's energy E

$$\theta(E) \sim \frac{\int Bdl}{E} + \delta_{SR}, \quad (3)$$

where δ_{SR} is a small correction term from synchrotron radiation. It can be shown that $\delta_{SR} \sim (\int Bdl)^3$ and does not depend on the particle energy E . In this study we neglect synchrotron radiation effects. However, detailed simulation studies should account for this correction.

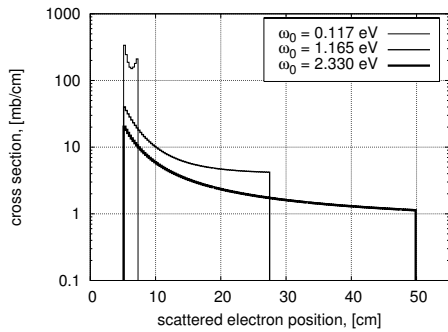


Figure 4: Scattered electrons distribution in the DP for three ω_L values, $\varepsilon=250$ GeV, an arc length of $L=48.5$ m, and a perfect 3 m long magnet with $B=0.28$ T.

distance between the beam position $X_{beam} = X(E_{beam})$ and that of the edge electrons $X_{edge} = X(E_{edge})$, where the cut-off energy of the edge electrons is directly transformed into a sharp edge location.

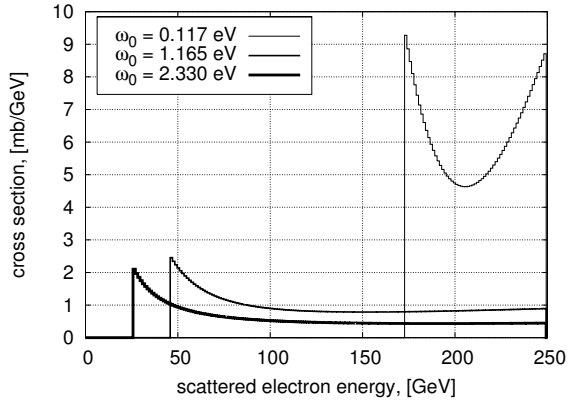


Figure 3: Scattered electron energy spectra for three laser energies ω_0 , $\varepsilon=250$ GeV and $\alpha=8$ mrad.

After the magnet all particles propagate in free space of length L (spectrometer arc length) up to the detector plane (indicated as DP in Fig. 1). In our setup, θ is in the order of some millirad and therefore the electron transverse position in the detector plane is approximated by

$$X(E) = X_0 + A/E, \quad (4)$$

where $A \sim L \cdot \int Bdl$ and X_0 the non-deflected photon position, determined by the center-of-gravity of the backscattered photons.

Fig. 4 represents the position range of backscattered electrons at the detector plane for 250 GeV beam particles and three laser energies. The electrons cover the dis-

According to eqs.(2) and (4), $X(E_{beam})$ and $X(E_{edge})$ can be expressed as

$$X_{beam} \equiv X(E_{beam}) = X_0 + A/E_{beam} \quad (5)$$

$$X_{edge} \equiv X(E_{edge}) = X_{beam} + A \frac{4\omega_0}{m^2} \quad (6)$$

and hence the beam energy can be deduced from

$$E_{beam} = \frac{m^2}{4\omega_0} \cdot \frac{X_{edge} - X_{beam}}{X_{beam} - X_0} . \quad (7)$$

Thus, E_{beam} can be determined from the electron rest mass m , the well-known laser energy ω_L and three particle positions which have to be deduced from the experiment: X_0 , X_{beam} and X_{edge} . The beam position X_{beam} can be measured by a high resolution BPM, while monitoring the positions of the edge electrons X_{edge} and the photon center-of-gravity X_0 needs dedicated high spatial resolution detectors. X_{edge} can e.g. be obtained from the position distribution of backscattered electrons via fitting the edge spectrum similar to the photon energy spectrum as performed at the VEPP-4M collider [5] using a HPGe detector, see Fig. 5.

It is important to mention that within this scheme precise beam energy measurements do not require precise knowledge of the absolute B-field integral. This is in contrast to the approach of measuring E_{beam} directly from the energy of the edge electrons, where absolute field integral information of the spectrometer magnet must exist with high precision.

The error of the beam energy, which has to be monitored with $\Delta E_{beam}/E_{beam} \lesssim 10^{-4}$, can be estimated from eq.(7) as

$$\frac{\Delta E_{beam}}{E_{beam}} = \frac{X_{edge}}{X_{edge} - X_{beam}} \left(\frac{\Delta X_{edge}}{X_{edge}} \right) \oplus \frac{X_{edge}}{X_{edge} - X_{beam}} \left(\frac{\Delta X_{beam}}{X_{beam}} \right) \oplus \frac{\Delta X_0}{X_{beam}} . \quad (8)$$

For the particular set of spectrometer parameters as used in Fig. 4, X_{beam} turns out to be close to 5 cm, and to achieve $\Delta E_{beam}/E_{beam}$ better than 10^{-4} , X_{beam} and X_0 (see also the last two terms in eq.(8)) have to be determined with accuracy of about $3 \mu\text{m}$.

The precision of X_{Edge} can be evaluated from the number of scattered electrons near the edge and the width of the edge, $\sigma_{X_{edge}}$. A non-zero edge width is supposed to be caused by several effects of which the most important ones are internal energy and angular spreads of the beam particles at the Compton IP. Such effects, which cause $\sigma_{X_{edge}}$ to be finite, define together with the statistics, the precision of X_{Edge} as

$$\Delta X_{edge} = \sqrt{\frac{2 \cdot \sigma_{X_{edge}}}{\frac{dN}{dx}(X_{edge})}} . \quad (9)$$

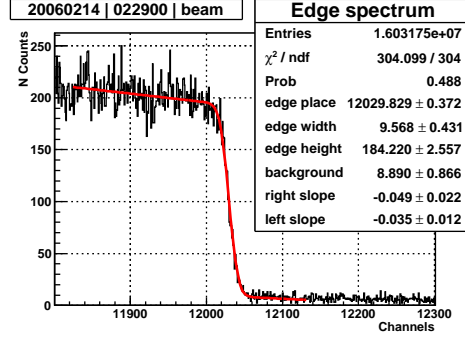


Figure 5: Compton backscattered photon energy spectrum measured by 120 ml HPGe detector at the VEPP-4M collider ($\simeq 0.5 \text{ keV/ch}$)

The behaviour of the first term in eq.(8) is shown in Fig. 6 against the beam energy for three laser types. Here, the following assumptions were made: a) the number of Compton events per bunch crossing is 10^6 , b) the electron detection efficiency is 100%, c) the B-field integral is linear proportional to the beam energy enabling X_{beam} to be independent on E_{beam} and d) smearing of X_{edge} is mainly caused by the angular spread of the electrons, which was assumed of 5 mrad. It can be noticed that, within the assumptions made, beam energy uncertainties of better than 10^{-4} are achievable, and lasers with short wavelengths are preferred. In particular, the 1.165 eV line of an infrared laser is much better suited than the far-infrared CO_2 laser.

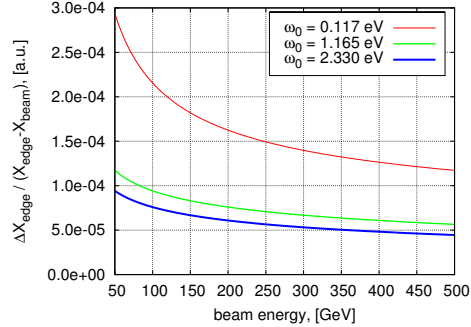


Figure 6: Precision of X_{edge} versus the beam energy for three laser energies..

Generation of 10^6 Compton scatters from $2 \cdot 10^{10}$ electrons per ILC bunch requires however a $Nd : YAG$ laser of typically 10 ps pulse duration and a pulse power of 20 mJ to be focused to a spot size of $\sim 50 \mu m$ at the Compton IP [6], as an example. Such a laser that matches the pattern of the ILC bunches with sufficient pulse power is at present commercially not available, hence further R&D is needed. It has also been shown in [6] that multiple scattering and non-linear corrections within the Compton process are of no concern, despite the large laser power required.

More details on precisions of the beam energy on statistics, which is to a large extent controlled by ΔX_{edge} , respectively, the first term in eq.(8), can be deduced from Fig. 7. Here, $\frac{\Delta X_{edge}}{X_{edge} - X_{beam}}$, which is the only statistics dependent term in (8), is shown against the

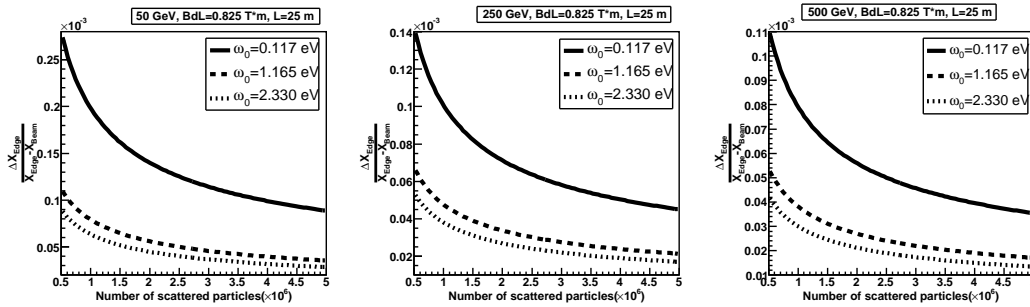


Figure 7: The first term of eq.(8) as a function of the number of Compton events ($\times 10^6$) per bunch crossing for three beam and laser energies.

number of Compton events per bunch crossing. These numbers were derived assuming a) the beam spot size is $50 \mu m$ at the detector plane in x and y, b) the internal energy spread is 0.15%, c) the accuracies on beam position and photon center-of-gravity are both $1 \mu m$ and the field integral equals $\int Bdl = 0.84 Tm$. One notices, for event rates less than 10^6 some improvements of $\frac{\Delta E_{beam}}{E_{beam}}$ can be achieved by maintaining larger event rates. This is

mostly evident for a CO_2 laser. Event rates beyond a few millions would have however less or negligible impact for better uncertainties of the beam energy. Whether such large event rates per bunch crossing can be realized depends mainly on ongoing laser developments.

On the other hand, even if we intend to measure the energy of each ILC bunch, there is no need to adjust the Compton luminosity or the laser power for 10^6 events per bunch crossing. From eqs.(6) and (7) follows that the numerator in eq.(7), $X_{edge} - X_{beam}$, is only coupled to spectrometer parameters such as the B-field integral and the drift distance L , and does not depend on the beam energy. Since bunch-to-bunch energy variations are supposed to proceed rapidly and spectrometer parameters change at a much larger timescale, we might, for each bunch, record the beam position X_{beam} and the position spectrum of electrons close to the edge. Accumulating these informations over many bunches provides a precise $X_{edge} - X_{beam}$ value, which is not rendered by insufficient bunch related Compton events. However, the denominator in eq.(7), $X_{beam} - X_0$, has to be measured for each bunch crossing, which can be performed by a high resolution BPM and, because of the large backscattered photon yield, by a precise center-of-gravity position device.

3 Spectrometer locations within the Beam Delivery System

In order to locate the spectrometer within the Beam Delivery System (BDS) [7] some basic constraints have to be accounted for. These constraints are caused by physics arguments related to systematical and statistical errors of each component of the spectrometer, additional background from Compton electron interactions with downstream magnets as well as space limitations within the BDS. In this section some pros and cons of possible locations of the Compton spectrometer within the BDS are shortly discussed.

3.1 Practical restrictions

In order to measure Compton backscattered electrons and photons, they have to leave the vacuum chamber, assumed to be a pipe of 20 mm diameter. This constrains the B-field integral $\int Bdl$ and the drift distance L between the magnet and the detector plane.

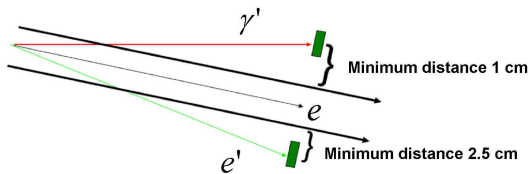


Figure 8: Illustration of spacing requirements at the detector plane.

for the sake of illustration the minimum distance between the beam pipe wall and the center of the photon detector should be, for practical reasons, in the order of 10 mm, while the center of the electron detector might be 25 mm away from the wall as illustrated in Fig. 8. These numbers should not be considered as strict, but thought to indicate the space requirements for reasonable particle position measurements. Since the distance to the electron detector is not really a concern, the location of the photon detector being only 20 mm off the beam

According to eq.(4), the space between the center-of-gravity of the backscattered photons and the beamline as well as between the edge electrons and the beam depends on the parameter A , which is proportional to the product $A \sim L \cdot \int Bdl$.

Therefore, A might be changed either by B-field or drift distance L variations, or both simultaneously. For the moment we fix $\int Bdl$ such that the bending angle for beam particles is 1 mrad and allow L to vary. For

needs special care. Accepting these numbers, a 3 meter long magnet with a B-field of 0.28 T (corresponding to $\int Bdl=0.84$ Tm) combined with a drift distance of 20 m ensures such minimal separations.

The dependence of the first term in eq.(8), $\frac{\Delta X_{edge}}{X_{edge}-X_{beam}}$, as a function of L is displayed in Fig. 9 for three beam and laser energies.

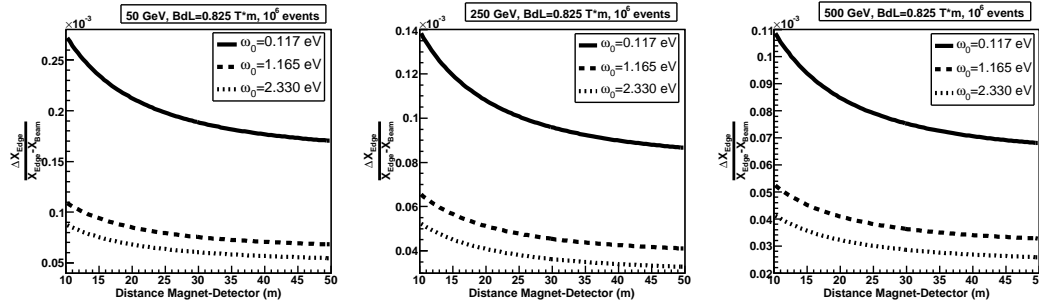


Figure 9: The first term of eq.(8) against drift distance L for three beam and laser energies.

Clearly, $\frac{\Delta X_{edge}}{X_{edge}-X_{beam}}$ does not strongly dependent on L , especially for high energy lasers, provided the drift distance is at least 20 m. The dependence becomes somewhat more pronounced when the spot size of the beam at the detector plane is substantially larger than $50 \mu\text{m}$ assumed so far.

Since A is proportional to the product $L \cdot \int Bdl$, it is totally equivalent to keep either $\int Bdl$ constant and to vary L or the opposite. An increase of the B-field has however carefully studied because additional beam emittance dilution has to be limited.

Last not least, Fig. 10 shows the beam energy uncertainty $\frac{\Delta E_{beam}}{E_{beam}}$ as a function of ΔX_{edge} , where ΔX_{edge} should be now understood as the total error of the electron edge position.

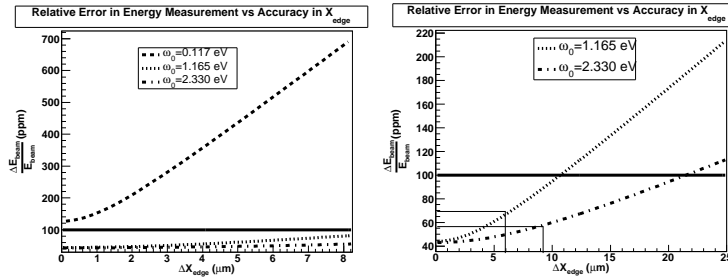


Figure 10: Left: $\frac{\Delta E_{beam}}{E_{beam}}$ as a function of ΔX_{edge} for three laser energies. Right: zoom of the left-hand figure for two laser energies. The horizontal line indicates the precision limit of a 100 ppm beam energy error.

The left part of Fig. 10 reveals that using a CO_2 laser $\frac{\Delta E_{beam}}{E_{beam}}$ rises strongly with increasing ΔX_{edge} . But more important is the error of the beam energy at $\Delta X_{edge} = 0$,

i.e. for perfect edge position information. This error exceeds 10^{-4} , respectively, 100 parts per million (ppm), which means a CO_2 laser should not be considered as an option for the proposed Compton spectrometer. Employing an Nd:YAG infrared or green laser is much more suitable as seen in the right-hand side of Fig. 10. In particular, for an infrared laser ($\omega_0 = 1.165$ eV) a $6 \mu\text{m}$ uncertainty on ΔX_{edge} provides a beam energy uncertainty of 66 ppm. To keep the uncertainty of the incident energy at 100 ppm, ΔX_{edge} has to be known with $10 \mu\text{m}$. A green laser ($\omega_0 = 2.33$ eV) allows somewhat to relax this constraint.

Tab. 1 summarizes, for a laser with $\omega = 1.165\text{eV}$, the individual error terms of eq.(8) utilizing a spectrometer magnet with 1 mrad beam bending power. The uncertainties shown assume for ΔX_{edge} , ΔX_{beam} and ΔX_0 $6 \mu\text{m}$, $1 \mu\text{m}$ and $1 \mu\text{m}$, respectively.

Beam Energy (GeV)	50		250		500	
Distance L (m)	25	50	25	50	25	50
$\frac{X_{edge}}{X_{edge}-X_{beam}} \left(\frac{\Delta X_{edge}}{X_{edge}} \right)$ (ppm)	79	68	46	41	38	33
$\frac{X_{edge}}{X_{edge}-X_{beam}} \left(\frac{\Delta X_{beam}}{X_{beam}} \right)$ (ppm)	80	40	46	24	42	22
$\frac{\Delta X_0}{X_{beam}}$ (ppm)	40	20	40	20	40	20

At $E_{beam} = 50$ GeV, accuracy of the beam energy results to 119 ppm for $L = 25$ m, whereas it is reduced to 66 ppm at 250 GeV beam energy. These numbers show that as long as L is larger or close to 25 m no restrictions would exist to perform beam energy measurements with 100 ppm or better precision. Furthermore, drift distances of $L \geq 25$ m also ensure sufficient large separation of the Compton backscattered photons from the beamline.

3.2 Possible locations within the BDS

Although the today's beam delivery system [7] is believed to be further developed within the next years, basic properties are assumed to be unchanged. We propose three alternatives for possible locations of the Compton spectrometer, but keeping major design parameters unaltered.

An overall view of the BDS is shown in Fig. 11, where also potential locations for the Compton spectrometer are indicated.

Common to all alternatives is the demand to locate the spectrometer upstream of the energy collimation system^b in order to avoid large background (muons) excess to the expected background from normal collimation losses [8].

The straight-forward approach suggests to locate the spectrometer into a sufficient free-space region within the BDS. The amount of space needed, of the order of 60-70 m, is determined by the 25 m long drift space together with the spectrometer magnet plus at least two ancillary magnets to compensate the bending of the spectrometer dipole and the drift spaces between them. Very upstream of the e^+e^- IP, such free space exists, see Fig. 11. Whether however the addition of new bends increases the beam emittance to non-tolerable values has to be checked. First estimates indicate an emittance dilution of about 0.5% for a 250 GeV beam.

^bThis system performs efficient removal of halo particles which lie outside the acceptable range of energy spread.

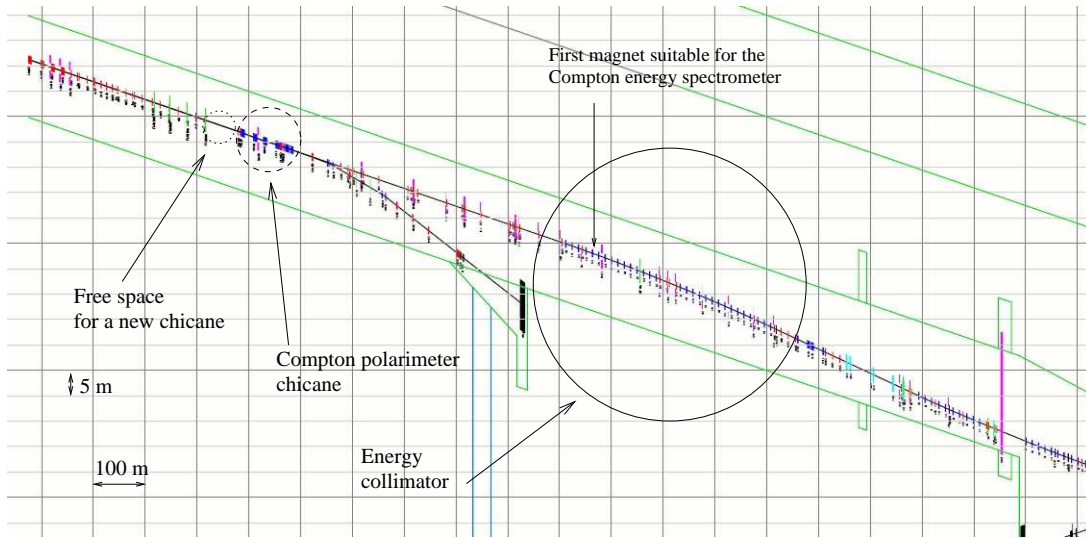


Figure 11: Scheme of the BDS with possible locations of the Compton spectrometer.

A suitable alternative for the spectrometer location consists in employing magnets of the present BDS for the spectrometer. At the beginning of the energy collimation section (see Fig. 11) several magnets^c might be combined to provide the desired bending power. In particular, such a combination of magnets would provide sufficient particle separation if the laser IP is e.g. located before the magnet marked in Fig 11. After passing magnet 6 in the chain, separation between Compton backscattered γ -rays and the beamline becomes 18 mm, while the distance of the beamline to the edge electrons, being laser dependent, is 98 mm for an infrared laser ($\omega_0 = 1.165$ eV). Thus, by locating the detector close to magnet 7 convenient position measurements for all particle species can be performed. Since this alternative does not require additional magnets, any further beam emittance growth is a priori avoided. However, the aperture of the magnets integrated into the system has to be continuously increased towards the bending direction allowing the edge electrons to pass in B-fields with properties as demanded. For example, at the exit of magnet 6 the uniformity of the B-field should extend up to about 100 mm in the bending direction.

The third option for a Compton spectrometer location consists in employing the magnetic chicane proposed for high energy polarization measurements [9]. In particular, the four magnets of the polarimeter chicane with its laser IP in the mid-point is proposed to be supplemented by a second IP for E_{beam} measurements, which is either located upstream of the first magnet or in between the first and second magnet. However, whether both measurements can be merged into one common concept needs dedicated studies.

^cEach magnet has a B-field of 291.68 Gauss, a length of 2.4 m and space in between of 12.3 m.

4 Summary

The BPM-based energy spectrometer [2] now under investigation is considered as the primary tool for accurate ILC beam energy monitoring. But experiences from LEP and SLD emphasize that more than one technique should be employed for precise \sqrt{s} determination and cross-calibration of absolute energy data is mandatory. Therefore, a new approach to perform beam energy measurements is suggested in this study. A spectrometer utilizing Compton backscattering of laser light on beam electrons seems to provide precisions for E_{beam} of 10^{-4} or better, on a bunch-to-bunch basis without beam disruption. Properties of such a spectrometer are discussed with the conclusion that no serious performance limitations are visible.

More details on the proposed Compton energy spectrometer will appear in a forthcoming paper [10].

References

- [1] Slides:
<http://ilcagenda.linearcollider.org/contributionDisplay.py?contribId=179&sessionId=78&confId=1296>.
<http://ilcagenda.linearcollider.org/contributionDisplay.py?contribId=180&sessionId=78&confId=1296>.
- [2] V.N. Duginov et al., *The Beam Energy Spectrometer at the International Linear Collider*, LC-DET-2004-031 (2004).
- [3] R. Klein *et al.* Nucl. Instrum. Meth. **A384** 293 (1997);
R. Klein *et al.* Nucl. Instrum. Meth. **A486** 545 (2002).
- [4] Ian C. Hsu, Cha-Ching Chu and Chuang-Ing Yu, Phys. Rev. **E54** 5657 (1996).
- [5] N. Muchnoi, S. Nikitin and V. Zhilich, *Fast and Precise Beam Energy Monitor Based on the Compton Backscattering at the VEPP-4M Collider*,
Proceedings of EPAC06, Edinburgh, Scotland, 26-30 Jun 2006
<http://accelconf.web.cern.ch/AccelConf/e06/PAPERS/TUPCH074.PDF>.
- [6] H.J. Schreiber, *Compton Backscattering as a Tool for Precise Beam Energy Measurement*,
<http://ilcagenda.linearcollider.org/contributionDisplay.py?contribId=30&sessionId=26&confId=1049>.
- [7] A. Seryi et al. Proceedings of PAC07, Albuquerque, New Mexico, USA, June 25-29, 2007;
ILC BDS lattice online repository: <http://www.slac.stanford.edu/mdw/ILC/2006e/>.
- [8] L. Keller, private communication.
- [9] N. Meyners, V. Gharibyan and K.P. Schüler, Proceedings of the 2005 International Linear Collider Workshop, p. 871, Stanford, California, USA, 18-22 March, 2005;
K.O. Eysler, these Proceedings.
- [10] N. Muchnoi, H.J. Schreiber and M. Viti, in preparation.

Progress Report for the BPM Energy Spectrometer Test Experiment at ESA

B. Maiheu¹, C. Adolphsen⁸, R. Arnold⁸, S. Boogert⁷, G. Boorman⁷, M. Chistiakova²,
V. Duginov⁵, F. Gournaris¹, C. Hast⁸, M. Hildreth⁶, Yu. Kolomensky², S. Kostromin⁵,
K. Kumar⁹, A. Lyapin¹, D. McCormick⁸, D. Miller¹, N. Morozov⁵, J. Ng⁸, E. Petigura²,
M. Sadre-Bazzaz², H.-J. Schreiber⁴, M. Slater³, Z. Szalata⁸, M. Thomson³, M. Viti⁴, D. Ward³,
M. Wing¹, M. Woods⁸

¹*University College London, UK*

²*University of California, Berkeley and Lawrence Berkeley National Laboratory, USA*

³*University of Cambridge, UK*

⁴*Deutsches Elektronen Synchrotron (DESY - Zeuthen), Germany*

⁵*Joint Institute for Nuclear Research (JINR), Russia*

⁶*University of Notre Dame, USA*

⁷*Royal Holloway University of London, UK*

⁸*Stanford Linear Accelerator Center (SLAC), USA*

⁹*University of Massachusetts Amherst, USA*

The main physics programme of the International Linear Collider (ILC) requires a measurement of the beam energy with a relative precision of 10^{-4} or better. To achieve this goal a spectrometer using high resolution beam position monitors (BPM) and accurately monitored bending magnets has been proposed. A prototype spectrometer chicane using 4 dipoles is now commissioned in End Station A (ESA) at SLAC, intending to demonstrate the required stability of this method and investigate possible systematic effects and operational issues. In this contribution we will describe the experimental setup for this ESA test experiment (T-474/491), which has been finalised during two runs in 2007, and present results from the BPM commissioning runs in 2006.

1 Introduction

The design of the International Linear Collider is driven by the broad precision physics programme of electroweak, Higgs, QCD and possible SUSY measurements. The uncertainty on the energy of the colliding electron and positron bunches contributes directly to the systematic error on e.g. top quark W and Higgs masses [2], making a precise energy measurement of the beam of crucial importance. At LEP2, an energy spectrometer was successfully commissioned, achieving an accuracy of 1.9×10^{-4} [3]. Dipoles in the bending sections of the storage ring were used to induce a deflection of the lepton beam. With accurate knowledge of the total integrated field of these bending magnets together with a measurement of the deflection itself, one can derive the energy of the beam. The ILC energy spectrometer has similar design requirements in terms of accuracy, however to limit the emittance growth due to synchrotron radiation in the beam delivery system, the introduced dispersion in the spectrometer chicane has been restricted to 5 mm. Also, at the ILC the measurement has to be done in a single shot. High resolution RF cavity BPM systems are therefore preferred to strip-line or button BPMs as these can achieve resolutions well below a micron [4], needed for a precision energy measurement.

As a proof of principle, a test beam experiment (T-474/491) was proposed [5] at ESA at the Stanford Linear Accelerator Center (SLAC), focusing on studying the achievability and

more importantly the stability and systematics of this type of energy measurement in a linac. The aim is to identify operational issues and provide practical guidelines for constructing the ILC energy spectrometer.

End Station A provides an ideal facility for ILC test experiments. It features a 28.5 GeV electron beam with a bunch charge of 1.6×10^{10} , an energy spread of 0.15 %, a repetition rate of 10 Hz and a nominal bunch length of about $500 \mu\text{m}$, all (except energy) similar to the ILC baseline specifications. The incoming beam orbit is stabilised both in horizontal and vertical planes using a feedback system consisting of 4 RF cavity BPMs as well as 4 corrector magnets equipped with trim coils. These trim coils can also be used for a rough calibration of the BPM system.

2 Experimental setup

The T-474/491 experiment started in 2006 with two BPM commissioning runs and was extended with the full spectrometer chicane during two runs in 2007. The experimental setup as of July 2007 is depicted in figure 1. The BPM system consists of different S-band

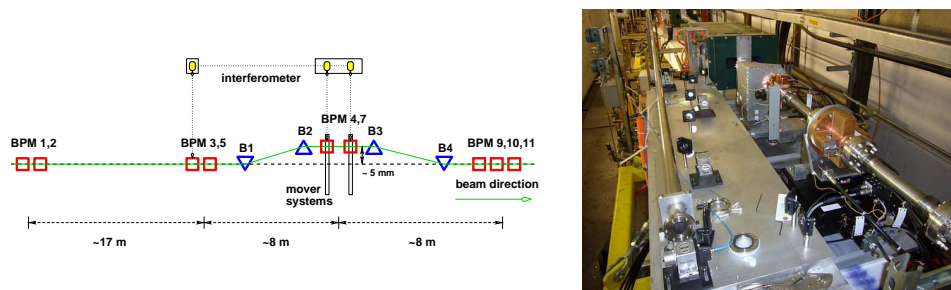


Figure 1: The T-474/491 beam line setup as of July 2007 showing the relevant BPM stations and dipole bending magnets (B). An interferometer monitors the horizontal mechanical stability of BPM 3 and BPMs 4 and 7 at the chicane centre.

cavity BPMs, all having resonant frequencies of about 2.9 GHz. BPMs 3, 4 and 5 are prototype BPMs for the ILC main linac [6] and are cylindrical cavities with a waveguide coupling system providing signals for both horizontal and vertical planes. They are designed to minimise the coupling of modes other than the position sensitive dipole mode. BPMs 1 and 2 and the triplet 9,10,11 are old SLAC rectangular cavities. BPM 7 is a new prototype which has been designed specifically for ILC energy spectrometer purposes in terms of mode suppression, resolution and decay time. The raw RF signals coming from the cavities were put through a system of filters and amplifiers and were down-mixed to about 83 MHz and 23 MHz in case of the BPM7 prototype. The resulting waveforms were digitised using 14 bit 119 MS/s sampling ADCs. Further extraction of the position and tilt information was done using algorithms in software [7], [4]. Both BPM4 and BPM7 are placed on their own 2D precision mover system for both calibration and tracking the beam when operating the chicane as the dynamic range of the BPMs is limited to about $\pm 1 \text{ mm}$.

The chicane is formed by four 94 cm long dipole magnets. Their characteristics were studied during a measurement campaign [8] at the SLAC magnetic measurement facility. The field integral for all 4 magnets was found to be uniform at the 10^{-4} level over $\pm 15 \text{ mm}$

horizontally from the magnet central axis and they are monitored during data taking by NMR probes. The induced fields of about 0.115 T cause a horizontal translation of the 28.5 GeV beam of roughly 5 mm at the centre of the chicane.

Compared to the two runs in 2006, various hardware upgrades were implemented to better understand the systematic effects that were observed during the BPM commissioning (see below). A calibration tone system in which the BPM processor electronics were fed in between machine pulses with a triggered, constant level tone was deployed, so it became possible to monitor gain drifts in the electronics, e.g. due to temperature variations. Two BPMs at high dispersion points (500 mm) in the ESA extraction line were commissioned along with charge-sensitive toroids for event-level monitoring of the beam energy and bunch charge. Furthermore, two Helmholtz coils were installed, enabling us to perform fast calibrations for the BPM system. An interferometer that was already present for the 2006 runs has been relocated to monitor the horizontal mechanical stability of the BPMs at the centre of the chicane as well as one BPM in front of the chicane.

3 Analysis results

Analysis is nearing completion for the BPM commissioning runs in 2006. First of all the resolution of the individual BPMs was assessed and more importantly the precision of the orbit reconstruction, which is of fundamental importance for the energy measurement. The resolution of a BPM is essentially the minimum change in beam position which the BPM can detect in one pulse. Table 1 shows the resolutions for data run 1421. They are defined here as the Gaussian spread of the distribution of the residual offset from the predicted beam position obtained by a linear regression analysis within a triplet or using the entire orbit. For all but BPMs 1 and 2, sub-micron resolutions were measured as well as for the orbit. This meets our requirement for spectrometer studies.

BPM	σ_x	σ_y
1, 2	2.53 μm	4.15 μm
3, 4, 5	0.69 μm	0.61 μm
9, 10, 11	0.25 μm	0.31 μm
Orbit	0.73 μm	0.91 μm

Table 1: The resolution of the BPM stations and orbit reconstruction (run 1421), where we have taken BPMs 1 and 2 and BPMs 9-11 to predict the position in BPM 3.

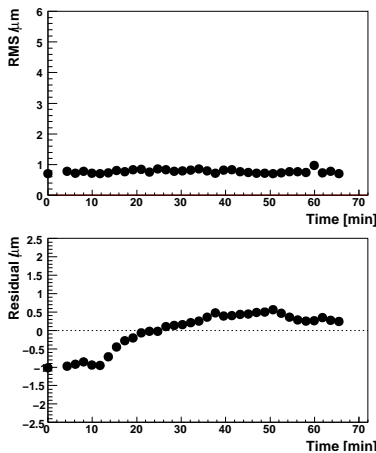


Figure 2: The resolution and residual stability over an hour.

What is more important for the operation of the ILC spectrometer is the stability of this measurement. Temperature and other environmental effects can affect for example the amplitude and phase response of the processing electronics or change the physical shape of the cavity. Ground motion can affect the mechanical stability of the system, rendering the orbit determination less accurate. Results from an hour long measurement of the resolution and the stability of the orbit are shown in figure 2. Even though the resolution itself does not appear to change drastically over the course of an hour, the residual offset itself does. Understanding these drifts was the underlying motivation for installing the calibration tone system discussed above.

During the March 2007 run, the full chicane was com-

missioned and some first spectrometer data was taken. Figure 3 shows an energy feedback scan in 50 MeV steps, as seen by the spectrometer chicane. Preliminary analysis of this data shows an encouraging energy resolution of about 6.6 MeV or about 230 ppm [8]. Detailed systematic and stability analysis with the extensive data set taken in July is in progress.

4 Summary

The energy spectrometer test experiment (T474/491) at SLAC's End Station A is now fully commissioned and has taken its first good spectrometer data during two runs in 2007. The analysis of the data taken during two BPM commissioning runs in 2006 is approaching completion. So far, we already demonstrated sub-micron precision of the orbit reconstruction with systematic drifts of about $1 \mu\text{m}$ over the course of an hour. This corresponds to a drift of 200 ppm on the energy measurement. In-depth understanding of the nature of these systematics is now possible thanks to hardware upgrades such as a calibration tone system and an interferometer. The analysis of the data taken during the 2007 March and July runs, will provide a "proof of principle" for an ILC BPM-based spectrometer.

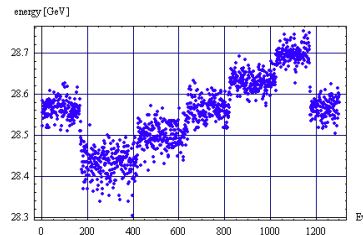


Figure 3: Energy scan as seen by the spectrometer

Acknowledgements

This work was supported by the Commission of the European Communities under the 6th Framework Programme "Structuring the European Research Area", contract number RIDS-011899 and by the US Department of Energy. We also wish to express our gratitude to the SLAC directorate and especially to the MCC operators for their kind help during the ESA running periods.

References

- [1] Slides: Progress Report for the BPM Energy Spectrometer Test Experiment at ESA
<http://ilcagenda.linearcollider.org/contributionDisplay.py?contribId=451&sessionId=78&confId=1296>
- [2] S. Boogert and F. Gournaris, Determination of dL/dE and total CM energy, *These proceedings*.
- [3] R. Assmann et al, Calibration of Center-of-Mass Energies at LEP2 for a precise measurement of the W Boson Mass, *Eur. Phys. J.* **C39** 253-292 (2005).
- [4] S. Walston et al, Performance of a high resolution cavity beam position monitor system, *Nucl. Inst. and Meth.* **A 578** 1-22 (2007)
- [5] M. Hildreth et al, BPM-based energy spectrometer, *SLAC Test Beam Request No. T-474*. June 11, 2004.
- [6] Z. Li, S-Band Cavity BPM For ILC, *Talk given at ALCPG, ILC Snowmass 2005 Conference*, Contribution ILCAW0901.
- [7] D. Whittum, Y. Kolomensky, Analysis of an Asymmetric Resonant Cavity as a Beam Monitor, *Rev. Scientific Instr.* **70** 2300 (1999)
- [8] R. Arnold et al., Magnetic measurements and simulations for a 4-magnet dipole chicane for the international linear collider. *Proceedings of PAC07*, THPMS038

Data Acquisition and Global Detector Network

Conveners: P. Le Du, D. Haas

Trigger/Data Acquisition Issues

Patrick Le Dû

DAPNIA – CEA Saclay
91191 Gif sur Yvette Cedex– FRANCE

This paper summarizes the current Trigger and Data Acquisition view of the four detector concepts of the worldwide study of the International Linear Collider (ILC) study group. First, a better knowledge of the ILC physics and machine event backgrounds and data bandwidths of the various sub-detectors will give the size of the full data flow of the read out system. Second, the concept of 'Software Trigger' architecture with its consequences on the read-out electronics designs under development is discussed. Third, some preliminary ideas for the event selection and analysis will be presented. Finally, a generic architecture model of the DAQ system uniform across each concept will be presented with a possible implementation based on ATCA.

1 Introduction

1.1 The Machine parameters and conditions

The ILC machine consists of two separate independent linear superconducting electrons accelerators of 16 km long with and energy of 500 GeV/c to 1TeV/c maximum and a luminosity up to $2 \cdot 10^{34} \text{ cm}^{-2} \text{ s}^{-1}$.

In contrast to currently operated or built colliders, such as HERA, Tevatron or LHC, which have a continuous rate of equidistant bunch crossings the ILC has a pulsed operation mode. For the nominal parameter set [7] the ILC will have

- ~3000 bunch crossings in about 1ms,
- 300 ns between bunch crossings inside a bunch train
- ~200 ms without collisions between bunch trains.

This operation mode results in a burst of collisions at a rate of ~3MHz over 1ms followed by 200ms without any interaction. The integrated collision rate of 15 kHz is moderate compared to the LHC and corresponds to the expected event building rate for the LHC experiments. One or two interaction points (IP) are foreseen. The size of the beam at the Interaction Point will be few μm needs a rapid feedback between each bunch train to optimize the luminosity.

1.2 Experimental features and detectors requirements

The ILC machine is a precision machine complementarily to LHC which is a discovery one. The physics goals require higher precision in jet and momentum resolution and better impact parameter resolution than any other collider detector built so far. As a consequence, ILC should strive to do physics with *all* final states by measuring charged particles in jets more precisely (the 'Particle flow' paradigm in calorimeters), with a good separation of charged and neutrals. Jets & leptons are the fundamental quanta of the signature of a physics process to be selected and recorded in any HEP detector. Compared to previous e^+e^- experiments at LEP for example, they must be identified and measured well enough to discriminate between Z's, W's, H's, Top, and new states. This requires a non-trivial task improving jet resolution

by a factor of two. Charged Particle tracking detectors must precisely measure 500 GeV/c leptons for Higgs recoil studies. This requires 10 times better momentum resolution than LEP/SLC detectors and 1/3 better on the Impact Parameter of SLD! To catch multi-jet final states (e.g. t-tbar H has 8 jets), need real 4π solid angle coverage with full detector capability. Never been done such hermiticity and granularity! Compared to LHC, its looks less demanding. ILC Detector doesn't have to cope with multiple minimum bias events per crossing, high rate triggering for needles in haystacks, radiation hardness, hence many more technologies available, where better intrinsic performance is possible. But ILC detectors does have to cover full solid angle, record all the available CM energy, measure jets and charged tracks with unparalleled precision, measure beam energy and energy spread, differential luminosity, and polarization, and tag all vertices, hence better performance and more technology development is needed. This improved accuracy can only be achieved by a substantial bigger number of readout channels.

1.3 Trigger and Data Acquisition requirements

As outlined in all 4 detector concept studies [1,2,3,4] the data acquisition (DAQ) system of a detector at the ILC has to fulfill the needs of a high luminosity, high precision experiment without compromising on rare or yet unknown physics processes. Although the maximum expected physics rate, of the order of a few kHz, is small compared to the most recent hadrons colliders, Peak rates within a bunch train may reach several MHz due to the bunched operation. In addition the ILC physics goals require higher precision in jet and momentum resolution and better impact parameter resolution than any other collider detector built so far. This improved accuracy can only be achieved by a substantial bigger number of readout channels.

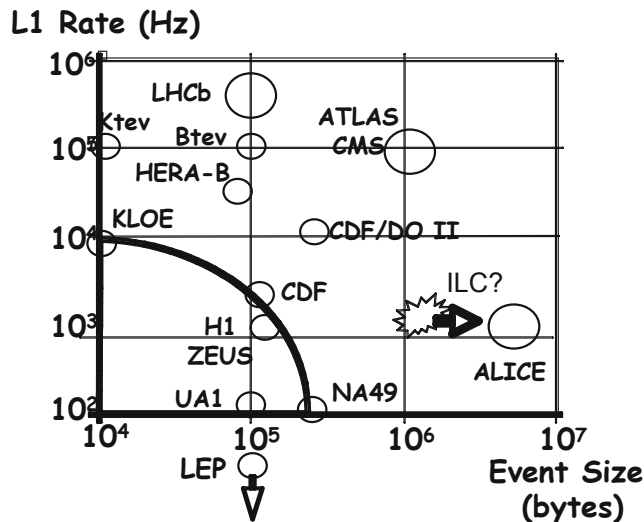


Fig. 1. Data rate and volume compared to previous and present large collider experiment

Taking advantage of the bunched operations mode at the ILC, event building without a hardware trigger, followed by a software based event selection was proposed [5] and has been adopted by all detector concept studies. This will assure the needed flexibility, scalability and will be able to cope with the expected complexity of the physics and detector data without compromising on efficiency.

TABLE I
ILC VERSUS LHC DETECTOR CHANNELS COUNTS

Subdeteor	LHC	ILC
Pixels	150 M	1 to 10 G
Microstrips	10 M	30 M
Fine grain tracker	400 K	1,5 M
Calorimeters	200 K	30 to 100 M

The increasing numbers of readout channels for the ILC detectors will require signal processing and data compression already at the detector electronics level as well as high bandwidth for the event building network to cope with the data flow. The currently built LHC experiments have up to 10^8 front-end readout channels and an event building rate of a few kHz, moving data with up to 500 Gbit/s [6]. The proposed DAQ system will be less demanding in terms of data throughput although the number of readout channels is likely to be a factor of 10 larger. The rapid development of fast network infrastructures and high performance computing technologies, as well as the higher integration and lower power consumption of electronic components are essential ingredients for this data acquisition system. Furthermore it turned out that for such large systems a restriction to standardized components is vital to achieve maintainability at an affordable effort, requiring commodity hardware and industry standards to be used wherever possible. Details of the data acquisition system depend to a large extent on the final design of the different sub detector electronic components, most of which are not fully defined to date. Therefore the DAQ system presented here will be rather conceptual, highlighting some key points to be addressed in the coming years.

2 Conceptual architecture

2.1 Software Trigger

The burst structure of the collisions at the ILC immediately leads to the suggested DAQ system:

- dead time free pipeline of 1 ms,
- no hardware trigger,
- front-end pipeline readout within 200 ms and event selection by software.

The high granularity of the detector and the roughly 3000 collisions in 1 ms still require a substantial bandwidth to read the data in time before the next bunch train. To achieve this, the detector front end readout has to perform zero suppression and data condensation as much as possible. Due to the high granularity it is mandatory to have multiplexing of many channels into a few optic fibers to avoid a large number of readout cables, and hence reduce dead material and gaps in the detector as much as possible.

2.2 Data Read Out and collection

The data of the full detector will be read out via an event building network for all bunch crossings in one train. After the readout, the data of a complete train will be situated in a single processing node. The event selection will be performed on this node based on the full event information and bunches of interest will be defined. The data of these bunches of interest will then be stored for further physics analysis as well as for calibration, cross checks and detector monitoring. Figure 1 shows a conceptual diagram of the proposed data flow. a programmable interface to the front end readout, the event data buffer which will allow storing data of several trains and the standardized network interface to the central DAQ system.

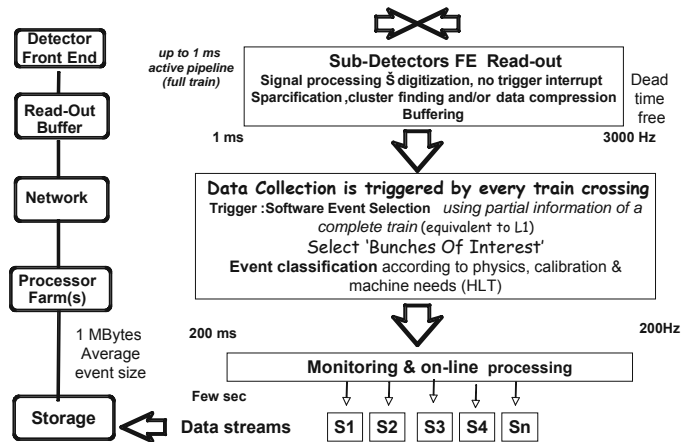


Fig. 2. Data flow and software trigger concept.

The programmable interface should enable one common type of readout unit to adapt to the detector specific front end designs. To allow for variations in the readout timing to more than 200 ms the readout units could be equipped with event data buffers with multiple train capacity. The full event is built via the event building network into a single data processing node which will perform final data processing, extract and apply online calibration constants and will select the data for permanent storage

In the data processing node the complete data of all bunch crossings within a train will be available for event processing. Distributing data of one train over several processing nodes should be avoided because sub detectors such as the vertex detector or the TPC will have overlapping signals from consecutive bunch crossings and unnecessary duplication of data would be needed. Event selection is performed in these data processing nodes such that for each class of physics process a specific finder process will identify the bunch crossings which contain event candidates and mark them as 'bunches of interest'. All data for the 'bunches of interest' will be fully processed and finally stored permanently for the physics analysis later on. By using software event selection with the full data available, a maximum event finding efficiency and the best possible flexibility in case of unforeseen conditions or physics processes is ensured. The best strategy for applying these finders and processing the data, depends on the topology of the physics processes to be selected and their background processes. This has to be further studied and optimized based on full Monte Carlo simulations.

Several trains will be built and processed in parallel in a farm of data processing nodes and buffering in the interface readout units will allow for fluctuations in the processing time.

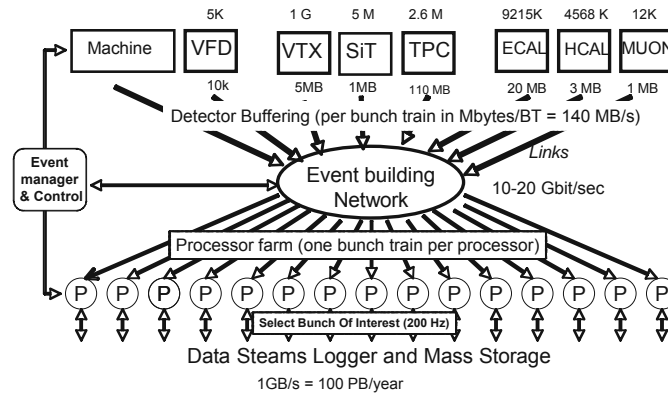


Fig. 3. Data Collecture Architecture and data flow of the GLD detectors concept

Using commodity components like PCs and standardized network components allows for the scaling of the processing power or network bandwidth according to the demands. The use of off-the-shelf technology for the network and the computing units will ease maintainability and allow to profit from the rapid development in this area. The DAQ system will also profit from the use of a common operating system, for example Linux, and high level programming languages already at the event building and event finding stage, making the separation of on-line and off-line code obsolete and therefore avoid the need to rewrite, and debug, code for on-line or off-line purposes. This results in a more efficient use of the common resources.

3 Systems boundaries

3.1 Detector front end electronics

The amount of data volume to be collected by the DAQ system is dominated by pair background from the machine. Simulations for the nominal ILC parameters [7] at $E_{cm} = 500\text{GeV}$ for the LDC [2] show in the vertex detector 455, 189 and 99 hits per bunch crossing for layer 1, 2 and 3 respectively. In the TPC volume roughly 18000 hits are produced. Similar studies for the other concepts confirm the high background near the beam pipe.

Except for the inner layers of the vertex detector the occupancy for a full train imposes no constraints onto the readout scheme. For the inner vertex detector layers the data has to be read out during the train to keep the hit density low enough not to compromise on the tracking performance. For the SiD main tracker the ability for bunch identification to reduce the background especially in the forward region is studied.

For the SiW based ECAL systems the high granularity requires large multiplexing on the front end detectors with an adequate multi hit capability and efficient hit detection or zero suppression. Single chips with hit detection, charge and time digitization and multi hit storage capacity for up to 2048 channels were proposed by several groups.

For the TPC novel readout technologies are developed with reduced ion feedback to allow for

a gateless operation with sufficient gas amplification for a period of 1ms. The electronic noise of the front end systems or the detectors themselves is a third, possibly very dangerous, source of data volume in a trigger less system and has to be sufficiently under control or be suppressed by the front end data processing.

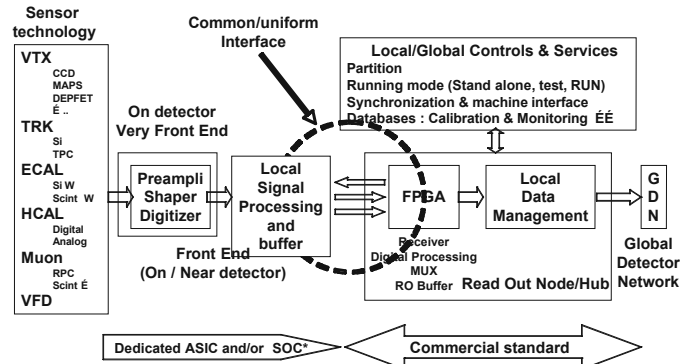


Fig. 4. Current view of a uniform read out architecture .

The high granularity of the detector systems and the increased integration of electronic at the detector front end, will result in large power dissipations. To avoid excessive cooling needs, all detector systems investigate the possibility of reducing the power at the front end electronics by switching power off between trains (power cycling). This has to be balanced against power up effects, the readout time needed between trains and the ability to collect data between trains for calibration purposes, e.g. cosmic muon tracks.

3.2 Machine Interface

The machine operation parameters and beam conditions are vital input for the high precision physics analysis and will therefore be needed alongside the detector data. Since the amount of data and time structure of this data is similar, a common data acquisition system and data storage model should be used. Up to now very little has happened to integrate the DAQ for the beam delivery system into the physics data flow. It is mainly assumed that integration of parts or all of the machine parameters should be straight forward due to the programmable interface units and the network based structure of the DAQ system.

3.3 Detector Control and Monitoring

The data acquisition and its operation is closely coupled to the detector status and detector conditions, as well as the machine conditions. Hence it is proposed that the detector slow control and the conditions monitoring is tightly linked to the DAQ system by an overall experiment control system.

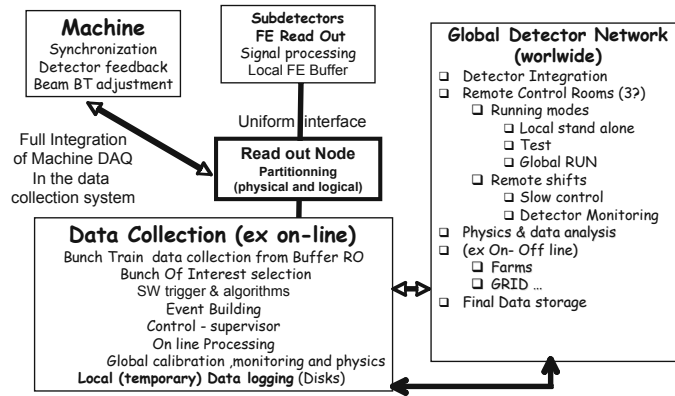


Fig. 5. Block diagram of system boundaries

For detector commissioning and calibration the DAQ system has to allow for partial detector readout as well as local DAQ runs for many sub components in parallel. The DAQ system has to be designed such that parts of a detector component or complete detector components can be excluded from the readout or be operated in local or test modes without disturbing the physics data taking of the remaining parts.

3.4 On - Off line boundaries

The notion of ON line and OFF line analysis is now completely obsolete due to the progress of hardware and software technologies (FPGA's, memories, processor, network bandwidth, embedded algorithms...). The figure 6 presents a possible integrated computing model.

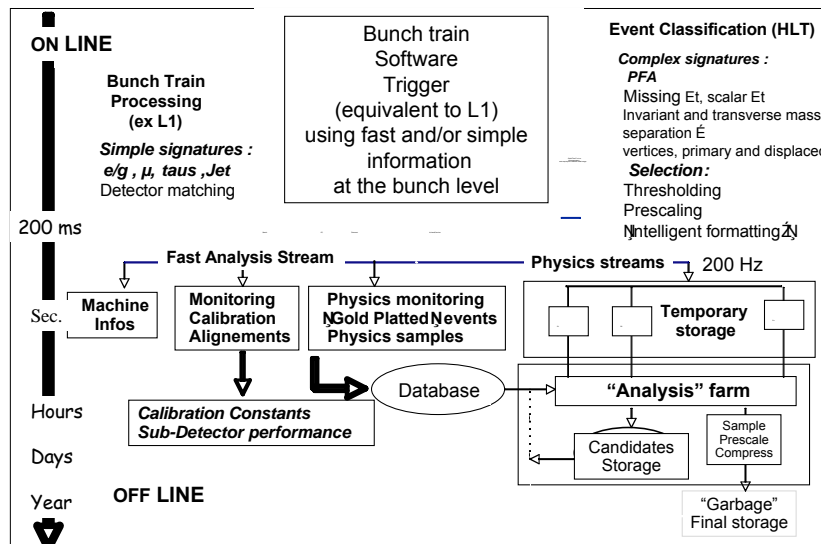


Fig 6. ILC Trigger and data acquisition possible computing model

To benefit from the online software event selection an accurate online calibration is needed. Strategies for calibrating and monitoring the detector performance as well as efficient filter strategies have to be worked out. Simulation studies will be needed in the coming years to prepare this in more detail.

3.5 3.5 Global Detector Networking

The ILC as well as the detector will be operated by truly worldwide collaborations with participants around the world. The global accelerator network (GAN) and global detector network (GDN) has been proposed to operate both the machine and the detector remotely by the participating sites. This in turn requires that the data acquisition system, as well as the detector control, be designed with remote control and monitoring features built in from the start.

4 Issues and Outlook

Although for the main DAQ system commodity components some generic R&D is needed to prepare the decisions. A DAQ pilot project should be planned to serve as a frame for R&D on the front end readout uniform interface, the machine and detector DAQ interface, detector slow control issues, online calibration and event selection strategies. Recent developments on data collection technology (for example ATCA [8]) should be followed and if possible explored to gain the necessary experience needed for the final DAQ technology choice.

In addition some architectural and technical studies should be made soon like the integration of a cosmic trigger that has been proven to be very useful for debugging purpose in the past during the commissioning phase. However, the compatibility with the power cycling scheme should be studied. The clock system, machine synchronization and timing distribution is another field of technical investigation. The experience of LHC could be useful.

Finally, a common work between the machine control group is foreseen on the subjects like ATCA and GAN. The figures presented in this report are presentation slides available on ref [10]. I would like to thanks Dr. Gunter Eckerlin from DESY for its contribution and useful discussions .we had together.

5 Reference

- [1] Detector Outline Document for the Large Detector Concept, July 2006.
- [2] GLD Detector Outline Document, July 2006W
- [3] Outline Document for the Fourth Concept Detector, August 2006
- [4] SiD Detector Outline Document, May [
- [5] TESLA Technical Design Report DESY 2001-11, ECFA 2001-209, March 2001
- [6] CMS TRIDAS Project, CERN/LHCC 2002-26, CMS TDR 6.2, December 2002
- [7] Suggested ILC Beam Parameter Range, Tor Raubenheimer, Feb, 2005
- [8] ATCA Short Form Spec., http://www.picmg.org/pdf/PICMG_3_0_Shortform.pdf
- [9] IEEE RT2007 proceedings G. Eckerlin and P. le Dû Trigger/Data Acquisition Issues and Challenges for the Next Generation of Experiments at the Future International Linear Collider
- [10] Slides
<http://ilcagenda.linearcollider.org/contributionDisplay.py?contribId=535&sessionId=83&confId=1296>.

The DAQ for the EUDET pixel telescope

Daniel Haas (Daniel.Haas@cern.ch) *

Université de Genève - Département de Physique Nucléaire et Corpusculaire
24, quai Ernest-Ansermet, 1211 Genève 4 - Switzerland

The EUDET pixel telescope [4] needs a flexible and performant data acquisition system (DAQ). Data throughput at raw data level is high and even demanding after data reduction. The integration of devices under test is provided at different levels and easy for the user. The DAQ system presented is platform independent, lightweight but scalable and outputs data as Lcio streams for the ILC software framework.

1 Introduction

The EUDET pixel telescope consists in its current implementation of up to 6 planes of monolithic active pixel sensors of 256x256 pixels with a single point resolution of 2 to 3 μm . It provides a testbench for different pixel sensor technologies and provides seamless integration of devices under tests (DUT). While in raw data taking mode, a data size of up to 2.4 MB per event is reached. So even at low trigger rates of a few Hertz, the DAQ system must assure a data throughput of some tens of megabytes per second and higher trigger rates would be difficult to achieve. Thus, the DAQ for the pixel telescope provides a data compression at the hardware level, reducing data to about 50 kB per event.

2 DAQ overview

Figure 1 shows a sketch of the components of the data acquisition. The data from the sensors is read via frontend boards and then transferred to an intermediate readout and data reduction board (EUDRB [5]), where the data can be compressed. A MVME6100 then collects the data of different EUDRBs inside a VME64x crate. The data is then sent to the main DAQ PC via gigabit ethernet. This PC also collects the information from the trigger logic unit (TLU, see Section 4) and eventually from the device under test.

Different scenarios for the integration of DUTs are foreseen:

- Integration at hardware level: This needs a special purpose hardware interface that should be able to read out the telescope sensors and the DUT as well. While the EUDRB implements this possibility, this approach is only feasible for very dedicated DUTs.
- Integration at software level: The DUTs will provide their own DAQ hardware, but the data will then be treated by a common DAQ software. This approach will eventually be used for some dedicated DUTs, but requests a lot of manpower from the EUDET collaboration.

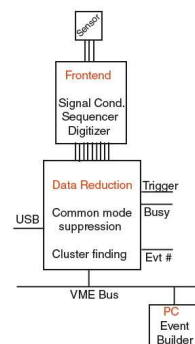


Figure 1: Data acquisition scheme of the EUDET pixel telescope.

*For the EUDET Collaboration

- Integration at data level: Both the beam telescope and the DUT use their own dedicated hardware and software, and the data streams are combined online by inter process communication. The synchronization of events and the configuration of the different devices during start-up can be difficult in this scenario.
- Integration at trigger level (Figure 2): This will be the default scenario. Different hardware and software can be used for the beam telescope and the DUT. The synchronization of the events is done via a simple trigger, busy and reset logic provided by the TLU and the events are combined off-line. To avoid slippage of event numbers between the DUT and the beam telescope, the TLU can provide a dedicated event number, to be read out by the DUT as well, thus guaranteeing a perfect match between an event from the telescope and the DUT.

3 The EUDRB

The data reduction and readout board (EUDRB) that has been developed by INFN Ferrara/Milano is described in detail in [5]. It collects the data from the frontend boards and has the following features:

- 20 MHz readout of 4 parallel input chains,
- Altera FPGA running at up to 80 MHz,
- independent daughter boards for analog and digital input,
- SRAM memory with space for 1 million 48bit-long words for the readout of up to 3 frames in succession,
- on board zero suppression algorithm and
- a readout either by USB 2.0 or VME64x, offering maximum flexibility.

In addition, the EUDRB allows to clock out the event number from the TLU and store it in the event data.

4 The trigger logic unit (TLU)

For the data integration at trigger level, the University of Bristol has developed a dedicated trigger logic unit for EUDET [6]. It is based around an off-the-shelf FPGA board. It has LVDS and/or TTL interfaces to the beam-telescope readout and any DUTs, PMT signal and/or NIM level signal interfaces to the beam-trigger and a USB interface to the DAQ. The data handshake between TLU and the DUT can be done in a simplified trigger/busy/reset mode or in a more sophisticated trigger data handshake, where the event number is clocked out by the DUT. The TLU is controlled and configured via an USB interface. Over the USB, additional information like the event timestamp and internal scalers is available.

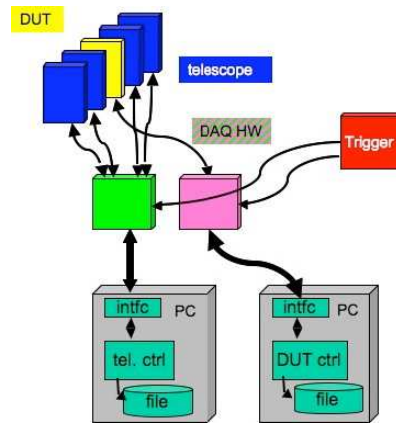


Figure 2: Integration of the DUT at trigger level.

5 The data acquisition software framework

The software framework for the data acquisition is constructed around a global run control and interprocess communication using sockets. A sketch of the different processes is shown in Figure 3. Producer tasks connect to the hardware of the beam telescope, to the TLU and eventually to a DUT in case of its full integration at software level. Data is sent from the producers to a central data collector and can be monitored by different processes. Control messages and status informations are sent to the logger process.

The software framework has been written platform independent. In the current, the beam-telescope producer runs on a Power-PC VME CPU under Linux, the TLU producer on a PC with Linux and the main run control, monitoring and logging under MacOSX. Windows systems are currently not used but supported using cygwin. Incoming data is stored on a 2 TB RAID 10 disk array and transferred to the GRID for conversion to lcio format and data analysis using the ILC software framework.

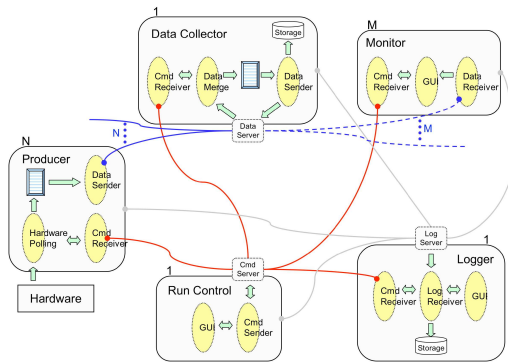


Figure 3: Interprocess communication of the DAQ software framework

6 Summary

A competitive DAQ system has been developed for the EUDET beam-telescope. Ease-of-use and platform independence for users of the telescope has been a main issue. The DAQ has been used successfully in testbeams at DESY and CERN in summer 2007 and will be further improved for upcoming tests. A full data chain from the readout of the pixel sensors up to the storage on the GRID has been established.

References

- [1] Slides:
<http://ilcagenda.linearcollider.org/contributionDisplay.py?contribId=358&sessionId=83&confId=1296>
- [2] <http://www.eudet.org>
- [3] <http://europa.eu.int/comm/research/fp6>
- [4] D. Haas, *A pixelated telescope for the E.U. detector R&D*, in these proceedings.
- [5] C. Bozzi, *The data reduction board of the EUDET pixel telescope*, in these proceedings.
- [6] Eudet-Memo-2007-02: D. Cussans, *Description of the JRA1 Trigger Logic Unit*, see <http://www.eudet.org>

Prototype DAQ for Calorimetry at Future ILC Experiments

David Bailey¹ for CALICE-UK[♦]

¹ – School of Physics and Astronomy, University of Manchester,
Oxford Road, Manchester M13 9PL

CALICE-UK are developing a prototype data-acquisition (DAQ) system for calorimeters at future ILC experiments. This DAQ system will be implemented using FPGAs and built using commodity components and networking hardware. The EUDET ECAL technical prototype will be used to demonstrate the feasibility of this approach. The design philosophy is presented, along with a possible implementation using PCI-express cards mounted in PCs, which act as data receivers and network interfaces.

Introduction

One of the most challenging aspects of calorimetry at the ILC is to successfully implement particle flow. This technique is the leading candidate to achieve the required excellent jet energy resolution vital to exploit the physics potential of the machine. The key to successful particle flow is a highly granular calorimeter, allowing the clean separation of showers from individual particles – in essence a tracking calorimeter. This approach leads to the requirement to handle very large quantities of data from the many readout channels.

The beam structure of the ILC, with a bunch train of 1 ms duration followed by a quiet gap of 200 ms, requires the detector readout electronics to digitise and time-stamp and buffer data from each bunch crossing during the bunch train and then read out the entire data sample during the inter-train gap with no triggering. All event classification and selection will be performed quasi-online by processor farms, so the main task of the DAQ is to send the data to mass-storage with no deadtime. It is also vital that no data be lost through buffer overflows or congestion in the network. Figure 1 shows the philosophy of the DAQ design.

Due to the very high number of readout channels and the necessity to minimise costs it is highly desirable to use commodity components wherever possible instead of developing bespoke solutions. This naturally leads to using powerful FPGAs and standard networking protocols as the building blocks of the DAQ system. Prototypes have been built using commercial FPGA development boards to receive data over Ethernet and store it to disk over PCI-express. Strategies for sending the data over a standard Ethernet-based network have also been investigated.

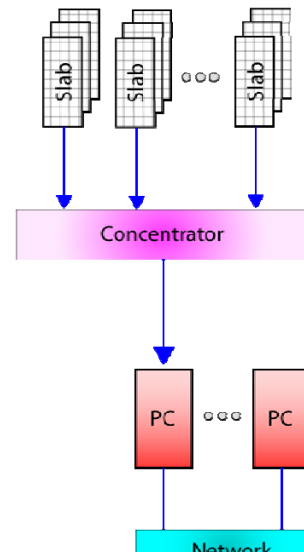


Figure 1: The DAQ uses a classic funnel design, concentrating the data in stages before sending it to storage.

[♦] This work is supported by the STFC and also by the Commission of the European Communities under the 6th Framework Programme Structuring the European Research Area, contract number RII3-026126.

The Front End

The detector signals are buffered and digitised by the Very Front End (VFE) ASICs. The interface to the VFE and DAQ system is provided by a sub-detector specific interface (DIF) board. This has been prototyped using a Xilinx Spartan FPGA development board. The VFE ASICs along the so called ECAL “slab” are emulated in FPGAs, allowing the development of the necessary control signals in the DIF. The DAQ interface is currently USB or Ethernet for simplicity of testing. Figure 2 shows the prototype system under test in Cambridge. It is anticipated that the production DIF will have a high-speed, bi-directional serial link to the DAQ and a connection to a neighbouring DIF for redundancy in case of failure of the primary DAQ link. The link to the DAQ must be shielded and the current implementation envisages using HDMI cables to carry the serial data and a clock as they are compact, readily available and can be made halogen-free. It may also be possible to add a prompt signal, carried on spare conductors in the HDMI cable, to inject test triggers or provide an input for a cosmic trigger.

It is envisaged that all the serial links will be encoded using 8B10B over LVDS.

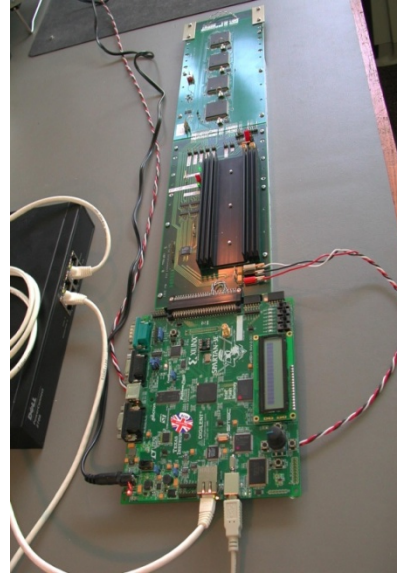


Figure 2: Prototype DIF connected to simulated EUDET ECAL VFE electronics.

DAQ System

A schematic of the on-detector DAQ system is shown in Figure 3. The first-level data concentrator (LDA in the figure) provides synchronous clock and control information to a number of DIFs. It also aggregates the data from the same DIFs. The redundant DIF-DIF connection is also shown. It provides a surrogate serial link for readout and a clock.

The LDAs buffer and frame the data for transmission over long, optical links to the off-detector receiver infrastructure. The downstream (off detector) links need not be synchronous with the accelerator clock as meta-data will be added to the data stream so that it is completely self-describing. Depending on where the external clocks are connected to the DAQ system, it may be necessary for the upstream (i.e. to the detector) to be synchronous, fixed latency serial links. Regardless of this requirement on the off-detector links, all the LDA-DIF serial links must be synchronous and of fixed latency to ensure the concurrent arrival of control signals at the VFE electronics. The complete DAQ system is

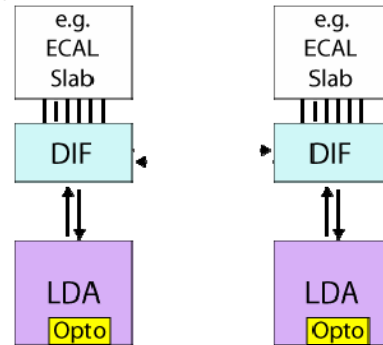


Figure 3: Schematic of the DAQ links between the front end electronics and first level concentrator (LDA).

shown schematically in Figure 4. Since all the sub-detector-specific control signals are generated by the DIF electronics, the entire DAQ chain from the DIF links to the off-detector infrastructure can be common between all components (subject to readout rate requirements) allowing commoditisation.

The off detector receiver (ODR) has been prototyped on a Xilinx Virtex4 development board supplied by PLDApplications [1]. A complete gigabit Ethernet layer has been implemented in the FPGA, capable of driving both optical and copper physical layers through the on-board SFP cages. This Ethernet capability has been used to investigate the data transfer rates over PCI-express from the card to disk and also to evaluate efficient network protocols to transfer data direct from the cards into packet-based networks [2]. At present the ODR is implemented using an FPGA on an PCI-express card, however if the ILC machine control infrastructure chooses to standardise on a crate-based system, such as ATCA, it would be possible to move the ODR systems to that infrastructure with minimal modification due to the use of standard network and interconnection protocols for data transmission.

The performance of the prototype ODR has been investigated using the Ethernet interface to provide an input data stream which is then subsequently written to the disk of the host PC. An example of the data-transfer rates to disk is shown in Figure 5.

Summary

CALICE-UK are prototyping the major components of a high-rate, scalable DAQ infrastructure that is based on readily available commodity commercial components. It will be used to read out the EUDET calorimeter technical prototypes.

References

- [1] <http://www.plda.com>. [2] See the proceedings of IEEE NPSS Real Time Conference 2007 for details.

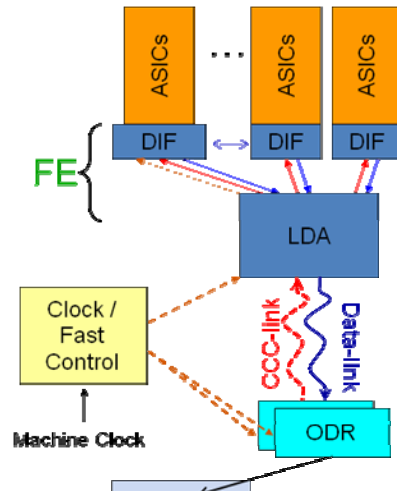


Figure 4: Schematic of the entire DAQ showing front-end, clock and control and off-detector components. Dotted lines indicate potential synchronous, fixed latency links.

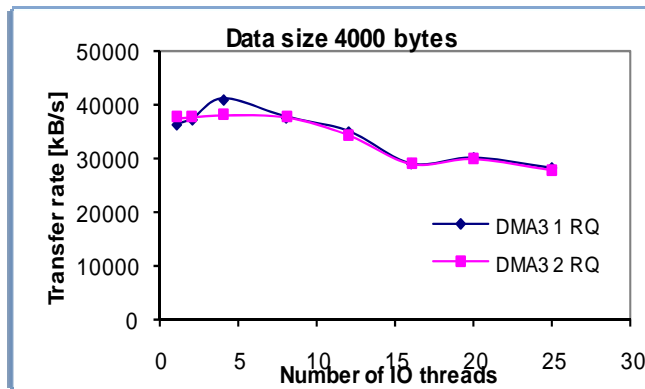


Figure 5: Example performance of the ODR data transfer rate to disk.

CALICE-DAQ communication and DAQ software

V. Bartsch¹ for the CALICE DAQ groups

1- University College London - Department of Physics and Astronomy
Gower Street, London WC1E 6BT, UK

This note describes work on the data acquisition system for a calorimeter of the future International Linear Collider (ILC) within the CALICE collaboration. Focus is on options for the network, requirements of the clock, a potential bottle neck for the control data and a use case analysis of the software for the data acquisition system.

1 Introduction

The planned data acquisition system is developed within the EUDET project which is scalable to the data rates which will occur in the final calorimeter and therefore give input to the Technical Design Report of one of the detectors. The work is carried out within the CALICE-UK groups.

The current design of the data acquisition (DAQ) system distinguishes between the very front-end electronics (VFE), which is located on the detection slabs and consists of ASICs, and the front-end electronics (FE), which is located at the end of the detection slab and consists of a FPGA and control systems. The closest part of the FE to the VFE is the detector interface (DIF) which has to be customized to the choice of the detector type and the VFE choices. The DIF translates the data into a common format. Therefore any other FE component is independent of the choices of the detection layer. Several DIFs are connected to a link data aggregator (LDA) which sends the data over an optical link to the off detector receiver (ODR). The ODR is a PCI (Peripheral Component Interconnect) card within a DAQ PC from where the data will be saved to disk. It is estimated that the total data volume to be read out from the calorimeter is about 5 Gb or about 1 Mb per slab for one bunch train, i.e. about 5 Mb/s for a slab.

2 Network and Switching

Between the LDA and the ODR a fast network of optical cables is envisaged. In order to reduce the overall cost of the hardware the work on the network is focussed on testing options for a 10 Gb/s network. On the ODR side it has been successfully shown that high bandwidth usage of over 9 Gb/s using PCIe 10Gig cards from Myricom [1] can be performed. Tests with multiple 10 Gb/s transfers are ongoing. To simulate data transfers from the LDA to the ODR a FPGA based Ethernet system using RAW frames has been setup and successfully tested with bi-directional communications in a request-response mode. The plan is to study multiple receivers talking to more than one FPGA system.

The performance of dispatching and routing tasks of a network switch between the LDA and the ODR is investigated. The motivation is to have high data-taking efficiency. Because the transport format of the data needs to be customized in order to allow for clock and control data to be uploaded to the slab an optical switch needs to be used. A 16x16 fibre multi mode optical switch has been purchased from Polatis [2].

3 Clock

It is understood that a machine clock will be used which will be fed into the ODRs. The clock will then be distributed to the LDAs which then distributes the clock to the DIFs. In turn the DIFs distribute the clock to the VFE. For debugging and test purposes an interface of the machine clock to the LDAs and the DIFs needs to be introduced. A couple of constraints on the clock have been identified:

- The machine clock will be running at a frequency around 50 MHz with low jitter. The fast commands will be accurate to a period of the machine clock. This requires a fixed latency in the command channel.
- The ODR needs to be running on a frequency of 125 MHz due to the link specifications of the optical link connection between the ODR and the LDA.
- The LDA derives the machine clock with low jitter. It is estimated that a jitter less than 1 ns is needed for the detectors.
- The bunch spacing is about 320 ns which corresponds to 3.125 MHz. Therefore at the DIF the machine clock needs to be divided by a factor 16. Due to the long time between bunch trains it would be helpful to have a fast command which determines the bunch clock phase with respect to the machine clock.

4 Single Event Upset

A study of single event upsets (SEUs) is part of the study of the configuration data which need to be send to the FE. The study tries to identify bottle necks which could arise. SEUs can occur in the electronics if a particle (typically a neutron, proton or pion above a certain threshold energy about 20 MeV) traverses the electronics and generates enough electron-hole pairs in the active area of the silicon material such that a change in the state of the circuit occurs. Typically these changes can be reset in FPGAs and therefore SEUs do not lead to permanent damage. However in order to reset the FPGAs at a reasonable rate one needs to know the rate at which SEUs occur.

For this study detector simulations using PYTHIA and MOKKA with the TESLA design have been performed for physics events which occur frequently according to the TESLA TDR [3]. In this study WW, QCD and $t\bar{t}$ events were simulated. The particle spectra of particles traversing the ECAL front-end electronics were generated. It was shown that all of these simulations were dominated by QCD events.

It has been shown that the SEU rate arising from physics events with today's FPGAs lies in the area to several days for today's FPGAs in the TESLA ECAL. Thus requiring the FPGAs in the ECAL to be reset at a higher rate to mitigate these effects. It needs to be noted that this study only comprises physics events. The machine background has only been studied partially up to now.

The occupancy resulting from physics events of the ECAL barrel could be determined from the simulations. It is estimated to be 5×10^{-4} per bunch train for physics events. The

occupancy is expected that this number will rise when you consider the machine background and noise. A linear collider note describing the study in more detail and adding radiation backgrounds is under development.

5 DAQ software

The requirements of the DAQ software for the technical calorimeter prototype within the EUDET project are currently discussed and use cases have been constructed. From the use cases it became clear that a state machine for the start and the close down of the DAQ needs to be used. The transitions need to take into account to check the status and the communication of the system, the configurations need to be distributed to the VFE before any data can be taken. It also needs to be noted that all of the checks and distributions of configurations need to be saved in a book keeping database.

A point of discussion is how to store the data. This depends on the data rate. Three scenarios have been envisaged: For data rates up to 200 Mb/s the data can be sent from a local disk on the DAQ PC to a central storage; for higher data rates a RAID array needs to be used; for data rates higher than about 1600 Mb/s the data can not be locally stored any more, but needs to be transferred in memory. Thus increasing the risk of failure of the data transfer. For the EUDET prototype an estimate has been made that the data rates of the DAQ will be about 400 Mb/s, however heavily depending on the detector and VFE choices.

6 Conclusion

In this note the design and development undertaken for the ILC calorimeter DAQ is presented. Special emphasis is put on the network, clock and configuration data as well as on the DAQ software. The ongoing research to provide a 10 Gb/s link solutions and an optical switch are described. The requirements for a clock system are discussed. An estimate for SEU rates deriving from physics events within the FE is given which is between about 40 days in the electromagnetic calorimeter of TESLA design. Concepts of use cases and the state machine for the DAQ software are discussed with the help of which a DAQ software will be designed.

References

- [1] <http://www.myri.com/Myri-10G/>
- [2] Polatis, Multimode Optical Switch Tray,
http://www.polatis.com/datasheets/polatis_ost305_02_01-s.pdf
- [3] T. Behnke et al., TESLA Technical Design Report, 2001
- [4] D. Bailey, Future DAQ directions, LCWS 2007, Hamburg, Germany

ATCA* for Machines

***Advanced Telecommunications Computing Architecture**

R. S. Larsen¹*

1 – Stanford Linear Accelerator Center – Electronics & ILC Divisions
Menlo Park California – USA

The Advanced Telecommunications Computing Architecture is a new industry open standard for electronics instrument modules and shelves being evaluated for the International Linear Collider (ILC). It is the first industrial standard designed for High Availability (HA). ILC availability simulations have shown clearly that the capabilities of ATCA are needed in order to achieve acceptable integrated luminosity. The ATCA architecture looks attractive for beam instruments and detector applications as well. This paper provides a brief overview of ongoing R&D including application of HA principles to power electronics systems.

1 The Case for High Availability in Accelerator Systems

Large accelerators and detectors are production machines that require huge investments in capital cost, operations and maintenance for a successful result. In economic terms, a non-functioning machine is wasting capital at an enormous rate. Accelerators are typically designed to operate for extended periods on a 24/7 basis, followed by a period of inactivity to allow maintenance and re-staging of experimental apparatus. Ideally, the machines should be designed to run for the mission period without interruption.

Such an ideal is rarely met although some modern synchrotron light sources come close. Large particle detectors have inherently high redundancy to tolerate loss of isolated channels without interruption. However, the ILC machine itself consists of two 10 km linacs pointed at each other in which every critical component on every pulse must operate flawlessly. Stored beam machines enjoy some immunity to problems that happen between beam fills, but the ILC is a single-shot machine in which the loss of any non-redundant component (single point of failure) will interrupt operation. The simulations have shown that if the ILC is built with current technologies, it will be operable only about 15% of the time. High Availability design for the ILC is therefore a necessity, not an option.

High Availability of a complete machine involves many strategies. A common example for linacs is to include active standby RF stations to maintain design beam energy in case one or more units fail in service. At the same time, it is necessary to have physical access to repair the broken stations while the machine keeps running on the standbys. This has led to a key element of the current baseline design of the ILC, namely a second parallel tunnel to contain all the support equipment which is totally accessible while the beam is on. Similar problems with power supply failures has led to an investigation of partial redundancy modular designs in which a single module out of N modules in a supply can fail and be replaced without interruption of operation.

In the case of instrumentation and controls, although these low power components tend to be more reliable, the sheer numbers demand an aggressive approach using partial redundancy

* US Department of Energy Contract DE-AC03-76SF00515.

techniques and hot-swap repair strategies. Such designs require more intelligence to be built into the systems to detect and manage problems before they lead to machine interruption. The same intelligent diagnostics and platform management techniques need to be applied to all systems in the ILC.

Fortunately the ATCA system offers a huge advantage in a readily available industrially supported platform, as well as an example of features that can be copied to non-ATCA systems. The ILC R&D program intends to evaluate the platform for typical controls and instrumentation applications, many of which can be addressed with commercial off the shelf (COTS) components; while at the same time extending its capabilities to accommodate the high-performance circuitry peculiar to accelerators: Instruments such as sub-micron beam position monitors, highly integrated detector front ends, very high performance low level RF circuits for beam phase and timing control, and intelligent RF and DC power systems.

2 ATCA Features Summary

ATCA was invented by a large consortium of telecom providers under the PCI Industrial Computer Manufacturers Group (PICMG) which includes ~250 telecom, integrated circuit, modular instrument, shelf¹ and rack manufacturers. The telecom business segment alone is estimated at \$10B annually. Several telecom companies have announced that all future products will use this platform. Some labs have joined PICMG as Associate members in order to access all the standards as well as to potentially help develop features of interest to the physics community within the PICMG framework.

The loaded shelf is designed for availability of 0.99999, which it achieves by the partial redundancy of various components and a hot-swap feature. This corresponds to a downtime of 5 minutes per year. The key elements of a shelf are: 5-16 module slots; dual Shelf Manager cards to sense all operating conditions of all modules; backplane of 2.5 Gb/s serial connections between controller slots and all modules (typically star or dual star) or all modules to all modules (mesh); dual controllers; redundant 48V power supplies and redundant fans. The 48 volt bulk supply feeds all modules via individual lines so no power fault will take down the shelf. All secondary voltages are developed on each module which ensures future compatibility as chip voltages change in future. The shelf managers, controllers, application modules, power supplies and fans are all hot-swappable. Controllers and Shelf Managers are typically dual-redundant while power supplies and fans can be 1 of N redundant – in other words, able to operate with 1 of N sections failed, and hot-swappable so the shelf never has to be turned off to make the exchange.

The function of the Shelf Manager (SM) is to detect the health of any module in the shelf, monitor its current, voltages or temperature, disable its power if it malfunctions and signal the high level control systems to dispatch a repair person. Once there the person observes by a blue LED that the module needs replacement, makes the exchange which the SM detects and returns it to service.

A chief feature for Telecom is data throughput, since telephony consists of transmitting, receiving, routing and processing data, so the shelf is designed in full mesh mode to have a

¹ *Shelf* is a term used by the Telco industry for the crate or sub-rack that has been more commonly used in research. *Shelf* will be used in this document to be consistent with other AdvancedTCA documents.

throughput of 2.5 Tb/s. This throughput will increase as the base speed of serial data transmission keeps increasing. Parallel processing speed is of great interest to the large particle detector community. At the same time, backplanes can be easily tailored to the more modest speeds of machine controls systems so bandwidth is not wasted. Figure 1 shows several versions of shelves.

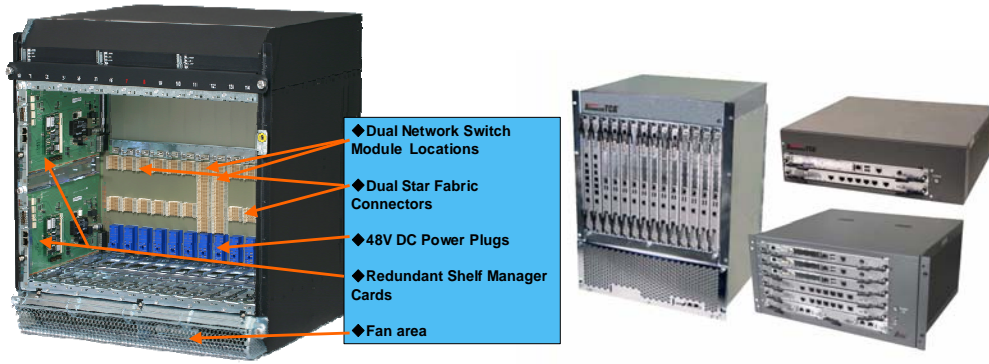


Figure 1: ATCA Shelf Options

3 Mezzanine Modules and Micro-ATCA Shelves

Since the investment in an ATCA module is substantial and processing and logic chips evolve rapidly, PICMG has developed options so that a base ATCA module can serve as a carrier board for several smaller modules. These mezzanines, Advanced TCA Cards (AMC), are also hot-swappable and different functions can be separated for future upgrades without affecting the base unit. Older types of mezzanine cards required the carrier to be removed before the mezzanine could be replaced. AMC's also allow design engineers to work on separate functions in parallel for faster overall development time of a system. In principle up to eight single wide single height AMC's can be plugged into a carrier. In addition, sizing options allow double wide and double high AMC's.

Where size permits, other standard mezzanines such as Industry Pack (IP) can be mounted on AMC's to gain entry to the ATCA platform. In this case the Mezzanine card becomes an adapter module for any IP function, thus allowing many more COTS industry choices when configuring a system.

A further option has been developed for packaging individual mezzanine cards in a separate much smaller shelf, called Micro-TCA (μ TCA). This packaging does not include full ATCA features but is of interest for small configurations where low cost is paramount and some loss of redundancy and control is tolerable. Figure 2 shows AMC and μ TCA shelf options.

4 Card Level Power Systems

Besides the maturing of multi-Gb/s serial data transmission and reception at the chip level to enable the ATCA technology, industry has introduced a suite of highly configurable hybrid power supply products designed for card-level applications. These are sophisticated 1 of N configurable miniature systems to simplify driving power-hungry dense components such as FPGAs and processors. The extremely high instantaneous switching currents needed to support high speed chips are provided by Point-of-Load regulators. The POL regulators can be monitored and controlled by the Shelf Manager. For example, the SM can adjust the conversion clock frequency and phase for noise minimization. Figure 3 is a block diagram of a typical suite of power components.

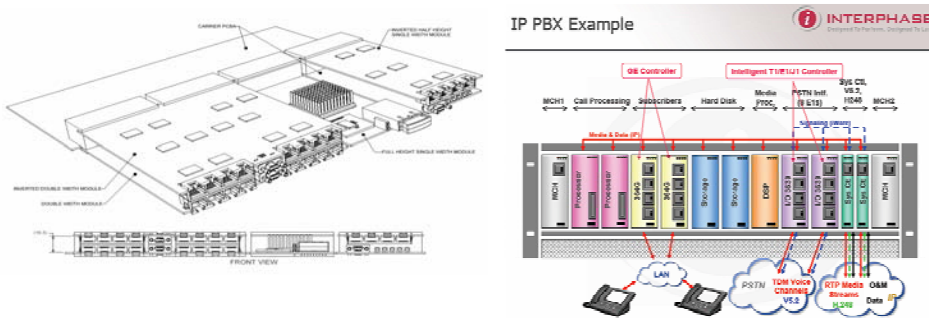


Figure 2: Mezzanine Boards on ATCA Carrier and µTCA Shelf

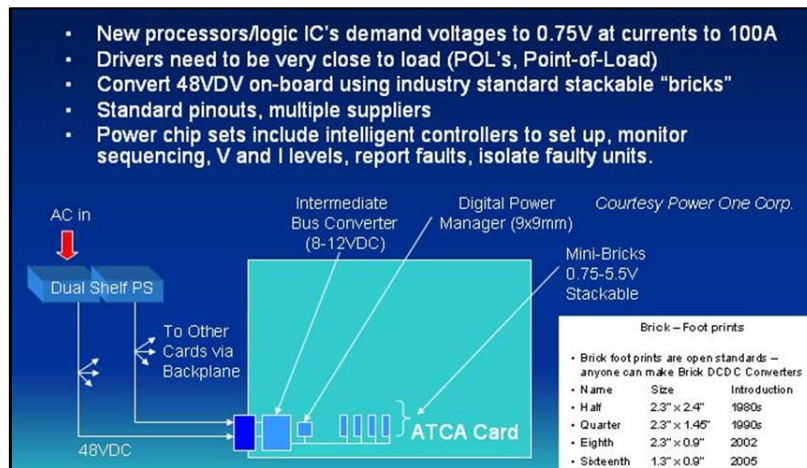


Figure 3: Board Level Intelligent Power System

5 Lab R&D Activities

SLAC, ANL, FNAL and DESY are engaged in exploratory evaluations of ATCA. SLAC in collaboration with University of Illinois Urbana Champaign and SAIC Corporation is

developing an ATCA carrier for a slave VME board in order to gain quick access to the ATCA platform for VME COTS products. SLAC is also developing a controls and interlock systems for an ILC 10 MW RF station in VME which will be ported to ATCA in a second iteration. ANL is developing high level software platforms for the ILC control system based on an ATCA technical and cost model. FNAL is evaluating the core control system as well as developing a beam position monitor controller on ATCA. DESY has several initiatives including porting a low level RF control system and investigating μ TCA for front end controls and interlock functions. At the 2007 IEEE Real Time Conference at FNAL in May 2007, an ATCA workshop was attended by 85 registrants. A number of vendors showed products, while the conference featured a number of papers on applications for a wide range of physics data acquisition and control experiments.

6 Conclusion

The ATCA system is a prime candidate for the core HA system for ILC controls. It also is a prime candidate for instrumentation modules providing analog interconnects and noise performance can be verified. The added cost of partially redundant systems seems reasonable. Similar principles are being applied in power electronics, specifically in DC and pulsed power supplies and high power pulse modulators. ATCA evaluations are aimed at understanding and demonstrating hardware and software in prototype settings, to verify architectures, performance and costs before ILC is ready for launch as a funded project by 2010.

7 Acknowledgments

The evaluations are being conducted by collaborators at the labs cited, joined by others who are not directly conducting R&D in their home labs. Key participants in the controls effort are John Carwardine (Lead) and Claude Saunders of ANL, Brian Chase, Manfred Wendt and Margaret Votava et al of FNAL, Stefan Simrock and Kay Rehlich of DESY, Michael Haney and Michael Kasten of UIUC, Shinichiro Michizono of KEK, and Robert Downing of SLAC and R.W. Downing Inc. Thanks also to the many others who are supporting these efforts as well as those in non-ILC labs undertaking independent efforts to employ the ATCA platform in experimental settings. Special thanks to Robert Downing for critiquing the manuscript.

8 References

[1] Slides:

<http://ilcagenda.linearcollider.org/contributionDisplay.py?contribId=372&sessionId=83&confId=1296>

[2] Availability and Reliability Issues for ILC, [T. Himel](#), [J. Nelson](#), [N. Phinney \(SLAC\)](#), [M. Ross \(Fermilab\)](#), SLAC-PUB-12606, Jun 27, 2007. 4pp, Contributed to Particle Accelerator Conference (PAC 07), Albuquerque, New Mexico, 25-29 Jun 2007

SLAC PUB 12822

Test Beam Contact

Conveners: M. Woods, J. Yu, F. Sefkow, K. Kawagoe

Overview on Test Beam Facilities

Kiyotomo Kawagoe

Kobe University - Department of Physics
1-1 Rokkodai-cho, Nada-ku, Kobe 657-8501 - Japan

ILC detectors are required to have precedented precision. Achieving this requires significant investment for detector test beam activities to complete the R&D needed, to test prototypes and (later) to qualify final detector system designs, including integrated system tests. This document describes an overview of current test beam facilities.

1 Introduction

ILC detectors are required to have precedented precision. Achieving this requires significant investment for detector test beam activities to complete the R&D needed, to test prototypes and (later) to qualify final detector system designs, including integrated system tests. To this purpose ILC Detector Test Beam Workshop (IDTB07) [2] was held at Fermilab in January 2007, where we started to write the roadmap document for ILC detector R&D test beams [3]. In this talk an overview of current test beam facilities was given based on the information collected at the IDTB07 workshop with some updates.

2 Facilities

Currently seven laboratories in the world provide eight beam test facilities; CERN PS, CERN SPS, DESY, Fermilab MTBF, Frascati, IHEP Protvino, LBNL and SLAC. In addition, three laboratories are planning to provide beam test facilities in the near future; IHEP Beijing starting in 2008, J-PARC in 2009 and KEK-Fuji available in fall 2007. Table 1 summarizes the capabilities of these facilities and their currently known availabilities and plans.

2.1 CERN

There are presently four beam lines at two machines; four in the east area of the PS and four in the north area at the SPS. A variety of targets are possible for the PS beams, including one that enhances electron yield by a factor 5~10, but T9/T10/T11 share the same target. For the SPS beams, H2/H4 and H6/H8 share targets. Up to three user areas are possible per beam, although some areas have been permanently occupied by major LHC users. H4 can be set up to produce a very pure electron beam, with energies up to 300 GeV. Low energy tertiary beams are possible in H2 and H8. In addition to test beams, there are two irradiation facilities at CERN. The Gamma Irradiation Facility (GIF), based on a ^{137}Cs source in the former SPS west area, provides 662 keV photons at up to 720 GBq. While 2007 may be the last year of operation, a new facility is under discussion. A proton and neutron irradiation facility in the PS east hall uses the 24 GeV primary protons from the PS to provide a $2 \times 2 \text{ cm}^2$ beam spot with 2.5×10^{11} protons/spill. Neutrons with a spectrum similar to the LHC can be obtained from a beam dump. With the start of the high-priority LHC program in 2008, there is considerable uncertainty about the future test beam running schedule. Three interleaved operational modes for the PS and SPS are envisioned in the LHC era, including LHC injection, LHC setup (with test beams in parallel), and delivery

Facility	Primary beam energy (GeV)	Particle types	Beam lines	Beam Inst.	Availability and plans
CERN PS	1–15	e, h, μ	4	Cherenkov, TOF, MWPC	Available, but reduced services during LHC commissioning
CERN SPS	10–400	e, h, μ	4	Cherenkov, TOF, MWPC	Available, but reduced services during LHC commissioning
DESY	1–6	e	3	Pixels	Available over 3 mo/yr
FNAL-MTBF	0.25–0.75	p, e, h, μ	1	Cherenkov, TOF, MWPC, Si-strips, Pixels	Continuous at 5% duty factor, except for summer shutdowns
Frascati	0.25–0.75	e	1		Available 6 mo/yr
IHEP-Beijing	1.1–1.5 0.4–1.2 (sec.)	e e, π , μ	3 3	Cherenkov, TOF, MWPC	Available in March 2008 or later
IHEP-Protvino	1–45	e, h, μ	4	Cherenkov, TOF, MWPC	Two one-month periods per year
KEK-Fuji	0.35–3.4	e	1		Available in fall 2007, for 8 mo/yr, as long as KEKB operates
LBNL	1.5; ≤ 0.06 ; ≤ 0.03	e; p; n	1	Pixels	Continuous
SLAC	28.5 1–20 (sec.)	e e, π , p	1		Shutdown in 2008-2009, with certain plans beyond

Table 1: Summary of test beam facilities along with their beam instrumentation, availability and plans.

to other programs, e.g., the neutrino program, and fixed target and test beam experiments. The study suggested about a 50% fraction in the delivery mode in 2008, rising to perhaps 85% by 2011, depending on experience. It remains to be seen what the actual availability will be in the coming years. However, operation of the SPS in test beam mode, and therefore the PS as well, is required to serve several fixed target experiments that are part of the core CERN physics program.

2.2 DESY

Three test beam lines are available, based on bremsstrahlung photons generated by a carbon fiber in the circulating beam in the DESY II synchrotron. Photons are converted in an external copper or aluminum target, spread into a horizontal fan by a dipole magnet, and then collimated. There are no external beam diagnostics or instrumentation available. However, the T24 area is being dedicated to EUDET, which will provide significant infrastructure. The facility will be down for the first half of 2008, but is otherwise available on a continuous

basis.

2.3 Fermilab

The Meson Test Beam Facility (MTBF) has recently completed a major upgrade in anticipation of the needs of the ILC community. By moving the target to shorten the decay path from about 1300 to 450 ft, reducing material in the beam line from 17.8 to 3.4% X_0 , and increasing the aperture and the momentum acceptance from .75 to 2%, the overall rate has been substantially improved in the new design and the momentum range has been extended below 4 GeV. In addition, the fraction of electrons in the beam has been enhanced. The Switchyard 120 (SY120) delivers main injector beams to the Meson Detector Building. It must run in conjunction with proton delivery to the pbar source and the neutrino programs. For the purposes of program planning, the MTBF is administratively limited to no more than a 5% impact on these other programs. The Accelerator Division has implemented both 1 second and 4 second spills. Possible configurations are one 4-second spill every minute, 12 hours/day; two 1-second spills every minute, 12 hours/day; and one 4-second spill every two minutes, 24 hours/day. It may also be possible to simulate the ILC beam structure of 1 ms beam followed by 199 ms gap. The MTBF test beam area is divided into two beam enclosures, although these cannot be operated independently. These enclosures are divided into six user stations and are supported by installed cables, gas lines, offices, and two climate controlled huts. Experiments are also supported by a tracking station, a new TOF system and differential Cherenkov detector, motion tables and video system, and a laser alignment system. Further enhancements to the Fermilab test beam capability are under consideration. The MCenter beam line, which houses the MIPP experiment, is currently not scheduled. The beam line has very attractive characteristics. Six beam species are available from 1~85 GeV, with excellent particle identification capabilities. The MIPP experimental setup could allow for a better understanding of hadron-nucleus interactions, thereby benefiting our understanding of hadronic shower development.

2.4 IHEP-Beijing

Three test beam lines are available at BES: two are to deliver primary electrons or positrons at 25 Hz to the E1 and E2 experimental areas, while secondary beams at 1.5 Hz are available in E3. The facility is already booked for all of 2007. It will undergo significant upgrade through March 2008, at which point the facility will be available on a continuous basis.

2.5 IHEP-Protvino

At least four high intensity and low intensity beam lines are available at IHEP-Protvino. Beam lines in the BV hall are produced from internal targets in proton synchrotron and have limited intensity. The extracted proton beam is also used to produce high-intensity primary and secondary test beams in the experimental gallery. Test beams are available in two period (April and November-December) for a total of about 2 months/year.

2.6 KEK and J-PARC

There are currently no test beam facilities at KEK. However, the Fuji test beam line is being implemented for fall 2007. This is based on bremsstrahlung photons from 8 GeV

high-energy beam particle collisions with residual gas in the KEKB Fuji straight section vacuum chamber. Photons are converted in a tungsten target and the conversion electrons are extracted to an experimental area outside the KEKB tunnel. The expected particle rate is continuously more than 100 electrons/s over a momentum range from 0.5 to 3.4 GeV. The facility will operate parasitically to KEKB, with availability about 240 days/year. Plans are developing for test beam facilities at J-PARC, which would be realized no earlier than 2009.

2.7 LBNL

Two test beam opportunities are offered, as well as dedicated beam lines for proton and neutron irradiation from the 88 inch cyclotron. A 1.5 GeV electron beam with tunable flux is available at 1 Hz from the injection booster for the ALS. This test area is equipped with a 4-plane beam telescope based on thinned CMOS pixel sensors. In addition, LOASIS is able to supply electron beams via TW laser wakefield acceleration. At present, it is possible to tune beam energies from 50 MeV to 1 GeV. There are also plans to extend the beam line for decreased intensity and to allow testing at different incident angles.

2.8 SLAC

A single beam line brings primary electrons from the main linac to End Station A (ESA), with energies up to 28.5 GeV and fluxes varying from 1.0×10^6 to 3.5×10^{10} /pulse. A secondary beam can be produced by putting the primary beam on a Be target in the beam-switchyard and accepting hadrons into the A-line, which makes a 0.5 degree angle with respect to the linac. Secondary electron or positron beams can also be created using collimators at the end of the linac, with fluxes adjustable down to one particle per pulse. The End Station A facility is well equipped with a shielded area for work with primary beam, and an open experimental region beyond for secondary beams. The beams are well instrumented.

Anticipating the end of the B Factory running in September 2008, the user-based test beam program in End Station A (ESA) will complete in Summer 2007, though some ILC tests will continue in ESA until September 2008. In 2009, the downstream 1/3rd of the linac will be used for the LCLS project with no plans for delivering test beams to ESA. The South Arc Beam Experiment Region (SABER) has been proposed as a follow-up to the Final Focus Test Beam Facility (FFTB). SABER would use the first 2/3 of the linac to deliver compressed, focused, primary electrons and positrons at 28.5 GeV to the south arc experimental region. This space may be suitable for smaller scale R&D experiments. SLAC is also considering an extension of the SABER proposal that would provide 28.5 GeV primary beams to the A-line, thereby restoring capability for both primary and secondary beams into End Station A. SABER is scheduled for operation in 2010, so a user test area could be restored in either the south arc or End Station A shortly afterward.

References

- [1] Slides:
<http://ilcagenda.linearcollider.org/contributionDisplay.py?contribId=429&sessionId=103&confId=1296>
- [2] URL: <https://conferences.fnal.gov/idtb07/>
- [3] *Roadmap for ILC Detector R&D Test Beams*, KEK Report 2007-3, FERMILAB-TM-2392-AD-DO-E, Unpublished (2007).

Beam Delivery System

Conveners: D. Angal-Kalinin, H. Yamamoto, A. Seryi

R&D STATUS OF ATF2 IP BEAM SIZE MONITOR (SHINTAKE MONITOR)

T. Suehara¹, H. Yoda¹, M. Oroku¹, T. Yamanaka¹, S. Komamiya¹,
T. Sanuki², T. Tauchi³, Y. Honda⁴ and T. Kume⁵

1- The University of Tokyo - Department of Physics
7-3-1 Hongo, Bunkyo, Tokyo - Japan

2- Tohoku University - Department of Physics
6-3 Aoba, Aramaki, Aoba, Sendai, Miyagi - Japan

3- KEK - Institute of Particle and Nuclear Studies

4- KEK - Accelerator Laboratory

5- KEK - Applied Research Laboratory
1-1 Oho, Tsukuba, Ibaraki - Japan

Shintake monitor[2] is a nanometer-scale electron beam size monitor. It probes a electron beam by an interference fringe pattern formed by split laser beams. Minimum measurable beam size by this method is less than 1/10 of laser wavelength. In ATF2, Shintake monitor will be used for the IP beam size monitor to measure 37 nm (design) beam size. Development status of the Shintake monitor, including fringe phase monitoring and stabilization, gamma detector and collimators, is described. In addition, we discuss the beam size measurement by Shintake monitor in ILC.

1 Overview

1.1 Shintake Monitor

Figure 1 shows a schematic of Shintake monitor. A photon beam from a YAG Laser (2nd harmonics, 532 nm wavelength) is split and go across the focal point of the electron beam line from the opposite direction to make an interference fringe pattern. Photons in the fringe interact with the electron beam by inverse-Compton scattering process.

The fringe pattern behaves as a kind of a modulation of photon density, so number of scattered photons can be modulated by scanning the phase of the laser fringe on the IP. Depth of the modulation of Compton photon density (N/N_0) depends on the electron beam size by,

$$\frac{\Delta N}{N_0} = \exp\left(-\frac{(2k_0\sigma_y)^2}{2}\right) \quad (1)$$

where k_0 is the laser wavenumber and σ_y is the beam size of y axis.

We can obtain the electron beam size by measuring this modulation depth with a gamma-ray monitor located downstream of the IP.

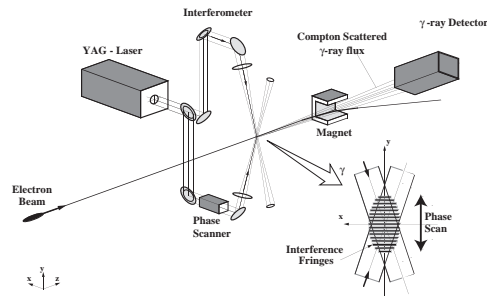


Figure 1: A schematic of Shintake monitor. Original figure from [3], partly revised.

1.2 Required Performance for ATF2

ATF2 (Accelerator Test Facility 2)[4] is a final focus test bench for ILC. It has 2 major goals, which are achievement and maintenance of 37 nm beam size by ILC-like beam optics and stabilization of beam position to nanometer level.

Shintake monitor is the key component to realize the first goal. It will be used for beam tuning as well as for confirming the achievement of 37 nm beam size. To meet the goal, 2 nm resolution will be required for the Shintake monitor. By Equation (1), 2 nm measurement error for 37 nm beam size corresponds to 3 % error of the modulation depth. In the following sections, we focus on the key techniques to realize 3 % resolution of the modulation depth.

2 Phase Control of the Laser Fringe

2.1 Required Fringe Stability

Phase fluctuation of the laser fringe on IP is one of the major error sources for the Shintake monitor. We performed a simulation study to estimate the stability requirement for 3 % modulation resolution.

The simulation result is shown in Figure 2. The graph shows that 3% resolution of the modulation depth requires 30 nm phase position stability. Considering other error factors, we should stabilize the fringe phase to 10 nm level. Note that the simulated position error is pulse-to-pulse jitter, and the real phase fluctuation may include slower vibration or drift, but we think the safety factor of 3 should suppress the error caused by the simulation model.

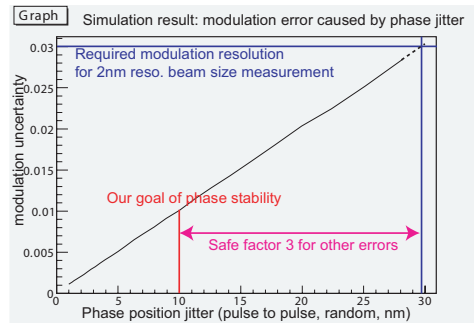


Figure 2: Effect of phase jitter on the modulation error.

2.2 Phase Monitor & Control

To achieve 10 nm phase stabilization, active phase stabilization system was developed. The phase monitor consists of an image sensor (Hamamatsu S9226) and a microscope lens (Nikon CF IC EPI Plan 100 x A). Split laser beams are guided into the microscope lens, forming an interference fringe pattern captured by the image sensor located at the back of the lens. The pixel size of the image sensor is $7.8 \mu\text{m}$, which is much larger than the fringe pitch at IP, but fringe magnification effect by the microscope lens makes the fringe pitch broaden to the observable range (a few tens of μm , depends on beam entering angle to the lens and the distance between the lens and the image sensor). An obtained spectrum by the image sensor is Fourier-transformed (online), and the phase at the peak of the power spectrum is used as the detected phase.

For phase control, we installed an optical delay line with a piezo stage (PI P-752.21C) to one of the split laser beam line. The stage has 0.2 nm resolution, and we use a 16 bit VME DAC (Advanet Advme2706) to indicate the position. The resolution on DAC is about 0.05 nm after the output voltage is reduced to 1/10 by resistor split. The frequency of feedback

control is 10 Hz, that is the repetition rate of the pulsed laser. For feedback algorithm, software PID control is implemented.

2.3 Result of Phase Stabilization

Because the fringe phase at IP cannot be directly measured, effect of the phase stabilization was evaluated by 2 image sensors. We use 1 sensor for stabilization and monitor another sensor to obtain the stabilization effect. The position of the sensors is selected symmetrically over IP (See the slide[1] for the geometry).

The stabilization result shows 0.034 radian (1.5 nm) stability in 1 minute window, and 0.133 radian (5.6 nm) stability in 10 minutes window using continuous-wave low power laser. Both meet 10 nm stability requirement of ATF2, but the stability is strongly depends on environmental conditions, including ground and air motion, temperature shift etc.

Stabilization study on pulsed laser is going on. Stability achieved up to now seems slightly worse, but we can expect 10 nm stabilization should be possible.

3 Collimators and Gamma Detectors

3.1 Beam Halo and Electron Collimator

The major background of the gamma detector is photons emitted by the electron beam halo hitting the beam pipe. Distribution of ATF2 beam halo was measured and the result was reported in [5]. Because the beam size at final focus magnets must be very large for strong focusing, the beam tail must be cut upstream to prevent background photons.

In ATF2, BPMs of upstream optics work as the collimators, but the effect should be confirmed by tracking simulation. We are preparing the tracking simulation now.

3.2 Gamma Detector

The proposed gamma detector for the Shintake monitor consists of several layers of CsI(Tl) scintillator. Thickness of layers is 10 mm for forward 4 layers, and 300 mm for a rear single layer. The average energy of Compton signal and background from beam pipe is much different, and with the forward layers we can obtain the S/N ratio using this energy difference. The result of simulation study is shown in [6].

Now we are going on detailed design and assembly of the detector.

3.3 Gamma Collimator

To reduce background photons at the detector, we plan to install a gamma collimator in front of the detector. The optimal collimator is cone-shaped, because signal photons are emitted from a point-source at IP and strictly restricted to forward angle by Lorenz-boost kinematics.

Aperture angle from IP	Signal / BG acceptance	Signal enhance ratio
2.20 mrad	95 % / 5 %	19
1.30 mrad	80 % / 1 %	80
0.83 mrad	60 % / 0.1 %	600

Table 1: Suppression ratio by gamma collimators.

The optimal radius of the collimator depends on S/N ratio. The fraction of background passing the collimator is strongly suppressed when narrowing the radius of the collimator, while the fraction of signal passing is rather mildly decreased. So, if the S/N ratio is very bad, narrower collimator is favored, while wider collimator is better when S/N ratio is not so bad. Suppression ratios by typical opening angles of the collimator is shown in Table 1.

4 Shintake Monitor for ILC

As a sub-micron beam size monitor, Shintake monitor can be useful for ILC or other future colliders. For using in ILC, several consideration should be needed.

- Because the beam energy of ILC is much larger than ATF2, the cross section of Compton scattering is lower, about 1/10 of ATF2. We need more laser beam energy or stronger laser focusing to obtain statistics enough.
- As the peak energy of the Compton scattering photons is almost the same as the beam energy, energy separation of signal and pipe-scattered background is not realistic. In addition, the energy of synchrotron radiation photons from focusing magnets is also larger in ILC, which should be cut by some kind of shields in front of the gamma detector.
- IP beam size of ILC is about 5 nm. For measuring 5 nm beam size, wavelength of the laser beam should be minimized. Within commercially available lasers, 193 nm excimer laser may have the shortest wavelength for high power pulsed beam. Using a 193 nm laser, 5 nm measurement is not impossible. Assuming the same resolution of the modulation depth measurement as ATF2 goal, the resolution on beam size is about ± 1 nm (20 %).

5 Summary and Outlook

Shintake monitor will be installed as an IP-BSM in ATF2 to measure 37 nm electron beam size. 10 nm stability of the laser fringe is necessary to achieve less than 5 % error on beam size measurement, and implementation of 10 nm level fringe stabilization is almost finished. Study and design of the gamma detector and collimators are going on. We plan to install the Shintake monitor in ATF2 IP region in early 2008 with the fringe stabilization system. Beam test of the gamma detector will be performed in this autumn and winter. By beginning of ATF2 commissioning run planned in end of 2008, the Shintake monitor will be ready for 37 nm beam size measurement (after some adjustment and tuning using the electron beams).

References

- [1] Slides:
<http://ilcagenda.linearcollider.org/contributionDisplay.py?contribId=128&sessionId=97&confId=1296>
- [2] T. Shintake, Nucl. Inst. and Meth., A311 455 (1992)
- [3] T. Shintake *et al.*, Proc. PAC95 (1995)
- [4] ATF2 Collaboration, ATF2 Proposal, KEK Report 2005-2 (2005)
- [5] T. Suehara *et al.*, Proc. NANOBEAM2005 (2005)
- [6] H. Yoda, Third ATF2 Project Meeting (2006)
<http://ilcagenda.linearcollider.org/contributionDisplay.py?contribId=7&materialId=slides&confId=1295>

High Resolution Cavity BPM for ILC Final Focal System (IP-BPM)

Tomoya Nakamura¹, Yosuke Honda², Yoichi Inoue³, Toshiaki Tauchi⁴, Junji Urakawa²,
Tomoyuki Sanuki⁵, Sachio Komamiya¹

1- The University of Tokyo - Dept of Physics
7-3-1, Hongo, Bunkyo-ku, Tokyo - Japan

2- KEK - ATF

1-1 Oho, Tsukuba, Ibaraki - Japan

3- Tohoku Gakuin University - Dept of Engineering
1-3-1 Tsuchitai, Aoba-ku, Sendai, Miyagi - Japan

4- KEK - Institute of Particles and Nuclear Studies
1-1 Oho, Tsukuba, Ibaraki - Japan

5- Tohoku University - Dept of Physics
6-3 Aoba, Aramaki, Aoba-ku, Sendai, Miyagi - Japan

IP-BPM (Interaction Point Beam Position Monitor) is an ultra high resolution cavity BPM to be used at ATF2, a test facility for ILC final focus system. Control of beam position in 2 nm precision is required for ATF2. Beam tests at ATF extraction line proved a 8.7 nm position resolution.

1 ATF2

ATF2 is an extension of ATF, a test facility for ILC accelerator development. ATF is the only facility today which can achieve beam emittance of the ILC specification. Experimental studies for ILC final focus is planned at ATF2, and is starting its operation at October, 2008.

There are two main goals for ATF2. First, achievement of 35 nm beam size at the IP. Second, control of beam position in 2 nm precision at the IP. Old model cavity BPMs at ATF have achieved 17 nm position resolution so far [2]. But to achieve the two goals, a BPM of 2 nm position resolution (IP-BPM) is required at ATF2. We have fabricated two hot models of IP-BPM, and tested its performance at ATF.

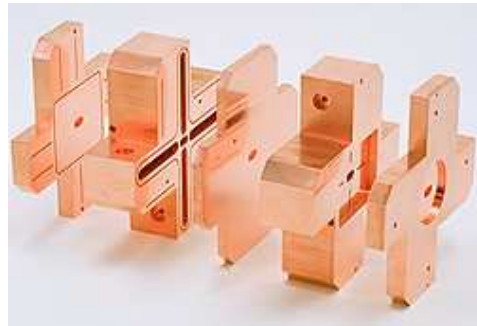


Figure 1: IP-BPM Block

2 Characteristics of IP-BPM

IP-BPM (See Figure 1) is a cavity BPM and uses di-pole mode signals to detect the beam position. The di-pole mode signal magnetically couples to the wave guides through the slots, and the signal is read out from coaxial antennas.

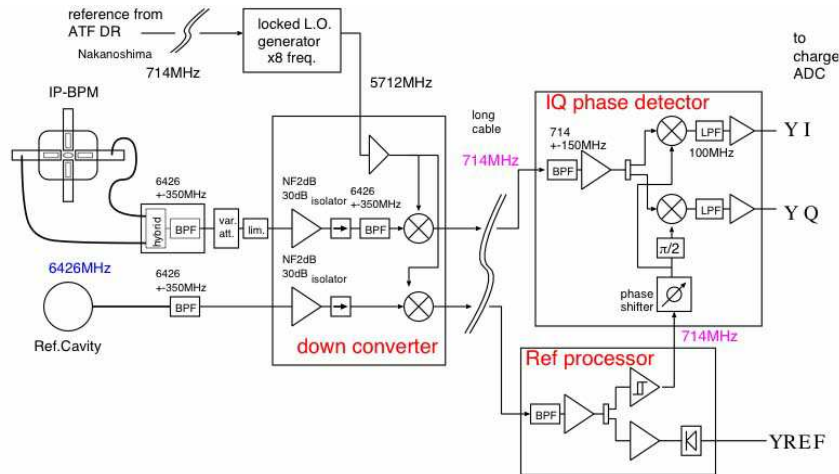


Figure 2: Measurement Scheme

IP-BPM has 3 main characteristics. (1) To measure the beam position perfectly independent in X and Y, the cavity is designed to be rectangular. The designed resonant frequency of X di-pole mode is 5.712 GHz, while Y di-pole mode is 6.426 GHz. The X-Y isolation was confirmed to be better than -50 dB. (2) It is designed to have low angle sensitivity, since the angle jitter would be large at IP, due to the strong focusing. We achieved this by designing the cavity length short ($L = 6$ mm). (3) It has a high coupling to achieve ultra high position sensitivity. The aperture of the beam pipe is designed to be small, to recover the coupling and position sensitivity which also reduces due to the short cavity length. The design value of coupling constant β for X, Y is 1.4 and 2.0, respectively.

3 Measurement Scheme

As shown in Figure 2, IP-BPM has a sensor cavity and a reference cavity for X and Y. The sensor cavity monitors the beam position using di-pole mode, while the reference cavity monitors the beam charge using mono-pole mode of same resonant frequency. The RF signals (6.426 or 5.712 GHz) from the cavities are quickly down converted to 714 MHz by a local oscillator, to minimize signal loss. The sensor signal enters a variable attenuator before the down converter, to enlarge dynamic range of the electricity, which is necessary when making calibration. Finally, the sensor signals are detected by the phase detector.

We can acquire I signals and Q signals, which are 90 degrees different in phase. Since beam angle signals or tilt signals of beam bunches are 90 degrees different in phase from position signals, through precise tuning we can divide position signals to I signals, and other signals to Q signals. To achieve this I-Q tuning, we need a beam synchronized phase origin. The reference cavity is used for this purpose, and it is down converted by the same local oscillator as used for the sensor signal, to maintain the phase relativity between reference signal and sensor signal. Also, to prevent the contamination of modes other than the di-pole modes, we use band-pass filters to select the di-pole mode of our concern.

4 Basic Tests

2 blocks (4 cavities) have been fabricated. Their basic performance was checked by the following experiments. (1) Their resonant frequencies, Q values, X-Y isolations were checked by using a network analyzer. Also, we tuned the reference cavity frequency to match that of the average of the 3 sensor cavities. (2) We made an R/Q measurement to estimate the cavity geometry and confirmed that the di-pole mode is sensitive to the beam position. R/Q of the cavity was measured through a bead perturbation measurement. (3) We carried out position and angle sensitivity tests at ATF extraction line. At position sensitivity measurements, we swept the beam against the cavity by controlling the steering magnets. We used a diode to detect signals, so the signal response to the beam position forms a V-shape (See Figure 3). At angle sensitivity measurements, we tilted the cavity against the beam by sandwiching shims between the BPM blocks and the stage. Even when the beam passes the cavity center, the signal is non-zero in this situation. This signal was compared with the equivalent position signal. As a result, IP-BPM position sensitivity was proved to be coincident with the expected value, also shown with lines in Figure 3. Also, angle sensitivity was proved to be reduced enough not to ruin the measurement.

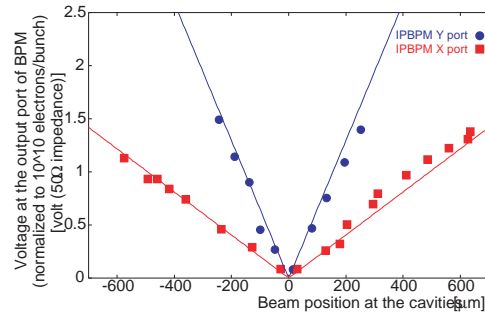


Figure 3: Position Sensitivity

5 I-Q Tuning

Contamination of angle signal would degrade the position resolution greatly. Precise decoupling of position signal and angle signal is critical for achieving ultra high position resolution.

We used 2 steering magnets to sweep the beam parallel. From the signal response, we were able to know the relative position of the 3 sensor cavities. We succeeded to align 3 cavities at same height in precision of a few microns, using shims to control the cavity height. This allowed us to keep the angle signal very small and tune the I-Q decoupling precisely.

6 Position Resolution Measurement

We used 3 cavities to determine the position resolution. From the upstream, we call them BPM1, BPM2, and BPM3. Our definition of "position resolution" is, $(\text{RMS of the residual between measured and predicted beam position at BPM2}) \times (\text{Geometry Factor})$. The prediction is made by using the beam information from BPM1 and BPM3.

Two types of measurements, calibration run and resolution run, were carried out. At calibration run we swept the beam against the cavities, while at resolution run we fixed the beam position and took statistics. Calibration run is for calibrating the I signal to the actual beam position. In order to enlarge the dynamic range of the detecting electronics, we set the variable attenuator at 40 dB, 30 dB, and 20 dB. We extrapolated the calibration slope for the non-attenuation case from those data. Then, resolution run was carried out

until enough statistics was achieved, especially for the non-attenuation case, 1 hour. To determine the position resolution, we used a linear regression analysis written below:

$$\begin{aligned}
 Y2I_{predicted} &= a_0 + a_1 * Y1I + a_2 * Y1Q + a_3 * Y3I + a_4 * Y3Q + a_5 * YREF \\
 &+ a_6 * X1I + a_7 * X1Q + a_8 * X3I + a_9 * X3Q + a_{10} * XREF \\
 Residual &= Y2I_{measured} - Y2I_{predicted}
 \end{aligned}$$

while Y(X)iI(Q) (i=1,2,3) stands for I(Q) signals from BPMi, and Y(X)REF stands for reference signals. The resolution will be calculated by the function below:

$$\text{Position Resolution} = \text{Geometry Factor} \times \frac{\text{RMS of Residual(ADC ch)}}{\text{Calibration Slope(ADC ch/nm)}}$$

Before the measurement, we calibrated the reference signal to beam charge. We made an appropriate data cut of $0.640 < \text{ICT} (\times 1.6\text{nC}) < 0.755$. As a result, the position resolution at non-attenuation case was proved to be $8.72 \pm 0.28 \pm 0.35$ nm, which is the best record in the world today (See Figure 4). The beam condition was 0.68×10^{10} e⁻/bunch, and the dynamic range was 4.96 μm. This result implies that the position resolution would be 5.94 nm for the ATF2 condition (10^{10} e⁻/bunch).

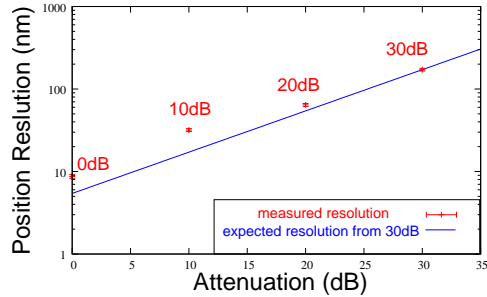


Figure 4: Position Resolution

In advance, thermal noise of the electricity was also checked. Signal from the same sensor cavity was divided into 2 and detected by the same detecting scheme. From the correlation of the two signals, we estimated the thermal noise, which determine the detecting limit of position signal. As a result, it was estimated to be 2.57 nm, under the condition of ATF2 (10^{10} e⁻/bunch). This result implies that by removing other noise, we can achieve resolution better than 3 nm by IP-BPM.

7 Summary

We developed a cavity BPM for the IP of ATF2, a test accelerator for ILC final focus system. As a result of beam tests, an ultra high position resolution of 8.72 nm was proved. Our goal is to improve the resolution to 2 nm, for nano-meter beam control at ATF2.

8 Acknowledgements

This work was supported by "Grant-In-Aid for Creative Scientific Research of JSPS (KAKENHI 17GS0210)". We thank for everyone involved in the ATF project for their cooperation.

References

- [1] Slides:
<http://ilcagenda.linearcollider.org/contributionDisplay.py?contribId=129&sessionId=97&confId=1296>
- [2] Y. Inoue, in preparation.

Permanent Magnet Final Quad

Y. Iwashita¹, T. Okugi², T. Tauchi², T. Omori², K. Kuroda², H. Yamamoto³, M. Kumada⁴

1 – Kyoto University – Institute for Chemical Research, Gokanosho, Uji, Kyoto 611-0011 – Japan

2 – KEK, 1-1 Oho, Tsukuba, Ibaraki 305-0801 – Japan

3 – Tohoku University – Graduate School of Science Research Center for Neutrino Science, 6-3 Aoba, Aramaki, Aoba-ku, Sendai-shi 980-8578 – Japan

4 – National Institution of Radiological Sciences, 4-9-1, Anagawa, Inage-ku, Chiba, 263-8555 – Japan

A quadrupole magnet for a final focus doublet of a linear collider made of permanent magnets has been investigated. The advantages of a permanent magnet quadrupole as a final focus quadrupole magnet would be its vibration free property together with its compactness. In order to make full use of these properties in a beamline strength adjustability has to be added. Current activities and future plans for R&D are described after a short history is presented.

1 Short History of the R&D

The series of R&D tasks were started from JFY (Japanese Fiscal Year) 2002 following approval of the program. A “Super Strong Permanent Magnet” scheme was utilized in the fabrication of magnets during this program. This is a so called extended Halbach configuration that enhances the field strength generated by use of soft magnetic materials such as permedur at the pole regions. A fixed strength Permanent Magnet Quadrupole (PMQ) was fabricated in the first FY, which achieved an integrated strength of 28.5T in 14mm bore diameter, where the outer diameter and the length were 130mm and 100mm, respectively (see Figure 1). The peak field gradient corresponds to 290T/m [2].

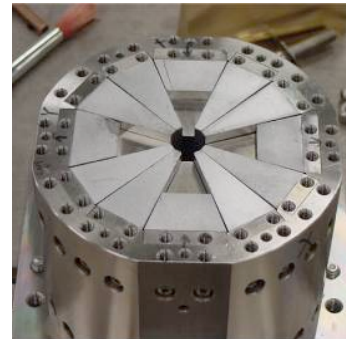


Figure 1 First prototype

A variable type PMQ was fabricated in FY2003, which uses the double ring structure (see Figure 2). The PMQ was divided into two nested rings with a rotatable outer ring while the inner ring is fixed. The rotation angle was restricted to only 0° and 90° to eliminate the skew component, which must be highly inhibited in Final Focus system in ILC. The outer part is further split lengthwise into four rings in a binary manner. It was measured in the next year at SLAC and found that it achieved integrated strength of from 3.47T to 24.4T with 1.4T steps at 20mm bore diameter (see Figure 3) [3,4]. FY2005

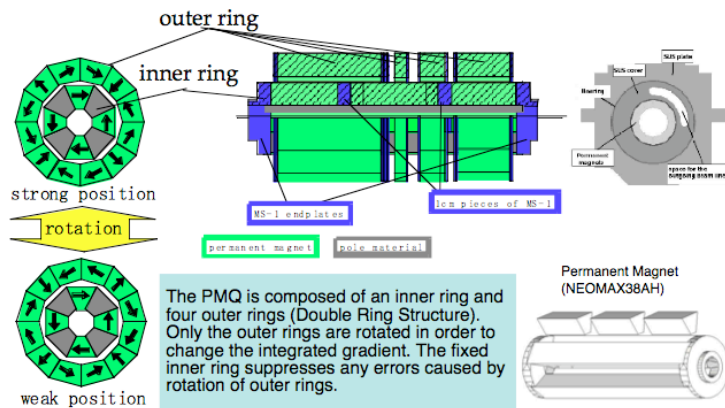


Figure 2 The double ring structure

was the last year of the first program and a minor modification was made to the second model to demonstrate a higher gradient by reducing the bore radius.

From FY2006 a subsequent program was approved (18204023(2006)), which includes a Permanent Magnet Sextupole (PMSx) for focusing of cold neutron beams. From this year a study of higher multipole field generation by permanent magnets is started, such as sextupoles and octupoles. Compact strong octupoles may be useful for beam tail folding. A PMSx that can modulate its strength at 25Hz was fabricated in the first FY (see Figure 4).

The frequency corresponds to that of the shortly coming pulsed cold neutron source at JPARC. The final system will have to be scaled twice to a 30mm bore diameter and about one meter length. Its gradient and capability of modulation was confirmed through experiments where the outer ring was driven by a 1.5kW motor. In order to overcome the large torque needed to rotate the outer ring, a flywheel helps to keep the rotation of the outer ring.

A second variable PMQ will be fabricated in FY2007 for 14mr crossing angle interaction point.

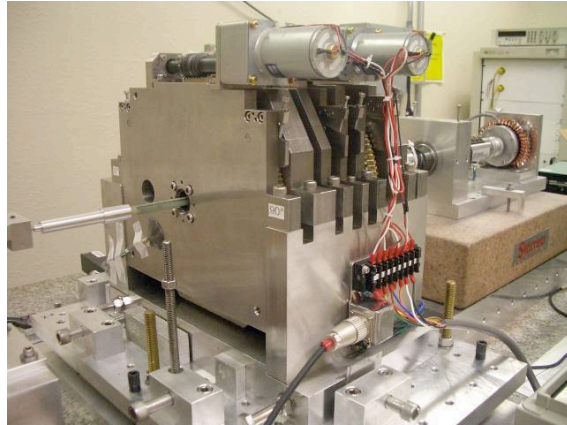


Figure 3 The 20mr Variable FFQ Magnet



Figure 4 A half scale model of a rapid cycling PMSx

2 PMQ for 14mr

The reduced crossing angle of 14mr made the double ring structure not applicable at least the closest part to the IP. Because of the narrow space available between the incoming beamline and outgoing beamline (4m x 14mr – 10mm x2), just a single ring structure has to be used, where both of the beamlines are assumed to require 10mm radius at the 4m location. In 1983, R.L.Gluckstern suggested a five-ring singlet [5]. Figure 5 shows the configuration of such a set of five rings whose lengths are the ratios as shown in the figure. The rotation angles, θ of the PMQ rings at even positions are opposite in sign against those at odd positions. The transfer matrix for such a system should be expressed by 4x4 matrix M, while those for each PMQ are written as:

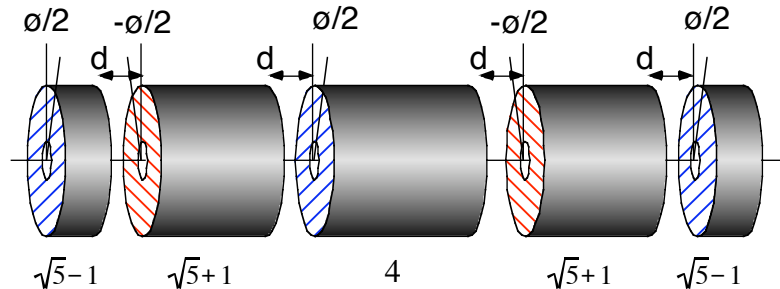


Figure 5 Five ring singlet. The numbers under the rings are the length ratios for the skew less condition when d=0.

$$\mathbf{M0} = \begin{pmatrix} \mathbf{M0}_{xx} & 0 & 0 \\ 0 & 0 & 0 \\ 0 & 0 & \mathbf{M0}_{yy} \end{pmatrix}, \mathbf{M1} = \begin{pmatrix} \mathbf{M1}_{xx} & 0 & 0 \\ 0 & 0 & 0 \\ 0 & 0 & \mathbf{M1}_{yy} \end{pmatrix}, \mathbf{M2} = \begin{pmatrix} \mathbf{M2}_{xx} & 0 & 0 \\ 0 & 0 & 0 \\ 0 & 0 & \mathbf{M2}_{yy} \end{pmatrix}.$$

Then the total transfer matrix \mathbf{M} is calculated as:

$$\mathbf{M} = \mathbf{R} \cdot \mathbf{M2} \cdot \mathbf{R}^{-2} \cdot \mathbf{M1} \cdot \mathbf{R}^2 \cdot \mathbf{M0} \cdot \mathbf{R}^{-2} \cdot \mathbf{M1} \cdot \mathbf{R}^2 \cdot \mathbf{M2} \cdot \mathbf{R}^{-1}.$$

By rewriting with sub matrices, \mathbf{M} can be written as

$$\mathbf{M} = \begin{pmatrix} \mathbf{M}_{xx} & \mathbf{M}_{xy} \\ \mathbf{M}_{yx} & \mathbf{M}_{yy} \end{pmatrix},$$

and the off-diagonal sub matrices become negligible when the lengths of the rings satisfy the relations stated before. It should be noted that the distances between rings are zero ($d=0$) in above case. A similar problem was solved for a case with $d=1\text{cm}$ case where summed PMQ length $L0+2L1+2L2$ is 20cm (total length is 24cm including four gaps), keeping $L0+2L2-2L1=0$. The rotation matrix \mathbf{R} should be substituted by $\mathbf{R} \cdot \mathbf{D}$, where matrix \mathbf{D} denotes a 1cm drift space. The off diagonal sub matrices are expanded in series up to 5th order for a solution. The ratios are solved as $L2:L1:L0=1.81046: 5: 6.37909$.

3 Preliminary Simulation Results

Assuming a field gradient of 140T/m and using 12 units of the five-ring-singlets, the total length becomes about 3m. Using this singlet train as a QD0, a preliminary fine tuning was carried out with matching requirement for Twiss parameters: $\alpha_x=\alpha_y=0$, $\beta_x=0.021\text{m}$, $\beta_y=400\mu\text{m}$, $\eta_x=0$ at IP, starting with the ILC deck “ilc2006b.ilcbds1” (14mrad version). The final θ of PMQ is 6.58 degree. Then off momentum matching was performed by re-optimizing K2 of sextupoles looking at the beam size at IP. The coupling between x and y was well suppressed and the final beam sizes at IP are $\sigma_x/\sigma_y = 656/5.44\text{nm}$ for $\gamma_{ex}/\gamma_{ey}=9.2\text{e-}6/3.4\text{e-}8\text{m}$ and $\sigma\delta=6\text{e-}4$ (636 / 5.25nm for original design). Although the optimization was

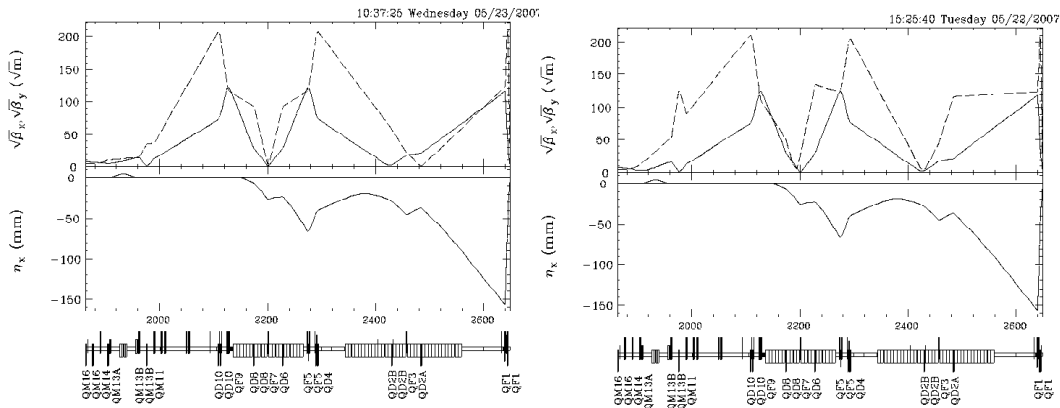


Figure 6 Optics with PMQ. top: original, bottom: using PMQ with partial optimization.

not fully performed such that octupoles were fixed, the result seems promising (see Figure 6). Further optimization will improve the results.

4 External Field of PMQ

The external field of the Halbach configuration is much smaller than that of coreless superconducting magnets, because the main part of the flux returns in the magnets (see Figure 7 and Figure 8). The leakage can be reduced if an iron case is used instead of nonmagnetic material such as stainless steel. Although it reduces the external field, solenoid field in the detector will magnetize the material. The magnitude depends on the number of segmentations of the ring; the more segmentations, the smaller leakage out side. Therefore such magnetic case for the external field shield may not be needed if the segmentation is fine enough. More than 20 segmentations may be enough to suppress the external field at a location of 46mm from the incoming beamline less than 30 gauss.

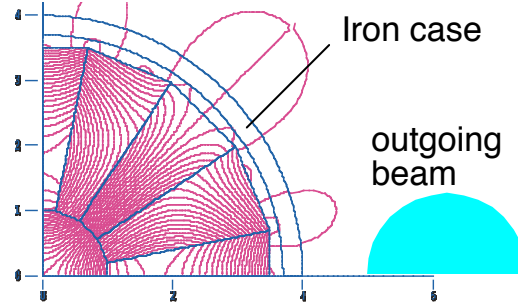


Figure 7 PMQ and out going beam.

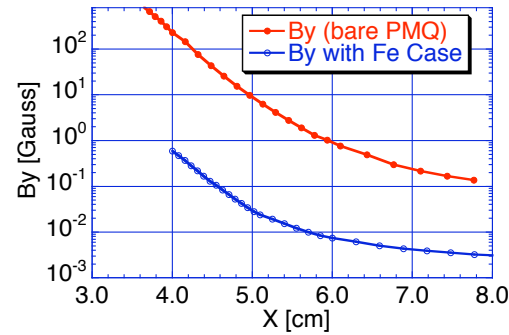


Figure 8 External stray field of PMQ.

5 Acknowledgements

Work partially supported by the Ministry of Education, Science, Sports and Culture, Grant-in-Aid for Scientific Research (A), 14204023(2002) , 18204023(2006) and the U.S. Department of Energy under contract number DE-AC02-76SF00515.

6 References

- [1] Slides:
<http://ilcagenda.linearcollider.org/contributionDisplay.py?contribId=130&sessionId=97&confId=1296>
- [2] Y. Iwashita, T. Mihara, E. Antokhin, M. Kumada, M. Aoki, "Permanent Magnet Quadrupole for Final Focus for Linear Collider", PAC03, May 12-16, Portland, OR, p2198-2200:
<http://accelconf.web.cern.ch/accelconf/p03/PAPERS/WPAB069.pdf>
- [3] T. Mihara, Y. Iwashita, M. Kumada, C.M. Spencer, E. Antokhin, "Super Strong Permanent Magnet Quadrupole for a Linear Collider" IEEE Transactions on Applied Supercond., **14**-2, pp.469-472, 2004
- [4] T. Mihara, Y. Iwashita, M. Kumada, C. M. Spencer, "Variable Permanent Magnet Quadrupole", IEEE Trans. on Applied Supercond., **16**-2, pp.224-7, 2006
- [5] R.L. Gluckstern and R.F. Holsinger: Adjustable Strength REC Quadrupoles, IEEE Trans. Nucl. Sci., NS-30, NO. 4, August 1983, http://epaper.kek.jp/p83/PDF/PAC1983_3326.PDF

Main Linac

Conveners: L. Lilje, H. Hayano, C. Adolphsen, N. Solyak

Vibration stability studies of a superconducting accelerating module at room temperature and at 4.5 K

Ramila Amirikas, Alessandro Bertolini, Wilhelm Bialowons

DESY
Notkestrasse 85, 22603 Hamburg, Germany

In this work we present a collection of results from a systematic investigation carried out at DESY on the mechanical stability of the quadrupole of a third generation (Type-III) FLASH (Free electron LASer in Hamburg) cryomodule (named Module 6). The results are of interest for the International Linear Collider (ILC) [2] and the European X-ray Free Electron Laser (XFEL) [3] cryomodule design, planned in both cases as a further evolution of the FLASH Type III one. Vibration level and mechanical transfer functions (TF) have been measured covering a large variety of conditions: from room temperature to 4.5 K, starting from the installation of the quadrupole on the cold mass during the module assembly and ending with data taken with the cryomodule in fully operating conditions at the CryoModule Test Bench (CMTB) facility.

1 Introduction

FLASH Type-III Module 6 is equipped with a string of eight 9-cell superconducting cavities, capable to operate with an average gradient of ~ 27 MV/m, and with a superconducting quadrupole located at the end of the module. Cavities, operating at 2 K and the quadrupole, operating at 4.5 K, suspended from the Helium Gas Return Pipe (HeGRP), supported from above by three posts consisting of large diameter thermal insulating fiberglass pipes [4]. The mechanical stability of the quadrupole was investigated by measuring the TFs between the key components of the cryomodule (vacuum vessel, HeGRP, quadrupole) using inertial velocity sensors (geophones and broadband seismometers), and the DESY site ground motion as broadband excitation source of vibrations (The root mean square (rms) displacement in the 1-80 Hz band can exceed 100 nm during working days [5]). This approach allows to discriminate the effect of the internal mechanics of the module from the effects of the cryostat support/girder and from environmental vibration sources, providing a picture which is totally site independent, therefore, usable for the ILC and the XFEL module design and for beam dynamics simulations.

2 Room temperature measurements

2.1 Quadrupole versus vacuum vessel

The displacement PSD spectra are dominated at low frequencies (1-20 Hz) by the effects of the rigid body modes of the cryostat on its supports, and at higher frequencies by technical noise sources. The TF measurements (Figure 1) have shown no evidence for mechanical resonances up to ~ 40 Hz in the horizontal transverse direction and up to ~ 70 Hz in the vertical direction.

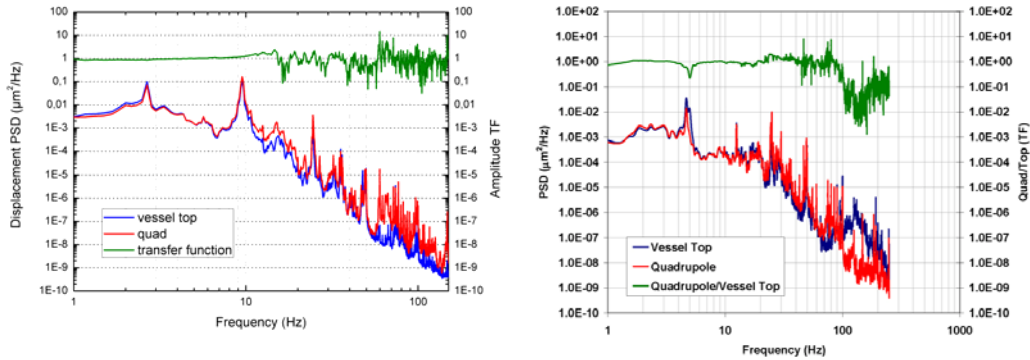


Figure 1: Quad vs. vessel top horizontal (left) and vertical (right) displacement PSDs and TFs.

2.2 Quadrupole versus HeGRP

The quality of the connection between the quadrupole and the HeGRP was tested first on the the Module 6 cold mass before the installation in the vacuum vessel (see Figure 2 left side).

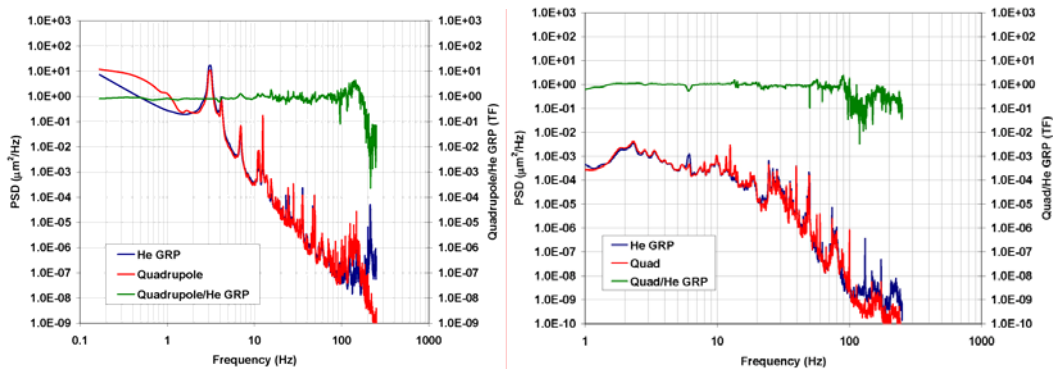


Figure 2: Quad vs. HeGRP: (left) horizontal displacement PSDs and TF measured during Module 6 assembly; the peaks below 10 Hz in the PSD are resonances of the assembly stand; (right) vertical displacement PSDs and TF measured with Module 6 on the CMTB.

The measurement was repeated on the module fully assembled and installed on the test bench to confirm the results (see Figure 2 right). Transfer functions show the absence of internal resonances up to 100 Hz in both vertical and horizontal transverse directions.

2.3 Stability along the module

The reduction of the vibration level is believed to be a reason for positioning of the quadrupole at the center of the cryostat. This is perhaps the major change in the ILC cryomodule design (Type-IV) with respect to the FLASH Type-III and future XFEL cryomodule prototype.

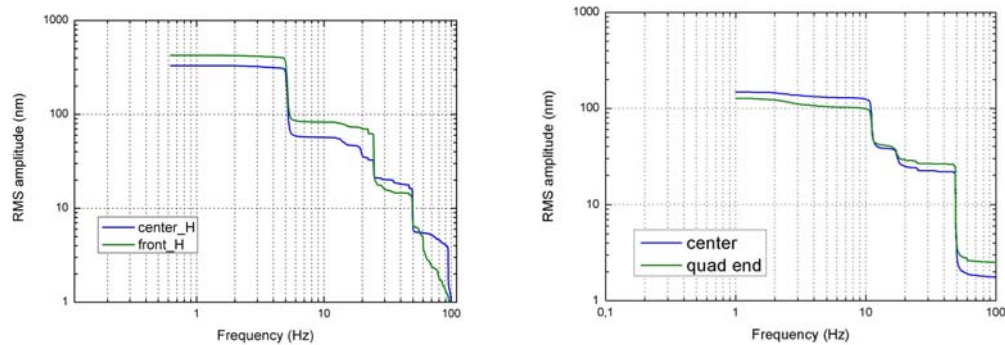


Figure 3: Quadrupole end vs. center horizontal rms comparison: inside the HeGRP with the module sitting on concrete blocks (left). On top of the vessel with Module 6 installed on the CMTB (right); in this configuration, a slightly larger amplitude was measured at the center.

To make a preliminary comparison between the two layouts, geophones have been positioned along the Module 6 length inside the HeGRP. In the horizontal axis the data show an integrated rms amplitude larger (up to ~ 30 % from 2 to 100 Hz) at the quadrupole end with respect to the center of the module (see Figure 3 left). Smaller differences (~ 10 %) were found in the vertical direction. Similar results were obtained by repeating the test on top of the vacuum vessel. Data taken at the CMTB (Figure 3 right) show a better matching and the clear influence of the cryostat supports (transverse rocking mode moved from 4.7 to 11 Hz, with a better girder-support interface and connection of the module to the endcaps).

3 Measurements at 4.5 K

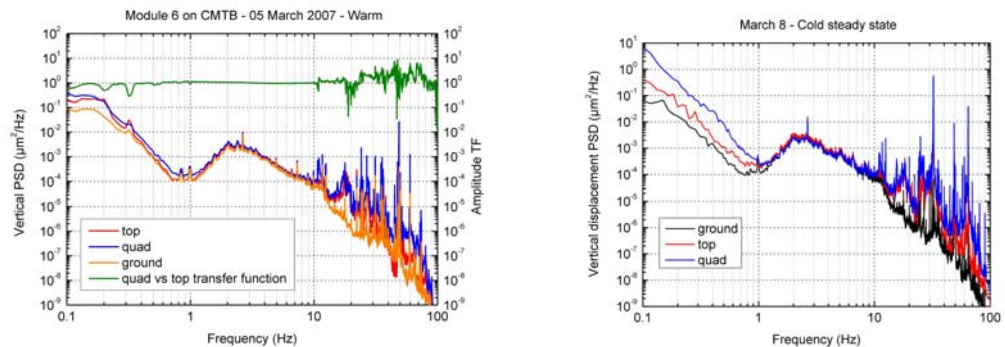


Figure 4: PSD spectra measured on the CMTB floor, on top of the vacuum vessel and on the quadrupole at room temperature (left), and in cold steady state with RF off (right).

Vertical vibrations of the quadrupole at 4.5 K have been measured using a commercial geophone [6]. The sensor could operate at cryogenic temperatures without loss of sensitivity, providing nanometer resolution even in the 1-10 Hz frequency band, region not covered by

the existing data because of the lack of resolution of cooled piezo accelerometers [7]. No difference (Figure 4) between reference room temperature data and measurements done during cold operation was found up to 30 Hz: the quadrupole position simply tracks the ground motion, with some amplification due to the effects of the vessel supports (coupling with the rocking modes at 11 and 18 Hz, resonance at 27 Hz). At higher frequencies, besides the common lines from the technical systems (the insulation vacuum pump at 48.6 Hz the strongest one), the onset of a strong anharmonic vibration, with fundamental frequency ~30 Hz, detectable both inside and outside of the cryostat and on the hall floor, was observed. The effect, not related to the module design, has been identified as a thermal acoustic oscillation originated by a flow sensor, with direct transition to room temperature, installed outside of the cryomodule upstream of the inlet valve of the quadrupole 4.5 K feed line [8]. A clear correlation between the vibration amplitude (ranging from 200 nm up to one micron rms on the quadrupole) and the settings of the same valve was in fact discovered, and no similar phenomenon was observed afterwards during the tests of Module 5 Type-III cryomodule [9]. No effect from the high power RF was observed in this experiment (data not shown here).

4 Summary

This study has proven the reliability of the FLASH Type III mechanical design with the quadrupole at the end of the module. In the frequency range 1-10 Hz, vibration spectra of the quadrupole are shaped by the local seismic activity. Amplification of the ground motion, mostly in the horizontal axis, only occurs due to the rigid body modes of cryostat on its supports, perhaps the most relevant engineering issue to improve the quadrupole stability. At high frequencies (> 20 Hz) lines from technical noise sources are dominant. A continuous monitoring of the FLASH linac cryomodules, using cooled geophones, is planned to confirm during machine operation the promising results obtained at the CMTB.

5 Acknowledgements

The authors would like to thank the DESY MKS Division. This work is supported by the Commission of the European Communities under the 6th Framework Programme “Structuring the European Research Area”, contract number RIDS-011899.

6 References

- [1] Slides: <http://ilcagenda.linearcollider.org/contributionDisplay.py?contribId=88&sessionId=56&confId=1296>
- [2] ILC Reference Design Report (2007).
- [3] XFEL Technical Design Report, ed. M. Altarelli *et al.* (2006).
- [4] C. Pagani, D. Barni, M. Bonezzi and J.G. Weisend, *Advances in Cryogenic Engineering*, 45, Plenum Press, New York (1999).
- [5] R. Amirikas, A. Bertolini, W. Bialowons and H. Ehrlichmann, EUROTeV-Report-2005-023-1 (2005).
- [6] Oyo Geospace Model GS-11D, <http://www.geospacelp.com>
- [7] R. Amirikas, A. Bertolini, W. Bialowons and H.D. Brueck, EUROTeV-Report-2006-036 (2006).
- [8] R. Lange and B. Petersen, DESY MKS Division, private communication (2007).
- [9] R. Amirikas, A. Bertolini, W. Bialowons, EUROTeV-Report-2007-059, in preparation.

Coupler Kick

Igor Zagorodnov and Martin Dohlus

Deutsches Elektronen-Synchrotron , Notkestrasse 85, 22603 Hamburg, Germany

The transverse kick due to cavity couplers can negatively affect the beam emittance. For example, in the International Linear Collider (ILC) the intense bunches encounter many hundreds cavities with couplers. In this contribution we estimate two different effects: the kick due to asymmetry of the external accelerating field (coupler RF kick) and the kick due to electromagnetic field of the bunch scattered by the couplers (coupler wake kick). The wakefield due to the couplers could be main source of the emittance dilution in ILC and a new HOM couplers orientation is suggested to reduce the wake by factor ~ 12 .

1 Introduction

The International Linear Collider (ILC) project [2] uses short, intense bunches, which encounter a lot of cavities with couplers. As it is shown in Fig. 1 the couplers violate the rotational symmetry of the cavities and produce transverse kicks on the axis. It can negatively affect the beam stability and the beam emittance.

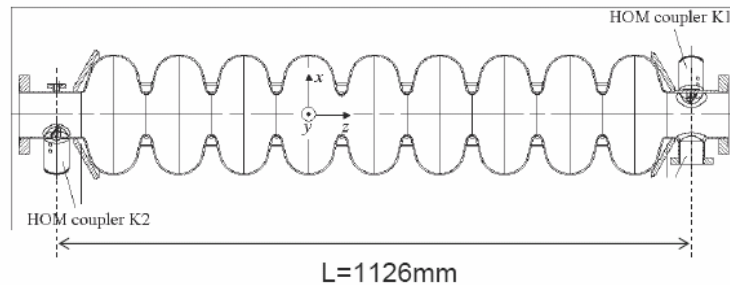


Figure 1: TESLA cavity with couplers.

In this contribution we estimate two different effects: the kick due to asymmetry of the external accelerating field (coupler RF kick) and the kick due to electromagnetic field of the bunch scattered by the couplers (coupler wake kick). In the calculation we consider not only the main coupler but higher order mode (HOM) couplers as well. The wakefield due to the couplers could be main source of the emittance dilution in ILC and a new HOM couplers orientation is suggested to reduce the wake by factor ~ 12

2 Geometry description and notation

In ILC and European XFEL [4] projects the design of the main accelerator will be based on the TESLA technology [5]. Each TESLA cavity is supplied with one main coupler and two HOM couplers (see Fig. 1). The design and orientation of the couplers in the European XFEL project are shown in Fig. 2. The radius of the pipe is equal to 39 mm and the couplers penetrate into the pipe up to the radius of 30 mm.

In the following estimations we consider the Gaussian bunch $\lambda(s)$ with rms width σ . The kick factor and the rms kick for wake potential $W_{\perp}(s)$ are given by

$$k_{\perp} = \langle W_{\perp} \rangle = \int W(s)\lambda(s)ds, \quad k_{\perp}^{rms} = \left\langle (W_{\perp} - k_{\perp})^2 \right\rangle^{0.5}.$$

The kick factor must be compensated for with orbit correctors. The rms kick gives the head-tail difference in the kick which is very difficult to correct and which leads to "banana" shape of the bunch.

The estimations of wakepotentials are obtained for a quite long bunch $\sigma = 1\text{mm}$. However, the transverse wake has already the capacitive character and we can state that the wake kick remains the same for the shorter bunches [6]

3 Wakefields of the TESLA couplers

3.1 Numerical code and accuracy estimation

To estimate the short range wakefields of the couplers in the pipe (without cavities) we have used a 3D, time-domain finite-difference program ECHO [7]. It has two features that make these 3D calculations tractable: (1) a method to reduce the so-called "mesh dispersion", and (2) an indirect method [8] of calculating wakes in 3D structures that eliminates long downstream beam pipes.

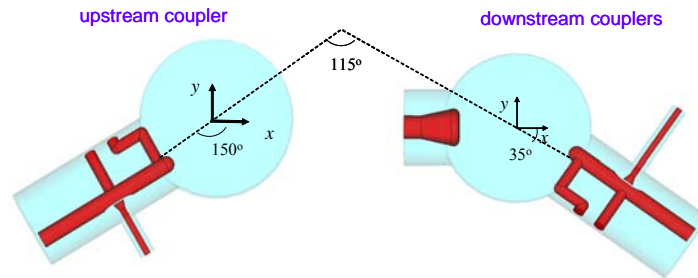


Figure 2: The geometry and the orientation of the TESLA couplers.

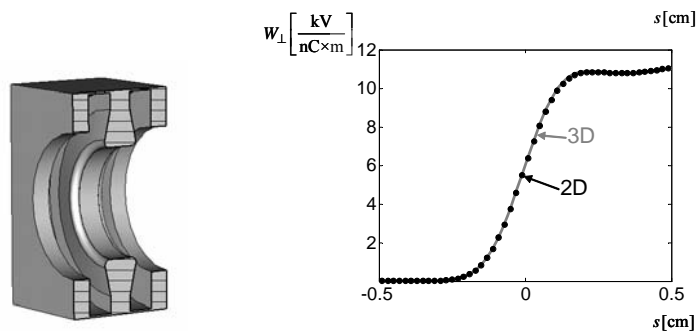


Figure 3: The axially symmetric approximation of the main coupler geometry and the accuracy check.

Table 1: Convergence and accuracy tests.

	2.5D, $\sigma/h=5$	2.5D, $\sigma/h=10$	3D, $\sigma/h=5$	Abs.error
$k_{ }$, kV/nC	2.205	2.195	2.241	0.05
$\partial k_{\perp} / \partial r$, kV/nC/m	5.820	5.817	5.89	0.07
$ k_{\perp}(0) $, kV/nC	0	0	1e-6	1e-6

In order to choose the mesh and check the accuracy of the 3D results we have considered an axially symmetric approximation of the main coupler geometry (see Fig.3). The results obtained with 2.5D and 3D codes are given in Fig. 3 and Table 1.

3.2 The couplers wake kick near to the axis

The kick factors of *downstream* and *upstream* couplers (see Fig. 2) are given as

$$\mathbf{k}_{\perp}^{\text{down}}(x, y) = \begin{pmatrix} -0.0069 \\ -0.0094 \end{pmatrix} + \begin{pmatrix} 3.2 & -1.1 \\ -1.1 & -1.0 \end{pmatrix} \begin{pmatrix} x[\text{m}] \\ y[\text{m}] \end{pmatrix} \begin{bmatrix} \text{kV} \\ \text{nC} \end{bmatrix},$$

$$\mathbf{k}_{\perp}^{\text{up}}(x, y) = \begin{pmatrix} -0.0142 \\ -0.0095 \end{pmatrix} + \begin{pmatrix} 1.02 & 1.15 \\ 1.15 & 0.07 \end{pmatrix} \begin{pmatrix} x[\text{m}] \\ y[\text{m}] \end{pmatrix} \begin{bmatrix} \text{kV} \\ \text{nC} \end{bmatrix}.$$

The rms kick can be related to the kick factor as $\mathbf{k}_{\perp}^{\text{rms}} = \mathbf{k}_{\perp} / \sqrt{3}$.

Fig. 4 shows the vector norms of the wake rms kick, RF rms kick (see next section) and the cavity rms kick [9] for the ILC bunch with charge $Q=1\text{nC}$ and length $\sigma=300\mu\text{m}$ versus offset from the axis.

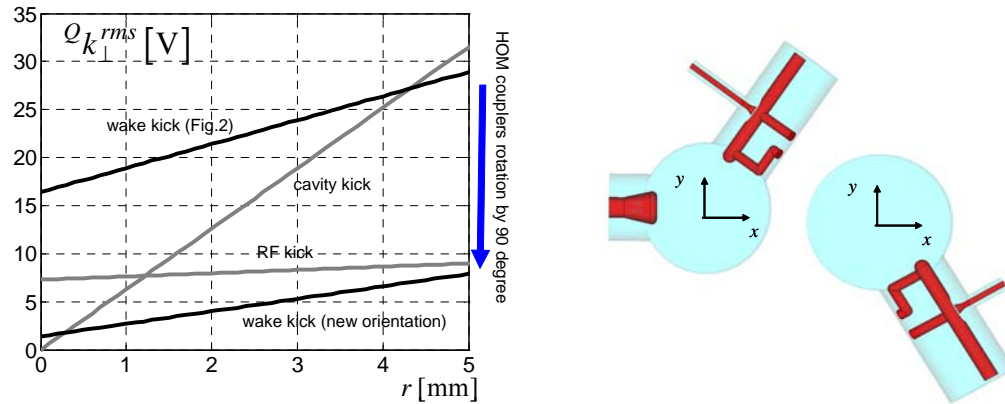


Figure 4: Kicks vs. offset and the new orientation of HOM couplers.

The coupler wake kick makes the main contribution. It can be reduced by factor ~ 12 with the help of rotation of the HOM couplers by 90 degrees as shown in Fig. 4. The kick factor of this new configuration is

$$\mathbf{k}_{\perp}(x, y) = \begin{pmatrix} -0.0025 \\ -0.0002 \end{pmatrix} + \begin{pmatrix} 2.33 & 0.04 \\ -0.02 & 1.1 \end{pmatrix} \begin{pmatrix} x[\text{m}] \\ y[\text{m}] \end{pmatrix} \begin{bmatrix} \text{kV} \\ \text{nC} \end{bmatrix}.$$

Let us note that we have calculated the coupler kick in infinite pipe without cavities. As the cavity irises have radius 35 mm which is smaller than the pipe radius of 39 mm we expect that the coupler wake kick could be reduced by a factor ~ 1.4 .

4 The RF coupler kick near the axis

The couplers destroy rotational symmetry of the TESLA cavity. With the help of the MAFIA field solver [10] we have estimated [11] the asymmetry effect on the external accelerating field due to the couplers existence and obtained the RF rms kicks as

$$\begin{aligned} \mathcal{Q} \mathbf{k}_{\perp}^{rms} &= \text{Im}(\mathbf{V}_n V_z) k \sigma, & \mathbf{V}_n &= \mathbf{V}_n^{down} + \mathbf{V}_n^{up}, & k &= 2\pi c^{-1} f, \\ \mathbf{V}_n^{down} \cdot 10^4 &= \begin{pmatrix} -0.25 + 0.52i \\ 0.32 + 0.05i \end{pmatrix} + \begin{pmatrix} -40 - 20i & 29 + 37i \\ 29 + 5i & 38 + 18i \end{pmatrix} \begin{pmatrix} x[\text{m}] \\ y[\text{m}] \end{pmatrix}, \\ \mathbf{V}_n^{up} \cdot 10^4 &= \begin{pmatrix} -0.57 + 0.07i \\ 0.41 + 0.03i \end{pmatrix} + \begin{pmatrix} 11 - 7i & 34 + 1.5i \\ 34 + 2i & -10 + 6i \end{pmatrix} \begin{pmatrix} x[\text{m}] \\ y[\text{m}] \end{pmatrix}, \end{aligned}$$

where *up* and *down* mean upstream and downstream couplers, correspondingly. Figure 4 shows the total RF rms kick for accelerating voltage $V_z = 15\text{MV}$ and frequency $f = 1.3\text{GHz}$.

5 Acknowledgements

We thank CST GmbH for letting us use CST Microwave Studio for the meshing for the ECHO simulations.

6 References

- [1] Slides: <http://ilcagenda.linearcollider.org/contributionDisplay.py?contribId=89&sessionId=56&confId=1296>
- [2] ILC Reference Design Report (2007).
- [3] M. Dohlus et al, TESLA 20002-05, (2002).
- [4] Report No. DESY-2002-167, DESY (2002).
- [5] TESLA Technical Design Report (2001).
- [6] G. Stupakov et al, Phys. Rev. ST Accel. Beams 10, 054401 (2007)
- [7] I. Zagorodnov and T. Weiland, Phys. Rev. ST Accel. Beams 8, 042001 (2005).
- [8] I. Zagorodnov, Phys. Rev. ST Accel. Beams 9, 102002 (2006).
- [9] I. Zagorodnov and T. Weiland, PAC 2003, p. 3249 (2003).
- [10] MAFIA Collaboration, MAFIA manual, CST GmbH, Darmstadt (1997).
- [11] M. Dohlus, http://www.desy.de/~dohlus/2004/2004.09.holgers_seminar/asym&kick_sep2004.pdf

Damping Rings

Conveners: A. Wolski, S. Guiducci, J. Gao, M. Zisman

UPDATE ON ION STUDIES*

Guoxing Xia and Eckhard Elsen

DESY, Hamburg, Germany

The effect of ions has received one of the highest priorities in R&D for the damping rings of the International Linear Collider (ILC). It is detrimental to the performance of the electron damping ring. In this note, an update concerning the ion studies for the ILC damping ring is given. We investigate the gap role and irregular fill pattern in the ring. The ion density reduction in different fills is calculated analytically. Simulation results are presented.

1 Introduction

Ions are recognized as a potential current limitation in storage rings with negatively charged particle beams [1]. The ions mainly come from beam-gas collisions. In some circumstances, they are trapped in the potential well of the beam. They couple to the motion of the beam and lead to adverse effects such as beam emittance growth, betatron tune shift and spread, collective instabilities and beam lifetime reductions [2].

There are two kinds of ion effects in electron storage rings. One is the conventional ion trapping which occurs when the circulating beam traps ions after multiple turns. It can be cured by introducing a few successive empty RF bucket (gaps), which are long compared to the inter-bunch spacing. In this case, the ions are strongly focused by the passing electron bunches in the beginning and then over focused in the gap. With a sufficiently large gap, the ions can be driven to large amplitudes, where they form a diffuse halo and do not affect the beam. However, in high current storage rings or linacs with long bunch trains, the ion accumulation during the passage of a single bunch train may cause a transient instability which is called fast ion instability (FII) [3, 4]. For the electron damping ring of the ILC, the bunch intensity is large and the bunch spacing is small and the fast ion instability is potentially striking [5]. Since the vertical beam emittance is much smaller (2 pm) than the horizontal one (0.5 nm), the FII is much more serious in the vertical plane.

In this note, the linear theory of ion effect is briefly recalled in section 2. In section 3, the gap effect in the fill is studied and the ion density reduction due to mini-trains in different fill patterns is investigated analytically. Section 4 shows the simulation results of FII for mini-trains. A short summary is given in the end.

2 Linear theory of ion effects

Without gaps in the fill, the ions with a relative molecular mass greater than A will be trapped in the beam potential, where,

$$A = \frac{N_0 r_p L_{sep}}{2\sigma_y(\sigma_x + \sigma_y)} \quad (1)$$

here, N_0 denotes the number of particles per bunch, r_p the classical radius of proton, L_{sep} the bunch spacing, $\sigma_{x,y}$ the horizontal and vertical beam size, respectively. It can be seen

*This work is supported by the Commission of the European Communities under the 6th Framework Programme "Structuring the European Research Area", contract number RIDS-011899.

Beam parameters	Fill pattern		
	Case A	Case B	Case C
Number of bunches	5782	4346	2767
Particles per bunch [10^{10}]	0.97	1.29	2.02
Bunch spacing [bucket]	2	2	4
Number of trains	118	82	61
Bunches per train f_2	0	0	23
Gaps between trains g_2	0	0	28
Bunches per train f_1	49	53	22
Gaps between trains g_1	25	71	28
FII char. growth time at train end [10^{-9} s]	3.922	4.527	4.030
FII expo. growth time with 30% ion freq. spread [10^{-6} s]	6.889	6.892	6.913
Coherent tune shift at train end	0.325	0.325	0.324

Table 1: Typical fill patterns in the ILC damping ring.

that the minimum trapped mass is closely related to the beam size. By using the beam parameters of three typical fill patterns in the ILC damping ring, from case A to case C as shown in Table 1 [6], the minimum trapped mass along the ring for two fill pattern case A and C is shown in Figure 1 and Figure 2 respectively. The number of bunches decreases from A to C while the particles per bunch increase to maintain a comparable overall charge. Here we take one sextant of the ring as an example.

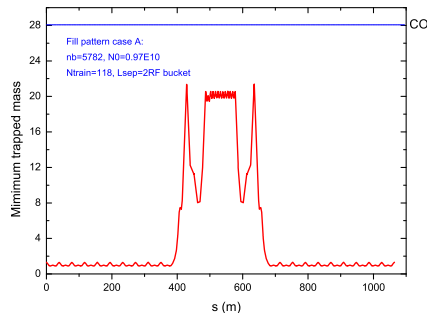


Figure 1: Minimum trapped mass for fill pattern case A.

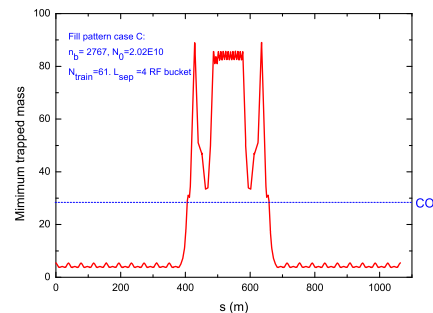


Figure 2: Minimum trapped mass for fill pattern case C.

It can be seen that for the fill pattern case A, all the CO ions will be trapped in the beam along the ring. While for the fill pattern case C, the CO ions can not be trapped in some parts of the ring.

The linear theory [3, 4] gives characteristic growth rate of FII which strongly depends on the bunch intensity, number of bunches, transverse beam size and the residual gas pressure. It can be estimated as

$$\tau_c^{-1}(s^{-1}) = 5p[Torr] \frac{N_0^{3/2} n_b^2 r_e r_p^{1/2} L_{sep}^{1/2} c}{\gamma \sigma_y^{3/2} (\sigma_x + \sigma_y)^{3/2} A^{1/2} \omega_\beta} \quad (2)$$

where p is the residual gas pressure, n_b is the bunch number, r_e and r_p are the classical radius of electron and proton respectively, c is the speed of light, γ is the relativistic gamma factor, A is the atomic mass number of the residual gas molecules and ω_β is the vertical betatron frequency. The ion coherent oscillation frequency ω_i is given by

$$\omega_i = \left(\frac{4N_0 r_p c^2}{3AL_{sep}\sigma_y(\sigma_x + \sigma_y)} \right)^{1/2} \quad (3)$$

However, the ion motion becomes decoherent because the vertical ion frequency depends on the horizontal position. Furthermore, the existence of various ion species and the variation of the beam size along the ring also introduce a spread in the ion oscillation frequency. Taking into account the ion coherent frequency spread, the linear theory gives the coupled bunch motion in the bunch train rising as $y \sim \exp(t/\tau_e)$, and in this case the exponential growth rate is given by

$$\tau_e^{-1} [s^{-1}] = \frac{1}{\tau_c} \frac{c}{2\sqrt{2}l_{train}(\Delta\omega_i)_{rms}} \quad (4)$$

where $(\Delta\omega_i)_{rms}$ denotes the rms spread of the ion coherent frequency as the function of the azimuthal position around the ring. $l_{train} = n_b L_{sep}$ the bunch train length. For the baseline design of the ILC damping ring, simulation shows the spread of ion coherent frequency to be about 30% [7].

If the ions are trapped in the beam potential, they give rise to additional focusing to the beam. The ion induced coherent tune shift is given by

$$\Delta Q_{y,coh} = \frac{\beta_y r_e \lambda_{ion} C}{\gamma 4\pi \sigma_y (\sigma_x + \sigma_y)} \quad (5)$$

here C is the circumference of ring, β_y is the vertical beta function, $\lambda_{ion} = \sigma_i N_0 n_b p / kT$ is the ion line density, σ_i is the ionization cross section (1.86 Mbarn and 0.31 Mbarn for carbon monoxide and hydrogen ions, respectively at beam energy of 5 GeV). k is Boltzmann constant and T is the temperature. By using beam parameters of the ILC baseline damping ring [8], the FII characteristic growth time, exponential growth time with 30% ion coherent frequency spread and ion induced coherent tune shift at bunch train end for a single long bunch train case are analytically estimated in Table 1. A CO partial pressure of 1 nTorr is assumed here. It can be seen that the growth time is extremely fast for the case of one long train. Even with 30% ion frequency spread, the FII growth time is still faster than one revolution period (22 μ s). The ion induced tune shift is large at a gas pressure of 1 nTorr for CO, so a lower vacuum gas pressure is critical to alleviate FII effect.

3 Gap effect in the fill

In the previous section, one long bunch train has been assumed and the ions are trapped by the bunch train. The trapping condition is disturbed when the fill pattern consists of a number of short bunch trains (mini-trains) with gaps in between. In the following, we will analyze the gap effect and ion density in different fill patterns.

The ions inside the beam are defined as those ions within $\sqrt{3}\sigma$ of the beam centroid. Note that the growth rate of FII is proportional to the ion density [9]. The diffusion of the ions during the gaps increases the size of ion cloud and therefore reduces the ion density.

With a gap introduced in the bunch train, one can estimate the density of the ions in the beam after the clearing gap as [2]

$$\rho_i \approx \frac{\rho_{i0}}{\sqrt{(1 + L_{gap}^2 \omega_x^2)(1 + L_{gap}^2 \omega_y^2)}} \quad (6)$$

where ρ_{i0} is the ion density at the end of the one bunch train, L_{gap} is the gap length between two adjacent bunch trains, $\omega_{x,y}$ are the ion oscillation frequencies as follows

$$\omega_{x,y}^2 = \frac{2N_0 r_p}{L_{sep} A \sigma_{x,y} (\sigma_x + \sigma_y)} \quad (7)$$

For the ILC damping ring, the harmonic number $h = 14516$, the circumference $C = 6695.057$ m. We made an analytic estimation of the relative ion density reduction versus train gap spacing. The result is shown in Figure 3. It can be seen that the relative ion density diminishes with respect to the bunch train gap spacing. If the gap length is larger than 30 RF bucket, the ion density is about 10% of the initial ion density. Beyond 30 RF bucket, the ion density no longer changes significantly. Taking into account the transient beam loading effect, train gap should not be too long. For current ILC damping ring fill patterns, the length of train gap varies from 25 to 71 RF bucket. Meanwhile, in order to evaluate the effect of the gaps, an Ion-density Reduction Factor (*IRF*) is defined as [9]

$$IRF = \frac{1}{N_{train}} \frac{1}{1 - \exp(-\tau_{gap}/\tau_{ion})} \quad (8)$$

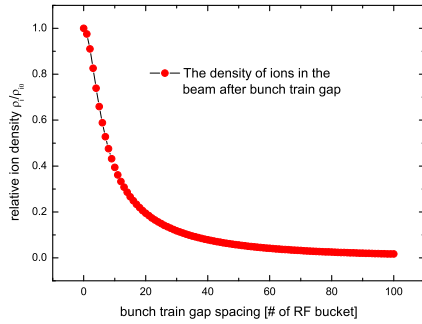


Figure 3: The density of the residual ions in the beam after the bunch train gap.

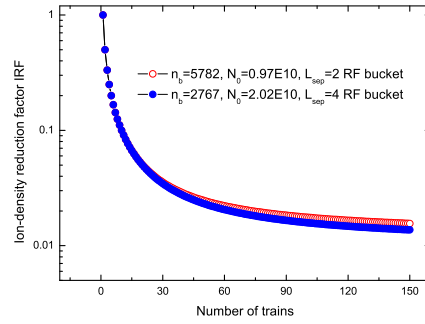


Figure 4: IRF factor in OCS6 damping ring for fill pattern A and C.

where N_{train} is the number of trains, τ_{ion} is the diffusion time of the ion cloud which can be estimate from Eq.(3). *IRF* is the ratio of the ion density with gaps and without gaps. In one long bunch train case, the ring is completely filled and the ions can accumulate indefinitely. With a fixed gap, a larger number of shorter bunch train helps to keep the ion density low. However, for a fixed ring circumference and total number of bunches, the length of gap shrinks as the number of bunch trains increases. The optimum fill pattern depends on the diffusion time, the circumference, and number of bunches. Figure 4 shows the *IRF*

versus number of trains in OCS6 damping ring for fill pattern case *A* and *C* respectively. It can be seen here if the harmonic number and ring circumference are fixed, the *IRF* reduces with respect to the number of trains. Beyond 60 trains the *IRF* does not change a lot.

The beam parameters of the ILC damping ring are listed in Table 2.4-1 of Ref. [8]. There are 5 different fills in this ring. For different fill patterns, the total number of particles is kept constant so that the specified luminosity can be achieved.

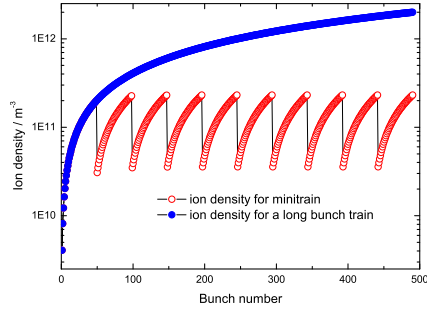


Figure 5: Ion density in fill pattern case *A*.

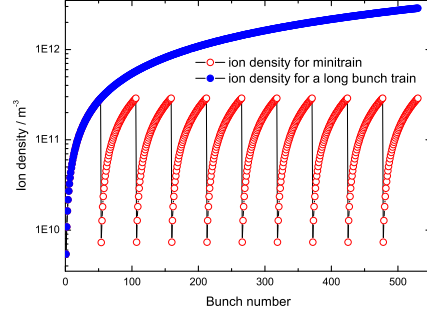


Figure 6: Ion density in fill pattern case *B*.

The ion density for different fill patterns case *A*, *B* and *C* are shown in Figure 5, Figure 6 and Figure 7 respectively for ten bunch trains. The CO partial pressure is 1.0 nTorr. It can be seen that the ion density for a single long bunch train will increase linearly with respect to the bunch number. However, if the gaps are introduced between the adjacent bunch trains, the ion density is reduced significantly. It also indicates that the ion density for mini-trains can quickly reach the peak value after the first few bunch trains. For the fill patterns *A*, *B* and *C*, the mini-trains can reduce the ion density by about two orders of magnitudes comparing to a single long bunch train. Since the growth rate of FII is proportional to the ion density, it indicates that the growth rate of FII can be reduced by a factor of 100. In this case, the FII can be potentially damped by a fast feedback system.

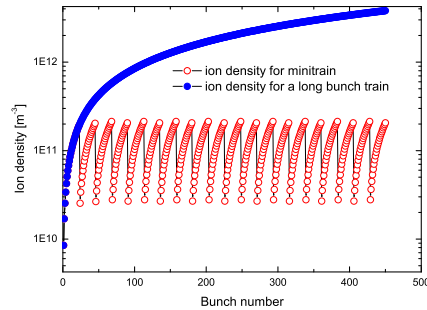


Figure 7: Ion density in fill pattern case *C*.

4 Simulation study of FII in the ILC damping ring

A weak-strong code is used to simulate the FII in the ILC electron damping ring [10]. The effect of mini-trains is taken into account. Figure 8 shows the growth of the vertical oscillation amplitude versus number of turns for a single long bunch train and for mini-

trains of fill pattern A. The 5782nd bunch is recorded here. It can be seen when the gap is

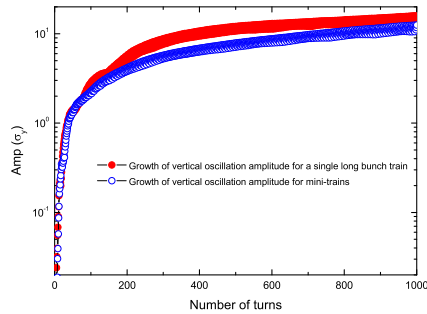


Figure 8: Growth of vertical oscillation amplitude for a single bunch train and mini-trains in fill pattern case A in a CO pressure of 1nTorr.

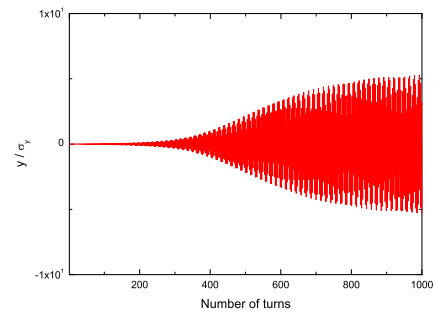


Figure 9: The 5782nd bunch centroid oscillation in the fill pattern case A.

introduced in the bunch trains, the growth of vertical oscillation slows down. This is because in the case the ion density for mini-trains is less than that of a single long bunch train case in Figure 5. Figure 9 shows the bunch centroid oscillation versus number of turns in the fill pattern case A. The 5782nd bunch is recorded here. We can see the bunch centroid begins to oscillate with small amplitude and then reaches the saturation after about 600 turns [11]. This is also one of the characteristics of the FII.

5 Conclusion

Gaps between bunch trains can significantly reduce the ion density in the ILC damping ring; a gap exceeding 30 RF bucket reduces the ion density by a factor 10. Depending on fill pattern the ion density diminishes by about two orders of magnitude compared to one long bunch train case. Simulation shows the growth of vertical oscillation amplitude to be attenuated with gaps in the fill.

References

- [1] Slides:
<http://ilcagenda.linearcollider.org/contributionDisplay.py?contribId=334&sessionId=65&confId=1296>
- [2] J.M. Byrd *et al.*, SLAC-PUB-7389 (1996).
- [3] T. Raubenheimer and F. Zimmermann, Phys. Rev. E **5** 5487 (1995).
- [4] G.V. Stupakov, T. Raubenheimer and F. Zimmermann, Phys. Rev. E **5** 5499 (1995).
- [5] A. Wolski *et al.*, LBNL-59449 (2006).
- [6] M. Kuriki, *et al.*, ILC-Asia-2006-03 (2006).
- [7] L. Wang, talks at ILCDR07 Workshop in Frascati, (2007).
- [8] G. Aarons, *et al.*, ILC-Report-2007-01 (2007).
- [9] L. Wang, *et al.*, SLAC-PUB-12643 (2007).
- [10] G. Xia, *et al.*, Proceedings of EPAC06, MOPLS133, Edinburgh, UK (2006).
- [11] G. Xia, *et al.*, Proceedings of PAC07, THPMN016, Albuquerque, New Mexico, USA (2007).

Depolarisation in the damping rings of the ILC

L.I. Malysheva¹ and D.P. Barber^{2*}

1- Department of Physics - The University of Liverpool
Liverpool, L69 7ZE - UK

2- Deutsches Elektronen-Synchrotron - DESY
22603 Hamburg - GERMANY

Spin polarisation will play an important role in the physics programme of the International Linear Collider (ILC). A well designed and aligned damping ring should not produce any significant depolarisation. This is confirmed by simulations using the code SLICKTRACK. However, it should be recognised that there is no full decoherence of the horizontal components of spins.

1 Overview

If highly spin-polarised electron and positron beams are to be available at the interaction point(s) of the ILC, it is essential that the damping rings cause no significant depolarisation. However, enhancement of synchrotron radiation by the wigglers in damping rings has the potential to cause spin depolarisation via the spin-orbit coupling embodied in the Thomas-BMT (T-BMT) equation [1]. Thus a special study of depolarisation in the ILC damping rings has been made [2]. In principle there are three effects which can either reduce the value of the polarisation at the interactions point(s) or add uncertainty to the direction of the polarisation at the interaction point(s). These are respectively the effect of synchrotron radiation just mentioned, and two effects related to a possible mismatch of the incoming spin distribution with the “ideal” spin distribution of particles with non-zero orbital amplitudes.

2 The effect of synchrotron radiation

Spins precess in the magnetic fields according to the T-BMT equation. But the stochastic nature of the emission of synchrotron radiation puts some random motion (noise) into the particle orbits. In the (non-uniform) quadrupole fields, the noise is transmitted to the spin motion and initially mutually parallel spins can start to spread out so that the beam becomes depolarised. In principle, synchrotron radiation can also lead to a build up of polarisation via the Sokolov-Ternov (ST) effect [1] but in damping rings this can be neglected since the alternating fields in the wigglers ensure that the asymptotic ST polarisation is very low. Also, the ST build-up rate is very low.

As a part of a study to determine the optimal damping ring configuration for the ILC, the depolarisation for a few damping ring designs (e.g., the OCS and TESLA lattices) has been estimated [2]. Since the beam is not at equilibrium, a Monte-Carlo simulation of the effect of stochastic photon emission was carried out using the code SLICKTRACK [3]. Even with typical misalignments (1/3 mm misalignments and 1/3 mrad roll for quadrupoles) the loss of polarisation is negligible both for the design energy of 5.006 GeV and close to a first

*Also Visiting Staff Member at the Cockcroft Institute, Daresbury Science and Innovation Campus, and at the University of Liverpool, UK.

order spin-orbit resonance at 4.8 GeV. See for example fig. 1 in [4]. A similar conclusion emerges from simulations with SLICKTRACK for the (newer) OCS6 lattice at 5.0 GeV. The simulations were performed both for a small energy spread (± 45 KeV) expected for injected electron bunches and for the large initial transverse emittances and initial energy spread of ± 25 MeV, expected for the positrons from the positron source of the ILC baseline-design.

3 The invariant spin field and the associated effects

Whereas radiative depolarisation is irreversible, the other two effects are mainly associated with radiationless, i.e., reversible, equations of spin motion. Both can be understood in terms of the so-called “invariant spin field” \hat{n} [5, 6] which describes the direction of the equilibrium polarisation at each point in phase space. The natural “reference direction” for describing spin motion in a storage or damping ring is the unit vector \hat{n}_0 , the periodic solution (of unit length) of the T-BMT equation on the closed orbit [1]. In a properly aligned damping ring \hat{n}_0 will be just a few milliradians from the vertical. In e^\pm storage rings \hat{n}_0 gives the direction of the equilibrium polarisation of the whole beam. If the beam is in equilibrium with non-zero emittances and spins are set initially parallel to \hat{n}_0 , instead of \hat{n} , the polarisation will fluctuate. See, for example, fig. 9 in [6]. Nevertheless, at the low energies of the damping rings, the effects of such fluctuations are negligible away from spin-orbit resonances. Note that earlier work with MERLIN for 1.98 GeV in the NLC damping rings [7, 8] which confirmed the positions of spin-orbit resonances, did not include synchrotron radiation and was therefore concerned with just these kinds of fluctuations.

A second and much more important effect which is of basically the same nature is illustrated in fig. 1 for electrons in the OCS6 lattice when the initial relative energy spread is ± 45 KeV. Here, all spins are initially tilted by 100 mrad from \hat{n}_0 , along the same direction. The first (top) curve shows the mean square angle of tilt. It is so large that it is not significantly influenced by synchro-betatron motion and synchrotron radiation. The other two curves show the mean squared projections of the spins on the radial and longitudinal directions. They oscillate almost sinusoidally as the polarisation vector basically just precesses around \hat{n}_0 . However, the peak-to-peak range is slightly less than 10000 mrad^2 , indicating that there is some decoherence, due to synchrotron radiation, of the projections of spins on the plane perpendicular to \hat{n}_0 . In fact the distribution of the projections comes to equilibrium with respect to the rotating mean direction, with an r.m.s. spread of about 14 degrees and this is consistent with a simple model [9]. Thus, contrary to common expectation, there is no complete decoherence of the spin projections. The same is true for large initial energy spreads. So, if the injected polarisation is tilted sufficiently from \hat{n}_0 , the direction of the polarisation vector at ejection and, in turn, that of the polarisation vector at the interaction point(s) will depend on the time at which the ejection kickers are fired. The injected polarisation should therefore be set sufficiently parallel to \hat{n}_0 , or for these damping rings, to the vertical.

4 Conclusions

New SLICKTRACK simulations for the ILC damping ring lattice support our earlier conclusion that the depolarisation is negligible and that the horizontal projections of the spins of the electron bunches injected into damping ring need not rapidly decohere. It is therefore important that the polarisation vector be properly aligned prior to injection. More details

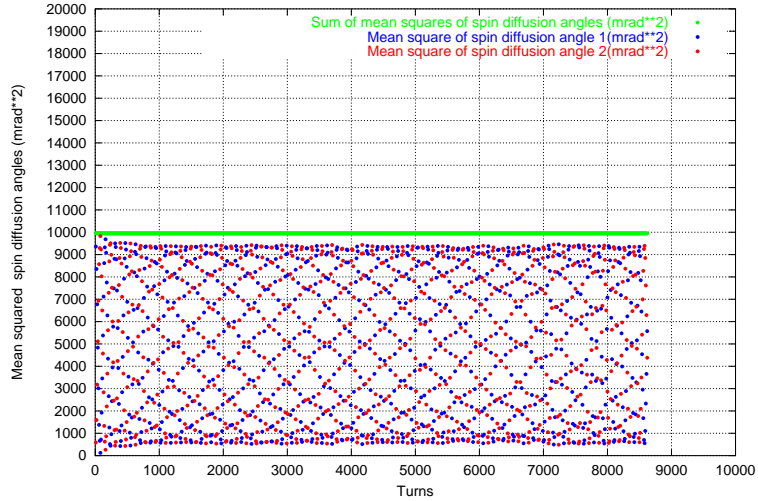


Figure 1: OCS6: mean squared spin angles at 5 GeV for a synchrotron tune of 0.0638, sampled every 10 turns for about 7 transverse damping times.

and results of simulations for positrons with their large initial energy spread will be provided in an extended version of this paper, published as a Cockcroft report. See [10] too.

References

- [1] D.P. Barber and G. Ripken, Handbook of Accelerator Physics and Engineering, Eds. A.W. Chao and M. Tigner, World Scientific, 3rd edition (2006).
- [2] A. Wolski *et al.*, Configuration studies and recommendations for the ILC Damping Rings, LBNL-59449, Cockcroft-06-04 (2006).
- [3] D.P. Barber *et al.*, Polarisation in the eRHIC electron(positron)ring, Cockcroft-04-01 (2004).
- [4] L.I. Malysheva *et al.*, *Depolarization effects at the ILC*, 17th International Spin Physics Symposium (SPIN2006), Kyoto, Japan (2006).
- [5] D.P. Barber, J.A. Ellison and K. Heinemann, Phys. Rev. ST Accel. Beams **7**(12), 124002 (2004).
- [6] K. Heinemann and G.H. Hoffstaetter, Phys.Rev. **E 54**(4) 4240 (1996).
- [7] A. Wolski and D. Bates, LCC-0155, CBP Tech Note-326 (2004).
- [8] N.J. Walker, "MERLIN", <http://www.desy.de/~merlin>
- [9] K. Heinemann, DESY Report 97-166 (1997) and arXiv physics/9709025.
- [10] Slides:
<http://ilcagenda.linearcollider.org/contributionDisplay.py?contribId=252&sessionId=92&confId=1296>

Status of the ATF Damping Ring BPM Upgrade Project

C. Briegel¹, N. Eddy¹, B. Haynes¹, J. May², D. McCormick², J. Nelson², D. Nicklaus¹, P. Prieto¹,
R. Rechenmacher¹, T. Smith², N. Teranuma³, J. Urakawa³, D. Voy¹, M. Wendt¹, M. Woodley²

1- Fermi National Accelerator Laboratory
P. O. Box 500, Batavia, IL 60510-0500 - U.S.A.

2- Stanford Linear Accelerator Center
2575 Sand Hill Road, Menlo Park, CA 94025 - U.S.A.

3- KEK High Energy Accelerator Research Organization
1-1 Oho, Tsukuba, Ibaraki 305-0801 - Japan

A substantial upgrade of the beam position monitors (BPM) at the ATF (Accelerator Test Facility) damping ring is currently in progress. Implementing digital read-out signal processing techniques in line with an optimized, low-noise analog downconverter, a resolution well below 1 μm could be demonstrated at 20 (of 96) upgraded BPM stations. The narrowband, high resolution BPM mode permits investigation of all types of non-linearities, imperfections and other obstacles in the machine which may limit the very low target aimed vertical beam emittance of < 2 pm. The technical status of the project, first beam measurements and an outlook to its finalization are presented.

1 Introduction

An important goal of the ILC beam studies at the KEK ATF damping ring is to generate and extract a beam with low vertical emittance (< 2 pm). This requires various optimization methods to steer the beam along an optimum (golden) orbit with minimum disturbance to non-linear field effects. A high resolution BPM system is a mandatory tool to achieve this goal, requiring a resolution in the 100 nm range operating in a “narrowband” mode. Many related beam studies will be triggered with this high resolution BPM tool, e. g. damping process and minimization of the damping time, beam based alignment (BBA) studies, including offset drift investigations, analysis/correction of various unwanted effects (coupling, chromaticity, noise, etc.). A wideband, turn-by-turn mode of moderate resolution ($< 10 \mu\text{m}$) also has to be provided for injection/extraction, and some special beam studies. The BPM’s may also be used within a orbit feedback system at a later stage. The ATF DR BPM Upgrade Project is a KEK/SLAC/Fermilab collaboration that addresses the problem by installing new hard-, firm- and software for read-out and signal processing of the 96 installed button-type BPM pickups in the ATF damping storage ring:

- 714 MHz-to-15 MHz downmix- and calibration-module, located inside the ATF tunnel.
- VME-based digital signal processing and timing electronics, based on the commercial *Echotek* digital receiver.
- Various FPGA-firmware, diagnostics software, and an EPICS interface to the ATF control system.

2 The ATF Damping Ring

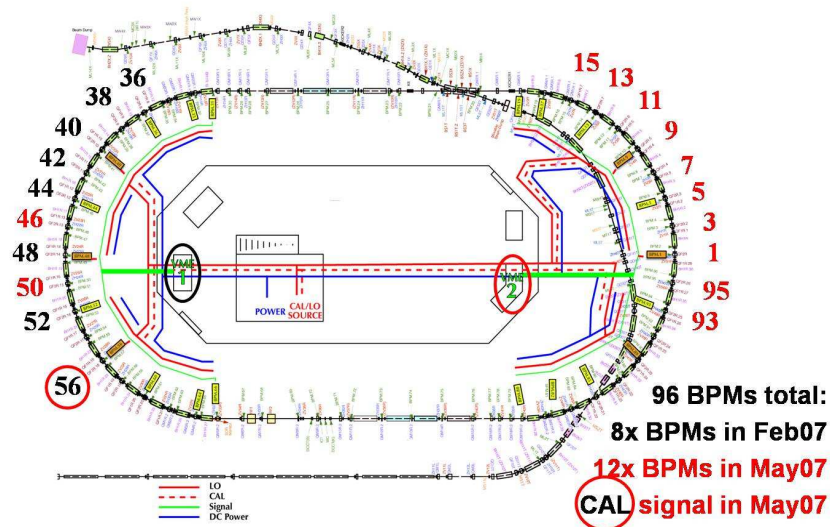


Figure 1: Layout of the ATF damping ring

Fig. 1 shows the layout of the approximately 140 m circumference ATF damping ring located at KEK, Japan, as of May 2007. It utilizes injection from a S-Band linac and extraction to the dump beam-line at the same location in the upper straight section, at a beam energy of 1.28 GeV; the 714 MHz RF cavities are located at the lower straight section. As indicated, 20 out of 96 button-style BPM's are upgraded with the new read-out system, which is located in the tunnel (distributed analog downconverters) and in two air-conditioned huts outside the tunnel (VME 1 and VME 2) accommodating the VME crates.

beam energy E	=	1.28 GeV
beam intensity, single bunch	\approx	1.6 nC $\equiv 10^{10}$ e ⁻ /bunch $\equiv I_{\text{bunch}} = 3.46$ mA
beam intensity, multibunch (20)	\approx	22.4 nC $\equiv 0.7 \cdot 10^{10} \times 20$ e ⁻ $\equiv I_{\text{bunch}} = 48.5$ mA
accelerating frequency f_{RF}	=	714 MHz
revolution frequency f_{rev}	=	$f_{\text{RF}}/330 = 2.1636$ MHz $\equiv t_{\text{rev}} = 462.18$ ns
bunch spacing t_{bunch}	=	$t_{\text{RF}}/2 = 2.8011$ ns
batch spacing t_{batch}	=	$t_{\text{rev}}/3 = 154.06$ ns
horizontal betatron tune	\approx	15.234 $\equiv f_{\text{h}} \approx 506$ kHz
vertical betatron tune	\approx	8.567 $\equiv f_{\text{v}} \approx 1200$ kHz
synchrotron tune	\approx	0.0045 $\equiv f_{\text{s}} \approx 9.7$ kHz
repetition frequency f_{rep}	=	1.56 Hz $\equiv t_{\text{rep}} = 640$ ms
beam time t_{beam}	=	460.41 ms (\equiv turn # 996170)

Table 1: Beam parameters of the ATF damping ring

Table 2 lists some machine and beam parameters of the ATF damping ring. In standard operation a single bunch is injected from the S-Band linac on axes into the damping ring. After ≈ 200 ms all injection oscillations are fully damped and the beam remains for another 400 ms in the machine before being extracted. This operation repeats at a 640 ms cycle time, and also allows for multibunch fillings of 3 batches, each up to 20 bunches spaced by 2.8 ns, in case the beam extraction is suppressed.

3 The BPM Upgrade

3.1 Overview

A Resolution of 10-20 μm is measured with the current ATF BPM read-out system. This does not meet the requirements for the corrections of non-linear effects in the ATF damping ring, and to achieve the ultimate low vertical beam emittance. A first initiative to upgrade the BPM read-out system was started in 2006, based on analog downmix modules and digital down converter receivers from Echotek, achieving 0.5-2 μm RMS resolution.

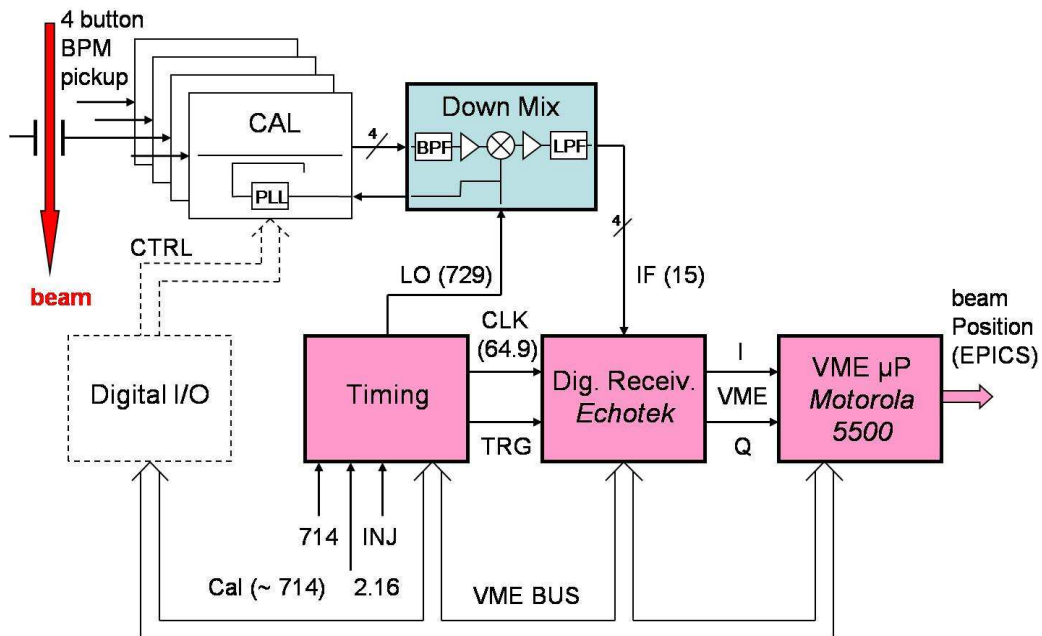


Figure 2: Schematic overview of the upgraded BPM hardware (one pickup = four channels).

Fig. 2 gives an overview of the new BPM read-out hardware, shown for single button-style pickup. The four electrode signals of each button-style BPM pickup – the only unchanged component – are processed separately up to the VME CPU, where the actual position normalization and calibration takes place. All analog hardware, i. e. downmix modules and calibration signal generation (under development), is located in the tunnel; all digital

hardware is located in two VME crates in the corresponding west and east arc huts. The upgraded hardware consists of:

- The *downmix module* receives the four signals from the button-style pickup, filters the 714 MHz frequency content ($BW \approx 10$ MHz), and downconverts this signal to a 15.1 MHz output signal.
- The *calibration/test signal* generation is under development, a principal function test at ATF proved the feasibility.
- Each of two *VME chassis* outside the tunnel holds:
 - A set of 5 *Echotek* digital receiver modules with each 8 channels to read-out two BPM's.
 - A *timing module* to generate all required trigger, clock and RF signals.
 - A *Motorola* 5500 CPU controller board for data collection and post-processing.
 - A *digital I/O* module was used temporarily, the final design of the calibration unit will make use of a CAN fieldbus for it's control.

3.2 Button-style BPM Pickup

The ATF damping ring is equipped with a total of 96 button-style BPM pickup stations. The button electrodes are mounted under a rotation of 45° into the beam pipe of circular cross-section (24.4 mm diameter), to avoid the direct synchrotron light. The 12 mm diameter button electrodes span 15.7 % (equiv. 56.4°), which results in an electrical beam-to-electrode coupling of 15.9 % for a centered beam.

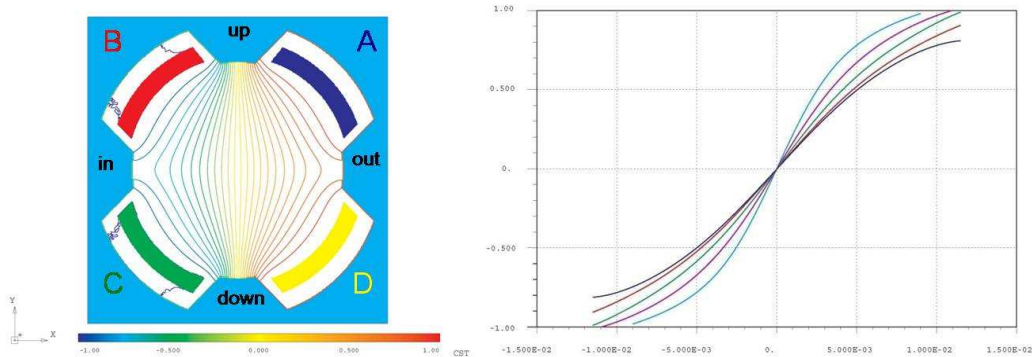


Figure 3: Horizontal position characteristics of the ATF damping ring button-style BPM pickup.

Fig. 3 shows the results of a numerical analysis, i. e. solving the *Laplace* equation for the 2D cross-section. The normalized position characteristics are plotted in terms of equipotentials:

$$\phi_{hor} = \frac{(\phi_A + \phi_C) - (\phi_B + \phi_D)}{\sum \phi} \quad \phi_{vert} = \frac{(\phi_A + \phi_B) - (\phi_C + \phi_D)}{\sum \phi}$$

which are identical in horizontal (shown) and vertical plane, due to the pickup symmetry. A 5th order 1D polynomial fit at $\phi_{hor}(y = 0)$, resp. $\phi_{vert}(x = 0)$ approximates this result, and is implemented in the read-out software to calibrate the intensity values of the four electrodes to a beam displacement:

$$\text{Pos}[mm] = 9.35\phi + 1.00\phi^3 + 7.79\phi^5$$

A more accurate 2D fit is also prepared to correct for the higher order non-linearities, but not yet implemented in the read-out software.

The high-pass like transfer impedance of the pickup was estimated analytically, resulting in a value of $Z_b \approx 0.735 \Omega$ at the operation frequency on the downconverter input $f_{in} = 714 \text{ MHz}$.

3.3 Analog Signal Processing

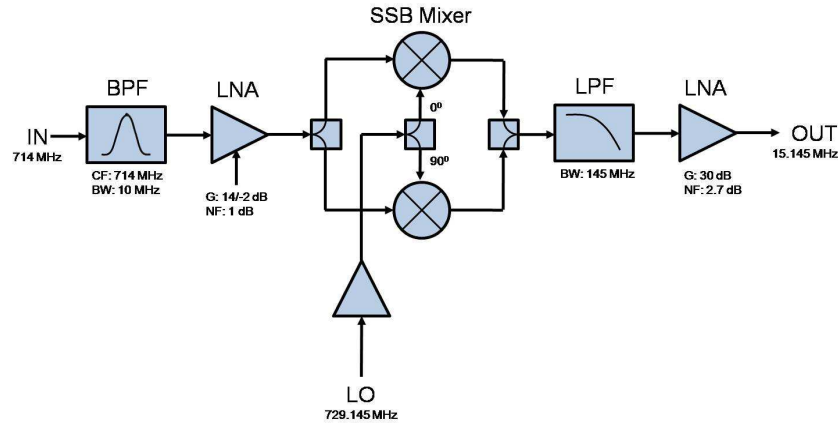


Figure 4: Analog downconverter schematics, one (of four) channel shown.

The analog bandwidth and sampling rate of the analog-to-digital converter (ADC), as well as other hardware specifications, limit the uses of the digital signal processing in the Digital Down Converter (DDC) receiver to analog signal frequencies $< 40 \text{ MHz}$ (by using under-sampling techniques this upper frequency limit could be extended somewhat). The transfer impedance of the button electrodes is poor at frequencies $< 100 \text{ MHz}$, thus a high signal frequency has to be used to get a sufficient good S/N-ratio. For this reason an analog downconverter, including filters and gain-stages, is switched in front of the DDC receiver, to pre-process the button signals accordingly. Fig. 4 shows a simplified block diagram of a single channel of this downmix module, which is located in the tunnel close to each BPM pickup station. The required $f_{LO} = 729.145 \text{ MHz}$ signal is fanned-out from the VME timing- and frequency generation module, supplying a image-rejection (SSB) mixer to convert the bandpassed pickup electrode signals $f_{IN} = 714 \text{ MHz}$ to $f_{IF} = 15.145 \text{ MHz}$. The downconverter unit includes a gain switchable low-noise amplifier (LNA), as well as gain and filter stages in the IF section.

3.4 Digital Signal Processing

Following the analog downconverter, the four BPM signals are digitized and digitally down-converted to baseband in a commercial 8-channel digital receiver board (*Echotek ECGR-GC814*). Each of the 8 DDC channels on this VME64X board is made up of a combination of an ADC (*AD6644*), *GC-4016* (TI DDC), FPGA, and a 128 KW FIFO.

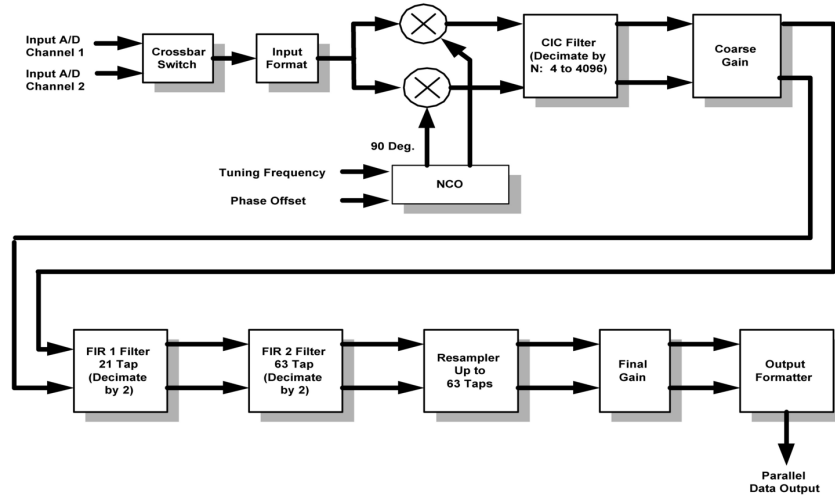


Figure 5: *Texas Instruments GC-4016, “Graychip”* digital downconverter (DDC), one (of four) channel.

The key of the digital signal processing is the 4-channel *GC-4016 “Graychip”* ASIC (Fig.5). Each selected channel receives the digitized 15.145 MHz IF data and produces a filtered, decimated stream of I-Q data pairs for each BPM channel. This data is further processed in the VME front end processor to generate the final intensity value computed by taking the square root of the sum of the squares of the I-Q pair for each channel (button electrode signal). The displacement (beam position) information is finally computed by combining the data of all electrode channels according to the equation shown in section 3.2.

All DDC NCO’s are programmed to 15.14545 MHz, shifting the IF frequency to baseband. Once the BPM signal is at baseband the decimation rate of the 5-stage CIC filter is set to 4 in the wideband mode (the minimum decimation achievable in the ASIC), but to 2747 in the narrowband mode, a rate calculated from the combination of the RRC FIR filter response and decimated clock frequency.

The lowpass FIR filters (CFIR and PFIR) that follow the CIC stage in the *wideband mode* are fundamentally calculated to notch out the 2.1636 MHz revolution frequency harmonics, still present in the digitized signal. This is achieved by combining the number of FIR taps (32 taps) and clock rate in a way that the low-pass sinc function zeros appear at $n \times 462.18$ ns. With these settings 4 data points per turn are sampled, allowing the consecutive acquisition of 32k turn-by-turn data. The bandwidth of ≈ 500 kHz (wideband mode) gives a true turn-by-turn time resolution, thus permits the measurement of betatron and synchrotron tunes. beam orbits at injection or ejection, etc. As the wideband mode data acquisition is

externally triggered and the VME timing provides flexible delay functions, beam orbits can be taken at injection, ejection, or any other selectable time during the damping cycle.

The CIC high decimation rate used in the *narrowband mode* produces a 2 kHz moving average filter. Further filtering in the CFIR and PFIR sections are implemented as root raised cosine (RRC) filters, obtaining a band rejection greater than 90 dB and bandwidth of 1 kHz. This bandwidth rejection allows the processing of 714 MHz BPM signals in presence of 714.2 MHz calibration tone simultaneously by using two adjacent DDC channels, with one NCO tuned to 15.145 MHz and the second one to 14.945 MHz. The desired IF signal is shifted to baseband and the unwanted one is filtered by the RRC FIR filter. The resulting I-Q pair from each adjacent channel is stored in the FIFO and sorted by the front end for processing.

The narrowband filter output is started at the 500,000 turn after injection and the data rate is $f_{CLK}/\text{total decimation rate} = 69.236171 \text{ MHz}/10988 = 6.30107 \text{ kHz}$, an averaged value is clocked out every $158.7 \mu\text{s}$. The DDC is programmed to output 1280 points, corresponding to 200 milliseconds of orbit data which is further averaged with a boxcar filter to filter out 50 Hz component from the magnet power supplies.

4 First Results and Outlook

During operation in February and May 2007 seven dedicated, plus some parasitic machine shifts were used for commissioning and testing the upgraded BPM stations with beam. First (preliminary) results show a substantial reduction on the beam intensity ($\approx 50\times$), degrading the beam position measurements. In wideband mode, betatron ($f_h \approx 387 \text{ kHz}$, $f_v \approx 1212 \text{ kHz}$) and synchrotron tunes ($f_h \approx 9.7 \text{ kHz}$) could be identified, the short-time, broadband turn-by-turn resolution is a few *mum*. In narrowband mode an SVD algorithm was applied, after additional filtering and removal of 50 Hz components, in order to distinguish between BPM systematics and beam motion. Using this method a narrowband resolution of 200-400 nm (preliminary!) could be estimated. As first application a series of beam based alignment (BBA) measurements were taken, showing a substantial improvement ($> 10\times$) on the reproducibility of the quad-to-BPM offset.

The final goal for the ATF damping ring BPM collaboration is the upgrade of a substantial amount ($\approx 2/3$, or even all!) of the 96 BPM stations with this high resolution read-out system, to supply a powerful tool to minimize the vertical beam emittance. The BPM hardware also has to include a calibration system to detect long term drift effects degrading the reported beam position, even during beam operation. Therefore a revised analog downconverter and calibration unit is under currently development. A prototype will be tested in late 2007, It will include remote control and test functions, and needs dedicated software support. In early 2008 a decision has to be made on the production quantity of these analog modules and the total number of upgraded BPM's, to allow the realization within spring 2008.

5 Acknowledgments

Special thanks to Marc Ross, who started this activity as part of the US-Japan linear collider beam instrumentation collaboration efforts.

Sources

Conveners: D. Scott, M. Kuriki, A. Brachmann

Positron Source Target Development Update

I.R. Bailey^{1,2} *

1 - Cockcroft Institute
Daresbury Laboratory, Warrington, Cheshire, WA4 4AD - UK

2 - University of Liverpool - Dept of Physics
Liverpool, L69 7ZE - UK

The future International Linear Collider (ILC) will require of order 10^{14} positrons per second to fulfil its luminosity requirements. The current baseline design produces this unprecedented flux of positrons using an undulator-based source. In this concept, a collimated beam of photons produced from the action of an undulator on the main electron beam of the ILC is incident on a conversion target.

In the baseline design, the photon beam is directed at a thin, rotating, water-cooled target wheel. In this paper I review the role of the target in the positron source and present plans for a first prototype.

1 Introduction

In the baseline design for the ILC positron source an intense photon beam is used to produce positrons from a conversion target [1]. The intensity and bunch structure of the photon beam require a novel target design which has previously been presented in [2]. Updated details have recently been published in the ILC Reference Design Report [3]. The main characteristics of the photon beam and target are reviewed in sections 2 and 3 of this paper.

A concern with the current design is the effect of eddy current generated in the target wheel rim due to the interaction between the rotating metal surface and the magnetic field of the adjacent capture optics. In collaboration with Lawrence Livermore National Laboratory and the Stanford Linear Accelerator Centre in the US, the Cockcroft Institute and Daresbury Laboratory in the UK are currently in the process of developing a first prototype of the target wheel with the aim of investigating the eddy current and benchmarking the associated numerical simulations. Recent simulations [1] differ in their predictions for the eddy current power losses by as much as 50%. Details of the prototype are given in section 4 of this paper, and future work is summarized in section 5.

2 Photon beam characteristics

The intense circularly polarised photon beam from the helical undulator insertion device of the ILC positron source will have the same time-structure as the main ILC electron beam [3]: nominally 5 pulses per second, with each pulse having a duration of approximately 1 ms. The undulator will have a total active length of 147 m, giving photons with a first harmonic energy of 10.06 MeV.

The required undulator length of 147 m has been determined assuming that the target is immersed in the magnetic field of a pulsed flux concentrator in order to maximize the

*On behalf of the members of the ILC positron source target groups at the University of Liverpool and Daresbury Laboratory.

positron capture efficiency. With this geometry, the average integrated power of the uncollimated photon beam will be approximately 131 kW, with each bunch of photons carrying a total energy of approximately 10 J and consisting of order 10^{13} photons.

3 Target design

The proposed target wheel consists of a circular titanium alloy (Ti-6%Al-4%V) rim connected to a central drive shaft by five equally-spaced radial struts. The wheel will be oriented with the photon beam parallel to the drive shaft, such that the photons strike the rim, which has a radial width of 30 mm and an axial thickness of 0.4 radiation lengths (14 mm). The target will be positioned 500 m downstream of the centre of the undulator, giving a photon beam spot with a rms radius of approximately 2 mm.

Particle tracking simulations [4] predict that approximately 8% of the power of the photon beam will be dissipated in the target. The total energy deposition from each photon pulse is therefore expected to be approximately 22 J/g for a rim speed of 100 ms^{-1} (compared with 0.9 kJ/g for a static target).

As the target wheel will be housed in a vacuum vessel at a pressure of 10^{-7} Torr or less, the wheel will be cooled by water flowing through the hollow drive shaft via a rotating water union and through an internal water-cooling channel contained inside the target rim.

4 Prototype

The prototype wheel will closely resemble the baseline target but will not have internal water cooling channels, and will be operated in air rather than in a vacuum. In addition, there are no plans to expose this first prototype to a photon or other particle beam, as its main purpose is to investigate eddy currents. The mechanical design and data acquisition system for the prototype are discussed in sections 4.1 and 4.2 respectively. The experimental programme is outlined in section 4.3.

4.1 Mechanical design

The prototype target wheel is being manufactured from the same titanium alloy as specified for the baseline target and will have the same outer diameter, radial wheel width and number of spokes. The thickness of the prototype wheel will be 16.6 ± 0.1 mm, which corresponds to a standard thickness of Ti plate. The drive shaft will connect the wheel via a flexible coupling to a 15 kW drive motor and will be supported by two Plummer block bearing units.

The (constant) magnetic field will be generated by a water-cooled dipole electromagnet with cylindrical pole caps 250 mm in diameter. The minimum pole gap envisaged during operation of the rotating wheel is 50 mm, which allows for a maximum peak field of 1.5 T. The magnet support structure will enable the fraction of the wheel rim immersed in the high-field region to be adjusted by varying the relative distance between the centre of the wheel and the centre of the pole caps. The magnet geometry limits the maximum length of the immersed arc to be 190 mm.

Simulations predict that the eddy current induced heating in the prototype for a 1 T field at 2000 rpm could be as high as 10 kW. As the prototype does not have an internal cooling channel, this heat must be dissipated by another mechanism. Initial calculations show that convective cooling of the rotating wheel in air at room temperature will lead to

an equilibrium temperature of the wheel rim of approximately 200° C. It is anticipated that a jet of cold dry air will be used to increase the cooling rate.

4.2 Data acquisition

The data acquisition system will consist of a PC interfaced to the power supplies (for the drive motor and the magnet) and a suite of transducers. A rotary torque sensor will be mounted on the drive shaft to measure the torque acting on the wheel. Infra-red sensors and thermocouples will be used to monitor the temperature of the magnet polecaps, target rim, drive shaft and support structures. An optical system will be used to monitor the angular velocity of the drive shaft. Uniaxial accelerometers will be mounted on each of the two bearing units to measure jitter due to vibrational instabilities and component fatigue. Finally, a Hall probe will be used to monitor the magnetic field between the pole caps.

4.3 Experimental programme

Following balancing and initial commissioning, the first phase of the experiment will aim to measure vibrations of the wheel as a function of angular velocity in the absence of a magnetic field. During the second (subsequent) phase of the experiment, the magnetic field strength and wheel speed will be systematically incremented and the resulting torque and temperature readings will be compared with the predictions of the computer simulations. During the third phase of the experiment, the wheel will be operated for long periods and the components will be monitored for wear. Additional investigations into methods of adjusting the conductivity of the wheel rim may also be carried out.

5 Summary and Outlook

A design for a titanium target wheel that satisfies the requirements of the ILC baseline positron source has been developed, and construction has begun of a target wheel prototype to investigate eddy currents effects. Further prototypes to demonstrate the cooling and vacuum systems are also envisaged.

Acknowledgments

This work is supported in part by the Commission of the European Communities under the 6th Framework Programme “Structuring the European Research Area”, contract number RIDS-011899.

References

- [1] Slides:
<http://ilcagenda.linearcollider.org/contributionDisplay.py?contribId=486&sessionId=61&confId=1296>
- [2] I.R. Bailey *et al.*, EPAC 2006 Conf. Proc. 2484 (2006).
- [3] G. Aarons *et al.*, “ILC Reference Design Report”,
<http://www.linearcollider.org/>.
- [4] A. Ushakov *et al.*, EPAC 2006 Conf. Proc. 2478 (2006).

Radiation Damage of the ILC Positron Source Target

Andriy Ushakov and Sabine Riemann *

DESY
Platanenallee 6, D-15738 Zeuthen - Germany

The radiation damage of the positron source target for the International Linear Collider (ILC) has been studied. The displacement damage in target material due to multi-MeV photons has been calculated by combining FLUKA simulations for secondary particle production, SPECTER data for neutron displacement cross-sections and the Lindhard model for estimations of displacement damage by ions. The radiation damage of a stationary Ti6Al4V target in units of displacements per atom (dpa) has been estimated for photons from an undulator with strength 0.92 and period 1.15 cm. The calculated damage is 7 dpa. Approximately 12.5% of displacement damage result from neutrons.

1 Introduction

At the International Linear Collider (ILC) positrons will be generated by multi-MeV photons produced in the helical undulator striking a Ti-alloy target of 0.4 radiation length thickness. The main ILC positron source parameters (see [2]) are shown in Table 1.

e ⁻ drive beam energy	150 GeV
Undulator K-value	0.92
Undulator period	1.15 cm
Undulator-target distance	500 m
e ⁺ per bunch at IP	$2 \cdot 10^{10}$
Bunches per pulse	2625
Pulse repetition rate	5 Hz

Table 1: ILC positron source parameters [2].

PKA is slowed-down by interactions with other atoms, which are called 'Secondary Knock-on Atoms' (SKAs). If the PKA energy is high enough (few tens keV for metals [3]), PKAs and SKAs will produce a displacement cascade or even many cascades. Most of the created vacancies and self-interstitial atoms annihilate each other. At the end of this recombination phase, only some residual point defects remain.

The goal of this article is to estimate the radiation damage of the positron source target by multi-MeV photons generated in a helical undulator.

2 Damage modeling

The photons are generated by the radiation of relativistic electrons passing through the periodic, helical magnetic field of the undulator. The undulator is installed part way along main

*Work supported by the Commission of the European Communities under the 6th Framework Programme "Structuring the European Research Area", contract number RIDS-011899.

electron linac, in a chicane arrangement, where the electron energy has reached 150 GeV. Positrons are produced from multi-MeV photons by means of pair production in the field of a nucleus in a conversion target. When a nucleus is excited by photons at energies of giant resonances, one or more nucleons may be knocked out. These secondary particles collide with lattice atoms and induce damage of the target.

The generation of secondary particles by a photon beam has been calculated using FLUKA [4]. A major advantage of FLUKA is its capability to calculate electromagnetic showers in matter as well as neutron fluxes and atomic recoil effects. The Monte-Carlo code is well suited to describe residual nuclei in electromagnetic and hadronic cascade processes. The FLUKA output data for secondary photons, neutrons, protons, deuterons, tritons, ^3He , alpha particles and recoil nuclei from the nuclear reactions have been used for radiation damage calculations. The FLUKA output includes the positions and momenta of secondary particles. Fig. 1 shows neutron energy distribution and energy spectrum of recoil nuclei in the Ti-alloy target generated by undulator photons (see Table 1).

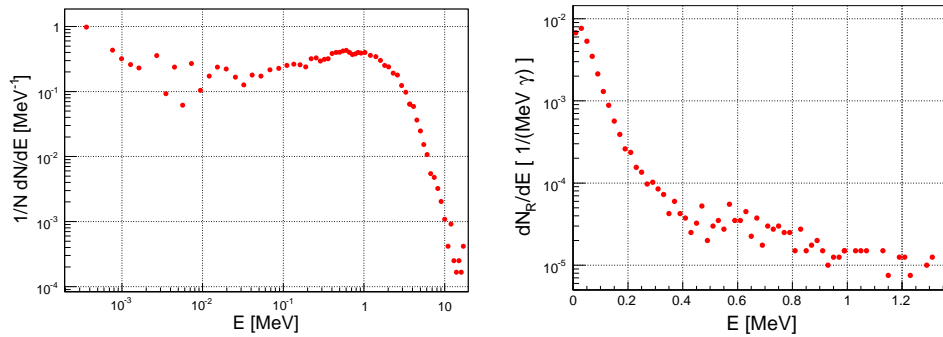


Figure 1: Energy distribution of neutrons (left) and recoil nuclei (right) in the Ti-alloy target.

Following the approach used in [5] the calculations of displacements in the target material have been performed separately for damage induced by neutrons, ions and recoil nuclei. For estimations of displacements induced by neutrons the energy dependent displacement cross-sections from SPECTER code have been used [6]. Fig. 2 shows the neutron damage cross-section σ_d created by the photon beam generated in a helical undulator with $K = 0.92$ and $\lambda = 11.5$ mm.

The number of atoms displaced by neutrons (dpa_n) is the product of σ_d and total neutron fluence ϕ_n : $dpa_n = \sigma_d \phi_n$.

In order to estimate the target damage it is necessary to know the power of the photon beam incident on the target. The re-

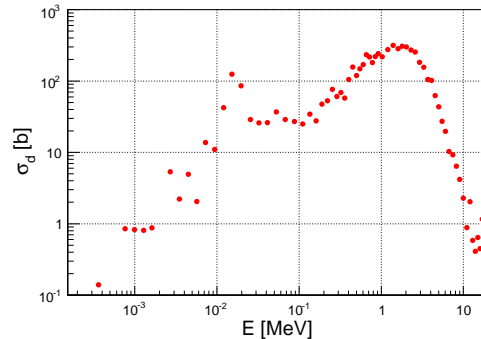


Figure 2: Neutron damage cross-section, σ_d , induced by a photon beam generated in a helical undulator with $K = 0.92$ and $\lambda = 11.5$ mm.

quired photon beam power has been derived from the positron production in the Ti6Al4V target (90% of Ti, 6% of Al and 4% of V) with a thickness of 0.4 radiation length and taking into account positron beam losses after the target. The positron yield defined as ratio of number of positrons emerging from the target and number of photons hitting the target is $2.25 \cdot 10^{-2}$. Almost 28% of the positrons are captured, accelerated and match the acceptance of the dumping ring. Hence, for the nominal ILC positron source parameters (Table 1) $7 \cdot 10^{16}$ photons per second are required corresponding to 117 kW average photon beam power. Fig. 3 shows the transverse dpa distribution induced by neutrons after 5000 hours of source operation averaged over the full target thickness.

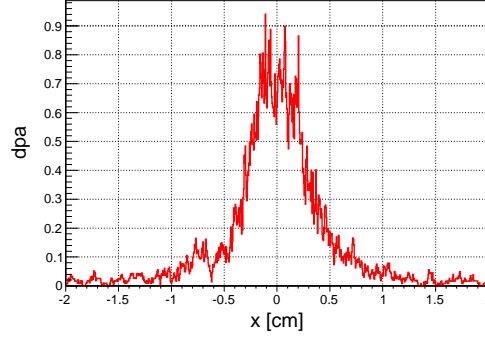


Figure 3: Transverse space distribution of neutron induced dpa in a Ti6Al4V target after 5000 hours irradiation.

For the calculation of displacements induced by ions and recoil nuclei the Linhard model [7] has been used. The dpa produced by ions, dpa_i , has been determined as

$$dpa_i = \sum_j \frac{\hat{E}_j}{L} \frac{\phi_j}{N_a},$$

where ϕ_j and \hat{E}_j are fluence and damage energy of j-type projectiles (protons, deuterons, tritons, ^3He , alpha particles, heavy particles and recoil nuclei), and N_a is the number of target atoms per cm^2 . L is the cascade multiplication threshold,

$$L = E_b + E_c + E_d,$$

where E_b is the energy binding an atom to its lattice site, E_c is the energy of the slow projectile to be captured by a vacant lattice site, E_d is the energy for displacing an atom permanently from its lattice site. The atom could be displaced if $\hat{E} \geq L$. In our estimations $L = 2E_d/0.8$ has been used as recommended by [7]. $E_d = 40$ eV for Ti, V and $E_d = 27$ eV for Al [6]. The damage energy has been approximated as (see [7])

$$\hat{E} = \frac{E}{1 + k_L(\varepsilon + 0.40244\varepsilon^{3/4} + 3.4008\varepsilon^{1/6})},$$

where E is the energy of projectile particle, and ε is a dimensionless energy,

$$\varepsilon = \frac{E}{E_L}, \quad E_L = \frac{Z_1 Z_2 e^2}{a_{12}} \frac{1+A}{A},$$

$$k_L = \frac{32}{3\pi} \sqrt{\frac{m_e}{M_2}} \frac{(1+A)^{3/2} Z_1^{2/3} Z_2^{2/3}}{(Z_1^{2/3} + Z_2^{2/3})^{3/4}}.$$

Z_1 and M_1 are the atomic number and mass of the projectile, Z_2 and M_2 are the atomic number and mass of the target atom, $A = M_2/M_1$, e is the charge of the electron, a_{12} is a Thomas-Fermi screening length of the atom [8]

$$a_{12} = \left(\frac{9\pi}{128} \right)^{1/3} \frac{a_H}{(Z_1^{2/3} + Z_2^{2/3})^{1/2}},$$

where a_H is the Bohr radius.

The number of displaced atoms in the Ti6Al4V target induced by ^{48}Ti recoils is shown in Fig. 4 as function of ^{48}Ti energy. Figure 5 shows dpa averaged over target thickness induced by neutrons, protons, ions (deuterons, tritons, ^3He , alpha particles, heavy particles) and all recoil atoms after 5000 hours of source operation. These results are quantitative only, because the 'damage area' used for the estimations has been defined by the size of the photon beam. This area has been frozen after the first inelastic photon-nucleus interaction and does not include the real displacement cascade development. The reason for such essential simplification was the inability of FLUKA to transport recoil atoms. Hence, the results shown in Figure 5 could be used only for relative comparisons.

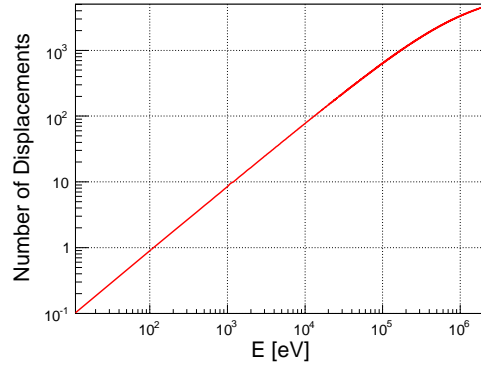


Figure 4: Number displaced atoms by ^{48}Ti recoils in Ti6Al4V target as function of ^{48}Ti energy.

Displacements induced by neutrons are one order of magnitude less than dpa by recoil atoms; damage by protons and ions (deuterons, tritons, ^3He , alpha particles and heavy particles) is smaller by two orders of magnitude. Taking into account the transport of recoil atoms will increase the damage area essentially or decrease the fluence of recoil atoms and results in a reduced dpa value. That is demonstrated in Fig. 5 and Fig. 3: Considering only neutrons and neutron transport the maximal dpa value is reduced from 8.7 to 0.9 (scaling factor is approximately 10). The estimated total dpa value induced by all secondary particles and their transport is 7 dpa after applying the scaling factor.

3 Summary

The radiation damage of stationary target for an ILC positron source has been estimated using a simplified model. The Ti6Al4V target was hit by 117 kW photon generated in a

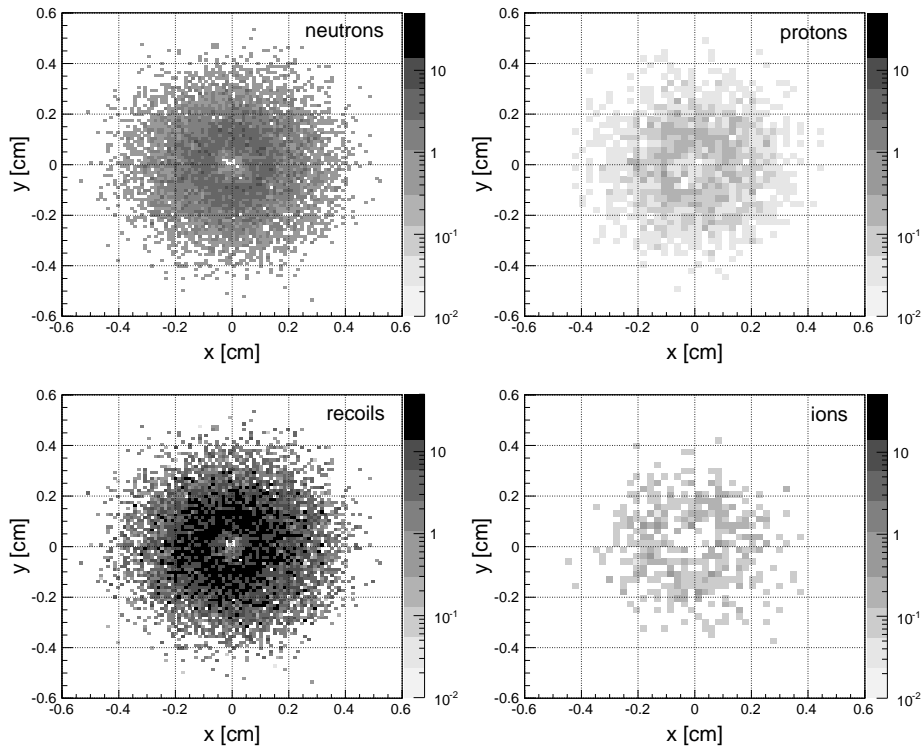


Figure 5: Average dpa induced by neutrons, protons, ions and recoil atoms (without taking into account secondary particle transport).

helical undulator with strength 0.92 and period 1.15 cm. The calculated damage is about 7 dpa after 5000 hours of positron source operation. The main contribution to dpa is induced by recoil atoms, only approximately 12.5% of displacement damage result from neutrons.

References

- [1] Slides: <http://ilcagenda.linearcollider.org/contributionDisplay.py?contribId=488&sessionId=61&confId=1296>
- [2] ILC Reference Design Report, <http://www.linearcollider.org/rdr/>
- [3] R.E. Stoller and L.R. Greenwood, J. Nucl. Mater. **271-272** 57 (1999).
- [4] A. Fassò, A. Ferrari, J. Ranft, and P.R. Sala, CERN-2005-10 (2005).
- [5] B. D. Wirth, P. Monasterio, W. Stein, UCB-NE-5015 (2005).
- [6] L. R. Greenwood and R. K. Smither, ANL/FPP/TM-197 (1985).
- [7] Mark T. Robinson, J. Nucl. Mater. **216** 1 (1994).
- [8] J. Lindhard, V. Nielsen, and M. Scharff, Kgl. Danske Videnskab. Selskab, Mat. Fys. Medd. 36, No. 10 (1968).

Robust Spin Polarisation Status

I.R. Bailey^{1,2}, D.P. Barber^{1,3}, A. Hartin⁴, L.I. Malysheva^{1,2}, G.A. Moortgat-Pick^{1,5},
E. Baynham⁷, A. Birch^{1,6}, T. Bradshaw⁷, A. Brummitt⁷, S. Carr⁷, J.A. Clarke^{1,6},
P. Cooke², J.B. Dainton^{1,2}, Y. Ivanyushenkov⁷, L.J. Jenner^{1,2,*}, A. Lintern⁷, O.B. Malyshev^{1,6},
J. Rochford⁷, D.J. Scott^{1,2,6}, L. Zang^{1,2}

¹ Cockcroft Institute, Daresbury Laboratory, Warrington, Cheshire WA4 4AD, U.K.

² Department of Physics, University of Liverpool, Oxford St., Liverpool, L69 7ZE, U.K.

³ DESY, Deutsches Elektronen Synchrotron, Notkestraße 85, D-22607 Hamburg, Germany

⁴ John Adams Institute, Oxford University Physics, Oxford OX1 3RH, U.K.

⁵ Institute of Particle Physics Phenomenology, University of Durham, Durham DH1 3LE, U.K.

⁶ STFC ASTeC Daresbury Laboratory, Daresbury, Warrington, Cheshire WA4 4AD, U.K.

⁷ STFC Rutherford Appleton Laboratory, Chilton, Didcot, Oxfordshire OX11 0QX, U.K.

The heLiCal collaboration has undertaken the task of creating a complete cradle to grave spin-tracking simulation of the positrons in the ILC. SLICKTRACK is the main software code being used for this purpose; it has been updated to include full non-commuting spin dynamics and will be upgraded to handle non-linear orbital motion. So far, spin dynamics have been simulated in the damping rings, beam delivery system and main linac. The theoretical uncertainties associated with beam-beam interactions at the ILC have been evaluated.

1 Introduction

The heLiCal collaboration is a group of around 25 people from institutions mainly within the UK. The remit of the collaboration is to develop reliable software tools which will allow the ILC to be optimised for spin polarisation as well as luminosity via full cradle-to-grave simulations. This has been identified as high priority by the Global R&D board. As such, simulations of depolarising effects in the damping rings, beam delivery system, main linac and during bunch-bunch interactions have been carried out. In addition, simulations of spin transport through the entire positron source have been performed. This is to enable background reduction and unlock sensitivity to new physics.

2 Depolarisation

The spin state of particles within a bunch can change with respect to each other by photon emission or classical precession through inhomogeneous magnetic fields. This is described by the Thomas-Bargmann-Michel-Telegdi equation:

$$\delta\theta_{spin} \propto \frac{g-2}{2} \gamma \delta\theta_{orbit} \quad (1)$$

more commonly known as the T-BMT equation. Here depolarisation is a term used to describe the uniformity of spin directions within the bunch; the physical spin angles are usually not of concern.

*l.j.jenner@cockcroft.ac.uk

3 Beam-Beam Interactions

The program CAIN [2] analytically evaluates both sources of depolarisation that occurs during beam-beam interactions at the ILC. Normal perturbation theory cannot be used when very large fields are present, as is the case in these types of interactions. A quasi-classical approximation has been used which has been demonstrated to be valid in these conditions [2, 4, 5]. Modelling of both coherent and incoherent background pairs resulting from these interactions has been added into CAIN. Studies of the effect of polarisation on the Breit-Wheeler process show a decrease in the number of photons produced; this is because it is strongly dependent on the initial photons states. This was carried out for a number of ILC beam parameter sets.

4 Damping Rings

Previously [3] results have been presented showing that spin motion in the 6 km DR (OCS) of the ILC, including both spin precession and synchrotron radiation effects in the presence of realistic magnet misalignments (1/3 mm misalignments and 1/3 mrad roll for quadrupole), leads to negligible depolarisation both at the design energy of 5.066 GeV and close to a spin-orbit resonance at 4.8 GeV.

Updated simulations using SLICKTRACK [7] with the “OCS6” damping ring lattice at 5.0 GeV show that the sum of the mean squares of the angles of tilts of spins away from the direction of the equilibrium polarisation (approximately vertical) to be less than 0.1 mrad², even after 8000 turns (8 damping times). At 4.8 GeV the sum of the mean squares of the angles was shown to reach approximately 40 mrad² after 8000 turns, which still represents a negligible degree of depolarisation. I.e. the ratio of final to initial polarisations in this case is $\cos(\sqrt{40} \text{ mrad}) \approx 0.99998$. These simulations were carried out assuming the narrow energy spread (± 45 keV) expected for injected electron bunches. Similar simulations have also been carried out for the OCS6 damping ring lattice at 5 GeV assuming an initial energy spread of ± 25 MeV, much greater than the natural energy spread of the damping ring, as expected for positrons coming from the ILC baseline positron source. In this case the sum of the mean squares of the spin angles after 8000 turns was found to be approximately 20 mrad² which is once again negligible. It was also shown that in this case, as in the previous simulations, the horizontal projections of the spin vectors of an electron or positron bunch do not fully decohere after 8000 turns, i.e. if the spins are tilted from the vertical at injection then their projections do not fan out uniformly in the horizontal plane during damping, even if the initial energy spread is large. In further work, the effect of the length of the injected positron bunches on this conclusion will be investigated.

5 Beam Delivery System

SLICKTRACK has been modified to include a “single pass” mode and then applied to the 2 mrad crossing-angle arm of the older design of the ILC BDS. Realistic misalignments were included as in the damping ring analysis. Simulations showed a total spin precession of approximately 332 degrees and an absolute decrease in the polarisation of 0.06% or less. These figures are consistent with those obtained by Smith et al using the BMAD computer program [1]. Our work will be repeated using updated versions of the BDS lattice consistent with the RDR.

6 Main Linac

The SLICKTRACK computer code has also been modified to include acceleration effects and then applied to the ILC main linac. Spin precession of approximately 26 degrees is expected in the Earth-following linac, and SLICKTRACK simulations of the spin motion show the ratio of the final to initial polarisations of particle bunches travelling through the linac is approximately $\cos(10^{-4}\text{rad})$.

7 CONCLUSIONS AND OUTLOOK

Possible depolarisation effects at the ILC have been studied for the damping ring, main linac, beam delivery system and during the beam-beam interactions for a range of ILC parameters as part of an ongoing rolling study.

- An analysis of depolarisation processes during ILC beam-beam interactions was carried out. The current CAIN implementation of depolarisation through spin precession has been shown to be valid for ILC energies.

- The polarisation dependence of coherent and incoherent pair production at the interaction point has been studied, and these effects are currently being incorporated into CAIN. This work is ongoing, but initial results from CAIN indicate a substantial decrease in low energy incoherent pair production when polarisation effects are included.

- The SLICKTRACK software package has been extended to simulate the spin dynamics through the ILC BDS and main linac. All simulations show very small amounts of depolarisation, as expected.

- Additional SLICKTRACK simulations of the ILC damping ring lattices support our earlier results showing that the horizontal projections of the spin vectors of the electron and positron bunches injected into the damping rings do not rapidly decohere. It is therefore very important that the vectors be properly aligned prior to injection.

- SLICKTRACK is being extended to include non-linear orbital motion, allowing a detailed study of spin motion in non-linear elements such as sextupoles and wigglers.

References

- [1] ILC-Note-2007-012, J.C. Smith, *Depolarisation Study in the International Linear Collider*.
- [2] K. Yokoya, P. Chen, SLAC-PUB-4692, 1988; K. Yokoya, 'User's Manual of CAIN', Version 2.35, April 2003.
- [3] EuroTeV-Report-2006-037, G. Moortgat-Pick et al., *Spin Tracking at the ILC*.
- [4] V. N. Baier and V. M. Katkov, Phys. Lett. A **280** (2001) 275; V. N. Baier and V. M. Katkov, Phys. Rept. **409** (2005) 261.
- [5] G. Moortgat-Pick et al., Cockcroft-07-22 (in preparation).
- [6] V.N. Baier, A.G. Grozin, hep-ph/0209361.
- [7] D.P. Barber, et al., Cockcroft-04-01.

HARDWARE DEVELOPMENT and STUDY for ILC POSITRON SOURCE PARAMETERS

L.V. Kravchuk¹, V.A. Moiseev¹, A.N. Naboka¹, V.V. Paramonov¹, A.K. Skasyrskaya¹,
K. Floettmann², F. Stephan²

1- Institute for Nuclear Research of the RAS
117312, Moscow, Russia

2- Deutsches Elektronen-Synchrotron, DESY
22609, Hamburg, 15738, Zeuthen, Germany

Some components of the normal conducting Positron Pre-Accelerator (PPA) in the ILC Positron Source will operate [1] in hard combination of high fields, long pulse and strong radiation. This case an experimental verification of operational ability in a conditions, mostly close to operational regime, becomes necessary. Moreover, some particularities of the PPA operating regime and beam structure require more consideration.

1 Accelerating sections

The PPA capture sections will operate with an accelerating gradient of up to 15 MV/m in combination with long RF pulses ($\sim 1ms$). Developed in INR and now constructing in DESY, the CDS Booster Cavity (BC) for the Photo Injector Test facility (PITZ), DESY, Zeuthen, will operate at the same conditions and is a full scale, high RF power prototype [2] of the PPA capture cavities. A low RF level test program has been performed to investigate cells production results, to verify RF tuning procedure, brazing procedure and cells parameters change after brazing. All cavity components are produced in industry. Tuning procedure has been established. Both operating and coupling mode frequencies were adjusted to target values for total cavity assembly, without individual cells tuning. Electric field distribution along the cavity axis confirms compensated structures advantage - high stability with respect cells parameters deviations. Cavity RF tuning before brazing is completed, Figure 1. Multi - step brazing procedure in vacuum is now under way. Brazed cavity components are shown in Figure 2. Symmetrical RF coupler, with two input windows, is developed for the cavity. Cavity completion and commissioning will be in nearest future. Start of operation is sheduled for 2008 summer.



Figure 1: Cavity assembly for RF tuning

2 Focusing elements

The solenoid in the first PPA part, together with focusing elements in the part of beam separation and collimation, should withstand against high radiation flux. The special technology is developed in INR for focusing elements, operating in a conditions of high radiation flux. A special water cooled conductor with mineral insulation is used. The example of dipole

coil is shown in Figure 3. There are no organic or plastic components in the conductor and conductor life-time is equal to initial components (copper and insulating oxide) life-time.

3 Methodical study

For the total PPA accelerating system the CDS structure has been proposed in [2]. Some particularities of CDS operation were considered in simulations and compared with the same effects in another structures, both standing and traveling wave, proposed in SLAC [3] for the same purpose.

With high accelerating gradient ($E_0 T \approx 15 \frac{MV}{m}$) CDS operation the maximal magnetic field $H_{smax} \sim 60 \frac{kA}{m}$ at the end of coupling windows will be realized, resulting in power pulse loss density $P_{dmax} = 1.55 \cdot 10^7 \frac{W}{m^2}$. These are sufficient for pulsed RF heating effect, values. This effect in CDS PPA options is considered in [4] and compared with the same effect in simple π -structure [3]. Instead of higher local temperature rise in CDS PPA, an effect summary for both structures is the same. Pulsed RF heating effect is not essential for PPA structures in comparison with this effect in successfully operating DESY RF Gun cavities, [4]. Mode danger can be structure non uniform pulsed heating, caused by particle losses.

An average heat in PPA capture sections is $\sim 25 \frac{kW}{m}$. Cooling CDS capability, taking into account real RF losses distribution, has been considered in two approaches. In engineering approach a prescribed heat exchange coefficient value at the cooling channels surface, estimated from approximate semi-empirical relations, is used. In conjugated approach we start from turbulent flow parameters simulation in cooling channels and solve self consistent heat exchange problem cavity body - cooling fluid. Results of all simulations show - the CDS structure has a sufficient reserve in cooling capability.

PPA beam loading effect, taking into account specific beam pulse structure, is considered in [5]. Our simulations show - for PPA output e^+ energy $\approx 400 MeV$ standing wave structure saves at least two RF channels.

References

- [1] ILC Reference Design Report. <http://www.linearcollider.org>
- [2] M. Krasilnikov et al., PAC 2005, p. 1030, 2005.
- [3] J.W. Wang, et al., Pros. PAC 2005, p. 2827, 2005.
- [4] V.V Paramonov, A.K. Skasyrskaya. TESLA-FEL report 2007-04, DESY, Hamburg, 2007.
- [5] V.V. Paramonov, K. Floettmann. Proc. 2006 Linac, p. 355, 2006.

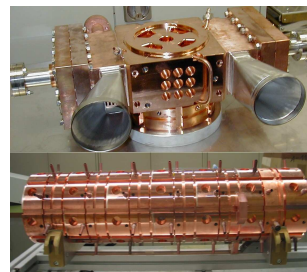


Figure 2: Brazen RF coupler cell (top) and half-cavity part, 7 periods (bottom)



Figure 3: Dipole coil made from conductor with mineral insulation

Accelerator Physics

Conveners: D. Schulte, K. Kubo, P. Lebrun

Update on the Status of BDSIM

S. P. Malton^{1*}, G. A. Blair¹, I. Agapov², A. Latina², O. Dadoun^{3 †}

1- John Adams Institute/Royal Holloway University of London
Egham, Surrey - UK

2- CERN
Geneva - Switzerland

3- Laboratoire de l'Accélérateur Linéaire
Orsay, Paris - France

Recent updates to the status of the BDSIM particle tracking code are presented. In particular, we describe efforts to combine the secondary particle generation of BDSIM with the wakefield calculations of PLACET in order to quantify backgrounds from collimating elements in the beam delivery system of the International Linear Collider. Further recent updates to BDSIM are also introduced.

1 Introduction

BDSIM [1] is an extension to the Geant4 [2] toolkit. It combines accelerator style particle tracking with Geant4 Runge-Kutta based tracking. Beamline elements are implemented through C++ classes, each with an associated stepper function which implements the particle transportation inside this element. The full Geant4 physics processes are available, and non-Geant processes can be added as separate C++ classes. The motivation is to permit fast tracking within the beampipe, while being able to generate backgrounds from beam/material interactions.

2 Wakefields

As a single-particle tracking code, BDSIM does not take account of intra-particle effects such as wakefield generation in collimating elements. In order to correctly model the backgrounds induced by wakefield kicks, some method is required to interface BDSIM with another code that is capable of performing the necessary calculations.

PLACET [3] is a multi-particle tracking code which simulates the dynamics of the beam in the presence of wakefields. Particle bunches are divided into slices longitudinally and the induced wakefield of each slice is applied to all those which follow. In cases where particles are near to the beampipe aperture, the wakefield kick may be sufficient to cause these particles to interact with the beampipe material. BDSIM is capable of generating the secondary particles in this situation, while PLACET is not.

*malton@pp.rhul.ac.uk

†Work supported in part by the STFC LC-ABD Collaboration, the British Council, and by the Commission of European Communities under the 6th Framework Programme Structuring the European Research Area, contract number RIDS-011899

2.1 BDSIM

BDSIM is a single-particle tracking code; wakefields are a multi-particle effect. Calculation of the wakefield kicks requires a description of the full bunch at the appropriate location. In order to generate this, a sensitive volume is introduced prior to the element, which transfers particles from the urgent stack to the postpone stack. This pauses the tracking of each particle in turn at this location. When the requested number of particles has been tracked up to this point, the clean up routine passes the bunch description to PLACET through a temporary fifo. BDSIM then listens on the same fifo, waiting for PLACET to return the distribution of particles from after the collimator. Tracking continues in BDSIM from the end of the previous run.

2.2 PLACET

As a multi-particle code, PLACET has a full description of the bunch at each point of tracking. Routines were added to insert a new bunch description at a given location, in this case at the entrance to a collimating element, and also to output the bunch description.

2.3 Tracking

The implementation described above simply calls PLACET to perform tracking in wakefield regions. However the purpose of this interface is to quantify the backgrounds caused by near-wall particles which are kicked into the beampipe by wakefield effects. This requires that the tracking be done by BDSIM. Ideally, BDSIM will use the bunch description returned by PLACET to calculate the wakefield kicks $\Delta x' = x'_{\text{after collimator}} - x'_{\text{before collimator}}$ (and similarly for $\Delta y'$) and apply these at the centre of the collimator logical volume.

The process currently requires that equivalent decks are available in both PLACET and gmad. The CLIC deck (dated 28/11/05) has been used so far as a test system. However, as tracking in PLACET is only relevant in the collimating elements, it should be possible to generate the same results with *only* the collimating elements in the PLACET input file.

3 Further Developments

Arbitrary materials definitions can now be placed in the gmad file to generate materials that are not already included in BDSIM using the `material` command like this:

```
CarbonDioxide : material, density=1e-14, components={"C","O"},
componentsWeights{1,2}
```

Chemical elements which have not been previously defined may also be included using the `atom` keyword:

```
ytterbium : atom, Z=70, A=174, symbol="Yb"
```

Currently this allows for the inclusion of materials in which every molecule is identical. Further refinements will allow the user to specify a mixture of materials by fractional weight. This will generate a more accurate description of common accelerator (tunnel) materials

such as soil and concrete.

The BDSIM installation has now been updated to make use of gcc4.0, CLHEP2.0.x.x and Geant4.9.0. Numerous bugfixes have also been included.

4 Future updates

BDSIM is continually evolving. A short list of the updates intended for inclusion in future releases includes:

- The integration of the OpenScientist framework [4] to allow interactive pan and zoom functionality in the visualisation.
- Design of realistic magnet element geometries to be built by default. This would replace the current default cylindrical elements.
- Support for a GDML/XML input format, such as LCDD [5] complementary to the gmad and Mokka/SQL formats.
- Polarisation tracking is supported in later versions of Geant4. This facility should be utilised by BDSIM.
- Further output data options, such as energy deposition by element. This would include dosimetry/activation.

5 Conclusions

The implementation of data transfer between the single- and multi-particle codes has been completed. This in effect calls PLACET to track through wakefield regions during BDSIM tracking; further refinements will use the bunch description from PLACET to calculate the wakefield kicks so that they can be applied in BDSIM and near-wall particles will interact with the beampipe material. Updated Materials input from gmad file. The current development version can be obtained from CVS at <http://cvs.pp.rhul.ac.uk/cvsweb.cgi/BDSIM>. The next major release, version 0.4, is expected by the end of October.

References

- [1] I. Agapov *et al.*, *BDSIM - Beamline Simulation Toolkit Based on Geant4*, EuroTev-Report-2006-035 (2006).
- [2] Geant4 Users' Guide,
<http://geant4.web.cern.ch/geant4/>
- [3] Daniel Schulte, *The Tracking Code PLACET*, Users' Manual, (2000)
- [4] G. Barrand, *OpenScientist. Status of the Project*, Proceedings of CHEP04, Interlaken, Switzerland (2004)
- [5] LCDD Homepage
<http://lcsim.org/software/lcdd/>
- [6] Slides:
<http://ilcagenda.linearcollider.org/contributionDisplay.py?contribId=221&sessionId=67&confId=1296>

Metrology

Conveners: M. Schlösser, R. Sugahara, R. Ford

Active Stabilization of a Mechanical Structure

L. Brunetti¹, N. Geffroy¹, B. Bolzon¹, A. Jeremie¹, J. Lottin², B. Caron², R. Oroz²

1- Laboratoire d'Annecy-le-Vieux de Physique des Particules
LAPP-IN2P3-CNRS-Université de Savoie

BP110, F-74941 Annecy-le-Vieux Cedex, FRANCE

Phone: +33450091600, Fax: +33450279495, contact person : E-mail: brunetti@lapp.in2p3.fr

2- Laboratoire SYstèmes et Matériaux pour la MEcatronique

BP80439, F-74944 Annecy-le-Vieux Cedex, FRANCE

Phone: +33450096560, Fax: +33450096543

This article [1] refers to a particular stage of our attempt to reach the stabilization of the linear collider final focus quadrupole. All along this final focus, an absolute displacement has to be lower than the third of nanometre above a few hertz. The presented intermediary step consists in doing active vibrations control of an elementary mechanical structure in cantilever mode which is similar to the final focus. We consider mainly the active compensation and the latest results on a large prototype. Other aspects are also treated such as modelling, active isolation and instrumentation dedicated to the ground motion.

1 The context and the approach

In order to attenuate the motion at the end of a mechanical structure in cantilever mode, the sources of the displacement have to be analysed. In fact, there are two different sources of disturbance, as presented by figure 1.

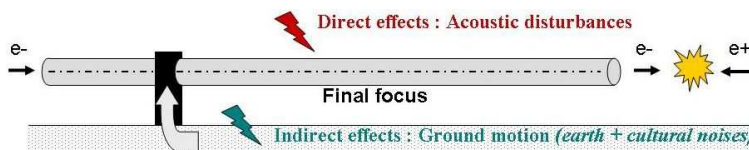


Figure 1: Different sources of disturbance which excite a mechanical structure

The main perturbation is the ground motion, which is in fact a combination of the earth motion lower than 1 hertz and of the cultural noise (pumps, motors, etc.) starting above 1 hertz. This disturbance will be transmitted by the clamping to the structure. Consequently the whole system (clamping and structure) is mainly excited vertically. The second influence is the acoustic perturbations which have a direct effect on the structure and which will excite it in all directions, affecting all resonant modes. Figure 2 represents the ground motion (left figure) and the acoustic pressure without added external disturbances (right figure) measured at LAPP.

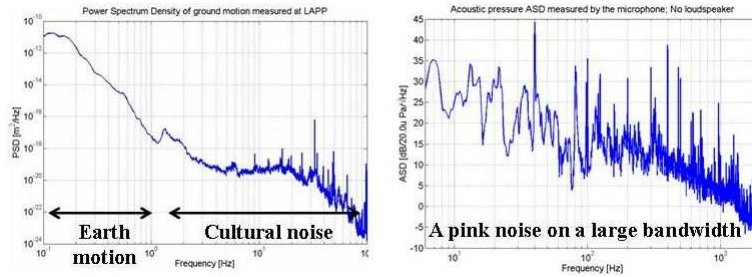


Figure 2: Example of ground motion (left) and acoustic pressure (right) measured at LAPP

As a consequence, we can differentiate two types of motion: the motion of the entire system via the vertical displacement of the clamping due to ground motion [2] and the motion of the mechanical structure itself due to acoustic disturbances [3]. First of all, the stabilization requires isolating the whole system from the ground using active and passive isolation in order to attenuate the vertical displacement of the clamping. In this manner, an almost null displacement of the clamping can be obtained. There is still to cancel the direct effects applied to the structure itself, in order to maintain it in a straight horizontal position along its axis. The only possible solution is then the active compensation, meaning to apply a force that creates a motion in opposition with the motion created by the acoustic disturbance. This study refers mainly to the active compensation, because there are already industrial solutions for the active isolation. The former will be nevertheless treated in the last part.

2 First approach for active compensation

2.1 The first algorithm

For the purpose of controlling the structure motion using the active compensation, one needs an adapted algorithm. In automatics, a controller is generally based on a representative model of the process by optimising the transfer of the system. Considering the final focus, it is too complicated to compute a fine model which is able to reproduce with accuracy the behaviour of this complex mechanical structure, so we consider that the model is unknown. The innovation of this algorithm consists of working only with the measurable behaviour of the process. Furthermore, we have taken into consideration that the measured motion of the mechanical structure does not present itself as a white noise, but is composed of many independent frequencies, some of which are amplified. We have then decided to control independently every main frequency. That means there must be as many algorithms that run at the same time as there are frequencies to reject.

This algorithm is based on the estimation of the effects of disturbances and it computes a sinusoidal control for each disturbance frequency [4]. The principle for one frequency is described in figure 3.

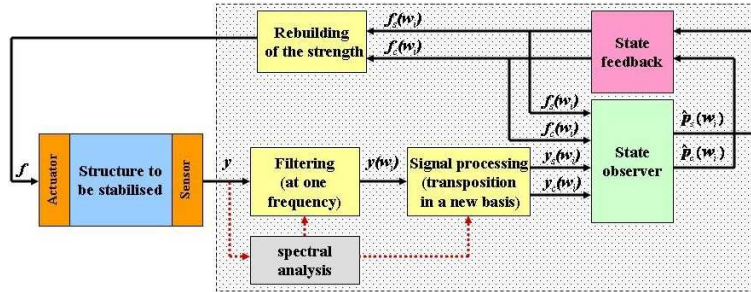


Figure 3: The initial developed algorithm for active compensation

2.2 The experimental setup

In order to validate this algorithm and to analyse its efficiency and robustness, the prototype presented in figure 4 was built [4].

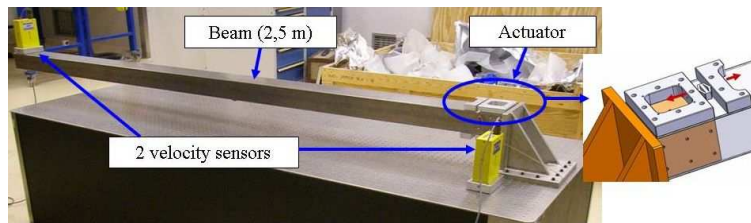


Figure 4: The built mock-up which has similar geometry to the final focus quadrupole

The prototype is composed of a 2,5 meters long steel beam in cantilever mode, just as planned for the final focus. To define the instrumentation, one has to consider the required accuracy and study the impact on the mechanical structure. The velocity sensor SP500B has been chosen, because of its light weight, its small size and its magnetic insensitivity. This sensor is able to measure ultra-low level vibrations because of its very low noise: 0.085 nm integrated noise from 4Hz to 75Hz measured at LAPP. Concerning the actuators, assemblies of piezoelectric patches (APA 25XS from the CEDRAT Company) are used. They allow creating very low displacements at a nanometre scale all along the beam.

2.3 The first results at a nanometre scale

The sensor used for the measurement in the feedback loop was placed at the end of the beam, the part that needs to be stabilised. A second sensor is placed on the clamping in order to measure the perturbation given by the ground motion. We also use an actuator located as close as possible to the clamping, in flexion mode. Figure 5 represents the result of the stabilization in a natural environment, with no added external disturbances. The first two modes of flexion of the beam can be recognized (large peaks) and a lot of unknown other disturbances can be noticed (narrow peaks).

For this test, one of the narrow peaks has been arbitrarily selected (the surrounded peak) and we can observe that the rejection is efficient. It is possible to parallelize the algorithms that reject each of these narrow peaks, in order to reduce as much as possible the motion of the mechanical structure. As a conclusion, we can state that this algorithm is able to reject narrow peaks at a nanometre scale. However, for the eigenfrequencies, this method is quite limited, because working at selected frequency is not sufficient enough to treat a bandwidth.

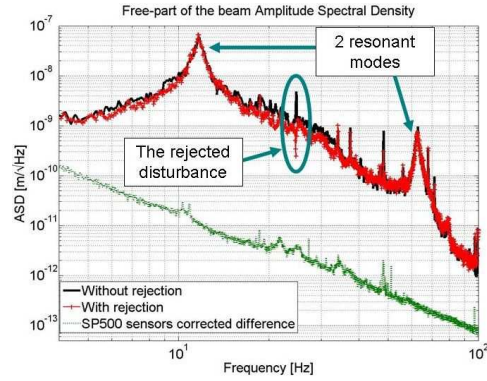


Figure 5: ASD of the displacement at the end of the beam with and without rejection

3 Improvement by using a new algorithm

3.1 The method

The aim of this chapter is to complete the previous method in order to be able to treat all sorts of disturbances, including the frequencies which correspond to the resonant modes of the structure. Because of its complexity, a complete model of the system is too difficult to obtain. Moreover, it is quite limited to work only at a selected frequency, so an intermediary solution was chosen, which consists in using a local model for the different large peaks (meaning the resonant modes of the structure). This algorithm is based on a command with internal model control [5] as described in figure 6 :

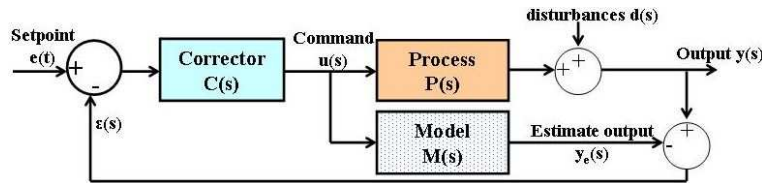


Figure 6: Principle of a classic command with internal model control

It is necessary to consider the transfer function in closed loop of this algorithm :

$$Y(s) = \frac{C(s)P(s)e(s) + [1 - C(s)M(s)]d(s)}{1 + [P(s) - M(s)]C(s)} \quad (1)$$

This equation allows revealing the two fundamental rules of this algorithm. First, in order to follow the setpoint, the controller should be exactly equal to the inverse of the model. Next, to cancel the disturbances, the model doesn't require being exactly equal to the process but only to be an approximation of it, which is an important advantage considering the difficulty in estimating an accurate model. To reach our specific problem of

stabilization, this method has been adapted to our needs. The particularity of our approach is that one algorithm is dedicated only to a bandwidth, so that, instead of using a complete model, only a local one which represents the process on the desired bandwidth is defined. The advantage is that this local model can be defined, having only a basic knowledge of the process behaviour. This knowledge is easy to estimate in experimental mode. The adaptation of the command with internal model control for one bandwidth is described in figure 7 . Notice that the measured and the estimated signals are filtered with a band pass filter in order to process only the desired bandwidth without disturbing the neighbour frequencies. Furthermore, different algorithms can be run in parallel in order to stabilize different bandwidths.

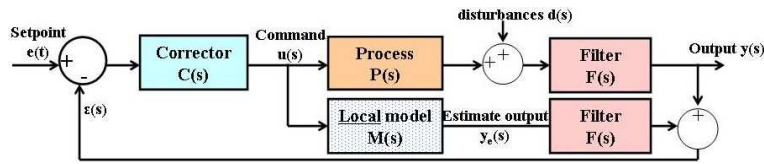


Figure 7: Adaptation of a classic command with internal model control

3.2 Test of the algorithm using a finite element model of the prototype

First of all, this feedback loop algorithm has been tested using a numerical approach in order to evaluate its efficiency. For this step, we computed a finite element model of the prototype under the software SAMCEF. This allowed us to obtain the dynamics equation:

$$M\ddot{u}(t) + C\dot{u}(t) + K(u) = f_p(t) \quad (2)$$

where M is the mass matrix, C is the damping matrix and K the stiffness matrix.

This method allows predicting with accuracy the mechanical structure response in all points in terms of displacement, velocity and acceleration. From the previous dynamics equation, a state-space model is created, using the MATLAB software [6], which can be integrated in a SIMULINK application. It can then be executed with the feedback loop in a simulation test application, as presented in figure 8. An efficient tool is obtained this way. It allows adjusting the feedback loop, increasing the test possibilities (multiple configurations for instrumentation) and analysing the behaviour of the entire beam during an active vibration control.

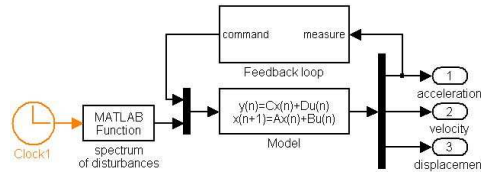


Figure 8: Simulation of the feedback loop with the computed model of the prototype

3.3 Experimental tests

Once this simulation step was completed, the developed feedback-loop algorithm was tested on the large prototype, in the same configuration as previously, with a natural environment.

Two bandwidths were processed, each of them corresponding to a resonant mode of the mechanical structure (12 and 68 Hz). Figure 9 represents the transfer function between the measured displacement at the end of the beam and the measured displacement at the clamping, with and without rejection (left plot) and the integrated displacement root mean square at the clamping and at the end of the beam with and without rejection (right plot).

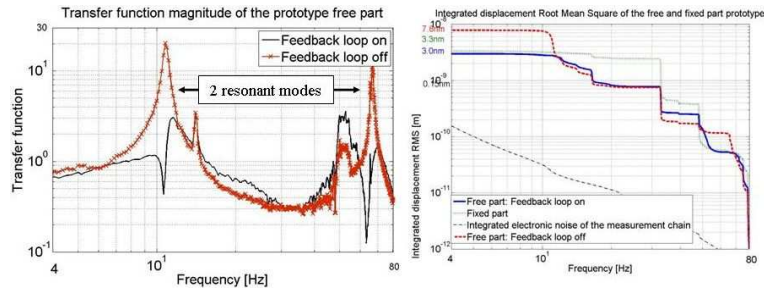


Figure 9: Transfer function between the motion at the end of the beam and the one at the clamping (left) and the integrated displacement RMS with and without rejection (right)

These results reveal that for the two treated bandwidths the algorithm is efficient, since the amplification is considerably reduced. However, the results can be improved, because the processing of a bandwidth has a small detrimental influence on neighbouring frequencies. Even without additional optimization, the displacement at the end of the beam is equal or even lower than the displacement of the clamping. It is expected that when the adjustments will be finished, the absolute displacement of the mechanical structure will be lower than the nanometre, by performing only the active compensation.

4 Combination between active compensation and active isolation

There are two manners of attenuating the motion of a mechanical structure: active compensation and active isolation. The aim of this part is to present the latest experiment done by combining active compensation with active isolation using an industrial solution: an active table with 4 STACIS active isolators, produced by the company TMC [7] (see figure 10).

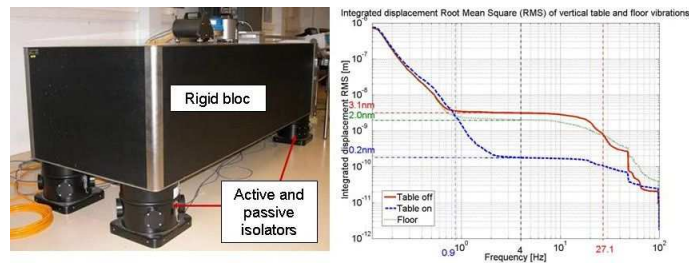


Figure 10: The active table TMC and an obtained integrated displacement RMS

When the beam is placed on this active table, a very low displacement on the clamping is obtained, of about 0.16 nanometres (3 nm with the table OFF). The measured displacement at the end of the beam (without active compensation) is lower than a nanometre (0.25 nm). This displacement is already very low. We also applied the active compensation at approximately the same ratio as previously. The result is a very low displacement, actually an absolute stabilization about a tenth of nanometre, as can be observed in figure 11. This test proves that the instrumentation is not a limitation and that it is possible to stabilize at the tenth of nanometre scale. Now, the objective is to succeed in obtaining the same results but in an environment with more perturbations, meaning when the motion of the structure, is about a few tens of nanometres. Another target is to obtain these results not only on a selected point of the beam, but along the whole length.

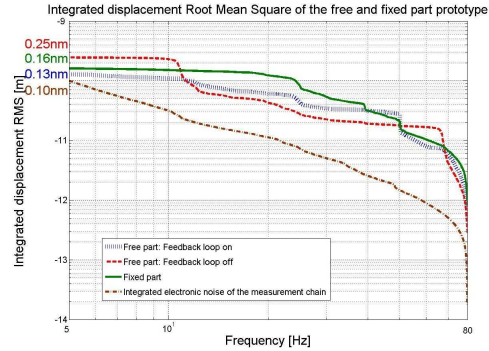


Figure 11: Integrated displacement RMS obtained with the combination of active compensation and active isolation

5 Other development

The active compensation is not enough for treating the case of the future linear collider final focus, because the ground motion (so the clamping displacement) in many measured sites [8] is already greater than the imposed tolerance. In this context, because of the price and the magnetic sensitivity of industrial active tables, we have begun to study the possibility of developing a low cost table [9].

In fact, the principle is based on a mixture of passive isolation and an active solution using actuators. The passive isolation material acts like a low resonant filter, meaning that it attenuates all the high frequency disturbances but amplifies the low frequency ones. Consequently, the high frequency disturbances are already attenuated by the passive solution, so it remains only to reject the low frequency amplified disturbances using the active isolation. In order to reproduce this phenomenon, a small elementary active table has been developed (see figure 12).

This table is composed of two superposed layers. The first one for passive isolation with rubber and the second one for active isolation with actuators (APA25XS). Furthermore, two accelerometers (Endevco 86) are placed on the base and on the table in order to measure the motions at these given points. The figure 13 presents the transfer function between the displacement measured by the sensor on the base of the small table and the displacement measured by the second sensor on the top of it.

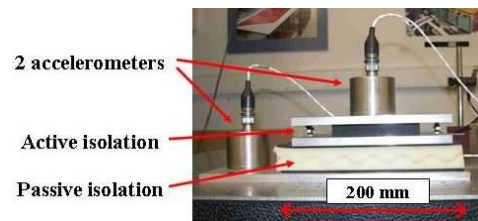


Figure 12: The small elementary active table

We can notice that the behaviour of this rubber (passive isolation) is similar to the behaviour of a resonant low pass filter.

For the active part, an adapted algorithm is required. Contrary to the active compensation, in this case it is possible to determine a model of the built table, so a classical algorithm can be used. We have selected an algorithm (LQG) [10], adapted to noisy systems, so to the seismic domain. This part is currently under development and the next step will be to transpose this study on a large mock-up with industrial rubber, in order to offer a complete solution with the active compensation.

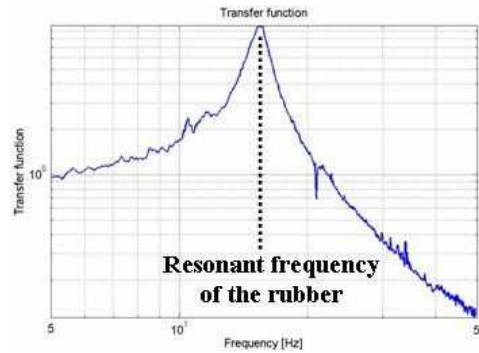


Figure 13: Transfer function on our table

6 Acknowledgments

This work is supported by the Commission of the European Communities under the 6th Framework Programme "Structuring the European Research Area" (RIDS-011899). We also thank the CERN team for allowing us to use their TMC active table.

7 Bibliography

References

- [1] Slides:
<http://ilcagenda.linearcollider.org/contributionDisplay.py?contribId=288&sessionId=90&confId=1296>
- [2] J.Lottin, A.Jeremie *et al.*, Vibration stabilisation for the final focus magnet of a future linear collider, REM 2005, Annecy-le-Vieux, July 2005.
- [3] B.Bolzon, "Direct impact of acoustic noise on the vibrations of a free-fixed beam", ILC 2006 workshop, May 2006, LAL Orsay,
<http://ilcagenda.linearcollider.org/contributionDisplay.py?contribId=39&sessionId=16&confId=293>
- [4] L.Brunetti *et al.*, "Status Report on Active Stabilisation of a Linear Collider Final Focus Quadrupole Mock-Up", EUROTeV-Report-2006-097.
- [5] Y. -S. Lee and S. J. Elliott, "Active position control of a flexible smart beam using internal model control", Journal of Sound and Vibration 242, Issue 5, 2001, pp 767-791.
- [6] N.Geffroy *et al.*, "Creation of a State-Space Model from a Finite Element Model for the active control algorithm efficiency tests", EUROTeV-Report-2007-054.
- [7] B.Bolzon *et al.*, "Modelling of simple cases in view of active stabilisation for a future linear collider", NANOBEAM 2005, Kyoto, Japan.
- [8] R. Amirikas *et al.*, "Measurement of ground motion at various sites", EPAC 2006, Edinburgh, UK.
- [9] Christoph Montag, "Active stabilization of mechanical quadrupole vibrations for linear colliders", Nuclear Instruments and Methods in Physics Research A 378, 1996, pp 369-375.
- [10] Chih-Cherng Ho, Chih-Kao Ma, "Active vibration control of structural systems by a combination of the linear quadratic Gaussian and input estimation approaches", J. Sound and Vib. 301, 2007, pp 429-449

Simulation of LiCAS Error Propagation

G. Grzelak¹, A. Reichold², J. Dale², M. Dawson², J. Green²,
Y. Han², M. Jones², G. Moss², B. Ottewell², R. Wastie²,
D. Kämpfner³, J. Prenting³, M. Schlösser³

1- University of Warsaw - Institute of Experimental Physics,
ul. Hoża 69, 00-681 Warsaw - Poland

2- University of Oxford - Department of Physics
Denys Wilkinson Building, Keble Road, Oxford OX1 3RH - United Kingdom

3- Deutsches Elektronen Synchrotron, DESY,
Notkestrasse 85, 22607 Hamburg - Germany

Linear Collider Alignment and Survey (LiCAS) R&D group is proposing a novel automated metrology instrument dedicated to align and monitor the mechanical stability of a future linear high energy e^+e^- collider. LiCAS uses Laser Straightness Monitors (LSM) and Frequency Scanning Interferometry (FSI) [2, 3] for straightness and absolute distance measurements, respectively. This paper presents detailed simulations of a LiCAS system operating inside a Rapid Tunnel Reference Surveyor (RTRS train). With the proposed design it is feasible to achieve the required vertical accuracy of the order of $\mathcal{O}(200)$ μm over 600 m tunnel sections meeting the specification for the TESLA collider [4].

1 Principle of the LICAS-RTRS train operation

In figure 1 the schematic view of the LiCAS train operating in the accelerator tunnel is presented. The train is composed of 6 cars, the distance between the centres of neighbouring cars is $\sim 4.5 m$. Each car is equipped with 4 CCD cameras and two beam splitters (BS) constituting the straightness monitor. The straightness monitor measures the transverse translation (T_x, T_y) and transverse rotation (R_x, R_y) with respect to a z axis defined by the laser beam passing through all cars in a vacuum pipe. The laser beam is reflected back using the retro-reflector (RR) located in the last car, illuminating the upper CCD cameras of the straightness monitors. 6 FSI lines placed in the same vacuum pipe between each pair of cars are responsible for the distance measurement along the z axis (T_z). In addition a clinometer located on each car provides a measurement of rotation around the z axis (R_z). When the train stops in front of the wall markers it firstly measures the relative position and rotation of all cars with respect to the first car. This defines the local reference frame of the train in which the location of the wall mounted reference markers are measured next. This procedure is repeated for each train stop. Each marker is measured up to 6 times. Finally the coordinates of each marker, expressed in the local train frames are transformed to the frame of the first train (the global frame) by fitting them to each other under the constraint that wall markers have not moved during the entire measurement.

2 Opto-geometrical model of the LICAS-RTRS train

In order to study the expected precision on the position reconstruction of the tunnel reference markers a simulation of the LiCAS survey train was performed. To describe the sensing parts of the train the SIMULGEO [5] package was used which allows for modelling

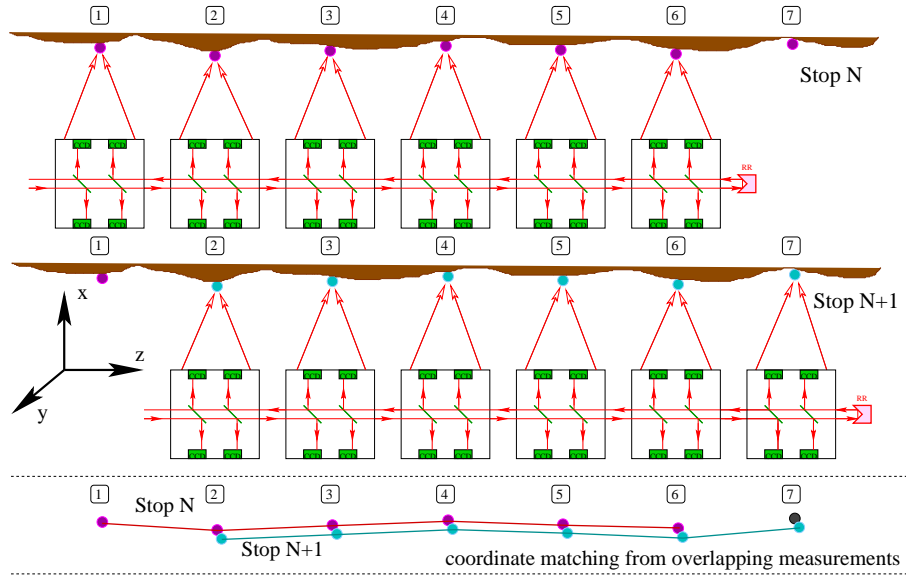


Figure 1: Principle of the LiCAS train operation. Top view of the two train stops along the accelerator tunnel are presented. For detailed description see text.

of the opto-geometrical systems. This software is also capable of performing the full error propagation including correlations between various sub-components linked via common mechanical supports.

2.1 Results of the train simulations

Presented results were obtained assuming the intrinsic resolution of the CCD cameras and FSI lines equal to $\sigma_{CCD} = \sigma_{FSI} = 1 \mu m$. The assumed precision of the clinometer was $\sigma_{tilt} = 1 \mu rad$. The simulation was performed under the assumption that all calibration constants (positions and rotations of CCD cameras, beam splitters, FSI light sources and retro-reflectors) are known to the accuracy of $\sigma_{pos} = 1 \mu m$ for positions and $\sigma_{ang} = 1 \mu rad$ for angles.

The long-distance operation of the train inside the accelerator tunnel was simulated by a set of many identical trains displaced by $4.5 m$ (distance between stops), each pair of them coupled via 5 overlapping wall markers. SIMULGEO calculations provide very precise results (taking into account correlations between subcomponents of the system) based on the exact opto-geometrical model of the survey procedure. However, from the numerical point of view, such an approach, manipulating large matrices, is very time and memory consuming. The 20 train stop results ($90 m$ tunnel section) were obtained after 34 hours of CPU time using $1 GB$ RAM memory on a $2 GHz$ machine (the rank of the used matrix was of the order of 10 000). The numerical complexity of these calculations scale like N^2 , where N is the number of involved coordinates. The simulation of the full $600 m$ tunnel section would require more than 7 weeks of CPU time.

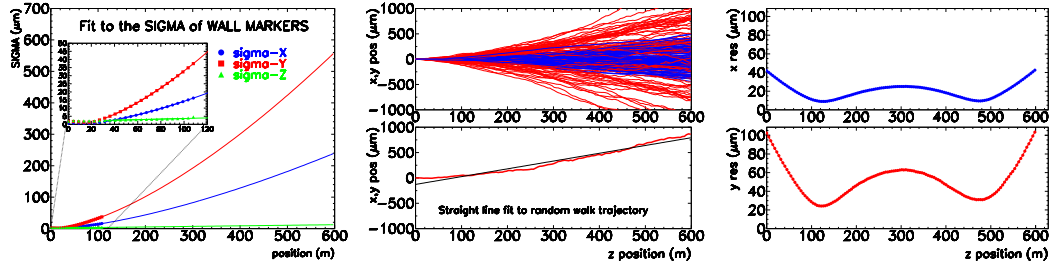


Figure 2: LiCAS train simulation (left plot): insertion contains the results of the exact simulation obtained with the SIMULGEO, extrapolated on the main plot to the 600 m tunnel section using the formula from the random walk model. Examples of the random walk trajectories (upper middle plot) and straight line fit to selected trajectory (lower middle plot). RMS of the residua distribution from the straight line fit to the random walk trajectories: horizontal (upper right plot) and vertical direction (lower right plot).

2.2 Random walk model

To overcome the above mentioned limitations a simplified analytical formula inspired by a random walk model was derived to extrapolate the SIMULGEO predictions over long tunnel sections:

$$\sigma_{xy,n} = \sqrt{l^2 \sigma_\alpha^2 \frac{n(n+1)(2n+1)}{6} + \sigma_{xy}^2 \frac{n(n+1)}{2}}, \quad \sigma_{z,n} = \sqrt{\sigma_z^2 \frac{n(n+1)}{2}} \quad (1)$$

where n is the wall marker number, l is the effective length of the ruler (here: distance between cars), and the corresponding errors are the parameters of the random walk: σ_α is the angular error, σ_{xy} are the transverse errors and σ_z is the longitudinal error. In this approach the procedure of accelerator alignment resembles the construction of a long straight line using short ruler. The overall error is a convolution of the precision of the ruler and the precision of the placement of the ruler with respect to the previous measurement. The asymptotic behaviour of the formulae from equation no. 1 is: $\sigma_{xy,n} \sim n^{\frac{3}{2}}$, and $\sigma_{z,n} \sim n$. This fast growth of errors (especially for transverse directions) is a consequence of the fact that the errors are highly correlated and the precision of the n^{th} element depends on the precision of all previous points. Formulae 1 were fitted to the SIMULGEO points determining σ_α , σ_{xy} , σ_z and then extrapolated over a 600 m tunnel section (fig. 2 left plot). The obtained predictions refer to the precision of the placement of the n^{th} accelerator component with respect to the first one. However this is not the ultimate measure of the quality of the accelerator alignment. The relevant parameter is the mean deviation of each component from the ideal straight line which can be expected from the above procedure. To obtain the final prediction on the deviation of the alignment from the straight line a series of random walk trajectories was generated using the parameters fitted to the SIMULGEO points (fig. 2 middle column). A straight line was fitted to each trajectory and the corresponding residua were calculated. The extracted RMS values of the residua distributions for each marker along 600 m provide the measure of the accuracy of the whole procedure. Because of high correlation between errors for n^{th} and $(n+1)^{\text{th}}$ marker the generated trajectories exhibit

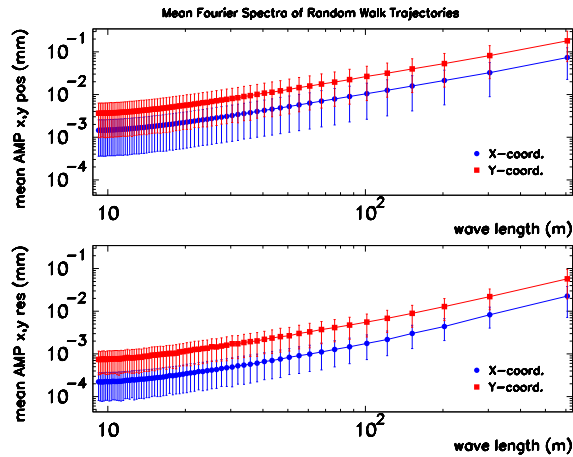


Figure 3: Fast Fourier Transformation (FFT) of random walk alignment trajectories. Mean value for position amplitude (upper plot) and residua amplitude (lower plot) from several Monte Carlo generations is presented.

much smaller oscillations that would be expected from completely random process. Figure 2 (right column) summarises the results obtained in this analysis demonstrating that the vertical precision of the order of $\mathcal{O}(100 \mu m)$ over $600 m$ is feasible.

2.3 Spectral analysis of the alignment trajectories

In order to study the spectra of the alignment trajectories obtained from the LiCAS Random Walk model the Fast Fourier Transformation (FFT) was performed. In figure 3 the mean values of the position and residua amplitude for several Monte Carlo generations is presented for $600 m$ tunnel section. The spectra are dominated by the long wave length components reaching the amplitude of about $50 \mu m$ at $600 m$. In the future more realistic model should also include the white noise component from the short distance 'stake out' measurements.

References

- [1] Slides: <http://ilcagenda.linearcollider.org/contributionDisplay.py?contribId=281&sessionId=90&confId=1296>
- [2] P.A. Coe, D. F. Howell and R. B. Nickerson "Frequency scanning interferometry in ATLAS: remote, multiple, simultaneous and precise distance measurements in a hostile environment", Meas. Sci. Technol. 15 (2004) 2175-2187.
- [3] A.F. Fox-Murphy et al., "Frequency scanned interferometry (FSI): the basis of the survey system for ATLAS using fast automated remote interferometry", Nuclear Instruments and Methods in Physics Research A 383 (1996) 229-237.
- [4] "TESLA, The Superconducting Electron-Positron Linear Collider with an Integrated X-Ray Laser Laboratory", Technical Design Report, DESY 2001-011.
- [5] L. Brunel, "SIMULGEO: Simulation and reconstruction software for optogeometrical systems", CERN CMS Note 1998/079.

GROUND MOTION DATA FOR INTERNATIONAL COLLIDER MODELS

J T Volk, P LeBrun, V Shiltsev, S Singatulin
Fermi National Accelerator Laboratory USA

The proposed location for the International Linear Collider (ILC) in the Americas region is Fermilab in Batavia Illinois. If built at this location the tunnels would be located in the Galena Platteville shale at a depth of 100 or more meters below the surface. Studies using hydro static water levels and seismometers have been conducted in the MINOS hall and the LaFrangé Mine in North Aurora Illinois to determine the level of ground motion. Both these locations are in the Galena Platteville shale and indicate the typical ground motion to be expected for the ILC. The data contains both natural and cultural noise. Coefficients for the ALT law are determined. Seismic measurements at the surface and 100 meters below the surface are presented.

1 Introduction

The proposed location for the International Linear Collider in the Americas region is at Fermilab in Northern Illinois. The preferred depth is 100 or more meters below the surface in the Galena Platteville dolomite. Fermilab and Budker institute have been collaborating on Hydro Static Level systems to measure ground motion for many years. Two of the current systems are in the near MINOS hall on the Fermilab site and the LaFrangé (formerly Conco Western [1]) mine in North Aurora Illinois). Both systems are in the Galena Platteville dolomite. Both systems use Budker institute designed and produced HLS systems to measure the change in floor level. Understanding ground motion due to natural and cultures sources are important for modeling the ILC accelerators and storage rings.

2 Apparatus

The MINOS system has 4 HLS sensors and the LaFrangé Mine has 6 sensors. In both systems the sensors are spaced 30 meters apart. This is similar to the quadrupole spacing proposed for the ILC (37.956 meters). A sensor consists of a stainless steel pool connected with 12.7 mm ID polyethylene tubing to adjoining pools. In the body of the pool there is a temperature sensor that records the water temperature and allows for corrections to be made for expansion due to temperature changes. Each pool sits on a plate with adjustable legs to allow for leveling of each sensor relative to the others.

On top of the pool is the sensor and electronics. The sensor measures the capacitance of the gap between the sensor face and the top of the water. The sensor is heated to prevent condensation; this would interfere with the precision of the measurements. Each sensor has been calibrated before installation. The gap measurement is accurate to 1 micro meter over a range of 10 mm.

A power and data cable daisy chains between each sensor. The data is read out through a National Instruments card into a PC. Software reads out the data at 1 minute (maximum read out of 100 hertz) and stores the data for later analysis.

volk@fnal.gov

Work supported by the U.S. Department of Energy under contract No. DE-AC02-76CH03000

LCWS/ILC 2007

853

Both systems are checked every business day to ensure the sensors and computers are functioning. At the end of every month data taking is automatically stopped and re started. A reset pulse is sent out to each sensor in case a software hang occurred. Figure 1 shows a pool and sensor.

The MINOS hall system became operational in December of 2005 and the LaFrance Mine was rebuilt and became operational in September of 2006.



Figure 1: Budker HLS sensor

With few exceptions for computer hangs there are data for every minute of every month since then. These data are available via a Fermilab data base. The data base is updated every month. The data base is available at <http://rexdb01.fnal.gov:8081/ilc/ILCGroundApp.py/index> The data is timed stamped in one minute intervals using Central time. All levels are in micro meters, temperatures are in degrees C and pressure is in kilo Pascal.

3 Long Term Trends

Data for both systems were compressed by doing a ten minute average of levels and temperatures. This allowed for time plots and Fast Fourier Transforms (FFTs) to be done on the data to reveal trends in natural and cultural noise. Figure 2 is a plot of the difference between 2 sensors 90 meters apart in the MINOS hall for the month of January 2006.

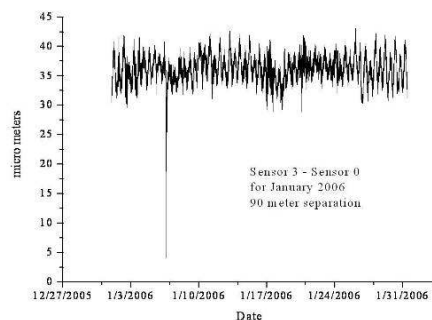


Figure 2: Differences in two sensors 90 meters apart at the MINOS hall for Jan 06

The fast sine wave is due to tidal motion this has a period of 12.4 hours. There is a slower sine wave with a period of 1 week these are the spring and neap tides caused by the relative phases of the sun and moon. The spike that occurs in the first week is due to monthly sump pump testing. There are two electric sump pumps that drain water from the sump pit. The water in the pit varies from a

maximum of 75% full to 25% full. As a back up there is a diesel powered sump pump that is run for 30 minutes each month. This test fully drains the sump pit thereby causing a tilt in the floor. After the test is finished the floor tilts back to it nominal position. Figure 3 shows an expanded view of the sump pump test.

Figure 4 is the same data for December 2005 through March of 2007. The sump pump tests are visible as sharp lines the dip that occurs in the summer months of 2006 may be seasonal more data is required to evaluate this. Figure 5 is a similar plot for the LaFränge data. This is a ten minute average of the difference between two sensors 150 meters apart. There is a clear yearly variation in the motion of the floor.

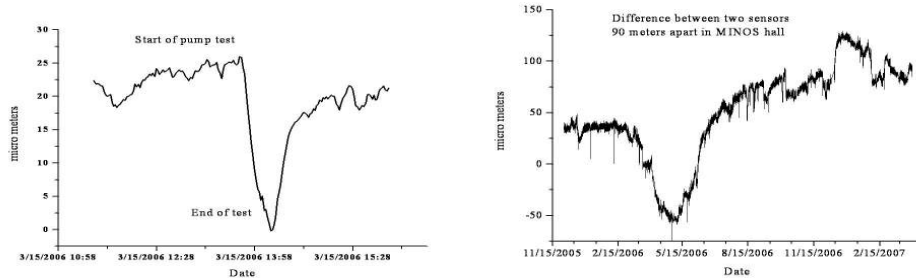


Figure 3: Tilt in floor due to sump pump test Figure 4: Differences in two sensors 90 meters apart at the MINOS hall for Dec 05 to Mar 07

Figure 6 is a Fast Fourier transform of the MINOS data. There is a clear spike at 12.4 hours from the tidal motion and a peak at the 28 day point for the sump pump test.

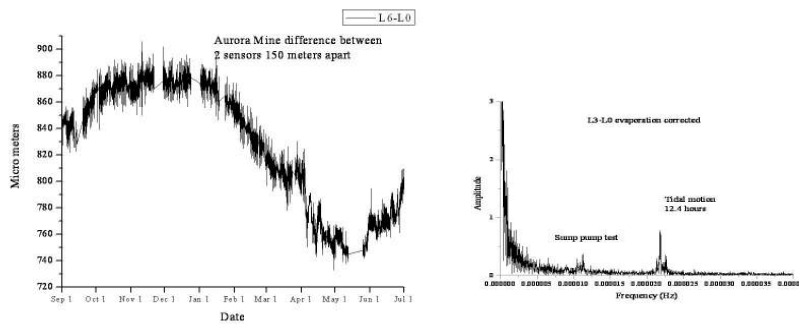


Figure 5 Difference between two sensors 150 meters apart in LaFränge mine Figure 6: shows the FFT for the MINOS data

4 ATL Law

The ATL law was originally proposed in 1991[2 & 3] to describe the relative displacement between two distant ground points. The empirical rule states that the relative displacement dX of two points at distance L apart grows in time T as

$$\langle dX^2 \rangle = 2ATL$$

Where A is on the order of $10^{-5\pm 1} \mu\text{m}^2/\text{s}\cdot\text{m}$ and depends on location. The MINOS and LaFrangé mine data can be used to determine this constant for the Fermilab area. The process is to first calculate the second differences for the system. In the case of the MINOS data there are four sensors L0 through L3 two second differences can be calculated these are;

$$SD012 = L0-2L1-L2$$

$$SD123 = L1-2L2-L3$$

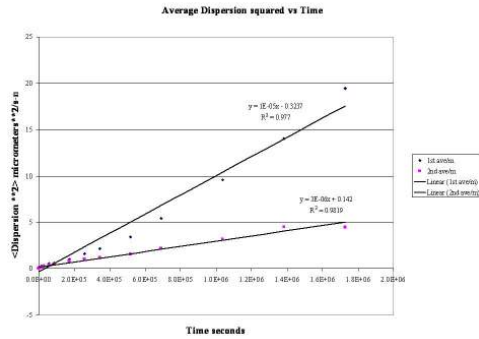


Figure 7 Time vs. average of dispersion yielding the constant for A

Where L0, L1, L2 and L3 are the levels recorded for each sensor in micrometers. The dispersion is then calculated by subtracting the second differences for various time increments ranging for 1 minute (the smallest time value) up to several weeks.

$$D_SD012 = SD012(t) - SD012(t+i)$$

$$D_SD123 = SD123(t) - SD123(t+i)$$

These values are then squared and average for each time increment. The slope of a plot of the means square dispersion versus time yields twice the value of A.

Figure 7 shows data for November 2006 taken in the MINOS hall. The value of A is 5 to $1.5 \cdot 10^{-6} \mu\text{m}^2/\text{s}\cdot\text{m}$.

5 Seismic Motion

Two Budker seismometers one for vertical and one for horizontal were used to measure ground motion in the range of 1 hertz to 200 hertz. Base line measurements were made at the surface on a concrete slab similar measurements were made in the MINOS near hall at a depth of 100 meters below the surface. Figure 8 and 9 show the activity for the surface measurements. There are screw compressors at the Central Helium Liquefier that generate at 4.6 hertz signal all over the site.

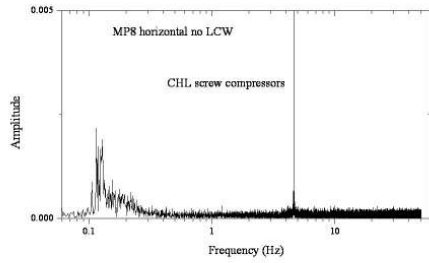


Figure 8 horizontal motions on surface at Fermilab

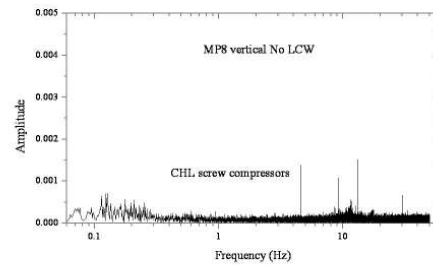


Figure 9 vertical motions on surface at Fermilab

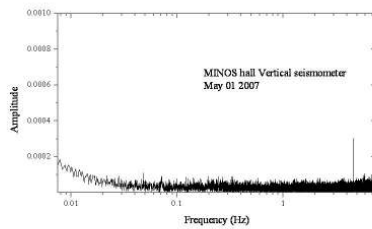


Figure 10 vertical motions 100 meters below surface

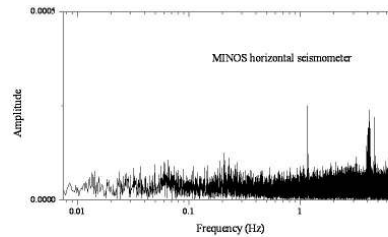


Figure 11 horizontal motions 100 meters below surface

It is clear that there is some attenuation of the culture noise. This is important for the ILC in that many sources of cultural noise can not be eliminated.

6 Conclusions

Data has been collected for over 14 months in a HLS system installed at the depth that the ILC would be built in Illinois. The value of the constant A in the ATL law has been determined to be $5 \text{ to } 1.5 \cdot 10^{-6} \mu\text{m}^2/\text{s}\cdot\text{m}$. In addition a parameterization for tidal motion has been presented. These can be used in modeling the ILC. Cultural seismic noise is attenuated with depth.

7 References

- [1] V Shiltsev et al "VLHC/NLC "Slow Ground motions studies in Illinois" PAC 2001
- [2] B.A. Baklavkov et al "Investigation of Correlation and Power Characteristics of Earth Surface Motion in the UNK Complex Region" PAC 1991
- [3] B.A. Baklavko et al "Study of Seismic Vibrations for the VLEPP Linear Collider" Tech Phys v.38 p 894

Polarization

Conveners: G. Moortgat-Pick, S. Riemann

Polarization aspects in radiative neutralino production

Herbert K. Dreiner, Olaf Kittel*, and Ulrich Langenfeld

Physikalisches Institut der Universität Bonn
Nußallee 12, 53115 Bonn - Germany

We study the impact of beam polarization on radiative neutralino production $e^+e^- \rightarrow \tilde{\chi}_1^0\tilde{\chi}_1^0\gamma$ at the International Linear Collider. We show that longitudinal polarized beams significantly enhance the signal and simultaneously reduce the Standard Model background from radiative neutrino production $e^+e^- \rightarrow \nu\bar{\nu}\gamma$. We point out that the radiative production of neutralinos could be the only accessible SUSY particles, if neutralinos, charginos, sleptons, as well as squarks and gluinos are too heavy to be pair-produced in the first stage of the ILC at $\sqrt{s} = 500$ GeV.

1 Introduction

The Minimal Supersymmetric Standard Model (MSSM) is a promising extension of the Standard Model of particle physics (SM) [2]. At the International Linear Collider (ILC) [3], the masses, decay widths, couplings, and spins of the new SUSY particles can be measured with high precision [4]. In particular, the lightest states like pairs of neutralinos, charginos, and sleptons, can be studied in the initial stage of the ILC, with a center-of-mass energy $\sqrt{s} = 500$ GeV, and a luminosity of $\mathcal{L} = 500 \text{ fb}^{-1}$. The lightest SUSY state is a pair of radiatively produced neutralinos [5–12]

$$e^+ + e^- \rightarrow \tilde{\chi}_1^0 + \tilde{\chi}_1^0 + \gamma. \quad (1)$$

The signal is a single high energetic photon, radiated off the incoming beams or off the exchanged selectrons, and missing energy, carried by the neutralinos [13–15].

2 Signal and background

The main Standard Model background is photons from radiatively produced neutrinos $e^+e^- \rightarrow \nu\bar{\nu}\gamma$ [14, 15]. In order to quantify whether an excess of signal photons from radiative neutralino production, $N_S = \sigma\mathcal{L}$, can be observed over the SM background photons, $N_B = \sigma_B\mathcal{L}$, we define the theoretical significance S , and the signal to background ratio r [11]

$$S = \frac{N_S}{\sqrt{N_S + N_B}} = \frac{\sigma}{\sqrt{\sigma + \sigma_B}}\sqrt{\mathcal{L}}, \quad r = \frac{N_S}{N_B} = \frac{\sigma}{\sigma_B}. \quad (2)$$

For example, a theoretical significance of $S = 1$ implies that the signal can be measured at the statistical 68% confidence level. If the experimental error of the background cross section is 1%, the signal to background ratio must be larger than 1%. A detection of the signal requires at least

$$S > 1 \quad \text{and} \quad r > 1\%. \quad (3)$$

*Speaker

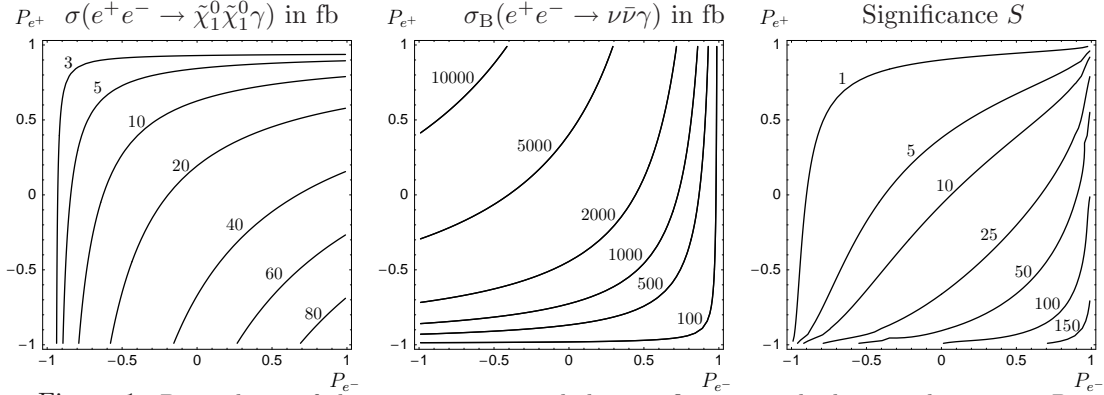


Figure 1: Dependence of the cross sections and the significance on the beam polarizations P_{e^-} , P_{e^+} with $\sqrt{s} = 500$ GeV, $\mathcal{L} = 500$ fb $^{-1}$ for SPS1a with $\mu = 352$ GeV, $M_2 = 193$ GeV, $\tan\beta = 10$, $m_0 = 100$ GeV, $m_{\tilde{\chi}_1^0} = 94$ GeV, and $m_{\tilde{e}_{R(L)}} = 143(204)$ GeV [11].

3 Cuts on photon angle and energy

For the tree-level calculation of the cross sections σ for signal and background, we use the formulas for the amplitudes squared as given in Ref. [11]. To regularize the infrared and collinear divergences, we apply cuts on the photon scattering angle θ_γ and energy E_γ [11]

$$|\cos\theta_\gamma| \leq 0.99, \quad 0.02 \leq x \leq 1 - \frac{m_{\tilde{\chi}_1^0}^2}{E_{\text{beam}}^2}, \quad x = \frac{E_\gamma}{E_{\text{beam}}}, \quad (4)$$

The upper cut on the photon energy $x^{\text{max}} = 1 - m_{\tilde{\chi}_1^0}^2/E_{\text{beam}}^2$ is the kinematical limit of radiative neutralino production. This cut also reduces much of the on-shell Z boson contribution to the background from radiative neutrino production [11]. Note that the ratios r and S do not depend very sensitively on the choice of the cuts $|\cos\theta_\gamma| \leq 0.99$ and $0.02 \leq x$, since signal and background have very similar distributions in energy E_γ and angle θ_γ .

4 Numerical Results

We present numerical results of the signal and background cross sections with emphasis on their dependence on the beam polarization [16], and on the higgsino and gaugino mass parameters μ and M_2 , respectively. Finally we discuss a mSUGRA scenario, where radiative production of neutralinos is the only accessible SUSY state at $\sqrt{s} = 500$ GeV.

4.1 Beam polarization dependence

In Fig. 1, we show the beam polarization dependence of the signal $\sigma(e^+e^- \rightarrow \tilde{\chi}_1^0\tilde{\chi}_1^0\gamma)$ and background cross sections $\sigma_B(e^+e^- \rightarrow \nu\bar{\nu}\gamma)$. In the SPS 1a scenario [17], the neutralino is mostly bino, such that radiative neutralino production dominantly proceeds via right selectron \tilde{e}_R exchange. The background, radiative neutrino production, mainly proceeds via W boson exchange. Thus positive electron beam polarization P_{e^-} and negative positron beam polarization P_{e^+} enhance the signal cross section and reduce the background at the

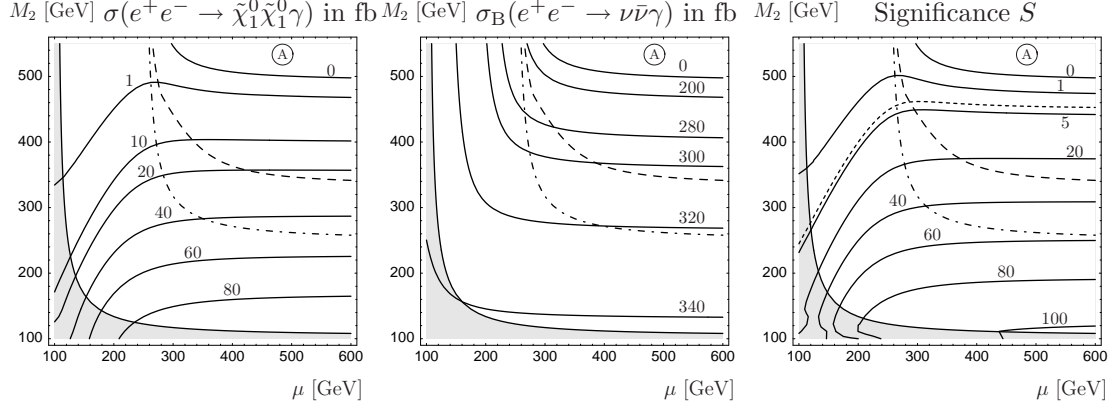


Figure 2: Dependence of the cross sections and the significance on μ , M_2 with $\sqrt{s} = 500$ GeV, $\mathcal{L} = 500 \text{ fb}^{-1}$, $(P_{e^-}, P_{e^+}) = (0.8, -0.6)$, and $\tan\beta = 10$, $m_0 = 100$ GeV [11]. The dashed line indicates the kinematical limit $m_{\tilde{\chi}_1^0} + m_{\tilde{\chi}_2^0} = \sqrt{s}$, and the dot-dashed line the kinematical limit $2m_{\tilde{\chi}_1^\pm} = \sqrt{s}$. Along the dotted line the signal to background ratio is $\sigma/\sigma_B = 0.01$. The area A is kinematically forbidden by the cut on the photon energy E_γ , see Eq. (4). In the gray area $m_{\tilde{\chi}_1^\pm} < 104$ GeV.

same time, such that the significance is greatly enhanced, see Fig. 1. For beam polarizations of $(P_{e^-}, P_{e^+}) = (0.8, -0.3)[(0.8, -0.6)]$, the signal cross section is $\sigma(e^+e^- \rightarrow \tilde{\chi}_1^0 \tilde{\chi}_1^0 \gamma) = 56[70]$ fb, the background is $\sigma_B(e^+e^- \rightarrow \nu\bar{\nu}\gamma) = 540[330]$ fb, such that the significance is $S = 50[80]$, and the signal to background ratio is $r = 10\%[20\%]$. These results should motivate a detailed experimental analysis including Monte Carlo studies [15, 18].

4.2 Dependence on μ and M_2

In Fig. 1, we show contour lines of the signal $\sigma(e^+e^- \rightarrow \tilde{\chi}_1^0 \tilde{\chi}_1^0 \gamma)$ and background cross section $\sigma_B(e^+e^- \rightarrow \nu\bar{\nu}\gamma)$ in the μ - M_2 plane. The signal is decreasing for increasing M_2 , since the neutralino mass $m_{\tilde{\chi}_1^0}$ and the selectron mass $m_{\tilde{e}_R}$ are increasing. For decreasing values of $\mu \lesssim 300$ GeV, the bino component of the neutralino is decreasing, leading to a decreasing signal cross section $\sigma(e^+e^- \rightarrow \tilde{\chi}_1^0 \tilde{\chi}_1^0 \gamma)$. Note that the background cross section also depends on μ and M_2 , since the kinematical cuts include the neutralino mass, see Eq. (4). In Fig. 1, we also indicate the kinematical limits of the production of neutralinos $e^+e^- \rightarrow \tilde{\chi}_1^0 \tilde{\chi}_2^0$ (dashed line) and charginos $e^+e^- \rightarrow \tilde{\chi}_1^+ \tilde{\chi}_1^-$ (dot-dashed line). Above these lines, the radiative production of neutralinos is the only kinematically allowed SUSY state, which can however be observed with a significance of up to $S = 20$.

4.3 The only state to be observed?

Consider, as an example, the mSUGRA scenario $M_0 = 200$ GeV, $M_{1/2} = 415$ GeV, $A_0 = -200$ GeV, and $\tan\beta = 10$. In this scenario, we have $M_2 = 349$ GeV, $\mu = 560$ GeV, and the particle masses are $m_{\tilde{\chi}_{1(2)}^0} = 180(344)$ GeV, $m_{\tilde{\chi}_1^\pm} = 344$ GeV, $m_{\tilde{\tau}_1} = 253$ GeV, $m_{\tilde{e}_{R(L)}} = 261(356)$ GeV. The neutralinos, charginos and selectrons are too heavy to be pair produced at $\sqrt{s} = 500$ GeV. However, neutralinos can still be radiatively produced. In

(P_{e^+}, P_{e^-})	(0 0)	(0 0.8)	(-0.3 0.8)	(0 0.9)	(-0.3 0.9)	(-0.6 0.8)
$\sigma(e^+e^- \rightarrow \tilde{\chi}_1^0 \tilde{\chi}_1^0 \gamma)$	4.7 fb	8.2 fb	11 fb	8.6 fb	11.2 fb	13 fb
$\sigma_B(e^+e^- \rightarrow \nu \bar{\nu} \gamma)$	3354 fb	689 fb	495 fb	356 fb	263 fb	301 fb
S	1.8	7	11	10	15	17
r	0.1%	1.2%	2.2%	2.4%	4.3%	4.4%

Table 1: Cross sections, significance S , and signal to background ratio r , for different sets of beam polarizations, for $\sqrt{s} = 500$ GeV, $\mathcal{L} = 500$ fb $^{-1}$, and $M_0 = 200$ GeV, $M_{1/2} = 415$ GeV, $A_0 = -200$ GeV, $\tan \beta = 10$ [12].

Table 1, we show the cross section and the background from radiative neutrino production for different sets of beam polarizations with $P_{e^+} = 0, -0.3, -0.6$ and $P_{e^-} = 0, 0.8, 0.9$. Polarized beams enhance the signal, in particular the background is strongly reduced by a high degree of electron polarization $P_{e^-} = 0.9$. Note that without beam polarization, the signal cannot be observed.

4.4 Summary and conclusions

A pair of radiatively produced neutralinos $e^+e^- \rightarrow \tilde{\chi}_1^0 \tilde{\chi}_1^0 \gamma$ is the lightest state of SUSY particles to be produced at e^+e^- colliders. The signal is a single high energetic photon and missing energy. The signal could not be observed at LEP due to the large background from radiative neutrino production $e^+e^- \rightarrow \nu \bar{\nu} \gamma$. At the ILC, however, polarized beams enhance the signal and simultaneously reduce the background. We have shown that the significance for observing the signal can be as large as $S = 100$, and that the signal to background ratio can be as large as $r = 20\%$. These results should motivate detailed experimental studies, to learn as much as possible about Supersymmetry through the process of radiatively produced neutralinos.

References

- [1] Slides:
<http://ilcagenda.linearcollider.org/contributionDisplay.py?contribId=53&sessionId=69&confId=1296> and
<http://ilcagenda.linearcollider.org/contributionDisplay.py?contribId=247&sessionId=92&confId=1296>
- [2] H. E. Haber and G. L. Kane, Phys. Rept. **117**, 75 (1985).
- [3] <http://www.linearcollider.org/wiki/doku.php>
- [4] See, for example, J. A. Aguilar-Saavedra *et al.*, Eur. Phys. J. C **46** (2006) 43 [arXiv:hep-ph/0511344].
- [5] A. Datta, A. Datta and S. Raychaudhuri, Phys. Lett. B **349** (1995) 113 [arXiv:hep-ph/9411435].
- [6] S. Ambrosanio, B. Mele, G. Montagna, O. Nicosini and F. Piccinini, Nucl. Phys. B **478** (1996) 46 [arXiv:hep-ph/9601292].
- [7] A. Datta, A. Datta and S. Raychaudhuri, Eur. Phys. J. C **1** (1998) 375 [arXiv:hep-ph/9605432].
- [8] S. Y. Choi, J. S. Shim, H. S. Song, J. Song and C. Yu, Phys. Rev. D **60** (1999) 013007 [arXiv:hep-ph/9901368].
- [9] H. Baer and A. Belyaev, [arXiv:hep-ph/0111017].
- [10] A. Datta and A. Datta, Phys. Lett. B **578** (2004) 165 [arXiv:hep-ph/0210218].
- [11] H. K. Dreiner, O. Kittel and U. Langenfeld, Phys. Rev. D **74** (2006) 115010 [arXiv:hep-ph/0610020].
- [12] H. K. Dreiner, O. Kittel and U. Langenfeld, arXiv:hep-ph/0703009.

- [13] G. W. Wilson, LC-PHSM-2001-010.
- [14] A. Birkedal, K. Matchev and M. Perelstein, Phys. Rev. D **70** (2004) 077701 [arXiv:hep-ph/0403004].
- [15] C. Bartels, Diploma Thesis, *Model-independent WIMP searches at the ILC*, DESY 2007.
- [16] G. A. Moortgat-Pick *et al.*, arXiv:hep-ph/0507011.
- [17] B. C. Allanach *et al.*, in *Proc. of the APS/DPF/DPB Summer Study on the Future of Particle Physics (Snowmass 2001)* ed. N. Graf, Eur. Phys. J. C **25** (2002) 113 [eConf **C010630** (2001) P125] [arXiv:hep-ph/0202233].
- [18] C. Bartels *et al.*, in preparation.

Incoherent pair background processes with full polarizations at the ILC

A. Hartin¹ *

Oxford University - Physics Department
Keble Road, Oxford OX3 7TF- UK

Incoherent background pair production processes are studied with respect to full polarizations of all states. Real initial photon polarizations are obtained via a QED calculation of the beamstrahlung process. Virtual photon polarizations are related to the electric field of the colliding bunches at the point of pair production. An explicit expression for the virtual photon polarization vector is developed and found to have no circular polarization component. Pair polarization states are highly dependent on initial state circular polarization and are consequently produced almost unpolarized. The Breit-Wheeler cross-section with full polarizations is calculated and coded into the CAIN pair generator program. Numerical evaluations of the ILC, operating with the seven proposed collider parameter sets, shows that there are 10 – 20% less low energy pairs than previously thought. Collider luminosity, as calculated by CAIN, remains the same.

1 INTRODUCTION

The International Linear Collider will collide polarized particle bunches to produce physics processes of interest and background events. The polarization states of both the bunch particles and the collective field of the bunch are important parameters affecting cross-sections and hence final particle states. It is important to calculate precisely the full polarization effects and this will be done here for incoherent background pair processes resulting from beam-beam interactions. A theoretical exposition will be required and the program CAIN will be modified for full polarizations in order to produce numerical results.

There are three incoherent background pair processes considered to produce background e^\pm pairs at the ILC. The Breit-Wheeler process, has two real photons in its initial state. The Bethe-Heitler and Landau-Lifshitz processes contain initial states of one and two virtual photons respectively. The flux of virtual photons is established using the well known Weizsacker-Williams virtual photon approximation. In all three processes, once the initial particle states are established, the same Breit-Wheeler cross-section is used to calculate the total number of background pair particles produced via beam-beam collisions. Three important theoretical expressions are necessary; the polarization of initial real and virtual photon states, the Breit-Wheeler cross-section containing all polarization states, and the polarization of final states.

2 THEORY

Real photons engaged in pair production processes are produced via the beamstrahlung process. The present version of CAIN contains full polarizations for this process and the representation in Stokes parameters is given in equation 5.510 of the CAIN manual [1]. An expression for virtual photon polarization states in terms of Stokes parameters has to be developed. The Stokes parameter of a

*This work is supported in part by the Commission of the European Communities under the 6th Framework Programme "Structuring the European Research Area", contract number RIDS-011899.

virtual photon with 3-momentum \hat{k} can be written in terms of the normalised polarization vector $(\hat{e}_x, \hat{e}_y, \hat{k}_z)$ as

$$\begin{aligned}\xi_1 &= \hat{e}_x \hat{e}_y^* + \hat{e}_y \hat{e}_x^* \\ \xi_2 &= \Im[\hat{e}_y \hat{e}_x^* - \hat{e}_x \hat{e}_y^*] \\ \xi_3 &= \hat{e}_x \hat{e}_x^* - \hat{e}_y \hat{e}_y^*\end{aligned}\tag{1}$$

To obtain an explicit form for the Stokes parameters it is recognised that the virtual photon polarization vector can be identified with the spectral component E_ω of the electric field of the particle bunch. The expression for E_ω is written down first from the expansion of the electric field E_q of a single relativistic particle of speed v in plane waves with wave vector $q = (q_x, q_y, q_z)$. The electric field of a bunch of N such charges is a product of the Gaussian form factor of the bunch and E_q integrated over all wave vector components [2]. The spectral component of the collective field at position (x, y) is written finally

$$E_\omega^{x,y} = -\frac{ie}{\pi v} \iint \frac{q_{x,y}}{q_x^2 + q_y^2} F(q) \exp(ixq_x + iyq_y) dq_x dq_y\tag{2}$$

where $F(q) = N \exp[-\frac{1}{2}(q_x \sigma_x)^2 - \frac{1}{2}(q_y \sigma_y)^2]$

Equation 2 is a difficult Fourier transform over two variables. Progress is made by separating variables via a Taylor expansion of $\frac{1}{q_x^2 + q_y^2}$. Fourier transforms in q_x and q_y are then easily calculated and terms in the Taylor expansion turn out to be dependent on a ratio of transverse beam sizes $\frac{\sigma_y}{\sigma_x}$. For the flat beam envisaged for the ILC, this ratio is very small and only the first term in the Taylor expansion is required. The spectral component of the beam field turns out to be

$$\begin{aligned}E_\omega^x &= -\frac{e}{\pi v} \exp(-\frac{x^2}{2\sigma_x^2}) \frac{x}{\sigma_x^3} \left[\exp(-\frac{y^2}{2\sigma_y^2}) + y \sqrt{\frac{\pi}{2}} \text{Erf} \left(\frac{y}{\sqrt{2}\sigma_y} \right) \right] \\ E_\omega^y &= \frac{e}{\pi v} \sqrt{\frac{\pi}{2}} \exp(-\frac{x^2}{2\sigma_x^2}) \frac{1}{\sigma_x} \text{Erf} \left(\frac{y}{\sqrt{2}\sigma_y} \right)\end{aligned}\tag{3}$$

The expressions in equation 3 are numerically easy to calculate and are inserted into CAIN. The magnitude of the y component of the bunch field E_ω^y is much greater than that of the x component. This is consistent intuitively with the bunch being squeezed in y. Both components are real, rendering $\xi_2 = 0$, meaning that there is no circular polarisation of virtual photons. This is consistent with the constant crossed electromagnetic fields associated with relativistic charges.

In order to take advantage of the full polarisation of initial photons, the full Breit-Wheeler cross-section is required. At present in CAIN the cross-section σ^{circ} is written down only for the product of circular polarisations $\xi_2 \xi_2'$ of initial photons k and k' . The full cross-section σ^{full} is a sum over all polarisation states and functions of final electron energy ϵ and momentum p [3]. With some algebraic manipulation the two cross-sections can be written in similar form

$$\begin{aligned}
\sigma^{\text{circ}} &\propto 2\left(1 - h_2 + \frac{2\epsilon^2 - 1}{2\epsilon^2}\right) \sinh^{-1} p + \frac{p}{\epsilon} \left(3h_2 - 1 - \frac{1}{\epsilon^2}\right) \\
\sigma^{\text{full}} &\propto 2\left(1 - h_2 + \frac{2}{\epsilon^2}(h_1 + h_3) - \frac{h_3}{\epsilon^4}\right) \sinh^{-1} p \\
&\quad + \frac{p}{\epsilon} \left(3h_2 - 1 - h_1 - \xi_3 \xi'_3 - \frac{h_3}{\epsilon^2}\right)
\end{aligned} \tag{4}$$

where $h_1 = \xi_1 \xi'_1$ $h_2 = \xi_2 \xi'_2$
 $h_3 = 1 + \xi_3 + \xi'_3 + \xi_3 \xi'_3$

The final analytic expression required for a full investigation of polarization effects, are the polarizations of final states. These are specified by the e^\pm polarization vector $(\zeta_1, \zeta_2, \zeta_3)$ and can be written in terms of a sum over products of initial polarization states and a function $F_{jj'}^{ii'}$ of 4-vector scalar products [3]

$$\zeta_i = \frac{1}{F} \sum_{ijj'} F_{jj'}^{i0} \xi_j \xi'_j \quad \text{where} \quad F = \sum_{jj'} F_{jj'}^{00} \xi_j \xi'_j \tag{5}$$

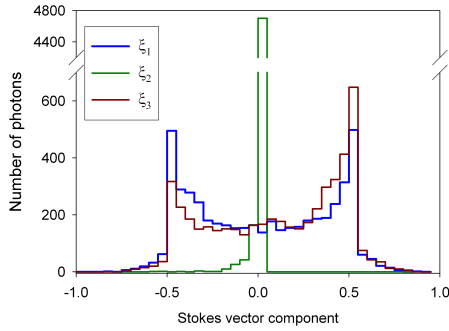


Figure 1: Stokes parameters of initial photons.

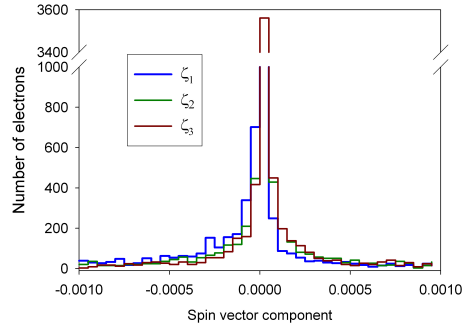


Figure 2: Polarization of final fermions.

3 NUMERICAL RESULTS

Modifications of the CAIN program were kept to a minimum by writing new analytic expressions in forms similar to those already existing in CAIN. The monte carlo scheme that determines whether a particular pair production process will take place relies on the Breit-Wheeler cross-section structure with respect to final electron energy and momentum (ϵ, p) (equation 4). Other required CAIN modifications were the extension of existing polarization vectors to all components, and use was made of the existing basis vector structure in CAIN.

Initial photon states, for both real and virtual particles, reveal almost no circular polarization component ξ_2 (figure 1). This is a consequence of the constant, crossed beam electromagnetic field which is source of real beamstrahlung photons and with which virtual photons are identified. The components of final e^\pm polarization vector are strongly dependent on the extent of circular polarization of initial photons. Consequently the pairs are produced with almost no polarization components (figure 2).

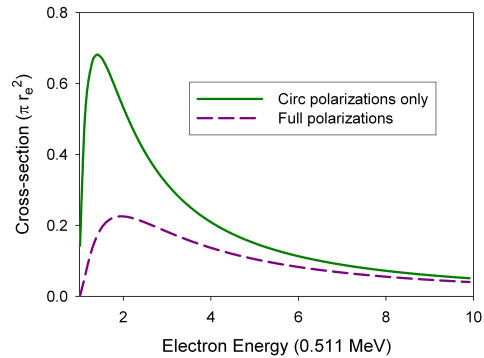


Figure 3: Breit-Wheeler cross-section.

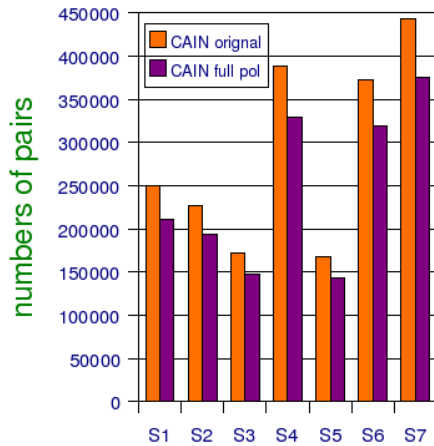


Figure 4: Pair numbers for seven parameter sets.

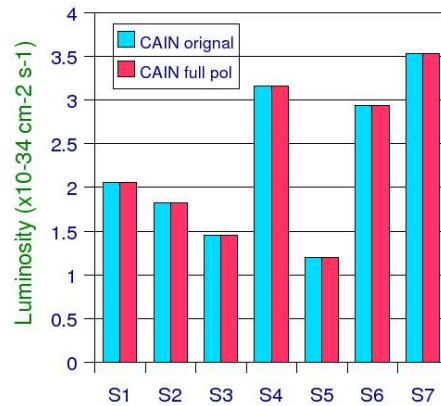


Figure 5: Luminosity for seven parameter sets.

A numerical investigation of the two cross-sections in equation 4 reveal the usual peak at low energies. However accounting for full polarizations reveals a substantially reduced cross-section for electron energies approximately less than 50 MeV (figure 3). It was expected that such a reduction in the Breit-Wheeler cross-section would result in less background pairs. It was also considered important to determine any effect on collision luminosity. So the modified CAIN program was run for all seven 500 GeV centre of mass collider parameter sets [4]. There was a 10 – 20% overall reduction in pairs (figure 4) with no discernible effect on collision luminosity (figure 5)

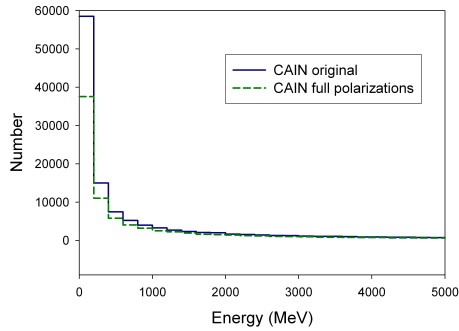


Figure 6: Energy of final pairs.

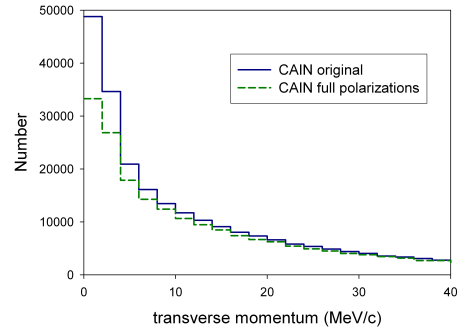


Figure 7: Transverse momentum of final pairs.

The energy and momentum of the new ensemble of expected pairs was also obtained. The short-fall in pair backgrounds was almost entirely made up of low energy and low transverse momentum pairs (figures 6 and 7).

4 CONCLUSION

The full polarizations of initial states, final states and the Breit-Wheeler cross-section have been investigated analytically and numerically. This enables the effect of full polarizations on three incoherent background pair processes to be determined. Real beamstrahlung photons have almost no circular polarization component. Virtual photon polarization is related to the constant, crossed bunch electric field at the point of production and likewise has no circular polarization component. The full Breit-Wheeler cross-section with all polarization states was written in similar form to the Breit-Wheeler cross-section with circular polarizations only. The CAIN program was modified and run for the seven parameter sets contemplated for the ILC with 500 GeV centre of mass collision energy. In all cases analysis of the full polarization effects revealed that there were 10 – 20% less low energy background pairs than was previously thought. At the same time there was no discernible change in collision luminosity.

References

- [1] CAIN Users Manual, Version 2.35 (2003)
- [2] R. Engel, A.Schiller, V.G. serbo, Z Phys C, 71 (1996) 651.
- [3] V.N. Baier, A.G.Grozin, hep-ph/0209361
- [4] T. Raubenheimer, "Suggested ILC Beam Parameter Range"

Polarised Geant4 – Applications at the ILC

Andreas Schälicke¹, Karim Laihem² and Pavel Starovoitov³

1- DESY

Platanenallee 6, 15378 Zeuthen - Germany

2- RWTH Aachen - Phys. Inst. IIIB

Physikzentrum, 52056 Aachen- Germany

3- NCPHEP BSU

M.Bogdanovich str. 153, 220040 Minsk - Belarus

Geant4 is a Monte Carlo simulation framework for the description of interactions of particles and matter. Starting with version 8.2 a new package of QED physics processes is available, allowing for the studies of interactions of polarised particles with polarised media dedicated to beam applications. In this contribution some details about the implementation are presented and applications to the linear collider are discussed.

1 Introduction

Programs that can simulate the complex interaction patterns of particles traversing matter are indispensable tools for the design and optimisation of particle detectors. A major example of such programs is Geant4 [2, 3], which is widely used in high energy physics, medicine, and space science. Different parts of this tool kit can be combined to optimally fulfil the users needs. A powerful geometry package allows the creation of complex detector configurations. The physics performance is based on a huge list of interaction processes. Tracking of particles is possible in arbitrary electromagnetic fields. However, polarisation has played only a minor role so far^a.

The new extension in the library of electromagnetic physics is dedicated to polarisation effects in beam applications [4]. It aims for a proper treatment of longitudinal polarised electrons/positrons or circularly polarised photons and their interactions with polarised matter.

Polarised versions of Bhabha/Møller scattering (B/MS), electron-positron annihilation (EPA), Compton scattering (CS), pair creation (PC), and bremsstrahlung (BS) are already part of the polarisation library. A polarised version of the Photoelectric Effect is in preparation.

Two basic problem classes are addressed:

- *Polarisation transfer* from initial beam particles to secondaries created in material interactions can be investigated. For instance, in the context of the ILC positron source a detailed study of the production mechanism of polarised positrons from photons emitted from a helical undulator is now possible.
- Interactions of polarised particles with polarised matter can be simulated. In general, asymmetries may be observed if beam and target particles are polarised. They manifest themselves in total cross sections as well as in differential distributions, which provides the basis of applications in *polarimetry*.

^aCompton scattering of linearly polarised photons is available since Geant4 version 3.1. Polarised Rayleigh scattering and Photoelectric effect of linearly polarised photons have been addressed recently.

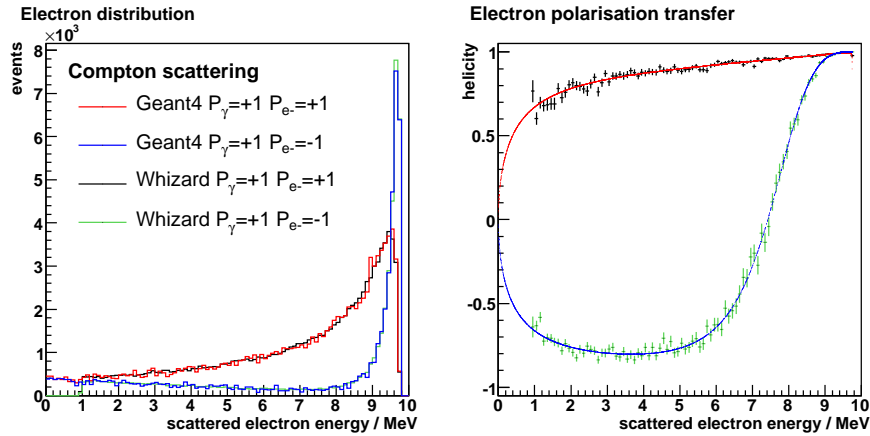


Figure 1: Compton scattering. Distribution (left) of electrons and their degree of polarisation (right) are compared with results from Whizard/O’mega for different initial state helicities [15].

These new features have already been exploited in the analysis of data from the E166 experiment [5], and are also used in studies for an anticipated low energy polarimeter [6] as well as in design and performance optimisation studies for an ILC positron source [7].

2 The new polarisation library

Several simulation packages for the realistic description of the evolution of electromagnetic showers in matter have been developed. A prominent example is EGS (Electron Gamma Shower)[8]. For this simulation framework, extensions with the treatment of polarised particles exist [9, 10]; the most complete has been developed by [11]. It is based on the matrix formalism [12], which enables a very general treatment of polarisation. However, the Flöttmann extension concentrates on evaluation of polarisation transfer, i.e. the effects of polarisation induced asymmetries are neglected, and interactions with polarised media are not considered. Another important simulation tool for detector studies is GEANT3 [13]. Here also some effort has been made to include polarisation [5, 14], but these extensions are not publicly available.

In general, the implementation of polarisation in the library in Geant4 follows very closely the approach by [12]. A *Stokes vector* is associated to each particle and used to track the polarisation from one interaction to another.

Five new process classes for CS, BS, B/MS, PC, EPA with polarisation are now available for physics studies with Geant4. The implementation has been carefully checked against existing references, alternative codes, and dedicated analytic calculations. Figure 1 shows exemplarily a comparison of electron distribution and polarisation transfer in Compton scattering using Whizard/O’mega^b [15]. Further details can be found in [16, 17].

^bWhizard/O’mega is a multipurpose matrix element generator allowing for polarisation in the initial state. It is dedicated to high energy collision with many particles in the final state, but can also be used to calculate polarised $2 \rightarrow 2$ cross sections, like e.g. Compton scattering.

3 Applications to the ILC

A key feature of the ILC will be that both beams – electrons and positrons – are polarised. With the new polarisation extension it is now possible to investigate details of the production mechanism and polarimetry options for electrons and, in particular, for positrons.

The degree of electron and positron polarisation should be known at least to an accuracy of a few per mill at the collision point to take full advantage of measurements with polarised beams.

3.1 Polarised positron source

In the baseline design of the ILC [19] polarised positrons are produced from circularly polarised photons created in an helical undulator hitting a thin Ti target. The spin of the photon is transferred to the electron-positron pairs produced resulting in a net polarisation of the particles emerging from the target. The positrons are captured just behind the target in a dedicated capture optics, i.e. an adiabatic matching device, and their degree of polarisation has to be maintained until they reach the collision point.

Figure 2 pictures energy distribution of photons and their degree of polarisation as expected from an ideal helical undulator with strength $K = 1$ and period $\lambda = 1$ cm. The resulting positron energy and polarisation distributions after the production target are shown in Figure 3.

3.2 Low energy polarimeter

For commissioning and optimisation of the ILC operation, an independent check of the polarisation near the creation point of positrons is recommended. A Bhabha polarimeter [6] is a promising candidate to realise a low energy positron polarisation measurement. There, a thin magnetised iron foil (few $10\mu\text{m}$ thick) is placed in the positron beam. A few of the positrons hitting the foil undergo Bhabha scattering. Rate and distribution of the scattered electrons and positrons depend on the polarisation of the beam, and can be exploited for polarimetry. The dominating background are bremsstrahlung positrons, which can be substantially reduced by looking at the electron distribution only.

The left part of Figure 4 shows an energy vs. angle distribution of electrons emerging from a $30\mu\text{m}$ iron foil hit by a beam with $2 \cdot 10^{10}$ positrons of 200 MeV. The right part of

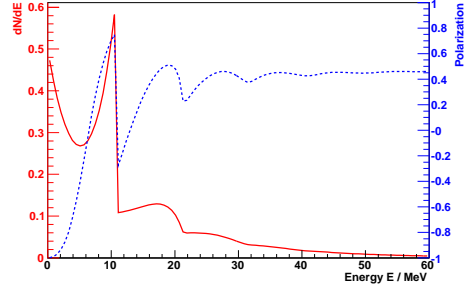


Figure 2: Energy (red) and polarisation (blue) of photons created in a helical undulator.

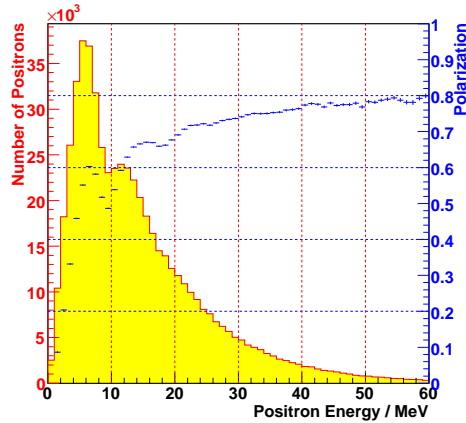


Figure 3: Energy (red) and polarisation (blue) of positrons after the production target of thickness $d = 0.4X_0$.

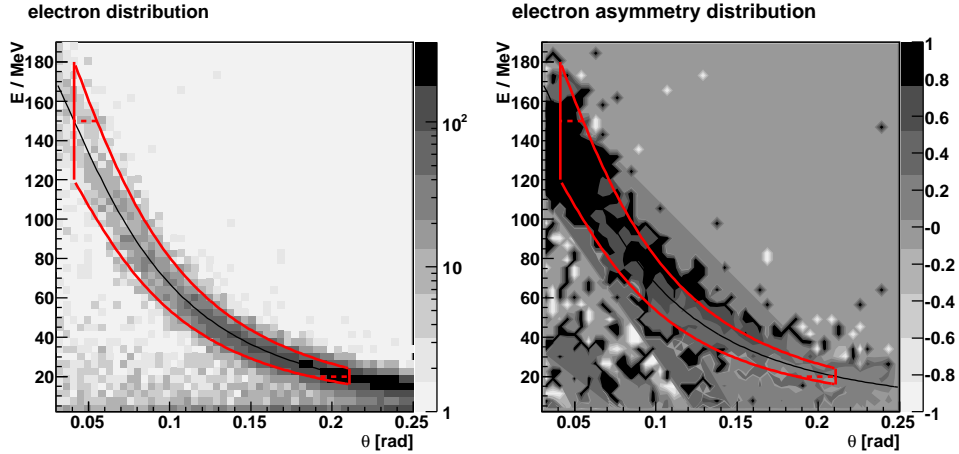


Figure 4: Angular distribution of electrons (left) and analysing power (right).

Figure 4 gives the corresponding analysing power. In the central acceptance approx. 10^4 electrons per positron bunch are expected with an analysing power of about 40%.

3.3 The E166 experiment

A proof-of-principle experiment has been carried out at SLAC to demonstrate the production of polarised positrons in a manner suitable for implementation at the ILC [5]. A helical undulator of 2.54 mm period and 1 m length produced circularly polarised photons, with a first harmonic endpoint energy of 8 MeV, when traversed by a 46.6 GeV electron beam. The polarised photons were converted to polarised positrons in a 0.2-radiation-length tungsten target. The polarisation of these positrons was measured at several energies using a Compton transmission polarimeter.

Geant4 simulations using the polarisation extension have been employed in the determination of the expected polarisation profile. These simulations also provided the basis for the determination of the analysing power needed to determine the polarisation of the produced positron beam. Further details may be found in [1, 16, 18].

4 Summary

Starting with version 8.2 a new package of QED physics processes has been added to the Geant4 framework, allowing studies of polarised particle interactions with polarised media. Applications include design and optimisation of a polarised positron source and beam polarimetry for a future linear collider facility.

Acknowledgements

The authors are indebted to A. Stahl as the initiator of this project, and also would like to thank T. Lohse and S. Riemann for fruitful collaboration, and helpful discussions.

References

- [1] Slides: <http://ilcagenda.linearcollider.org/contributionDisplay.py?contribId=253&sessionId=92&confId=1296>
- [2] S. Agostinelli *et al.* [GEANT4 Collaboration], Nucl. Instrum. Meth. A **506** (2003) 250.
- [3] J. Allison *et al.* [GEANT4 Collaboration], IEEE Trans. Nucl. Sci. **53** (2006) 270.
- [4] R. Dollan, K. Laihem and A. Schälicke, Nucl. Instrum. Meth. A **559** (2006) 185.
- [5] G. Alexander *et al.*, SLAC-TN-04-018, SLAC-PROPOSAL-E-166.
- [6] K. Laihem *et al.*, Proceedings of EPAC 2006, WEPLS045.
- [7] A. Ushakov *et al.*, Proceedings of PAC 2007, THPMN017.
- [8] W. R. Nelson, H. Hirayama, D. W. O. Rogers, SLAC-R-0265.
- [9] Y. Namito, S. Ban, H. Hirayama, Nucl. Instrum. Meth. A **332** (1993) 277.
- [10] J. C. Liu, T. Kotseroglou, W. R. Nelson, D. C. Schultz, SLAC-PUB-8477.
- [11] K. Flöttmann, PhD thesis, DESY Hamburg (1993); DESY-93-161.
- [12] W. H. McMaster, Rev. Mod. Phys. **33** (1961) 8; and references therein.
- [13] R. Brun *et al.*, CERN-DD/85/1.
- [14] J. Hoogduin, PhD thesis, Rijksuniversiteit Groningen (1997).
- [15] W. Kilian, LC-TOOL-2001-039; T. Ohl *et al.*, LC-TOOL-2001-040-rev.
- [16] K. Laihem, PhD thesis, Humboldt University Berlin, Germany, (2007).
- [17] GEANT4 physics reference manual, Part III, Electromagnetic Interactions, <http://geant4.web.cern.ch/geant4/UserDocumentation/UsersGuides/PhysicsReferenceManual/html/index.html>
- [18] P. Starovoitov *et al.*, in preparation.
- [19] ILC Reference Design Report, August 2007.

ILC Positron Production Target Simulation

V.Gharibyan

DESY - MDI
Hamburg - Germany

A photon-positron conversion target of the undulator or laser based polarized positron source is optimized using a modified GEANT-3 program adapted to count the spin transfer. High intensity positron beam with around 0.75 polarisation could be achieved choosing tungsten conversion target of 0.3 and 0.7 radiation lengths for the undulator and laser case respectively.

1 Positron Sources

Currently two scenarios are considered to generate polarized positrons for the ILC. Both are utilizing low energy circularly polarized photons and high energy electrons to boost these photons to MeV energies and then convert them into electron-positron pairs. Each method named after the photon source as undulator [1] or laser [2] based positron production. In

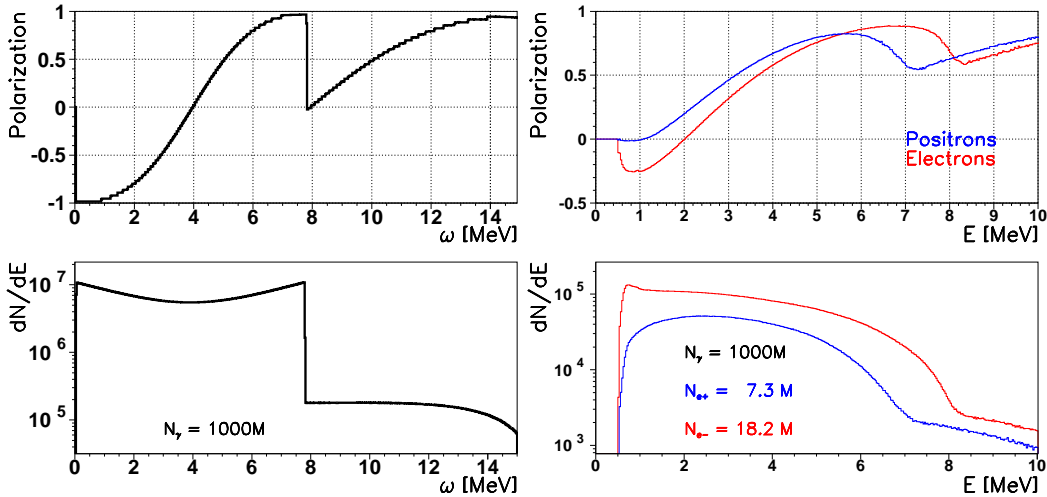


Figure 1: Polarisation distribution and spectrum of undulator photons (left) and positrons/electrons behind $0.2X_0$ tungsten (right).

this study [3] we will vary thickness and material of the production target to optimize the positron yield and polarisation.

2 Simulation Tools and Considered Polarized Processes

To achieve high number of positrons the target should be thick, of the order of one radiation length, $1X_0$ hence, the MeV photons may initiate showers, or at least 2-3 generations of particles and we would need a proper tracking tool like EGS or GEANT.

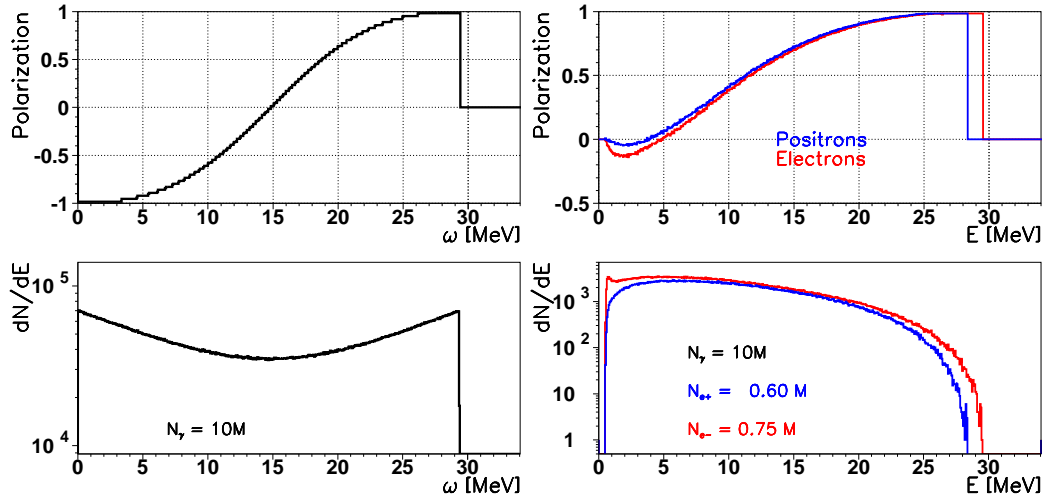


Figure 2: The same as in Figure 1 for a laser scattering Compton photons and $0.6X_0$ tungsten target

To address the polarisation issue one have to take care also about the polarisation tracking. This has been incorporated into the EGS by K. Flöttmann [4] and into the GEANT-4 by DESY-Zeuthen E166 group [5]. Here we will use GEANT-3 [6] modified in a way to account polarisation transfer in the processes summarized in table 1. For the multiple scattering and dE/dX energy loss continuous approximations there are certain difficulties to treat the depolarisation especially for energies below the critical E_C and this is mostly because lack of the theoretical and experimental input. Anyhow, for our calculations we use straight trajectory/no depolarisation for the dE/dX loss and $(q + \cos \theta)/(1 + q \cos \theta)$ approximation as depolarisation factor for a θ multiple scattering angle with $q = (\gamma^2 - 1)/(\gamma^2 + 1)$ where γ is the Lorentz factor.

3 Results

One example of the simulation outcome for a $0.2X_0$ tungsten is shown on Figure 1 where initial photons originate from a helical 1m long undulator with $k=0.19$ on a 46.6 GeV energy electron beam (E166 experiment configuration). On the lower right figure one can find also total number of the positrons/electrons for the 10^9 simulated initial photons. Figure 2 displays results for the initial Compton photons produced by a 532 nm laser, scattered on 1.3 GeV electrons with a crossing angle of 8 deg. Number of simulated Compton

Process	Particles
Pair creation	$\vec{\gamma} \rightarrow e^+ e^-$
Compton scattering	$\vec{\gamma} + e^- \rightarrow \vec{\gamma} e^-$
Photoeffect	$\vec{\gamma} + e^- \rightarrow e^-$
Annihilation	$e^+ + e^- \rightarrow \vec{\gamma}$
Bremsstrahlung	$e^- + N \rightarrow e^- + N + \vec{\gamma}$
Multiple Scattering	$e^- + N \rightarrow e^- + N$
Energy loss dE/dX	$e^- + Ne \rightarrow e^- + Ne^*$

Table 1: Modified GEANT-3 processes with polarisation transfer. Vector sign indicates polarized particle

events is 10^7 . Using positrons intensity dN/dE and polarisation P distributions we can form a product $P^2 dN/dE$ (Figure 3) to serve as a figure of merit for the target material and thickness optimization.

4 Optimal Target

To choose best production target we try tungsten and titanium changing their thickness by $0.04X_0$ steps, each time recording the positrons yield, polarisation and energy at the maximum figure of merit. Resulting numbers are displayed on Figure 4 and Figure 5 for the undulator and laser case respectively.

One can note that in general the positron polarisation depends weakly on the target thickness i.e. the target optimization could be done by maximizing only the positron yield. The distributions also indicate that the tungsten is preferable with a thickness of $0.3X_0$ for the undulator and $0.7X_0$ for the laser case.

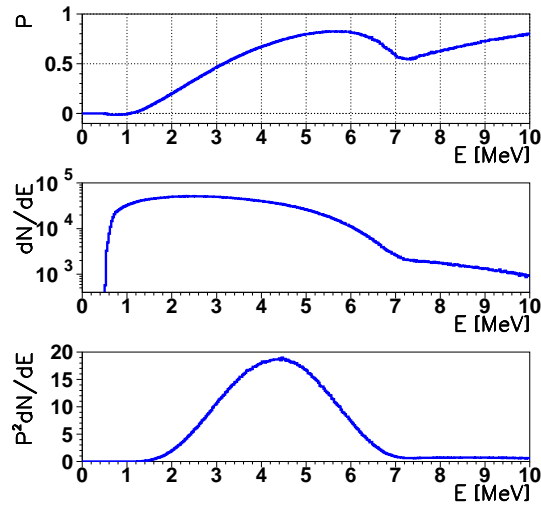


Figure 3: Figure of merit derived for the $0.2X_0$ W case. (Figure 1).

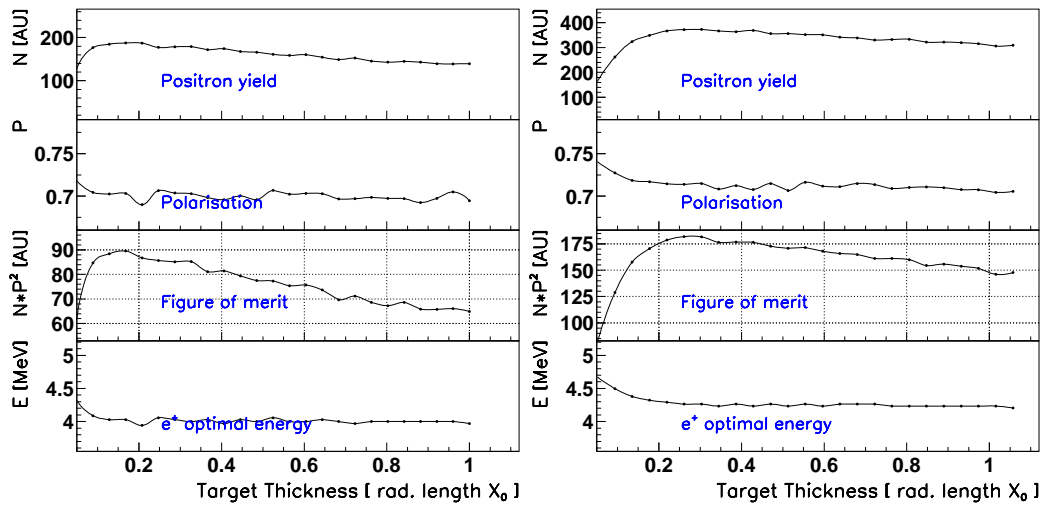


Figure 4: Undulator produced positrons intensity, polarisation, figure of merit and energy versus titanium (left) and tungsten (right) target thickness.

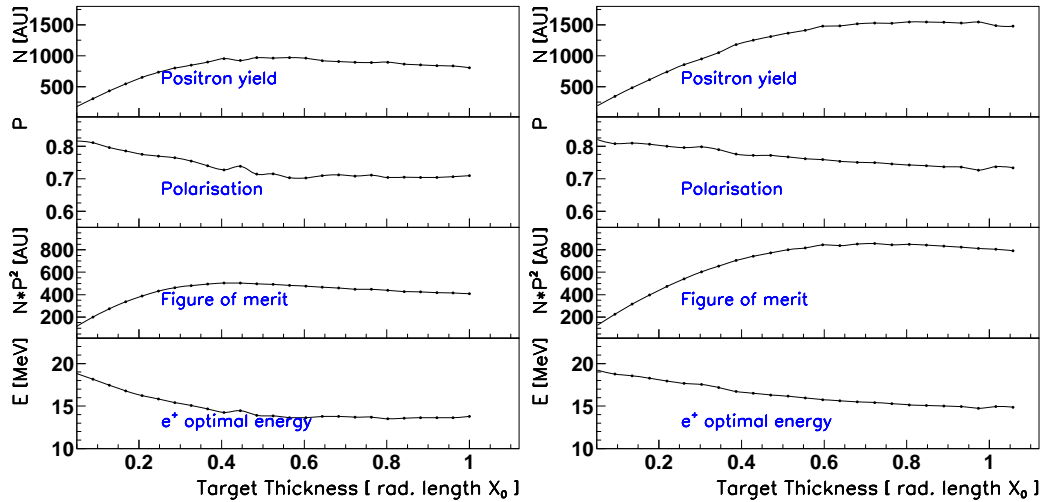


Figure 5: The same as in Figure 4 for the laser produced positrons.

5 Summary

In addition to the existing MC programs GEANT-3 is modified to count the polarisation. For energies lower than the critical, calculation errors could be large, special attention deserve multiple scattering and continuous energy loss.

For the target choice polarized calculations could almost be escaped, its sufficient to maximize the positron yield.

References

- [1] G. Alexander et al., "Undulator-based production of polarized positrons: A proposal for the 50-GeV beam in the FFTB", SLAC-TN-04-018.
- [2] K. Sakaue *et al.*, "Polarized positron generation based on laser Compton scheme and its polarization measurements," *Int. J. Mod. Phys. B* **21** (2007) 519.
- [3] Slides:
<http://desy.de/~vaagn/psource/LCWS-2007-gharibyan.pdf>
- [4] K. Flöttmann, "Investigations Toward the Development of Polarized and Unpolarized High Intensity Positron Sources for Linear Colliders", Ph.D. Thesis, DESY 93-161.
- [5] GEANT4 physics reference manual, Chapter Polarized Electron/Positron/Gamma Incident.
- [6] *GEANT - Detector Description and Simulation Tool* CERN Program Library Long Writeup W5013;

Low Energy Positron Polarimetry for the ILC

R. Dollan^{1*}, G. Alexander², T. Lohse¹, S. Riemann³, A. Schällicke³,
P. Schüler⁴, P. Starovoitov⁵, A. Ushakov^{3*}

1- Humboldt Universität zu Berlin - Institut für Physik

Newtonstr. 15, 12489 Berlin - Germany

2- Physics Department, Tel Aviv University,

Tel Aviv 69978 - Israel

3- DESY in Zeuthen

Platanenallee 6, 15738 Zeuthen - Germany

4- DESY in Hamburg

Notkestr. 85, 22603 Hamburg - Germany

5- National Center for Particle and High Energy Physics,

Bogdanovitch street 153, 220040 Minsk - Belarus

For the International Linear Collider (ILC) a polarized positron source based on a helical undulator is proposed. In order to control and optimize the degree of positron polarization a low energy polarimeter at the source is required. Methods to measure the positron polarization near the creation point are currently under study and will be discussed in this contribution.

Introduction

The physics potential of the ILC will be substantially broadened if both beams - the electron and the positron beam - are polarized [2]. But in comparison to polarized electrons the generation of polarized positrons is a challenge. Polarized electron sources based on photo emission from GaAs induced by circularly polarized laser photons are operating and deliver electron polarization $P_{e^-} > 80\%$ [3]. Regarding polarization, the SLC polarized electron source [4], for example, already meets the ILC requirements. For the production of polarized positrons a helical undulator based system is foreseen for the ILC [5–7]. Circularly polarized photons are created by an electron beam traversing a helical undulator. The photons hit a thin target producing electron-positron pairs and the circular polarization of the photons is transferred into longitudinal polarization of the created e^+e^- pairs. After being captured, pre-accelerated and separated from the electrons and the initial photon beam the positrons are transported to the damping ring and finally to the interaction region while the beam polarization has to be maintained.

At the interaction region the beam polarization will be measured with high accuracy ($\approx 0.25\%$) [8, 9]. However, for the optimization of the positron beam polarization as well as for the control of polarization transport also the degree of polarization near the positron source should be known at least with an accuracy of a few percent. Although an absolute polarization measurement is preferred, a low energy polarimeter should at least measure the relative beam polarization. It should be easy to handle, robust and fast.

*Supported by the European Commission under the Sixth Framework Program (FP6) “Structuring the European Research Area”, contract number RIDS-011899.

Table 1 shows the beam parameters at the positron source. Several methods to measure the polarization of such beam have been considered. To evaluate the feasibility and the performance of the respective methods simulation studies have been performed using GEANT4 with polarization extension [10, 11]. This extension was developed to describe the interaction of polarized beams with polarized matter.

Parameter	value
e^+ /bunch, N_{e^+}	$2 \cdot 10^{10}$
bunches/pulse, N_b	2620
Rep. Rate, f_{rep}	5 Hz
Energy, E	30 - 5000 MeV
Energy spread, $\Delta E/E$	10 %
Normalized emittance, ϵ^*	~ 3.6 cm
Beam size, $\sigma_{x,y}$	~ 1 cm

Table 1: Beam parameters at the positron source based on the RDR design values [5].

Polarimeter options

Most polarization measurements are based on the same principle: the polarized beam to be measured hits a polarized target (beam or fixed target). The scattering process is spin dependent hence the counting rates or the distribution of the scattered particles differ for different spin orientation of the beam particles and an asymmetry can be measured. This asymmetry depends also on the target polarization, thus, knowing the latter the beam polarization can be determined.

Laser Compton Polarimeter

A laser Compton polarimeter will be used to measure the polarization at the interaction region of the ILC [5]. The photons of a high intensity laser hit the low emittance positron or electron beam and are backscattered. The distribution of the scattered photons depends on the initial polarization of the positron or electron beam as well as on the laser polarization. Polarimeters of this type provide very high precision and were used, e.g. at SLC [12] and at HERA [13]. However, this method is not applicable for the low energy positrons at the source. The size of the positron beam before the damping ring will be too large to achieve reasonable interaction rates (see also Table 1). Also the asymmetry in the angular distribution of the scattered photons is very small for energies of a few GeV or below. Recent studies showed, that Compton polarimetry is possible after the damping ring at an energy of 5 GeV [14].

Bhabha Polarimeter

The cross section of Bhabha scattering (Eq. 1) depends on the polarizations, P_{e^+} , P_{e^-} , of the initial state particles;

$$\frac{d\sigma}{d\Omega} \sim \frac{(1 + \cos\vartheta)^2}{16\gamma^2 \sin^4\vartheta} \{ (9 + 6\cos^2\vartheta + \cos^4\vartheta) - P_{e^+}P_{e^-} (7 - 6\cos^2\vartheta - \cos^4\vartheta) \}. \quad (1)$$

If the incoming particles are longitudinally polarized, the maximal achievable asymmetry is $7/9 P_{e^+}P_{e^-}$ at a scattering angle $\vartheta = \pi/2$ (CMS) (see Fig. 1). This method has been used to measure the polarization of electrons with Møller polarimeters, for example at SLAC and at the VEPP-3 storage ring [15–18]. Corresponding to the design of the ILC [5] a Bhabha polarimeter could be applied after the positron pre-acceleration where the positron energy is in the range between 125 MeV and 400 MeV [19–22].

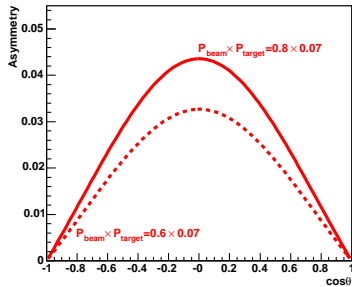


Figure 1: Two examples for the angular dependence of the Bhabha asymmetry (CMS, $P_{\text{beam}} = P_{e^+}$, $P_{\text{target}} = P_{e^-}$).

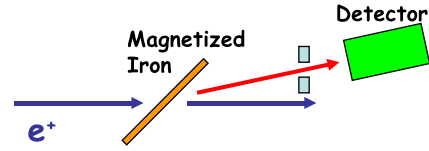
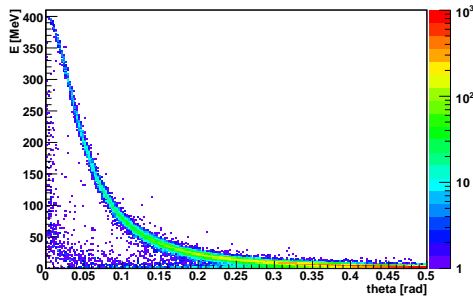
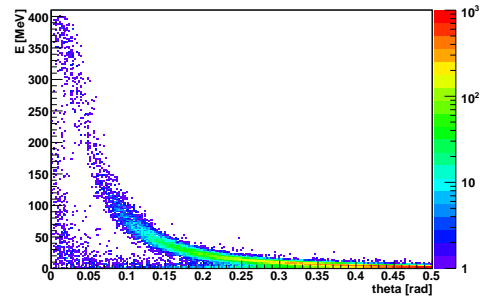


Figure 2: Sketch of a Bhabha polarimeter. Behind the target an appropriate mask system selects the angular range of interest.

Figure 2 shows the principle of a Bhabha polarimeter. The positron beam hits a thin magnetized iron foil. By reversing the target magnetization an asymmetry in the distribution of the scattered particles can be measured. Selecting only the scattered electrons, the background to the Bhabha process, which is dominated by Bremsstrahlung, can be significantly suppressed. First simulation studies have been done for energies of 200 MeV and 400 MeV.



(a) Target polarization $P_{e^-} = -100\%$.



(b) Target polarization $P_{e^-} = +100\%$.

Figure 3: The distribution of the Bhabha scattered electrons in bins of the energy E and the scattering angle ϑ (E_{beam} : 400 MeV, ΔE_{beam} : 10%, target: 30 μm Fe).

Figure 3, for example, shows the distribution of the scattered electrons depending on their energy and the scattering angle for opposite target polarizations in the case of 400 MeV beam energy. The asymmetry of these two distributions is shown in Figure 4. It is obvious, that, in addition to the selection of the angular range of interest by an appropriate shielding system, an energy spectrometer is needed. With optimal energy selection and angular cuts the average analyzing power is A_{e^-} ($P_{e^+} = 100\%$, $P_{e^-} = 100\%$) ≈ 40 -50% as the simulations show.

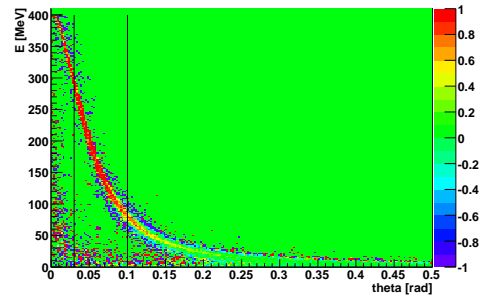


Figure 4: Asymmetry of the $E - \vartheta$ distribution of the Bhabha electrons. The vertical lines indicate the angular range of highest asymmetry.

To minimise the influence of multiple scattering in the target, the target foil should be as thin as possible. Estimations have shown that for the large beam size and the target thickness of about $30\ \mu\text{m}$ the beam divergence is increased by less than 10% for energies between 200 MeV and 400 MeV. So the low energy Bhabha polarimetry at the ILC positron source can be considered as almost non-destructive. A problematic issue is the heating of the target material. The temperature rise leads to a decrease in the magnetization of the target and thus to a reduction of the electron polarization. In an iron foil of $30\ \mu\text{m}$ thickness hit by a 250 MeV beam with the parameters as shown in Table 1 a heat-up of approximately 10 K per bunch is obtained. Assuming cooling by radiation the target temperature reaches an equilibrium at $T_{eq} \approx 500\ \text{K}$ resulting in a reduction of the electron polarization to approximately 93%. In addition, the distortion of the foil due to heating will have an influence on the accuracy of the measured asymmetry. To guarantee reliable measurements of the asymmetry the working temperature of the target has to be stable within relativ narrow limits.

Compton Transmission Polarimeter

An alternative method to measure the positron polarization is Compton transmission polarimetry. This method is based on the spin dependence of Compton scattering. The method is well known and has been used successfully at experiments at SLAC(E166) and KEK [6, 7, 23]. A fraction

of the positron beam is sent onto a thick target (1 to 3 radiation lengths) of high Z-material and is converted via Bremsstrahlung into polarized photons. The photons traverse a magnetized iron block and undergo Compton scattering with the shell electrons of the iron atoms. Behind the iron the survival rate of the photons is measured (Figure 5). The transmission probability $T^\pm(L)$ for photons through the iron block of length L depends on the polarization state of the photons P_γ and the shell electrons $P_{e^-}^{Fe}$ in the iron:

$$T^\pm(L) = e^{-nL\sigma_0} e^{\pm nLP_{e^-}^{Fe}P_\gamma\sigma_p} \quad , \quad (2)$$

n is the number density of atoms in the iron and σ_0 and σ_p are the unpolarized and the polarized Compton cross sections, respectively. The magnetization of the iron block and thus the electron polarization $P_{e^-}^{Fe}$ is reversed and the positron polarization can be determined from the resulting asymmetry in transmission.

The working point of a Compton transmission polarimeter is at energies well below 100 MeV, hence the ideal position at the ILC would be located after the capture section at energies of about 30 MeV. At energies higher then a few tens of MeV the pair-production cross section becomes more and more dominant over the Compton cross section and the method becomes inefficient. The advantages of a polarimeter of this type are the compact dimensions ($O(\sim 1\ \text{m})$) and the simple and robust setup. Disadvantages are the high energy deposition ($O(\sim \text{kW})$) in the target hence only a fraction of the positron beam can be used for measurements. Finally, the asymmetries are very small ($A \lesssim 1\%$).

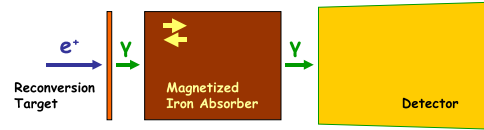


Figure 5: The principle of a Compton transmission polarimeter

Simulation studies using the polarization extensions of GEANT4 [11] were performed to test the performance of a Compton transmission polarimeter at the ILC. The parameters and results of these simulations are shown in Table 2. The optimization of target and absorber regarding e.g. heating of the material, beam fraction to use for polarimetry etc. are subject of an ongoing study.

Simulation parameters:		
beam energy E_{beam}		30 MeV
target material		tungsten
target thickness		$2X_0$
Fe absorber thickness		15 cm
electron polarization P_{e^-}		7.92 %
Simulation results:		
positron polarization P_{e^+}	asymmetry A	
30 %		$\approx 0.4 \%$
60 %		$\approx 0.8 \%$

Table 2: Results of a GEANT4 simulation for a Compton transmission polarimeter

Other options

Mott Polarimeter

Mott polarimeters measure transverse beam polarisation and are based on the electron scattering in the Coulomb field of heavy nuclei. Polarimeters of this type are widely used at operating energies of 10 eV to 1 MeV [24]. At higher energies (above ~ 10 MeV) the Mott scattering probability becomes very small and is dominated by Bhabha scattering and Bremsstrahlung. Furthermore, spin rotators would be needed to measure the longitudinal beam polarisation. Both facts make the Mott polarimetry not suitable for the ILC positron source.

Synchrotron radiation

The spin dependence of synchrotron radiation can be used to measure the transverse polarisation of positrons or electrons. This has been demonstrated at the VEPP-4 storage ring using a magnetic “snake” [25, 26]. At the ILC the method could be applied in the damping ring, where the positron energy is higher (5 GeV) and the beam polarization has to be transverse anyway. However, the effect is very small ($\sim 10^{-4}$ - 10^{-3} at $E_{beam} \sim 10$ - 100 GeV [26]). In addition, the short storage period of the positrons in the damping ring (O(ms)) will make it difficult to reduce the systematic uncertainties sufficiently to observe this effect at all.

Summary

Options for a design of a **Low Energy Positron Polarimeter** (LEPOL), to be placed at the ILC positron source have been described and discussed. The high intensity of the positron beam as well as its large spatial extension limit the number of polarimeter options. A Bhabha polarimeter, measuring the asymmetry in the distribution of the scattered electrons, is a promising candidate for a positron polarimeter at the ILC source. A detailed design study for a LEPOL is in progress.

References

- [1] The slides: <http://ilcagenda.linearcollider.org/contributionDisplay.py?contribId=256&confId=1296>.
- [2] G. Moortgat-Pick et al. arXiv:hep-ph/0507011, 2005.
- [3] T. Nakanishi et al. *Physics Letters A*, 158:345, 1991.
- [4] R. Alley et al. *Nucl. Instrum. Meth.*, A365:1–27, 1995.
- [5] ILC Reference Design Report. <http://www.linearcollider.org/cms/?pid=1000437>.

- [6] A. Mikhailichenko et al. *AIP Conf. Proc.*, 915:1095–1100, 2007.
- [7] G. Alexander et al. SLAC-TN-04-018, 2004.
- [8] N. Meyners et al. In the Proceedings of 2005 International Linear Collider Workshop (LCWS 2005), Stanford, California, 18-22 Mar 2005.
- [9] K. Moffeit et al. In the Proceedings of 2005 International Linear Collider Workshop (LCWS 2005), Stanford, California, 18-22 Mar 2005.
- [10] R. Dollan et al. *Nucl. Instrum. Meth.*, A559:185–189, 2006.
- [11] A. Schälicke et al. this proceeding.
- [12] Woods M. et al. arXiv:hep-ex/9611005, 1996.
- [13] M. Beckmann et al. *Nucl. Instrum. Meth.*, A479:334–348, 2002.
- [14] G. Alexander and P. Starovoitov. in preparation.
- [15] H. R. Band et al. *Nucl. Instrum. Meth.*, A400:24–33, 1997.
- [16] P. Steiner et al. *Nucl. Instrum. Meth.*, A419:105–120, 1998.
- [17] P. S. Cooper et al. *Phys. Rev. Lett.*, 34(25):1589–1592, 1975.
- [18] G. Alexander and I. Cohen. *Nucl. Instrum. Meth.*, A486:552–567, 2002.
- [19] G. Alexander et al. *Nonlin. Phenom. Complex Syst.*, 8:180–185, 2005.
- [20] G. Alexander and E. Reinherz-Aronis. arXiv:hep-ex/0505001, 2005.
- [21] A. Schälicke et al. Proceedings to the International Conference on Linear Colliders (LCWS 06), IISc, Bangalore, 2006, to appear in Pramana journal of physics.
- [22] A. Schälicke et al. Prepared for European Particle Accelerator Conference (EPAC 06), Edinburgh, Scotland, 26-30 Jun 2006, EUROTeV-Report-2006-078.
- [23] T. Omori et al. *Phys. Rev. Lett.*, 96(11):114801, 2006.
- [24] T.J. Gay and F.B. Dunning. *Rev. Sci. Instrum.*, 63:1635, 1992.
- [25] S. A. Belomestnykh et al. *Nucl. Instrum. Meth.*, A227:173–181, 1984.
- [26] A. E. Bondar and E. L. Saldin. *Nucl. Instrum. Meth.*, 195:577–580, 1982.

ATF2 Project Meeting

Convener: E. Elsen

ATF2 project: Final doublet support studies at LAPP

B. Bolzon¹, A. Jeremie¹, N. Geffroy¹, T.Tauchi²

1- LAPP-IN2P3-CNRS-Université de Savoie
BP110, F-74941 Annecy-le-Vieux Cedex, FRANCE

Phone: +33450091600, Fax: +33450279495, contact person : E-mail: bolzon@lapp.in2p3.fr

2- KEK-High Energy Accelerator Research Organization
1-1 Oho, 305-0801, Tsukuba, Ibaraki, JAPAN
Phone: 0081-29-864-5374

We investigated a support for the final doublets for ATF2. Its relative motion to the floor has to be below 6nm. Consequently, this support has to be very stiff and well fixed to the floor. We studied a steel lightweight honeycomb table whose first eigenfrequency in free configuration is at 230Hz. Some simple simulations and measurements to study the table resonant frequency evolutions for different boundary conditions were done.

1 Introduction

At ATF2, relative motion between the Shintake monitor (measuring the beam size) and the final doublets has to be below 6nm above 0.1Hz because beam-based feedback is efficient only below 0.1Hz due to the beam repetition rate of 1Hz [2]. Ground motion coherence is good up to a distance of 4-5 meters for frequencies below 10Hz [3] and so is the relative ground motion. The Shintake monitor and the final doublets being separated by 4 meters, they will be fixed on rigid mounts to move like ground motion. We are investigating a support for the final doublets for a relative motion to the floor below 6nm. We chose a steel lightweight honeycomb table manufactured by TMC [1]. This table has already been investigated for stabilization in the final focus system of the Compact Linear Collider (CLIC) at CERN [4].

2 Table eigenfrequencies

TMC Company has measured characteristics of the first resonant frequency of the table in free configuration [1]. The Guaranteed Minimum Resonant Frequency is at 230Hz with a Guaranteed Maximum factor Q of amplification at resonant frequency of 1.5. A quick and easy test has been done by putting the table on four rigid supports at the corners in order to measure its first eigenfrequency with lead masses of 1400Kg (weight of final doublets) and without. The experimental set-up is shown in figure 1. Guralp CMG-40T velocity sensors and ENDEVCO sensors [5] were used to measure vibrations from 0.1Hz to 40Hz and from



Figure 1: Experimental set-up

First resonant frequency	Measured	Simulated
Free configuration	230Hz	230Hz
Table on supports/no weight	74Hz	56Hz
Table on supports/1400kg	46Hz	26Hz

Table 1: Evolution of resonant frequencies

40Hz to 100Hz respectively. The measurements on the table were done on the middle where vibrations are the strongest. In order to identify eigenfrequencies of the table, its transfer function has been calculated with and without any masses on it. Figure 2 shows magnitudes of table transfer functions. Without any masses on it, the table amplifies mainly floor motion between 60Hz to 100Hz with a maximum amplification factor of 12 at 74Hz. With the lead masses on it, this important amplification goes to lower frequencies, between 30Hz and 70Hz, with a maximum amplification factor of 9 at 46Hz. These two main ground motion amplifications seem to be eigenfrequencies of the table. It has been checked by studying table transfer function phases that they have both a phase of 90 degrees with respect to ground motion which is typical of a resonant frequency. Consequently, putting the table on four supports at its corners decreases its performances: its first eigenfrequency goes from 230Hz in free configuration to 74Hz. Moreover, the weight of the final doublets makes it fall to 46Hz.

Table 1 shows a comparison between simulations and measurements on the evolution of the first table resonant frequency. The first eigenfrequency of the simulated table has been fixed at 230Hz in free configuration which is used as a reference. One can see that simulation results are representative of resonant frequency evolution with weight and boundary conditions. Another simulation of the table fixed directly to the floor on one entire face has been done. The first eigenfrequency is at 526Hz which is much higher than in free configuration (230Hz). When adding some masses of 1400Kg on the table, the first resonant frequency falls to 135Hz. Consequently, these boundary conditions increase table performances. This should be the preferred method of supporting the ATF2 final doublet.

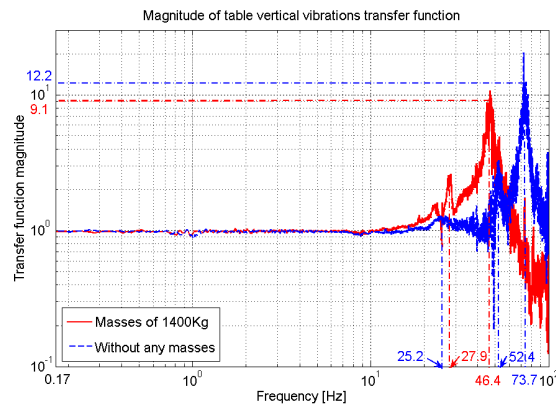


Figure 2: Table transfer function magnitudes

3 Relative motion between table and floor at ATF Ring

In order to have a value of relative motion between table and floor, the integrated Root Mean Square of relative motion has been calculated using ATF floor measurements.

Results are shown in figure 3 with and without masses of 1400kg. In the bandwidth where there are no resonant frequencies, relative motions between table and floor are probably due to supports : loss of coherence is probably due to non-linearities in vibration transmissibility between floor and table. Consequently, these results can be improved. The most important result is the integrated relative motion Root Mean Square which is only due to the amplification at the first eigenfrequency and to the damping above. In fact, it cannot be improved when keeping the same boundary conditions. With no weight on the table, the first eigenfrequency (not including the small peaks at lower frequency; see figure 2) is high enough (74Hz) to induce an integrated relative motion of only 0.9nm from 60Hz to 100Hz because of the amplification. But when putting some weight on the table, the first resonant frequency falls to 46Hz and induces an integrated relative motion of 4.6nm from 30Hz to 100Hz because of the amplification and damping above it.

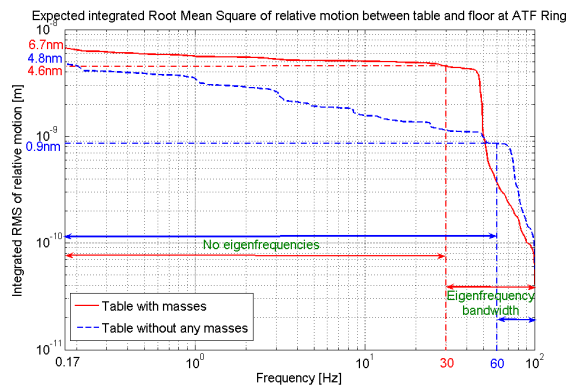


Figure 3: Expected integrated RMS of relative motion between table and floor at ATF

4 Conclusion

At ATF2, we plan on fixing the Final Doublet support on the entire bottom face of the table with some special concrete. This should push up the resonant frequency based on the simulation shown in this paper, and should be within ATF2 specifications. However, tests with the magnet (instead of lead bricks) are still to be done.

5 Acknowledgments

This work is supported by the French ANR and the France-Japan program FJPPL. We also thank the CERN team for allowing us to use their TMC active table.

6 Bibliography

References

- [1] "Technical Background" from TMC:
<http://www.quantumtech.com.br/teckbkgd.pdf>
- [2] H.Braun *et al.*, "ATF2 Proposal: V.1", CERN-AB-2005-035, KEK-REPORT-2005-2
- [3] Slides: T.Tauchi
<http://ilcagenda.linearcollider.org/getFile.py/access?resId=0&materialId=slides&confId=1453>
- [4] S.Redaeli *et al.*, "CLIC magnet stabilization studies", Proceedings of LINAC2004 TUP88, August 2004, pp.483-485.
- [5] Guralp CMG-40T and Endevco Model 86 accelerometer
http://www.geosig.com/downloads/leaflets/L_CMG-40T.pdf
<http://www.bksv.com/pdf/86.pdf>

Study of time-dependent corrections in the ATF2 beam-line

Philip Bambade, Yves Renier *

LAL, Univ Paris-Sud, IN2P3/CNRS, Orsay, France

Goals of ATF2 will be to provide beams with a few tens of nanometers and stability at the nanometer level. To achieve this, ground motion should be measured and the effects of element displacement on the beam at the Interaction Point (IP) should be well understood. Feedback systems should also be simulated with a ground motion generator which includes spatial coherence for effects to be computed realistically.

1 Introduction

The goal is to understand and simulate the effects of ground motion on the ATF2 beam, in order to design and implement suitable feedback. Effects from displacing each magnet on the beam position and size at the IP are first computed and interpreted. Feedback requirements are then analysed given measured ground motion properties and results from simulating an initial version are shown. Finally, some conclusions and prospects are given.

2 Effects of magnet displacements on the beam at the IP

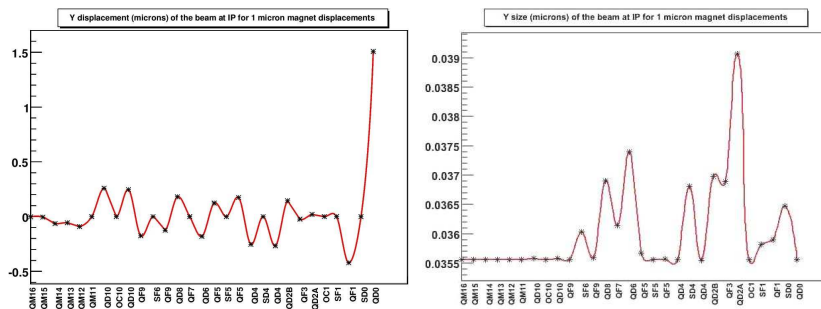


Figure 1: Displacement and size at IP for magnet displacements of 1 micron

Displacing a dipole magnet with constant field has no effect. For a quadrupole, it will however cause deflection since a dipole term appears from the linear field. Similarly, a displaced sextupole changes both the focusing and (slightly) the steering, through quadrupole and dipole terms. The beam offset and size changes at the IP depend both on the displaced magnet strengths and on the optical transport to the IP.

The result of displacing each ATF2 magnet on IP beam position and size is shown in Figure 1. The tightest tolerance for the beam position is for QD0 which is the strongest quadrupole. Displacing another quadrupole, QD2A causes the largest size increase due to the long drift to the next magnet group, which includes two strong sextupoles then traversed off-axis.

*Work supported in part by the EC under the FP6 "Research Infrastructure Action - Structuring the European Research Area" EUROTeV DS Project Contract no.011899 RIDS.

3 Effect of ground motion on the beam at the IP

3.1 Measurement of ground motion at the ATF site

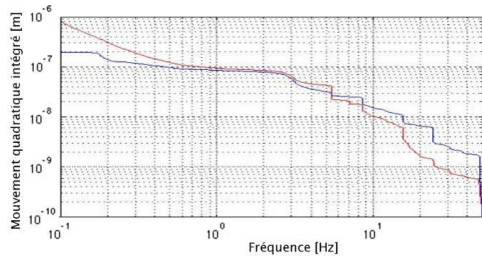


Figure 2: Integrated RMS displacement

Figure 2 shows the integrated RMS vertical displacement measured at KEK (courtesy of R. Sugahara), computed integrating from 50 Hz to each frequency on the abscissa.

For a 1 Hz bunch repetition rate, feedback can only be expected to work up to $\frac{1}{6}$ Hz. At that frequency, the ground motion amplitude is about 0.2 micron. For such amplitudes, the beam position and size at the IP would be affected at the level of 0.2 micron and 10%, respectively, given the sensitivities to QD0 and QD2A displacements in Figure 1. This would be even for perfect

feedback and would definitely not allow reaching ATF2 objectives. Fortunately, as QD0 is just about 1 m from the IP, there is very good coherence up to a few Hz. If mechanical structures supporting this magnet and the IP instrumentation are rigidly mounted to the floor, both will vibrate in phase and relative motion should be small and produce negligible effects at the IP.

However for about 10 other quadrupoles farther from the IP, 0.2 micron motions can still cause about 0.04 micron beam displacements. The global effect expected at the IP for fully incoherent motions of these other magnets is about $\sqrt{10} \times 0.04 = 0.125$ micron. Even with perfect feedback, for a repetition rate of 1 Hz, achieving stability at the level of the beam size must thus rely on some degree of coherence beyond just a few meters.

3.2 Simulation of the effects on the beam

The simulation process starts with a ground motion simulator, developed in MATLAB to recreate the Fourier spectra of the measured vibration and some of its coherence properties [2]. Data files are created as input to PLACET, a code which tracks particle distributions along the ATF2 beam line including magnet misalignments. Analysis is done in ROOT. Figure 3 (right) shows the vertical size and displacement obtained at the IP in the first 100 seconds. The size enhancement is small in this short time span ($< 10\%$), but displacements without feedback (dotted line) are 0.1 microns, which exceed the goal by an order of magnitude.

4 Feedback implementation

Position feedback according to the scheme shown in Figure 3 (left) was simulated with PLACET, with 5 nanometer errors for the BPMs used to measure the beam positions near the IP. The most efficient controller tried was the PID one, using Takahashi's method to choose the coefficients [1]. The corrector dipole is placed after the final doublet to avoid offsetting the beam in the last sextupoles.

This feedback improves the beam stability by a factor 3 and doesn't affect the beam size during the 100 seconds considered, see Figure 3 (right, plain line). Although a significant

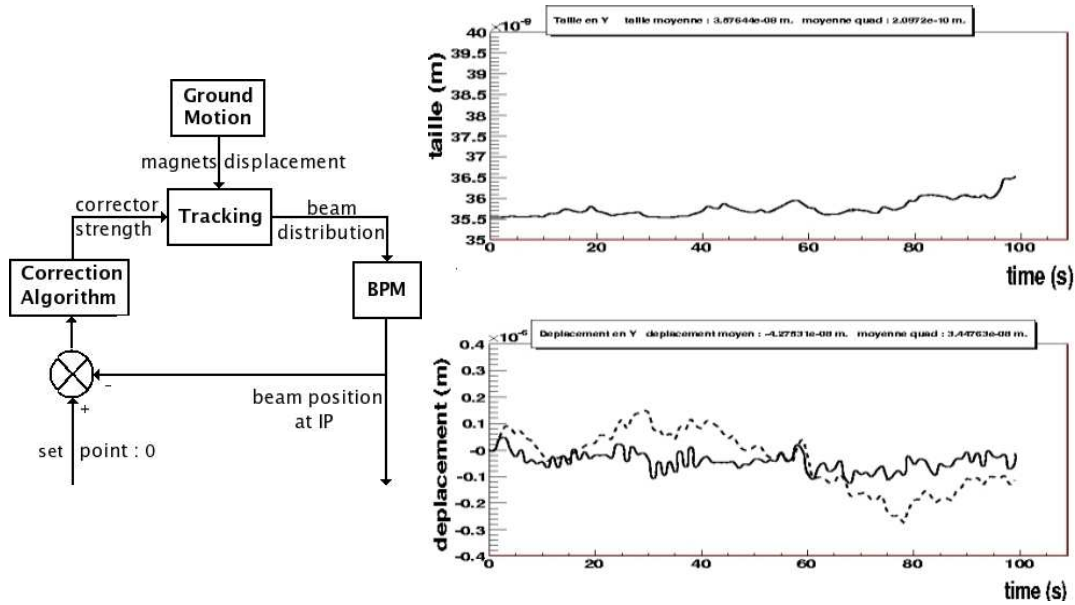


Figure 3: Left : Scheme of the feedback. Right : Size and displacement as function of time without/with feedback (dotted/plain).

improvement, the vertical position beam stability obtained is not sufficient to avoid affecting the beam size measurement. This may be explained in part by the ground motion generator used, which underestimates the coherence and is hence pessimistic [2].

5 Conclusion and prospects

The sensitivity of the ATF2 beam to ground motion has been studied. Simulating a correction feedback loop using a PID controller, improvements in stability by a factor 3 were obtained. This however remains about a factor 3 above specifications.

An improved generator representing coherence properties more reliably should be developed and other PID coefficients may need to be tried to reach the goals.

6 Acknowledgements

Thanks to Maria del Carmen Alabau Pons for her help using PLACET, to Benoît Bolzon for his help analyzing the ground motion data and to Ryuhei Sugahara for providing the ATF floor vibration measurements.

References

- [1] Slides: first presented at LCWS, second presented in a KEK weekly meeting
<http://ilcagenda.linearcollider.org/subContributionDisplay.py?subContId=1&contribId=213&confId=1296>
<http://ilcagenda.linearcollider.org/contributionDisplay.py?contribId=0&sessionId=0&confId=1740>
- [2] Y. Renier, P. Bambade and B. Bolzon, CARE/ELAN document-2007-004.

